Dissertation

Adrian Hochgesang, 2023
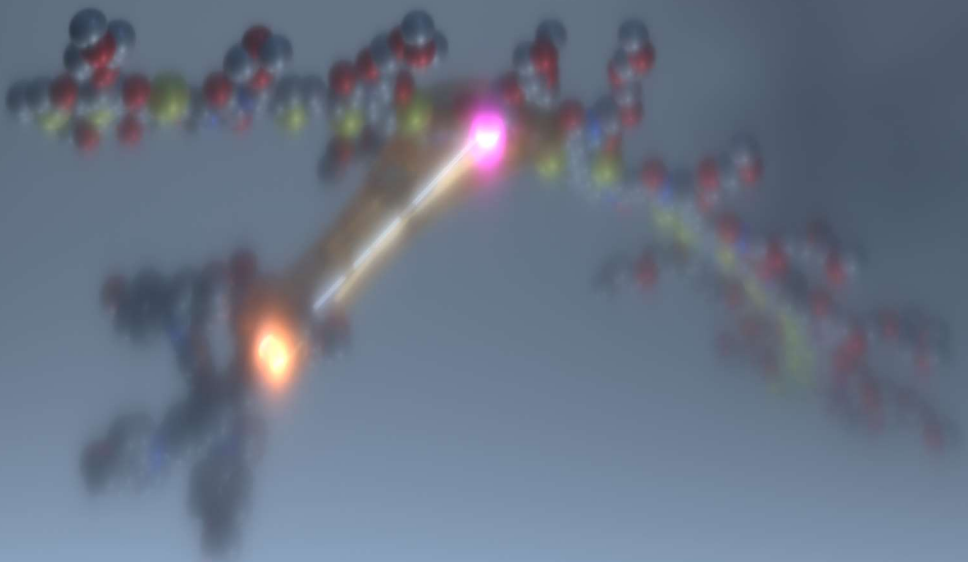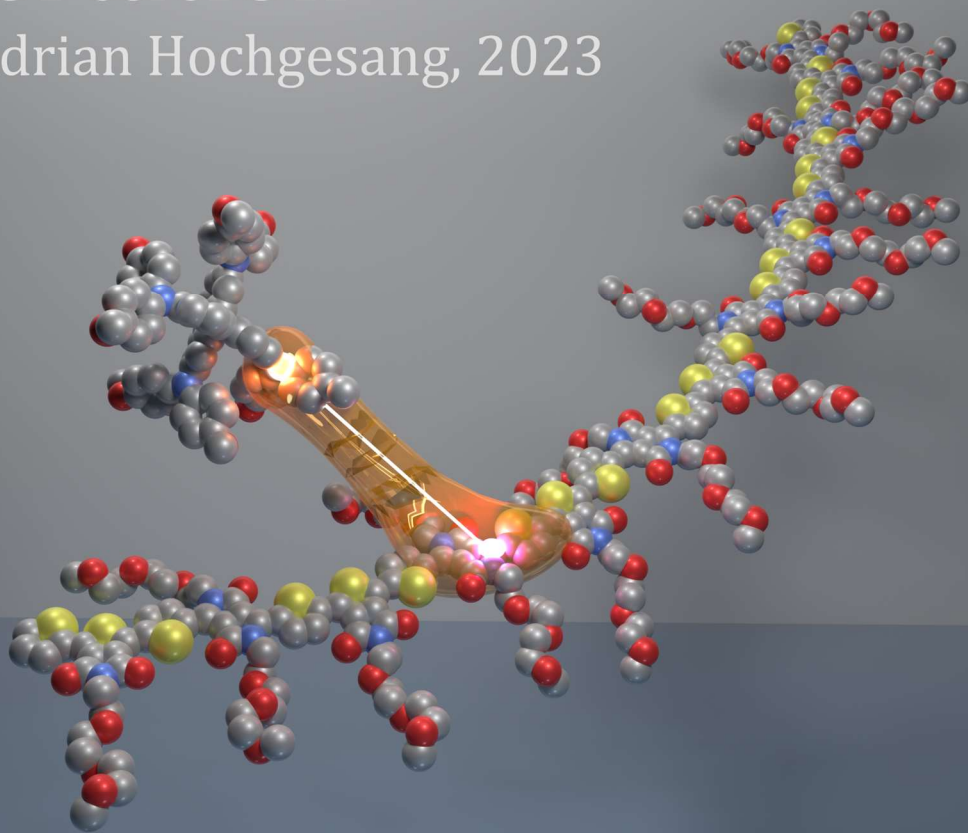
Novel doping methods and electrical characterization of doped organic semiconductors

Dissertation

zur Erlangung des akademischen Grades eines Doktors der Naturwissenschaften (Dr. rer. nat.) in der Bayreuther Graduiertenschule für Mathematik und Naturwissenschaften (BayNAT) der Universität Bayreuth

vorgelegt von

Adrian Gerhard Hochgesang

geboren in *Pegnitz*

Bayreuth, 2023

Die vorliegende Arbeit wurde in der Zeit vom Mai 2020 bis April 2023 in der Arbeitsgruppe Angewandte Funktionspolymere (AFuPo) am Lehrstuhl Makromolekulare Chemie I der Universität Bayreuth unter Betreuung von Herrn Prof. Dr. Mukundan Thelakkat angefertigt.

Vollständiger Abdruck der von der Bayreuther Graduiertenschule für Mathematik und Naturwissenschaften (BayNAT) der Universität Bayreuth genehmigten Dissertation zur Erlangung des akademischen Grades eines Doktors der Naturwissenschaften (Dr. rer. nat.).

Form der Dissertation: Kumulative Dissertation

Dissertation eingereicht am: 06.07.2023

Zulassung durch das Leitungsgremium: 18.07.2023

Wissenschaftliches Kolloquium: 16.04.2024

Amtierender Direktor der Graduiertenschule: Prof. Dr. Jürgen Köhler

Prüfungsausschuss:

Prof. Dr. Mukundan Thelakkat   (Gutachter)

Prof. Dr. Anna Köhler   (Gutachterin)

Prof. Dr. Markus Retsch   (Vorsitz)

Prof. Dr. Ralf Moos

(Weiterer Gutachter: Prof. Dr. Christian Müller)

Für meine Familie

Study hard what interests you the most in the most undisciplined, irreverent and original manner possible.

Richard Feynman

Table of Contents

Summary

Chemical doping is the key tool to transform the ever-growing chemical space of intrinsically insulating organic semiconductors into precisely tuneable, conducting materials. However, the number of available dopants is sparse and plagued by low doping efficiency, low stability and costly materials. In some cases, the doping mechanism has not been elucidated yet, excluding in-depth understanding of the system. In this thesis, novel dopants based on organic radical cations, transition metal salts and carbonates are synthesized and applied to organic semiconductors, with the aim of enhancing environmental stability of the doped state, a more efficient doping process or new doping strategies altogether. By using advanced photoelectron- and impedance spectroscopy, supplemented by spectroscopic- and electronic measurements, detailed doping mechanisms are provided to guide future research. *p*-dopants based on triphenylamine building blocks and their Janus-faced nature are the guiding concept throughout this work. Once oxidized, they form stable radical cations, serving as *p*-dopants suitable for a broad palette of organic semiconductors. Whereas in their neutral form, they are potent hole conducting materials.

First, we asked the scientific question, if the electron-deficient oxidized (doped) product of an organic semiconductor may be used as a *p*-dopant itself, showcasing the interconvertible behaviour of triphenylamine derivatives by accepting electrons into a partially filled HOMO. This HOMO-HOMO electron transfer mechanism was previously demonstrated for donor-acceptor polymers in our group. In Chapter 5, we expanded this concept by doping poly(3,4-ethylenedioxythiophene) homopolymers with Spiro-MeOTAD(TFSI)$_2$. Introducing branched alkyl side chains into the monomer prior to controlled Kumada catalyst transfer polymerization yields the readily oxidisable polymer PEDOT-C$_6$C$_8$ soluble in common organic solvents. By adding Spiro-MeOTAD(TFSI)$_2$ as a *p*-dopant, a conductivity similar to the commercially available blend PEDOT:PSS was achieved, however without requiring poly(styrene sulfonate) counter ions. The doped state was found to be resilient towards thermal stress and ambient conditions for up to 12 h with negligible loss in carrier mobility or conductivity. As a result, Spiro-MeOTAD(TFSI)$_2$ doped PEDOT-C$_6$C$_8$ can replace PEDOT:PSS in a multitude of applications, ranging from bioelectronics to flexible polymer electrodes.

Even efficient doping processes suffer from accumulation of dopant byproducts having a negative impact on charge transport. By utilizing an expanded HOMO-HOMO concept involving multielectron acceptors, we lowered the necessary amount of dopant to reach target conductivity. In this concept, we correlated the oxidation state of the dopant with the density of free carriers induced in the organic semiconductor. We provided a proof of principle by applying mono-, di- and tetracationic salts of different hole conductors as *p*-dopants for polar donor-acceptor polymers. Mott-Schottky impedance spectroscopy measurements reveal a linear relationship between dopant charge and free charge carrier density in the polymer. Besides a record doping efficiency of 24 % at 5 mol% Spiro-MeOTAD(PF_6)$_4$, no loss in carrier mobility was found due to the hole conducting properties of the neutral dopant. In addition, a synergistic effect between polymer polarity and doping efficiency was recorded. Thus, Chapter 6 successfully combines HOMO-HOMO electron transfer and multielectron acceptor in *p*-doping concept.

Our group previously introduced a novel dopant copper(II) bis(trifluoromethanesulfonyl)-imide for the pristine hole transporter Spiro-MeOTAD. In Chapter 7, the underlying mechanism is studied to understand, why copper(II) salt is highly effective in creating positive charges on Spiro-MeOTAD. *Via* co-evaporation, uniform films were prepared for UV/Vis/NIR-, ultraviolet photoelectron- and electron paramagnetic resonance spectroscopy. Initially, the formation of a coulombically bound [Spiro$^+$][Cu^I(TFSI)$_2^-$] was proven. The extraordinarily low binding energy of this salt and stability of the complex Cu^I(TFSI)$_2^-$ leads to a large fraction of free charge carriers Spiro$^+$, explaining the high efficiency of this dopant. Temperature dependent impedance measurements unravel a detrimental impact of Cu^I, trapping holes and reducing carrier mobility. This could be partially reverted by complexing Cu^I. Chapter 7 expands the present state of knowledge on organic *p*-doping mechanisms by increasing awareness of dopant byproducts and provides guidelines for designing transition metal salt dopants.

Lastly, we applied the synergy effect from Chapter 6 towards *n*-doping a polar acceptor-acceptor copolymer. We combined the strong acceptor moieties thienopyrrolodione (TPD) and diketopyrrolopyrrole (DPP) with polar ethylene glycol side chains to obtain the *n*-type polymer, poly(DPP-TPD). Caesium carbonate was chosen as the *n*-dopant, as it is less costly and can be naturally obtained compared to synthetical N-DMBI. FT-IR, X-ray and (inverse) ultraviolet photoelectron spectroscopy revealed thiophene deprotonation by the carbonate anion, leading to electron majority carriers. The high polarity helps to

accommodate CsHCO$_3$ as the byproduct without polymer morphology disruption. The resulting carbonate doped acceptor-acceptor polymer system delivers a highly competitive thermoelectric power factor of ca. 5.6·10^{-6} W m^{-1} K^{-2}. We could show, that carbonates undergo proton abstraction reaction during n-doping and are able to replace N-DMBI in a variety of applications.

In conclusion, this thesis provides detailed mechanistic insights and design strategies for p-doping as well as n-doping organic semiconductors using novel materials. It expands existing concepts towards highly efficient, universally applicable doping strategies.

Zusammenfassung

Chemisches Dotieren ist ein Schlüsselelement in der Transformation der stetig wachsenden Zahl an intrinsischen, isolierenden organischen Halbleitern hin zu individuell angepassten, leitfähigen Materialien. Die Anzahl der verfügbaren Dotierungsstoffe ist jedoch begrenzt. Zudem handelt es sich oft um teure Substanzklassen mit begrenzter Stabilität und Dotierungseffizienz. In vielen Fällen existiert kein wissenschaftlicher Konsens zum Mechanismus der Dotierungsreaktion, was das tiefgreifendes Verständnis des Systems erschwert. In dieser Arbeit werden neuartige Dotierungsmittel auf Basis von organischen Radikalkationen, Übergangsmetallsalzen und Carbonaten synthetisiert und auf organische Halbleiter angewendet. Das Forschungsziel ist die Verbesserung der Stabilität des dotierten Zustands bei Umgebungsbedingungen, eine Effizienzsteigerung des Dotierungsprozesses und die Verfolgung neuer Dotierungsstrategien. Durch den Einsatz fortschrittlicher Photoelektronen- und Impedanzspektroskopie, sowie Messungen der elektronischen und optischen Eigenschaften werden detaillierte Dotierungsmechanismen aufgeklärt, die als Basis für zukünftige Forschung dienen. Die Janusköpfigkeit der p-Dotierungsmittel basierend auf Triphenylamin-Bausteinen ist das Leitkonzept dieser Arbeit. Im oxidierten Zustand bilden sie stabile Radikalkationen, welche durch Elektronenaufnahme eine große Auswahl an organischen Halbleitern p-dotieren können. Im neutralen Zustand hingegen fungieren sie als potente Lochleiter.

In Kapitel 5 haben wir die wissenschaftliche Fragestellung erörtert, ob oxidierte, elektronenarme organische Halbleiter selbst als p-Dotierstoff verwendet werden kann. Dadurch kann das umschaltbare Verhalten von Triphenylamin-Derivaten demonstriert werden, indem Elektronen in das teilweise gefüllte HOMO aufgenommen werden. Dieser HOMO-HOMO-Elektronentransfermechanismus wurde bereits für Donor-Akzeptor-Polymere in unserer Forschungsgruppe nachgewiesen. In diesem Kapitel erweitern wir dieses Konzept durch Dotierung von Poly(3,4-ethylendioxythiophen) Homopolymeren. Die Einführung von verzweigten Alkylseitenketten in das Monomer mit anschließender kontrollierter Kumada catalyst transfer polymerization ergibt das leicht oxidierbare Polymer PEDOT-C_6C_8, welches in üblichen organischen Lösungsmitteln löslich ist. Durch die Zugabe von Spiro(TFSI)$_2$ als p-Dotierungsmittel wurde eine dem kommerziell erhältlichen Polymerblend PEDOT:PSS ähnliche Leitfähigkeit erzielt, ohne

Poly(styrolsulfonat) Gegenionen zu benötigen. Der dotierte Zustand erwies sich bis zu einer Dauer von 12 Stunden sich als stabil gegenüber thermischer Belastung und Umgebungsbedingungen, mit vernachlässigbarem Verlust der Ladungsträgerbeweglichkeit und Leitfähigkeit. Aus diesen Gründen kann mit Spiro-MeOTAD(TFSI)$_2$ dotiertes PEDOT-C$_6$C$_8$ PEDOT:PSS in einer Vielzahl von Anwendungen ersetzen, die von der Bioelektronik bis zu flexiblen Polymerelektroden reichen.

Ein bekanntes Problem selbst bei effizienten Dotierungsreaktionen ist die Störung des Ladungstransportes durch Akkumulation von End- und Nebenprodukten. Durch ein erweitertes HOMO-HOMO Konzept mit Multielektronenakzeptoren konnte ein Ansatz zur Verringerung der erforderlichen Dotierungsmenge zum Erreichen einer gewissen Leitfähigkeit erarbeitet werden. In diesem Konzept haben wir versucht, den Oxidationszustand des Dotierstoffs mit der Dichte der im organischen Halbleiter induzierten freien Ladungsträger zu korrelieren. Die Umsetzbarkeit dieses Konzeptes wurde bewiesen, indem mono-, di- und tetrakationische Salze von verschiedenen Lochleitern als *p*-Dotierungsmittel auf polare Donor-Akzeptor-Polymere angewendet wurden. Mott-Schottky Messungen mittels Impedanzspektroskopie zeigen eine lineare Beziehung zwischen der Wertigkeit des Dotierungsmittels und der freier Ladungsträgerdichte im Polymer. Neben dem Erreichen einer Rekord-Dotierungseffizienz von 24 % bei 5 Mol% Spiro-MeOTAD(PF$_6$)$_4$ wurde kein Verlust der Ladungsträgerbeweglichkeit, zurückzuführen auf die lochleitenden Eigenschaften des neutralen Dotierstoffs, festgestellt. Darüber hinaus wurde ein synergistischer Effekt zwischen der Polarität des Polymers (Dielektrizitätskonstante) und der Dotierungseffizienz attestiert. Kapitel 6 kombiniert erfolgreich das HOMO-HOMO Elektronentransfer und das Multielektronenakzeptor-Konzept in der *p*-Dotierung.

In der Vergangenheit wurde durch unsere Arbeitsgruppe ein neuartiges Kupfer(II)bis(trifluormethylsulfonyl)amid Salz als Dotierungsmittel für den Lochleiter Spiro-MeOTAD eingeführt. In Kapitel 7 wird der grundlegende Mechanismus aufgeklärt, um zu verstehen warum Kupfer(II)-Salze sehr effektiv Ladungen im Hostmaterial erzeugen können. Durch simultane physikalische Gasphasenabscheidung wurden homogene Filme für die Charakterisierung mittels UV/Vis/NIR, Ultraviolett-Photoelektronen- und Elektronenspinresonanz-Spektroskopie erzeugt. Zu Beginn der Reaktion wurde ein elektrostatisch gebundenes [Spiro$^+$][Cu^I(TFSI)$_2^-$] Salz gebildet. Die außerordentlich niedrige Bindungsenergie dieses Salzes, in Verbindung mit der hohen

Komplexstabilität von $Cu^I(TFSI)_2^-$ führt zu einem großen Anteil an freien Ladungsträgern Spiro$^+$, was die hohe Dotierungseffizienz erklärt. Durch temperaturabhängige Impedanzspektroskopie wurde Kupfer(I) als Fallenzustand identifiziert, was die Ladungsträgerbeweglichkeit erheblich verringert. Durch Zugabe von Bathocuproin, welches selektiv Kupfer(I) komplexiert, konnte dieser Effekt deutlich verringert werden. Kapitel 7 erweitert den Stand der Wissenschaft über *p*-Dotierungsmechanismen an organischen Halbleitern, insbesondere wird die zunehmende Bedeutung der Nebenprodukte der Dotierungsreaktion erläutert. Weiterhin werden Leitlinien zum Design neuartiger Übergangsmetallsalz-Akzeptoren festgelegt.

Im letzten Kapitel wurde der Synergieeffekt aus Kapitel 6 zur *n*-Dotierung eines polaren Akzeptor-Akzeptor-Copolymers genutzt. Durch Kombination der starken Akzeptor-Monomere Thienopyrrolodion (TPD) und Diketopyrrolopyrrol (DPP) mit polaren Ethylenglykol-Seitenketten wurde das *n*-Typ-Polymer Poly(DPP-TPD) zu erhalten. Als *n*-Dotierstoff wurde Cäsiumcarbonat gewählt, da es leicht verfügbar und im Gegensatz zu N-DMBI keinen synthetischen Ursprung hat. Durch FT-IR-, Röntgen- und (inverse) Ultraviolett-Photoelektronenspektroskopie wurde die Deprotonierung von Thiophen durch das Carbonat-Anion nachgewiesen, was zu Elektronen als Majoritätsträgern führt. Die hohe Polarität ermöglicht die Integration von $CsHCO_3$ als Nebenprodukt, ohne dass die Polymermorphologie gestört wird. Darüber hinaus weist das neuartige, mit Carbonat dotierte Akzeptor-Akzeptor-Polymersystem einen bemerkenswerten Leistungsfaktor von ca. $5.6 \cdot 10^{-6}$ W m^{-1} K^{-2} in thermoelektrischen Anwendungen auf. Wir konnten zeigen, dass Carbonate einfache Säure-Base-Reaktionen während der *n*-Dotierung eingehen und N-DMBI in einer Vielzahl von Anwendungen ersetzen können.

Zusammengefasst liefert diese Arbeit detaillierte mechanistische Einblicke und Designstrategien für die *p*- und *n*-Dotierung von organischen Halbleitern mit neuartigen Materialien. Sie erweitert bestehende Konzepte hin zu hocheffizienten, universell einsetzbaren Dotierungsstrategien.

1. Introduction

1.1 Introduction to impedance spectroscopy

1.1.1 Electrical impedance

Among the broad readership, the term "impedance spectroscopy", abbr. IS, is commonly used concurrently with EIS, or "electrochemical impedance spectroscopy" without clear differentiation. Electrochemical IS presupposes the presence of a solid-liquid interface in the experimental setup. In this work, the applied IS techniques are limited to all-solid-state samples. Hence, this chapter excludes peculiarities of electrochemical impedance spectroscopy experiments. For a broader introduction into impedance spectroscopy of solid-electrolyte interfaces, the reader is referred to the relevant literature[1–3].

Impedance spectroscopy is a tool to extract electrical information out of a system.[2] Often, this system consists of a two-port element, i.e., the material under investigation is brought into contact between two electrodes. If only steady-state, frequency-independent properties such as the DC (direct current) resistance of said sample are of interest, one can determine these properties by measuring the current i passing through the element at a given voltage v and calculating the resistance R_{DC} according to Ohm's Law (**Equation 1.1**).

$$R_{DC} = \frac{v}{i} \tag{1.1}$$

However, complex materials such as organic semiconductors can hardly be described using resistive processes alone. In addition, one may observe capacitive and/or inductive response upon applying an external potential to the setup. Capacitors (abbr. C) are comprised of a two-port element with a dielectric layer. Instead, upon applying a DC potential $v(t)$, one observes a sharp rise in potential, followed by a steady-state regime. This is caused by time t dependent accumulation of charge C at the electrode-insulator interface (**Equation 1.2**)[4]:

$$v(t) = \frac{1}{C} \int_0^t i(t)dt \qquad (1.2)$$

Charging the capacitance causes a current $i(t)$, which exponentially approaches zero over time, effectively blocking DC current. On contrary, inductances can be viewed as elements blocking alternating current (abbr. AC) of frequency f (**Equation 1.3**), here shown for strictly sinusoidal current of angular frequency $\omega = 2\pi f$:

$$v_{AC}(t) = V_0 \sin(\omega t) \qquad (1.3)$$

Inductive elements (abbr. L) are typically wire coils to enhance the inductance L but are present in any conductive material. The effect, which reduces the AC (or any changing) current, is created by current flowing through the inductor, inducing an electromotive force opposing the initial current flow according to Lenz' Law.[5] As a result, a potential difference occurs at the inductor (**Equation 1.4**).[4]

$$v(t) = L\frac{di(t)}{dt} \qquad (1.4)$$

An ideal resistor has no frequency-dependent term, therefore **Equation 1.1** holds for AC, as well as DC case. Inductive and capacitive elements however display a frequency-dependent AC resistance, otherwise known as reactance. Exciting capacitive or inductive elements with a sinusoidal AC signal (**Equation 1.3**) does not only lead to reactance, but also to a phase shift between input potential $V_{AC}(t)$ and current response $i(t)$ as shown in **Figure 1.1**.
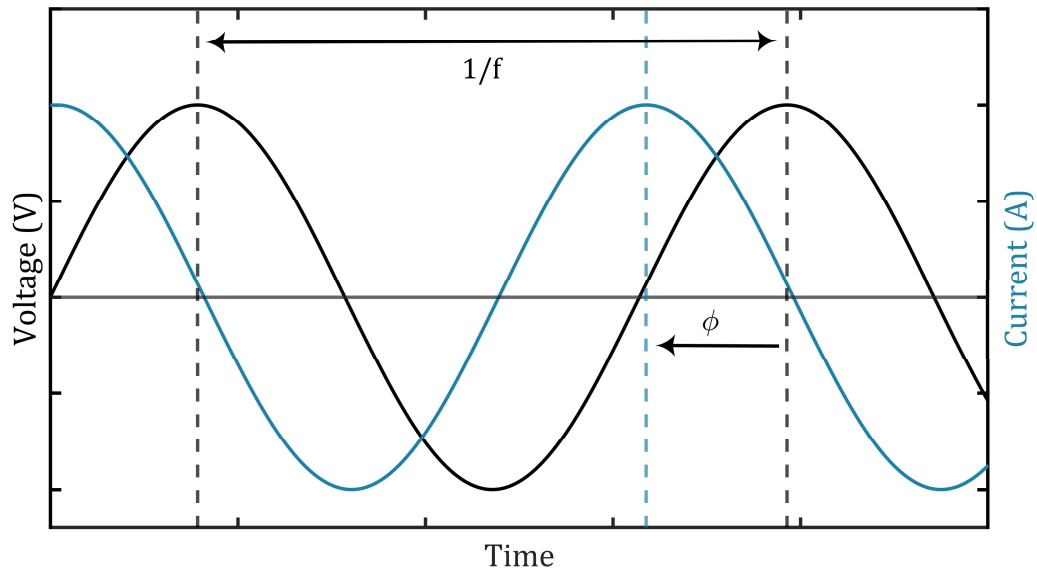
Figure 1.1. Phase shift φ of a current response $i(t)$ (blue) following excitation of a two-pole circuit element with a sinusoidal voltage (black) of period = 1/frequency. Reproduced from Ref.[1]

As we know the sinusoidal input function in **Equation 1.3**, represented as the black curve in **Figure 1.1**, is characterized by the frequency f, calculating the response of an arbitrary system in the frequency domain is of great value. First, the differential equations must be solved. Hence, **Equations 1.2** and **1.4** are transformed from the time domain (depending on *variable t*) into the frequency domain $f = t^{-1}$ (depending on *parameter s*) using a Laplace transform, which is defined as[4,6]:

$$F(s) = \mathcal{L}[f(t)] = \int_0^\infty f(t)e^{-st}dt \tag{1.5}$$

The first derivative of $f(t)$, $f'(t)$ is transformed as follows

$$\mathcal{L}[f'(t)] = \int_0^\infty f'(t)e^{-st}dt = f(t)e^{-st}\Big|_0^\infty - \int_0^\infty f(t)(e^{-st})'dt$$
$$= -f(0^+) + s\int_0^\infty f(t)e^{-st}dt = sF(s) - f(0^+) \tag{1.6}$$

Exemplary, a capacitor in series with a resistor is excited by an external arbitrary potential v(t), described by **Equation 1.6**:[4]

$$v(t) = i(t)R + \frac{1}{C}\int_0^t i(t)dt \qquad (1.7)$$

Transforming **Equation 1.7** using **Equation 1.5** yields

$$\mathcal{L}[V(t)] = \mathcal{L}\left[i(t)R + \frac{1}{C}\int_0^t i(t)dt\right] = RI(s) + \frac{1}{Cs}I(s) \qquad (1.8)$$

Where I(s) is the current in the Laplace plane, to which **Equation 1.8** is rearranged:

$$I(s) = \frac{1}{R+\frac{1}{sC}}V(s) \qquad (1.9)$$

The definition of a current $I(s)$ and potential $V(s)$ in the Laplacian plane allows to introduce a general description of the operational impedance $\hat{Z}$ upon passing through the passive resistive, capacitive or inductive elements:[4]

$$\hat{Z}(s) = \frac{\mathcal{L}[v(t)]}{\mathcal{L}[i(t)]} = \frac{V(s)}{I(s)} \qquad (1.10)$$

The impedance $\hat{Z}$ can now be understood as the expansion of Ohm's Law (**Equation 1.1**) for AC, introducing the phase shift φ besides the magnitude (or amplitude), which also occurs for the DC case (**Figure 1.1**). Defining $\hat{Z}$ *via* the ratio of Laplace transformed current and potential is especially useful for arbitrary excitation signals, whereas for periodic excitation signals, Fourier transform (FT) may be used. FT, similar to Laplace transform, maps a function $f(t)$ in a time window 0-T to the frequency (or spectral) domain $F(\omega)$:

$$F(\omega) = \int_0^T f(t)e^{-st}dt = \int_0^T f(t)e^{-i\omega t}dt \qquad (1.11)$$

where i^2-1 is the imaginary unit. Note, that for the Laplace transform (**Equation 1.5**), the parameter s was real, whereas for FT it is complex. This is useful, as Euler's formula (**Equation 1.12**) can be used to separate **Equation 1.11** into a real $F'(\omega)$ and imaginary part $F''(\omega)$, where $f(t)$ is integrated with a periodic function $\sin(\omega t)$ (**Equation 1.13**) or $\cos(\omega t)$ (**Equation 1.14**).[4]

$$e^{ix} = \cos(x) + i\sin(x) \tag{1.12}$$

$$F'(\omega) = \int_0^T f(t)\cos(\omega t)dt \tag{1.13}$$

$$F''(\omega) = i\int_0^T f(t)\sin(\omega t)dt \tag{1.14}$$

Further, the introduction of imaginary numbers and the complex plane provides a convenient way to evaluate and visualize AC current (phase and magnitude component) flow. To clarify this concept, we assume a periodic cosine excitation ΔV with angular frequency ωt and initial phase shift φ_1 (**Equation 1.15**):[4]

$$\Delta V = V_0 e^{i\varphi_1} e^{i\omega t} = \tilde{V} e^{i\omega t} \tag{1.15}$$

Once a system made of passive components (such as R, C or L) is excited with ΔV, a periodic current ΔI with initial phase shift φ_2 is flowing (**Equation 1.16**):

$$\Delta I = I_0 e^{i\varphi_2} e^{i\omega t} = \tilde{I} e^{i\omega t} \tag{1.16}$$

Note, that a periodic response ΔI can only be expected, if passive, *linear* two-port elements are present in the system, i.e. there is a linear dependency between a DC voltage V and current I flowing through the device.[7] $\tilde{V}$ and $\tilde{I}$ are time-invariant *phasors* i.e., the term $e^{i\omega t}$ is removed.[7] This step can be justified, as in a system excited with a single AC source, the (angular) frequency ωt is constant; only magnitude and phase angle of the current ΔI are changed.[8] Due to the absence of a frequency dependent term, the vectors are static on in the phasor diagram. Their length is representing the magnitude I_0 or V_0, whereas the angle is given by φ (**Figure 1.2a**):
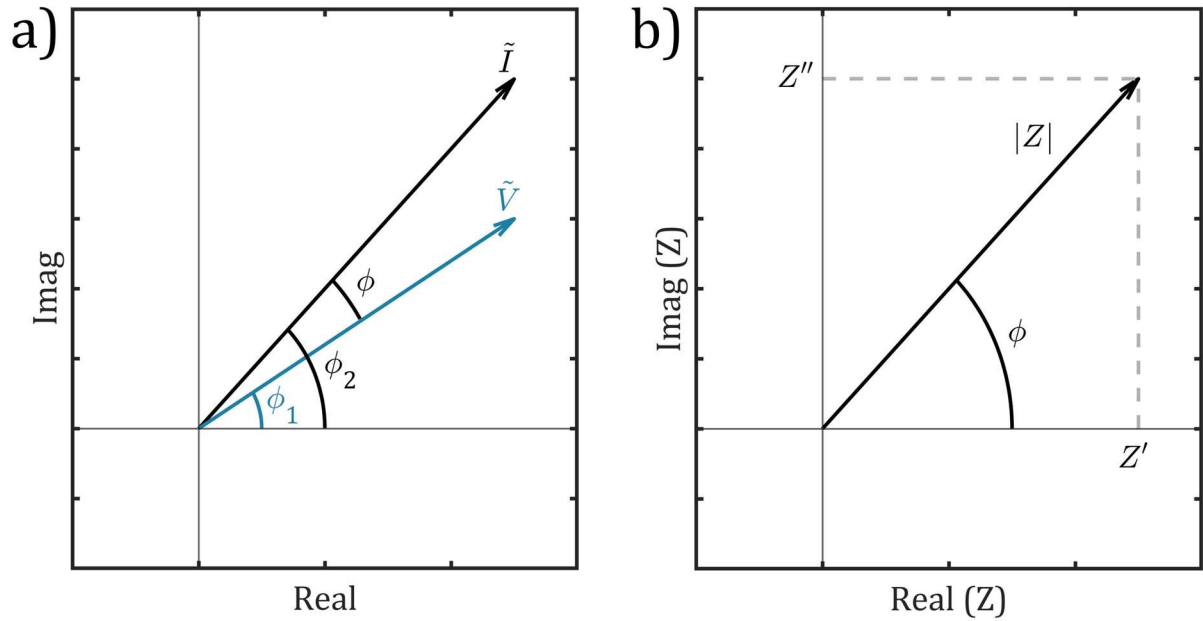
Figure 1.2. a) Phasor diagram in the complex plane of current and voltage phasors $\tilde{V}$ and $\tilde{I}$. φ_1 is the initial phase shift of the exciting AC voltage, φ_2 the phase shift of the current response. The phase angle between both phasors is denoted as φ. b) Complex plane plot of the impedance $\hat{Z}$ as a vector of length $|\hat{Z}|$ and angle φ. The rectangular coordinates of the y-axis are the imaginary- Z'' and real impedance part Z'. Reproduced from Ref.[9]

Conveniently, we can use the current and voltage phasors as the Fourier transformed vectors $V(t)$ and $I(t)$ to calculate the impedance $\hat{Z}(\omega t)$ for periodic excitations:

$$\hat{Z}(i\omega) = \frac{F[v(t)]}{F[i(t)]} = \frac{\Delta V}{\Delta I} = \frac{\tilde{V}}{\tilde{I}} \tag{1.17}$$

As evident from **Equation 1.17**, $\hat{Z}$ is a complex number and can be expressed with both an imaginary and real part according to Euler's relationship (**Equation 1.12**, **1.18**).[1]

$$\hat{Z}(i\omega) = |Z|(\cos(\varphi) + i\sin(\varphi)) = |Z|e^{i\varphi} = Z_{\text{Real}} + iZ_{\text{Imag}} \tag{1.18}$$

$$\text{Real}(\hat{Z}) = Z' = |Z|\cos(\varphi) \tag{1.19}$$

$$\text{Imag}(\hat{Z}) = Z'' = |Z|\sin(\varphi) \tag{1.20}$$

Similar to the phasor diagram (**Figure 1.2a**), the complex number $\hat{Z}$ can be visualized in a complex plane (or polar using magnitude and phase) plot (**Figure 1.2b**). As $\hat{Z}(i\omega)$ is

frequency dependent, the vector with magnitude $|Z|$ and phase angle φ points at different directions in the complex plane depending on the excitation frequency; yet it does not rotate at constant excitation frequency. $|Z|$ and φ can be interconverted with Z' and Z'':[10]
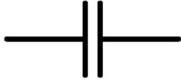
$$|Z| = \sqrt{Z''^2 + Z'^2} \tag{1.21}$$

$$\varphi = \tan^{-1}\left(\frac{Z''}{Z'}\right) \tag{1.22}$$

After defining the impedance Z (**Equation 1.10** and **1.17**) as an expansion of Ohm's law into the frequency domain (**Equation 1.1**), the focus is now set on the impedance of the three passive two-port elements, R, C and L. As shown earlier, an inductor is described by its differential **Equation 1.4**. FT and **Equation 1.17** can be used to solve this differential equation, which yields **Equation 1.23**[9]

$$I(i\omega) = \frac{V(i\omega)}{i\omega L} \rightarrow Z(i\omega) = i\omega L \tag{1.23}$$

Similarly, solutions are found for R and C and tabulated below (**Table 1.1**):
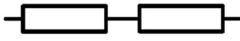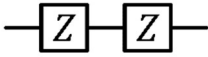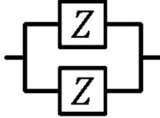
Table 1.1. AC impedances of resistive (R), inductive (L) and capacitive elements (C). Taken from Ref.[4]

Element	AC impedance	Symbol[a]
R	R	
C	$1/(i\omega C)$	
L	$i\omega L$	

[a] According to DIN EN 60617.

From these three passive elements, the resistor R, inductor L, and capacitor C, arbitrarily complex electrical systems can be constructed, using serial and/or parallel connections between the two-port elements. The resulting resistance R_{ges}, resp. impedance Z_{ges} of the whole circuit is the calculated from their individual contributions (**Table 1.2**).

Table 1.2. Calculation of circuit resistance R_{ges} and impedance Z_{ges} of series and parallel resistors and impedances. According to Ref.[11]

Connection	Formula
	$R_{ges} = R_1 + R_2 + \cdots + R_n = \sum\limits_{x=1}^{n} R_x$
	$\dfrac{1}{R_{ges}} = \dfrac{1}{R_1} + \dfrac{1}{R_2} + \cdots + \dfrac{1}{R_n} = \sum\limits_{x=1}^{n} \dfrac{1}{R_x}$
	$Z_{ges} = Z_1 + Z_2 + \cdots + Z_n = \sum\limits_{x=1}^{n} Z_x$
	$\dfrac{1}{Z_{ges}} = \dfrac{1}{Z_1} + \dfrac{1}{Z_2} + \cdots + \dfrac{1}{Z_n} = \sum\limits_{x=1}^{n} \dfrac{1}{Z_x}$

1.1.2 Visualization and analysis of impedances

A successful impedance analysis of device under test yields the frequency dependent, complex impedance Z. Besides a less-transparent mathematical treatment, the visualization of the results helps to rapidly identify common circuit elements and behaviour. As a typical example, consider a polymer sandwiched between two conductive electrodes, as shown in **Figure 1.3**. In order to analyse this circuit impedance (which can take arbitrarily complex forms), the electrical behaviour is modelled using an equivalent circuit (**Figure 1.3**, right).[9] In this case, a series resistor R_S to account for cable and electrode resistance and a parallel circuit consisting of bulk polymer resistance R_P and capacitance C_P is sufficient.
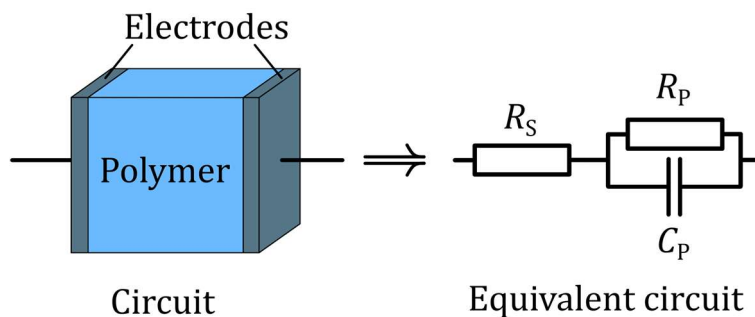
Figure 1.3. Model circuit of a polymer in between two conductive electrodes (left), which is electrically modelled for impedance analysis using an equivalent circuit (right) consisting of series resistor R_S and resistance R_P in parallel to capacitance C_P.

Z of the circuit shown in **Figure 1.3** can now be determined using **Table 1.1** and **1.2**:

$$Z(i\omega) = R_S + \cfrac{1}{C_P i\omega + \cfrac{1}{R_P}} \tag{1.24}$$

Equation 1.24 may be separated into real Real(Z) and imaginary part Imag(Z) (**Equation 1.25**).

$$\text{Real}[Z(i\omega)] = Z' = R_S + \frac{R_P}{1 + (\omega R_P C_P)^2} \tag{1.25}$$

$$\text{Imag}[Z(i\omega)] = Z'' = -\frac{\omega R_P C_P}{1 + (\omega R_P C_P)^2} \tag{1.26}$$

The numerical results of **Equations 1.25** and **1.26** can be conveniently displayed in a complex plane plot (see **Figure 1.2b**), often referred to as *Nyquist plot* (**Figure 1.4a**).[12]
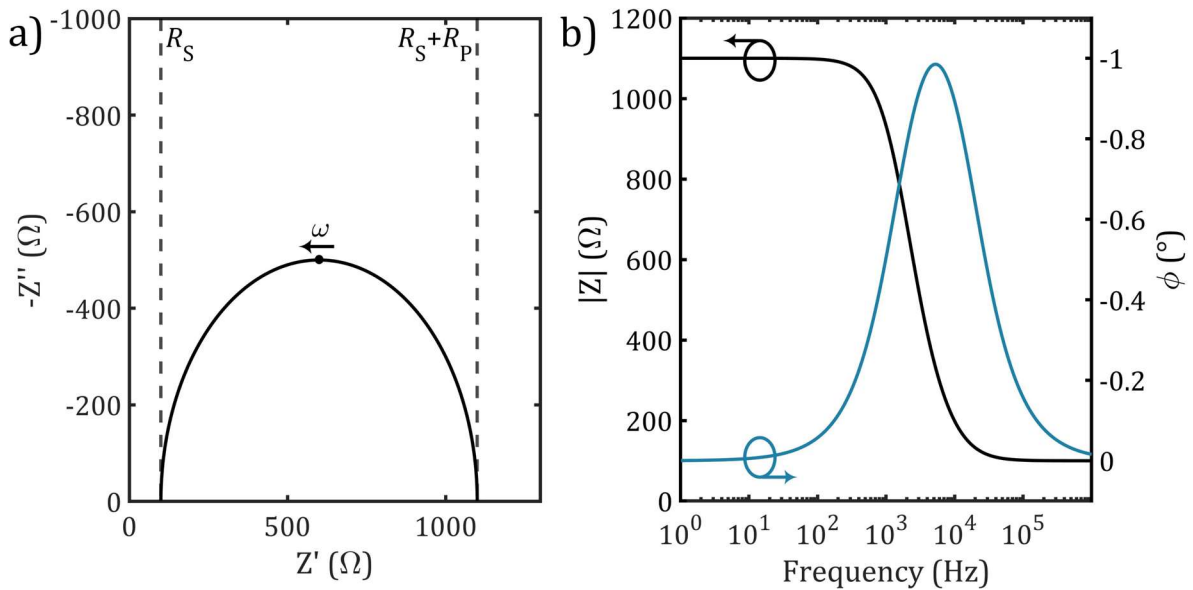
Figure 1.4. a) Nyquist plot of the complex impedance describing equivalent circuit from **Figure 1.3**. The series resistance R_S can be estimated from the low-frequency x-axis intercept, the parallel resistance R_P+R_S from the high-frequency x-axis intercept. b) Bode plot showing the logarithmic frequency dependent impedance $|Z|$ (left y-axis) and phase angle φ (right y-axis).

While the Nyquist plot contains frequency-dependent information, it may not be immediately obvious. Upon sweeping the AC excitation frequency from high to low

frequency, the data points move. The low frequency impedance is mostly real (no imaginary $-Z''$ component) and can be described as the sum of both series and parallel resistance R_S+R_P, as the parallel capacitance behaves as an open circuit at low frequencies. Contrarily, at high frequencies, the parallel capacitance acts as a short circuit ($R \approx 0\ \Omega$) and the circuit impedance is governed by the frequency-independent series resistance R_S. As the immediate frequency information is missing from a Nyquist plot (**Figure 1.4a**), the frequency dependent *Bode* plot is a common alternative in evaluation of impedance data (**Figure 1.4b**). Here, the absolute magnitude of impedance $|Z|$ and phase angle φ, calculated using **Equations 1.21** and **1.22**, are shown versus the measurement frequency.

1.1.3 Charge carrier mobility (μ) measurement using impedance spectroscopy

Impedance spectroscopy is a powerful tool to examine frequency-dependent behaviour of electronic devices such as (photo)diodes, transistors or capacitors. A multitude of parameters can induce such a frequency-dependency, one of them being the charge carrier mobility μ. As it is defined *via* drift velocity υ_D and electrical field E

$$\mu = \frac{|\upsilon_D|}{|E|} \tag{1.27}$$

it includes a velocity component (unit $\frac{m^2}{Vs}$) and is predestined to be measured using impedance spectroscopy.[13] It describes the charge carrier motion under applied electrical field and is an important figure of merit for both inorganic and organic semiconductors, as it limits the upper operational frequency of the device and current flow. The method of determining carrier mobilities using impedance spectroscopy is largely based on a seminal work by Shao and Wright, 1961.[14] A unipolar, space-charge limited diode (either holes or electrons acting as majority carrier, no mixed conduction) is first constructed. Unipolar transport can be controlled by a suitable selection of electrodes, such that the hole injection barrier is far smaller than the electron injection barrier. To reach hole-only space-charge limited (SCL) current transport, the semiconductor is sandwiched between two electrodes with a hole-injection barrier of less than 0.4 eV.[15] The device geometry fluorine-doped tin oxide (FTO)|polymer|Au as shown in **Figure 1.5** was used in this work.
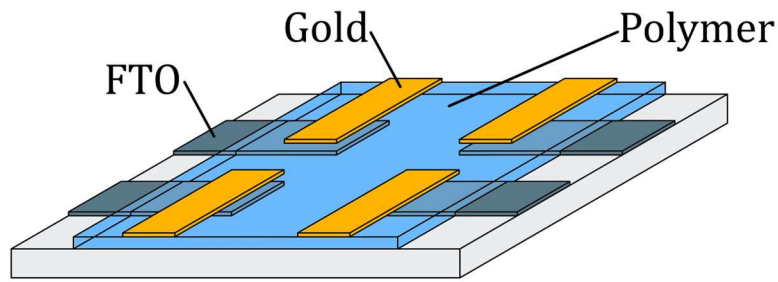
Figure 1.5. Schematic fluorine-doped tin oxide |polymer|Au device geometry for charge carrier mobility measurements of organic semiconductors using impedance spectroscopy.

If the device is biased with a DC voltage, one observes the SCL region after surpassing the ohmic region (slope = 1 in the *I-V* curve) and trap-filling limit. The SCL regime is characterized by a Mott-Gurney current-voltage characteristic:[16]

$$I = \frac{9}{8}\varepsilon_0\varepsilon_S\mu\frac{V^2}{L^3} \tag{1.28}$$

ε_0 is the vacuum permittivity, ε_S the dielectric constant of the semiconductor and L the semiconductor layer thickness. From **Equation 1.28**, it is obvious that the current is directly controlled by mobility and transit time $\tau_t = L^2/(\mu V)$.[17] Superimposing an AC component onto the DC bias under SCL conditions allows to modulate this space charge by injection of additional charges. Hole transport has characteristics of an inductive element, e.g. the current lags behind the AC excitation voltage.[18] Martens et al. refined this concept for organic semiconductors and found, that this inductive response vanishes once the frequency exceeds the average transit time of the carriers.[18,19] Crossing this frequency region creates various outcomes such as a loss in conductance above this specific transit frequency, which can be used to determine the mobility of the carriers.[14,17]

Aim of the impedance spectroscopy is now to characterize and quantize this carrier transit effect in a SCL diode. Often, the reciprocal impedance is used, the *admittance Y*:[10]

$$Y = Z^{-1} = G(\omega) + iB(\omega) = G(\omega) + i\omega C \tag{1.29}$$

$G(\omega)$ is the real conductance, $iB(\omega)$ the imaginary susceptance. Alternatively, the organic layer capacitance can be approximated by treating the whole sample as a single capacitance in simple device geometries (**Equation 1.30**). Here, $C(\omega)$ is calculated as the real part of the complex capacitance.[20]

$$C(\omega) = \frac{-Z''}{\omega(Z'^2 + Z''^2)}$$

(1.30)

This allows for a fast assessment of the device capacitance C, which is used to resolve the inductive effect of the space charge layer movement. Since the change in C is of interest, the negative differential susceptance -ΔB is used.[19]

$$-\Delta B = -\omega(C(\omega) - C_{\text{geo}})$$

(1.31)

C_{geo} is the geometric capacitance above the transit frequency, i.e. the device capacitance is independent from electronic effects and solely determined by its geometry and dielectric constant ($C_{geo} = \varepsilon A/L$; A: Area and L: Thickness). As a first step, the capacitance of the SCL diode is measured (**Figure 1.6a**).
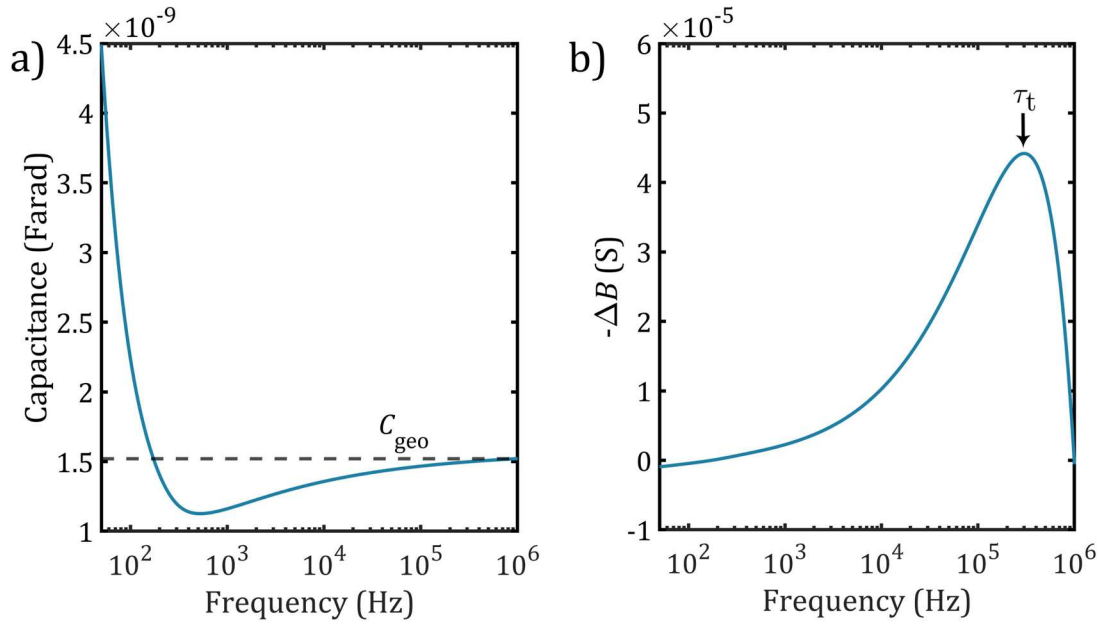
Figure 1.6. a) Frequency dependent capacitance of a biased SCL diode, calculated and offset for clarity from Ref.[18,21] Parameters used for Simulation: $\tau_t = 5 \cdot 10^{-3}$ s^{-1}, $M = 0.15$, $\alpha = 0.3$, $d = 600$ nm, Area = 1 mm^2, Offset = 6 nF. The geometrical capacitance C_{geo} is marked with a horizontal line. b) Negative differential susceptance $-\Delta B$ of the frequency dependent capacitance shown in a), calculated from **Equation 1.31**. The transit time τ_t is marked at the maximum of $-\Delta B$.

$C(\omega)$ steadily decreases upon increasing the applied AC frequency, reaching a minimum before approaching the high-frequency geometric capacitance. Applying **Equation 1.31** to $C(\omega)$ allows to identify τ_t, from which ultimately the charge carrier mobility μ can be evaluated (**Figure 1.6b**, **Equation 1.32**).[22]

$$\mu = 0.56 \frac{d^2}{0.56\tau_t V_{DC}} \tag{1.32}$$

d is the thickness of the active organic layer. Note, that μ obtained in this way is depending on the DC bias V_{DC} superimposed on the AC signal. For obtaining a field-free mobility μ_0, a Poole-Frenkel fit on mobilities obtained at different V_{DC} bias voltages can be used.[23] This method of obtaining charge carrier mobilities using impedance spectroscopy, has been used successfully in organic small molecules, semiconducting polymers and organic solar cells.[24–28]

1.1.4 Charge carrier density (*N*) measurement

As demonstrated in **Section 1.1.3**, capacitance (*via* impedance-) spectroscopy is a valuable tool to examine charge carrier dynamics in organic semiconductors. In recent years, this technique has emerged as indispensable in semiconductor characterisation.[29–32] Besides the charge carrier mobility μ, the ionized charge carrier density N_{A^-} is the second fundamental electronic properties directly affected by doping the semiconductor. Similar to mobility measurements a sandwiched device, FTO|Al$_2$O$_3$|polymer|Au is constructed (**Section 1.1.3**), albeit with an insulating Al$_2$O$_3$ layer in between one of the electrodes and the polymer (**Figure 1.7**).
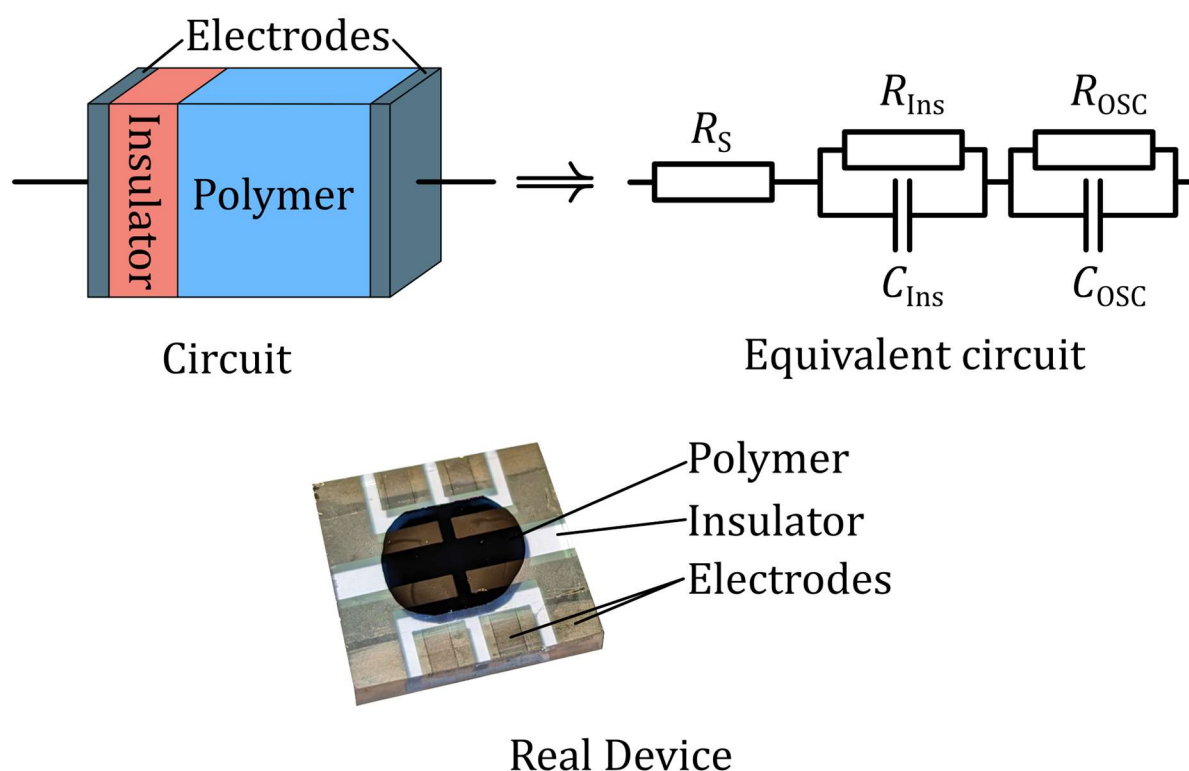
Figure 1.7. Left: Device structure of a metal-insulator-semiconductor (MIS) capacitor featuring an organic semiconductor. Right: Equivalent circuit modelling the impedance of the MIS device shown on the left. R_{Ins}: Insulator parallel resistance, C_{Ins}: Insulator capacitance, R_{OSC}: Organic semiconductor parallel resistance, C_{OSC}: Organic semiconductor capacitance. Bottom: Photo of a MIS capacitor device featuring a fluorine-doped tin oxide|Al$_2$O$_3$|polymer|Au stacking.

Commonly, this device architecture is referred to a metal-insulator-semiconductor (MIS) capacitor. Core principle of this setup is the variation of C_{OSC} upon changing the applied DC bias voltage V_G, whereas C_{Ins} is considered to be static. C_{Ins} can be calculated by treating the insulating layer with thickness d_{Ins}, permittivity $\varepsilon_0\varepsilon_{Ins}$ and area A as a plate capacitor (**Equation 1.33**).[33]

$$C_{Ins} = \frac{\varepsilon_0\varepsilon_{Ins}A}{d_{Ins}} \tag{1.33}$$

The sandwiched device configuration (**Figure 1.7**) necessitates the insulator and OSC capacitances to be in series, i.e. the total capacitance C perceived by the external impedance measurement is then calculated according to **Equation 1.34**.[34]

$$C = \frac{C_{Ins}C_{OSC}}{C_{Ins} + C_{OSC}} \tag{1.34}$$

Based on the sign and magnitude of V_G, which is applied to the metal electrode on top of the insulator, three different operational modes of the MIS capacitor can be discerned (**Figure 1.8**).
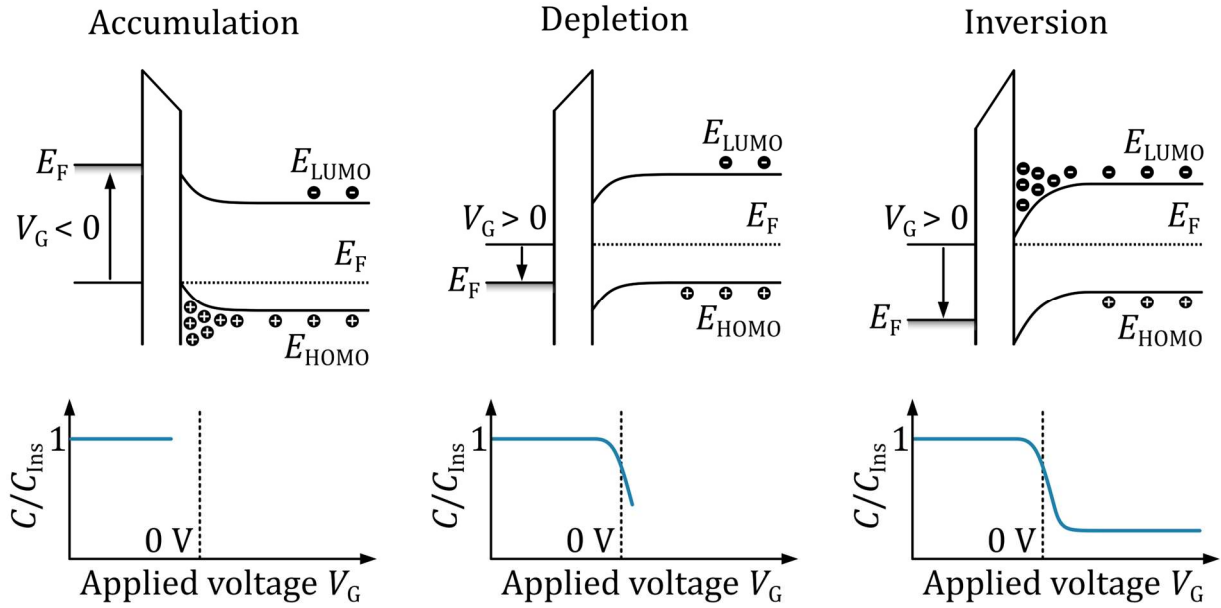
Figure 1.8. Upper half: Energy diagrams of a MIS capacitor with metallic gate, insulator and p-type OSC. E_{HOMO} denotes the HOMO energy, E_{LUMO} the corresponding LUMO energy and E_F the Fermi energy of the system. For negative gate voltages V_G, majority carriers (holes for p-type OSC) are accumulated on the semiconductor/insulator interface with the OSC bands bending upwards ("Accumulation"). A positive V_G causes the bands to bend downwards, depleting the semiconductor/insulator interface from majority carriers ("Depletion"). Applying an even more positive gate voltage moves E_F closer to the LUMO, enabling thermally generated minority charge carriers (i.e. electrons in the case of a p-type OSC) to populate the LUMO ("Inversion"). Lower half: Schematic plot of the ratio between the insulator capacitance C_{Ins} and device capacitance C at accumulation, depletion and inversion (high-frequency case). Reproduced from Ref.[13]

Upon operating the MIS capacitor in depletion mode (positive V_G), the width of the depletion layer varies drastically as V_G changes, and vanishes completely when being driven into the accumulation mode by applying a negative V_G for a p-type OSC (**Figure 1.8**). Ultimately, the total device capacitance the depends on the width w of the depletion layer in series with the insulator capacitance (**Equation 1.35**).[35,36]

$$C = \frac{1}{\frac{1}{C_{Ins}} + \frac{\sqrt{\frac{2\varepsilon_{OSC}\varepsilon_0(V_{Bi} - V_G)}{qN_A^-}}}{\varepsilon_{OSC}}} \tag{1.35}$$

$\varepsilon_{OSC}\varepsilon_0$ denotes the dielectric constant times vacuum permittivity of the OSC, V_{Bi} the built-in voltage, N_A^- the concentration of ionized acceptors/dopants and q the elementary charge. Therefore, C/C_{Ins} approaches 1 in the accumulation regime, as only C_{Ins} governs the total device capacitance C, which slowly decreases in the depletion mode due to an increased depletion layer width (this can be easily visualized as a plate capacitor with an increased dielectric layer thickness, **Figure 1.8**). Evidently, the depletion layer only persists in the depletion region, where dC^{-2}/dV_G can be used to extract the doping concentration N_A^- from the OSC layer using the *Mott-Schottky*-plot (**Equation 1.36**).[37,38]

$$\frac{d}{dV_G}\frac{1}{C^2} = \frac{2}{A^2 q \varepsilon_{OSC}\varepsilon_0}\frac{1}{N_A^-}$$

(1.36)

Where A^2 is the area of the MOS-capacitor. Conveniently, the inverse squared capacitance is plotted vs. V_G (in the depletion regime) and the slope is used to calculate N_A^-.[37] Often, **Equation 1.37** is used to derive the total device capacitance from the imaginary admittance data. Hereby, the device is treated as a R_{Series}-$(R_{Parallel}C)$ equivalent circuit.[38]

$$C(\omega) = \frac{iB(\omega)}{\omega}$$

(1.37)

There is no universal scientific consensus, as to which frequency should be used to measure C^{-2} in electrochemical systems.[39] Generally, the excitation frequency should be high enough to mask electrode polarisation effects and low-frequency leakage currents (typically in the kHz range).[33,40] Recently, using *pin*-structures (*p*-doped – *i*ntrinsic[undoped] - *n*-doped layer) has been proven to eliminate many drawbacks of conventional MIS devices, such as a low capacitance change $C(V_G)$ or insulator surface trap states.[41] C-V measurements on MIS diodes are often used to extract carrier densities from inorganic semiconductors (Si, Ge), metal-oxide semiconductors and insulators (TiO_2, SiO_2), semiconducting polymers, as well as small molecules.[42–47]

1.2 Organic semiconductors

1.2.1 Basics of organic semiconductors and chemical structures

If one were to draw a word cloud of all subjects related to semiconductors, the conventional inorganic semiconductors, especially silicon would display the largest share. Nevertheless, ever since the discovery of highly conductive organic semiconductors (OSC) by Shirakawa et al., their chemical space and applications kept on expanding; attracting significant scientific interest in the process (**Figure 1.9**).[48]
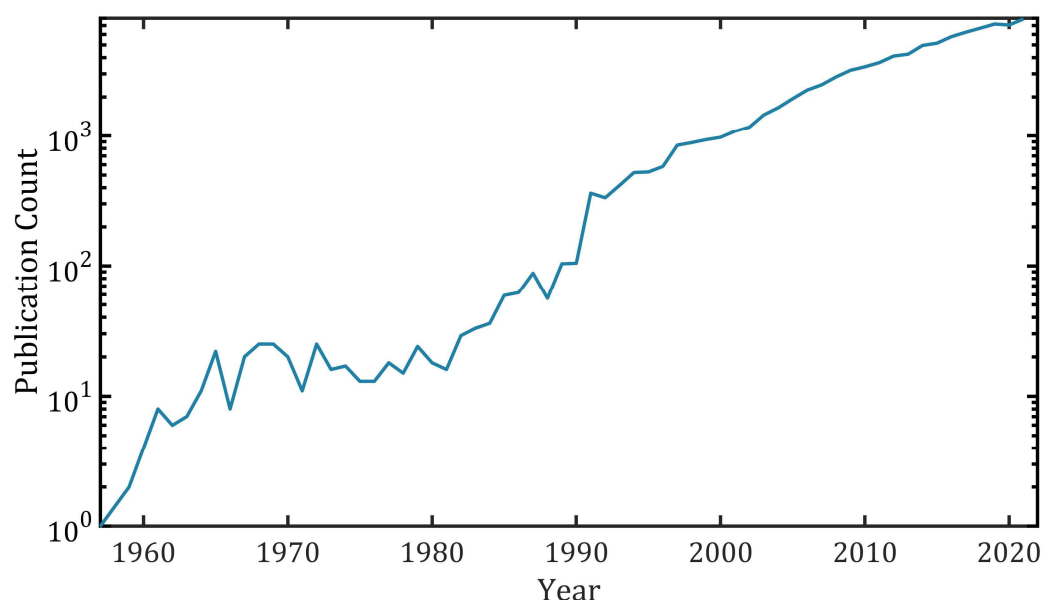
Figure 1.9. Number of organic semiconductor related publications contained in the WebOfScience. Accessed in April, 2022. Search query: "(((((ALL=(Organic Semiconductor)) OR ALL=(Organic Semiconductors)) OR ALL=(Semiconducting Small Molecule)) OR ALL=(Semiconducting Polymer)) OR ALL=(Conductive Polymer)) OR ALL=(Conductive Small Molecule)".

Owing to their magnitude of unique physical and chemical properties, OSCs are rivalling complementing conventional inorganic counterparts in many aspects and applications. These include, but are not limited to: i) Low cost synthesis, solution processability and large area fabrication, ii) Exceptionally high absorption coefficients in the visible range iii) Tailored chemical, morphological and electronic structure, and iv) Low intrinsic defect concentration (no single crystal growth necessary).[49] Contrary to rigid crystal structures

of most inorganic semiconductors, OSCs are characterized by a conjugated π-electron system, formed by sp²-hybridized carbon atoms (**Figure 1.10**).[50]
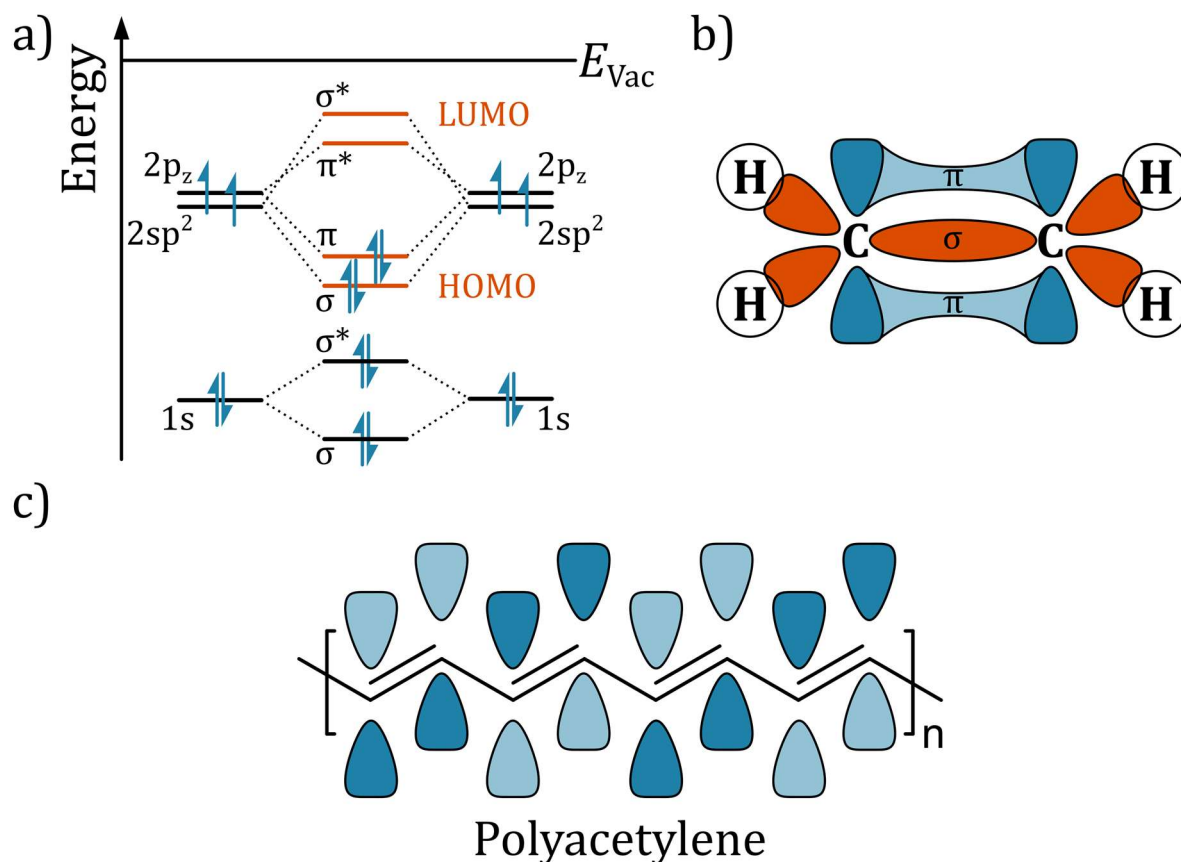
Figure 1.10. a) Schematic energy diagram of ethylene, the HOMO composed of σ and π bonding orbitals and LUMO of antibonding σ* and π* orbitals are marked in red. b) Molecular orbitals of ethylene, π orbitals shown in dark blue, sp² σ orbitals in red. Reproduced from Ref.[51] c) Conjugated π-electrons of polyacetylene, shown is the highest occupied molecular orbital.

As in the very simple case of ethylene, the carbon atoms are linked *via* a π orbital originating from the overlap of the two $2p_z$ orbitals, as well a σ orbital formed by the carbons sp² hybrid orbitals (**Figure 1.10b**). Here, the frontier orbitals, which dominate the electronic structure and optical properties of the molecule, consist of the highest occupied molecular orbital (abbr. *HOMO*) being the π orbital, and the lowest unoccupied molecular orbital (abbr. *LUMO*) represented by the antibonding π* orbital (**Figure 1.10a**).[51] This concept can be transferred to larger, unsaturated and conjugated molecules such as polyacetylene (**Figure 1.10c**). The more extended this π-system is, the

lower the energetic splitting (energetic distance between both orbitals in the MO-scheme) between bonding- and antibonding orbital, thus creating states in a favourable energy range of ca. 1.5 to 3 eV for optical absorption and electron injection.[50] σ and σ* orbitals close to the internuclear axis typically possess a fairly strong splitting, outside the range for efficient electronic interaction with visible light and injecting electrodes (> ca. 6 eV) and therefore have minimal impact on the electronic properties of OSCs.[51] Owing to their organic nature, a distinctive feature-set of OSCs can be formulated:

- OSCs are subject to comparatively weak van der Waals interactions and hydrogen-bonding between molecules. This causes the wavefunction describing the frontier orbitals to be strongly localized on each molecule, with very little overlap of adjacent sites.[52] Further, the bulk electronic properties are therefore largely dominated by the structure of the individual molecule.[52] Conjugated polymers are however subject to noncovalent interactions between chains, which can lead to crystallite formation and planarization of the backbone (increased conjugation length).[53]

- Charge transport between OSCs is dominated by charge carrier hopping between individual sites. The rate of transition is a function of spatial separation, energy difference and transfer integral (wavefunction overlap).[54,55]

- OSCs are subject to permanent electric dipole and/or quadrupoles. As a consequence, fundamental properties such as the ionization potential or work function show asymmetric behaviour, depending on the molecular orientation.[56,57] This anisotropy of electronic properties is not only found in bulk OSCs, but also thin films and single crystals.[58,59]

- OSCs are mostly based on carbon-carbon and carbon-heteroatom bonds, therefore showing a low dielectric constant of ~3 vs. ~12 for Si.[60,61] The most immediate consequence being the fairly strong exciton (coulombically bound electron-hole pair) binding energy. Upon light irradiation, OSCs form small-radius Frenkel-excitons, which tend to recombine, releasing heat.[62] In Si, these pairs form delocalized Wannier-Mott excitons, with far lower binding energies; hence the popularity of Si-based solar cells.[63]

- In the case of semicrystalline conjugated polymers, the energy levels almost merge together in long conjugated systems and these closely lying levels can be roughly

considered as valence band and conduction band (in analogy to inorganic SCs) as shown in **Figure 1.11** below.
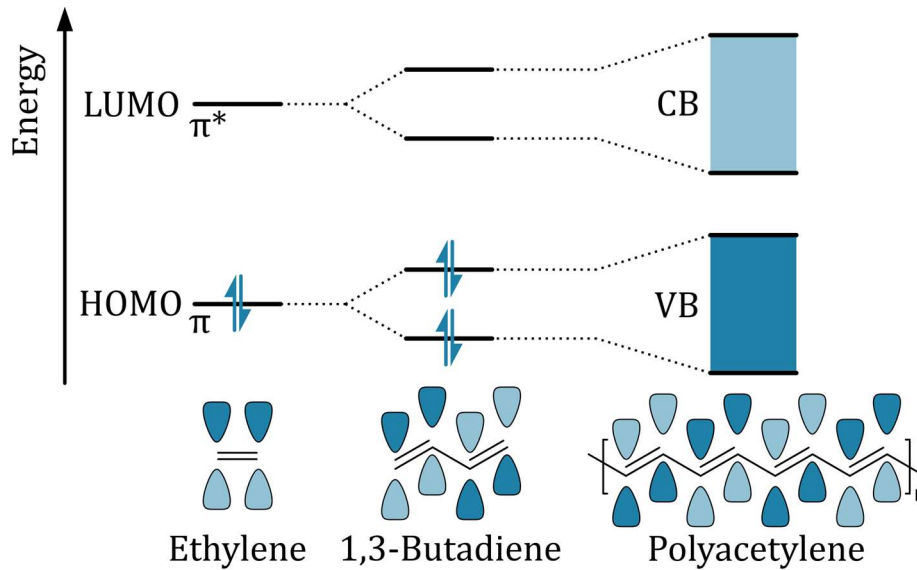
Figure 1.11. Schematic molecular orbital energy diagrams of ethylene, 1,3-butadiene and polyacetylene demonstrating the gradual transition from discrete energy levels to a band-like structure. Reproduced from Ref.[64]

However, in stark contrast to energetically clearly defined *bands* formed in metals and inorganic semiconductors, HOMO and LUMO orbitals form individual *states*, which are distributed in energy. This gives rise to a so-called *distribution of states* (abbr. DOS). One reason for the distribution of states, rather than being isoenergetic, is the absence of ordered intermolecular distances in (mostly) amorphous OSC solids and van der Waals coupling.[51] Bässler et al. showed, that this statistical fluctuation in intermolecular distance can be described by a Gaussian DOS (GDOS) $N(E)$ distributed in energy E (**Equation 1.38**).[65]

$$N(E)dE = \frac{N}{\sqrt{2\pi\sigma^2}} e^{\left(\frac{-E_0^2}{2\sigma^2}\right)} dE \qquad (1.38)$$

N is the total density of states, often the number of molecules per volume, whereas the width of the Gaussian distribution is defined by the standard deviation σ^2. The result is a statistical distribution of states in energy, compared to defined bands found in metals and inorganic semiconductors (**Figure 1.12**).
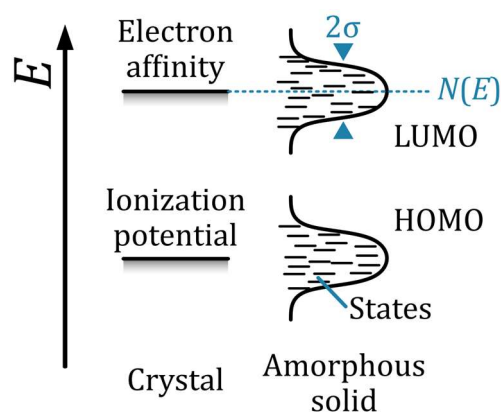
Figure 1.12. Energy diagram of the valence- (ionization potential) and conduction (electron affinity) band in a crystalline, inorganic semiconductor compared to the Gaussian distributed states in an amorphous OSC (right). The GDOS is characterized by its state density $N(E)$ and approximate full-width at half maximum 2σ. Reproduced from Ref.[65]

Besides stochastic variations in inter-site distance, site energy variations occur due to different dipole alignments with the polarizable environment. This type of disorder is also called *static disorder*.[51] Shape and σ^2 of the DOS may also be influenced by *dynamic disorder* introduced by coupling of site-energies with vibrational modes, leading to enhanced energetic disorder ("broadening of the DOS").[51,66] The DOS can also be calculated with an exponential distribution, with the advantages of having analytical solutions for charge transport and describing disordered tail states in superposition with a GDOS (**Equation 1.39**).[67,68]

$$N(E)dE = \frac{N}{E_0} e^{\frac{-E}{E_0}} dE$$
(1.39)

Here, E_0 determines the width of the exponential tail.[67] Ultimately, the actual DOS of disordered semiconductors is not strictly bound to one model, and may take more on complex, arbitrary shapes, which cannot be computed directly.[69] Yet, the DOS is the central core of many model describing the charge transport in OSCs.[67]

As mentioned in **Section 1.2.1**, OSCs consist mainly of sp^2 carbon chains. Inevitably, the chemical space of OSCs keeps expanding, with hundreds of new members being

discovered each year.[70,71] In **Figure 1.13**, some of the most intensive researched and in this work used small molecules and polymeric OSCs are presented.

PDPP[T]$_2$-EDOT PEDOT-C$_6$C$_8$ PDPP[T]$_2${TEG}$_2$-3-MEET P3HT

Copper phthalocyanine C60 Poly(9,9-dioctylfluorene) MEH-PPV

spiro-MeOTAD 4-MeO-TPD Pentacene

Figure 1.13. Various semiconducting polymers and small molecules commonly found in research.

Apart from fundamental OSC properties, their unique nature also implies charge transport and -generation vastly different from conventional inorganic semiconductors. These phenomena will be discussed in the following section.
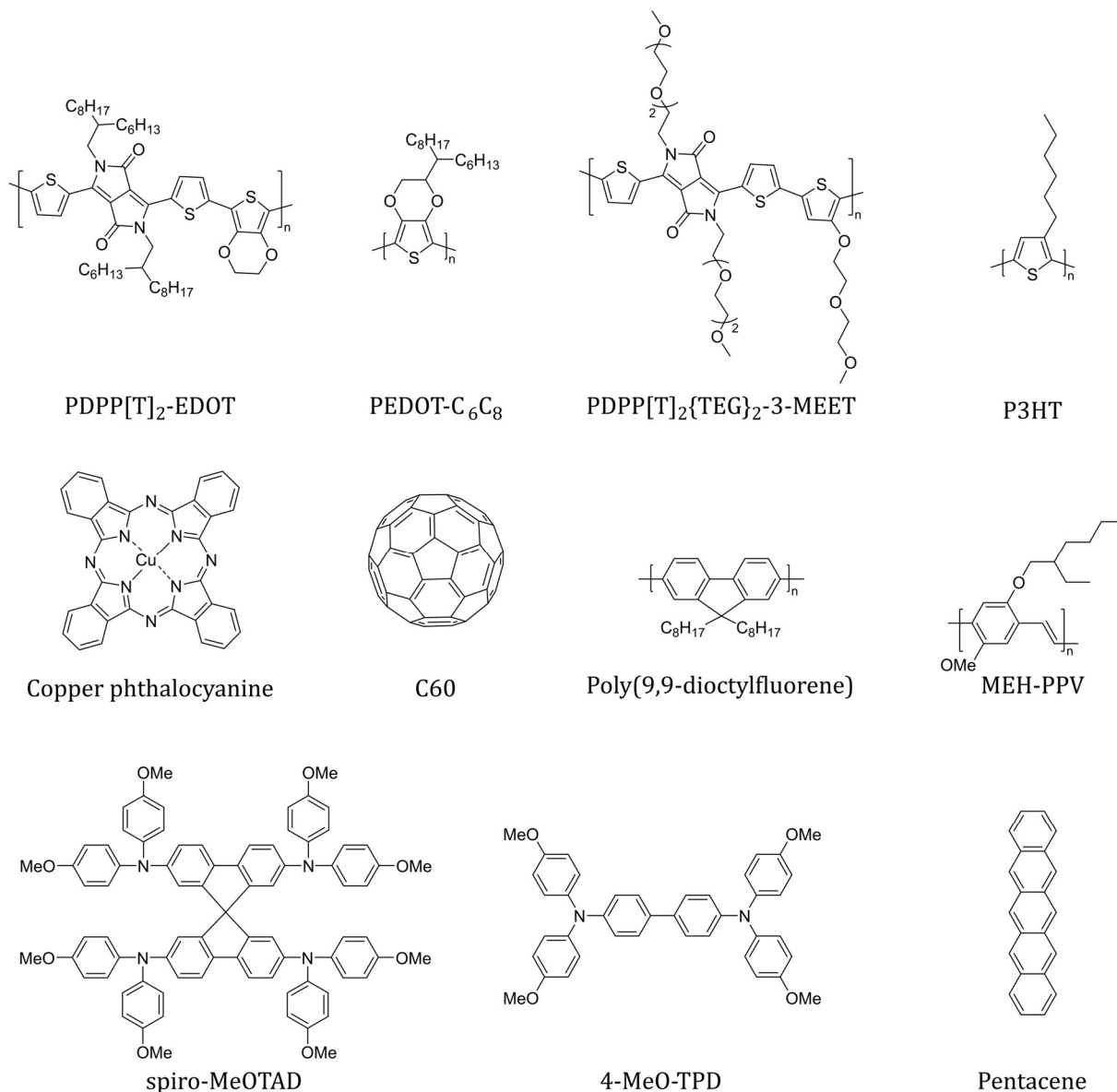
1.2.2 Charge generation in organic semiconductors

As introduced in **Chapter 1.2.1**, the electronic band diagram of a OSC can be defined *via* HOMO and LUMO position, spanning a band gap E_G = HOMO-LUMO. Both are described by a DOS, which itself contains no information on how these states are occupied. The energy limit, up to which states are filled with electrons according to Pauli exclusion principle, is called the *Fermi level* E_F.[72] It is no sharp transition, but rather an occupation probability $f(E)$ separating filled and empty electronic states, which varies with temperature T (**Equation 1.40**).

$$f(E) = \frac{1}{e^{\left(\frac{E-E_F}{k_B T}\right)} + 1}$$
(1.40)

k_B is the Boltzmann constant. Alike all semiconductor energy levels discussed in this paragraph, E_F is referenced to the *vacuum level* E_{Vac}. E_{Vac} is defined as the energy of an electron, which resides a few nanometers above the surface – far enough to eliminate the influence of any image forces. It is highly dependent on the surface dipole and chemical bonds (surface treatment, physisorption of foreign molecules, etc.).[73] Besides E_F, all energy levels relevant to the discussion on organic semiconductors are depicted in **Figure 1.14a**. The work function (WF) is defined as E_{Vac}-E_F and describes the energy barrier to remove an electron residing at E_F from the bulk solid into the local vacuum level.[74] Electron affinity (EA) and ionization potential (IP) values correspond approximately to the HOMO and LUMO energy positions w.r.t. vacuum level, respectively. From the Fermi occupation statistics $f(E)$ and the DOS distribution function $N(E)$, the density of occupied states (abbr. DOOS) can be derived (**Figure 1.14b**).[13]
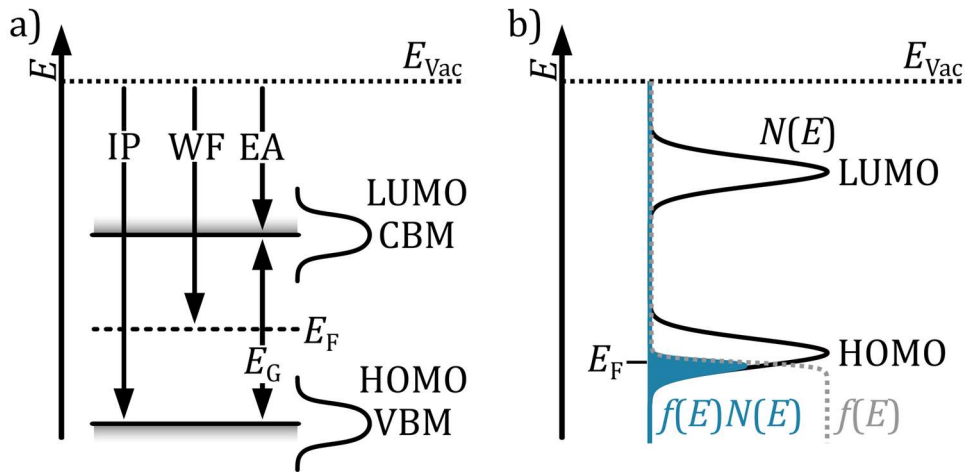
Figure 1.14. a) Energy levels of an organic semiconductors with a Gaussian DOS. Conduction band minimum (LUMO), valence band maximum (HOMO), Fermi level (E_F), band gap (E_G), electron affinity (EA), work function (WF) and ionization potential (IP) are referenced to the vacuum level E_{Vac}. Adopted from Ref.[74] b) Schematic representation of Gaussian HOMO and LUMO DOS $N(E)$ (**Equation 1.38**), Fermi distribution $f(E)$ (**Equation 1.40**) and the DOOS resulting from $f(E)N(E)$.

Filling of the states (akin to chemical reduction of the OSC bulk) causes E_F to gradually move towards lower energies (LUMO). Integration of the DOOS (blue marked area in **Figure 1.14b**) yields the electron- n and hole density p (charge carrier densities), depending on the integration limits (**Equation 1.41**, **1.42**).[13,75]

$$n = \int_{\text{LUMO onset}}^{\infty} N(E)f(E)dE \tag{1.41}$$

$$p = \int_{-\infty}^{\text{HOMO onset}} N(E)f(E)dE \tag{1.42}$$

In pristine organic semiconductors, the band gap typically ranges from ca. 1.4 in narrow band gap materials up to 3-4 eV in wide band gap materials.[76–78] Holes may be generated by thermally exciting an electron into the LUMO, a process which is balanced by charge neutrality condition $n = p$. The resulting charge carrier density $n = p = n_i$ is called the *intrinsic* charge carrier concentration and can be calculated using **Equation 1.43**.[13]

$$n_i = \sqrt{N_{\mathrm{HOMO}} N_{\mathrm{LUMO}}}\, e^{\left(-\frac{E_{\mathrm{G}}}{2 k_{\mathrm{B}} T}\right)} \tag{1.43}$$

here, N_{HOMO} and N_{LUMO} are the effective HOMO and LUMO density of states respectively; i.e. the total number of available states. Taking a typical E_{G} of 2 eV and $N_{\mathrm{HOMO}} = N_{\mathrm{LUMO}} = 10^{21}$ cm^{-3} results in a n_i of ca. $6 \cdot 10^3$ cm^{-3} at room temperature.[79] This value is extremely low in comparison to deliberately doped OSCs with reported charge carrier densities in the order of 10^{18} to 10^{20} cm^{-3} (see also **Chapter 1.3**).[80–82] The conductivity σ of a semiconductor is directly linked to the carrier concentration, elementary charge q and charge carrier mobility μ (**Equation 1.44**).[13]

$$\sigma = q n \mu \tag{1.44}$$

As a direct consequence of the low intrinsic carrier concentration, a pristine OSC (e.g., $\mu = 10^{-3}$ cm^2 V^{-1} s^{-1}, $n_i = 6 \cdot 10^3$ cm^{-3}, r.t.) is a rather bad conductor with $\sigma \approx 10^{-18}$ S cm^{-1}, well within the range of insulators. To put this into perspective, for low-density polyethylene, a common aliphatic and insulating polymer, a conductivity of roughly 10^{-17} S cm^{-1} was determined.[83] Hence, to transform insulating, intrinsic OSCs into useful materials for device applications, various means of generating additional charges are vital.

Mostly, four distinct phenomena to enhance p (or n) are known: i) chemical doping *via* chemical redox reactions, ii) electrochemical doping *via* charge injection or extraction through suitable electrodes, iii) photoeffect, i.e. separation of photogenerated excitons, or iv) shift of the Fermi level by field-effect.[50] The first case, chemical doping, the core topic of this work, will be explained in greater detail in **Chapter 1.3**.

1.2.3 Charge transport in organic semiconductors

As highlighted in **Section 1.2.1**, most OSCs are highly disordered materials, with a finite correlation length of the molecular orbitals. Further, the energy states of the individual molecules do not form a continuous band, but are distributed in energy (**Figure 1.12**).

Additional effects such as positional (no fixed positions on crystal lattice) and conformational disorder (polymer backbone twisting) further broaden the DOS.[67] Consequently, it comes as no surprise, that only a few examples of small-molecule single crystalline OSCs with low-temperature band-like transport are known in literature. Examples are naphthalene, perylene and anthracene, which need to be purified with extreme care, as every impurity disturbs the charge transport and creates crystallographic defects.[84,85] However, these special cases of charge transport under absence of phonon scattering in single-crystals at low-temperatures cannot be used to treat conventional, disordered OSCs (especially semiconducting polymers) and remain a niche application in devices.[86]

Instead, in most OSCs, charge transport *via* carrier hopping dominates.[51] In this process, either holes or electrons tunnel between strongly localized, filled states to empty ones in the disordered OSC bulk under the influence of an electric field.[55] The rate of carrier hopping events v_{ij} is often calculated using the Miller-Abrahams (**Equation 1.45**) or Marcus rate expression (**Equation 1.46**).

$$v_{ij} = v_0 exp\left(-\frac{2r_{ij}}{\alpha} - \frac{\varepsilon_j - \varepsilon_i + |\varepsilon_i - \varepsilon_j|}{2k_B T}\right) \tag{1.45}$$

$$v_{ij} = \frac{J_0^2}{\hbar}\sqrt{\frac{\pi}{4E_a k_B T}} exp\left(-\frac{2r_{ij}}{\alpha} - \frac{E_a}{k_B T}\right) exp\left(-\frac{\varepsilon_j - \varepsilon_i}{2k_B T} - \frac{(\varepsilon_j - \varepsilon_i)^2}{16k_B T E_a}\right) \tag{1.46}$$

v_0, α, r_{ij} and ε are the attempt-to-escape frequency, localization length (i.e., how quickly the wavefunction of a localized state decays with increasing distance from its center), distance between sites i and j as well as the energy of the site. J_0, $\hbar$ and E_a describe the transfer integral, or wavefunction overlap, between sites i and j, the reduced Planck constant and the polaron activation energy (where "polaron" refers to an electronic charge in the OSC coupled to phonons).[54,87] Whereas the Miller-Abrahams rate is suitable for low electron-phonon coupling and temperatures, the Marcus rate is also valid for strong electron-phonon coupling, which better represents highly polarizable OSCs.[67] From the expression of the available states (**Equations 1.38**, **1.39**), the occupation probability (**Equation 1.40**) and the transfer rate (**Equations 1.45**, **1.46**), models for the macroscopic description of charge transport can be developed. The world of charge transport models and research thereof is vast, hence only a small excerpt will be given in this section. For a more in-depth review on the subject of charge transport in disordered

organic materials, the reader is referred to the relevant literature.[51,67,88,89] Fishchuk et al. developed an analytical framework to describe charge transport in disordered OSCs using a Gaussian DOS and accounting for polaronic (E_a) and disorder (σ) effects at high temperatures using the Marcus rate expression. Using the effective medium approximation, a method which treats macroscopically inhomogeneous media, Fishchuk et al. derived a universal expression for the charge carrier mobility μ (**Equation 1.47**).[90,91]

$$\mu = \mu_0 \exp\left(-\frac{E_a}{k_B T} - \frac{1}{8q^2}\left(\frac{\sigma}{k_B T}\right)^2 + \frac{1}{2\sqrt{2}q^2}\left[\left(\frac{\sigma}{k_B T}\right)^{3/2} - \left(\frac{\sigma}{k_B T}\right)^{1/2}\right]\sqrt{\frac{e\alpha E}{\sigma}}\right) \quad (1.47)$$

Where μ_0 is a constant mobility, which is a function of the transfer integral J_0, $q = \sqrt{1 - (\sigma/E_a)(\sigma/k_B T)/8}$, σ the Gaussian DOS width, e the elementary charge and E the electric field. Parris et al. proposed a similar expression obtained *via* numerical computer simulations (**Equation 1.48**).[92]

$$\mu = \mu_0 \exp\left(-\frac{E_a}{k_B T} - 0.31\left(\frac{\sigma}{k_B T}\right)^2 + 0.78\left[\left(\frac{\sigma}{k_B T}\right)^{3/2} - 1.75\right]\sqrt{\frac{e\alpha E}{\sigma}}\right) \quad (1.48)$$

The main observation from **Equation 1.47** are the nonlinear temperate dependence of μ on T for small polaron activation energies, strongly decreasing μ with increasing polaron activation energy and a positive field dependency.[90] This model was verified by comparing the simulated mobilities with temperature- and field-dependent time-of-flight measurements on poly(methylphenylsilane).[90,93] Recently, the focus of research on charge transport in disordered OSCs has shifted towards the concept of transport energy (thermally equilibrated energy level, at which most of carrier hops contribute to conduction; can be different from E_F).[54] This theoretical tool does not rely on simple phenomenological assumptions or simulations in a regular lattice grid, yet yields very good descriptions for disordered OSCs.[54] Further, advances in molecular dynamic simulations have allowed the direct observation of time propagation of charge carriers in relatively large systems ($\sim 10^3$ organic molecules), instead of assuming charge transport mechanisms.[94] Also, efforts have been made to unify existing theories, with the goal of describing charge transport for various degrees of disorder and crystallinity in OSCs.[89]

Polaron hopping in disordered OSCs is highly sensitive towards a multitude of parameters, mostly the presence of charge carrier trap states, morphology and crystallinity. In addition, long- and short-range ordering, recombination and self-ordering may also play a role.[51] Trap states (often referred to simply as "traps") are mid-gap states in the energy diagram of an OSC, which provide energetically favourable residence sites for holes or electrons (**Figure 1.15**).
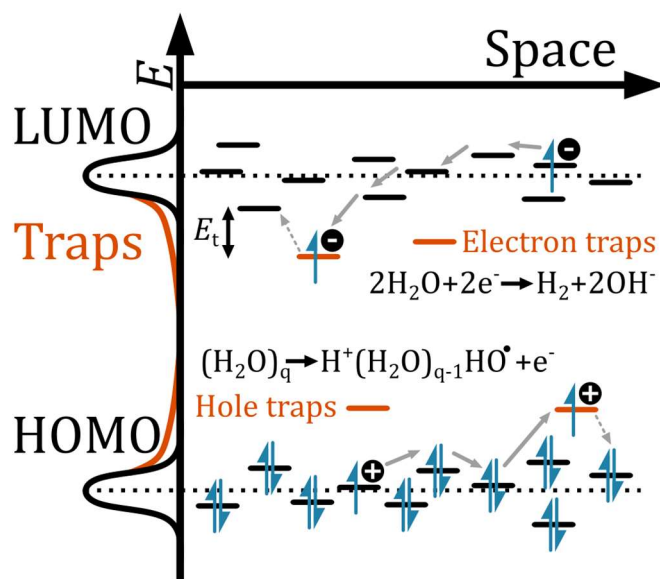
Figure 1.15. Energy structure of a disordered OSC with a Gaussian DOS and exponentially distributed trap states ("Traps"). Holes moving along an electric field may be trapped in hole traps higher in energy. One possible common reaction is the capture of a hole in water clusters $(H_2O)_q$ present, which yields a hydroxyl radical and hydrated oxonium ions. Similarly, electrons hopping in the LUMO are subject to electron traps deeper in energy located at trap energy E_t. If water is present, it can be reduced from the electrons/trapped, forming hydrogen. Adopted from Ref.[51,95,96]

Once captured in a trap site, charge carriers experience an energy barrier hampering their release back into the states responsible for transport. This barrier can be overcome by sufficient electrical fields, thermal energy or incident photons interacting with the OSC.[97] Shallow traps can release charge carriers at room temperature ($k_BT \approx 26$ meV), deeper traps often irreversibly capture holes or electrons.[97] Further, with increasing E_t, the trap site is located further in the band gap, eventually leading to trap-assisted recombination.[98] Besides obvious chemical impurities, such as water, oxygen or synthesis byproducts, intrinsic disorder like structural defects can also act as trapping

centers. Another important source of traps in devices are the interfaces to electrodes, insulators and other (organic) semiconductors.[97] Generally, any trap state is detrimental to polaron transport in OSCs, limiting the charge carrier mobility and degrading device performance.[99,100] As discussed earlier, OSCs are subject to rather weak van der Waals interactions, and therefore the coupling between hopping sites plays a major role for charge transport. This coupling is directly influenced by the morphology, crystallinity and molecular structure of the OSC. The impact of morphology and crystallinity on charge transport is typically higher for semiconducting polymers than for small molecules, as they have a lower degree of rotational freedom and kinetic hindrance to align properly in the solid state. One prominent example is the OSC poly(3-hexylthiophene) P3HT. Before the advent of Rieke-method, Grignard metathesis and Kumada catalyst transfer polymerisation enabling the synthesis of highly regioregular polyalkylthiophenes, regiorandom variants were prepared by oxidative polymerisation.[101–104] As Sirringhaus et al. demonstrated, increasing the ratio of head-tail coupling from 70 % to 96 % results in a ca. 4 orders of magnitude linear increase in the field-effect transistor (abbr. FET) mobility (**Figure 1.16a**). They attributed this to the preferential edge-on alignment of regioregular P3HT w.r.t. the substrate along the (100) direction, compared to a face-on alignment observed for less regioregular P3HT in the (010) direction (**Figure 1.16b**).
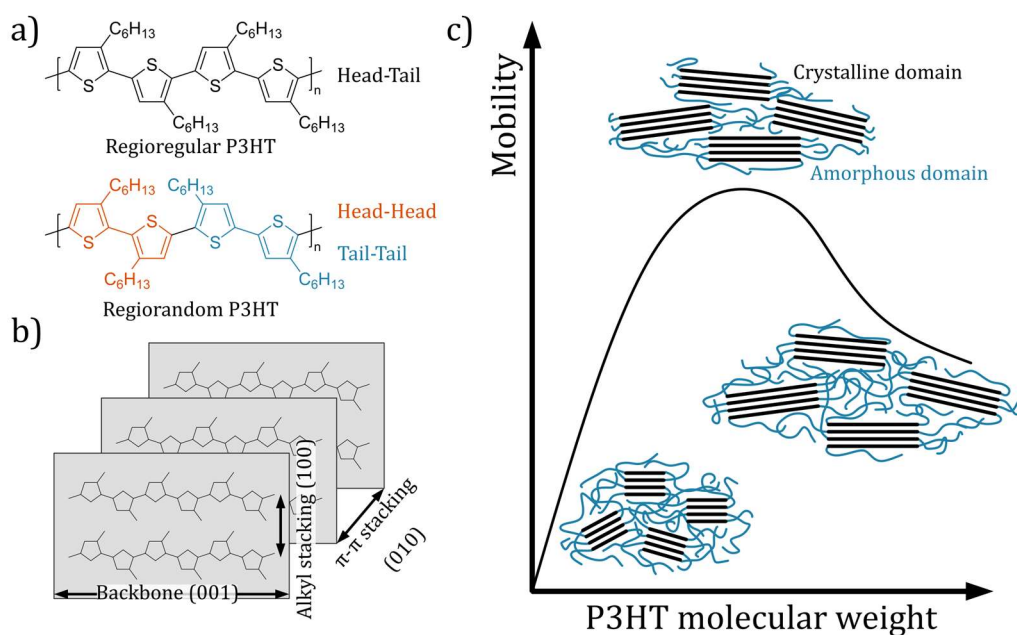
Figure 1.16. a) Regioregularity of P3HT with head-tail, head-head and tail-tail coupling in the main chain. b) Schematic P3HT packing in the crystalline domain with (hkl) indices. Along the (001) direction, the backbone length (long period) is shown, the alkyl stacking is along the (100) axis. The (010) plane is defined by the π- π stacking distance. Adopted from Ref.[105] c) Schematic correlation between the P3HT molecular weight and charge carrier mobility. The inset depicts the P3HT morphology with regular crystalline- and amorphous domains at low-, medium- and high molecular weight. Adopted from Ref.[106]

The chain length play another decisive role in the charge transport of P3HT. Starting from very short oligomers (ca. 2.5 kDa), the P3HT FET mobility increases by 3 orders of magnitude up to a molecular weight of ca. 7 kDa, followed by a constant mobility of 10^{-2} cm^2 V^{-1} s^{-1} up to ca. 18 kDa.[107] This has been attributed to a high degree of open chain ends and lower regioregularity in the low molecular weight P3HT, which forms crystalline, but isolated (by the amorphous region) microstructures.[108,109] At higher molecular weights, the crystalline domains dominate. Ballantyne et al. expanded this series up to 121 kDa and found a profound loss in mobility.[110] He reasoned the loss originates from lower ordering in high molecular weight P3HT films due to entanglement causing lower intra-chain mobility, chain twisting and less overlap between neighbouring chains (**Figure 1.16c**). Similar results were reported by Lohwasser et al., who made chain-folding and increase of the amorphous volume fraction responsible for the decreasing mobility.[106] Concluding, the charge transport can be modelled by selecting

appropriate theories, yet many extrinsic and intrinsic material properties govern the real-world device performance.

1.2.4 Interfaces and charge injection in organic semiconductors

In **Sections 1.2.1-1.2.3**, the isolated bulk properties of organic semiconductors are covered. Real-world devices however consist of many different interfaces, typically a OSC is sandwiched between two adjacent OSCs or electrodes. Hence, understanding the fine interplay and energetics between different (semi)conductive materials is the key for device engineering. A key concept is the Fermi level alignment at interfaces. If an OSC is brought into contact with a metallic electrode (which can supply or sink an infinite amount of electrons), the Fermi level aligns to form a constant value throughout the device stack to reach thermal equilibrium.[111] If the E_F of the OSC is higher in energy than the metal E_F before brought into contact, electrons are supplied from OSC to metal at contact, and *vice versa* if the E_F of the OSC is lower.[50] The process results in *band bending*, a term describing the variation in electronic energy levels as a function of the distance to the interface.[112] This is well described by the Mott-Schottky model, developed to treat inorganic semiconductor-metal interfaces by Mott et al. and later refined by Walter Schottky.[113,114]

Originally developed for inorganic semiconductors, the model falls short in some aspects for highly disordered OSCs with hopping type transport and low binding energy between adjacent molecules. Photoelectron spectroscopy, DFT and Kelvin probe studies on organic/metal interfaces have revealed a strong vacuum level shift at the first few nanometers, attributed to a surface dipole Δ rather than actual band bending only present in selected cases (e.g. C_{60}/Cu interface).[112,115-117] The combination of band bending and interface dipole for an metal/OSC interface is schematically shown in **Figure 1.17**.
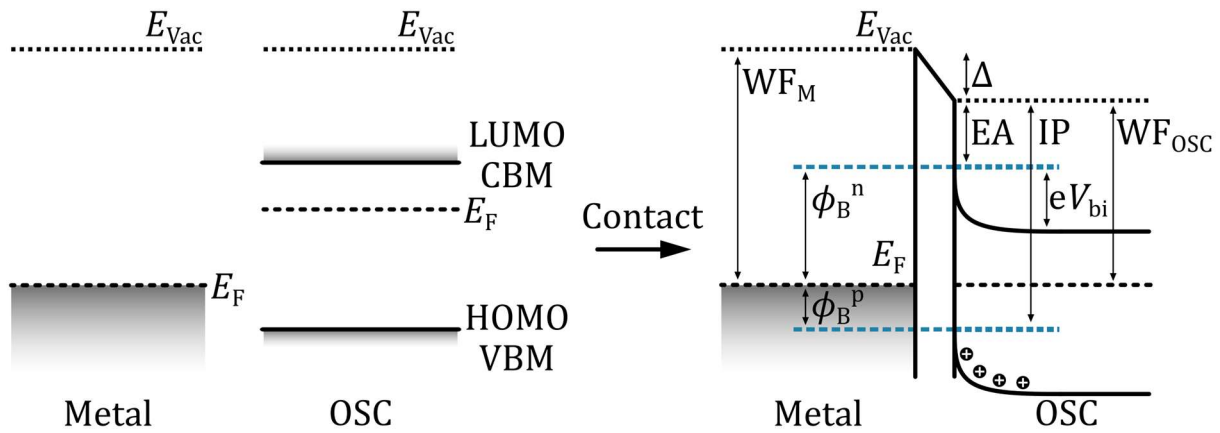
Figure 1.17. Alignment of organic semiconductor energy levels before (left) and after(right) contact with a metal. After Fermi level alignment, the interface dipole Δ in addition with band bending leads to shifts in electron affinity (EA, LUMO) and ionization potential (IP, HOMO) with formation of an electron depletion zone. A built-in potential V_{Bi} is formed across the space charge, equal to the difference between metal and OSC work function before contact plus Δ. Charges injected/extracted from the metal contact experience an energy barrier ϕ_B^n for electrons and ϕ_B^p for holes. Adopted from Ref.[112]

The contribution of true band bending to the energy level shifts may be as low as 0.1 eV, therefore Δ governs V_{bi} and injection behaviour in many OSCs.[50] The origin of Δ is still under debate as of 2022, major contributions include, but are not limited to: i) image charge screening by the metal, ii) variations in metal work function upon contact with organic matter, iii) chemical interactions, especially reactive polymers like PEDOT-PSS and iv) permanent dipoles present in the OSC.[116,118–124] Similar to metal/OSC interfaces, OSC/OSC heterointerfaces play a huge role in device engineering, predominantly in organic light emitting diodes and organic photovoltaic cells, where they help to combine or separate electron-hole pairs.[125–130] Compared to metal/OSC interfaces, the second participating OSC cannot infinitely supply charge carriers to support Fermi level alignment, so band bending (together with additional effects) occurs at both semiconductors. In most OSCs, the interface dipole is rather small, e.g. the vacuum levels align for many OSC pairs without significant vacuum level shift.[131] Notable exceptions are fluorinated copper phthalocyanine, P3HT:PCBM and pentacene:fullerene interfaces, either due to charge transfer or polarization effects.[132–134]

After Fermi level equilibrium is established, the metal electrodes can be utilized to extract or inject charges into a (multi)layered device. If the electrodes are able to supply more

charges than the bulk OSC can transport, a space-charge layer forms and the electrode is referred to as *ohmic*.[51] To achieve this condition, the injection barriers ϕ_B must be minimized. Evidence for true ohmic contacts can be gathered by measuring the current-voltage characteristics of the device and comparing the curve to the expected current flow for true space-charge limited current, according to the Mott-Gurney law (see **Equation 1.28**) after accounting for built-in potentials (**Figure 1.18**).[135]
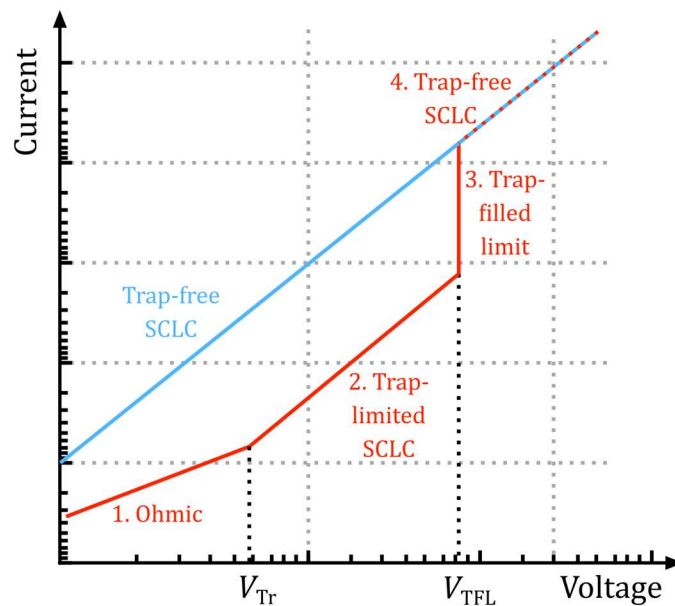
Figure 1.18. Schematic current-voltage characteristics of space-charge limited conduction (SCLC) in a dielectric material. V_{Tr} defines the limit, at which the number of injected chargers is equal to the thermally generated charges in the material. Above V_{TFL}, all charge carrier traps are filled. Reproduced from Ref.[136]

As a side effect, lowering ϕ_B results in an exponentially increased current flow in the semiconductor bulk, rendering the interface energetics vital for proper device operation.[137] To avoid excess injection barriers ϕ_B, high work function electrodes are selected for hole extraction/injection and low work function metals for electron extraction/injection (see **Figure 1.17**). These metals are then paired with appropriate *p*- (high WF) or *n*-type (low WF) OSCs; for example, Spiro-MeOTAD (E_{HOMO} = 4.92 eV) may be deposited on top of Au (WF $\approx$ 5.2 eV) to form a hole-injection contact.[138,139] However, the selection of suitable electrode materials can be restricted by the device itself, i.e. solar cells inherently rely on at least one electrode to be transparent in the optical range. Too tackle this problem, the electrode work functions can be tuned by surface-assembled

monolayers, plasma-treatment, or physical adsorption of organic molecules.[140–143] Similarly, by changing the Fermi level of the OSC adjacent to the electrode, a more efficient injection can be achieved. Popular choices for hole-injection layers are 2,3,5,6-tetrafluoro-7,7,8,8-tetracyanoquinodimethane, an electron deficient *p*-dopant, Lewis acids such as FeCl$_3$ or metal-oxides.[144–148] Notably, manufacturing conditions (absorption of monolayers onto electrodes), presence of mobile ions and device geometry too have a profound impact on the efficiency of charge injection.[135]

The process of charge injection itself often has been described by Fowler-Nordheim tunnelling or Richardson-Schottky emission - models which are based on inorganic semiconductors and are not sufficient to describe charge injection into disordered OSCs according to Köhler et al.[51] Besides band bending, which directly influences ϕ_B, the formation of an *image force* is important to understand the charge injection at metal/OSC interfaces (**Figure 1.17**).[149] An electron located in the OSC bulk at distance *x* from the electrode will experience an attractive force by inducing a positive charge on the electrode surface. This image force F_{imag} can be calculated as two point charges at a distance of 2*x* (**Equation 1.49**).[13]

$$F_{\text{imag}} = \frac{-q^2}{16\pi\varepsilon_0 x^2} \tag{1.49}$$

where ε_0 is the vacuum permittivity and *q* the elementary charge. When an electrical field *E* is applied to the metal/OSC junction, the potential energy *P(x)* of the band (e.g. VBM or CBM) is the sum of field strength and potential energy of an electron residing at distance *x* from the electrode (**Equation 1.50**).

$$P(x) = \frac{-q^2}{16\pi\varepsilon_0 x^2} - q|E|x \tag{1.50}$$

The maximum energy $\Delta\phi_B$, by which the barrier ϕ_B is lowered compared to the theoretical absence of any image force in a semiconductor is given by:

$$\Delta\phi_B = 2|E|x_{\text{m}} \tag{1.51}$$

where x_m the maximum of $P(x)$, which is located at:

$$x_m = \sqrt{\frac{q}{16\pi\varepsilon_{OSC}\varepsilon_0|E|}} \tag{1.52}$$

here, ε_{OSC} is the semiconductor permittivity. If charge carriers possess sufficient thermal energy, they can overcome the barrier ϕ_B-$\Delta\phi_B$ and are injected into the semiconductor. The schematic metal/semiconductor interface energetics and lowering of ϕ_B by image force are depicted in **Figure 1.19a**. Compared to Richardson-Schottky thermionic emission with barrier lowering, in metal/OSC interfaces distributed localized states have to be accounted for.[149] In a nutshell, thermally activated charges are injected the tail states of a Gaussian DOS, from where it performs a random walk under the influence of the image force coulomb potential and external potential (**Figure 1.19b**).[150]
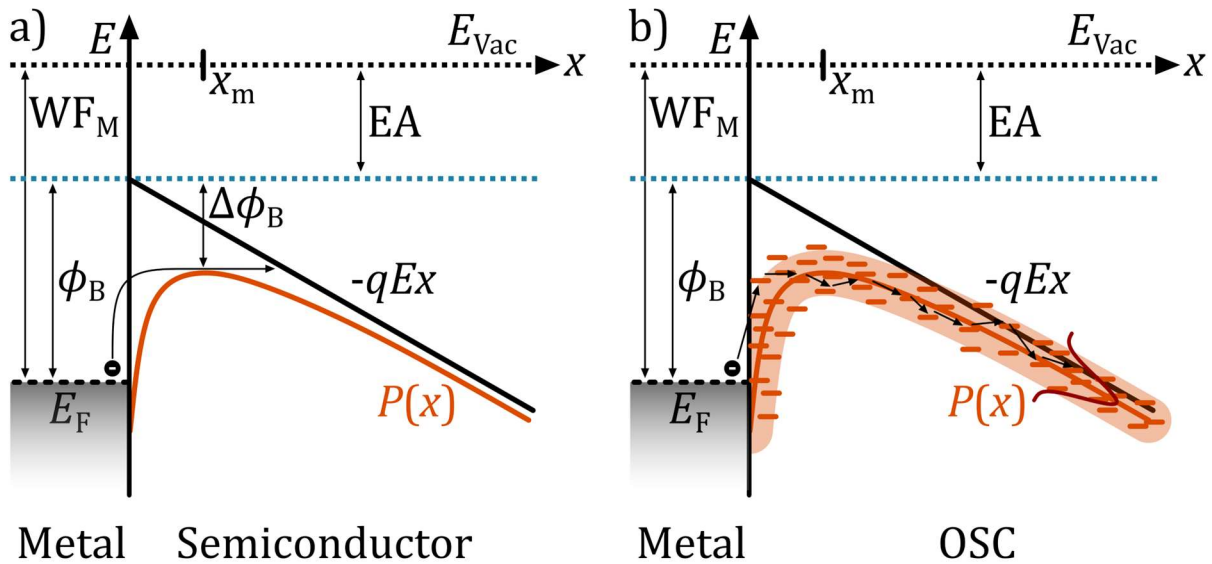
Figure 1.19. a) Energy level diagram of a metal/semiconductor junction with electron injection from metal with Fermi level E_F into the semiconductor with electron affinity EA. Schottky barrier ϕ_B is lowered by the image force by $\Delta\phi_B$. The total potential energy is given by $P(x)$, the applied electrical field by $-qEx$. The maximum of $P(x)$ is reached at a distance x_m from the metal electrode. b) Energy level diagram of a metal/OSC junction with injection of charges into a disordered semiconductor with Gaussian DOS (dark red) and potential $P(x)$. Note, that the charge carrier hopping events are distributed among the DOS. Adopted from Ref.[51]

1.3 Fundamentals of doping of organic semiconductors

As demonstrated in **Chapter 1.2**, organic semiconductors without any doping are of intrinsic nature. Control over the conduction properties of any semiconductor, which is mutually interconnected with the position of the Fermi level and charge carrier density, transforms the insulating OSC into a finely tuneable material. In fact, even though aniline derivatives such as dyes or its oxidation products are known for more than 100 years, intensive research on conductive polymers obtained from conjugated polymers dates back to the 1970s.[151,152] This class of materials is still very relevant as of 2022.[152] Although the synthesis of highly conductive polymers is known for a very long time, enhancing the carrier density of semiconducting pristine OSCs remains an challenge up to this day. Recently, significant progress on device performance and engineering by *doping* organic semiconductors has been made in the field of organic light emitting diodes, field-effect transistors, organic/inorganic hybrid solar cells and organic electrochemical transistors.[153–157] In the process of *doping*, the OSC undergoes a redox reaction or adduct formation with a *dopant*, ultimately leading to an enhanced majority carrier concentration accompanied by a shift of the Fermi level towards LUMO (*n*-doping) or HOMO (*p*-doping). Simplified, electrons are removed from the OSC HOMO and accepted by the *p*-dopant, or electrons are added to the OSC LUMO from the *n*-dopant. Besides few exceptions which will be discussed later in this section, two general doping mechanisms have been accepted today. First, if an integer number of electrons is transferred from OSC to dopant and *vice versa*, driven by an energy difference between the involved orbitals, the mechanism is known as *integer charge transfer* or *ion-pair formation* (abbr. IP).[158–164] Basic requirement for a *p*-type IP process is the EA of the dopant to be situated higher in energy than the OSC IE. Likewise, in the case of *n*-type doping, electrons are donated from the dopant IE lower in energy than the OSC EA (**Figure 1.20a**).
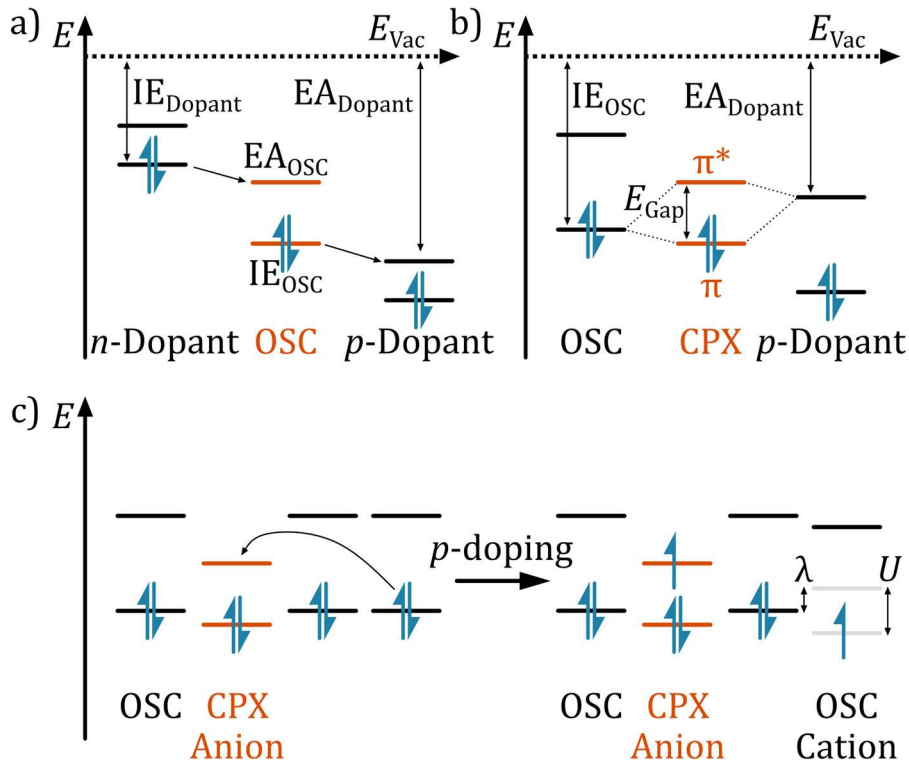
Figure 1.20. Schematic representations of the ion-pair formation doping (IP) process a) and charge transfer complex (CPX) formation b). The CPX process ultimately leads to the generation of free charge carrier by accepting electrons into the newly formed antibonding orbital of the CPX for *p*-doping c). The on-site Coulomb interaction U may cause splitting of the oxidized OSC HOMO into sublevels, as proposed by Koch et al.[175] Adopted from Refs.[81,158,165]

The IP process was employed to explain the prototypical systems P3HT *p*-doped with tetracyanoquinodimethane as well as various thiophene based donor-acceptor copolymers and small molecule triphenylamine derivatives.[160,165–167] After the initial electron transfer process, the formed ion pair is bound by electrostatic interactions. Typically, the binding energy is as high as several 100 meV, far higher than the thermal energy available at room temperature (k_BT ≈ 26 meV). Consequently, only a small fraction of the ion pairs dissociates to yield mobile and free charge carriers responsible for bulk electric current measurable.[168–170] However, energetic- (see **Section 1.2.1**) as well as morphological disorder and disorder induced by the doping process itself have been speculated to lower this value; enabling room temperature dissociation of the dopant:OSC ion pair.[79,171–173] During *p*-doping, an electron is removed from the OSC HOMO,

effectively forming a singly-occupied molecular orbital (abbr. SOMO). Likewise, a SOMO is formed after adding an electron to the antibonding LUMO during n-doping. The doping process concurs with OSC lattice reorganisation and bond length adaptation, i.e. the SOMO is a polaronic state in OSCs.[174] Removing or adding a second electron from the SOMO forms a bipolaron, where two charges are residing on one site. Koch et al. proposed a splitting of the OSC cation SOMO into an unoccupied sublevel situated above the HOMO of the neutral OSC, and a singly occupied sublevel below (**Figure 1.20c**). On-site Coulomb interaction U as well as lattice relaxation λ upon oxidation (in the case of a positive polaron) was brought forward as a root cause.[81,175] While it is conceptually easy to understand, that the ionization energy a cation is higher than the ionization energy of a neutral molecule - which leads to the downshift of the SOMO compared to the neutral OSC HOMO – the presence and nature of the upshifted unoccupied level remains under debate as of 2024.

Tietze et al. studied the underlying statistics of co-evaporated IP systems and proposed three distinct regimes based on the ratio of dopant and Fermi level position.[47,176] Starting from the pristine OSC with E_F located mid band gap, initial addition of a dopant causes the Fermi level too shift towards the HOMO (for p-doping). As explained in **Section 1.2.3**, hole traps are typically located lower in energy then the VBM (**Figure 1.15**). As E_F approaches E_t, the trap states are being oxidized and therefore passivated (i.e., these sites are then already occupied by hole), hence why it is named *trap-filling* regime. In this regime, all introduced holes are consumed by the traps without forming free holes in the OSC bulk. As these localized tail states have negative impact on carrier mobility, filling them greatly increases the OSC performance in device heterojunctions and transistors.[177–179] Due to the low density of trap states ($10^{17} – 10^{19}$ cm^{-3}) in the DOS, ultralow doping levels < 1 mol% are sufficient to reach the trap-filling regime, as demonstrated on ruthenium(pentamethylcyclopentadienyl)(1,3,5-trimethylbenzene) dimer doped C_{60} by Olthof et al.[180,181] Once E_F has crossed E_t in the *dopant saturation* regime, further added dopant molecules create free holes in the HOMO of the OSC. At high doping concentrations the *dopant reserve* regime is reached, the position of E_F saturates and is pinned at the transport energy of the HOMO.[182] Concurrently, the high number of ionized dopants leads to an increased number of free hole capture processes. Hence, the doping efficiency drastically reduces in the dopant reserve regime, experimentally confirmed by

Tietze et al. employing ultraviolet photoelectron spectroscopy (abbr. UPS) studies on p-doped N,N,N',N'-tetrakis(4-methoxyphenyl)benzidine.[47]

Once hybridization between OSC and dopant frontier orbitals play a major role and form new bonding and antibonding states, the mechanism is known as *charge transfer complex formation* (abbr. CPX).[165,183–187] Hybridization may also occur, if EA of the dopant is situated lower in energy than the OSC IE for p-type doping, which is one of the main advantages over the IP process.[81,165,188] *Via* linear combination of the OSC molecular orbitals, new bonding and antibonding CPX orbitals are formed (**Figure 1.20b,c**).[189] Méndez et al. showed, that the energy gap E_{Gap} between HOMO$_{CPX}$ and LUMO$_{CPX}$ can be estimated based on a Hückel model (**Equation 1.53**).[188]

$$E_{Gap} = 2\sqrt{\left(HOMO_{OSC} - LUMO_{Dopant}\right)^2 + 4\beta^2} \tag{1.53}$$

Hence, the CPX energy gap depends on both the OSC HOMO and dopant LUMO position (for p-type doping), as well as the resonance integral β, which represents the amount of intermolecular coupling between dopant and OSC. For quaterthiophene doped with 2,3,5,6-tetrafluoro-7,7,8,8-tetracyanoquinodimethane (abbr. F$_4$TCNQ), an E_{Gap} of 0.9 eV was reported.[165] As the charge (electrons residing in the OSC HOMO) is effectively shared in the CPX between OSC and p-dopant, it is referred to as fractional charge transfer.[189] However, this initial fractional charge transfer does not yield mobile free charge carriers. Instead, the newly formed CPX is charge neutral and requires additional activation steps to generate free charge carriers.[81] In the case of p-doping, the empty antibonding CPX state above the OSC HOMO DOS accepts electrons from a nearby neutral OSC, a thermally activated process (**Figure 1.20c**).[81] It is this OSC cation, which ultimately leads to an enhanced bulk conductivity. Compared to IP, a CTC typically results in a lower fraction of OSC molecules ionized, as E_{Gap} is larger than the available energy at room temperature, hence only a small fraction of the antibonding CPX orbital is occupied (for p-type doping).[190] As of 2022, no clear guidelines are established, whether an OSC:dopant system can be assumed to follow either IP or CPX processes. However, co-facial alignment between OSC and a planar dopant such as F$_4$TCNQ seems to facilitate CPX formation.[189] This has been observed in conjunction with quaterthiophene, 2,7-didecyl[1]benzothieno[3,2-b][1]benzothiophene, tetrathiafulvalene and thiophene-based quinoxaline copolymers.[160,165,188,191] Bulkier dopants such as C$_{60}$F$_{36}$, an increasing

chain length for polymer OSCs, mild processing conditions (e.g. lower temperature, lower solvent polarity) tend to facilitate IP.[38,192–195]

A series of doping pathways aside from pure charge transfer have been described in literature, which do not fall in line with IP or CPX formation. One historically important case is Brønsted acid doping, where protonating the OSC by strong acids introduces a positive charge. The protonation step can be followed by a hole transfer from OSC-H$^+$ to a neutral OSC, generating a radical cation and polaron.[196] Introduced in 1985 as a viable tool to enhance to conductivity of poly(aniline), modern acid doping approaches involve 4-ethylbenzenesulfonic acid for thienothiophene copolymers and mineral acid doped poly(3,4-ethylenedioxythiophene):poly(4-styrene sulfonate) materials.[197–199] Hydride doping has been observed for the dopant 4-(2,3-Dihydro-1,3-dimethyl-1H-benzimidazol-2-yl)-N,N-dimethylbenzenamine, n-doping the OSC *via* hydride transfer. The exact mechanism, possibly involving additional hydrogen atom and electron transfer, is still under debate.[200,201] Lewis acids and bases enjoy a much greater popularity among research groups, owing to their broader OSC compatibility. Common Lewis acids include trimethylaluminium, boron trichloride, boron trifluoride, tris(pentafluorophenyl)borane and tris(pentafluorophenyl)alane, which have been extensively researched for donor-acceptor small molecules by Welch et al.[202] Recent studies focus on tris(pentafluorophenyl)borane, mostly due to the low LUMO energy, hydrophobic nature and solubility in common organic solvents.[156,203,204] Current findings by Yurash et al. suggests the formation of a water-Lewis acid complex protonating the OSC (where water acts as a Lewis base), generating a positively charged polaron.[46] Using Lewis bases, n-doping can be realised. Russ et al. introduced a general Lewis base n-doping concept for [6,6]-phenyl-C$_{61}$-butyric acid methyl ester, naphthalene diimide and diketopyrrolopyrrole small molecules using tethered tertiary amines.[205] The concept was expanded to donor-acceptor copolymers, which can be efficiently n-doped using lithium benzoate, tetrabutylammonium hydroxide and various tetraalkylammonium halide salts.[206–210] In **Figure 1.21**, the most common p- and n-type dopants are categorized based on their frontier orbital energy levels.
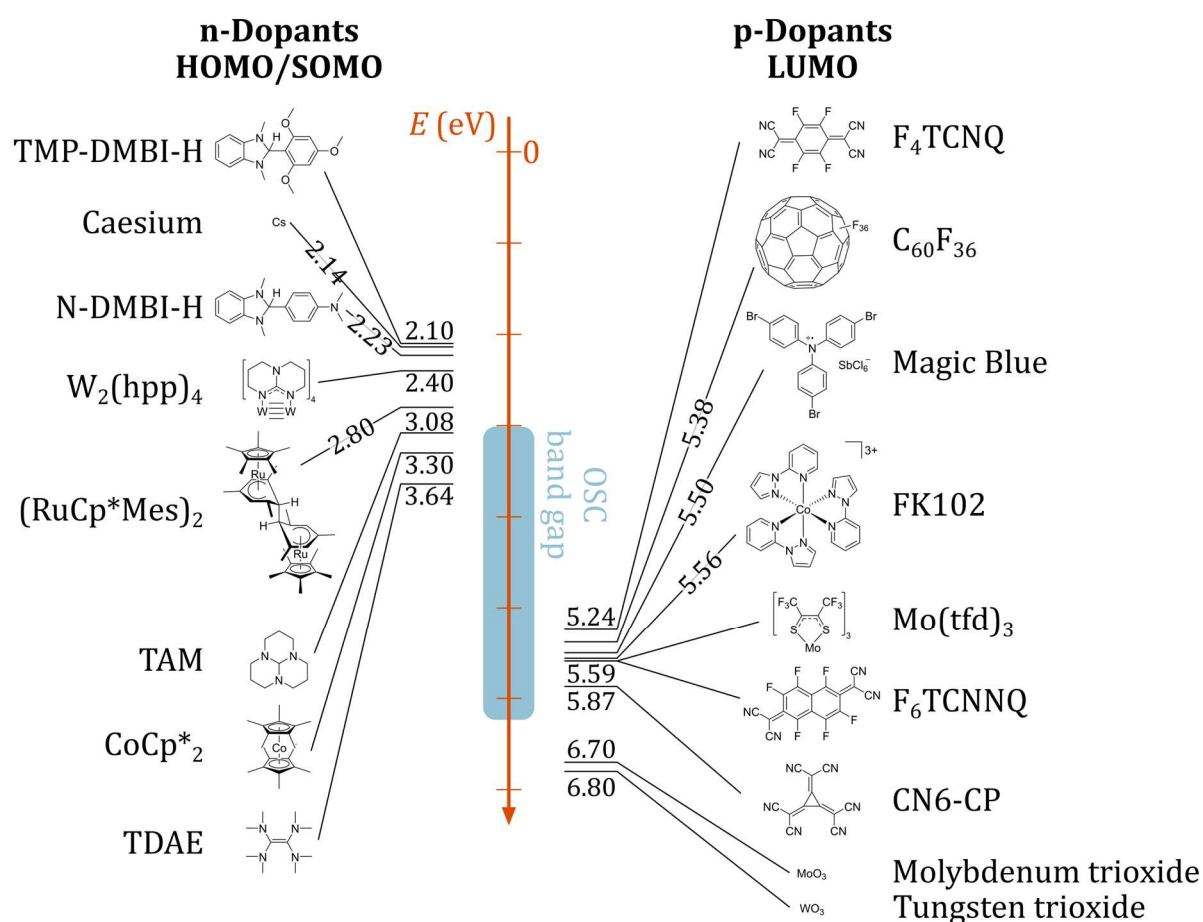
Figure 1.21. Overview of the HOMO, resp. SOMO values of common *p*-type dopants and LUMO values of *p*-type dopants. Values taken from Refs.[200,211–226] The HOMO value of FK102 was converted from cyclovoltammetry half wave potential vs. normal hydrogen electrode potential. For TMP-DMBI-H, N-DMBI-H and TAM, the SOMO values after hydrogen radical abstraction from the dopant molecule are shown. The blue-shaded region marks the typical band gap of the OSCs.

Doping OSCs is a process requiring careful control over the reaction conditions. The amount of dopant in the OSC can be calculated by considering the molar ratio MR, where n_{Dop} are the moles of dopant and n_{OSC} the moles of OSC (**Equation 1.54**). For polymeric OSCs with a broadly distributed molecular weight, typically the molar mass of the repeating unit is used in this calculation.

$$\text{MR} = \frac{n_{\text{Dop}}}{n_{\text{OSC}}}$$

(1.54)

MR can be converted to doping (or molar) concentration c_{Dop} by **Equation 1.55**.[227]

$$c_{Dop} = 100\% \frac{MR}{MR + 1} \tag{1.55}$$

After a certain MR of dopant is fed into the system, the doping efficiency η_{Dop} can be used to quantify the efficiency of the doping reaction. It describes the ratio of free charge carriers N_{Free} to total number of dopant molecules N_{Dop} in the OSC. Aforesaid, doping in OSCs generally is a two-step reaction. Consequently, η_{Dop} is the product of both initial ionization $\eta_{Ionization}$ and ion-pair dissociation $\eta_{Dissociation}$ efficiency (**Equation 1.56**).[228]

$$\eta_{Dop} = \eta_{Ionization}\eta_{Dissociation} = \frac{N_{Free}}{N_{Dopant}} \tag{1.56}$$

1.3.1 Preparation of doped organic semiconductors

To prepare doped OSC materials for e.g., device applications, appropriate doping reaction conditions must be selected. Contrary to inorganic semiconductors with doping levels ranging from parts per thousand (degenerate doping) to parts per billion (low doping), organic semiconductors may require several tens of mole percent to achieve appreciable conductivity.[168,229,230] Correspondingly, preparation methods have a profound impact on the device performance, as the dopant has to be incorporated without disrupting the OSC microstructure or provoking phase separation. For sublimable small molecule OSCs, a common method is vacuum co-deposition *via* physical vapor deposition. Here, both OSC and dopant are loaded into separate crucibles (effusion cells) facing the sample surface to be coated in a distance of ca. 10-100 cm in a vacuum chamber. Typically, the chamber is pumped down to ca. 10^{-5} mbar or less to increase the mean free path of the evaporated or sublimed molecule. The crucibles are heated above the sublimation, resp. melting temperature of the materials, creating a flux of material directed towards the sample, at which the OSC and/or dopant get mixed up in the gas phase and is re-deposited due to the lower surface temperature.[231] Placing shutters above the crucibles or controlling the temperature allows to fine-tune the ratio of OSC and dopant emitted from both crucibles, effectively changing the doping concentration in the deposited bulk material. Zhou et al. prepared hole injection layers for organic light emitting diodes using 4,4′,4″-tris(N,N-

diphenyl-amino)triphenylamine co-evaporated with F$_4$TCNQ, lowering the driving voltage and increasing the efficiency.[144] Using segmented shutters, the OSC and dopant can be co-evaporated with molar ratios as low as 10^{-5}, enabling far greater control than solution based techniques.[176]

Due to the simplicity, solution doping is a popular approach for both polymeric and small molecule OSCs, especially in solution processed devices.[232,233] Here, both OSC and dopant are dissolved in separate stock solutions. Upon adding the required amount of dopant stock solution, stirring/mixing allows OSC and dopant to react and often distribute homogeneously. In this context, a similar polarity or complementary structural features favour uniform mixing. Subsequent thin film deposition *via* e.g. spin-coating yields OSC films of uniform morphology. This approach has been successfully applied to *p*-dope a wide range of polymers, *inter alia*, poly(3-hexylthiophene) and poly(9,9-dioctylfluorene-*alt*-benzothiadiazole) with F$_4$TCNQ; enhancing the conductivity by several orders of magnitude.[234] Under anhydrous conditions, *n*-doping of a small molecule with 4-(2,3-dihydro-1,3-dimethyl-1*H*-benzimidazol-2-yl)-N,N-dimethylbenzenamine (abbr. N-DMBI) derivatives can be achieved.[235] Major drawbacks include doping induced phase segregation in polymer semiconductors and low solubility of some dopants, such as F$_4$TCNQ.[236,237] To overcome these drawbacks, sequential doping techniques were introduced. In a sequential doping method, the film preparation step of the OSC and doping reaction are separated, allowing for higher quality films than simultaneous deposition, especially for immiscible dopants. The doping process can be conducted by immersing the OSC film into a dopant solution, spin-coating or thermal evaporation.[238–240] If solution based techniques are employed, care must be taken to ensure the solvents are orthogonal to each other.[241] Additionally, a lateral gradient in doping concentration can be introduced by controlling the dopant diffusion, which was demonstrated for poly[2,5-bis(3-tetradecylthiophen-2-yl)thieno[3,2-*b*]thiophene] doped with F$_4$TCNQ.[242] By separating the dopant ions (e.g. F$_4$TCNQ$^-$ after IP process) from the polymer OSC crystallites, a 3-15 times higher conductivity compared to solution doping was achieved in poly(3-hexylthiophene).[236] Another method to exclude chemical dopants and their potential harmful side products from the OSC bulk is electrochemical doping. The OSC is deposited on a conductive substrate and placed inside an electrochemical cell. This cell is equipped with a platinum counter electrode, a reference electrode and an electrolyte. Using an external potentiostat, the potential applied at the OSC can be tuned to force the

bulk to undergo redox processes, being either oxidized (*p*-doped) or reduced (*n*-doped). To maintain charge neutrality, the holes or electrons in the OSC are compensated by counter ions from the electrolyte. Due to the high level of control, electrochemical doping was used to study fundamental properties of doped semiconductors like poly(benzimidazobenzophenanthroline) and polypyrrole for thermoelectric applications.[243,244] Further, electrochemical doping is the key working principle of organic electrochemical transistors, i.e. the conductivity of an OSC channel material between source and drain electrode is controlled *via* selective electrochemical oxidation/reduction. Hence, this method enables high transconductance devices, chemical sensors and dual-mode transistors by de-doping self-doped polymeric OSCs.[157,245,246] However this method is limited by the need for a wet electrochemical system, requires this additional doping step and is less suitable to dope bulk OSC material for large scale applications.

1.3.2 Importance of doped OSCs in OFET, OPV, TE and OECT

In general, doping increases the majority charge carrier concentration and enables efficient charge injection and -transport, properties fundamental for device engineering.[49] Therefore, doping has proven vital for the performance of modern OSC devices and applications.

Organic field effect transistors (OFETs): For solid state amplification and switching applications, OFETs are feasible. The basic setup of a bottom contact bottom gate OFET consists of interdigitated source and drain electrodes as well as an electrically isolated gate electrode modulating the field in the channel of the transistor (**Figure 1.22a**). By changing the applied gate voltage V_G, the carrier density at the isolator/OSC interface can be modulated, which controls the source-drain current I_D (identical to the accumulation regime in a MIS capacitor **Figure 1.8**). Efficient charge injection and low contact resistance at the source and drain electrodes is vital for OFET operation and is the focus of interest for many studies (see injection barrier in **Figure 1.17**).[247–250] Doping helps to minimize the contact resistance for certain metal-semiconductor material combinations and improves the charge injection. Ante et al. showed a significant decrease of the contact resistance from 660 Ω cm to 390 Ω cm in dinaphtho-[2,3-b:2',3'-f]thieno[3,2-b]thiophene

OFETs doped with NDP-9, a commercial dopant.[251] Similarly, the contact resistance for pentacene based OFETs was lowered by a factor of three upon introducing F$_4$TCNQ between OSC and Au electrodes.[252] Besides contact doping, OFET bulk doping (often called channel doping, as only a thin layer at the interface between isolator and OSC is responsible for the OFET operation) is used to tune the intrinsic majority carrier concentration N_A. This in turn directly influences the threshold voltage V_{Th}, the point at which the transistor turns on (**Equation 1.57**).[182]

$$V_{Th} \approx V_{Fb} + \frac{q N_A d_{Dop}}{C_{Ox}}$$
(1.57)

V_{Fb} is the flatband potential (i.e., the potential at which band bending is minimized, see **Figure 1.8**), q the elementary charge, d_{Dop} the thickness of the doped layer and C_{Ox} the oxide capacitance. Altering V_{Th} has great impact on OFET performance, especially for integrated circuits where well-defined turn-on voltages are required.[253] By increasing the channel hole concentration using a *p*-dopant in a *p*-channel OFET, V_{Th} typically shifts towards more positive values, which was shown for F$_6$TCNNQ doped pentacene OFETs by Liu et al. Using the *n*-dopant tetrakis(hexahydropyrimidinopyrimidine)ditungsten(II), they were also able to revert the V_{Th} trend towards more negative gate potentials.[254] Ma et al. could prove the same trend for *p*-doped polymeric OSCs. Using between 0.1 and 0.6 mol% F$_4$TCNQ, they were able to increase V_{Th} from -6.0 V up to 40 V. Simultaneously, a significant increase in mobility and on/off-ratio (ratio of source-drain current in the off vs. on state in OFETs) occurred, which they attributed to higher P3HT crystallinity and molecular orientation.[255] Summarizing, doping introduces unprecedented flexibility in tuning the switching behaviour of OFETs.
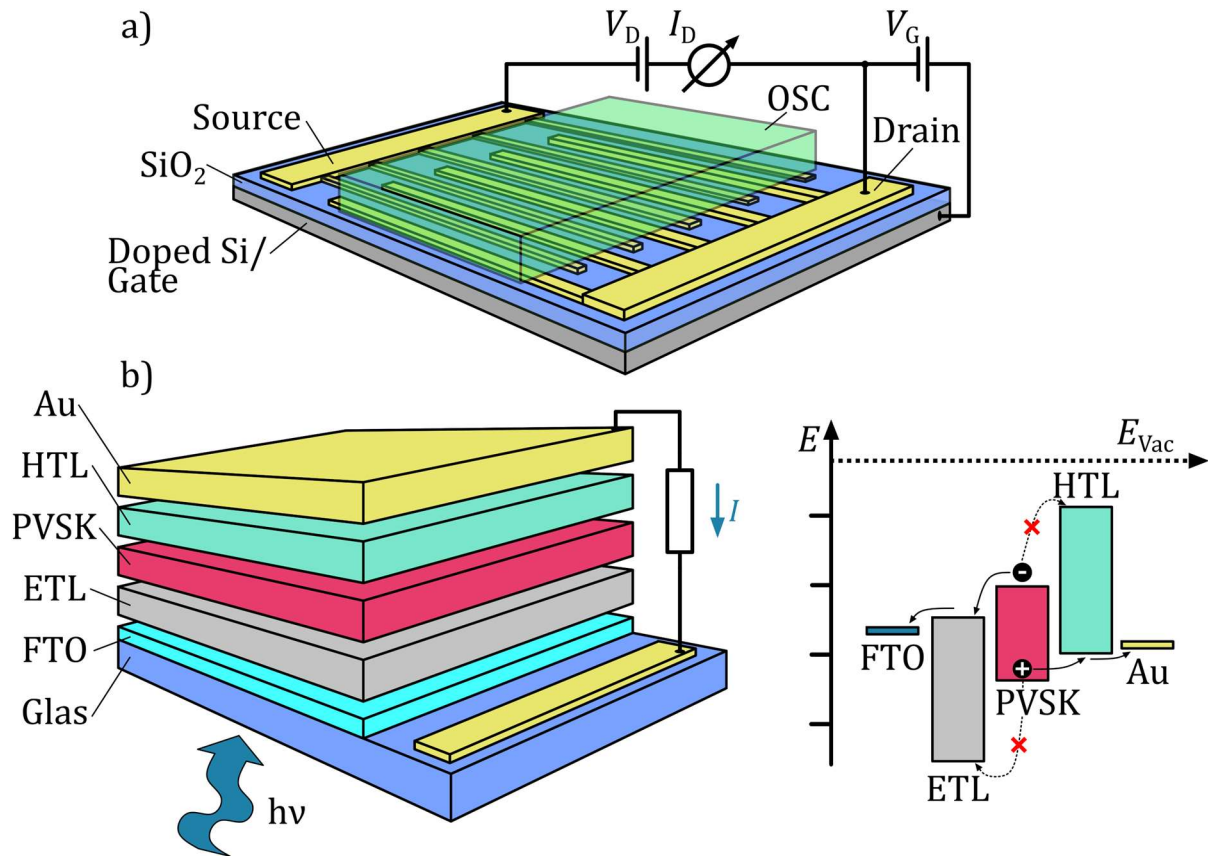
Figure 1.22. a) Schematic overview of an organic field effect transistor (OFET) in the bottom contact bottom gate configuration. b) Schematic stack of a perovskite (abbr. PVSK) solar cell with conductive transparent oxide (fluorine doped tin oxide, FTO), electron transport layer (ETL), hole transport layer (HTL) and gold top electrode. The HOMO and LUMO values of the electron- and hole transport layer are aligned, such that holes are blocked from being injected into the ETL and *vice versa*. Doping manipulates the HTL and ETL WF and can be used to tune the extraction and blocking behaviour.

Organic and hybrid organic/inorganic photovoltaic devices (OPV): These devices rely heavily on doped charge extraction layers (electron transport layer ETL and hole transport layer HTL) to improve the power output. This is achieved mostly by a complex interplay between increased conductivity, charge carrier mobility and alignment of the frontier orbitals at interfaces upon doping.[256] Whereas organic solar cells are based on OSCs for light absorption and exciton (coulombically bound electron-hole pair) generation, perovskite solar cells (PVSK) use perovskites of the formula ABX_3 as the absorption and charge generation layer. X typically is a halogen (Br, I, Cl), the octahedral B sites are occupied by divalent cations (often Pb^{2+} or Sn^{2+}) and the cuboctahedral A sites

consist of large cations, most often methyl ammonium.[257] Compared to inorganic semiconductors, perovskites offer unique properties: High absorption coefficients in the optical range, shallow trap states, solution processability and low exciton binding energy of ca. 16 meV for methyl ammonium lead iodide MAPbI$_3$ (organic heterojunctions: ca. 0.3-0.7 eV).[258–260] Hole transport layer (abbr. HTL) engineering is crucial for improving the fill factor and power conversion efficiency in both PVSK and fully organic solar cells (**Figure 1.22b**).[261,262] By doping the HTL, significant increases in electrical conductivity can be achieved, in combination with an adjustment of the HTL work function. Lowering of the HTL work function also helps to efficiently extract charges and increase the electron blocking behaviour. N2,N2,N2′,N2′,N7,N7,N7′,N7′-octakis(4-methoxyphenyl)-9,9′-spirobi[9H-fluoren]-2,2′,7,7′-tetramine, abbr. Spiro-MeOTAD, and its derivatives are one of the most widely used organic HTL materials based on triphenylamines.[263–266] Using 12 mol% of the *p*-dopant tris(4-bromophenyl)ammoniumyl hexachloroantimonate, Snaith et al. reported a 10 fold increase in hole mobility to $\mu_h = 1.6 \cdot 10^{-3}$ cm^2 V^{-1} s^{-1} compared to pristine Spiro-MeOTAD.[267] Adding 7.7 mol% tris(2-(1H-pyrazol-1-yl)-4-*tert*-butylpyridine)-cobalt(III)tris(bis(trifluoromethylsulfonyl)imide)) to Spiro-MeOTAD increases the conductivity by a factor of 280, in turn enhancing the power conversion efficiency from 5.0 % to 8.1 % by increasing the open circuit voltage of the cell (low charge extraction barrier).[268] Different doping approaches include molybdenum trioxide interface doping, F$_4$TCNQ doped Spiro-MeOTAD and the use of already doubly oxidized Spiro-MeOTAD(TFSI)$_2$.[269–271] For the electron transport layer (abbr. ETL), metal oxides like TiO$_2$, SnO$_2$ and ZnO have found their way into high performance perovskite solar cells.[272] Only few reports exist on doped organic ETLs. Xia et al. prepared [6,6]phenyl-C$_{61}$-butyric acid methyl ester (abbr. PCBM) ETL in a conventional methyl ammonium lead iodide solar cell. By adding (9*Z*)-octadec-9-enamide as a *n*-dopant, the short-circuit current drastically increased, leading to a power conversion efficiency enhancement from 10.05 % to 12.69 %.[273] By replacing (9*Z*)-octadec-9-enamide with N-DMBI, Kim et al. could boost the short-circuit current of PCBM ETL based perovskite solar cells from 19.1 mA cm^{-2} (no dopant added) to 21.3 mA cm^{-2} (5 wt% dopant).[274] To sum up, doping charge transport layers in photovoltaic devices enables OSCs to efficiently transform light into usable electrical energy.

Organic thermoelectric devices (TE): Recently, organic thermoelectric materials have gained significant scientific interest and breakthroughs.[275–277] Fundamentally, TE

materials can be used to convert heat dissipation (arising from a difference in thermal energy between two conductors) into electrical current *via* the Seebeck effect.[278] The performance of the material in TE applications can be classified by the figure of merit *ZT*, calculated from the Seebeck coefficient *S*, conductivity *σ*, temperature *T* and thermal conductivity κ (**Equation 1.58**).[279]

$$ZT = \frac{S^2 \sigma T}{\kappa} \tag{1.58}$$

As the in-plane thermal conductivity is often cumbersome to determine for thin film organic materials, the power factor *PF* is usually reported instead of *ZT* (**Equation 1.59**).[280]

$$PF = S^2 \sigma \tag{1.59}$$

Doping enables increased TE performance by leveraging *σ*. In addition, the Seebeck coefficient, a function of the energy difference between Fermi- E_F, which is charge carrier density dependent, and transport energy E_t can be effectively modulated by doping (**Equation 1.60**).[243]

$$S = \frac{k_B}{q} \frac{E_t - E_F}{k_B T} \tag{1.60}$$

In real-world TE devices, both *n*- (negative Seebeck coefficient) and *p*-type (positive *S*) OSCs are doped separately and later on combined to obtain a higher maximum output power. However, *S* and *σ* are inversely proportional, connected by the empirical relationship $S \propto \sigma^{-1/4}$.[281] Hence, highly controlled doping processes must be employed to obtain a maximum in ZT. For *p*-type OSCs, poly(3,4-ethylenedioxythiophene) (abbr. PEDOT) is one of the most popular choices for TE devices, as it can be efficiently *p*-doped using poly(4-styrene sulfonic acid) PSS, reaching record ZT values of 0.42.[282–284] The concept of controlled doping for TE enhancement can also be applied for donor-acceptor copolymers. Wu et al. noted, that by changing the *p*-dopant from F4TCNQ (E_{LUMO} = -5.24 eV) to CN6CP (E_{LUMO} = -5.87 eV), the PF of the thieno[3,4-*b*]thiophene based donor-acceptor copolymer PTbTTVT could be increased from 5.6 to 42.8 µW m^{-1} K^{-2}. They argue,

that by using a *p*-dopant with deeper LUMO level, the driving force for electron transfer from polymer HOMO and consecutively σ is higher.[285] For selenium-substituted diketopyrrolopyrrole donor-acceptor copolymers, *p*-doping *via* immersion in $FeCl_3$ solution leads to a maximum PF of $364\,\mu W\,m^{-1}\,K^{-2}$. Together with the low thermal conductivity, a record ZT value of 0.22 ± 0.03 at 55 °C was obtained, which is partially attributed to the increased ordering in the polymer and doping capabilities of $FeCl_3$.[286] Recently, the attention has shifted towards hybrid materials incorporating carbon nanotubes and OSCs. Ito et al. demonstrated, that by *n*-doping a carbon nanotube-poly(ethylene glycol) composite with 1-butyl-3-methyl-imidazolium-hexafluorophosphate, a highly flexible TE generator could be obtained.[287]

By careful selection of the dopant, *n*-type TE operation can be optimized as reported by Un et al. The fluorinated donor-acceptor copolymer FBDPPV was treated with the *n*-dopants N-DMBI, a dimeric derivative $(N\text{-}DMBI)_2$ and the *n*-dopant $(RCp^*mes)_2$. Compared to conventional N-DMBI reaching $5\,\mu W\,m^{-1}\,K^{-2}$ at 30 mol%, $(N\text{-}DMBI)_2$ yields a PF of $7\,\mu W\,m^{-1}\,K^{-2}$ at 10 mol% dopant. This is achieved by the higher reducing capability and less microstructure disruption of the polymer by using $(N\text{-}DMBI)_2$.[288] Hence, the fine interplay between Seebeck coefficient and electrical conductivity can be manipulated by doping to create novel high performance TE materials.

Organic electrochemical transistors (OECTs): Signal switching and amplifying devices play a huge role in our everyday life. Conventional OFETs rely on the field effect to enhance the free carrier concentration in the channel, thus modulating the source-drain current. In 1984, White et al. introduced an alternative to the OFET, the organic electrochemical transistor (abbr. OECT).[289] It can be understood as an OFET, where the insulator is replaced by an electrolyte capable of penetrating the bulk OSC (**Figure 1.23**).[290]
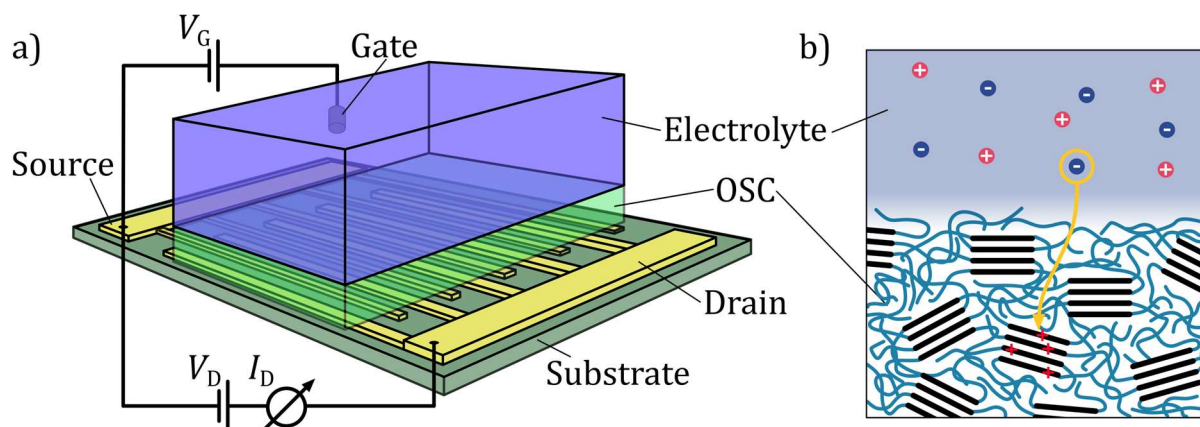
Figure 1.23. a) Schematic overview of an organic electrochemical transistor (OECT). The electrolyte is in contact with the OSC, the gate voltage V_G is applied at the gate electrode situated inside the liquid electrolyte. b) Schematic overview of the interface reactions between electrolyte and OSC. Upon oxidizing (*p*-doping) the OSC by applying a negative V_G, counterions from the electrolyte can drift into the OSC *via* amorphous regions to compensate the polaron charges. Adopted from Refs.[291,292]

Hence, the source-drain current I_D can be controlled by V_G which electrochemically dopes the OSC. One of the key advantages compared to OFETs are i) the low threshold voltage, i.e. the gate voltage, which has to be supplied in order for current to flow between source and drain and ii) sensitivity to ions in the OSC bulk.[293,294] This makes OECTs highly competitive in the field of bioelectronics, where aqueous systems dominate and voltages < 1 V are required to prevent electrolysis and cell damage.[295–297] As ions penetrate the OSC bulk, a concurrent transport of both ions and electrons/holes (termed *mixed conduction*) is crucial for the OECT performance.[298] Strategies for mixed conduction in OSCs include doped conjugated polyelectrolyte blends (e.g. PEDOT:PSS), conjugated polyelectrolytes such as poly[6-(thiophen-3-yl) hexane-1-sulfonate tetraalkylammonium] (abbr. PTHS) or donor-acceptor copolymers with ion compatible ethylene glycol side chains.[290,291,299,300] The ability of the OECT to convert a potential stimulus into a drain current variation can be quantified by the transconductance g_m, which is defined as $\Delta I_D / \Delta V_G$.[301] OSCs enabling high g_m are therefore highly sought after material classes. Intrinsically doped PEDOT, in which charges are compensated by poly(4-styrene sulfonate) allows the OECT to be fully conductive without applying V_G. Upon switching to a positive V_G, the PEDOT is de-doped and reverted back a non-conductive state. This OECT behaviour with conductive polymers is known as *depletion mode*. Keene

et al. de-doped PEDOT using secondary and tertiary amines for *enhancement mode* OECTs. Here, the OECT is switched off without gate bias, showing no loss in long-term stability (> 1000 operational cycles) nor mobility (ca. 2 cm^2 V^{-1} s^{-1}) compared to PEDOT:PSS OECTs.[302] Anchoring the counterions to the side chain of a conjugated polymer produces self-doped conjugated polyelectrolytes, which eliminates the need for e.g. PSS. Nguyen-Dang et al. showed, that this type of doping enables the OECT to operate in both enhancement- and depletion mode by switching the polarity of drain-source voltage and V_G.[246] A similar concept was used by Inal et al., who introduced an OECT based on PTHS. This self-doped P3HT derivative enables a high g_m of $(2.0 \pm 0.2)\,\mu$S in enhancement mode.[303] Hence, de-doping offers a great potential to switch the current voltage characteristics of conductive polymer OECTs. PSS may also be substituted by *p*-toluene sulfonic acid (abbr. TOS), *p*-doping PEDOT to yield PEDOT:TOS. Jimison et al. used PEDOT:TOS poly(ethylene glycol) composite OECTs and found excellent biocompatibility with mammalian cells while maintaining a g_m of 768 μS.[304] *n*-type OSCs have been used in OECT applications, albeit suffering inherent instability towards water and air. This is caused by low lying LUMO energies, rendering the reduced state highly susceptible towards water or oxygen reduction.[96] By *n*-doping a naphthalene diimide bithiophene donor-acceptor copolymer with tetra-*n*-butylammonium fluoride, Paterson et al. demonstrated a transconductance increase from 1.8 μS to 10.5 μS as a result of higher mobility. After doping, g_m retains 97 % of its initial value after storage in phosphate-buffered saline solution for 132 days – a record shelf-life for *n*-type OECTs as of 2023.[305] In a nutshell, doping offers great potential to enhance the performance of OECTs by increasing stability, transconductance and the possibility to modify their mode of operation. Doping is not limited to OECTs, but drastically impacts a majority of devices incorporating OSCs today, highlighting the importance of this research field.

1.4 Photoelectron spectroscopy

At the heart of each photoelectron spectroscopy (abbr. PES) experiment is the *photoelectric effect*. It was discovered by Heinrich Hertz in 1887 while studying the impact of ultraviolet light on the spark length between different metal electrodes.[306] Albert Einstein later explained, that upon irradiation of matter with sufficient quantized photon energy, (photo)electrons are emitted with a kinetic energy E_{Kin}.[307] PES measures the photoelectrons angle, E_{Kin} and intensity to gain information about the samples composition and density of states.[308] For that, the sample surface is irradiated with monochromatic photons of known energy. This source differentiates the two main PES experimental setups: *X-Ray photoelectron spectroscopy* (abbr. XPS) and ultraviolet *photoelectron spectroscopy* (abbr. UPS). The former commonly utilizes Mg Kα (1253.6 eV) and Al Kα (1486.6 eV) X-Rays to excite the sample surface.[309,310] Here, K denotes the principal quantum number *n* of the vacant level (K = 1, L = 2, M = 3, etc.), which is created upon ejection from an electron of the metals inner shell. α denotes, that the electron filling the vacant state originates from *n*+1 = 2 (L-shell).[311] In a UPS setup, ultraviolet radiation produced by electrical gas discharge lamps excite the sample. These lamps emit mostly He(I) (21.22 eV) and He(II) (40.81 eV) lines. As UPS radiation energy is only a fraction of the X-Ray source, different states in the sample are excited: XPS ionizes mostly core electrons, whereas UPS is used to study the valence shell electrons (lowest binding energy).[312] Upon generation, the radiation enters a ultra-high vacuum chamber (< 10^{-8} mbar) and is focussed on the sample surface at an incident angle α. The photoelectrons emitted at a take-off angle θ are then collected by an electrostatic energy analyzer, which separates the electrons based on their kinetic energy. Finally, a detector integrates the intensity of the photoelectrons (**Figure 1.24**).[313,314] Besides photoelectrons, interaction of matter in vacuum with X-Rays additionally produces Auger electrons and causes X-Ray fluorescence, which can be analysed but are not subject of this paragraph.[311] In a nutshell, Auger lines are produced by a double ionization process. Upon photoionization, the vacancy on the inner shell gets filled by an outer shell electron. The excess energy causes a second electron from the outer shell to be ejected and detected by PES.[315]
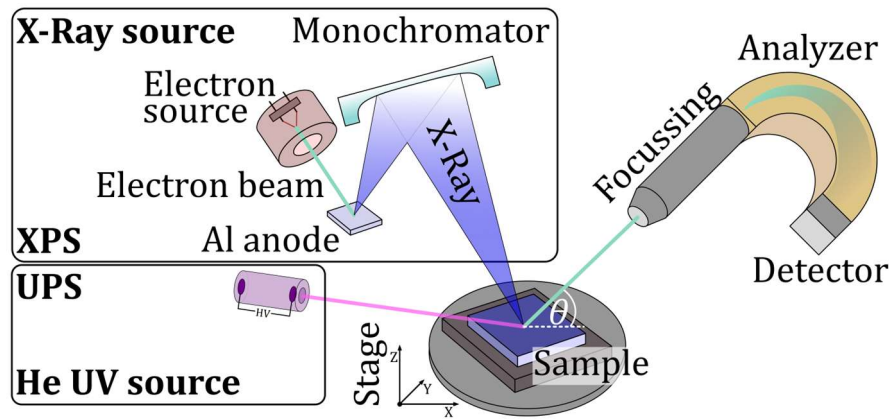
Figure 1.24. Schematic overview of a combined X-Ray- and ultraviolet photoelectron spectroscopy (XPS/UPS) setup. All parts shown operate under ultra-high vacuum. Adopted from Ref.[314]

If we consider energy conservation, the kinetic energy E_{Kin} of the emitted photoelectrons can be calculated from the excitation source wave length v, the binding energy E_{Bind} and sample work function ϕ_{Sample} (**Equation 1.61**).[316,317]

$$E_{Kin} = \hbar v - \phi_{Sample} - |E_{Bind}| \qquad (1.61)$$

where $\hbar$ is the Planck constant divided by 2π (or reduced Planck constant). Hence, for a photoelectron to be emitted from a sample with a kinetic energy E_{Kin}, it has to overcome the binding energy (difference between excited state and Fermi energy) and work function. The surplus energy is then translated to E_{kin}. This photoelectric effect in PES experiments can be modelled by three distinctive steps: i) photoexcitation of the state, followed by ii) movement of the generated electrons to the sample surface and iii) photoelectron emission into vacuum.[318] In a real-world experimental PES setup, the detector work function $\phi_{Detector}$ may not be identical with the sample work function, due to being constructed from dissimilar materials.[319,320] Especially in the case of UPS, the electrically conductive sample is connected to the metal body of the spectrometer. This causes the Fermi energies of the sample and spectrometer/detector to align, which induces a vacuum level shift from sample to spectrometer (**Figure 1.25**).
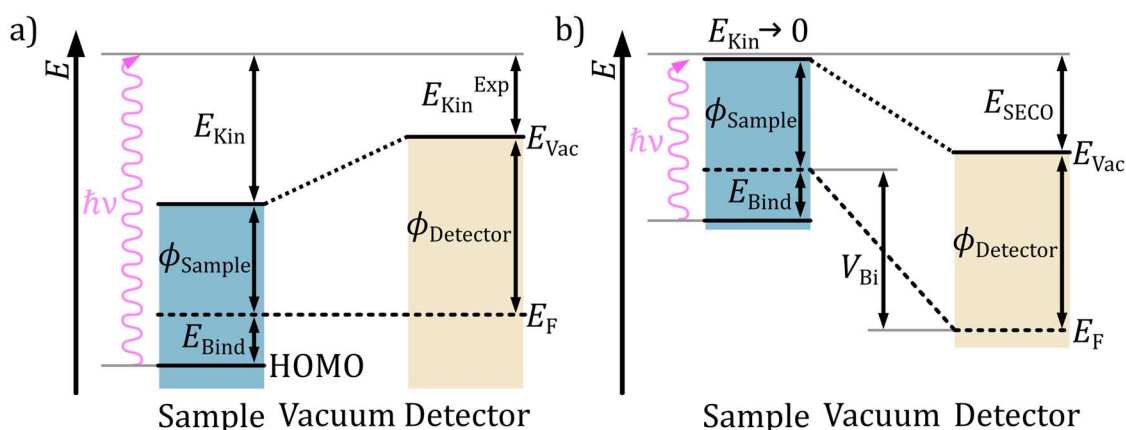
Figure 1.25. a) Schematic energy diagram of a sample, which is electrically connected to the detector of a photoelectron spectrometer (causing Fermi energy alignment). The photoelectron emitted with a kinetic energy E_{Kin} is experimentally observed having the apparent kinetic energy E_{Kin}^{Exp} if the detector work function $\phi_{Detector}$ is different from the sample work function ϕ_{Sample}. b) Application of an external bias voltage V_{Bi} to accelerate photoelectrons of low kinetic energy towards the detector. This allows the secondary electron cut-off (SECO) to be detected. Adopted from Refs.[319,320]

Thus, the apparent kinetic energy E_{Kin}^{Exp} detected by the PE spectrometer is smaller than the real kinetic energy E_{Kin}, if the detector work function is greater than the sample work function (**Figure 1.25a**). This causes E_{Bind} in a PES experiment to be dependent of $\phi_{Detector}$ instead of ϕ_{Sample} (**Equation 1.62**).

$$|E_{Bind}| = \hbar\nu - \phi_{Detector} - E_{Kin}^{Exp} \tag{1.62}$$

$\phi_{Detector}$ can be calibrated by measuring the Fermi edge (photoelectrons with highest kinetic energy) of reference metals.[314] Finally, from the known incoming photon energy $\hbar\nu$ and $\phi_{Detector}$, the E_{Bind} is obtained. Usually, the intensity of emitted photoelectrons vs. binding energy is plotted after a successful PES experiment. The outcome of this experiment can be used to analyse the composition and binding states of the sample. E_{Bind} obtained from a typical XPS experiment can be related to the orbital energies of the states *via* the *Koopman theorem*. It states, that the binding energy $E_{Bind}(j)$ of a certain state is equal to its one-electron (i.e orbital) energy ε_j (**Equation 1.63**).[318]

$$E_{\text{Bind}}(j) = -\varepsilon_j \qquad\qquad\qquad (1.63)$$

In simple terms, the ionization energy (which is actually measured in XPS, as the state is emitting a photoelectron) is approximately equal to its neutral orbital state.[321,322] If orbital relaxations and charge screening in inner core levels cannot be neglected, Koopmans theorem may not hold true.[318] However, care must be taken in interpreting binding energies, as PES is a surface sensitive technique and may not represent bulk properties. Upon irradiation with X-rays or UV radiation, electrons are generated up to few μm deep inside the bulk sample. While trying to escape into the vacuum, these electrons undergo inelastic scattering processes, loosing kinetic energy. By applying **Equation 1.62**, these scattered "secondary" photoelectrons are perceived as states with higher binding energy. Only the electrons generated in the top-most layer of the sample are emitted without scattering and give rise to a sharp peak in the photoelectron intensity characteristic for the respective element.[323] This short inelastic mean free path λ_{IMP} describes the average photoelectron distance travelled without undergoing inelastic scattering. Besides the electronic structure of the observed element(s), λ_{IMP} is predominantly affected by the excitation photon energy.[313] By comparing different photon energies, a parabola shape is obtained, with a minimum λ_{IMP} of ca. 0.5 nm at roughly 10^2 eV photoelectron energy.[324] The information depth of a XPS experiment with inelastic scattering is therefore limited to roughly 2-5 nm, that from a UPS experiment to even 1 nm, rendering PES a highly surface sensitive technique.[325,326]

Following the energy conservation in **Equation 1.61** and the schematic energies involved (**Figure 1.25a**), the photoelectrons with the lowest binding energy are emitted from the Fermi energy of the sample. This onset in photoelectron emission is called *valence band maximum* (abbr. VBM) or *Fermi edge* and is characterized by a Fermi photoelectron intensity distribution convoluted with a Gaussian slit function.[317] Generally, the PES energy scale is calibrated such, that all binding energies are referenced to the Fermi edge, which is set to zero (BE = 0).[317] This is usually performed by referencing the VBM to the measured Fermi edge of sputter cleaned gold.[327] Sample charging *via* accumulation of photoelectrons on the surface in insulators and/or misalignment of spectrometer and sample Fermi energy (bad contacts) leads to a shift of the recorded binding energies.[328]
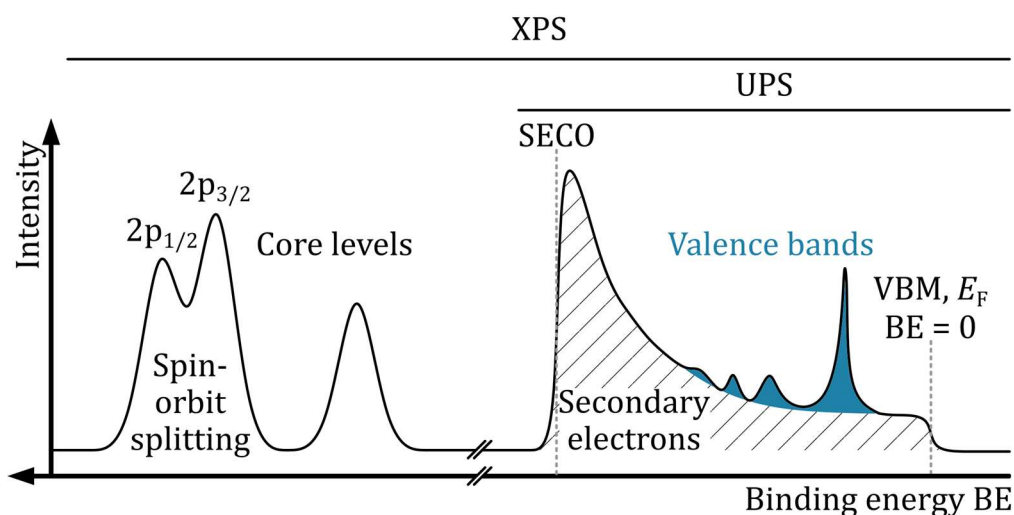
Figure 1.26. Schematic XPS and UPS spectra involving core-levels with spin-orbit splitting, valence bands and the valence band maximum. In UPS, the *secondary photoelectron cut-off* (abbr. SECO) marks the region where the kinetic energy of the inelastic scattered electrons approaches zero. Adopted from Refs.[317,329]

Below the VBM, signals from the valence bands are recorded in a PES experiment. These states represent the frontier orbitals, originating from the samples HOMO (**Figure 1.26**). As XPS energy resolution is fourfold lower and is less sensitive towards inelastic scattering, the valence band states are usually studied with UPS.[330] Moving further towards higher binding energy, an increase in photoelectron intensity followed by a steep, step-like decay to near zero is observed only in UPS. This phenomenon is called *secondary photoelectron cut-off* (abbr. SECO). It is caused by $E_{Bind} + \phi_{Detector}$ approaching $\hbar\nu$, thus E_{Kin}^{Exp} of the ejected (secondary) photoelectrons is too low to leave the sample surface (**Equation 1.62**). As this would pose a problem for measuring the SECO, the sample is often biased with a negative voltage V_{Bi} with respect to the spectrometer Fermi energy (**Figure 1.25b**). The potential difference accelerates the photoelectrons from the SECO region towards the detector, enabling a correct measurement (effectively shifting E_F and hence the BE scale by V_{Bi}). From the midpoint of the SECO position E_{SECO}, ϕ_{Sample} can be determined (**Equation 1.64**).

$$\phi_{Sample} = \phi_{Detector} + E_{SECO} + qV_{Bi} \tag{1.64}$$

where q is the elementary charge. If the PES instrument is correctly calibrated, such that VBM occurs at BE = 0 for a metallic reference sample, **Equation 1.64** can be rewritten to **Equation 1.65**. Otherwise, the difference between valence band maximum energy E_{VBM} and E_{SECO} must be used.[327,331]

$$\phi_{\text{Sample}} = \hbar\nu - E_{\text{SECO}} - qV_{\text{Bi}} = \hbar\nu - (E_{\text{VBM}} - E_{\text{SECO}}) - qV_{\text{Bi}} \tag{1.65}$$

From the position of the VBM (which is > 0 eV for organic samples, i.e. E_F is positioned above the valence band states), the HOMO energy E_{HOMO} can be deduced according to **Equation 1.66**.[332]

$$E_{\text{HOMO}} = \phi_{\text{Sample}} + (|qV_{\text{Bi}}| - E_{\text{VBM}}) \tag{1.66}$$

To report changes in ϕ_{Sample} independent from vacuum level shifts or sample charging effects, often the hole-injection barrier (abbr. HIB) is reported, which is defined as the energy difference between ϕ_{Sample} and E_{HOMO}. It is worth mentioning, that the valence bands obtained from a PES experiment are not to be confused by the actual DOS of the sample (see **Figure 1.12**). Despite visual similarity, the photoelectrons recorded in PES are not only dependent on the DOS, but also on the take-off angle, wave function, polarization, orientation of the molecules and photon energy.[52,333] At higher energies than the valence band states lie the core levels responsible for σ-bonds (see **Figure 1.10**). As the BE of core levels far exceeds the photon energy of UPS, X-Ray photoelectron spectroscopy is used to study core states. The power of XPS lies in the fact, that each element in the periodic table has characteristic binding energies and hence can be used to probe the sample composition. Apart from the lightest elements He and H_2, every element can be detected. The intensity I of a core level peak is a directed by multitude of parameters - the atomic density n, the exciting photon flux f, the photoelectric cross section σ, the angular efficiency factor ϕ_{Ang}, the efficiency of photoelectron generation γ, the sample area A, the efficiency of photoelectron detection T and finally the emitted photoelectron mean free path λ (**Equation 1.67**).[334]

$$I = nf\sigma\phi_{\text{Ang}}\gamma AT\lambda \tag{1.67}$$

While f, ϕ_{Ang}, A, and T are instrument-, resp. sample specific quantities, the photoelectric cross section depends on the atomic number Z. Scofield found σ to be increasing with principal quantum number (e.g. $\sigma_{Li\,2s} < \sigma_{Na\,2s} < \sigma_{K\,2s}$) and decreasing when moving to higher azimuthal quantum number (e.g. $\sigma_{Na\,2s} > \sigma_{Na\,2p1/2}$).[335] Along with photoelectron peaks and Auger lines, satellite peaks are frequently encountered in a XPS spectrum.[314] Satellite peaks, appearing as weaker duplicates of the main peak and may have two independent origins: i) insufficient filtering capability of the X-Ray monochromator and/or ii) shake-up or shake-down processes. In a shake-up process, the photoelectron exiting the atom simultaneously excites outer shell electrons to higher lying orbitals, in turn losing a small amount of kinetic energy (which the PES interprets as having a higher BE).[336] Especially in metals, photoelectrons ejected from core levels can excite valence band electrons above the Fermi edge, and thus exit the atom with lower E_{Kin}. This causes a continuous shake-off loss tail above the BE of the main core level peak.[314] In conjugated π-systems like (doped) OSCs, shake-up peaks occur frequently due to π-π* transitions of the aromatic system.[337] Another phenomenon often observed in transition metal ions is multiplet- or spin-orbit splitting of a core level peak (**Figure 1.26**). Unpaired electrons in outer, low BE shells lead spin-orbit coupling with either antiparallel or parallel spin orientation, which splits the core level peak.[314]

By far the most prominent feature of core level peaks is their sensitivity towards the chemical environment of the element. A change in core level BE occurs, when the electrostatic potential experienced by the core level electron is altered by removing or adding electron density from the valence bands. In other words, excess negative charge in the valence bands screens the charge on the nucleus, lowering the binding energy of core states.[317] This BE change, denominated *chemical shift*, is used to differentiate oxidation states of elements, e.g. carbon (**Figure 1.27**).[338]
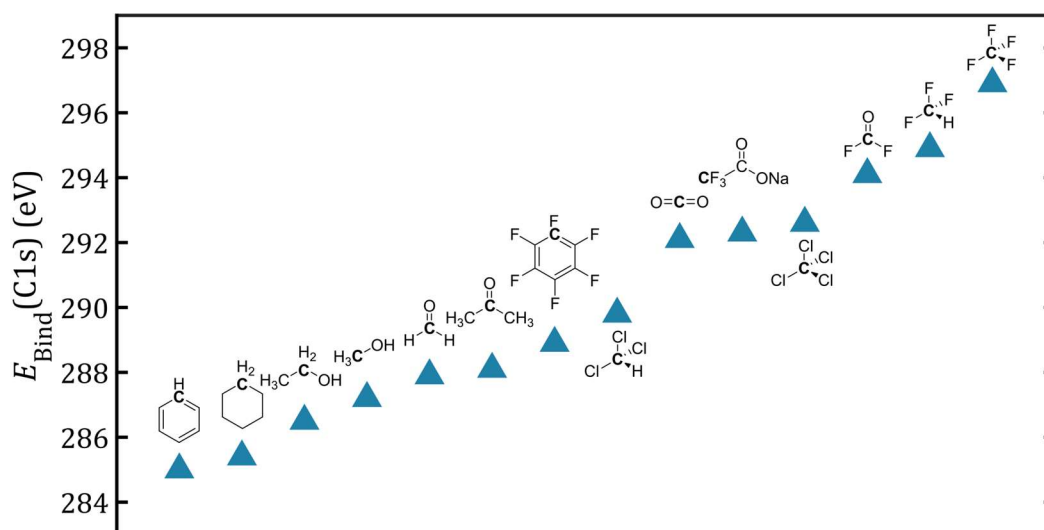
Figure 1.27. XPS chemical shifts of the carbon 1s core level peak of various organic substances. Carbon atom marked in bold. Data taken from Ref. and referenced to 285 eV.[339]

In molecules with multiple oxidation states per element, such as ethanol, the C 1s core peak is a convolution of both contributions. By deconvoluting the peak, information about the individual contributions can be obtained.

1.4.1 Characterisation of doped organic systems using XPS

Albeit core levels have minor influence on the electronic properties dictated by the frontier orbitals (valence bands), XPS has found widespread use in investigating fundamental properties of doped organic systems. In the highly conductive, doped polymer semiconductors, XPS analysis is a popular choice to determine the doping level. For *p*-methyl benzenesulfonate (abbr. tosylate) and poly(styrene sulfonate) (abbr. PSS⁻) doped PEDOT, Xing et al. determined a doping concentration of 25 % tosylate and 50 % PSS⁻ counter ion on the polymer surface. This was achieved by monitoring the sulfur 2p and oxygen 1s signals of pristine and doped polymer.[340] Further, the doping level of tosylate doped PEDOT can be enhanced by a factor of ca. 3 by choosing alcohols over ketone based solvents during the oxidative polymerization. Kim et al. studied this effect

by comparing the area ratios of sulfur 2p signals originating from sulfonate and thiophene sulfur.[341] Using ethylene glycol surfactant in vacuum vapour phase polymerised PEDOT boosts the doping level from 16.4 % (no surfactant) to 28.4 % (15 wt% ethylene glycol). As published by Fabretto et al., the doping level can be conveniently accessed by the oxygen 1s ratio between tosylate and PEDOT oxygen.[342] Chiu et al. applied a similar sulfur 2p peak area analysis and found, that sulfate ions may also act as dopants towards PEDOT, yielding a doping level of 11.6 %.[343] Liu et al. demonstrated, that by measuring the chlorine to carbon atomic ratio using XPS, the doping level of hydrogen chloride (acid) doped poly(aniline) can be determined.[344] Deconvoluting the nitrogen 1s peak into quinone diimine and benzene diamine contribution, Zeng et al. could show, that protonation by HCl likely occurs at the nitrogen atoms in the quinoid poly(aniline) units.[345] XPS also delivers fundamental insight into doping reactions of poly(alkyl thiophene) OSCs. Hintz et al. studied the photooxidative *p*-doping process of poly(3-hexylthiophene) (abbr. P3HT). The oxygen uptake was monitored by the oxygen 1s : sulfur 2p peak area ratio and coincided with a BE shift of all core levels towards lower binding energies upon light exposure. This was attributed to a Fermi energy shift towards the HOMO, effectively *p*-doping P3HT (see **Figure 1.25**, **1.28**).[346]
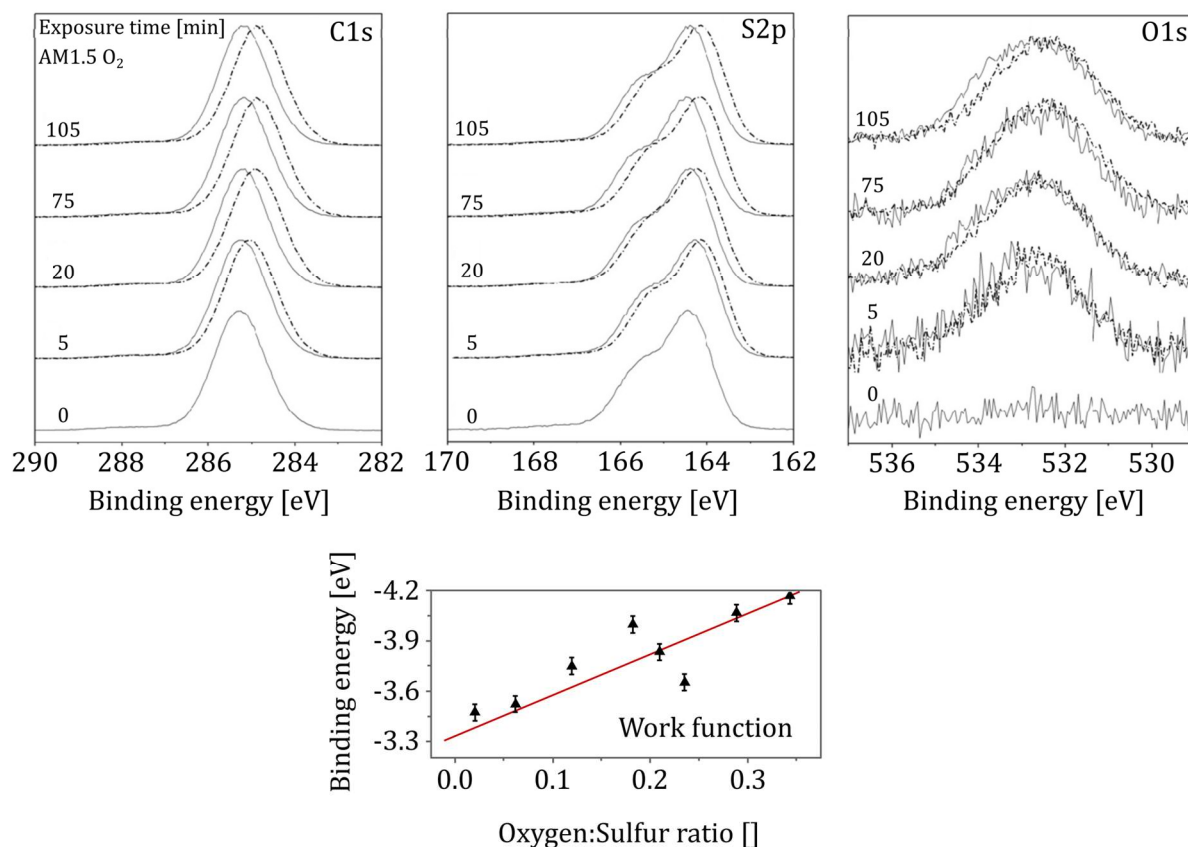
Figure 1.28. Top: Carbon 1s, sulfur 2p and oxygen 1s core level spectra of P3HT films illuminated with AM1.5 solar radiation and exposed to pure oxygen (dotted lines). Exposure times are given in minutes. The films were subsequently annealed at 423 K under vacuum (10^{-3} mbar) for 10 min, shown as solid lines. As the instrument is referenced such that the Fermi energy is located at 0 eV binding energy, a shift of the core level peaks towards lower binding energies suggests a lower distance between P3HT HOMO and Fermi energy. Bottom: Work function of the exposed P3HT films measured by UPS as a function of the oxygen to sulfur ratio determined by XPS. Oxygen is introduced into P3HT by means of oxidation, hence the oxygen to sulfur ratio increases. A shift in the work function towards lower energies (closer to the P3HT HOMO) indicates *p*-doping. The workfunction was calculated using **Equation 1.65** with V_{Bi} = -5 V and the position of the SECO E_{SECO}. Adopted and reprinted with permission from H. Hintz, H. Peisert, H.-J. Egelhaaf, T. Chassé, *J. Phys. Chem. C* **2011**, *115*, 13373-13376. Copyright 2011 American Chemical Society.

The same BE shift can be observed by using the strong chemical oxidant $FeCl_3$ to *p*-dope sexithiophene. Oeter et al. reported a $|\Delta E_{Bind}(\text{carbon 1s})|$ of ca. 0.8 eV at 70 %

FeCl₃:sexithiophene doping ratio.[347] *p*-doping may not lead to a core level shift, but instead induce π-π* shake-up lines, as observed in AsF₅ doped *para*-distyrylbenzene.[348] Besides doping processes, the complementary de-doping reactions can be quantified using XPS. Storing FeCl₃ doped poly(alkyl thiophenes) in ambient atmosphere at room temperature results in loss of free charge carriers over time *via* de-doping. Wu et al. showed, that the FeCl₄⁻ chlorine 2p signal loses intensity over time, escaping as HCl gas.[349] Molybdenum trioxide (abbr. MoO₃) is a powerful *p*-type dopant akin to FeCl₃ which can be used in vapour phase doping (see **Section 1.3.1**). XPS analysis revealed a significant sensitivity towards ambient moisture, which breaks up MoO₃ clusters and forms hydroxyl groups. Gwinner et al. optimized the poly(9,9-dioctylfluorene-*alt*-benzothiadiazole)/MoO₃ doped OSC system by excluding H₂O based on XPS results.[350] Combining XPS with sputter/etching techniques allows depth-profiling of elemental constitution, where after each XPS analysis cycle, a defined part of the sample surface is removed. For P3HT solution *p*-doped with phosphomolybdic acid, this technique has been applied by Kolesov et al. to investigate the dopant diffusion. They found ca. 10-20 nm dopant penetration into the pristine polymer film, which is dependent on the exposure time to the dopant solution (**Figure 1.29**).[351]
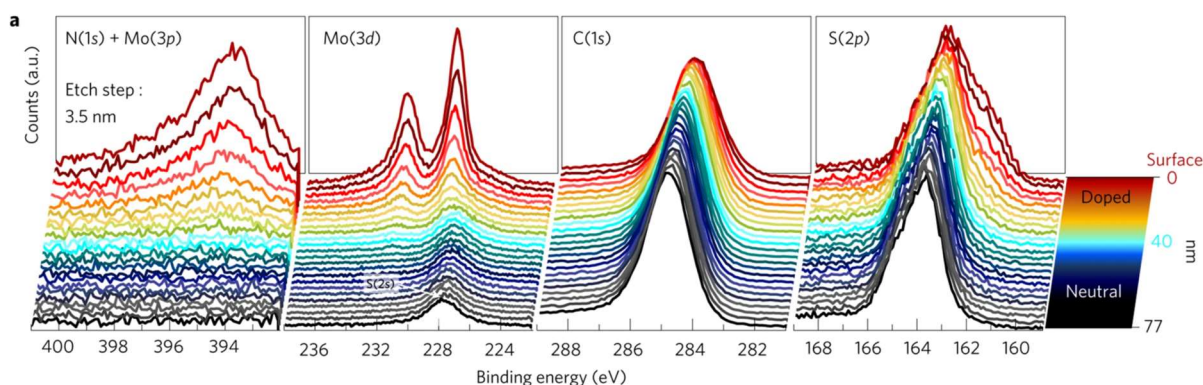

Figure 1.29. Depth-dependent XPS spectra of the N 1s, Mo 3d, C 1s and S 2p binding energy regions of a 210 nm thick phosphomolybdic acid doped P3HT film. The film was prepared by 1 min immersion doping of the P3HT film in 0.5 M phosphomolybdic acid nitromethane solution. The Mo 3d peak series shows a decay constant of 11 nm for the Mo 3d signal, indicating only limited penetration of the dopant into the P3HT film. Reproduced with permission from Springer Nature, V. A. Kolesov, C. Fuentes-Hernandez, W.-F. Chou, N. Aizawa, F. A. Larrain, M. Wang, A. Perrotta, S. Choi, S. Graham, G. C. Bazan, T.-Q. Nguyen, S. R. Marder, B. Kippelen, *Nature Mater.* **2017**, *16*, 474-480.

Lewis acids and bases have also been studied with the help of XPS. Tris(pentafluorophenyl)borane forms strong adducts with Lewis basic nitrogen sites in poly[2,6-(4,4-bis(2-hexadecyl)-4H-cyclopenta[2,1-b;3,4-b']dithiophene)-*alt*-4,7-(4,4-dihexadecyl-4H-cyclopenta[2,1-b:3,4-b']dithiophene-2,6-diyl)bis([1,2,5]thiadiazolo [3,4-c]pyridine)]. Yurash et al. verified the adduct formation by the presence of new nitrogen 1s core level peaks.[46] Wang et al. used tetraalkylammonium bromide salts as Lewis bases to *n*-dope a range of OSCs for photovoltaic applications. The relative BE shifts of the bromine 3d and nitrogen N1s peak were used as an indicator for the Lewis basicity of the Br⁻ anion.[209] To conclude, XPS core level analysis is a modern and indispensable tool to investigate composition and kinetics of doped organic systems. Its versatility allows the exploration of a broad pallet of doped organic systems.

1.4.2 Characterisation of doped organic systems using UPS

For doped OSCs, precise knowledge about the energy levels involved is essential to understand the system as a whole. UPS is sensitive towards all filled states in the valence band region of the OSC, hence it is particularly useful to investigate *p*-doped system. If the unpopulated states in the conduction band (LUMO etc.) are of interest in e.g. *n*-doped systems, *inverse photoelectron spectroscopy* (IPES) is used. Complementary to PES, electrons are accelerated towards the sample and the emitted photons are detected in IPES.[317] Combining PES and IPES spectra yields a comprehensive picture of both HOMO and LUMO states.[216] For more information about the subject of IPES, the reader is recommended to refer to the relevant literature.[317,352–354]

As doping primarily manipulates the occupation statistics of filled and empty states in the frontier orbitals, UPS is mostly used to determine the work function and HOMO position of doped OSCs.
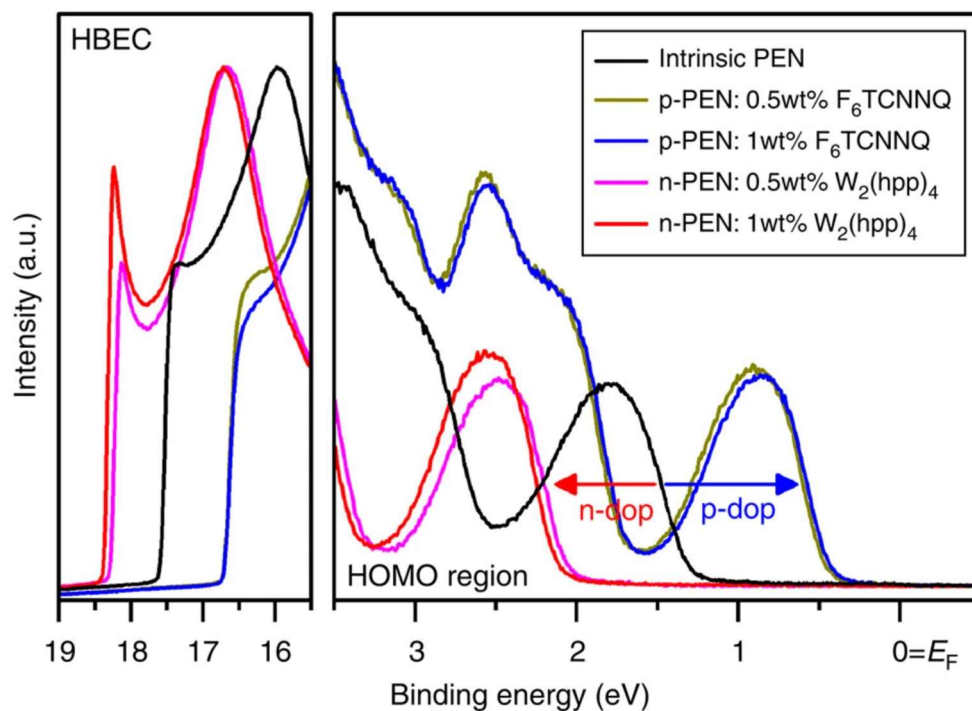
Figure 1.30. Binding energy of the OSC pentacene (PEN) in the pristine form (black curve), *p*-doped with F$_6$TCNNQ (olive and blue curves) and *n*-doped with W$_2$(hpp)$_4$ (pink and red curves) determined by UPS. Left: High binding energy cut-off (HBEC), identical to the SECO; right: valence band region (VBM). Reprinted from B. Lüssem, M. L. Tietze, H. Kleemann, C. Hoßbach, J. W. Bartha, A. Zakhidov, K. Leo, *Nat. Commun.* **2013**, *4*, 2775, which is licensed under a Creative Commons Attribution-NonCommercial-ShareAlike 3.0 Unported License. To view a copy of this license, visit http://creativecommons.org/licenses/by-nc-sa/3.0/.

Lüssem et al. studied the influence of the *p*-dopant F$_6$TCNNQ and the *n*-dopant W$_2$(hpp)$_4$ on the work function and HOMO position of the OSC pentacene using UPS.[355] An exemplary UPS binding energy spectrum of the doped pentacene is depicted in **Figure 1.30**. The work function of pristine PEN ϕ_{PEN} is calculated using **Equation 1.65**, with E_{SECO} = 17.59 eV and $\hbar\nu$ = 21.22 eV: ϕ_{PEN} = 21.22 eV – 17.59 eV = 3.63 eV. The spectrum shown is already corrected for V_{Bi}, hence it is not used in **Equation 1.65**. Upon *p*-doping pentacene, E_{SECO} shifts towards lower binding energies, which equates to a higher work function (E_F moves closer to the OSC HOMO, HIB of 0.43 eV at 1 wt% F$_6$TCNNQ). *n*-doping pentacene induces a E_{SECO} shift towards higher energies, lowering the work function (E_F moves closer to the OSC LUMO, HIB of 2.85 eV at 1 wt% W$_2$(hpp)$_4$). Using the valence band onset E_{VBM}, determined from the low binding energy region of the

UPS spectrum (**Figure 1.30**, right), the HOMO energy of pristine pentacene was calculated using **Equation 1.66**: E_{HOMO} = 3.63 eV + 1.31 eV = 4.94 eV. Neither *n*- nor *p*-doping significantly changes the HOMO energy of pentacene. In early studies by Oeter et al., oligothiophenes were *p*-doped with $FeCl_3$. Oeter et al. used UPS in early studies to track the doping reaction of $FeCl_3$ and oligothiophenes. The HOMO onset shifted ca. 1 eV towards the Fermi energy with increasing dopant concentration. In turn, the HIB was lowered, an unambiguous sign of *p*-doping.[356] More recent studies utilize UPS to study fundamental phenomena such as band bending in OSCs (**Figure 1.17**). Upward bending of the vacuum energy was observed for hexadecafluorophthalocyaninatozinc *n*-doped with tetrathianaphthacene. This was achieved by studying the work function evolution of evaporated, doped films with increasing film thickness up to ca. 140 nm by Tanaka et al.[357] Similarly, tetrafluorotetracyanoquinodimethane doped zinc phthalocyanine interfaces were investigated by Gao et al. The doped OSC forms a < 3.2 nm thick space-charge layer when deposited on a gold electrode as determined by UPS, which greatly boosts hole injection compared to the pristine OSC.[218] In more elaborate studies, Olthof et al. studied the interface dipole formation of doped OSCs on silver, indium-doped tin oxide and PEDOT:PSS substrates with UPS. Especially the all organic junction creates a very low interface dipole beneficial for charge injection.[168]

By careful control of ultralow doping ratios (molar ratio ranging from 10^{-1} to 10^{-4}), more subtle effects of the Fermi energy moving through the band gap can be observed with UPS. As discussed in previous **Section 1.2.3**, various localized states may be present above the HOMO (hole traps) or below the LUMO energy (electron traps) (**Figure 1.15**). Olthof et al. identified the transition between trap-filling regime (charges generated by doping are consumed in passivating traps) and formation of free-charge carriers in C_{60}, which was *n*-doped with a mesitylene pentamethylcyclopentadienyl ruthenium dimer. Upon investigating the change of the work function relative to the dopant molar ratio, a distinct change in slope marked the transition.[180] A comparable trend was found for $C_{60}F_{36}$ *p*-doped N,N,N',N'-tetrakis(4-methoxyphenyl)benzidine by Tietze et al. Both XPS core levels- and UPS valence band onsets shifted towards lower BE with increasing doping ratio, finally being pinned close to the HOMO position of the host. The UPS results were in accordance to classical semiconductor physics, on the basis of which a refined model for understanding doped OSCs was built.[47] Kröger et al. observed a similar two-regime work function shift in inorganic MoO_3 *p*-doped triphenylamine derivatives.[358]

UPS can be partially used to replace inverse PES by monitoring the HIB during *n*-doping OSCs. If the HIB increases upon doping, the Fermi energy moves away from the HOMO towards the LUMO. This was used by Naab et al. to develop dimeric benzimidazole dopants which are able to shift E_F closer to the LUMO of a semiconducting polymer compared to monomeric benzimidazole derivatives.[359] Further, UPS may partially replace or support impedance spectroscopy measurements to determine the doping efficiency. Tietze et al. used UPS measurement on *p*-doped zinc phthalocyanine of increasing film thickness to derive the depletion layer thickness and built-in potential, which are used to calculate the doping efficiency at various dopant ratios.[173] Finally, UPS also helps to unravel detrimental effects of doping, which are difficult to pinpoint with conventional spectroscopy. In the case of Li-TFSI doped N,N′-di(1-naphthyl)-N,N′-diphenyl-(1,1′-biphenyl)-4,4′-diamine, excessive doping ratios of 25 % increased the hole injection barrier as determined by UPS. In turn, this lowered the doping efficiency and current density in hole-only organic diodes.[360] To put it concisely, UPS enables a deep insight into fundamental energies related to doping – work function, HOMO position, doping efficiency and interface energetics in devices to name a few. Both UPS and XPS represent complementary methods enabling high quality research on doped organic systems.

References

[1]   V. F. Lvovich, *Impedance Spectroscopy: Applications to Electrochemical and Dielectric Phenomena*, John Wiley & Sons, Inc., Hoboken, NJ, USA, **2012**.

[2]   O. Kanoun, Ed., *Impedance Spectroscopy: Advanced Applications: Battery Research, Bioimpedance, System Design*, De Gruyter, **2018**.

[3]   M. E. Orazem, B. Tribollet, *Electrochemical Impedance Spectroscopy*, John Wiley & Sons, Inc., Hoboken, NJ, USA, **2017**.

[4]   A. Lasia, *Electrochemical Impedance Spectroscopy and Its Applications*, Springer New York, New York, NY, **2014**.

[5]   E. Lenz, *Ann. Phys. Chem.* **1834**, *107*, 483.

[6]   M. A. B. Deakin, *Arch. Hist. Exact Sci.* **1992**, *44*, 265.

[7]   M. Hufschmid, *Grundlagen der Elektrotechnik: Einführung für Studierende der Ingenieur- und Naturwissenschaften*, Springer Vieweg, Wiesbaden [Heidelberg], **2021**.

[8]   W. Raith, *Lehrbuch der Experimentalphysik Bd. 2, Bd. 2,* De Gruyter, Berlin [u.a, **2006**.

[9]   E. Barsoukov, J. R. Macdonald, Eds., *Impedance Spectroscopy: Theory, Experiment, and Applications*, Wiley, **2005**.

[10]   J. R. Macdonald, W. B. Johnson, in *Impedance Spectrosc.* (Eds.: E. Barsoukov, J. R. Macdonald), John Wiley & Sons, Inc., Hoboken, NJ, USA, **2018**, pp. 1–20.

[11]   M. Marinescu, N. Marinescu, *Elektrotechnik für Studium und Praxis: Gleich-, Wechsel- und Drehstrom, Schalt- und nichtsinusförmige Vorgänge*, Springer Vieweg, Wiesbaden [Heidelberg], **2020**.

[12]   G. W. Walter, *Corros. Sci.* **1986**, *26*, 681.

[13]   S. M. Sze, K. K. Ng, *Physics of Semiconductor Devices*, Wiley-Interscience, Hoboken, NJ, **2007**.

[14]   J. Shao, G. T. Wright, *Solid-State Electron.* **1961**, *3*, 291.

[15]   T. Okachi, T. Nagase, T. Kobayashi, H. Naito, *Thin Solid Films* **2008**, *517*, 1331.

[16]   Mott, Nevill Francis, Gurney, Ronald Wilfred, *Electronic Processes in Ionic Crystals*, Oxford University Press, New York, NY, **1940**.

[17]   H. C. F. Martens, W. F. Pasveer, H. B. Brom, J. N. Huiberts, P. W. M. Blom, *Phys. Rev. B* **2001**, *63*, 125328.

[18]   H. C. F. Martens, H. B. Brom, P. W. M. Blom, *Phys. Rev. B* **1999**, *60*, R8489.

[19]   H. C. F. Martens, J. N. Huiberts, P. W. M. Blom, *Appl. Phys. Lett.* **2000**, *77*, 1852.

[20]   M. Itagaki, S. Suzuki, I. Shitanda, K. Watanabe, *Electrochemistry* **2007**, *75*, 649.

[21]   H. Xu, C. Tang, W.-J. Zhai, R.-L. Liu, Z. Rong, Q.-L. Fan, W. Huang, *Eur. Phys. J. Appl. Phys.* **2014**, *68*, 30202.

[22]   S. W. Tsang, S. K. So, J. B. Xu, *J. Appl. Phys.* **2006**, *99*, 013706.

[23]   P. W. M. Blom, M. J. M. de Jong, M. G. van Munster, *Phys. Rev. B* **1997**, *55*, R656.

[24]   R. Davis, A. N. Asokan, P. Predeep, *J. Inorg. Organomet. Polym. Mater.* **2020**, *30*, 4408.

[25]   N. D. Nguyen, M. Schmeits, H. P. Loebl, *Phys. Rev. B* **2007**, *75*, 075307.

[26]   F. Tinti, S. E. Debebe, W. Mammo, T. Yohannes, N. Camaioni, *Synth. Met.* **2011**, *161*, 794.

[27]   D. Poplavskyy, F. So, *J. Appl. Phys.* **2006**, *99*, 033707.

[28]   C. Melzer, E. J. Koop, V. D. Mihailetchi, P. W. M. Blom, *Adv. Funct. Mater.* **2004**, *14*, 865.

[29]   J. V. Li, G. Ferrari, Eds., *Capacitance Spectroscopy of Semiconductors*, Pan Stanford Publishing, Singapore, **2018**.

[30]   H. Hirwa, S. Pittner, V. Wagner, *Org. Electron.* **2015**, *24*, 303.

[31]   L. Bertoluzzi, P. Lopez-Varo, J. A. Jiménez Tejada, J. Bisquert, *J. Mater. Chem. A* **2016**, *4*, 2873.

[32]   E. von Hauff, *J. Phys. Chem. C* **2019**, *123*, 11329.

[33]   E. J. Meijer, A. V. G. Mangnus, C. M. Hart, D. M. de Leeuw, T. M. Klapwijk, *Appl. Phys. Lett.* **2001**, *78*, 3902.

[34]   P. K. Manda, L. Karunakaran, S. Thirumala, A. Chakravorty, S. Dutta, *IEEE Trans. Electron Devices* **2019**, *66*, 3967.

[35]   M. Prashanth Kumar, K. Logesh, S. Dutta, in *Phys. Semicond. Devices* (Eds.: R. K. Sharma, D. S. Rawal), Springer International Publishing, Cham, **2019**, pp. 69–74.

[36]   O. V. Kozlov, S. A. Zapunidi, *Synth. Met.* **2013**, *169*, 48.

[37]   M. Meier, S. Karg, W. Riess, *J. Appl. Phys.* **1997**, *82*, 1961.

[38]   P. Pahner, H. Kleemann, L. Burtone, M. L. Tietze, J. Fischer, K. Leo, B. Lüssem, *Phys. Rev. B* **2013**, *88*, 195205.

[39]   K. Darowicki, S. Krakowiak, P. Ślepski, *Electrochimica Acta* **2006**, *51*, 2204.

[40]   O. Almora, C. Aranda, E. Mas-Marzá, G. Garcia-Belmonte, *Appl. Phys. Lett.* **2016**, *109*, 173903.

[41]   H. Kleemann, B. Lüssem, K. Leo, *J. Appl. Phys.* **2012**, *111*, 123722.

[42]   F. P. Heiman, *IEEE Trans. Electron Devices* **1967**, *14*, 781.

[43]   Y. Fukuda, Y. Otani, Y. Itayama, T. Ono, *IEEE Trans. Electron Devices* **2007**, *54*, 2878.

[44]   M. C. K. Sellers, E. G. Seebauer, *Thin Solid Films* **2011**, *519*, 2103.

[45]   A. Tataroğlu, Ş. Altındal, *Microelectron. Eng.* **2008**, *85*, 2256.

[46]   B. Yurash, D. X. Cao, V. V. Brus, D. Leifert, M. Wang, A. Dixon, M. Seifrid, A. E. Mansour, D. Lungwitz, T. Liu, P. J. Santiago, K. R. Graham, N. Koch, G. C. Bazan, T.-Q. Nguyen, *Nat. Mater.* **2019**, *18*, 1327.

[47]   M. L. Tietze, L. Burtone, M. Riede, B. Lüssem, K. Leo, *Phys. Rev. B* **2012**, *86*, 035320.

[48]   H. Shirakawa, E. J. Louis, A. G. MacDiarmid, C. K. Chiang, A. J. Heeger, *J. Chem. Soc. Chem. Commun.* **1977**, *0*, 578.

[49]   B. Lüssem, M. Riede, K. Leo, in *Phys. Org. Semicond.* (Eds.: W. Brütting, C. Adachi), Wiley, **2012**, pp. 425–496.

[50]   W. Brütting, *Physics of Organic Semiconductors*, Wiley-VCH, Weinheim, **2005**.

[51]   A. Köhler, H. Bässler, *Electronic Processes in Organic Semiconductors: An Introduction*, Wiley-VCH Verlag GmbH & Co. KGaA, Weinheim, Germany, **2015**.

[52]   J.-P. Yang, F. Bussolotti, S. Kera, N. Ueno, *J. Phys. Appl. Phys.* **2017**, *50*, 423002.

[53]   D. Raithel, L. Simine, S. Pickel, K. Schötz, F. Panzer, S. Baderschneider, D. Schiefer, R. Lohwasser, J. Köhler, M. Thelakkat, M. Sommer, A. Köhler, P. J. Rossky, R. Hildner, *Proc. Natl. Acad. Sci.* **2018**, *115*, 2699.

[54]   A. V. Nenashev, J. O. Oelerich, S. D. Baranovskii, *J. Phys. Condens. Matter* **2015**, *27*, 093201.

[55]   H. Bässler, *Phys. Status Solidi B* **1993**, *175*, 15.

[56]   H. Fukagawa, H. Yamane, S. Kera, K. K. Okudaira, N. Ueno, *Phys. Rev. B* **2006**, *73*, 041302.

[57]   S. Duhm, G. Heimel, I. Salzmann, H. Glowatzki, R. L. Johnson, A. Vollmer, J. P. Rabe, N. Koch, *Nat. Mater.* **2008**, *7*, 326.

[58]   G. A. de Wijs, C. C. Mattheus, R. A. de Groot, T. T. M. Palstra, *Synth. Met.* **2003**, *139*, 109.

[59]   H. Yoshida, N. Sato, *Phys. Rev. B* **2008**, *77*, 235205.

[60]   W. C. Dunlap, R. L. Watters, *Phys. Rev.* **1953**, *92*, 1396.

[61]   M. P. Hughes, K. D. Rosenthal, N. A. Ran, M. Seifrid, G. C. Bazan, T. Nguyen, *Adv. Funct. Mater.* **2018**, *28*, 1801542.

[62]   J. Brebels, J. V. Manca, L. Lutsen, D. Vanderzande, W. Maes, *J. Mater. Chem. A* **2017**, *5*, 24037.

[63]   R. S. Knox, *Theory of Excitons*, Academic Pr, New York, **1972**.

[64]   M. Rehahn, *Chem. Unserer Zeit* **2003**, *37*, 18.

[65]   H. Bässler, *Phys. Status Solidi B* **1981**, *107*, 9.

[66]   M. Marcus, J. D. Milward, A. Köhler, W. Barford, *J. Phys. Chem. A* **2018**, *122*, 3621.

[67]   H. Klauk, Ed., *Organic Electronics II: More Materials and Applications*, Wiley, **2012**.

[68]   A. V. Nenashev, F. Jansson, J. O. Oelerich, D. Huemmer, A. V. Dvurechenskii, F. Gebhard, S. D. Baranovskii, *Phys. Rev. B* **2013**, *87*, 235204.

[69]   S. Baranovskii, O. Rubel, in *Springer Handb. Electron. Photonic Mater.* (Eds.: S. Kasap, P. Capper), Springer International Publishing, Cham, **2017**, pp. 1–1.

[70]   C. Kunkel, J. T. Margraf, K. Chen, H. Oberhofer, K. Reuter, *Nat. Commun.* **2021**, *12*, 2422.

[71]   C. Y. Cheng, J. E. Campbell, G. M. Day, *Chem. Sci.* **2020**, *11*, 4922.

[72]   U. K. Mishra, J. Singh, *Semiconductor Device Physics and Design*, Springer, Dordrecht, **2008**.

[73]   D. Cahen, A. Kahn, *Adv. Mater.* **2003**, *15*, 271.

[74]   A. Kahn, *Mater. Horiz.* **2016**, *3*, 7.

[75]   S. D. Baranovskii, *Phys. Status Solidi A* **2018**, *215*, 1700676.

[76]   P. Cheng, Y. Yang, *Acc. Chem. Res.* **2020**, *53*, 1218.

[77]   N. Kobayashi, H. Kuwae, J. Oshima, R. Ishimatsu, S. Tashiro, T. Imato, C. Adachi, S. Shoji, J. Mizuno, *J. Lumin.* **2018**, *200*, 19.

[78]   J. Ma, M. Idris, T. Y. Li, D. S. M. Ravinson, T. Fleetham, J. Kim, P. I. Djurovich, S. R. Forrest, M. E. Thompson, *Adv. Opt. Mater.* **2022**, *10*, 2101530.

[79]   V. I. Arkhipov, P. Heremans, E. V. Emelianova, H. Bässler, *Phys. Rev. B* **2005**, *71*, 045214.

[80]   M. Lehnhardt, S. Hamwi, M. Hoping, J. Reinker, T. Riedl, W. Kowalsky, *Appl. Phys. Lett.* **2010**, *96*, 193301.

[81]   I. Salzmann, G. Heimel, M. Oehzelt, S. Winkler, N. Koch, *Acc. Chem. Res.* **2016**, *49*, 370.

[82]   M. Koopmans, M. A. T. Leiviskä, J. Liu, J. Dong, L. Qiu, J. C. Hummelen, G. Portale, M. C. Heiber, L. J. A. Koster, *ACS Appl. Mater. Interfaces* **2020**, *12*, 56222.

[83]   V. Adamec, J. H. Calderwood, *J. Phys. Appl. Phys.* **1981**, *14*, 1487.

[84]   W. Warta, R. Stehle, N. Karl, *Appl. Phys. Solids Surf.* **1985**, *36*, 163.

[85]   N. Karl, J. Marktanner, R. Stehle, W. Warta, *Synth. Met.* **1991**, *42*, 2473.

[86]   N. Karl, *Synth. Met.* **2003**, *133–134*, 649.

[87]   G. F. Bassani, G. L. Liedl, P. Wyder, *Encyclopedia of Condensed Matter Physics*, Elsevier, Amsterdam Boston, **2005**.

[88]   V. Coropceanu, J. Cornil, D. A. da Silva Filho, Y. Olivier, R. Silbey, J.-L. Brédas, *Chem. Rev.* **2007**, *107*, 926.

[89]   C. Liu, K. Huang, W.-T. Park, M. Li, T. Yang, X. Liu, L. Liang, T. Minari, Y.-Y. Noh, *Mater. Horiz.* **2017**, *4*, 608.

[90]   I. I. Fishchuk, A. Kadashchuk, H. Bässler, S. Nešpůrek, *Phys. Rev. B* **2003**, *67*, 224303.

[91]   D. Stroud, *Superlattices Microstruct.* **1998**, *23*, 567.

[92]   P. E. Parris, V. M. Kenkre, D. H. Dunlap, *Phys. Rev. Lett.* **2001**, *87*, 126601.

[93]   H. Bässler, P. M. Borsenberger, R. J. Perry, *J. Polym. Sci. Part B Polym. Phys.* **1994**, *32*, 1677.

[94]   S. Giannini, J. Blumberger, *Acc. Chem. Res.* **2022**, *55*, 819.

[95]   Q.-M. Koh, C. G. Tang, M. C.-Y. Ang, K.-K. Choo, Q.-J. Seah, R.-Q. Png, L.-L. Chua, P. K. H. Ho, *Nat. Commun.* **2021**, *12*, 3345.

[96]   S. Griggs, A. Marks, H. Bristow, I. McCulloch, *J. Mater. Chem. C* **2021**, *9*, 8099.

[97]   H. F. Haneef, A. M. Zeidell, O. D. Jurchescu, *J. Mater. Chem. C* **2020**, *8*, 759.

[98]   S. Zeiske, O. J. Sandberg, N. Zarrabi, W. Li, P. Meredith, A. Armin, *Nat. Commun.* **2021**, *12*, 3603.

[99]   S. Anand, K. P. Goetz, Z. A. Lamport, A. M. Zeidell, O. D. Jurchescu, *Appl. Phys. Lett.* **2019**, *115*, 073301.

[100]   J. Kublitski, A. Hofacker, B. K. Boroujeni, J. Benduhn, V. C. Nikolis, C. Kaiser, D. Spoltore, H. Kleemann, A. Fischer, F. Ellinger, K. Vandewal, K. Leo, *Nat. Commun.* **2021**, *12*, 551.

[101]   T.-A. Chen, X. Wu, R. D. Rieke, *J. Am. Chem. Soc.* **1995**, *117*, 233.

[102]   R. S. Loewe, P. C. Ewbank, J. Liu, L. Zhai, R. D. McCullough, *Macromolecules* **2001**, *34*, 4324.

[103]   E. E. Sheina, J. Liu, M. C. Iovu, D. W. Laird, R. D. McCullough, *Macromolecules* **2004**, *37*, 3526.

[104]   A. Yokoyama, R. Miyakoshi, T. Yokozawa, *Macromolecules* **2004**, *37*, 1169.

[105]   M. Chowdhury, M. T. Sajjad, V. Savikhin, N. Hergué, K. B. Sutija, S. D. Oosterhout, M. F. Toney, P. Dubois, A. Ruseckas, I. D. W. Samuel, *Phys. Chem. Chem. Phys.* **2017**, *19*, 12441.

[106]   C. R. Singh, G. Gupta, R. Lohwasser, S. Engmann, J. Balko, M. Thelakkat, T. Thurn-Albrecht, H. Hoppe, *J. Polym. Sci. Part B Polym. Phys.* **2013**, *51*, 943.

[107]   R. Zhang, B. Li, M. C. Iovu, M. Jeffries-EL, G. Sauvé, J. Cooper, S. Jia, S. Tristram-Nagle, D. M. Smilgies, D. N. Lambeth, R. D. McCullough, T. Kowalewski, *J. Am. Chem. Soc.* **2006**, *128*, 3480.

[108]   J.-F. Chang, J. Clark, N. Zhao, H. Sirringhaus, D. W. Breiby, J. W. Andreasen, M. M. Nielsen, M. Giles, M. Heeney, I. McCulloch, *Phys. Rev. B* **2006**, *74*, 115318.

REFERENCES

[109]   R. J. Kline, M. D. McGehee, E. N. Kadnikova, J. Liu, J. M. J. Fréchet, *Adv. Mater.* **2003**, *15*, 1519.

[110]   A. M. Ballantyne, L. Chen, J. Dane, T. Hammant, F. M. Braun, M. Heeney, W. Duffy, I. McCulloch, D. D. C. Bradley, J. Nelson, *Adv. Funct. Mater.* **2008**, *18*, 2373.

[111]   M. Oehzelt, K. Akaike, N. Koch, G. Heimel, *Sci. Adv.* **2015**, *1*, e1501127.

[112]   H. Ishii, N. Hayashi, E. Ito, Y. Washizu, K. Sugi, Y. Kimura, M. Niwano, Y. Ouchi, K. Seki, *Phys. Status Solidi A* **2004**, *201*, 1075.

[113]   N. F. Mott, *Math. Proc. Camb. Philos. Soc.* **1938**, *34*, 568.

[114]   W. Schottky, *Z. Für Phys.* **1942**, *118*, 539.

[115]   I. G. Hill, A. J. Mäkinen, Z. H. Kafafi, *J. Appl. Phys.* **2000**, *88*, 889.

[116]   X. Crispin, V. Geskin, A. Crispin, J. Cornil, R. Lazzaroni, W. R. Salaneck, J.-L. Brédas, *J. Am. Chem. Soc.* **2002**, *124*, 8131.

[117]   X. Crispin, *Sol. Energy Mater. Sol. Cells* **2004**, *83*, 147.

[118]   E. Ito, Y. Washizu, N. Hayashi, H. Ishii, N. Matsuie, K. Tsuboi, Y. Ouchi, Y. Harima, K. Yamashita, K. Seki, *J. Appl. Phys.* **2002**, *92*, 7306.

[119]   M. Eremtchenko, D. Bauer, J. A. Schaefer, F. S. Tautz, *New J. Phys.* **2004**, *6*, 4.

[120]   C. Shen, A. Kahn, *Org. Electron.* **2001**, *2*, 89.

[121]   N. Koch, *ChemPhysChem* **2007**, *8*, 1438.

[122]   N. Koch, S. Duhm, J. P. Rabe, A. Vollmer, R. L. Johnson, *Phys. Rev. Lett.* **2005**, *95*, 237601.

[123]   J. C. Scott, *J. Vac. Sci. Technol. Vac. Surf. Films* **2003**, *21*, 521.

[124]   E. V. Tsiper, Z. G. Soos, W. Gao, A. Kahn, *Chem. Phys. Lett.* **2002**, *360*, 47.

[125]   S. Verlaak, D. Beljonne, D. Cheyns, C. Rolin, M. Linares, F. Castet, J. Cornil, P. Heremans, *Adv. Funct. Mater.* **2009**, *19*, 3809.

[126]   Y. Noguchi, Y. Miyazaki, Y. Tanaka, N. Sato, Y. Nakayama, T. D. Schmidt, W. Brütting, H. Ishii, *J. Appl. Phys.* **2012**, *111*, 114508.

[127]   M. Fathollahi, M. Ameri, E. Mohajerani, E. Mehrparvar, M. Babaei, *Sci. Rep.* **2017**, *7*, 42787.

[128]   Y. Chen, D. Ma, *J. Mater. Chem.* **2012**, *22*, 18718.

[129]   S. Rafique, S. M. Abdullah, K. Sulaiman, M. Iwamoto, *Renew. Sustain. Energy Rev.* **2018**, *84*, 43.

[130]   P. Heremans, D. Cheyns, B. P. Rand, *Acc. Chem. Res.* **2009**, *42*, 1740.

[131]   I. G. Hill, D. Milliron, J. Schwartz, A. Kahn, *Appl. Surf. Sci.* **2000**, *166*, 354.

[132]   W. Chen, S. Chen, H. Huang, D. C. Qi, X. Yu. Gao, A. T. S. Wee, *Appl. Phys. Lett.* **2008**, *92*, 063308.

REFERENCES

[133]   P. Sehati, S. Braun, L. Lindell, Xianjie Liu, L. M. Andersson, M. Fahlman, *IEEE J. Sel. Top. Quantum Electron.* **2010**, *16*, 1718.

[134]   M. Linares, D. Beljonne, J. Cornil, K. Lancaster, J.-L. Brédas, S. Verlaak, A. Mityashin, P. Heremans, A. Fuchs, C. Lennartz, J. Idé, R. Méreau, P. Aurel, L. Ducasse, F. Castet, *J. Phys. Chem. C* **2010**, *114*, 3215.

[135]   Y. Shen, A. R. Hosseini, M. H. Wong, G. G. Malliaras, *ChemPhysChem* **2004**, *5*, 16.

[136]   C.-P. Kwan, M. Street, A. Mahmood, W. Echtenkamp, M. Randle, K. He, J. Nathawat, N. Arabchigavkani, B. Barut, S. Yin, R. Dixit, U. Singisetti, Ch. Binek, J. P. Bird, *AIP Adv.* **2019**, *9*, 055018.

[137]   J. G. Simmons, *Phys. Rev. Lett.* **1965**, *15*, 967.

[138]   M. Goel, M. Siegert, G. Krauss, J. Mohanraj, A. Hochgesang, D. C. Heinrich, M. Fried, J. Pflaum, M. Thelakkat, *Adv. Mater.* **2020**, *32*, 2003596.

[139]   G. N. Derry, M. E. Kern, E. H. Worth, *J. Vac. Sci. Technol. Vac. Surf. Films* **2015**, *33*, 060801.

[140]   J. Rittich, S. Jung, J. Siekmann, M. Wuttig, *Phys. Status Solidi B* **2018**, *255*, 1800075.

[141]   D. M. Alloway, A. L. Graham, X. Yang, A. Mudalige, R. Colorado, V. H. Wysocki, J. E. Pemberton, T. R. Lee, R. J. Wysocki, N. R. Armstrong, *J. Phys. Chem. C* **2009**, *113*, 20328.

[142]   M. Fang, C. Zhang, Q. Chen, *Appl. Surf. Sci.* **2016**, *385*, 28.

[143]   F. Li, Y. Zhou, F. Zhang, X. Liu, Y. Zhan, M. Fahlman, *Chem. Mater.* **2009**, *21*, 2798.

[144]   X. Zhou, J. Blochwitz, M. Pfeiffer, A. Nollau, T. Fritz, K. Leo, *Adv. Funct. Mater.* **2001**, *11*, 310.

[145]   Y. Kim, S. Chung, K. Cho, D. Harkin, W.-T. Hwang, D. Yoo, J.-K. Kim, W. Lee, Y. Song, H. Ahn, Y. Hong, H. Sirringhaus, K. Kang, T. Lee, *Adv. Mater.* **2019**, *31*, 1806697.

[146]   J. Endo, T. Matsumoto, J. Kido, *Jpn. J. Appl. Phys.* **2002**, *41*, L358.

[147]   W.-J. Shin, J.-Y. Lee, J. C. Kim, T.-H. Yoon, T.-S. Kim, O.-K. Song, *Org. Electron.* **2008**, *9*, 333.

[148]   D.-S. Leem, H.-D. Park, J.-W. Kang, J.-H. Lee, J. W. Kim, J.-J. Kim, *Appl. Phys. Lett.* **2007**, *91*, 011113.

[149]   A. R. Hosseini, M. H. Wong, Y. Shen, G. G. Malliaras, *J. Appl. Phys.* **2005**, *97*, 023705.

[150]   H. Bässler, A. Köhler, in *Unimolecular Supramol. Electron. I* (Ed.: R. M. Metzger), Springer Berlin Heidelberg, Berlin, Heidelberg, **2011**, pp. 1–65.

[151]   H. Shirakawa, E. J. Louis, A. G. MacDiarmid, C. K. Chiang, A. J. Heeger, *J. Chem. Soc. Chem. Commun.* **1977**, 578.

[152]   S. C. Rasmussen, *ChemPlusChem* **2020**, *85*, 1412.

[153]   N. Hai, Z. Bo, T. Xian-Zhong, *Chin. Phys.* **2007**, *16*, 730.

[154]   B. H. Lee, G. C. Bazan, A. J. Heeger, *Adv. Mater.* **2016**, *28*, 57.

[155]   Y. Lin, M. I. Nugraha, Y. Firdaus, A. D. Scaccabarozzi, F. Aniés, A.-H. Emwas, E. Yengel, X. Zheng, J. Liu, W. Wahyudi, E. Yarali, H. Faber, O. M. Bakr, L. Tsetseris, M. Heeney, T. D. Anthopoulos, *ACS Energy Lett.* **2020**, *5*, 3663.

[156]   J. Luo, J. Xia, H. Yang, H. A. Malik, F. Han, H. Shu, X. Yao, Z. Wan, C. Jia, *Nano Energy* **2020**, *70*, 104509.

[157]   X. Wu, Q. Liu, A. Surendran, S. E. Bottle, P. Sonar, W. L. Leong, *Adv. Electron. Mater.* **2021**, *7*, 2000701.

[158]   K. Harada, M. Riede, K. Leo, O. R. Hild, C. M. Elliott, *Phys. Rev. B* **2008**, *77*, 195212.

[159]   P. Pingel, D. Neher, *Phys. Rev. B* **2013**, *87*, 115209.

[160]   F. Ghani, A. Opitz, P. Pingel, G. Heimel, I. Salzmann, J. Frisch, D. Neher, A. Tsami, U. Scherf, N. Koch, *J. Polym. Sci. Part B Polym. Phys.* **2015**, *53*, 58.

[161]   M. Pfeiffer, A. Beyer, T. Fritz, K. Leo, *Appl. Phys. Lett.* **1998**, *73*, 3202.

[162]   T. Glaser, S. Beck, B. Lunkenheimer, D. Donhauser, A. Köhn, M. Kröger, A. Pucci, *Org. Electron.* **2013**, *14*, 575.

[163]   B. Maennig, M. Pfeiffer, A. Nollau, X. Zhou, K. Leo, P. Simon, *Phys. Rev. B* **2001**, *64*, 195208.

[164]   K. Walzer, B. Maennig, M. Pfeiffer, K. Leo, *Chem. Rev.* **2007**, *107*, 1233.

[165]   H. Méndez, G. Heimel, S. Winkler, J. Frisch, A. Opitz, K. Sauer, B. Wegner, M. Oehzelt, C. Röthel, S. Duhm, D. Többens, N. Koch, I. Salzmann, *Nat. Commun.* **2015**, *6*, 8560.

[166]   P. Pingel, L. Zhu, K. S. Park, J.-O. Vogel, S. Janietz, E.-G. Kim, J. P. Rabe, J.-L. Brédas, N. Koch, *J. Phys. Chem. Lett.* **2010**, *1*, 2037.

[167]   J.-H. Lee, J. Lee, Y. H. Kim, C. Yun, B. Lüssem, K. Leo, *Org. Electron.* **2014**, *15*, 16.

[168]   S. Olthof, W. Tress, R. Meerheim, B. Lüssem, K. Leo, *J. Appl. Phys.* **2009**, *106*, 103711.

[169]   Y. Zhang, B. de Boer, P. W. M. Blom, *Adv. Funct. Mater.* **2009**, *19*, 1901.

[170]   P. Pingel, R. Schwarzl, D. Neher, *Appl. Phys. Lett.* **2012**, *100*, 143303.

[171]   G. Zuo, H. Abdalla, M. Kemerink, *Phys. Rev. B* **2016**, *93*, 235203.

[172]   A. Fediai, A. Emering, F. Symalla, W. Wenzel, *Phys. Chem. Chem. Phys.* **2020**, *22*, 10256.

[173]   M. L. Tietze, J. Benduhn, P. Pahner, B. Nell, M. Schwarze, H. Kleemann, M. Krammer, K. Zojer, K. Vandewal, K. Leo, *Nat. Commun.* **2018**, *9*, 1182.

[174]   S. Braun, W. R. Salaneck, M. Fahlman, *Adv. Mater.* **2009**, *21*, 1450.

[175]   S. Winkler, P. Amsalem, J. Frisch, M. Oehzelt, G. Heimel, N. Koch, *Mater. Horiz.* **2015**, *2*, 427.

REFERENCES

[176]   M. L. Tietze, P. Pahner, K. Schmidt, K. Leo, B. Lüssem, *Adv. Funct. Mater.* **2015**, *25*, 2701.

[177]   F. Deschler, E. Da Como, T. Limmer, R. Tautz, T. Godde, M. Bayer, E. von Hauff, S. Yilmaz, S. Allard, U. Scherf, J. Feldmann, *Phys. Rev. Lett.* **2011**, *107*, 127402.

[178]   M. M. Mandoc, F. B. Kooistra, J. C. Hummelen, B. de Boer, P. W. M. Blom, *Appl. Phys. Lett.* **2007**, *91*, 263505.

[179]   C.-T. Lee, H.-C. Chen, *Org. Electron.* **2011**, *12*, 1852.

[180]   S. Olthof, S. Mehraeen, S. K. Mohapatra, S. Barlow, V. Coropceanu, J.-L. Brédas, S. R. Marder, A. Kahn, *Phys. Rev. Lett.* **2012**, *109*, 176601.

[181]   P. J. Diemer, Z. A. Lamport, Y. Mei, J. W. Ward, K. P. Goetz, W. Li, M. M. Payne, M. Guthold, J. E. Anthony, O. D. Jurchescu, *Appl. Phys. Lett.* **2015**, *107*, 103303.

[182]   B. Lüssem, C.-M. Keum, D. Kasemann, B. Naab, Z. Bao, K. Leo, *Chem. Rev.* **2016**, *116*, 13714.

[183]   J. B. Torrance, *Acc. Chem. Res.* **1979**, *12*, 79.

[184]   M. Meneghetti, C. Pecile, *J. Chem. Phys.* **1986**, *84*, 4149.

[185]   E. F. Aziz, A. Vollmer, S. Eisebitt, W. Eberhardt, P. Pingel, D. Neher, N. Koch, *Adv. Mater.* **2007**, *19*, 3257.

[186]   I. Salzmann, G. Heimel, S. Duhm, M. Oehzelt, P. Pingel, B. M. George, A. Schnegg, K. Lips, R.-P. Blum, A. Vollmer, N. Koch, *Phys. Rev. Lett.* **2012**, *108*, 035502.

[187]   J. Yang, Y. Li, S. Duhm, J. Tang, S. Kera, N. Ueno, *Adv. Mater. Interfaces* **2014**, *1*, 1300128.

[188]   H. Méndez, G. Heimel, A. Opitz, K. Sauer, P. Barkowski, M. Oehzelt, J. Soeda, T. Okamoto, J. Takeya, J.-B. Arlin, J.-Y. Balandier, Y. Geerts, N. Koch, I. Salzmann, *Angew. Chem. Int. Ed.* **2013**, *52*, 7751.

[189]   I. E. Jacobs, A. J. Moulé, *Adv. Mater.* **2017**, *29*, 1703063.

[190]   S.-J. Yoo, J.-J. Kim, *Macromol. Rapid Commun.* **2015**, *36*, 984.

[191]   John. Ferraris, D. O. Cowan, V. Walatka, J. H. Perlstein, *J. Am. Chem. Soc.* **1973**, *95*, 948.

[192]   J. T. Liu, H. Hase, S. Taylor, I. Salzmann, P. Forgione, *Angew. Chem. Int. Ed.* **2020**, *59*, 7146.

[193]   K. E. Watts, B. Neelamraju, E. L. Ratcliff, J. E. Pemberton, *Chem. Mater.* **2019**, *31*, 6986.

[194]   O. Zapata-Arteaga, B. Dörling, A. Perevedentsev, J. Martín, J. S. Reparaz, M. Campoy-Quiles, *Macromolecules* **2020**, *53*, 609.

[195]   D. A. Stanfield, Y. Wu, S. H. Tolbert, B. J. Schwartz, *Chem. Mater.* **2021**, *33*, 2343.

[196] S. J. Ausserlechner, M. Gruber, R. Hetzel, H.-G. Flesch, L. Ladinig, L. Hauser, A. Haase, M. Buchner, R. Resel, F. Schürrer, B. Stadlober, G. Trimmel, K. Zojer, E. Zojer, *Phys. Status Solidi A* **2012**, *209*, 181.

[197] A. G. Macdiarmid, J.-C. Chiang, M. Halpern, W.-S. Huang, S.-L. Mu, L. D. Nanaxakkara, S. W. Wu, S. I. Yaniger, *Mol. Cryst. Liq. Cryst.* **1985**, *121*, 173.

[198] S. N. Patel, A. M. Glaudell, D. Kiefer, M. L. Chabinyc, *ACS Macro Lett.* **2016**, *5*, 268.

[199] L. Zhang, K. Yang, R. Chen, Y. Zhou, S. Chen, Y. Zheng, M. Li, C. Xu, X. Tang, Z. Zang, K. Sun, *Adv. Electron. Mater.* **2020**, *6*, 1900648.

[200] Y. Zeng, W. Zheng, Y. Guo, G. Han, Y. Yi, *J. Mater. Chem. A* **2020**, *8*, 8323.

[201] B. D. Naab, S. Guo, S. Olthof, E. G. B. Evans, P. Wei, G. L. Millhauser, A. Kahn, S. Barlow, S. R. Marder, Z. Bao, *J. Am. Chem. Soc.* **2013**, *135*, 15018.

[202] G. C. Welch, R. Coffin, J. Peet, G. C. Bazan, *J. Am. Chem. Soc.* **2009**, *131*, 10802.

[203] J. Liu, W. Liu, E. Aydin, G. T. Harrison, F. H. Isikgor, X. Yang, A. S. Subbiah, S. De Wolf, *ACS Appl. Mater. Interfaces* **2020**, *12*, 23874.

[204] J. Panidi, A. F. Paterson, D. Khim, Z. Fei, Y. Han, L. Tsetseris, G. Vourlias, P. A. Patsalas, M. Heeney, T. D. Anthopoulos, *Adv. Sci.* **2018**, *5*, 1700290.

[205] B. Russ, M. J. Robb, B. C. Popere, E. E. Perry, C.-K. Mai, S. L. Fronk, S. N. Patel, T. E. Mates, G. C. Bazan, J. J. Urban, M. L. Chabinyc, C. J. Hawker, R. A. Segalman, *Chem. Sci.* **2016**, *7*, 1914.

[206] G. Huseynova, E.-Y. Shin, W.-T. Park, Y.-Y. Noh, *Dyes Pigments* **2019**, *162*, 243.

[207] J. Kim, D. Khim, K.-J. Baeg, W.-T. Park, S.-H. Lee, M. Kang, Y.-Y. Noh, D.-Y. Kim, *Adv. Funct. Mater.* **2016**, *26*, 7886.

[208] Y. Hu, Z. D. Rengert, C. McDowell, M. J. Ford, M. Wang, A. Karki, A. T. Lill, G. C. Bazan, T.-Q. Nguyen, *ACS Nano* **2018**, *12*, 3938.

[209] R. Wang, B. Wang, J. Wang, X. Zhang, D. Zhang, D. Wei, X. Sun, H. Zhou, Y. Zhang, *J. Mater. Chem. A* **2019**, *7*, 25808.

[210] Y. Han, Z. Fei, Y.-H. Lin, J. Martin, F. Tuna, T. D. Anthopoulos, M. Heeney, *Npj Flex. Electron.* **2018**, *2*, 11.

[211] X. Lin, B. Wegner, K. M. Lee, M. A. Fusella, F. Zhang, K. Moudgil, B. P. Rand, S. Barlow, S. R. Marder, N. Koch, A. Kahn, *Nat. Mater.* **2017**, *16*, 1209.

[212] Z. Bin, J. Li, L. Wang, L. Duan, *Energy Environ. Sci.* **2016**, *9*, 3424.

[213] J. Hölzl, F. K. Schulte, in *Solid Surf. Phys.* (Eds.: J. Hölzl, F. K. Schulte, H. Wagner), Springer Berlin Heidelberg, Berlin, Heidelberg, **1979**, pp. 1–150.

[214] M. L. Tietze, B. D. Rose, M. Schwarze, A. Fischer, S. Runge, J. Blochwitz-Nimoth, B. Lüssem, K. Leo, J.-L. Brédas, *Adv. Funct. Mater.* **2016**, *26*, 3730.

[215] C.-Y. Yang, Y.-F. Ding, D. Huang, J. Wang, Z.-F. Yao, C.-X. Huang, Y. Lu, H.-I. Un, F.-D. Zhuang, J.-H. Dou, C. Di, D. Zhu, J.-Y. Wang, T. Lei, J. Pei, *Nat. Commun.* **2020**, *11*, 3292.

REFERENCES

[216]   C. K. Chan, W. Zhao, S. Barlow, S. Marder, A. Kahn, *Org. Electron.* **2008**, *9*, 575.

[217]   T. L. D. Tam, J. Xu, *J. Mater. Chem. A* **2021**, *9*, 5149.

[218]   W. Gao, A. Kahn, *Appl. Phys. Lett.* **2001**, *79*, 4040.

[219]   R. Meerheim, S. Olthof, M. Hermenau, S. Scholz, A. Petrich, N. Tessler, O. Solomeshch, B. Lüssem, M. Riede, K. Leo, *J. Appl. Phys.* **2011**, *109*, 103102.

[220]   S. Zhang, H. M. Hill, K. Moudgil, C. A. Richter, A. R. Hight Walker, S. Barlow, S. R. Marder, C. A. Hacker, S. J. Pookpanratana, *Adv. Mater.* **2018**, *30*, 1802991.

[221]   J. Burschka, A. Dualeh, F. Kessler, E. Baranoff, N.-L. Cevey-Ha, C. Yi, M. K. Nazeeruddin, M. Grätzel, *J. Am. Chem. Soc.* **2011**, *133*, 18042.

[222]   Y. Qi, T. Sajoto, S. Barlow, E.-G. Kim, J.-L. Brédas, S. R. Marder, A. Kahn, *J. Am. Chem. Soc.* **2009**, *131*, 12530.

[223]   F. Zhang, A. Kahn, *Adv. Funct. Mater.* **2018**, *28*, 1703780.

[224]   Y. Liu, B. Nell, K. Ortstein, Z. Wu, Y. Karpov, T. Beryozkina, S. Lenk, A. Kiriy, K. Leo, S. Reineke, *ACS Appl. Mater. Interfaces* **2019**, *11*, 11660.

[225]   J. Meyer, *J. Photonics Energy* **2011**, *1*, 011109.

[226]   J. Meyer, S. Hamwi, S. Schmale, T. Winkler, H.-H. Johannes, T. Riedl, W. Kowalsky, *J. Mater. Chem.* **2009**, *19*, 702.

[227]   M. L. Tietze, Molecular Doping Processes in Organic Semiconductors Investigated by Photoelectron Spectroscopy, TU Dresden, **2014**.

[228]   A. D. Scaccabarozzi, A. Basu, F. Aniés, J. Liu, O. Zapata-Arteaga, R. Warren, Y. Firdaus, M. I. Nugraha, Y. Lin, M. Campoy-Quiles, N. Koch, C. Müller, L. Tsetseris, M. Heeney, T. D. Anthopoulos, *Chem. Rev.* **2022**, *122*, 4420.

[229]   S. S. Li, W. R. Thurber, *Solid-State Electron.* **1977**, *20*, 609.

[230]   T. Menke, D. Ray, J. Meiss, K. Leo, M. Riede, *Appl. Phys. Lett.* **2012**, *100*, 093304.

[231]   S. M. Rossnagel, *J. Vac. Sci. Technol. Vac. Surf. Films* **2003**, *21*, S74.

[232]   H. Li, Z. Xu, J. Song, H. Chai, L. Wu, L. Chen, *Adv. Funct. Mater.* **2022**, *32*, 2110047.

[233]   G. Ge, J. Li, J. Wang, M. Xiong, X. Dong, Z. Li, J. Li, X. Cao, T. Lei, J. Wang, *Adv. Funct. Mater.* **2022**, *32*, 2108289.

[234]   K.-H. Yim, G. L. Whiting, C. E. Murphy, J. J. M. Halls, J. H. Burroughes, R. H. Friend, J.-S. Kim, *Adv. Mater.* **2008**, *20*, 3319.

[235]   D. Yuan, D. Huang, C. Zhang, Y. Zou, C. Di, X. Zhu, D. Zhu, *ACS Appl. Mater. Interfaces* **2017**, *9*, 28795.

[236]   I. E. Jacobs, E. W. Aasen, J. L. Oliveira, T. N. Fonseca, J. D. Roehling, J. Li, G. Zhang, M. P. Augustine, M. Mascal, A. J. Moulé, *J Mater Chem C* **2016**, *4*, 3454.

[237]   J. Li, G. Zhang, D. M. Holm, I. E. Jacobs, B. Yin, P. Stroeve, M. Mascal, A. J. Moulé, *Chem. Mater.* **2015**, *27*, 5765.

REFERENCES

[238]   Q. Zhang, Y. Sun, W. Xu, D. Zhu, *Energy Environ. Sci.* **2012**, *5*, 9639.

[239]   D. T. Scholes, S. A. Hawks, P. Y. Yee, H. Wu, J. R. Lindemuth, S. H. Tolbert, B. J. Schwartz, *J. Phys. Chem. Lett.* **2015**, *6*, 4786.

[240]   J. Li, C. W. Rochester, I. E. Jacobs, S. Friedrich, P. Stroeve, M. Riede, A. J. Moulé, *ACS Appl. Mater. Interfaces* **2015**, *7*, 28420.

[241]   A. R. Chew, R. Ghosh, Z. Shang, F. C. Spano, A. Salleo, *J. Phys. Chem. Lett.* **2017**, *8*, 4974.

[242]   T. Ma, B. X. Dong, G. L. Grocke, J. Strzalka, S. N. Patel, *Macromolecules* **2020**, *53*, 2882.

[243]   K. Xu, T. Ruoko, M. Shokrani, D. Scheunemann, H. Abdalla, H. Sun, C. Yang, Y. Puttisong, N. B. Kolhe, J. S. M. Figueroa, J. O. Pedersen, T. Ederth, W. M. Chen, M. Berggren, S. A. Jenekhe, D. Fazzi, M. Kemerink, S. Fabiano, *Adv. Funct. Mater.* **2022**, *32*, 2112276.

[244]   M. Li, C. Luo, J. Zhang, J. Yang, J. Xu, W. Yao, R. Tan, X. Duan, F. Jiang, *Surf. Interfaces* **2020**, *21*, 100759.

[245]   P. Lin, F. Yan, *Adv. Mater.* **2012**, *24*, 34.

[246]   T. Nguyen-Dang, S. Chae, J. Chatsirisupachai, H. Wakidi, V. Promarak, Y. Visell, T. Nguyen, *Adv. Mater.* **2022**, *34*, 2200274.

[247]   D. Natali, M. Caironi, *Adv. Mater.* **2012**, *24*, 1357.

[248]   X. Cheng, Y.-Y. Noh, J. Wang, M. Tello, J. Frisch, R.-P. Blum, A. Vollmer, J. P. Rabe, N. Koch, H. Sirringhaus, *Adv. Funct. Mater.* **2009**, *19*, 2407.

[249]   F. Ante, D. Kälblein, T. Zaki, U. Zschieschang, K. Takimiya, M. Ikeda, T. Sekitani, T. Someya, J. N. Burghartz, K. Kern, H. Klauk, *Small* **2012**, *8*, 73.

[250]   S.-W. Rhee, D.-J. Yun, *J. Mater. Chem.* **2008**, *18*, 5437.

[251]   F. Ante, D. Kälblein, U. Zschieschang, T. W. Canzler, A. Werner, K. Takimiya, M. Ikeda, T. Sekitani, T. Someya, H. Klauk, *Small* **2011**, *7*, 1186.

[252]   T. Minari, T. Miyadera, K. Tsukagoshi, Y. Aoyagi, H. Ito, *Appl. Phys. Lett.* **2007**, *91*, 053508.

[253]   J. Belasco, S. K. Mohapatra, Y. Zhang, S. Barlow, S. R. Marder, A. Kahn, *Appl. Phys. Lett.* **2014**, *105*, 063301.

[254]   X. Liu, D. Kasemann, K. Leo, *Appl. Phys. Lett.* **2015**, *106*, 103301.

[255]   L. Ma, W. H. Lee, Y. D. Park, J. S. Kim, H. S. Lee, K. Cho, *Appl. Phys. Lett.* **2008**, *92*, 063310.

[256]   T. H. Schloemer, J. A. Christians, J. M. Luther, A. Sellinger, *Chem. Sci.* **2019**, *10*, 1904.

[257]   M. Petrović, V. Chellappan, S. Ramakrishna, *Sol. Energy* **2015**, *122*, 678.

REFERENCES

[258]   W.-J. Yin, T. Shi, Y. Yan, *Adv. Mater.* **2014**, *26*, 4653.

[259]   M. Baranowski, P. Plochocka, *Adv. Energy Mater.* **2020**, *10*, 1903659.

[260]   L. Zhu, Y. Yi, Z. Wei, *J. Phys. Chem. C* **2018**, *122*, 22309.

[261]   W. Tress, N. Marinova, O. Inganas, M. K. Nazeeruddin, S. M. Zakeeruddin, M. Graetzel, in *2014 IEEE 40th Photovolt. Spec. Conf. PVSC*, IEEE, Denver, CO, USA, **2014**, pp. 1563–1566.

[262]   D. Bilby, B. Frieberg, S. Kramadhati, P. Green, J. Kim, *ACS Appl. Mater. Interfaces* **2014**, *6*, 14964.

[263]   H.-S. Kim, C.-R. Lee, J.-H. Im, K.-B. Lee, T. Moehl, A. Marchioro, S.-J. Moon, R. Humphry-Baker, J.-H. Yum, J. E. Moser, M. Grätzel, N.-G. Park, *Sci. Rep.* **2012**, *2*, 591.

[264]   N. J. Jeon, H. G. Lee, Y. C. Kim, J. Seo, J. H. Noh, J. Lee, S. I. Seok, *J. Am. Chem. Soc.* **2014**, *136*, 7837.

[265]   J.-H. Im, I.-H. Jang, N. Pellet, M. Grätzel, N.-G. Park, *Nat. Nanotechnol.* **2014**, *9*, 927.

[266]   H. Zhou, Q. Chen, G. Li, S. Luo, T. Song, H.-S. Duan, Z. Hong, J. You, Y. Liu, Y. Yang, *Science* **2014**, *345*, 542.

[267]   H. J. Snaith, M. Grätzel, *Appl. Phys. Lett.* **2006**, *89*, 262114.

[268]   J. H. Noh, N. J. Jeon, Y. C. Choi, Md. K. Nazeeruddin, M. Grätzel, S. I. Seok, *J. Mater. Chem. A* **2013**, *1*, 11842.

[269]   J. Xu, O. Voznyy, R. Comin, X. Gong, G. Walters, M. Liu, P. Kanjanaboos, X. Lan, E. H. Sargent, *Adv. Mater.* **2016**, *28*, 2807.

[270]   L. Huang, Z. Hu, J. Xu, K. Zhang, J. Zhang, J. Zhang, Y. Zhu, *Electrochimica Acta* **2016**, *196*, 328.

[271]   W. H. Nguyen, C. D. Bailie, E. L. Unger, M. D. McGehee, *J. Am. Chem. Soc.* **2014**, *136*, 10996.

[272]   L. Lin, T. W. Jones, T. C. Yang, N. W. Duffy, J. Li, L. Zhao, B. Chi, X. Wang, G. J. Wilson, *Adv. Funct. Mater.* **2021**, *31*, 2008300.

[273]   F. Xia, Q. Wu, P. Zhou, Y. Li, X. Chen, Q. Liu, J. Zhu, S. Dai, Y. Lu, S. Yang, *ACS Appl. Mater. Interfaces* **2015**, *7*, 13659.

[274]   S. S. Kim, S. Bae, W. H. Jo, *Chem. Commun.* **2015**, *51*, 17413.

[275]   Y. Zhang, Y.-J. Heo, M. Park, S.-J. Park, *Polymers* **2019**, *11*, 167.

[276]   J. Liu, B. van der Zee, R. Alessandri, S. Sami, J. Dong, M. I. Nugraha, A. J. Barker, S. Rousseva, L. Qiu, X. Qiu, N. Klasen, R. C. Chiechi, D. Baran, M. Caironi, T. D. Anthopoulos, G. Portale, R. W. A. Havenith, S. J. Marrink, J. C. Hummelen, L. J. A. Koster, *Nat. Commun.* **2020**, *11*, 5694.

[277]   H. Wang, J.-H. Hsu, S.-I. Yi, S. L. Kim, K. Choi, G. Yang, C. Yu, *Adv. Mater.* **2015**, *27*, 6855.

[278]   A. W. Van Herwaarden, P. M. Sarro, *Sens. Actuators* **1986**, *10*, 321.

[279]   N. Mateeva, H. Niculescu, J. Schlenoff, L. R. Testardi, *J. Appl. Phys.* **1998**, *83*, 3111.

[280]   W. Zhao, J. Ding, Y. Zou, C. Di, D. Zhu, *Chem. Soc. Rev.* **2020**, *49*, 7210.

[281]   B. Russ, A. Glaudell, J. J. Urban, M. L. Chabinyc, R. A. Segalman, *Nat. Rev. Mater.* **2016**, *1*, 16050.

[282]   O. Bubnova, Z. U. Khan, A. Malti, S. Braun, M. Fahlman, M. Berggren, X. Crispin, *Nat. Mater.* **2011**, *10*, 429.

[283]   O. Bubnova, M. Berggren, X. Crispin, *J. Am. Chem. Soc.* **2012**, *134*, 16456.

[284]   G.-H. Kim, L. Shao, K. Zhang, K. P. Pipe, *Nat. Mater.* **2013**, *12*, 719.

[285]   S. Wu, W. Xing, M. Zhu, Y. Zou, Y. Sun, W. Xu, D. Zhu, *J. Mater. Chem. C* **2021**, *9*, 4158.

[286]   J. Ding, Z. Liu, W. Zhao, W. Jin, L. Xiang, Z. Wang, Y. Zeng, Y. Zou, F. Zhang, Y. Yi, Y. Diao, C. R. McNeill, C. Di, D. Zhang, D. Zhu, *Angew. Chem. Int. Ed.* **2019**, *58*, 18994.

[287]   M. Ito, T. Koizumi, H. Kojima, T. Saito, M. Nakamura, *J. Mater. Chem. A* **2017**, *5*, 12068.

[288]   H. Un, S. A. Gregory, S. K. Mohapatra, M. Xiong, E. Longhi, Y. Lu, S. Rigin, S. Jhulki, C. Yang, T. V. Timofeeva, J. Wang, S. K. Yee, S. Barlow, S. R. Marder, J. Pei, *Adv. Energy Mater.* **2019**, *9*, 1900817.

[289]   H. S. White, G. P. Kittlesen, M. S. Wrighton, *J. Am. Chem. Soc.* **1984**, *106*, 5375.

[290]   J. Rivnay, S. Inal, A. Salleo, R. M. Owens, M. Berggren, G. G. Malliaras, *Nat. Rev. Mater.* **2018**, *3*, 17086.

[291]   A. Giovannitti, D.-T. Sbircea, S. Inal, C. B. Nielsen, E. Bandiello, D. A. Hanifi, M. Sessolo, G. G. Malliaras, I. McCulloch, J. Rivnay, *Proc. Natl. Acad. Sci.* **2016**, *113*, 12017.

[292]   J. Rivnay, R. M. Owens, G. G. Malliaras, *Chem. Mater.* **2014**, *26*, 679.

[293]   M. Berggren, A. Richter-Dahlfors, *Adv. Mater.* **2007**, *19*, 3201.

[294]   E. Zeglio, J. Eriksson, R. Gabrielsson, N. Solin, O. Inganäs, *Adv. Mater.* **2017**, *29*, 1605787.

[295]   D. Khodagholy, T. Doublet, P. Quilichini, M. Gurfinkel, P. Leleux, A. Ghestem, E. Ismailova, T. Hervé, S. Sanaur, C. Bernard, G. G. Malliaras, *Nat. Commun.* **2013**, *4*, 1575.

[296]   Y. Zhang, J. Li, R. Li, D.-T. Sbircea, A. Giovannitti, J. Xu, H. Xu, G. Zhou, L. Bian, I. McCulloch, N. Zhao, *ACS Appl. Mater. Interfaces* **2017**, *9*, 38687.

[297]   D. A. Bernards, G. G. Malliaras, G. E. S. Toombes, S. M. Gruner, *Appl. Phys. Lett.* **2006**, *89*, 053505.

[298]   A. Savva, R. Hallani, C. Cendra, J. Surgailis, T. C. Hidalgo, S. Wustoni, R. Sheelamanthula, X. Chen, M. Kirkus, A. Giovannitti, A. Salleo, I. McCulloch, S. Inal, *Adv. Funct. Mater.* **2020**, *30*, 1907657.

[299]   I. Gualandi, D. Tonelli, F. Mariani, E. Scavetta, M. Marzocchi, B. Fraboni, *Sci. Rep.* **2016**, *6*, 35419.

[300]   B. Ding, G. Kim, Y. Kim, F. D. Eisner, E. Gutiérrez-Fernández, J. Martín, M. Yoon, M. Heeney, *Angew. Chem.* **2021**, *133*, 19831.

[301]   D. Khodagholy, J. Rivnay, M. Sessolo, M. Gurfinkel, P. Leleux, L. H. Jimison, E. Stavrinidou, T. Herve, S. Sanaur, R. M. Owens, G. G. Malliaras, *Nat. Commun.* **2013**, *4*, 2133.

[302]   S. T. Keene, T. P. A. Pol, D. Zakhidov, C. H. L. Weijtens, R. A. J. Janssen, A. Salleo, Y. Burgt, *Adv. Mater.* **2020**, *32*, 2000270.

[303]   S. Inal, J. Rivnay, P. Leleux, M. Ferro, M. Ramuz, J. C. Brendel, M. M. Schmidt, M. Thelakkat, G. G. Malliaras, *Adv. Mater.* **2014**, *26*, 7450.

[304]   L. H. Jimison, A. Hama, X. Strakosas, V. Armel, D. Khodagholy, E. Ismailova, G. G. Malliaras, B. Winther-Jensen, R. M. Owens, *J. Mater. Chem.* **2012**, *22*, 19498.

[305]   A. F. Paterson, A. Savva, S. Wustoni, L. Tsetseris, B. D. Paulsen, H. Faber, A. H. Emwas, X. Chen, G. Nikiforidis, T. C. Hidalgo, M. Moser, I. P. Maria, J. Rivnay, I. McCulloch, T. D. Anthopoulos, S. Inal, *Nat. Commun.* **2020**, *11*, 3004.

[306]   H. Hertz, *Ann. Phys. Chem.* **1887**, *267*, 983.

[307]   A. Einstein, *Ann. Phys.* **1905**, *322*, 132.

[308]   J. H. D. Eland, *Photoelectron Spectroscopy: An Introduction to Ultraviolet Photoelectron Spectroscopy in the Gas Phase.*, Elsevier Science, Kent, **2014**.

[309]   A. N. Mansour, *Surf. Sci. Spectra* **1994**, *3*, 202.

[310]   K. Yates, R. H. West, *Surf. Interface Anal.* **1983**, *5*, 133.

[311]   G. N. Dolenko, O. K. Poleshchuk, J. N. Latosińska, in *Encycl. Spectrosc. Spectrom.*, Elsevier, **2017**, pp. 691–694.

[312]   J. B. Peel, E. I. von Nagy-Felsobuki, *J. Chem. Educ.* **1987**, *64*, 463.

[313]   M. Angst, Forschungszentrum Jülich, Eds., *Scattering Methods for Condensed Matter Research: Towards Novel Applications at Future Sources*, Forschungszentrum Jülich, Jülich, **2012**.

[314]   S. Hofmann, *Auger- and X-Ray Photoelectron Spectroscopy in Materials Science: A User-Oriented Guide*, Springer, Heidelberg ; New York, **2013**.

[315]   P. A. Naik, in *Encycl. Spectrosc. Spectrom.*, Elsevier, **2017**, pp. 725–734.

[316]   C. S. Fadley, *J. Electron Spectrosc. Relat. Phenom.* **2010**, *178–179*, 2.

[317]   S. Hüfner, *Photoelectron Spectroscopy*, Springer Berlin Heidelberg, Berlin, Heidelberg, **2003**.

[318]   S. Suga, A. Sekiyama, *Photoelectron Spectroscopy*, Springer Berlin Heidelberg, Berlin, Heidelberg, **2014**.

[319]   A. J. L. Hofmann, The Influence of Dipolar Doping on Charge Injection and Transport in Small Molecular Organic Semiconductors, Universität Augsburg, **2020**.

[320]   H. Ishii, K. Kudo, T. Nakayama, N. Ueno, Eds., *Electronic Processes in Organic Electronics: Bridging Nanostructure, Electronic States and Device Properties*, Springer Japan, Tokyo, **2015**.

[321]   J. C. Slater, *Phys. Rev.* **1955**, *98*, 1039.

[322]   W. G. Laidlaw, F. W. Birss, *Theor. Chim. Acta* **1964**, *2*, 181.

[323]   F. A. Stevie, C. L. Donley, *J. Vac. Sci. Technol. A* **2020**, *38*, 063204.

[324]   C. J. Powell, *J. Vac. Sci. Technol. A* **2020**, *38*, 023209.

[325]   S. Oswald, R. Reiche, *Appl. Surf. Sci.* **2001**, *179*, 307.

[326]   F. J. Himpsel, in *Charact. Mater.* (Ed.: E. N. Kaufmann), John Wiley & Sons, Inc., Hoboken, NJ, USA, **2012**, p. com061.pub2.

[327]   E. Itoh, M. Iwamoto, M. Burghard, S. Roth, *Jpn. J. Appl. Phys.* **2000**, *39*, 5146.

[328]   G. Greczynski, L. Hultman, *Prog. Mater. Sci.* **2020**, *107*, 100591.

[329]   E. A. Kraut, R. W. Grant, J. R. Waldrop, S. P. Kowalczyk, *Phys. Rev. B* **1983**, *28*, 1965.

[330]   C. S. Fadley, D. A. Shirley, *J. Res. Natl. Bur. Stand. Sect. Phys. Chem.* **1970**, *74A*, 543.

[331]   M. G. Helander, M. T. Greiner, Z. B. Wang, Z. H. Lu, *Appl. Surf. Sci.* **2010**, *256*, 2602.

[332]   S. Olthof, *Adv. Opt. Mater.* **2021**, *9*, 2100227.

[333]   N. Ueno, A. Kitamura, K. K. Okudaira, T. Miyamae, Y. Harada, S. Hasegawa, H. Ishii, H. Inokuchi, T. Fujikawa, T. Miyazaki, K. Seki, *J. Chem. Phys.* **1997**, *107*, 2079.

[334]   C. D. Wagner, L. E. Davis, M. V. Zeller, J. A. Taylor, R. H. Raymond, L. H. Gale, *Surf. Interface Anal.* **1981**, *3*, 211.

[335]   J. H. Scofield, *J. Electron Spectrosc. Relat. Phenom.* **1976**, *8*, 129.

[336]   M. A. Brisk, A. D. Baker, *J. Electron Spectrosc. Relat. Phenom.* **1975**, *7*, 197.

[337]   J. A. Gardella, S. A. Ferguson, R. L. Chin, *Appl. Spectrosc.* **1986**, *40*, 224.

[338]   N. S. McIntyre, S. Sunder, D. W. Shoesmith, F. W. Stanchell, *J. Vac. Sci. Technol.* **1981**, *18*, 714.

[339]   U. Gelius, P. F. Hedén, J. Hedman, B. J. Lindberg, R. Manne, R. Nordberg, C. Nordling, K. Siegbahn, *Phys. Scr.* **1970**, *2*, 70.

[340]   K. Z. Xing, M. Fahlman, X. W. Chen, O. Inganäs, W. R. Salaneck, *Synth. Met.* **1997**, *89*, 161.

[341]   T. Y. Kim, C. M. Park, J. E. Kim, K. S. Suh, *Synth. Met.* **2005**, *149*, 169.

[342]   M. Fabretto, C. Jariego-Moncunill, J.-P. Autere, A. Michelmore, R. D. Short, P. Murphy, *Polymer* **2011**, *52*, 1725.

[343]   W. W. Chiu, J. Travaš-Sejdić, R. P. Cooney, G. A. Bowmaker, *Synth. Met.* **2005**, *155*, 80.

[344]   C. Liu, J. Zhang, G. Shi, F. Chen, *J. Appl. Polym. Sci.* **2004**, *92*, 171.

[345]   X.-R. Zeng, T.-M. Ko, *J. Polym. Sci. Part B Polym. Phys.* **1997**, *35*, 1993.

[346]   H. Hintz, H. Peisert, H.-J. Egelhaaf, T. Chassé, *J. Phys. Chem. C* **2011**, *115*, 13373.

[347]   D. Oeter, Ch. Ziegler, W. Gopel, H. Naarmann, *Berichte Bunsenges. Für Phys. Chem.* **1993**, *97*, 448.

[348]   D. E. King, J. E. Fernandez, W. E. Swartz, *Appl. Surf. Sci.* **1990**, *45*, 325.

[349]   C.-G. Wu, Y.-R. Yeh, L.-N. Chien, *Polymer* **2000**, *41*, 5839.

[350]   M. C. Gwinner, R. D. Pietro, Y. Vaynzof, K. J. Greenberg, P. K. H. Ho, R. H. Friend, H. Sirringhaus, *Adv. Funct. Mater.* **2011**, *21*, 1432.

[351]   V. A. Kolesov, C. Fuentes-Hernandez, W.-F. Chou, N. Aizawa, F. A. Larrain, M. Wang, A. Perrotta, S. Choi, S. Graham, G. C. Bazan, T.-Q. Nguyen, S. R. Marder, B. Kippelen, *Nat. Mater.* **2017**, *16*, 474.

[352]   Th. Fauster, V. Dose, in *Chem. Phys. Solid Surf. VI* (Eds.: R. Vanselow, R. Howe), Springer Berlin Heidelberg, Berlin, Heidelberg, **1986**, pp. 483–507.

[353]   H. Yoshida, *J. Electron Spectrosc. Relat. Phenom.* **2015**, *204*, 116.

[354]   N. V. Smith, *Rep. Prog. Phys.* **1988**, *51*, 1227.

[355]   B. Lüssem, M. L. Tietze, H. Kleemann, C. Hoßbach, J. W. Bartha, A. Zakhidov, K. Leo, *Nat. Commun.* **2013**, *4*, 2775.

[356]   D. Oeter, Ch. Ziegler, W. Göpel, *Synth. Met.* **1993**, *61*, 147.

[357]   S. Tanaka, K. Kanai, E. Kawabe, T. Iwahashi, T. Nishi, Y. Ouchi, K. Seki, *Jpn. J. Appl. Phys.* **2005**, *44*, 3760.

[358]   M. Kröger, S. Hamwi, J. Meyer, T. Riedl, W. Kowalsky, A. Kahn, *Org. Electron.* **2009**, *10*, 932.

[359]   B. D. Naab, S. Zhang, K. Vandewal, A. Salleo, S. Barlow, S. R. Marder, Z. Bao, *Adv. Mater.* **2014**, *26*, 4268.

[360]   K. Kim, J. Jeong, M. Kim, D. Kang, S. W. Cho, H. Lee, Y. Yi, *Appl. Surf. Sci.* **2019**, *480*, 565.

2.

2. Objective of the thesis

Parallel to the global success of inorganic semiconductors during the ongoing digital revolution, organic semiconductors have begun to partially transform from fundamental research topics into commercial products. Organic light emitting diodes, found in many modern display technologies, are a prime example. As of today, the electronic properties of organic semiconductors are frequently tailored to their desired values using chemical doping. Especially in the fast-paced, emerging research areas of organic bioelectronics, organic thermoelectrics involving both *p*-type (donor) and *n*-type (acceptor) materials, doping technology as the key promoter is not keeping up. Despite recent advances in the field of organic dopants and considerable computational effort, it lacks performance, stability and a universal approach to unify doping strategies. The aim of this thesis is to enhance the performance of doped organic semiconductors by designing new doping materials and proposing novel concepts while applying advanced analytical methods. These methods will be based mostly on impedance- and photoelectron spectroscopy. In this work, we try to achieve this objective by four approaches build on one another.

In organic bioelectronics, PEDOT:PSS has emerged as a benchmark material for conductive, biocompatible polymers. However, it is a non-soluble blend and hence difficult to process into thin films. By designing a new doping strategy to vastly improve the performance and conductivity of soluble poly(3,4-ethylenedioxythiophene) homopolymers, we try to replace PEDOT:PSS and eliminate the need for a PSS counter ion. This approach will be realized by utilizing oxidized triphenylamines as *p*-dopants. The performance of the doped system will be examined by UPS, as well as mobility and conductivity electrical measurements. Here, we can benefit from knowledge gained in our seminal work on HOMO-HOMO electron transfer in 2020 to create a highly conductive system. Further, we will employ bis(trifluoromethanesulfonyl)imide counter ions to boost the environmental stability of the doped state, allowing it to be used in ambient conditions.

Current studies suggest, that the doping efficiency of typical dopants like N-DMBI or NOPF$_6$ is quite poor, dropping well below 10 % at 5 mol% dopant. By increasing the doping efficiency, we can decrease the required amount of dopant and minimize the accumulation of undesired side products in doped thin films. Hence, by coupling the second approach with the synthesis of covalently coupled multielectron acceptor *p*-dopants, we will expand the HOMO-HOMO concept to a more universal and efficient strategy. We intend to prove this concept by treating a polar donor-acceptor copolymer with either mono-, di- or tetracationic organic radical salt *p*-dopants. If more than one electron is accepted per dopant molecule, we can effectively decrease the dopant loading and confirm the charge carrier concentration and doping efficiency by Mott-Schottky measurements. Additionally, we try to limit the impact on the carrier mobility by exploiting the hole transport capabilities of the neutral dopant, which can be verified by frequency-dependent impedance measurements. Combining these advances should reward us with improvement in overall system performance compared to regular doping materials.

In a consecutive study, we revisit a doping concept published in 2019 by our group. In this work, we used copper(II) bis(trifluoromethanesulfonyl)imide as a powerful electron acceptor dopant for hole transport materials such as Spiro-MeOTAD in perovskite solar cells. We recognized, that transition metal salts offer a huge potential for next generation *p*-type dopants, due to the efficient charge carrier generation. By understanding the basic mechanism on a molecular level, their full performance potential can be unlocked. Using a set of advanced impedance spectroscopy methods tightly integrated with temperature control, we aim to unravel the thermodynamic equilibria of the reactants during doping. This allows us to identify the causal link between dopant design and doping efficiency. Additionally, we aim to identify possible detrimental aspects to this doping strategy and how to avoid them, in an attempt to formulate guidelines for further research. Based on the impact on carrier transport, these states are expected to be observable by studying the carrier mobility at various temperatures and doping concentrations.

Currently, there is an ever-increasing demand for *n*-type materials with outstanding figure of merits, such as conductivity, stability, low lying LUMO values and thermoelectric capability. To expand the scope of this work towards *n*-type materials, we shall develop a bulk dopant for polar acceptor-acceptor polymers. We selected alkali metal carbonates as a viable alternative to N-DMBI, as they are more readily available and stable. We set on to

develop a conclusive doping mechanism of proton abstraction by the carbonate for this system through inverse- and ultraviolet photoelectron spectroscopy studies. An important aspect is the morphological change during doping, which will be assessed with grazing-incidence wide-angle X-ray scattering. Improving the electron density on the polymer backbone could render this system applicable in many fields, such as thermoelectric devices for power generation from waste heat energy. Ultimately, proposing a doping mechanism and confirming the performance increase may broaden the horizon for doped *n*-type polymer research.

3. Overview of the thesis

This thesis addresses the synthesis of novel organic/inorganic dopants for organic semiconductors, along with the introduction of new chemical doping strategies. Insight into the properties of the doped systems is provided by using advanced electrical characterisation methods. Especially, solid-state devices were fabricated and detailed electrical analysis are given to characterize the doped systems using impedance spectroscopy, for the first time in the AFuPo research group. Specifically, Mott-Schottky analysis of impedance data of metal-insulator-semiconductor devices were used to elucidate charge carrier concentration. Since it is difficult to determine the charge carrier mobility of conducting systems (doped polymers in general) using conventional methods such as OFET or SCLC, the field dependent charge carrier mobilities of pristine and doped polymers were measured using negative differential susceptance ($-\Delta B$) method utilizing impedance spectroscopy on metal-semiconductor substrates. Additionally, in specific systems the mechanism of doping is resolved and explained in detail for the first time. Doping is the pillar of modern organic semiconductor research, transforming intrinsic insulators into tailored, sought-after conductive materials for energy storage and - conversion applications. Hitherto, the field is confronted with the requirement of high dopant levels, stability and performance issues, which are addressed in the different chapters of this dissertation. The work is divided into two major parts, focussing on either *p*- or *n*-doping. Chapters 5 to 6 cover the use of radical cation salts of triphenylamine derivatives as electron acceptors (*p*-dopants) for organic semiconductors, whereas Chapter 7 discusses the detailed mechanism of *p*-doping using $Cu(TFSI)_2$ salt. Chapter 8 deals with the viability of using diverse alkali metal carbonates as novel *n*-dopants for acceptor-acceptor polymers as well as the mechanism of this *n*-doping. (see **Figure 3.1** for a schematic overview). The chapters have been published in peer-reviewed journals as individual manuscripts and are presented here in a cumulative manner.

Chapter 5

p-Doping soluble PEDOT-C$_6$C$_8$ using Spiro-MeOTAD(TFSI)$_2$

Chapter 6

p-Doping of Polydiketopyrrolopyrroles using Multielectron Acceptor Salts

Impedance spectroscopy

Electrical Characterisation

Photoelectron spectroscopy

p-Doping of Spiro-MeOTAD using Cu(TFSI)$_2$

Chapter 7

n-Doping Acceptor-Acceptor Copolymers using Alkali Metal Carbonates

Chapter 8

Figure 3.1. Graphical overview of the Chapters 5-8 presented in this thesis, centred around the electrical characterisation using photoelectron- and impedance spectroscopy methods. The chapters were published under the following titles: A Solution-Processable Pristine PEDOT Exhibiting Excellent Conductivity, Charge Carrier Mobility, and Thermal Stability in the Doped State (Chapter 5), Highly Efficient Doping of Conjugated Polymers Using Multielectron Acceptor Salts (Chapter 6), Intricacies and Mechanism of p-Doping Spiro-MeOTAD Using Cu(TFSI)$_2$ (Chapter 7), Applicability and mechanism of Carbonates as *n*-Dopants for an Acceptor-Acceptor Polymer (Chapter 8).

Chapter 5: A Solution-Processable Pristine PEDOT Exhibiting Excellent Conductivity, Charge Carrier Mobility, and Thermal Stability in the Doped State

(Published in Macromol. Chem. Phys. **2021**, *222*, 2100123*)*

The controlled synthesis of soluble PEDOT-C$_6$C$_8$ conjugated polymer and chemical *p*-doping using oxidized Spiro-MeOTAD salts will be addressed in Chapter 5. The novel concept of HOMO-HOMO electron transfer using oxidized triphenylamine derivatives as *p*-dopants was previously introduced by our group, where two distinct advantages were

found: i) no deep lying LUMO required for the *p*-dopant, as the electron is accepted into a HOMO state, and ii) non-interfering doping byproducts, which can participate in hole transport.[1] We combined this promising concept with the need for soluble, highly conductive polymers for bioelectronics. Currently, the field is dominated by commercial PEDOT:PSS, an insoluble doped polymer blend which is processed as an aqueous dispersion. We substituted a EDOT monomer with solubilizing branched alkyl side chains, followed by controlled Kumada catalyst transfer polymerisation. This yields a well-controlled, narrowly distributed homopolymer PEDOT-C_6C_8 between 3 and 9.8 kg mol^{-1}, which is soluble in most aprotic, unipolar organic solvent (**Figure 3.2**) and can be doped at our will.
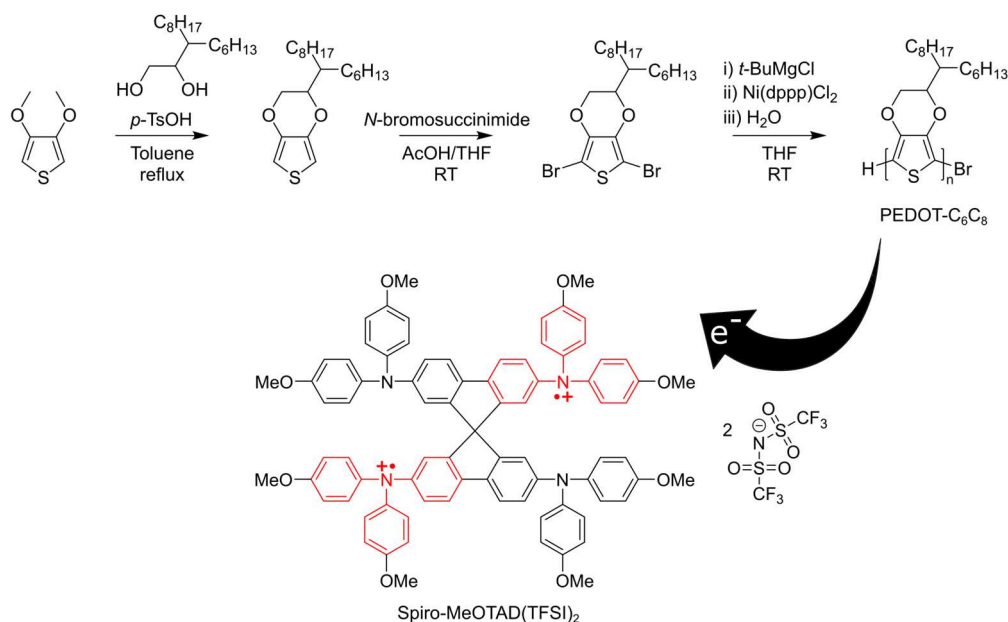
Figure 3.2. Synthesis of PEDOT-C_6C_8 from the EDOT monomer by Kumada catalyst transfer polymerisation presented in Chapter 6. The polymer is able to donate electrons to the *p*-dopant Spiro-MeOTAD(TFSI)$_2$. Adopted from Ref.[2]

In addition to excellent material properties, we conducted spectroelectrochemistry experiments to evaluate the oxidizability of PEDOT-C_6C_8. Upon oxidation, a distinct polaron absorption was recorded, with a low threshold voltage of +300 mV vs. Ag/AgCl in 0.1 M NaCl aqueous solution. We substituted the electrochemical doping by chemical doping using the *p*-dopant Spiro-MeOTAD(TFSI)$_2$. UPS confirmed the electron transfer from PEDOT-C_6C_8 to Spiro-MeOTAD(TFSI)$_2$, inducing a very low hole-injection barrier of only 100 meV at 2.5 mol% dopant. All electrical characterizations as well as UPS studies

were conducted to understand the mechanism and efficiency of doping. We obtained a highly stable doped system, showing no significant conductivity decrease from $1.1 \cdot 10^{-3}$ S cm^{-1} at 10 mol% dopant after being stored under ambient conditions for 12 h. Further, we note that the addition of Spiro-MeOTAD(TFSI)$_2$ has no appreciable impact on hole transport as confirmed by mobility studies. This chapter presents PEDOT-C$_6$C$_8$, a solution processable alternative to PEDOT:PSS, which can be made electrically conductive by the HOMO-HOMO doping concept.

Chapter 6: Highly Efficient Doping of Conjugated Polymers Using Multielectron Acceptor Salts

(Published in Macromol. Rapid Commun. **2021**, *42*, 2100443*)*

Doping efficiency is the major figure of merit to characterise the performance of a doped system. It quantifies the efficiency of generating free charge carriers from the total amount of dopant molecules added. Most doped organic systems are known to respond with an exponential decrease of the doping efficiency with increasing doping concentration, limiting the improvement of doping at high dopant concentrations. Hence, we tackle this problem by combining the HOMO-HOMO doping concept with molecules containing multiple triphenylamine units. Ethylene glycol side chain substituted donor-acceptor polymers are mixed with mono-, di- and tetravalent multielectron acceptor salts derived from different triphenylamine derivatives (**Figure 3.3**). The results are compared to a conventional monovalent *p*-dopant, NOPF$_6$. An excellent morphological compatibility between polar polymer and highly charged dopant molecules was found by XPS mapping of solution co-processed thin films.
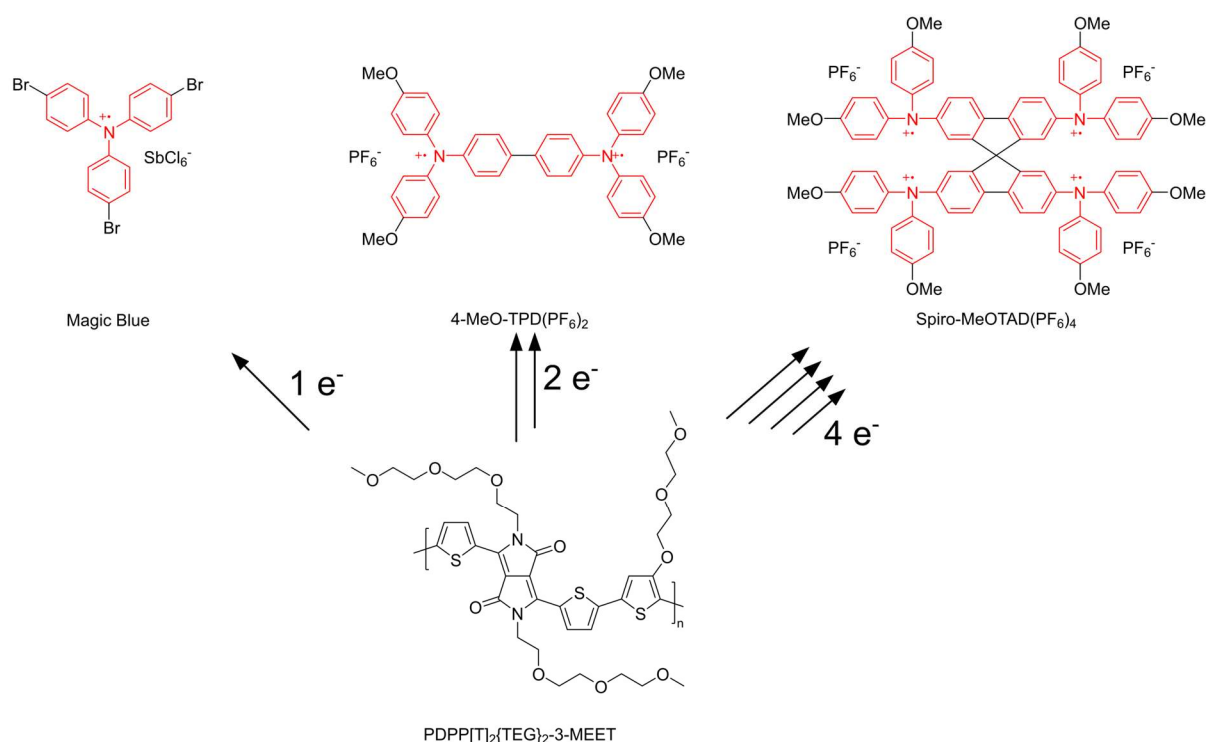
Figure 3.3. Studied *p*-dopants in Chapter 7: Magic Blue (monoelectron acceptor, left) and multielectron acceptors 4-MeO-TPD(PF$_6$)$_2$ (two-electron acceptor, middle) as well as Spiro-MeOTAD(PF$_6$)$_4$ (four-electron acceptor, right). PDPP[T]$_2${TEG}$_2$-3-MEET serves as the host material. Adopted from Ref.[3]

UPS and cyclic voltammetry studies on the HOMO energy levels of both dopant and host materials reveal the possibility of an exothermic electron transfer from polymer to dopant salts which was verified by UV/Vis/NIR spectroscopy. The tetravalent cation induced the highest polaron density, equivalent to positive charges on the polymer backbone. This was supported by thin film conductivity measurements, where the multielectron acceptors showed up to ca. 200-fold increase in conductivity compared to single electron acceptors. Mott-Schottky impedance spectroscopy measurements provided a proof for our concept, revealing a linear relationship between charge on the dopant and induced carrier density. Hence, we could reduce the necessary amount of dopant to induce an identical hole density on the polymer host by 75 % compared to Magic Blue while reaching a conductivity of 0.2 S cm^{-1} at 5 mol% Spiro-MeOTAD(PF$_6$)$_4$. Further, we monitored the doping efficiency of multielectron acceptor salts and found them to be up to one order of magnitude higher than NOPF$_6$, a standard material in doping research. Besides, the efficiency retention was more pronounced at increasing doping

concentrations (up to 24 % for Spiro-MeOTAD(PF$_6$)$_4$) compared to a steep loss for NOPF$_6$ (< 3 %) at 5 mol%. The polar ethylene glycol side chains also help to boost the doping efficiency by providing a higher dielectric constant of the system, lowering the necessary energy to dissociate the charge transfer state formed upon doping. This was verified by comparing the doping experiments with a polymer carrying lower polarity branched alkyl side-chains instead of polar oligo ethylene glycol as substituents. In the hydrophobic polymer, the doping efficiency was effectively decreased by 50 %. To conclude, this chapter introduces novel di- and tetracationic multielectron acceptor dopants for organic semiconductors, inducing a higher conductivity, carrier density and doping efficiency compared to standard single electron acceptors. Polymer – dopant compatibility was tuned by increasing the polymer polarity, which creates a synergistic effect boosting the electrical performance of the system.

Chapter 7: Intricacies and Mechanism of p-Doping Spiro-MeOTAD Using Cu(TFSI)$_2$

(Published in Adv. Electron. Mater. **2022**, *8*, 2200113*)*

Spiro-MeOTAD is a popular choice for hole transport materials in organic solar cells. To improve the device efficiency, Spiro-MeOTAD is commonly doped with organic acceptors such as F$_4$TCNQ or air oxidation in presence of LiTFSI and *t*-butyl pyridine. Previously, our group published a new concept of co-evaporating the novel *p*-dopant Cu(TFSI)$_2$ and Spiro-MeOTAD to produce a highly uniform and conductive hole transport film. Despite being efficient, the underlying mechanism and interaction between transition metal salts and triphenylamines remained elusive. By studying the doping reaction between co-evaporated Spiro-MeOTAD and Cu(TFSI)$_2$ in detail, we provide mechanistic insights into transition metal *p*-doping. Using UPS and optical spectroscopy experiments, we found that the electron transfer from Spiro-MeOTAD to Cu(TFSI)$_2$ to be highly exothermic, resulting in a temperature independent formation of the charge transfer salt [Spiro-MeOTAD^{x+}][Cu^{I}(TFSI)$_2^-$]$_x$ (**Figure 3.4**).
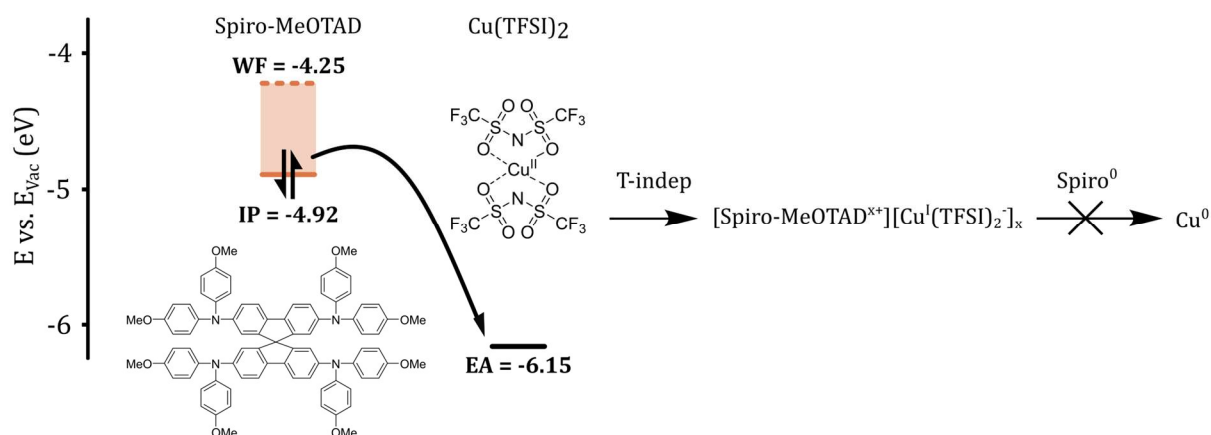
Figure 3.4. Oxidation of Spiro-MeOTAD (left) by temperature-independent electron transfer to Cu(TFSI)$_2$ during co-evaporation, as reported in Chapter 5. Cu(TFSI)$_2$ is reduced to the copper(I) salt [Spiro-MeOTAD^{x+}][Cu^I(TFSI)$_2^-$]$_x$, but is not reduced to metallic copper(0). Adopted from Ref.[4]

No further reduction of copper(I) to copper(0) occurred, which was explained by copper(I) stabilization with TFSI$^-$ ligands and verified by elemental analysis. The high doping efficiency found in earlier studies can then be explained by the low Coulombic binding energy of this salt, requiring a mere 11-19 meV to dissociate into free charge carriers Spiro-MeOTAD^{x+}, far lower than the available room temperature thermal energy of ca. 26 meV. Quantification of the doping efficiency *via* impedance spectroscopy yielded a value of (52 ± 6.4) % at 10 mol% dopant. This results in a significant increase over conventional organic *p*-dopants such as F$_6$TCNNQ or C$_{60}$F$_{36}$, both lying below 10 % doping efficiency at 10 mol% and above. Testing the electrical conductivity of the doped system revealed a temperature independent regime below 150 K, which is unusual for Arrhenius-activated systems like doped organic semiconductors. As this phenomenon could not be explained by published physical models, extensive temperature-dependent Mott-Schottky and impedance measurements were conducted. Monovalent copper was identified as a potent trap state, which is frozen out/inactivated below 150 K. Bathocuproine as a selective copper(I) complexing agent is able to revert this effect to a certain extent. Complemented by energetical analysis of the charge carrier hopping, the complete picture of all reaction steps occurring during Cu(TFSI)$_2$ doping Spiro-MeOTAD was drawn. In short, we have demonstrated the necessity of fully understanding the underlying mechanism in an organic doping reaction. Transition metal doping with

Cu(TFSI)$_2$ is presented as a highly efficient strategy, if the impact of metal ions on the hole transport is accounted for.

Chapter 8: Applicability and mechanism of Carbonates as n-Dopants for an Acceptor-Acceptor Polymer

n-type organic semiconductors are becoming increasingly sought-after for thermoelectric applications, organic electrochemical sensors and photovoltaics. However, the *n*-doped state is considerably less stable towards ambient conditions than *p*-doped systems, which is exacerbated by a lack of suitable *n*-dopants as well as acceptor polymers with low lying LUMO values. Hence, we approach this problem by designing a novel polar *n*-type acceptor-acceptor copolymer, which is *n*-doped in a new approach using abundant Cs$_2$CO$_3$. By lowering the LUMO of the polymer, we increase the stability of the *n*-doped system towards oxidation. For caesium carbonate, conflicting explanations can be found in literature to explain the doping mechanism for small molecule OSCs, while it is entirely unknown for semiconducting polymers. In electrical conductivity measurements, we measured eight orders of magnitude increase upon adding 40 mol% Cs$_2$CO$_3$, comparable to the reference *n*-dopant N-DMBI. Seebeck measurements confirmed electrons as the majority carrier type for the carbonate doped polymer. This was accompanied by a rather high power factor of $(5.59 \pm 0.39) \cdot 10^{-6}$ W m^{-1} K^{-2}, exceeding the performance figures of N-DMBI doped donor-acceptor *n*-type polymers. To investigate the underlying mechanism further, we conducted FT-IR and XPS studies. A distinct change in electron density at the unsubstituted thiophene comonomer occurred due to deprotonation. We correlated this to the Brønsted basicity of a series of alkali metal- and organic carbonates, where a less basic carbonate resulted in a lower conductivity. Inverse- and regular photoelectron spectroscopy studies were conducted to investigate the impact of doping on HOMO and LUMO orbitals. Although the deprotonation leads to the formation of localized intragap states, electrons are transported mostly in the LUMO. Finally, GIWAXS measurements revealed the formation of crystalline CsHCO$_3$ after doping, with only minor morphological changes after addition of the carbonate. To conclude, this work provides a novel *n*-doping pathway for acceptor polymers following the unusual base *n*-doping

mechanism. The bulk carbonate doping offers a great potential for applications in energy conversion.

References

[1]   M. Goel, M. Siegert, G. Krauss, J. Mohanraj, A. Hochgesang, D. C. Heinrich, M. Fried, J. Pflaum, M. Thelakkat, *Adv. Mater.* **2020**, *32*, 2003596.

[2]   P. Schmode, A. Hochgesang, M. Goel, F. Meichsner, J. Mohanraj, M. Fried, M. Thelakkat, *Macromol. Chem. Phys.* **2021**, *222*, 2100123.

[3]   G. Krauss, A. Hochgesang, J. Mohanraj, M. Thelakkat, *Macromol. Rapid Commun.* **2021**, *42*, 2100443.

[4]   A. Hochgesang, S. Biberger, J. Grüne, J. Mohanraj, F.-J. Kahle, V. Dyakonov, A. Köhler, M. Thelakkat, *Adv. Electron. Mater.* **2022**, 2200113.

4. Individual contributions to joint publications

In this chapter, the individual contributions to the manuscripts published within the framework of this research work are explicitly stated for each author.

4.1 "Intricacies and Mechanism of p-Doping Spiro-MeOTAD Using Cu(TFSI)$_2$"

Published as a research article in *Advanced Electronic Materials* **2022**, 2200113 by Adrian Hochgesang, Simon Biberger, Jeannine Grüne, John Mohanraj, Frank-Julian Kahle, Vladimir Dyakonov, Anna Köhler and Mukundan Thelakkat.

I prepared co-evaporated and solution processed films for all experiments presented in this research article. I measured room temperature optical spectroscopy, room- and temperature dependent Mott-Schottky devices, temperature dependent electrical conductivity, mobility and activation energies for hopping transport and charge transfer state dissociation. Furthermore, I measured room- and temperature dependent doping efficiency. I measured the mobility of copper(I) mixed Spiro-MeOTAD using the negative differential susceptance method. The planning and conceptualization of this research project and experiments was partially done by me. Furthermore, I wrote and corrected the manuscript and supporting information, as well as plotted all data.

Simon Biberger conducted temperature-dependent optical spectroscopy and CELIV measurements, as well as wrote the respective part in the manuscript and supporting information.

Jeannine Grüne conducted (temperature-dependent) EPR spectroscopy and evaluated the data. Further, she prepared and corrected the corresponding section in the manuscript.

John Mohanraj conducted UPS spectroscopy and evaluated the data.

Frank-Julian Kahle supported CELIV measurements and helped in evaluating the data.

Vladimir Dyakonov, Anna Köhler and Mukundan Thelakkat supervised the project and corrected the final manuscript.

4.2 "A Solution-Processable Pristine PEDOT Exhibiting Excellent Conductivity, Charge Carrier Mobility, and Thermal Stability in the Doped State"

Published as a research article in *Macromolecular Chemistry and Physics* **2021**, *222*, 2100123 by Philip Schmode, Adrian Hochgesang, Mahima Goel, Florian Meichsner, John Mohanraj, Martina Fried and Mukundan Thelakkat.

Adrian Hochgesang and Philip Schmode contributed equally to this work and planned the research work together.

Philip Schmode partially conceptualized the research project and wrote a preliminary manuscript. He synthesized and characterized the polymers and conducted spectroelectrochemical measurements, OFET experiments and optical spectroscopy of the pristine polymer.

I wrote and corrected the finalized manuscript. Further, I curated the data and plotted all figures. Further, I measured optical spectroscopy of the doped samples and zero-field mobility *via* impedance spectroscopy. Further, I measured the room temperature thin film conductivities of the doped samples.

Mahima Goel measured the thermal and environmental stability of the doped state *via* electrical conductivity measurements.

Florian Meichsner supported Philip Schmode in preparing the polymer. Further, he determined the polymerisation kinetics.

John Mohanraj conducted ultraviolet photoelectron spectroscopy of the doped and pristine samples.

Martina Fried synthesized the dopant used in this study.

Mukundan Thelakkat supervised the project and corrected the manuscript.

4.3 "Highly Efficient Doping of Conjugated Polymers Using Multielectron Acceptor Salts"

Published as a research article in *Macromolecular Rapid Communications* **2021**, *42*, 2100443 by Gert Krauss, Adrian Hochgesang, John Mohanraj and Mukundan Thelakkat.

Adrian Hochgesang and Gert Krauss contributed equally to the project conceptualization, writing of this manuscript and supporting information. Charge carrier density measurements by optical spectroscopy and Mott-Schottky measurements were also done with equal work contribution.

I synthesized the dopants and characterised their properties. I prepared samples to measure the charge carrier density using Mott-Schottky measurements of $NOPF_6$ doped films. In addition, I measured the zero-field mobilities of the neutral triphenylamine precursors. Further, I measured the dielectric permittivity of the polymers and fabricated the corresponding devices. In addition, I conducted sample preparation and ultraviolet photoelectron spectroscopy of the polymers, dopants and doped systems.

Gert Krauss synthesized and characterized the polymers. He prepared samples, conducted optical spectroscopy as well as spectroelectrochemical measurements and evaluated the data. He prepared devices and measured the thin film electrical conductivities and thermal activation energies. Further, he plotted all data and prepared all figures for the manuscript and supporting information.

John Mohanraj determined the chemical composition of the dopants *via* X-ray photoelectron spectroscopy. Further, he was involved in the correction of the manuscript.

Mukundan Thelakkat supervised the project and corrected the manuscript.

4.4 "Applicability and mechanism of Carbonates as n-Dopants for an Acceptor-Acceptor Polymer"

Published as a research article in *Advanced Functional Materials* **2023**, DOI:10.1002/adfm.202300614, forthcoming, by Adrian Hochgesang, Andreas Erhardt, John Mohanraj, Meike Kuhn, Eva M. Herzig, Selina Olthof and Mukundan Thelakkat.

This article was published with shared first authorship between Adrian Hochgesang and Andreas Erhardt.

During our investigation, we developed the concept of proton-abstraction doping in our system together. We designed the conducted experiments and performed the doping reaction together. Andreas Erhardt and myself wrote the manuscript and designed the figures together.

I wrote 50 % of the manuscript and corrected the finalized version of the manuscript. I synthesized the TEA_2CO_3 dopant. I performed solution doping experiments to prepare doped samples and analysed the products using NMR and MALDI-TOF. I performed XPS as well as UPS analysis on doped samples and evaluated the data. Further, I measured thermoelectric parameters, performed the NMR doping study, TGA, Impedance, Stability and FTIR analysis.

Andreas Erhardt wrote 50 % of the manuscript and corrected the finalized version of the manuscript. He synthesized the monomers and polymers used in this study. Furthermore, he prepared doped samples and measured electrical conductivity, temperature-dependent conductivity and conducted GIWAXS sample preparation and data interpretation. He performed Flash-DSC, OFET and UV/Vis/NIR-spectroscopy and evaluated the data.

John Mohanraj conducted regular and inverse ultraviolet photoelectron spectroscopy of the doped and pristine samples and assisted in data evaluation.

Meike Kuhn performed measurement of GIWAXS on doped and pristine samples.

Eva M. Herzig helped and assisted in evaluating GIWAXS data.

Selina Olthof assisted in evaluating photoelectron spectroscopy data.

Mukundan Thelakkat supervised the project and corrected the manuscript.

5

5

5. A SOLUTION-PROCESSABLE PRISTINE PEDOT EXHIBITING EXCELLENT CONDUCTIVITY, CHARGE CARRIER MOBILITY, AND THERMAL STABILITY IN THE DOPED STATE

5. A Solution-Processable Pristine PEDOT Exhibiting Excellent Conductivity, Charge Carrier Mobility, and Thermal Stability in the Doped State

Philip Schmode[#][†], Adrian Hochgesang[#][†], Mahima Goel[†], Florian Meichsner[†], John Mohanraj[†], Martina Fried[†] and Mukundan Thelakkat[†][§]*

[†] Applied Functional Polymers, University of Bayreuth, Universitätsstr. 30, 95440 Bayreuth, Germany

[§] Bavarian Polymer Institute (BPI), University of Bayreuth, Universitätsstr. 30, 95440 Bayreuth, Germany

[#] **equally contributing authors**

* Corresponding Author
E-mail: mukundan.thelakkat@uni-bayreuth.de

Abstract

PEDOT:PSS [poly(3,4-ethylenedioxythiophene) polystyrene sulfonate] is a widely used insoluble conducting polymer, which is therefore processed from dispersions. In this work, PEDOT homopolymers (PEDOT-C_6C_8 1 and 2) highly soluble in common solvents like toluene, tetrahydrofuran, and chloroform are synthesized with a high control of molecular weight and low dispersity using Kumada catalyst transfer polymerization of a newly synthesized EDOT monomer carrying a branched alkyl substituent. Pristine PEDOT-C_6C_8 allows the use in accumulation mode transistors with a high charge carrier mobility of $5 \cdot 10^{-4}$ cm^2 V^{-1} s^{-1}. Moreover, these polymers can be doped in a controlled fashion, reaching conductivities of 10^{-3} S cm^{-1} at 10 mol% of a dopant, Spiro-MeOTAD(TFSI)$_2$. The doped state is remarkably stable, retaining 80 % of the initial value after annealing under nitrogen at 100 °C and being exposed to ambient atmosphere for up to 12 h. During doping, the hole injection barrier decreases and reaches an impressively low value of 130 meV at only 2.5 mol% dopant loading without loss in carrier mobility; as monitored using ultraviolet photoelectron- and impedance spectroscopy. This new design concept leading to highly soluble polymers with well-controlled molecular weights provides solution-processable PEDOT dopable in a well-controlled fashion.

5.1 Introduction

π-conjugated semiconducting polymers as well as their doped counterparts called conductive polymers, which show a good charge transport, low oxidation potential, and a high stability of the oxidized state, are of great interest in the field of organic thermoelectrics, solar cells, and in organic bioelectronics.[1-3] The most widely used p-type

conducting polymer is PEDOT:PSS [poly(3,4-ethylenedioxythiophene) polystyrene sulfonate], which is commonly processed as a dispersion in water due to its insoluble nature.[4,5] It is mainly transparent (80–95 %) within low thickness ranges and exhibits high conductivity of up to 4600 S cm^{-1}, catching up with elemental metals such as mercury $(1 \cdot 10^4$ S cm$^{-1})$.[6-8] PEDOT:PSS is a mixture of two ionomers, where PSS has the function of doping the short PEDOT segments and stabilizing their oxidized state. In this mixture, the short PEDOT segments (7–18 units) are surrounded by the PSS chains with a much higher molecular weight, forming a dispersion in solution and a granular structure in thin films.[9] These unique properties predestine PEDOT:PSS for both high-volume applications such as antistatic coatings as well as specialized fields of research on doped polymers like thermoelectrics or organic solar cells.[10-13] However, there is a big demand for soluble undoped PEDOT polymers due to its low oxidation potential and feasibility of processing thin films from solutions. The advantages of doped PEDOT:PSS are overshadowed by drawbacks such as: i) long-term and thermal instability of thin films; ii) limited solubility in organic solvents; and iii) intrinsically conductive nature hampering the use of undoped material in devices requiring a normally off-behavior, for example, accumulation mode organic field effect transistors (OFET).[14,15] This inherent limitation has instigated recent interest in developing suitably substituted PEDOT homopolymers, which are highly soluble in pristine form, processable from solution and more importantly dopable in a controlled and desired fashion for, for example, bioelectronics and thermoelectric applications.[16,17] The key challenge in synthesizing soluble PEDOT homopolymers is to select suitable substituents guaranteeing solubility, while still maintaining high molecular weights, because unsubstituted PEDOT is insoluble even at a few repeating units. In addition, the useful electrical properties of PEDOT:PSS, for example, high conductivity, should also be achieved in the new PEDOT homopolymers. Incorporating suitable substituents is a viable strategy, which is also shown in other conjugated polymers like poly(3-hexylthiophene) to improve the solubility and processability of the resulting polymer. In low band gap polymers, a common way to increase the solubility is to introduce branched aliphatic side chains.[18] Various approaches to tackle this challenge of making PEDOT polymers soluble were published, ranging from cyclic alkyl-substituted 3,4-ethylenedioxythiophenes (EDOT) and 3,4-propylenedioxythiophenes (PProDOT) over acyclic linear alkyl branched dioxythiophenes to more elaborate polar sidechains such as sulfonates or ethers.[19-23]

5. A SOLUTION-PROCESSABLE PRISTINE PEDOT EXHIBITING EXCELLENT CONDUCTIVITY, CHARGE CARRIER MOBILITY, AND THERMAL STABILITY IN THE DOPED STATE

Caras-Quintero previously published dihexyl-substituted PEDOT homopolymers employing acid-catalyzed transetherification to form the corresponding EDOT monomers, which were subsequently polymerized by electrochemical oxidation.[24] Recently, Pittelli introduced branched (ethylhexyl-) and unbranched (octyl-) alkyl-substituted poly(dioxythiophenes) synthesized by oxidative polymerization using FeCl$_3$, to obtain doped polymers, however suffering from broad polydispersities (Đ = 1.8–3.8).[25] Yet, no report on a controlled polymerization of soluble PEDOT homopolymer was published until Bhardwaj et al. functionalized an ethylenedioxythiophene monomer with a hexyl side chain and used the controlled polymerization technique of Kumada catalyst transfer polymerization (KCTP) to achieve a PEDOT-C$_6$ homopolymer.[26] Nevertheless, they achieved a polymer with low molecular weight of 4 kg mol^{-1}, indicating that the hexyl side chains did not enhance the solubility of the final polymer sufficiently. We introduced branched side chains to overcome this issue and synthesized a new generation of dibrominated EDOT monomer, to obtain a sufficiently high molecular weight and well-controlled PEDOT homopolymer soluble in common organic solvents. A new monomer synthesis route was developed to obtain an EDOT monomer with a branched 2-hexyldecyl (C$_6$C$_8$) side chain. In this study we present highly soluble PEDOT homopolymer having controlled molecular weight, low polydispersity as synthesized in a living fashion, utilizing KCTP. The two resulting highly defined polymers, differing in the polymer chain lengths, were investigated with spectro-electrochemistry measurements to evaluate their electrochemical oxidizability. Furthermore, the charge carrier mobility in accumulation mode OFETs was measured for the pristine samples. The change in work function and hole injection barrier of doped states of PEDOT-C$_6$C$_8$ polymer obtained by adding Spiro-MeOTAD(TFSI)$_2$ dopant were monitored using ultraviolet photoelectron spectroscopy (UPS). The influence of doping on charge carrier mobility was studied using the negative differential susceptance ($-\Delta B$) method, applying impedance spectroscopy experiments.[27] To summarize, our strategy offers a route to synthesize soluble pristine PEDOT polymers with controlled molecular weights, which allow any degree of doping in solution in a well-controlled fashion, and the doped state was found to be remarkably stable, retaining 80 % of the initial value for 12 h in ambient atmosphere after annealing under nitrogen at 100 °C.

5.2 Results and Discussion

In this study, we first synthesized the new polymer PEDOT-C_6C_8 starting from 3,4-dimethoxythiophene 1 as shown in **Figure 5.1a**. Detailed synthetic procedures for the substituent are given in the experimental part.[28] A transetherification between 3-hexylundecane-1,2-diol and 3,4-dimethoxythiophene results in EDOT-C_6C_8 monomer 2 carrying a branched C_6C_8 side chain. For the use in the Kumada catalyst transfer polymerization, a further dibromination step is necessary, which was accomplished using N-bromosuccinimide in CH_3COOH/THF to yield the monomer 3. We chose two different monomer to nickel catalyst ratios [M]$_0$/[Ni(dppp)Cl$_2$] (30/1 and 10/1) to synthesize PEDOT-C_6C_8 1 and 2, which should deliver theoretical molecular weights of 3500 and 10500 g mol^{-1}. Furthermore, a study of the polymerization kinetics was conducted in a separate experiment (**Figure 5.1b**). We observed a very rapid increase in molecular weight in the first 30 min of the polymerization before the molecular weight levels off indicating a chain-growth mechanism typically found in KCT polymerizations.[29] After the first 30 mins, the polymer chain grows less rapidly reaching almost a plateau after 4 h. To determine the molecular weight distribution and dispersity of PEDOT-C_6C_8 1 and 2, we used size exclusion chromatography (SEC) and MALDI–TOF analysis (see **Table 5.1**, **Figure 5.1c**). SEC measurements revealed well-defined monomodal distributed with low dispersities, but the elution with THF using PS calibration resulted in almost identical molecular weights for the two polymers (**Figure S5.2**, Supporting Information). However, the difference in molecular weights could be clearly resolved in MALDI-TOF analysis, showing peak molecular weights of 3 (≈ 9 repeating units) and 10 kg mol^{-1} (≈ 27 repeating units), respectively (**Figure 5.1c**), as expected from the monomer/catalyst ratio. In both MALDI-TOF spectra the molecular weight of the repeating unit (352 g mol^{-1}) could be confirmed for the peak series. The second peak series of the spectra of PEDOT-C_6C_8 1 can be attributed to the doubly charged species of the ionized polymer. Commercially available PEDOT:PSS such as Clevios P is composed of high molecular weight PSS chains (400 kg mol^{-1}) and short PEDOT segments of only 1000–2500 g mol^{-1}, which translates to ≈ 7–18 repeating units.[9] By eliminating PSS (later for doping), we can increase the content of electroactive PEDOT with a high degree of control over the molecular weight. We can deduce two advantages of our approach using a 2-hexyldecyl

side chain monomer in PEDOT polymers: i) no copolymerization necessary to achieve sufficient solubility; ii) high degree of control over molecular weight using KCTP; and iii) low polydispersity (**Table 5.1**).
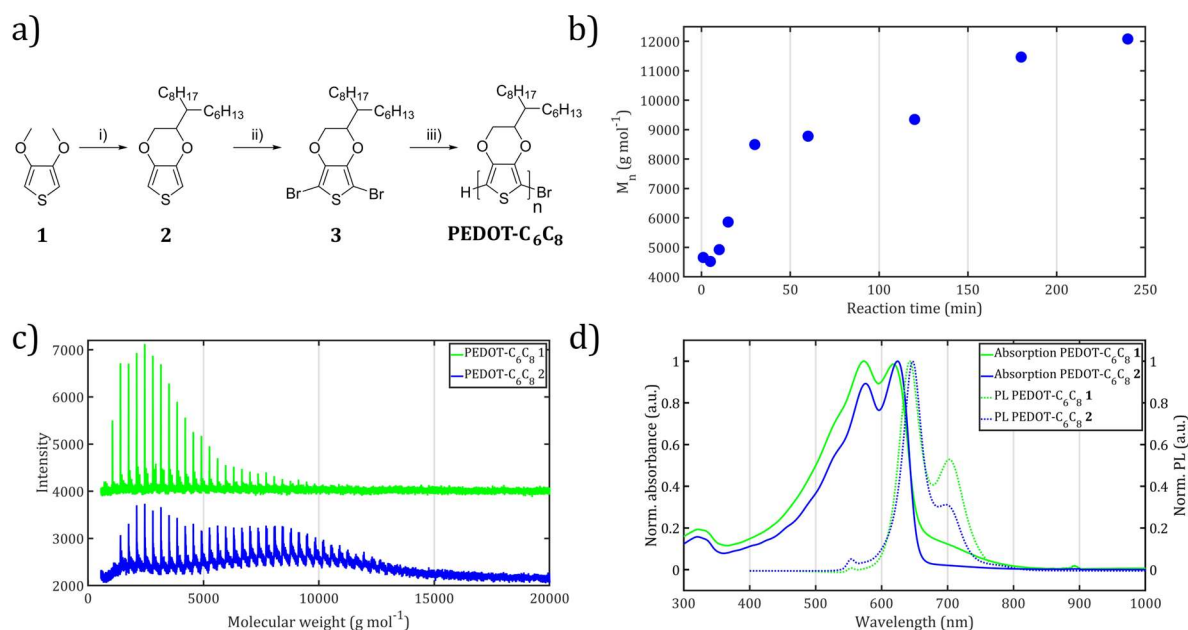
Figure 5.1. a) Scheme of polymer synthesis for PEDOT-C_6C_8 1 and 2: i) 3-hexylundecane-1,2-diol, p-TsOH, toluene, reflux; ii) N-bromosuccinimide, CH_3COOH/THF, RT; iii) t-BuMgCl, THF, RT, Ni(dppp)Cl_2, H_2O. b) Kinetic plot of PEDOT-C_6C_8 polymerization with monomer to nickel catalyst ratios $[M]_0$/[Ni(dppp)Cl_2] 100:1. M_n determined by SEC using THF as eluent, 1,2-dichlorobenzene as internal reference and narrowly distributed polystyrene standards. c) MALDI-TOF spectra of PEDOT-C_6C_8 recorded with dithranol as matrix. d) UV/Vis absorption and photoluminescence (PL) spectra of PEDOT-C_6C_8 1 and 2 in THF solution, with a polymer concentration of 0.02 mg ml^{-1}.

5. A SOLUTION-PROCESSABLE PRISTINE PEDOT EXHIBITING EXCELLENT CONDUCTIVITY, CHARGE CARRIER MOBILITY, AND THERMAL STABILITY IN THE DOPED STATE

Table 5.1. Characteristics of the two synthesized copolymers PEDOT-C$_6$C$_8$ 1 and 2, determined *via* SEC, MALDI-TOF, and OFET experiments.

	M_P MALDI-TOF (kg mol^{-1})[a]	Đ[b]	Repeating units[c]	μ_{hole}^{OFET} (cm^2 V^{-1} s^{-1})
PEDOT-C$_6$C$_8$ 1	3	1.38	9	$1.6 \cdot 10^{-4}$
PEDOT-C$_6$C$_8$ 2	9.8	1.19	27	$5.0 \cdot 10^{-4}$

[a] Dithranol was used as a matrix material, dilution 1:1000.

[b] SEC with polystyrene calibration and THF as eluent.

[c] Calculated from peak molecular weight determined in MALDI-TOF.

Optical properties play a vital role in devices incorporating PEDOT thin films such as organic solar cells, which were assessed consecutively *via* UV/Vis/NIR spectroscopy. UV/Vis/NIR absorption and emission studies in THF solution reveal, that both polymers exhibit similar vibronically resolved absorption and photoluminescence features, as well as an identical optical bandgap (**Figure 5.1d**). The as-synthesized sample PEDOT-C$_6$C$_8$ 1 exhibits absorption at wavelengths higher than 680 nm compared to PEDOT-C$_6$C$_8$ 2, indicating in-situ doping in the former. From the absorption or PL spectra, qualitative information regarding aggregation in solution was deduced. Both polymers exhibit highly ordered absorption spectra, in which the 0–0 transition peak for both polymers can be distinguished at 638 nm and the 0–1 transition peak at 584 nm, respectively.[30] It can be stated that both PEDOT polymers are highly aggregated in every solvent we tested (chloroform, hexane, THF, etc.). By introducing an aliphatic 2-hexyldecyl side chain, we expect an increased solubility of the pristine PEDOT-C$_6$C$_8$ 2 homopolymer. To test our hypothesis, we conducted solubility studies, summarized in **Table 5.2** below.

Table 5.2. Maximum solubilities of PEDOT-C_6C_8 2 in anhydrous organic solvents at RT.

Solvent	Solubility (g L^{-1})[a]	Solvent	Solubility (g L^{-1})[a]	Solvent	Solubility (g L^{-1})[a]
Toluene	34.1 ± 5.20	CHCl$_3$	25.1 ± 3.33	Ethyl acetate	0.43 ± 0.15
CH$_2$Cl$_2$	29.9 ± 0.60	1,4-Dioxane	0.67 ± 0.05	Acetonitrile	0.29 ± 0.18
THF	27.0 ± 0.40	Hexane	0.47 ± 0.06	Dimethylformamide	Insoluble[b]

[a] Solubilities determined by preparing a saturated PEDOT-C_6C_8 2 solution in solvent of choice and weighing the mass of the concentrated polymer after evaporation of a known volume of supernatant solution, averaged over three samples.

[b] No influence of prolonged heating on solubility was found.

Pristine PEDOT-C_6C_8 2 offers exceptional solubility of up to 34.1 g L^{-1} in nonpolar, aprotic solvents such as toluene and chlorinated solvents like dichloromethane and trichloromethane. Surprisingly, we were able to dissolve moderate amounts of PEDOT-C_6C_8 even in 1,4-dioxane, ethyl acetate, and hexane. Poor compatibility was found with the highly polar solvents acetonitrile and dimethylformamide. Bu et al. synthesized copolymers of dihexyl-substituted EDOT with the intended aim of high solubility in organic solvents and achieved a solubility of 1.82 g L^{-1} in dichloromethane, affirming the advantages of our homopolymer design strategy.[31] We investigated the thermal stability of the polymers using thermogravimetric analysis and observed that even the lower molecular weight polymer PEDOT-C_6C_8 1 is stable until 321 °C ($T_{5\%\text{weight loss}}$) under nitrogen atmosphere (**Figure S5.3**, Supporting Information). PEDOT:PSS on the other hand is prone to thermal decomposition at much lower temperatures, showing multiple degradation steps, namely water loss below 200 °C and PSS degradation at 230 °C before the ultimate oxidation at 420 °C.[32] The tendency of oxidizability (doping) of both polymers was monitored with spectro-electrochemistry measurements in a three-electrode assembly. Here, we monitored the changes in the absorption spectra of the polymer films in an aqueous NaCl electrolyte when they are subjected to increasing

electrochemical doping potentials from 0 to 900 mV in 100 mV steps. The resulting continuous changes in the absorption spectral features and the difference absorption spectra are shown for PEDOT-C_6C_8 2 as an example in **Figures 5.2a** and **5.2b**, respectively. Upon applying a doping potential in the range of 300 to 400 mV, the characteristic polaron absorption between 680 and 1100 nm arises, while concurrently the main $\pi-\pi^*$ absorption decreases and finally vanishes completely at 900 mV, which make theses polymers very attractive for transparent electrode applications in the highly doped state (**Figure 5.2a** and **Figure S5.3**, Supporting Information).[33] The electrochromism of PEDOT-C_6C_8 is comparable to PEDOT:PSS thin films in aqueous solution. In the pristine state, the former offers a larger bandgap (lower absorption onset) and therefore higher transmittance in the visible range than electrochemically de-doped PEDOT:PSS.[34] PEDOT-C_6C_8 1 behaves similarly (data of PEDOT-C_6C_8 1 can be found in **Figure S5.4**, Supporting Information). Between our polymers, a small variation is observed in the onset potential values, where PEDOT-C_6C_8 1 shows a lower onset of 300 mV versus Ag/AgCl compared to PEDOT-C_6C_8 2 having an onset of 400 mV (**Figure 5.2c**). However, the concentration of the electrochemically doped species saturates at about 700 to 800 mV versus Ag/AgCl for both polymers, indicating that probably the oxidation mechanism and the tendency of oxidation in both polymers are similar.
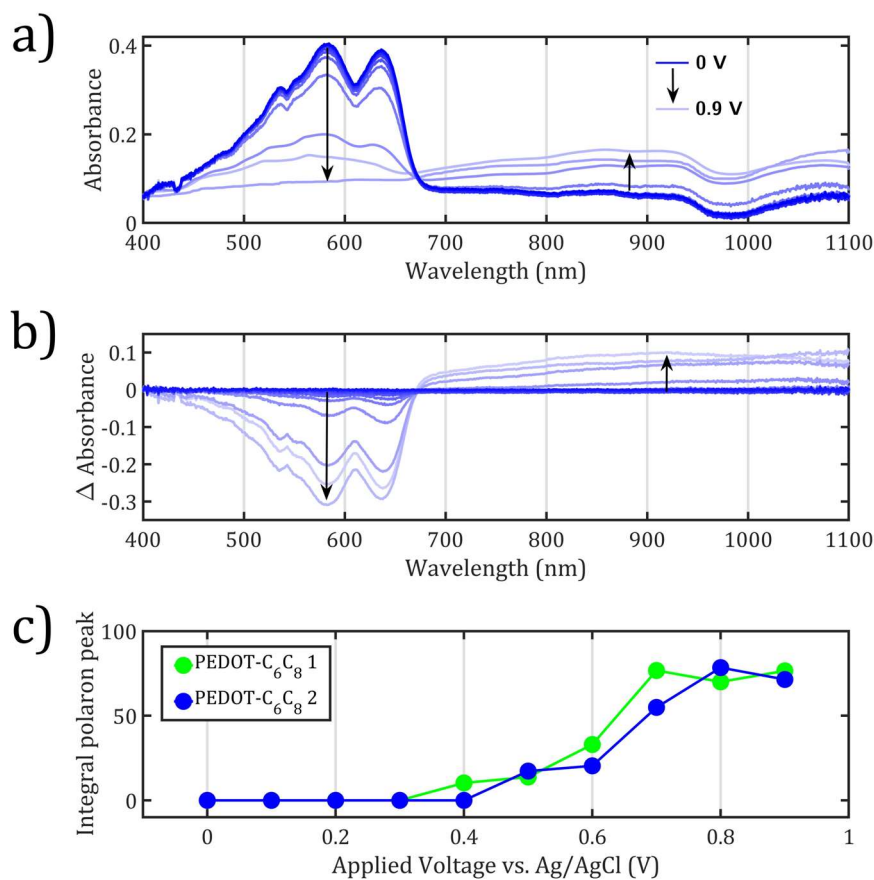
Figure 5.2. a) Spectro-electrochemistry measurements of thin polymer films on ITO of PEDOT-C$_6$C$_8$ 2. The spectra were measured in 0.1 M NaCl when the films were biased from 0 to 0.9 V in a three-electrode setup with an Ag/AgCl reference electrode and a Pt counter electrode. −100 mV versus Ag/AgCl was applied prior to SEC measurement for de-doping residual oxidized states. ITO transmittance cut-off below 400 nm is not shown. b) Difference spectra of doped PEDOT-C$_6$C$_8$ 2 obtained by subtracting the absorption spectra of the polymers in the neutral state (0 V) from the absorption spectra under different applied potentials from 0 to 900 mV. The arrow indicates the direction of spectral changes. c) Correlation of the concentration of polarons indicated by the integrals (obtained by integrating the area under the curve between 680–1100 nm corresponding to the increasing polaron concentration) versus applied potential.

From the low intensity of the polaron absorption shown in **Figure 5.2**, we can expect a low charge carrier density (N_D) of pristine PEDOT-C$_6$C$_8$ contrary to PEDOT:PSS, which is typically used in depletion-mode organic field-effect transistors due to its inherently

conductive nature. This intrinsic behavior allows PEDOT-C_6C_8 to be used in normally-off accumulation mode OFETs, which is inconceivable for PEDOT:PSS without significant chemical changes to the PEDOT backbone or additional de-doping chemistry.[35] The hole mobilities in pristine state, an important electronic property, of both the polymers in undoped state were investigated in commercially available OFET substrates containing different channel lengths ranging from 10 to 20 μm. By plotting the square root of the drain current I_D versus the gate voltage V_G the hole mobility was calculated (see **Equation S5.1**, Supporting Information). Hole mobility values of $1.6 \cdot 10^{-4}$ cm^2 V^{-1} s^{-1} (PEDOT-C_6C 1, **Figure S5.5**, Supporting Information) and $5.0 \cdot 10^{-4}$ (PEDOT-C_6C_8 2; **Figure S5.6**, Supporting Information) were obtained, with an ON/OFF ratio in the range of $2 \cdot 10^3$ to $9 \cdot 10^3$. Undoped, solution processable EDOT-thiophene alternating oligomers show comparable performance in accumulation mode OFETs with $\mu_h = 6 \cdot 10^{-4}$ cm^2 V^{-1} s^{-1}.[36] PEDOT-C_6C_8 2, the higher molecular weight polymer with 27 repeating units, shows only a 3 times higher charge carrier mobility compared to the low molecular weight one with nine repeat units. This indicates that the dependence of hole mobility on molecular weight is not very pronounced after about nine repeating units, unlike in many other polythiophenes such as P3HT, where orders of magnitude improvement is observed for high molecular weight samples.[37] The facile polaron formation upon electrochemical doping indicates good chances of obtaining a conducting polymer *via* chemical doping akin to acid-doped PEDOT:PSS. To test our hypothesis, we exploited the concept of *p*-doping through HOMO-HOMO electron transfer by employing Spiro-MeOTAD(TFSI)$_2$ as the *p*-dopant due to its deep singly occupied acceptor levels. (−5.3 eV, chemical structure shown in **Figure 5.3a**).[27,38,39] We used this kind of electron transfer doping method due to the high stability of the doped state.[27] PEDOT-C_6C_8 1 (3 kg mol^{-1}) displays slight in situ doped behavior in the pristine state, which could not be chemically de-doped fully by treatment with the reducing agent sodium dithionite. Therefore, PEDOT-C_6C_8 2 was selected for further chemical doping experiments and for a detailed consequent study of the electronic properties. PEDOT-C_6C_8 2 was first investigated to determine the absolute ionization potential and work function in pristine state using UPS. The recorded valence band maximum (VBM) and secondary electron cut-off (SECO) regions of the pristine PEDOT-C_6C_8 2 film with respect to E_F are shown in **Figure 5.3c**. The onset of the VBM is located 460 meV below E_F. Considering the optical band gap (ca. 1.8 eV) of the polymer, E_F is positioned near to the HOMO, suggesting an

intrinsic p-type nature of the polymer. The measured ionization potential (-4.48 eV) emphasizes its shallow HOMO levels, which could facilitate exothermic electron transfer from the polymer HOMO to lower lying unoccupied levels, for example, Spiro-MeOTAD(TFSI)$_2$ HOMO (possibly SOMO) positioned at -5.3 eV, effectively p-doping PEDOT-C$_6$C$_8$. UPS studies by Xing et al. on as-prepared, neutral PEDOT prior to PSS doping revealed a similar HOMO value of -4.7 eV, with a reported work function of -4.0 eV.[40] This similarity excludes effects of the introduced C$_6$C$_8$ side chain on the frontier orbitals, preserving the useful oxidizability of PEDOT:PSS. Further, the change in the electronic levels of PEDOT-C$_6$C$_8$ 2 as a function of dopant molar ratio was monitored through UPS measurements (**Figure 5.3c** and **5.3d**). The measured VBM and SECO regions of PEDOT-C$_6$C$_8$ 2 doped with Spiro-MeOTAD(TFSI)$_2$ up to 2.5 mol% are shown in **Figure 5.3c**. With increasing dopant concentration from 0.5 up to 1.25 mol%, E_F continues to shift closer to the VBM of PEDOT-C$_6$C$_8$ 2, decreasing the hole injection barrier; concurrently, SECO also moves towards the lower binding energy region, shifting down the work function value, as typically observed in p-doped systems.[27] These changes are plotted in **Figure 5.3d** and the absolute values are collected in **Table S5.7**, Supporting Information. Further increase in the dopant concentration up to 2.5 mol% practically coalesce the polymer VBM with E_F, thus reducing the hole injection barrier down to 130 meV. This is an impressive value for a p-type polymer with a remarkably low dopant content (2.5 mol%), which emphasizes the facile and controlled oxidative nature of PEDOT-C$_6$C$_8$, as well the efficient doping ability of Spiro-MeOTAD(TFSI)$_2$.[27]
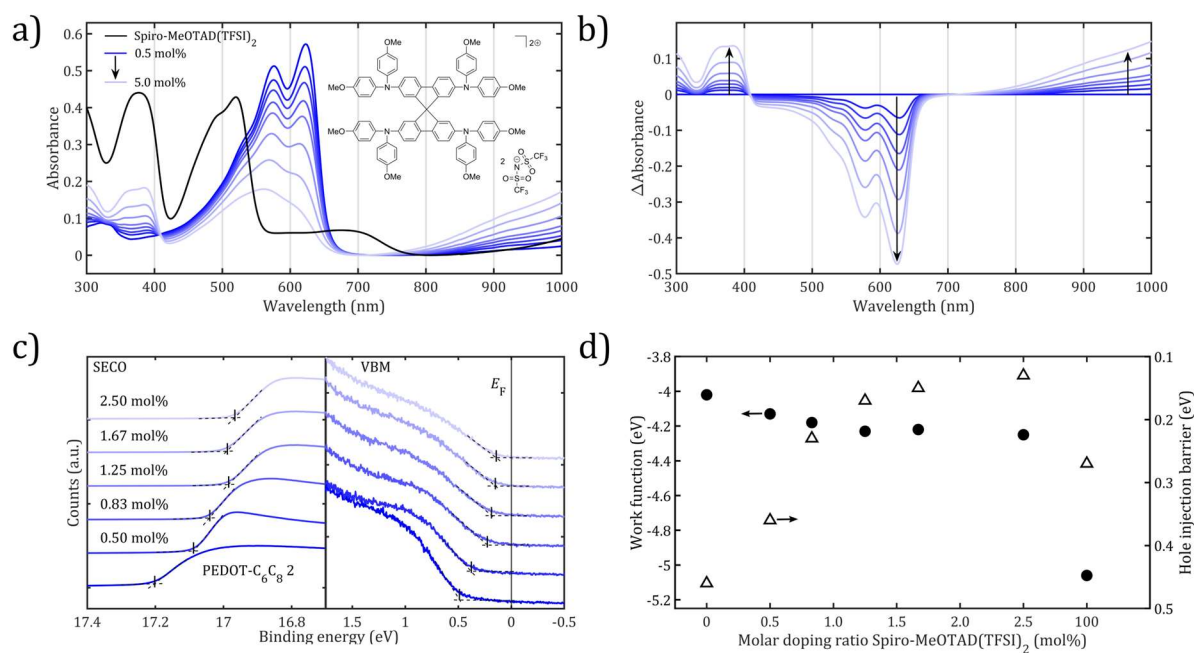
Figure 5.3. a) UV/Vis/NIR spectra of 0.02 mg mL^{-1} PEDOT-C$_6$C$_8$ 2 in anhydrous THF doped with Spiro-MeOTAD(TFSI)$_2$. The concentration of Spiro-MeOTAD(TFSI)$_2$ was increased from 0.5 mol% (dark blue) up to 5.0 mol% (faint blue). Absorption spectrum of 100 mol% Spiro-MeOTAD(TFSI)$_2$ referenced in THF (0.01 mg mL^{-1}) is also shown (black). Inset shows the chemical structure of the *p*-dopant Spiro-MeOTAD(TFSI)$_2$. b) Difference spectra were obtained by subtracting the absorption of the pristine PEDOT-C$_6$C$_8$ 2 reference from the chemically doped polymer solutions. The spectra were recorded under N$_2$ atmosphere in a sealed quartz glass cuvette of 1 cm optical path length. c) UPS measurement of the secondary electron cut-off region (SECO, left) and the valence band maximum (VBM, right) of PEDOT-C$_6$C$_8$ 2 doped with increasing amounts of Spiro-MeOTAD(TFSI)$_2$. d) Workfunction (left *y*-axis) and hole injection barrier (right *y*-axis) of pristine PEDOT-C$_6$C$_8$ 2 and Spiro-MeOTAD(TFSI)$_2$ and their mixtures as measured by UPS.

After assessment of the involved energy levels, which clearly allow for exothermic electron transfer from PEDOT-C$_6$C$_8$ HOMO to Spiro-MeOTAD(TFSI)$_2$ HOMO and evaluating the influence of doping on work function using UPS, we monitored the polaron formation on the polymer by UV/Vis optical spectroscopy during chemical doping. The *p*-doping process was investigated *via* a UV/Vis absorption titration experiment, in which aliquot amounts of Spiro-MeOTAD(TFSI)$_2$ were added to a PEDOT-C$_6$C$_8$ 2 solution, and consequent spectral changes were observed, as shown in **Figure 5.3a** and **5.3b**. With

increasing dopant concentration, as similar to SEC experiment, a continuous and linear rise in polaron absorption in the range of 680 to 1100 nm and concomitant decrease of the neutral main $\pi-\pi^*$ absorptions at 638 and 584 nm were observed. The linear increase of the integral of polaronic peak absorption of the doped polymer solutions (integrated between isosbestic point at 716 and 1000 nm) with the molar percentage of Spiro-MeOTAD(TFSI)$_2$ dopant in solution is given as an inset in **Figure 5.4a**. In addition a strong feature around 370 nm arises with increasing molar ratio of Spiro-MeOTAD(TFSI)$_2$, possibly originating from the residual or reduced dopant content (compare the absorption of pure dopant shown as a black curve in **Figure 5.3a**).
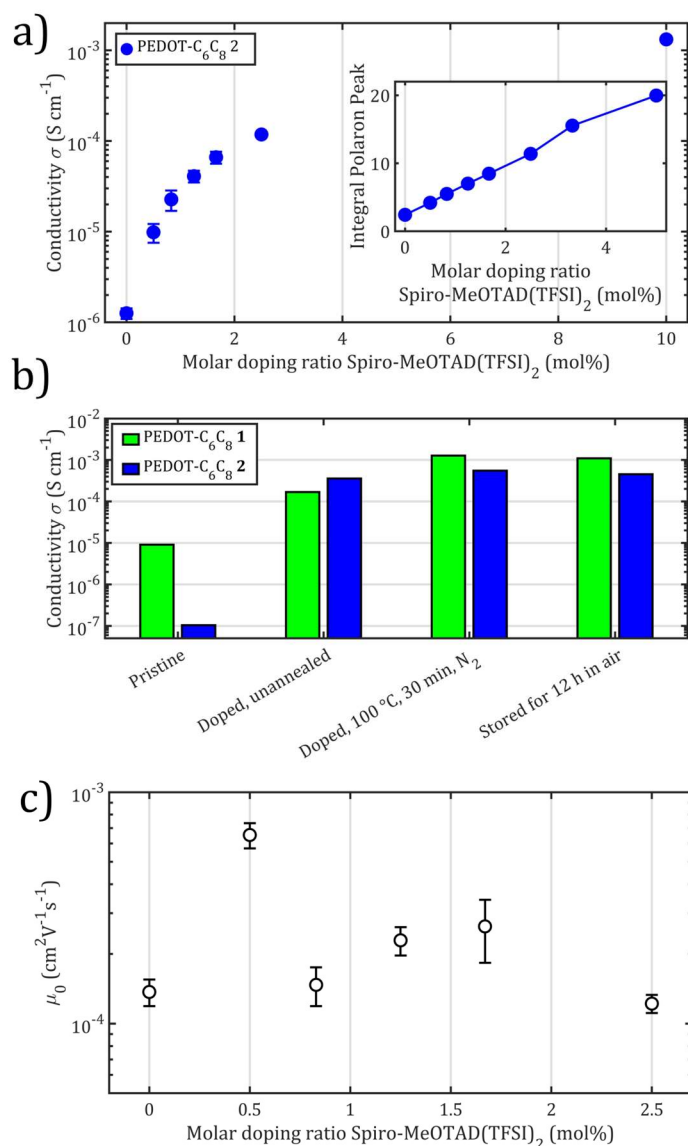
Figure 5.4. a) Thin film conductivities of PEDOT-C_6C_8 2 doped with Spiro-MeOTAD(TFSI)$_2$ as a function of molar dopant ratio with an inset showing the linear correlation between the integral of polaronic peak absorption of the doped polymer solutions (integrated between isosbestic point at 716 and 1000 nm) and the molar percentage of Spiro-MeOTAD(TFSI)$_2$ dopant in solution. b) Electrical conductivity (pristine, doped unannealed, doped annealed at 100 °C under N$_2$ for 30 min and 100 °C, 30 min N$_2$ annealed samples after 12 h storage in air) of PEDOT-C_6C_8 1 and 2, which were doped with 10 mol% of Spiro-MeOTAD(TFSI)$_2$. c) Zero-field mobilities μ_0 of PEDOT-C_6C_8 2 doped with different amounts of Spiro-MeOTAD(TFSI)$_2$ as measured by negative differential susceptance ($-\Delta B$) method on metal-semiconductor devices. The field-free mobilities were obtained by extrapolating log(μ(F)) versus $F^{0.5}$ plots towards the y-intercept.

5. A SOLUTION-PROCESSABLE PRISTINE PEDOT EXHIBITING EXCELLENT CONDUCTIVITY, CHARGE CARRIER MOBILITY, AND THERMAL STABILITY IN THE DOPED STATE

As UV/Vis/NIR absorption experiments provide clear evidence for polaron formation and UPS studies confirm the gradual shift of the workfunction towards VBM on doping, we conducted conductivity studies on the chemically doped PEDOT-C_6C_8 to assess the influence of doping on conductivity and the stability of the formed polaronic states as shown in **Figure 5.4a** and **5.4b** and **Tables S5.2** to **S5.6**, Supporting Information. Sufficient delocalization and mobility of these charge carriers may result in significantly enhanced electrical conductivity. The electrical conductivities of pristine and doped polymers in thin films were measured on as cast and annealed films. Varying the molar ratio of Spiro-MeOTAD(TFSI)$_2$ to PEDOT-C_6C_8 2 reveals a steady increase in conductivity, which asymptotically reaches $1.32 \cdot 10^{-3}$ S cm^{-1} (**Figure 5.4a**). For pristine as-cast films, PEDOT-C_6C_8 1 show the unusual high conductivity value of 10^{-5} S cm^{-1}, which can be explained only due to possible in situ doping *via* air oxidation. On the other hand, the pristine PEDOT-C_6C_8 2 exhibited an electrical conductivity of $1.04 \cdot 10^{-7}$ S cm^{-1}. Upon doping with 10 mol% Spiro-MeOTAD(TFSI)$_2$, both polymers gain orders of magnitude in electrical conductivity, precisely PEDOT-C_6C_8 1 to $3.58 \cdot 10^{-4}$ S cm^{-1} and PEDOT-C_6C_8 2 reaching $1.10 \cdot 10^{-3}$ S cm^{-1} (**Figure 5.4b**). In comparison to other reported PEDOT homopolymers, acid-doped side-chain functionalized PEDOT-S conductivity was reported as $2 \cdot 10^{-4}$ S cm^{-1} by Cutler et al.[22] Poly(3,4-propylenedioxythiophene) PProDOT doped with the electron acceptor Ni(tfd)$_2$ reached $1.2 \cdot 10^{-3}$ S cm^{-1}, whereas branched alkyl side-chain PProDOT oxidized with tris(4-bromophenyl)ammoniumyl hexachloroantimonate displays a similar conductivity of ca. 10^{-3} S cm^{-1}, rendering our reported PEDOT-C_6C_8 system highly competitive in the limited chemical space of doped soluble PEDOT homopolymer materials.[17,25] In addition, PEDOT:PSS typically lacks fine tuneability of the electrical conductivity below 1 S cm^{-1} necessary in, for example, hole-transport layers for solar cells, with most reports focusing on post-treatment to induce metal-like conductivities for electrode applications.[7,41,42] Aside from controlled polymerization, as well as high solubility in a broad range of solvents and tunable conductivity in films processed from solution, resilience against environmental factors such as oxygen, water, and heat are key requirements for use in commercial applications. To evaluate the thermal stability of our pristine and doped PEDOT-C_6C_8 system, we studied the changes in electrical conductivity in details after: i) heating under inert atmosphere, followed by; ii) heating of the same samples in ambient atmosphere; and iii) after storage at room

temperature for 12 h. The annealing protocols and all the conductivity data are summarized in under **Tables S5.3** to **S5.6**, Supporting Information. First, we annealed stepwise the as-cast polymer films at 100° C up to 30 min under nitrogen atmosphere (**Figure 5.4b**). Our measurements indicate that annealing under inert atmosphere marginally enhances the conductivity of doped films, which is in agreement with the high exothermicity found for the p-doping process in UPS experiments. Further, to probe the stability of doped films against humid and oxygen rich environments at elevated temperatures, we further annealed the oxidized films stepwise (30 and 120 min) at 100 °C in air. On annealing in air, an initial minor decrease in conductivity of 14 % (PEDOT-C_6C_8 1) and 18 % (PEDOT-C_6C_8 2) was observed in the first 30 min, which then stabilizes fully. After all the annealing steps, on storing the samples for 12 h in air at RT, we could confirm that the conductivity of doped films remains virtually unchanged for both PEDOT-C_6C_8 1 and 2 confirming very high stability of these doped polymers. Contrarily, both pristine polymers display signs of air-doping after prolonged exposure to ambient atmosphere, resulting in enhanced conductivity values compared to as-cast pristine films. Commercially available PEDOT:PSS degrades to ca. 63 % of the initial conductivity at 100 °C for 12 h in ambient atmosphere, further highlighting the remarkable stability of our new generation chemically doped PEDOT-C_6C_8 against thermal and environmental factors.[43] As outlined in our OFET experiments, the electrical mobility μ is not only important in field-effect transistors (according to **Equation S5.1**, Supporting Information), but also dictates the electrical conductivity σ together with the charge carrier density N_D and elementary charge e in unipolar (i.e. single carrier type) systems *via* **Equation 5.1** and consequently influences derived variables, for example, the Seebeck coefficient S in organic thermoelectric materials.[44]

$$\sigma = eN_{D}\mu \tag{5.1}$$

Since it is difficult to determine the charge carrier mobility of conducting systems (doped polymers in general) using conventional methods such as OFET or SCLC methods, we determined field dependent charge carrier mobilities of pristine and doped of PEDOT-C_6C_8 2 using negative differential susceptance ($-\Delta B$) method utilizing impedance spectroscopy on metal-semiconductor substrates. A detailed description of this method and the **Equations S5.3** to **S5.7**, Supporting Information, used for the calculation of

charge carrier mobility are given (**Figures S5.1** and **S5.7**, Supporting Information). In **Figure 5.4c**, the zero-field charge carrier mobilities of the pristine and doped PEDOT-C_6C_8 2 are plotted versus the dopant concentration. The measured zero-field mobility μ_0, $1.37 \cdot 10^{-4}$ cm^2 V^{-1} s^{-1} for pristine sample (at 0 mol% dopant) is comparable with μ values from OFET measurements ($\mu_{OFET} = 5 \cdot 10^{-4}$ cm^2 V^{-1} s^{-1}), proving the applicability of the negative differential susceptance ($-\Delta B$) method. Adding 0.5 mol% of Spiro-MeOTAD(TFSI)$_2$ to PEDOT-C_6C_8 2 increases μ_0 by a factor of 4.8 from $1.37 \cdot 10^{-4}$ to $6.53 \cdot 10^{-4}$ cm^2 V^{-1} s^{-1}, possibly due to trap filling process. Further dopant addition up to 2.5 mol% proves to have no detrimental effect on charge transport, albeit yielding zero-field mobilities comparable to pristine sample, consistent with the doping of highly disordered OSC systems as shown by Arkhipov et al.[45] Field-dependent mobilities of doped PEDOT:PSS were reported to be $4.5 \cdot 10^{-2}$ cm^2 V^{-1} s^{-1} in OFET-structures with calculated carrier densities of 10^{20} cm^{-3}.[46] By applying **Equation 5.1** to μ_0 and σ of PEDOT-C_6C_8 at 2.5 mol% Spiro-MeOTAD(TFSI)$_2$, a carrier density of ca. $6 \cdot 10^{18}$ cm^{-3} can be estimated. By decreasing N_D, μ is commonly decreased concurrently in organic semiconductors.[47] Taking this relationship into account, PEDOT-C_6C_8 offers a well-balanced mobility at high conductivities. Our study proves chemical p-doping based on HOMO-HOMO electron transfer yields delocalized and mobile charge carriers resulting in an exceptionally stable and highly conductive PEDOT-C_6C_8 system. **Table S5.8**, Supporting Information, summarizes the parameters determined with OFET, impedance, and conductivity measurements.

5.3 Conclusion

In summary, we synthesized a highly soluble, branched alkyl side chain bearing PEDOT homopolymer *via* controlled Kumada catalyst transfer polymerization. A new monomer synthesis route was developed to obtain a 3,4-ethylenedioxythiophene monomer Br$_2$-EDOT-C_6C_8, carrying branched alkyl chains. MALDI-TOF and SEC measurements revealed well-defined polymers with low polydispersity and molecular weights of up to 10 kg mol^{-1} ($\approx$ 27 repeating units). Absorption and photoluminescence spectroscopy confirmed a high degree of aggregation in solutions of PEDOT-C_6C_8. In contrast to well-

established, intrinsically conductive PEDOT:PSS, we were able to fabricate accumulation mode organic field effect transistors using this PEDOT polymer delivering a promising hole mobility of $5 \cdot 10^{-4}$ cm^2 V^{-1} s^{-1}. Furthermore, the ease of PEDOT-C$_6$C$_8$ oxidation is explained by spectro-electrochemistry and UPS measurements. On employing the hole conductor salt, Spiro-MeOTAD(TFSI)$_2$ as a *p*-type dopant for PEDOT-C$_6$C$_8$ results in a high conductivity of $1.3 \cdot 10^{-3}$ S cm^{-1} for 10 mol% dopant. Deeper insight into the doped states using UPS, UV/Vis/NIR absorption, and impedance spectroscopic measurements highlights the reduced hole injection barrier of oxidized PEDOT-C$_6$C$_8$, while conserving its original charge carrier mobility. The doped polymer exhibits a remarkable stability against thermal and environmental factors, retaining a conductivity value of $1 \cdot 10^{-3}$ S cm^{-1} after annealing at 100 °C in nitrogen for 30 min and storing in ambient atmosphere for up to 12 h. This outstandingly stable doped state mimicking PEDOT:PSS could help to ease the availability of solution processable conducting polymers. This work opens a new pathway to obtain highly soluble, solution processable PEDOT homopolymers having controlled molecular weights, which are chemically dopable in a desired fashion.

5.4 Experimental Section

General

Anhydrous solvents with a purity of > 99.5 % for synthesis and spectroscopical characterization were purchased from Thermo Fisher Scientific. Reagent-grade solvents and reagents for synthesis were supplied by Sigma-Aldrich. All reagents were used without further purification. In the following the synthesis of the branched alkyl substituent and monomer (**Scheme S5.1**, Supporting Information), as well as polymer, (**Figure 5.1a**) is described.

Synthesis 2-Hexyldecanal

25 mL DMSO in 620 mL dichloromethane was added to a dry Schlenk flask under nitrogen atmosphere. Thereafter, 12.4 mL (144 mmol, 1.40 equiv.) oxalyl chloride was added at −72 °C and stirred for 30 min. Then, at −72 °C, 25 g (103 mmol) 1,2-hexyldecan-1-ol were added and stirred again for 30 min. Subsequently, 73.8 mL (532 mmol, 5.16 equiv.) NEt_3 was added dropwise and reacted at rt for 24 h. 30 ml deionized water was added to the reaction mixture which then was extracted three times with 30 ml of diethyl ether. The organic phase was washed with a 10 % HCl solution. Subsequently, the reaction product was washed with a saturated $NaHCO_3$ solution and with a saturated NaCl. The crude product was purified *via* column chromatography over silica with ethyl acetate:*n*-hexane 1:5. (Yield: 23.1 g, 93 %)

^{1}H NMR (300 MHz; ppm, CDCl$_3$, δ_H): 0.88 (t, 6H), 1.14–1.7 (m, 24H), 2.22 (m, 1H), 9.57 (d, 1H).

Synthesis 2-Hexyldecene

41 g (115 mmol, 1.2 equiv.) methyltriphenylphosphonium bromide was dissolved in 580 mL THF at −78 °C in a dry Schlenk tube under nitrogen. Meanwhile, 12.9 g (114.8 mmol, 1.2 equiv.) potassium *t*-butoxide was dissolved in anhydrous THF and added to the reaction mixture. The mixture was stirred for 1 h at −78 °C. 23 g 2-hexyldecanal (96 mmol, 1 equiv.) were dissolved in 96 mL THF and slowly added to the mixture at −78 °C and stirred for 1 h. Then, the reaction mixture was allowed to warm up

to room temperature and stirred overnight. The mixture was diluted with 250 mL *n*-hexane and filtered over Celite. The raw product was purified *via* column chromatography over silica with *n*-hexane as eluent. (Yield: 14.7 g, 65 %)

^{1}H NMR (300 MHz; ppm, CDCl$_3$, δ_H): 0.88 (t, 6H), 1.14–1.42 (m, 24H), 1.94 (s, 1H), 4.88–5.01 (m, 1H), 5.43–5.6 (m, 2H)

Synthesis of 3-Hexylundecane-1,2-diol

The synthesis was done according to Plietker et al. with minor modifications.[28] 18 mL H$_2$SO$_4$ (18.3 mmol, 0.2 equiv.) and 29.4 g NaIO$_4$ (137 mmol, 1.5 equiv.) were dissolved in 60 mL water in a flask and cooled down to 0 °C. An aqueous suspension of 95 mg RuCl$_3$ (0.46 mmol, 0.005 equiv.) in 5 mL water was added slowly to the solution. 274 mL ethyl acetate was added and the suspension was stirred for 5 min. 274 mL acetonitrile were added and the suspension was again stirred for 5 min. 22 g 2-hexyldecene (91 mmol, 1 equiv.) was slowly added and the mixture was stirred for 5 min. The reaction mixture was poured into saturated solutions of 690 mL NaHCO$_3$ and 910 mL Na$_2$S$_2$O$_3$. The organic phase was dried over Na$_2$SO$_4$. The product was purified *via* column chromatography over silica with *n*-hexane:ethyl acetate 5:1. (Yield: 9.73 g, 39 %)

^{1}H NMR (300 MHz; ppm, CDCl$_3$, δ_H): 0.88 (t, 6H), 1.14–1.42 (m, 24H), 2.01 (s, 1H), 3.50–3.59 (m, 1H), 3.61–3.77 (m, 2H)

Synthesis of 2-(Pentadecan-7-yl)-2,3-dihydrothieno[3,4-b] [1,4] dioxine – Compound 2

To a three-necked flask equipped with an argon purge 3,4-dimethoxythiophene **1** (1 g, 6.935 mmol) were added 3-hexylundecane-1,2-diole (3.779 g, 13.87 mmol), *p*-toluenesulfonic acid monohydrate (0.120 g, 3.467 mmol), and 25 mL anhydrous toluene. The solution was heated at 90 °C for 24 h. After this time, another two equivalents of the diol were added, and the reaction was conducted for another 3 h before it was allowed to cool to room temperature. The reaction mixture was mixed with ethyl acetate and washed twice with a saturated sodium bicarbonate solution. After removal of the solvent, the remaining crude product was isolated by column chromatography (silica gel, *n*-hexane:dichloromethane 8:2). (Yield: 1.54 g, 63 %)

^{1}H NMR (300 MHz; ppm, CDCl$_3$, δ_H): 0.90 (t, 6H), 1.14–1.42 (m, 24H), 1.68 (s, 1H), 3.95–4.03 (m, 2H), 4.06–4.13 (q, 1H), 4.14–4.20 (dd, 1H), 6.31 (s, 2H)

Synthesis of 5,7-Dibromo-2-hexyl-2,3-dihydrothieno[3,4-b] [1,4] dioxine – Compound 3

N-bromosuccinimide (1.633 g, 9.173 mmol) was dissolved in a mixture of THF (30 ml) and acetic acid (30 ml) and cooled to 0 °C using an ice bath. 2-(pentadecan-7-yl)-2,3-dihydrothieno[3,4-b] [1,4] dioxine **2** (1.54 g, 4.368 mmol) was added against an argon stream dropwise at 0 °C and the solution was stirred at rt for 4 h under the exclusion of light. The solution was then extracted with diethyl ether and washed with water, saturated solution of sodium bicarbonate, and 1 molar solution of sodium hydroxide. The organic phase was dried over anhydrous $MgSO_4$, filtered, and concentrated. The raw product was purified by column chromatography over silica with *n*-hexane:dichloromethane 8:2 as eluent. (Yield: 1.87 g, 84 %)

^{1}H NMR (300 MHz; ppm, $CDCl_3$, δ_H): 0.90 (t, 6H), 1.14–1.42 (m, 24H), 1.68 (s, 1H), 3.95–4.03 (m, 2H), 4.06–4.13 (q, 1H), 4.14–4.20 (dd, 1H)

Synthesis of Poly(2-(pentadecan-7-yl)-2,3-dihydrothieno[3,4-b] [1,4] dioxine) PEDOT-C₆C₈

5,7-dibromo-2-hexyl-2,3-dihydrothieno[3,4-b] [1,4] dioxine **3** (1 eq.) was added to a dry flask under argon and the vessel was evacuated once again and flushed with nitrogen. Then the concentration was set with anhydrous THF to 0.5 mol L^{-1} and *t*-butylmagnesiumchloride (1.22 M in THF, 0.96 equiv.) was added dropwise. The reaction mixture was stirred for 20 h under the exclusion of light. Then the reaction mixture was diluted with anhydrous THF to 0.1 mol L^{-1}. The respective amount of Ni(dppp)Cl$_2$ (suspension in 2–3 mL anhydrous THF) was added in one portion to start the polymerization. After 4 h the polymerization was quenched with water. The mixture was concentrated, and the polymer was precipitated in methanol. Furthermore, the polymer was purified by Soxhlet extraction with *n*-hexane, methanol, and chloroform and dried under vacuum.

^{1}H NMR (300 MHz; ppm, $CDCl_3$, δ_H): 0.88 (t, 6H), 1.14–1.42 (m, 24H), 1.94 (s, 1H), 4.01–4.57 (m, 4H)

5.5 Acknowledgements

5.6 Conflicts of Interest

The authors declare no conflict of interest.

5.7 References

[1]   X. Wu, A. Surendran, J. Ko, O. Filonik, E. M. Herzig, P. Müller-Buschbaum, W. L. Leong, *Adv. Mater.* **2019**, *31*, 1805544.

[2]   S. Kee, H. Kim, S. H. K. Paleti, A. El Labban, M. Neophytou, A.-H. Emwas, H. N. Alshareef, D. Baran, *Chem. Mater.* **2019**, *31*, 3519.

[3]   B. Vaagensmith, K. M. Reza, M. N. Hasan, H. Elbohy, N. Adhikari, A. Dubey, N. Kantack, E. Gaml, Q. Qiao, *ACS Appl. Mater. Interfaces* **2017**, *9*, 35861.

[4]   H. Shi, C. Liu, Q. Jiang, J. Xu, *Adv. Electron. Mater.* **2015**, *1*, 1500017.

[5]   W. Lövenich, *Polym. Sci., Ser. C* **2014**, *56*, 135.

[6]   J. E. Mccarthy, C. A. Hanley, L. J. Brennan, V. G. Lambertini, Y. K.Gun'ko'ko, *J. Mater. Chem. C* **2014**, *2*, 764.

[7]   B.J. Worfolk, S.C. Andrews, S. Park, J. Reinspach, N. Liu, M.F. Toney, S. C. B. Mannsfeld, Z. Bao, *Proc. Natl. Acad. Sci. USA* **2015**, *112*, 14138.

[8]   F. C. Walsh, *Trans. IMF* **1991**, *69*, 107.

[9]   U. Lang, E. Müller, N. Naujoks, J. Dual, J. Dual, *Adv. Funct. Mater.* **2009**, *19*, 1215.

[10]   S. N. Karri, P. Srinivasan, *Mater. Sci. Energy Tech.* **2019**, *2*, 208.

[11]   Z. Fan, J. Ouyang, *Adv. Electron. Mater.* **2019**, *5*, 1800769.

[12]   R. Yue, J. Xu, *Synth. Met.* **2012**, *162*, 912.

[13]   W.-C. Lai, H.-C. Yu, S.-H. Yang, T.-F. Guo, P. Chen, L.-J. Lin, H.-C. Hsu, A. Singh, C.-W. Chu, *Org. Electron.* **2019**, *73*, 266.

[14]   M. Hokazono, H. Anno, N. Toshima, *J. Electron. Mater.* **2014**, *43*, 2196.

[15]   A. Giovannitti, D.-T. Sbircea, S. Inal, C. B. Nielsen, E. Bandiello, D.A. Hanifi, M. Sessolo, G. G. Malliaras, I. Mcculloch, J. Rivnay, *Proc. Natl. Acad. Sci. USA* **2016**, *113*, 12017.

[16]   D. Minudri, D. Mantione, A. Dominguez-Alfaro, S. Moya, E. Maza, C. Bellacanzone, M. R. Antognazza, D. Mecerreyes, *Adv. Electron. Mater.* **2020**, *6*, 2000510.

[17]   J. F. Ponder, A. K. Menon, R. R. Dasari, S. L. Pittelli, K. J. Thorley, S. K. Yee, S. R. Marder, J. R. Reynolds, *Adv. Energy Mater.* **2019**, *9*, 1900395.

[18]   T. Weller, M. Breunig, C. J. Mueller, E. Gann, C. R. Mcneill, M. Thelakkat, *J. Mater. Chem. C* **2017**, *5*, 7527.

[19]   E. E. Havinga, C. M. J. Mutsaers, L. W. Jenneskens, *Chem. Mater.* **1996**, *8*, 769.

[20]   P. Das, B. Zayat, Q. Wei, C. Z. Salamat, I.-B. Magdău, R. Elizalde-Segovia, D. Rawlings, D. Lee, G. Pace, A. Irshad, L. Ye, A. Schmitt, R. A. Segalman, T. F. Miller, S. H. Tolbert, B. S. Dunn, S. R. Narayan, B. C. Thompson, *Chem. Mater.* **2020**, *32*, 9176.

[21]   J. F. Ponder, B. Schmatz, J. L. Hernandez, J. R. Reynolds, *J. Mater.Chem. C* **2018**, *6*, 1064.

[22]   C. A. Cutler, M. Bouguettaya, T.-S. Kang, J. R. Reynolds, *Macromolecules* **2005**, *38*, 3068.

[23]   L. R. Savagian, A. M. Österholm, J. F. Ponder, K. J. Barth, J. Rivnay, J. R. Reynolds, *Adv. Mater.* **2018**, *30*, 1804647.

[24]   D. Caras-Quintero, P. Bäuerle, *Chem. Commun.* **2004**, 926.

[25]   S. L. Pittelli, M. De Keersmaecker, J. F. Ponder Jr, A. M. Österholm, M. A. Ochieng, J. R. Reynolds, *J. Mater. Chem. C* **2020**, *8*, 683.

[26]   D. Bhardwaj, Shahjad, S. Gupta, P. Yadav, R. Bhargav, A. Patra, *ChemistrySelect* **2017**, *2*, 9557.

[27]   M. Goel, M. Siegert, G. Krauss, J. Mohanraj, A. Hochgesang, D. C. Heinrich, M. Fried, J. Pflaum, M. Thelakkat, *Adv. Mater.* **2020**, *32*, 2003596.

[28]   B. Plietker, M. Niggemann, *Org. Lett.* **2003**, *5*, 3353.

[29]   R. H. Lohwasser, M. Thelakkat, *Macromolecules* **2011**, *44*, 3388.

[30]   S. T. Turner, P. Pingel, R. Steyrleuthner, E. J. W. Crossland, S. Ludwigs, D. Neher, *Adv. Funct. Mater.* **2011**, *21*, 4640.

[31]   H.-B. Bu, G. Götz, E. Reinold, A. Vogt, R. Azumi, J. L. Segura, P. Bäuerle, *Chem. Commun.* **2012**, *48*, 2677.

[32]   N. Romyen, S. Thongyai, P. Praserthdam, G. A. Sotzing, *J. Mater. Sci.: Mater. Electron.* **2013**, *24*, 2897.

[33]   S. Inal, G. G. Malliaras, J. Rivnay, *J. Mater. Chem. C* **2016**, *4*, 3942.

[34]   D. G. Harman, R. Gorkin, L. Stevens, B. Thompson, K. Wagner, B. Weng, J. H. Y. Chung, M. I. H. Panhuis, G. G. Wallace, *Acta Biomater.* **2014**, *14*, 33.

[35]   J. Fan, S. S. Rezaie, M. Facchini-Rakovich, D. Gudi, C. Montemagno, M. Gupta, *Org. Electron.* **2019**, *66*, 148.

[36]   M. Turbiez, P. Frère, M. Allain, C. Videlot, J. Ackermann, J. Roncali, *Chem. - Eur. J.* **2005**, *11*, 3742.

[37]   C. R. Singh, G. Gupta, R. Lohwasser, S. Engmann, J. Balko, M. Thelakkat, T. Thurn-Albrecht, H. Hoppe, *J. Polym. Sci., Part B: Polym. Phys.* **2013**, *51*, 943.

[38]   U. B. Cappel, T. Daeneke, U. Bach, *Nano Lett.* **2012**, *12*, 4925.

[39]   W. H. Nguyen, C. D. Bailie, E. L. Unger, M. D. Mcgehee, *J. Am. Chem. Soc.* **2014**, *136*, 10996.

[40]   K. Z. Xing, M. Fahlman, X. W. Chen, O. Inganäs, W. R. Salaneck, *Synth. Met.* **1997**, *89*, 161.

[41]   V. M. Le Corre, M. Stolterfoht, L. Perdigón Toro, M. Feuerstein, C. Wolff, L. Gil-Escrig, H. J. Bolink, D. Neher, L. J. A. Koster, *ACS Appl.Energy Mater.* **2019**, *2*, 6280.

[42]   P. Sakunpongpitiporn, K. Phasuksom, A. Sirivat, **Polym. Int.** 2021.

[43]   S. Bontapalle, S. Varughese, *Polym. Degrad. Stab.* **2020**, *171*, 109025.

[44]   F. Zhang, C.-A. Di, *Chem. Mater.* **2020**, *32*, 2688.

[45]   V. I. Arkhipov, P. Heremans, E. V. Emelianova, H. Bässler, *Phys. Rev.B* **2005**, *71*, 045214.

[46]   Q. Wei, M. Mukaida, Y. Naitoh, T. Ishida, *Adv. Mater.* **2013**, *25*, 2831.

[47]   S. Olthof, S. Mehraeen, S. K. Mohapatra, S. Barlow, V. Coropceanu, J.-L. Brédas, S. R.

Marder, A. Kahn, *Phys. Rev. Lett.* **2012**, *109*, 176601.

5.8 Supporting Information

5.8.1 Methods

1H-NMR: Spectra were recorded in deuterated $CDCl_3$ on a Bruker Avance 250 spectrometer at 300 MHz at room temperature. Chemical shifts are noted in ppm and coupling constants in Hz. All spectra were calibrated according to the residual solvent peaks ($CDCl_3$, δ = 7.26 ppm).

Size exclusion chromatography (SEC): SEC was performed utilizing a Waters 515 HPLC pump and THF with 0.25 wt% tetrabutylammonium bromide (TBAB) as eluent at a flow rate of 0.5 mL min^{-1}. A volume of 100 µL of polymer solution (1-2 mg mL^{-1}) was injected with a 707 Waters auto-sampler into a column setup comprising a guard column (Agilent PLgel Guard MIXED-C, $5 \cdot 0.75$ cm, particle size 5 µm) and two separation columns (Agilent PLgel MIXED-C, $30 \cdot 0.75$ cm, particle size 5 µm). Polymer size distributions were monitored with a Waters 998 photodiode array detector at 254 nm and a Waters 414 refractive index detector. Narrowly distributed polystyrene standards were used for calibration and 1,2-dichlorobenzene as an internal reference.

UV/Vis Spectroscopy: UV/Vis spectra were recorded on a Jasco V-670 spectrophotometer. The spectra were recorded in quartz cuvettes with an internal diameter of 10 mm. The thin polymer films were spin-coated from methanol and from mixtures of methanol and THF on glass substrates.

Spectro-electrochemistry Measurements: Thin films were prepared on ITO coated glass substrates. Measurements were carried out using a UV/Vis spectrometer (OceanOptics USB 2000+) integrated with an Ivium CompactStat potentiostat. A Pt mesh was used as the counter electrode and an Ag/AgCl electrode as the reference electrode. The indicated voltages were applied versus V_{OC} for 10 s until the current stabilized prior to recording of

the spectrum. A voltage of -100 mV vs. Ag/AgCl was applied prior to SEC experiment to de-dope the semiconductive polymer film electrochemically.

Organic Field Effect Transistors (OFETs): Bottom gate/bottom contact organic field effect transistors (OFET Gen4) were purchased from Fraunhofer IPMS. *n*-doped silicon (doping at the surface n ~ $3 \cdot 10^{17}$ cm^{-3}) was used as the surface and gate electrode. The dielectric consists of a 230 ± 10 nm layer of silicon oxide. Each substrate consisted of 16 devices with a constant channel width of 10 mm and varying channel length of 2.5–20 μm. The source and drain electrodes were a 30 nm thick gold layer on a 10 nm ITO adhesion layer. The devices were prepared by cleaning in acetone and subsequently in iso-propanol in an ultrasonic bath for 10 min, followed by 15 min treatment in an ozone oven at 50 °C and subsequent silanization by 45 min treatment in a bath of 1 wt% octadecyltrichlorosilane (ODTS) in toluene at 60 °C. The devices were rinsed with toluene and *i*-propanol and dried. Thin polymer films were spun cast from 6 mg mL^{-1} chloroform solutions at a spinning speed of 3000 rpm under ambient conditions. All devices were stored and measured under nitrogen atmosphere. The I-V-characteristics were measured using an Agilent B1500 semiconductor parameter analyzer. Using **Equation S5.1** the charge carrier mobilities were calculated from the slope of the $(I_d)^{0.5}$ – V_g plots.

$$I_d = \frac{W}{2L} C_i \mu (V_g - V_t)^2 \qquad\qquad (S5.1)$$

Ultraviolet Photoelectron Spectroscopy: UPS measurements were carried out on a PHI 5000 VersaProbe III system fitted with a He discharge light source providing stable and continuous He I and He II lines, under ultrahigh vacuum (ca. 10^{-10} mbar). PEDOT-C_6C_8 2 (pristine and doped with Spiro-MeOTAD(TFSI)$_2$) samples for UPS measurements were spin cast on clean ITO (15 Ω square^{-1}) substrates using anhydrous THF solutions (3 mg mL^{-1}) in a N$_2$ filled glovebox. The thickness of the spun films is ca. 30 nm, measured by using dummy samples in a profilometer. The samples were directly transported to the UPS instrument by using a N$_2$ filled, sealed stainless steel transport vessel without exposing them to the ambient conditions. The Fermi level E_F position of the polymer samples (doped and pristine) were referenced to the Fermi level of sputter-cleaned Au foil. The energy resolution of the valence band maximum (VBM) and secondary electron

cut-off (SECO) is 0.15 eV, which is derived from the full-width half-maximum of the Au Fermi edge.

Conductivity σ Measurements: Prepared substrates (OFET Gen 4) were purchased from Fraunhofer IPMS. In these substrates, an *n*-doped silicon (doping at the surface $n \approx 3 \cdot 10^{17}$ cm^{-3}) bulk layer has a 230 ± 10 nm layer of silicon oxide as the dielectric layer. The source and drain electrodes were a 30 nm thick gold layer on a 10 nm ITO adhesion layer. The substrates were cleaned with acetone and subsequently with iso-propanol in an ultrasonic bath for 5 minutes. The polymers (10 mg mL^{-1}) and appropriate amounts of dopant (MDR = 0.1, where, MDR is defined as: moles of oxidized Spiro-MeOTAD(TFSI)$_2$ / moles of repeating unit) were dissolved at room temperature in THF and thin films were spin coated (1000 rpm for 90 s) on precleaned substrates for conductivity measurements. All steps of sample preparation were performed in argon filled glovebox. Each substrate (chip) consists of four groups with four identical transistors, with a channel length of 2.5, 5, 10 and 20 µm respectively and a constant channel width of 1 cm. For calculating conductivity, the source-drain current I_{DS} was measured as a function of the source-drain voltage V_{DS} (± 2 V), without applying a gate potential V_G. An increase in the drain potential V_{DS} led to a linear increase in the current I_{DS}. From the linear fit of the I-V plots, the slope of was used to calculate the conductivity using the following equation:

$$\sigma = \frac{slope \cdot L}{W \cdot d} \tag{S5.2}$$

where L is channel length, W is channel width (1 cm, constant) and d is the layer thickness, which was measured with Dektak Profilometer.

Mobility Measurements (-ΔB): All following steps were conducted under inert atmosphere (nitrogen) and in absence of H$_2$O (< 1 ppm) and O$_2$ (< 1 ppm). 10.0 mg of PEDOT-C$_6$C$_8$ 2 were dissolved in 667 µL of THF and stirred for 15 min at rt. A dopant stock solution of 150 µL 5 mg mL^{-1} Spiro-MeOTAD(TFSI)$_2$ in THF (2.8 µmol mL^{-1}) was prepared. The dopant stock solution was stirred for 15 min at rt. To obtain the desired molar ratios of

PEDOT-C_6C_8 repeating units to Spiro-MeOTAD(TFSI)$_2$, the following amounts of dopant stock solution were added to 100 µl of the polymer solution: 0 mol% (0 µL), 0.5 mol% (7.6 µL), 0.83 mol% (12.7 µL), 1.25 mol% (19.0 µL), 1.67 mol% (25.0 µL) and 2.50 mol% (38.0 µL). The PEDOT-C_6C_8 2 : Spiro-MeOTAD(TFSI)$_2$ solutions were stirred for 15 min at rt. TEC-7 (XOP glass, 1" · 1" · 2.2 mm, 6 – 8 Ω square^{-1}, ~ 500 nm FTO on glass) substrates were etched with dilute HCl/Zn-dust. After obtaining the etched electrode pattern, the substrates were brushed manually with sodium dodecyl sulfate and deionized water, followed by ultra-sonication in 2 vol% aqueous hellmanex-III solution, water, acetone and isopropanol. The substrates were blown dry with nitrogen and pre-treated with O_3/UV for 15 min at 50 °C. The doped PEDOT-C_6C_8 films were deposited on top of the electrodes utilizing spin coating (30 µL, 1 krpm, 50 s, no annealing, static solution application) under inert atmosphere. To avoid edge effects, a part of the conductive electrodes was masked with Kapton tape, which was removed after the OSC deposition. 100 nm of Au was thermally evaporated on top of the OSC layer using a shadow mask to complete the device stack. The impedance of the devices was measured with a two-electrode setup and increasing electrical field (1 MHz to 100 Hz, 25 points per frequency decade, 0-2 V_{Bias} in 15 voltage steps, 10 mV_{RMS}) using a Metrohm Autolab PGSTAT204 equipped with an FRA32M module. The NOVA 2.1.4 Software package provided by Metrohm, Germany was used to process the impedance data. The ITO back contact was connected to the working electrode (WE) and sense (S), while the Au top electrode was connected to the counter electrode (CE) and reference electrode (RE). Devices under test were shielded from ambient light and external electrical fields. From the imaginary Z'' and real Z' impedance, the capacitance of the organic layer was extracted assuming an R_S(RC) equivalent circuit:

$$\hat{Z}(i\omega)_{\text{R(RC)}} = R_{\text{Series}} + \frac{1}{i\omega C_{\text{Parallel}} + \frac{1}{R_{\text{Parallel}}}} \tag{S5.3}$$

Which can be solved for C_{Parallel} to yield:

$$C_{\text{Parallel}} = \frac{Im(Z)}{(-Im(Z)^2 + (Re(Z) - R_S)^2)\omega} \tag{S5.4}$$

The geometric capacitance C_{Geo} of each device was determined in the high frequency region of the $C(\omega)$ plot (**Figure S5.1**).
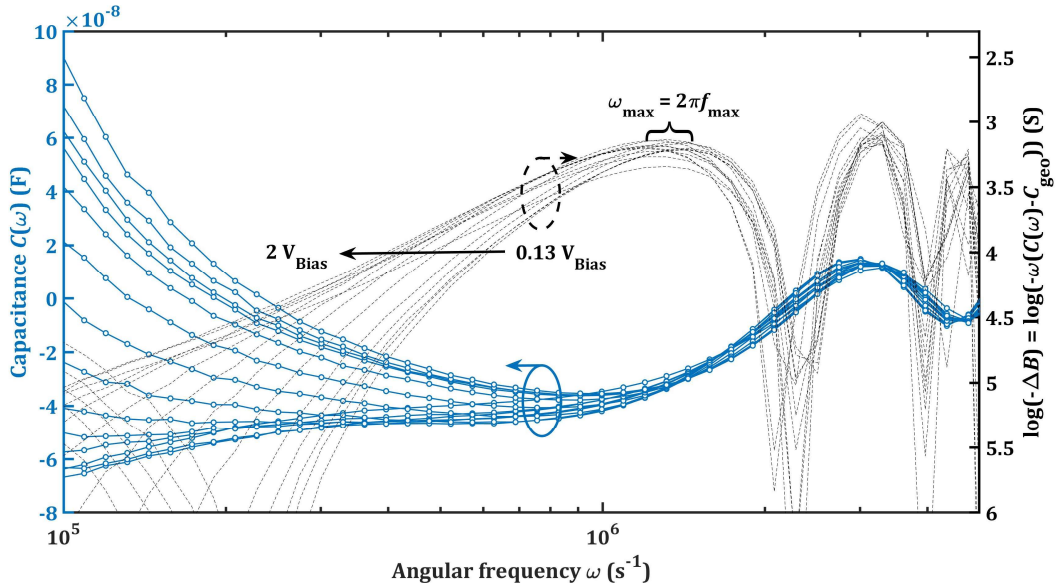
Figure S5.1. Angular frequency ω dependent capacitance $C(\omega)$ of an ITO/66 nm PEDOT-C_6C_8 2:1.66 mol% Spiro-MeOTAD(TFSI)$_2$/Au device (blue, left y-axis) and logarithmic negative differential susceptance -ΔB calculated by **Equation S5.5** (black, right y-axis). A bias voltage ranging from 0.13 V to 2 V was applied during the measurement. From the maximum ω_{max} of – ΔB, the transit time τ_{tr} (**Equation S5.6**) and consecutively, the mobility μ can be calculated (**Equation S5.7**).

Together with the measured capacitance, the mobility was extracted from the negative differential susceptance $-\Delta B$ at different electrical fields. The negative differential susceptance $-\Delta B$ can be calculated according to **Equation S5.5**.

$$-\Delta B = -\omega\big(C(\omega) - C_{geo}\big) \tag{S5.5}$$

The global maximum f_{max} of the $-\Delta B(f)$-plot was extracted and used to calculate the transit time τ_{tr}

$$\tau_{tr} = 0.56 f_{max}^{-1} \tag{S5.6}$$

Local maxima above the transit frequency without physical meaning were discarded. The mobility can then be extracted as

$$\mu = \frac{4}{3} \frac{d^2}{\tau_{\text{tr}} V_{\text{Bias}}} \qquad (S5.7)$$

with d being the thickness of the organic layer. The zero-field mobility μ_0 was calculated by extrapolating the obtained Poole-Frenkel type field dependency.

5.8.2 Experimental

For the synthesis and structural analysis of the dopant Spiro-MeOTAD(TFSI)$_2$, refer to the published paper under reference no. 27 in main text of **Chapter 5**.

3-hexylundecane-1,2-diol
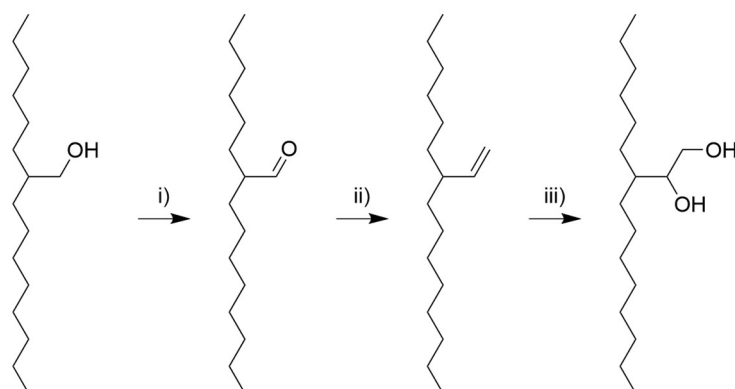
Scheme S1. **i)** 2-hexyldecan-1-ol 1, oxalyl chloride, TEA, -72 °C **ii)** KO*t*-Bu, methyltriphenylphosphonium bromide, -78 °C, **iii)** NaIO$_3$, RuCl$_3$, RT, acetone, water, ethyl acetate, RT.

5.8.3 Supporting Measurements
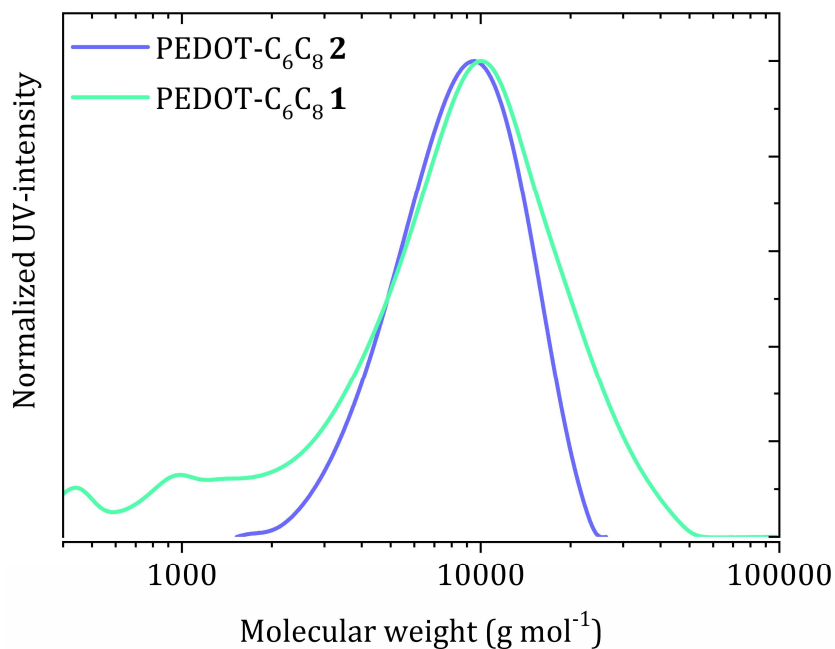
Figure S5.2. SEC chromatograms measured with THF as eluent and narrowly distributed polystyrene as calibration materials.
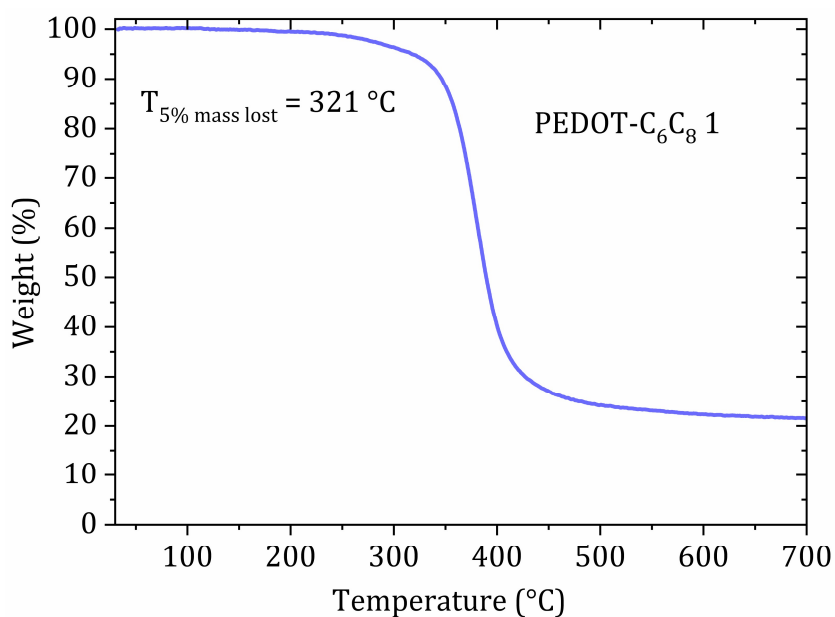
Figure S5.3. TGA measurement of PEDOT-C_6C_8 1 under nitrogen with a heating rate of 10 K min^{-1}.
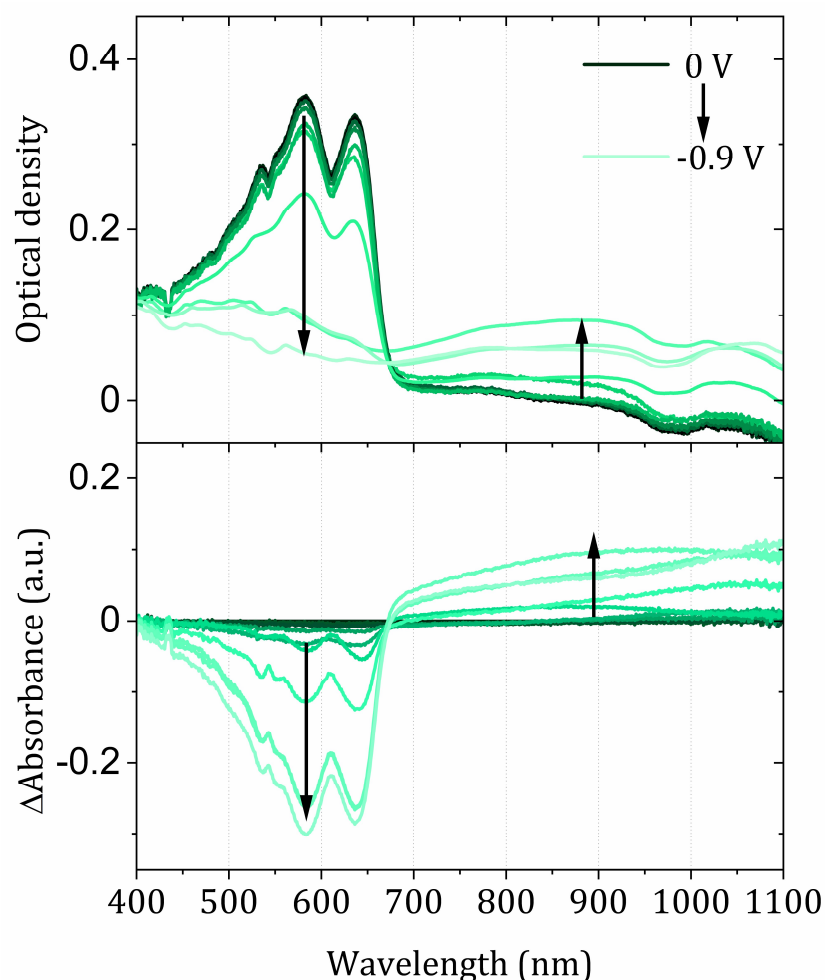
Figure S5.4. a) Spectro electrochemistry measurements of thin polymer films on ITO of PEDOT-C_6C_8 1 respectively. The spectra were measured in 0.1 M NaCl when the films were biased from 0 V to 0.9 V in a three-electrode setup with an Ag/AgCl reference electrode and a Pt counter electrode. Difference spectra obtained by subtracting the absorption spectra of the polymer in the neutral state (0 V) from the absorption spectra under different applied potentials during the in situ electrochemical oxidation of PEDOT-C_6C_8 2 by applying a potential from 0 to 900 mV. The pristine absorption in the 400-680 nm range decreases with a concomitant increase in polaron absorption in the range of 680 to 1100 nm. The arrow indicates the direction of spectral changes.
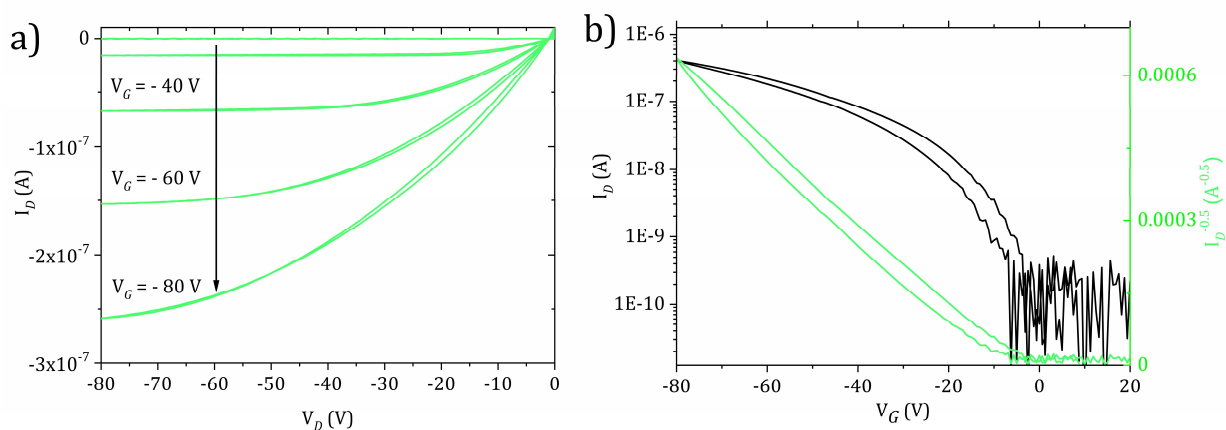
Figure S5.5. OFET output (a) and transfer curve (b) of PEDOT-C_6C_8 1, measured in a bottom-gate (Si), bottom-contact (Au) geometry in range from 0 V to -80 V.
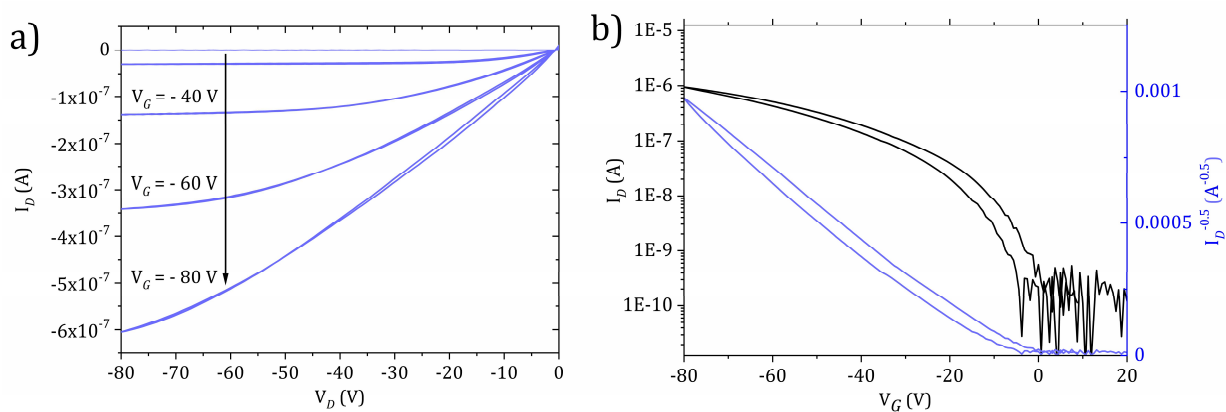
Figure S5.6. OFET output (a) and transfer curve (b) of PEDOT-C_6C_8 2, measured in a bottom-gate (Si), bottom-contact (Au) geometry in range from 0 V to -80 V.
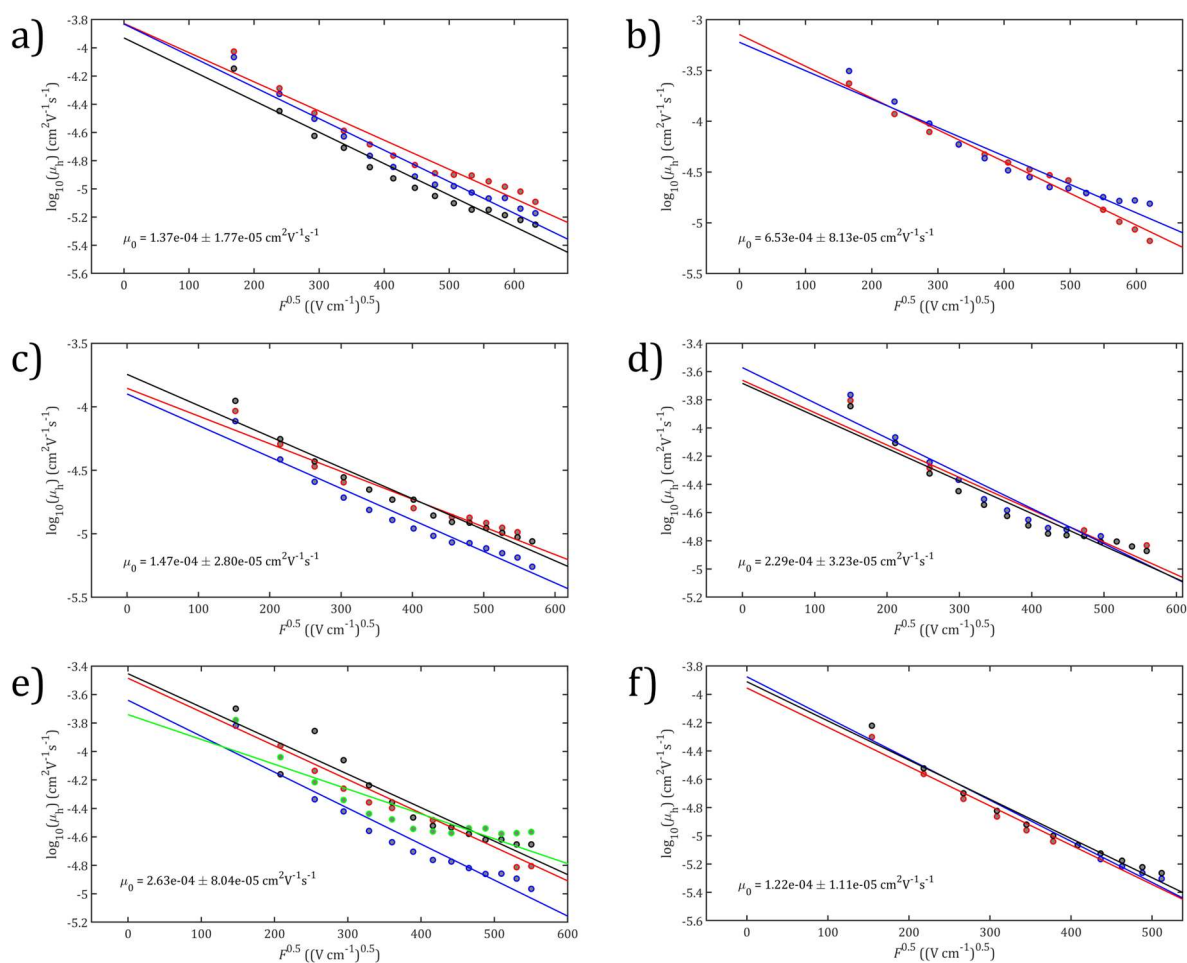
Figure S5.7. Field dependent mobilities of PEDOT-C_6C_8 2 doped with a) 0 mol%, b) 0.5 mol%, c) 0.83 mol%, d) 1.25 mol%, e) 1.67 mol% and f) 2.50 mol% Spiro-MeOTAD(TFSI)$_2$. Inset values show the calculated average mobility with standard deviation of each concentration.

5. A SOLUTION-PROCESSABLE PRISTINE PEDOT EXHIBITING EXCELLENT CONDUCTIVITY, CHARGE CARRIER MOBILITY, AND THERMAL STABILITY IN THE DOPED STATE

Table S5.1. Characteristics of the two synthesized copolymers PEDOT-C_6C_8 1 and 2, determined *via* SEC and MALDI-TOF experiments.

	[M]/[Ni] (mol)	Theoretical molecular weight (kg mol^{-1})	$M_{n,SEC}$[a] (kg mol^{-1})	$M_{p,MALDI-TOF}$[b] (kg mol^{-1})	Đ$_{SEC}$[a]	Repeating units[c]
PEDOT-C_6C_8 1	10	3.5	10	3	1.38	9
PEDOT-C_6C_8 2	30	10.5	9.5	9.8	1.19	27

[a] SEC with polystyrene calibration and THF as eluent.

[b] Dithranol was used as matrix material, dilution 1:1000.

[c] Calculated from peak molecular weight determined in MALDI-TOF.

Table S5.2. Summary of the measured conductivities (as cast, no annealing) with interdigitated electrode geometry (2.5 μm apart) of PEDOT-C_6C_8 2 doped with different amounts of Spiro-MeOTAD(TFSI)$_2$.

Doping ratio (mol%)	Thickness (nm)	Conductivity (S cm^{-1}) Channel length (2.5 μm)
0	40	$1.26 \cdot 10^{-6} \pm 0.17 \cdot 10^{-6}$
0.50	41	$9.85 \cdot 10^{-6} \pm 2.31 \cdot 10^{-6}$
0.83	48	$2.27 \cdot 10^{-5} \pm 0.57 \cdot 10^{-5}$
1.25	40	$4.09 \cdot 10^{-5} \pm 0.60 \cdot 10^{-5}$
1.67	48	$6.62 \cdot 10^{-5} \pm 0.99 \cdot 10^{-6}$
2.50	39	$1.18 \cdot 10^{-4} \pm 0.06 \cdot 10^{-4}$
10.0	18	$1.32 \cdot 10^{-3} \pm 0.07 \cdot 10^{-3}$

Table S5.3. Summary of the measured conductivities of pristine PEDOT-C_6C_8 1 in thin films (as cast, annealed at 100 °C for 5 min under N_2, annealed at 100 °C for 30 min under N_2, annealed at 100 °C for 30 min in air and annealed at 100 °C for 120 min, stored in air for 12 h after annealing) with different widths of interdigitated electrodes (2.5, 5, 10 and 20 μm). Annealing experiments were conducted successively with the same samples.

PEDOT-C_6C_8 1 pristine Thickness: 54.71 nm	Conductivity (S cm^{-1}) Channel length (2.5 μm)	Conductivity (S cm^{-1}) Channel length (5 μm)	Conductivity (S cm^{-1}) Channel length (10 μm)	Conductivity (S cm^{-1}) Channel length (20 μm)	Conductivity (S cm^{-1}) Average of four channels
As cast	-	$9.12 \cdot 10^{-6}$	$9.13 \cdot 10^{-6}$	-	$9.12 \cdot 10^{-6}$
Annealed at 100 °C for 5 min under N_2	$9.14 \cdot 10^{-6}$	$9.13 \cdot 10^{-6}$	$1.82 \cdot 10^{-6}$	$0.73 \cdot 10^{-6}$	$5.20 \cdot 10^{-6}$
Annealed at 100 °C for 30 min under N_2	-	$9.13 \cdot 10^{-6}$	$1.82 \cdot 10^{-6}$	$1.10 \cdot 10^{-6}$	$4.02 \cdot 10^{-6}$
Annealed at 100 °C in air for 30 min	$18.2 \cdot 10^{-6}$	$9.13 \cdot 10^{-6}$	$3.65 \cdot 10^{-6}$	$3.65 \cdot 10^{-6}$	$8.66 \cdot 10^{-6}$
Annealed at 100 °C in air for 120 min	$22.8 \cdot 10^{-6}$	$18.2 \cdot 10^{-6}$	$7.31 \cdot 10^{-6}$	$3.65 \cdot 10^{-6}$	$12.99 \cdot 10^{-6}$
Stored for 12 h in air @RT	$31.9 \cdot 10^{-6}$	$54.8 \cdot 10^{-6}$	$1.10 \cdot 10^{-6}$	$7.3 \cdot 10^{-6}$	$23.78 \cdot 10^{-6}$

5. A SOLUTION-PROCESSABLE PRISTINE PEDOT EXHIBITING EXCELLENT CONDUCTIVITY, CHARGE CARRIER MOBILITY, AND THERMAL STABILITY IN THE DOPED STATE

Table S5.4. Summary of the measured conductivities of doped PEDOT-C_6C_8 1, with 10 mol% of Spiro-MeOTAD(TFSI)$_2$ in thin films (as cast, annealed at 100 °C for 5 min under N_2, annealed at 100 °C for 30 min under N_2, annealed at 100 °C for 30 min in air and annealed at 100 °C for 120 min, stored in air for 12 h after annealing) with different widths of interdigitated electrodes (2.5, 5, 10 and 20 μm). Annealing experiments were conducted successively with the same samples.

PEDOT-C_6C_8 1 pristine Thickness: 94.55 nm	Conductivity (S cm^{-1}) Channel length (2.5 μm)	Conductivity (S cm^{-1}) Channel length (5 μm)	Conductivity (S cm^{-1}) Channel length (10 μm)	Conductivity (S cm^{-1}) Channel length (20 μm)	Conductivity (S cm^{-1}) Average of four channels
As cast	$1.58 \cdot 10^{-4}$	$1.58 \cdot 10^{-4}$	$2.11 \cdot 10^{-4}$	$1.48 \cdot 10^{-4}$	$1.69 \cdot 10^{-4}$
Annealed at 100 °C for 5 min under N_2	$5.29 \cdot 10^{-4}$	$5.28 \cdot 10^{-4}$	$7.40 \cdot 10^{-4}$	$8.46 \cdot 10^{-4}$	$6.60 \cdot 10^{-4}$
Annealed at 100 °C for 30 min under N_2	$1.32 \cdot 10^{-3}$	$1.05 \cdot 10^{-3}$	$1.05 \cdot 10^{-3}$	$1.69 \cdot 10^{-3}$	$1.28 \cdot 10^{-3}$
Annealed at 100 °C in air for 30 min	$1.05 \cdot 10^{-3}$	$1.05 \cdot 10^{-3}$	$1.05 \cdot 10^{-3}$	$1.27 \cdot 10^{-3}$	$1.10 \cdot 10^{-3}$
Annealed at 100 °C in air for 120 min	$1.05 \cdot 10^{-3}$	$1.05 \cdot 10^{-3}$	$1.05 \cdot 10^{-3}$	$1.27 \cdot 10^{-3}$	$1.10 \cdot 10^{-3}$
Stored for 12 h in air @RT	$1.05 \cdot 10^{-3}$	$1.05 \cdot 10^{-3}$	$1.05 \cdot 10^{-3}$	$1.27 \cdot 10^{-3}$	$1.10 \cdot 10^{-3}$

Table S5.5. Summary of the measured conductivities of pristine PEDOT-C_6C_8 2 in thin films (as cast, annealed at 100 °C for 5 min under N_2, annealed at 100 °C for 30 min under N_2, annealed at 100 °C for 30 min in air and annealed at 100 °C for 120 min, stored in air for 12 h after annealing) with the corresponding channel length of the transistor (2.5, 5, 10 and 20 µm). Experiment conducted successively with the same samples.

PEDOT-C_6C_8 1 pristine Thickness: 44.32 nm	Conductivity (S cm^{-1}) Channel length (2.5 µm)	Conductivity (S cm^{-1}) Channel length (5 µm)	Conductivity (S cm^{-1}) Channel length (10 µm)	Conductivity (S cm^{-1}) Channel length (20 µm)	Conductivity (S cm^{-1}) Average of four channels
As cast	$0.56 \cdot 10^{-7}$	$1.12 \cdot 10^{-7}$	$1.12 \cdot 10^{-7}$	$1.35 \cdot 10^{-7}$	$1.04 \cdot 10^{-7}$
Annealed at 100 °C for 5 min under N_2	$5.64 \cdot 10^{-7}$	$1.12 \cdot 10^{-7}$	$1.12 \cdot 10^{-7}$	$0.32 \cdot 10^{-7}$	$2.05 \cdot 10^{-7}$
Annealed at 100 °C for 30 min under N_2	$45.1 \cdot 10^{-7}$	$6.76 \cdot 10^{-7}$	$4.51 \cdot 10^{-7}$	$3.16 \cdot 10^{-7}$	$1.49 \cdot 10^{-6}$
Annealed at 100 °C in air for 30 min	$3.38 \cdot 10^{-6}$	$0.90 \cdot 10^{-6}$	$1.24 \cdot 10^{-6}$	$1.80 \cdot 10^{-6}$	$1.83 \cdot 10^{-6}$
Annealed at 100 °C in air for 120 min	$8.46 \cdot 10^{-6}$	$2.25 \cdot 10^{-6}$	$2.25 \cdot 10^{-6}$	$3.16 \cdot 10^{-6}$	$4.03 \cdot 10^{-6}$
Stored for 12 h in air @RT	$16.9 \cdot 10^{-6}$	$6.20 \cdot 10^{-6}$	$6.76 \cdot 10^{-6}$	$3.61 \cdot 10^{-6}$	$8.37 \cdot 10^{-6}$

5. A SOLUTION-PROCESSABLE PRISTINE PEDOT EXHIBITING EXCELLENT CONDUCTIVITY, CHARGE CARRIER MOBILITY, AND THERMAL STABILITY IN THE DOPED STATE

Table S5.6. Summary of the measured conductivities of doped PEDOT-C_6C_8 2, with 10 mol% of Spiro-MeOTAD(TFSI)$_2$ in thin films (as cast, annealed at 100 °C for 5 min under N$_2$, annealed at 100 °C for 30 min under N$_2$, annealed at 100 °C for 30 min in air and annealed at 100 °C for 120 min, stored in air for 12 h after annealing) with the corresponding channel length of the transistor (2.5, 5, 10 and 20 μm). Experiment conducted successively with the same samples.

PEDOT-C_6C_8 1 pristine Thickness: 44.32 nm	Conductivity (S cm^{-1}) Channel length (2.5 μm)	Conductivity (S cm^{-1}) Channel length (5 μm)	Conductivity (S cm^{-1}) Channel length (10 μm)	Conductivity (S cm^{-1}) Channel length (20 μm)	Conductivity (S cm^{-1}) Average of four channels
As cast	$4.77 \cdot 10^{-4}$	$2.86 \cdot 10^{-4}$	$2.86 \cdot 10^{-4}$	$3.82 \cdot 10^{-4}$	$3.58 \cdot 10^{-4}$
Annealed at 100 °C for 5 min under N$_2$	$4.77 \cdot 10^{-4}$	$4.77 \cdot 10^{-4}$	$4.77 \cdot 10^{-4}$	$3.82 \cdot 10^{-4}$	$4.53 \cdot 10^{-4}$
Annealed at 100 °C for 30 min under N$_2$	$4.77 \cdot 10^{-4}$	$4.77 \cdot 10^{-4}$	$4.77 \cdot 10^{-4}$	$5.73 \cdot 10^{-4}$	$5.53 \cdot 10^{-4}$
Annealed at 100 °C in air for 30 min	$4.77 \cdot 10^{-4}$	$4.77 \cdot 10^{-4}$	$4.77 \cdot 10^{-4}$	$3.82 \cdot 10^{-4}$	$4.53 \cdot 10^{-4}$
Annealed at 100 °C in air for 120 min	$4.77 \cdot 10^{-4}$	$4.77 \cdot 10^{-4}$	$4.77 \cdot 10^{-4}$	$3.82 \cdot 10^{-4}$	$4.53 \cdot 10^{-4}$
Stored for 12 h in air @RT	$4.77 \cdot 10^{-4}$	$4.77 \cdot 10^{-4}$	$4.77 \cdot 10^{-4}$	$3.82 \cdot 10^{-4}$	$4.53 \cdot 10^{-4}$

Table S5.7. Calculated work function, ionization potential and hole injection barrier values for pristine and p-doped PEDOT-C_6C_8 2 films with spiro-MeOTAD(TFSI)$_2$ from UPS measurements.

Doping ratio (mol%)	Work function (eV)	Ionization potential (eV)	Hole injection barrier (eV)
0	-4.02	-4.48	0.46
0.50	-4.13	-4.49	0.36
0.83	-4.18	-4.41	0.23
1.25	-4.23	-4.40	0.17
1.67	-4.22	-4.38	0.15
2.50	-4.25	-4.38	0.13
100	-5.06	-5.33	0.27

Table S5.8. OFET and impedance characteristics of PEDOT-C_6C_8 1 and 2 determined in bottom-gate (Si), bottom-contact (Au) transistors and metal-semiconductor (MS) devices. The hole mobility μ_{hole}, was estimated out of the transfer curves (**Figure S5.5**, **S5.6**) and Poole-Frenkel plots (**Figure S5.7**). Conductivity measurement of the polymers as cast, doped as cast with Spiro-MeOTAD(TFSI)$_2$ and the conductivity after storing the film in air for 12 h. The thickness of the polymer films was determined with a Dektak Stylus profilometer.

	OFET		$-\Delta B$	Conductivity			Thickness
	$\mu_{hole,average}$ (cm^2 V^{-1} s^{-1})	ON/OFF ratio	$\mu_{0,average}$ (cm^2 V^{-1} s^{-1})	$\sigma_{pristine,\ as\ cast}$ (S cm^{-1})	$\sigma_{doped,\ as\ cast}$ (S cm^{-1})	$\sigma_{in\ air}$ (S cm^{-1})	(nm)
PEDOT-C_6C_8 1	$1.6 \cdot 10^{-4}$	$2 \cdot 10^3$	-	$9.12 \cdot 10^{-6}$	$1.28 \cdot 10^{-3}$	$1.10 \cdot 10^{-3}$	95 ± 9
PEDOT-C_6C_8 2	$5 \cdot 10^{-4}$	$9 \cdot 10^3$	$1.37 \cdot 10^{-4}$	$1.04 \cdot 10^{-7}$	$5.53 \cdot 10^{-4}$	$4.53 \cdot 10^{-4}$	105 ± 10

5. A SOLUTION-PROCESSABLE PRISTINE PEDOT EXHIBITING EXCELLENT CONDUCTIVITY, CHARGE CARRIER MOBILITY, AND THERMAL STABILITY IN THE DOPED STATE

6. Highly Efficient Doping of Conjugated Polymers Using Multielectron Acceptor Salts

Gert Krauss[#†], Adrian Hochgesang[#†], John Mohanraj[†] and Mukundan Thelakkat[†§]*

[†] Applied Functional Polymers, University of Bayreuth, Universitätsstr. 30, 95440 Bayreuth, Germany

[§] Bavarian Polymer Institute (BPI), University of Bayreuth, Universitätsstr. 30, 95440 Bayreuth, Germany

[#] **equally contributing authors**

* Corresponding Author
E-mail: mukundan.thelakkat@uni-bayreuth.de

6. HIGHLY EFFICIENT DOPING OF CONJUGATED POLYMERS USING MULTIELECTRON ACCEPTOR SALTS

Abstract

Chemical doping is a vital tool for tuning electronic properties of conjugated polymers. Most single electron acceptors used for *p*-doping necessitate high dopant concentrations to achieve good electrical conductivity. However, high-molar doping ratios hamper doping efficiency. Here a new concept of using multielectron acceptor (MEA) salts as dopants for conjugated polymers is presented. Two novel MEA salts are synthesized and their doping efficiency towards two polymers differing in their dielectric properties are compared with two single electron acceptors such as $NOPF_6$ and magic blue. Cutting-edge methods such as ultraviolet photoelectron spectroscopy/X-ray photoelectron spectroscopy (XPS), impedance spectroscopy, and density of states analysis in addition to UV/Vis/NIR absorption, spectroelectrochemistry, and Raman spectroscopy methods are used to characterize the doped systems. The tetracation salt improves the conductivity by two orders of magnitude and quadruples the charge carrier concentration compared to single electron acceptors for the same molar ratio. The differences in charge carrier density and activation energy on doping are delineated. Further, a strong dependency of the carrier release on the polymer polarity is observed. High carrier densities at reduced dopant loadings and improved doping efficacies using MEA dopants offer a highly efficient doping strategy for conjugated polymers.

6.1 Introduction

In recent years, doped conjugated polymers have emerged into different areas of applications and the scientific interest in this field of research is unbroken. A variety of modern devices require doped conjugated polymers as their active materials, for example, in high-mobility OFETs,[1-3] as novel thermoelectric materials[4] or in organic photovoltaics.[5,6] Inherently insulating conjugated polymers primarily require doping in order to achieve high electrical conductivity. During molecular doping, the conjugated polymer transfers electrons to the dopant (*p*-type doping leading to oxidized radical cation states) or back (*n*-type doping resulting in radical anion states). These redox processes introduce one preferred majority carrier type, e.g., holes in the case of *p*-doping

and causes the shift of the Fermi level towards either valence band (*p*-doping) or conduction band (*n*-doping).[7] Depending on the electronic structure and sterical demands of the host:dopant system, hybridization of the frontier orbitals with a concomitant formation of charge transfer complexes or redox reactions can be observed. The simplest doping mechanism is described by the integer charge transfer, where an integer number of electrons is transferred between the host and dopant. During *p*-type doping, the redox process occurs in which electrons are transferred from highest occupied molecular orbital (HOMO) of the conjugated polymer to empty lowest unoccupied molecular orbital (LUMO) or partially filled singly occupied molecular orbital (SOMO) of the dopant.[8] The most common *p*-type dopants are tetracyanoquinodimethane (F_4TCNQ)[9-11] and its derivative, hexafluorotetracyanonaphthoquinodimethane (F_6TCNNQ).[12] Other dopants are conventional oxidizing agents like iron(III)chloride ($FeCl_3$), nitrosonium tetrafluoroborate ($NOBF_4$) or nitrosonium hexafluorophosphate ($NOPF_6$),[4,13,14] which are usually capable of accepting one electron per dopant molecule. This circumstance necessitates the employment of high dopant loadings in the range of 20 mol% or more in order to achieve appreciable electrical conductivities required for the intended application.[11,15] By doping, the charge carrier concentration is increased and ideally the conductivity and charge carrier mobility are enhanced concurrently,[16] predominantly in the low-doping regime (<1 mol%) due to filling of deep-lying trap states.[17] On the other hand, it is accepted that excessive amounts of dopants have detrimental effects on the polymer microstructure and film morphology, leading to decreased charge transport properties.[18-20] Lying dormant, the acceptor anions or the ionized dopant molecules act as Coulombic traps, i.e., charge carriers are temporarily bound by these trap states and contribute significantly less to the overall current.[21] This problem is amplified by a rapidly decreasing doping efficiency with increasing doping ratio, meaning that less and less dopants participate in the desired redox reaction.[8,22] As a consequence, the introduced molar dopant amounts need to be kept as low as possible to fully exploit the potential of both, high doping efficiency as well as good charge transport in the doped conjugated polymer. In this context, it is known that radical cation salts of hole transport materials (HTMs) such as spiro-MeOTAD^{2+}(TFSI$^-$)$_2$ or MeOTPD$^+$(TFSI$^-$) can be used as additives to the pristine spiro-MeOTAD (2,2',7,7'-Tetrakis[N,N-di(4-methoxyphenyl)amino]-9,9'-spirobifluorene) to redistribute the charges

(comproportionation) and thus to improve the electrical conductivity of the latter.[23-25] Inspired by this fact, we have earlier demonstrated the proof of principle of a highly thermally stable doping strategy for conjugated polymers where spiro-MeOTAD^{2+}(TFSI$^-$)$_2$ was employed for HOMO–HOMO electron transfer with a conjugated polymer.[26] In a similar fashion, Hofmann et al. showed that a singly oxidized triarylammonium radical cation salt, tris(4-bromophenyl) ammonium hexachloroantimonate (Magic Blue), is capable of p-doping a variety of conjugated polymers.[27] In most of these reported cases, only one electron is accepted by such a radical cation dopant molecule and therefore to achieve high conductivity high molar dopant ratio is required. Since spiro-MeOTAD can be theoretically oxidized to a tetracation salt and MeOTPD to its dication salt, here we ask a fundamental question on the efficacy of such multivalent radical cation salts as multielectron acceptors (MEAs). Our motivation is based on the idea that theoretically the tetracation salt of spiro-MeOTAD should exhibit the highest degree of doping for the same molar dopant ratio, if it can take up four electrons from the conjugated polymer. This can then fulfill the requirement of desired low doping levels, as explained earlier, if we can make use of multication salts. To study this, we chemically synthesized fully oxidized novel radical cation salts, spiro-MeOTAD^{4+}(PF$_6^-$)$_4$ and MeOTPD^{2+}(PF$_6^-$)$_2$ and addressed the feasibility and efficacy of using such multication salts (which are themselves HTMs) as MEA dopants for two different polydiketopyrrolopyrroles (PDPPs) differing in their polarity and dielectric constants. To quantify the results, we compare the properties of the doped systems with those doped with the well-known monoradical cation salts, magic blue as well as NOPF$_6$. We study in detail how the doping efficiency and the electronic properties of the doped polymers change. The three triphenylamine radical cation salts having oxidation states 1, 2, and 4 used here are: tris(4-bromophenyl)ammonium hexachloroantimonate ("Magic Blue", D2), N,N,N′,N′-tetrakis(4-methoxyphenyl)benzidine hexafluorophosphate ("MeOTPD^{2+}(PF$_6^-$)$_2$", D3) and 2,2″,7,7″-tetrakis[N-(4-methoxyphenyl)amino]-9,9′-spirobifluorene hexafluorophosphate (spiro-MeOTAD^{4+}(PF$_6^-$)$_4$ D4). Here the dication salt D3 and tetracation salt D4 are expected to have very similar electronic energies and absorption features, thus enabling a fair comparison of doping efficiency just based on their capacity to accept two or four electrons, respectively. Two DPP-based polymers with varying hydrophilicity, but similar electronic properties were selected as host materials to study the changes in electrical conductivity, charge carrier mobility and charge carrier density imparted by the different

dopants in environments of different polarity. We address the following scientific questions in this work.

1. Can the tetracation dopant D4 (spiro-MeOTAD^{4+}(PF$_6^-$)$_4$) generate four times the charge carrier density compared to single electron acceptors, NOPF$_6$ or Magic Blue?

2. What are the consequences on electrical conductivity, charge carrier mobility and activation energy on using triphenylamine radical cation salts, which are themselves HTMs, as *p*-dopants compared with the conventional redox-dopant NOPF$_6$?

3. How does the polarity of the host polymer affect the doping process?

Here, the compatibility of dopant and host as a key requirement for efficient doping is studied using X-ray photoelectron spectroscopy (XPS) mapping. The electronic properties and energy levels of the dopants and polymers are assessed by ultraviolet photoelectron spectroscopy (UPS). The doping process is monitored using optical absorption spectroscopy as well as UPS. The electrical conductivity and thermal activation energy thereof are measured to study the impact of different dopants on macroscopic charge transport properties, depending on the polymer polarity and polarizability. To study the differences in charge carrier density in the doped polymers using mono-, di-, and tetracation salt dopants as compared to single electron oxidants and to determine the resulting doping efficiency, impedance spectroscopy experiments were performed. We also elucidated how HTM-dopants such as D3 and D4 differ on their influence on the charge carrier density, charge carrier mobility, activation energy for charge transport and density of states of doped polymers compared to a non-HTM dopant such as NOPF$_6$. Altogether, we present a comprehensive and comparative study of a series of triarylamine cation salt dopants with increasing oxidation state from 1 to 4 in two different DPP-polymers, thus highlighting the benefits and drawbacks, if any, of multiple oxidized triarylamine based HTM-dopants. Thereby, the electrical conductivity gained by doping with 5 mol% of a tetracation dopant spiro-MeOTAD^{4+}(PF$_6^-$)$_4$ is 255 times higher than that obtained with an equal molar amount of NOPF$_6$. Thus, we introduce an elegant concept for highly efficient doping of conjugated polymers using multielectron acceptors at unprecedented low dopant molar ratios, opening up innovative and novel *p*-doping strategies.

6.2 Results and Discussion

The chemical structures of all the dopants and conjugated polymers investigated in this work are displayed in **Figure 6.1a**. We studied two PDPPs with an identical backbone structure consisting of a thiophene-flanked DPP-core (DPP[T]$_2$) and 3-(2-(2-methoxyethoxy)ethoxy)thiophene (3-MEET) as comonomer. The presence of 3-MEET as comonomer helps to maintain a low ionization potential in the range of 4.6 eV.[28] These are donor–acceptor polymers capable of undergoing *p*-doping.[29,30] The DPP[T]$_2$ core is either equipped with hydrophilic triethylene glycol {TEG} substituents in the polymer PDPP[T]$_2${TEG}$_2$-3-MEET denoted as P1, or hydrophobic 2-hexyldecyl {2-HD} chains in the polymer PDPP[T]$_2${2-HD}$_2$-3-MEET, denoted as P2. Both polymers exhibit sufficient solubility in common organic solvents. Further, the replacement of the 2-HD substituents with TEG chains leads to an increase of the fraction of ethylene glycol from 13 to 52 wt%. Due to this, a difference in miscibility between the dopant salts and polymer can be expected and the dissociation of generated charge transfer state may be facilitated by the higher dielectric constant due to ethylene glycol groups. This may influence both charge carrier mobilities and electrical conductivities.[11,31,32] The three HTM-dopants are based on the common basic structural motif triphenylamine and have different oxidation states. The singly oxidized Magic Blue (D2) carrying hexachloroantimonate as counter ion was purchased. The new dication salts, N,N,N′,N′-tetrakis(4-methoxyphenyl)benzidine hexafluorophosphate (D3, MeOTPD^{2+}(PF$_6^-$)$_2$) and the tetracation salt, 2,2″,7,7″-tetrakis[N,N-di(4-methoxyphenyl)amino]-9,9′-spirobifluorene hexafluorophosphate (D4, spiro-MeOTAD^{4+}(PF$_6^-$)$_4$) were chemically synthesized by reacting the pristine molecules, MeOTPD and spiro-MeOTAD with carefully dried nitrosonium hexafluorophosphate in large molar excesses required for complete oxidation under extremely dry conditions and argon atmosphere (see Supporting Information). UPS was conducted on thin film samples of P1, P2, and D2 to D4 on ITO to assess the HOMO energy levels and work functions (**Figure S6.1**, Supporting Information). From the energy diagram in **Figure 6.1b** it is apparent, that both polymers exhibit very similar ionization potentials of 4.6–4.7 eV, in accordance with the fact that the polymer backbones are identical, which dictate the HOMO energy levels. All three triarylamine dopants, D2 to D4 are thermodynamically capable of oxidizing the polymers, as their partially occupied

HOMOs (5.7, 5.3, and 5.3 eV, respectively) lie well below those of the polymers. From the measured SOMO levels, the most exothermic electron transfer from polymer to dopant can be expected for D2, followed by D3 and D4. We postulate that the doping-mechanism of the HTM-dopants occurs *via* integer charge transfer, as hybridization and the formation of charge-transfer complexes is unlikely in these sterically demanding dopants and nonplanar polymers.[33,34] First we confirmed the uniform distribution of the dopants in our doped polymer thin films using an XPS mapping technique for 5 mol% D2, D3, and D4 (highest molar ratio) over an area of 0.56 mm^2. By selecting binding energies which are exclusive to either the polymer (thiophene sulfur 2p$_{3/2}$) or dopant (antimony 3d$_{3/2}$ or fluorine 1s), we could demonstrate a uniform distribution of D2 to D4 in both polymers with a lateral resolution of 10 μm (**Figure 6.1c** to **6.1h**). High miscibility in both alkyl- and TEG side chain substituted polymers results in astonishing compatibility of our HTM dopants with semiconducting PDPP polymers. This also excludes inhomogeneities, which may otherwise will have to be considered in the electrical characterizations and interpretations of the resulting thin films.
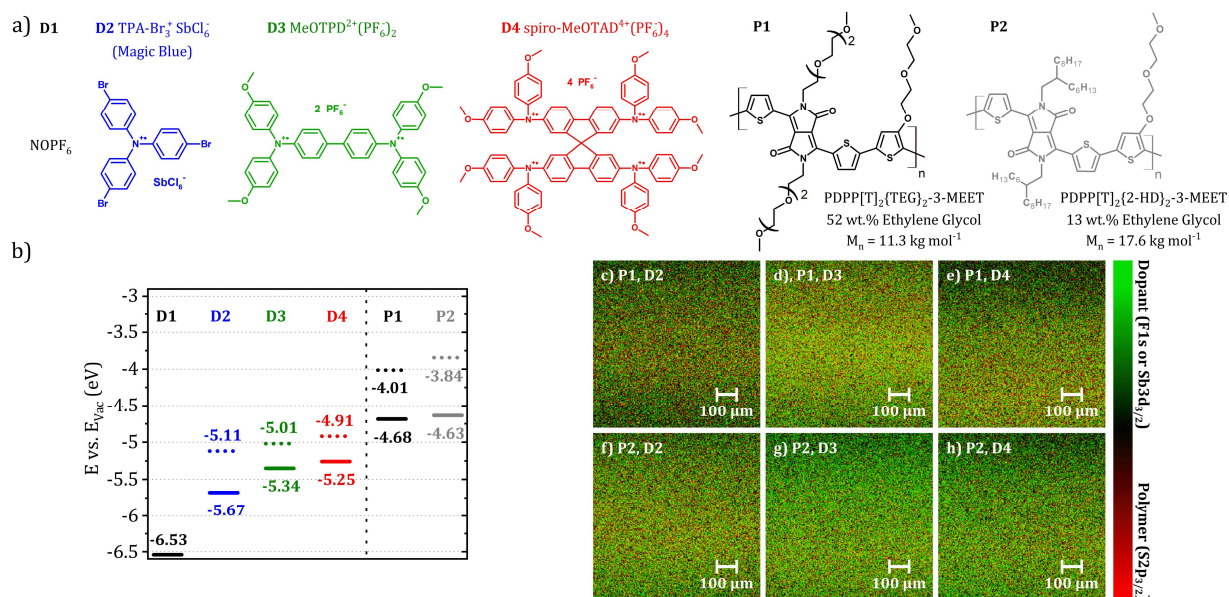
Figure 6.1. a) Structures of the studied dopants D1 (NOPF$_6$, black), D2 (Magic Blue, blue), D3 (MeOTPD^{2+}(PF$_6$)$_2$, green), D4 (spiro-MeOTAD^{4+}(PF$_6$)$_4$, red) and the polymers P1 (PDPP[T]$_2${TEG}$_2$-3-MEET, black) and P2 (PDPP[T]$_2${2-HD}$_2$-3-MEET, gray). b) Ionization potentials (solid lines) and work function (dotted lines) of D2–D4, P1, and P2 w.r.t. vacuum level as obtained from UPS experiments. D1 value taken from ref. [35]. c)–h) XPS elemental maps of P1 and P2 doped with 5 mol% D2, D3, and D4 over an area of 750 by 750 µm featuring a lateral resolution of 10 µm. Colors represent the peak intensity of the mapped elements at a particular binding energy, which are exclusive to either polymer or dopant. P1 and P2 are attributed to their thiophene sulfur 2p$_{3/2}$ (165 eV, red) signal, D2 to the antimony 3d$_{3/2}$ (539 eV, green) signal, D3 and D4 to the fluorine 1s signal (688 eV, green).

6.2.1 Dopant Characterization

The triarylamine based cation salts D2–D4 were thoroughly characterized using additional spectroscopic methods such as UV/Vis/NIR and Raman spectroscopy as given in **Figure S6.2** and **Figure S6.3** of the Supporting Information, respectively. All the triarylamine dopants, D2–D4 feature an absorption at ≈ 700 nm due to localized HOMO–LUMO transitions of the triphenylamine moiety (**Figure S6.2**, Supporting Information).[35] The close similarity of electronic levels of D3 and D4 are reflected both in the HOMO energy values (both ≈ 5.3 eV) as well as in the maximum absorption in the near-infrared region at ≈ 900 nm, which arises due to optically induced hole transfer from the triarylamine unit to the linking bridge leading to this strong and broad absorption. This peak is obviously not visible in Magic Blue for the lack of any bridging units between the Ar_3N units.[35] It is to be noted that D3 shows similar absorption signatures as a reported dication obtained from MeOTPD by oxidation using a silver salt of perfluorinated alkoxyaluminates.[36] A small shoulder visible in the absorption spectrum of D2 at 630 nm is explained by symmetry breaking of the tris(4-bromophenyl)amine radical cation, which is not present in D3 and D4 due to their twisted arrangement of the phenyl groups around the nitrogen centers.[36,37] In the Raman spectra of thin films (**Figure S6.3**, Supporting Information) typical aromatic hydrocarbon stretching vibrations are present; most notably, the C–H out-of-plane wagging from mono substituted benzene (908 cm^{-1}, Δ), C–H in plane bending from benzene rings (1175 cm^{-1}, *) and C–N stretching (1320 cm^{-1}, +) are observable. C–C stretching bands are susceptible to quinoid to benzoid transitions of the mesomeric structures. This explains the higher intensity of the more stabilized quinoid vibration in the biphenyl bridged cations, MeOTPD^{2+}(PF$_6$)$_2$ and spiro-MeOTAD^{4+}(PF$_6^-$)$_4$ (1564 cm^{-1}) as compared to the energetically more favored benzoid structure in the less stabilized Magic Blue (1606 cm^{-1}).[36,38] The redox behavior and energy levels of our dopants and their pristine states are further studied by measuring the frontier orbitals using cyclic voltammetry (CV), as well as differential pulse polarography (DPP) by sequentially oxidizing the pristine molecules (**Figure S6.4**, Supporting Information). All the values are summarized in **Table 6.1**, together with the UPS values.

Table 6.1. HOMO energy E^{HOMO} values of neutral tris(4-bromophenyl)amine (TPA-Br$_3$), MeOTPD, and spiro-MeOTAD obtained by cyclic voltammetry (CV) half wave potential and differential pulse polarography (DPP) peak potential. Oxidation states of the corresponding peaks are given as (+x) in brackets. Ionization potential IP and workfunction WF were obtained by ultraviolet photoelectron spectroscopy on D2, D3, and D4.

| Compound | CV[a] | DPP[a] | Compound | UPS[b] | |
| | E^{HOMO}(+x) | | | IP | WF |
	(eV)	(eV)		(eV)	(eV)
TPA-Br$_3$	-5.69 (+I)	-5.81 (+I)	D2	-5.67	-5.11
MeOTPD	-5.50 (+I)	-5.51 (+I)	D3	-5.34	-5.01
	-5.77 (+II)	-5.76 (+II)			
Spiro-MeOTAD	-5.38 (+I)	-5.39 (+I)	D4	-5.25	-4.91
	-5.53 (+II)	-5.54 (+II)			
	-5.75 (+IV)	-5.75 (+IV)			

[a] Measured in anhydrous dichloromethane (sample concentration 10^{-3}–10^{-5} M) using supporting electrolyte: 0.1 M TBAPF$_6$, reference electrode: Ag/AgNO$_3$, counter electrode: Platinum disk, and working electrode: platinum disk at a scan rate: 100 mV s^{-1}, at rt and ambient pressure. For DPP measurements, a pulse size of 20–50 mV with 100 ms pulse duration was chosen. The half wave potentials $E^{1/2}$ versus Ag/AgNO$_3$ were referenced to the vacuum level by E^{HOMO}(compound) = [$-e\{E^{1/2}$(compound vs ref. Ag/AgNO$_3$) – ($E^{1/2}$(Fc/Fc$^+$ vs Ag/AgNO$_3$)}] + E^{HOMO}(Fc/Fc$^+$ vs E_{Vac}, solvent corrected). The ferrocene reference half-wave potential $E^{1/2}$(Fc/Fc$^+$ vs Ag/AgNO$_3$) was determined to be +0.10 V in DCM at a scan rate of 100 mV s^{-1}, E_{HOMO}(Fc/Fc$^+$ vs E_{Vac}, solvent corrected) was taken as -5.16 eV.[40] For complete dataset, see **Table S6.1** of the Supporting Information.

[b] UPS was measured on 20 nm thin films of D2, D3, and D4 on ITO.

To avoid radical cross-coupling of the dopants, high scan rate was chosen for CV, which results in large peak-to-peak separation energies ΔE_P (**Table S6.1**, Supporting Information). All the pristine molecules show fully reversible redox cycles; the number of redox peaks depending on the number of nitrogen centres (**Figure S6.4**, Supporting Information). Obviously, TPA-Br$_3$ shows a single reversible oxidation, whereas MeOTPD exhibits two (mono- and dication) and spiro-MeOTAD three (mono-, di-, and tetracation) oxidation steps in both CV and DPP measurements. The monooxidation step of MeOTPD to MeOTPD^{1+} and the dioxidation step of spiro-MeOTAD^{1+} to spiro-MeOTAD^{2+} are almost degenerate in energy (−5.50 and −5.53 eV, respectively, in CV). This indicates that most probably, spiro-MeOTAD^{2+} resembles the monocation, MeOTPD^{1+} electronically. Therefore, it can be deduced that spiro-MeOTAD^{2+} consists of two decoupled MeOTPD^{1+} radical cations anchored at one common spiro carbon center, rather than a doubly charged MeOTPD^{2+} moiety linked to another neutral half. The chemical structures of all four possible spiro-MeOTAD oxidation states are compiled in **Figure S6.5** of the Supporting Information. Moreover, both spiro-MeOTAD^{1+} and MeOTPD^{1+} possess sufficient low ionization potentials or E_{HOMO} of −5.38 and −5.50 eV, making exothermal multielectron electron transfer from P1 or P2 (IP = 4.6–4.7 eV) feasible to reach the zero oxidation states of both D3 and D4. The peak current obtained from the DPP experiment is directly related to the amount of electrons transferred and the concentration of the redox species, which is constant in our experiment.[39] When comparing the differential pulse polarogram peak current of spiro-MeOTAD^{2+} and spiro-MeOTAD^{4+} signal, a two electron oxidation process from dication to tetracation can be inferred (**Figure S6.4b**, Supporting Information). This implies an intrinsically unstable triply charged spiro-MeOTAD^{3+}, consistent with an earlier report by Zhang et al.[40] Quantitative X-ray photoelectron spectroscopy analysis was employed to obtain the atomic composition (N/P) of D3 and D4 powder samples (see **Table S6.2**, Supporting Information). By comparing the theoretical nitrogen to phosphorous atomic ratios (N/P = 1 for both tetracation, D4 and dication D3) to experimentally determined nitrogen 1s and phosphorous 2p signal integral ratios (1.2 and 1.4, respectively), average contents of at least 60 % for D3 and 80 % for D4 can be assessed from XPS. Considering all the supporting data from CV, DPP, UPS, and XPS, it can be very well concluded that the di- and tetracation organic salts D3 and D4 were successfully synthesized, where both dopants are capable of exothermal multielectron transfer from the polymers P1 and P2.

6.2.2 Monitoring of the Doping Process

As a first step to study the charge transfer between dopants and polymers, we performed UV/Vis/NIR absorption spectroscopy experiments, as it is a simple, yet powerful technique to probe changes in electronic states due to doping of polymers. Prior to chemical doping, the changes in spectral features of polymers P1 and P2 on electrochemical oxidation were determined by spectroelectrochemical (SEC) measurements in solution to identify the polaron features. For this, both polymers were biased from zero to +800 mV oxidation potential in 200 mV steps and absorption spectra are measured (**Figure 6.2a**). The ground-state absorptions for both P1 and P2 are located at 820 nm and upon electrochemical oxidation, the ground state absorption is bleached and new polaronic features appear at ≈ 1200 nm in the near-infrared region. The detailed absorption spectra for P1 and P2 for all the dopant concentrations ranging from 0.1 to 5 mol% for D1–D4 are shown in **Figure S6.6** of the Supporting Information. **Figure 6.2b** shows the absorption spectra of chemically doped P1 and P2 for the four different dopants D1–D4 at a typical 2 mol% dopant concentration in 0.01 mg mL^{-1} polymer solution. For both polymers, the MEAs, D3 and D4 show pronounced doping effects compared to the monovalent dopants D1 and D2. For all dopant concentrations, the TEG substituted polymer P1 exhibit the highest polaron absorption intensities in the increasing order from D2, over D3 to D4. Similarly, in the 2-hexyldecyl substituted polymer P2, a lower and less gradually expressed polaron absorption is observed with both D1 and D2. To delineate the changes in the absorption spectra, difference spectra were plotted in **Figure 6.2c**. Difference spectra are obtained by subtracting the spectrum of the pristine polymer from each spectrum of the doped polymers, thus emphasizing spectral changes upon doping. The upper plot in **Figure 6.2c** shows the difference spectra of the TEG substituted polymer P1 at a typical dopant concentration of 2 mol% for all four dopants. It shows a clear trend with increasing polaron intensity from D1 over D2 to D3 and D4. In the lower part, the difference plots for the alkyl substituted polymer P2 are shown. As before, only low doping can be achieved using D1, and the intensity of the polaron absorption increases with the oxidation state of the dopants. A notable difference for P2 is that D1 and D2 yield similar and low polaron intensities, as compared to D3 and D4. For dopant molar ratios up to 2 mol% (**Figure 6.2c**), there is no other considerable difference

between P1 and P2 in terms of polaron intensity. However, for the dopant D4, a higher
absolute polaron absorption was measured in the case of the hydrophilic polymer P1 as
compared to the hydrophobic derivative P2 at 5 mol% doping ratio (**Figure 6.2d**). This
can be attributed probably due to better miscibility of D4 in the former at higher
concentrations. Similar behavior was previously observed by Kroon et al., who doped
ethylene glycol substituted polythiophenes using F_4TCNQ and found an improved
solubility and conductivity by the introduction of polar side chains.[11] This can be
explained as follows: for a successful molecular doping, the polar dopants must access the
conjugated polymer backbone whereby the glycol substitution assists this mixing and
therefore, a more steady and uniform doping process is attained with the more
hydrophilic polymer P1.
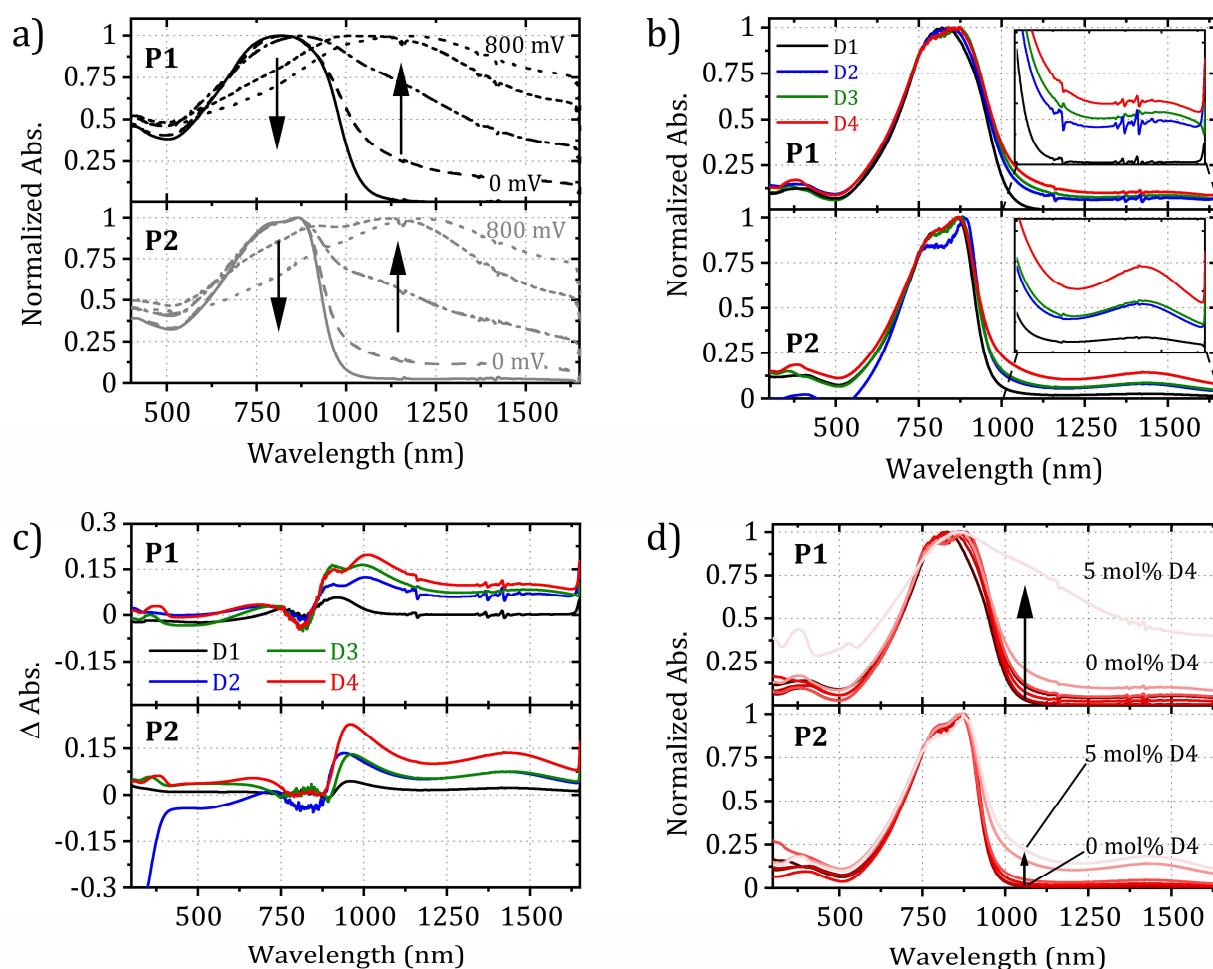
Figure 6.2. a) Spectroelectrochemical spectra of the polymers P1 and P2 in DCM obtained by biasing from 0 mV to +800 mV. A de-doping step of −100 mV was applied prior to measurement to ensure pristine polymer samples. b) Comparison of the optical absorption spectra of the doped P1 and P2 for four different dopants. D1–D4 at 2 mol% dopant loading in 0.01 mg mL^{-1} polymer solution. c) Comparative difference spectra of both polymers with 2 mol% dopant loading, obtained by subtracting the pristine polymer absorption from the oxidized polymer absorption (b). d) Change in absorption for P1 on doping with 0 to 5 mol% D4 in DCM. Spectra (b–d) obtained under inert and anhydrous conditions.

Concomitant with polymer doping, the formation of reduced dopant species can be expected and consequently their original absorption changes. The pristine precursors (non-oxidized forms) of D2–D4 absorb only below 400 nm. To identify the optical signatures of intermediate reduction products of D3 and D4, i.e., MeOTPD^{+}(PF$_6^{-}$) monocation and spiro-MeOTAD^{2+}(PF$_6^{-}$)$_2$ dication salts, these were prepared by titration

of their respective neutral precursors MeOTPD or spiro-MeOTAD using the necessary equivalents of oxidizing agents. Spectra of these salts can be found in **Figure S6.2b** of the Supporting Information. Both exhibit pronounced NIR absorption at ≈ 1500 nm with almost no absorption at 900 nm (typical absorption for the dopant D3 and D4, **Figure S6.2a**). Since the polaron absorption of P1 and P2 overlaps with the absorption of the reduced dopant intermediates at about 1500 nm, it is very difficult to elucidate the contribution of the reduced species toward near infrared absorption. It is to be noted that the contribution of the reduced species at low molar dopant regime is negligibly small. However, the increase in absorption below 400 nm can be attributed to the neutral triarylamine species of the dopants, even though the molar amount of the dopant used is very small. Nevertheless, it is valid to focus on the polaron absorptions for the first estimate of the doping process. It is clearly demonstrated, that D4 introduces a much higher polaron concentration than all other dopants for the whole dopant concentration up to 5 mol% in both polymers P1 and P2 studied here, regardless of the polarity of the polymer.

6.2.3 Impact on the Electrical Conductivity and Activation Energies

The above discussed absorption studies have proven the highly efficient doping of polymers by the multication salts in general and the highly pronounced nature of doping using D4. The coulombically bound polaron-counter ion pair can now release electrons upon thermal activation, thus increasing the bulk conductivity. **Figure 6.3a** shows the electrical conductivity values of the doped systems measured in thin films in the range of zero to 5 mol% dopants for both the hydrophilic polymer P1 and the hydrophobic polymer P2. Interestingly, an increase in electrical conductivity over one to two orders of magnitude develops within 1 mol% of doping for any dopant for both P1 and P2. Below 1 mol% dopant concentrations, no big differences among the doping capabilities of D1–D4 are discernible. This initial strong increase of the conductivity at low doping concentrations is well-known in the literature and characteristic for filling of energetically deep lying states in highly disordered systems.[41] On increasing dopant concentration, substantial differences for the four different dopants, as well as for the two polymers are evident. For example, above 1 mol%, the conductivity of doped P1 increases drastically

for D3 and D4, whereas it levels off for D1 and D2, with the highest conductivity reached for the samples doped with D4 throughout the whole dopant concentration range. The final value for P1 doped with D3 reaches $1.9 \cdot 10^{-2}$ S cm^{-1} and with D4 0.2 S cm^{-1} is obtained at 5 mol% dopant. In comparison, D1 and D2 increase the bulk conductivity of P1 to a mere $9.1 \cdot 10^{-4}$ S cm^{-1}, and $1.1 \cdot 10^{-3}$ S cm^{-1}, respectively (**Tables S6.4** and **S6.5**, Supporting Information). Thus, the tetracation salt D4 causes two orders and D3 results in one order of magnitude higher conductivity compared to monocation salts D1 and D2 at 5 mol% doping. In the hydrophobic polymer P2 also a strong increase in electrical conductivity is observed at lower dopant loadings, which however increases slower than in the hydrophilic polymer. This can be attributed to the lack of glycol-substitution leading to a decreased accessibility of the polar dopants to the polymer backbones and therefore, to a lower efficiency of polaron formation in P2. In P2, D1 and D2 have an identically lower doping effect as compared to D3 and D4. Here, the final conductivity values at 5 mol% reach $1.8 \cdot 10^{-4}$ and $2.3 \cdot 10^{-4}$ S cm^{-1} for D1 and D2, respectively, and $2.6 \cdot 10^{-3}$ and $1.7 \cdot 10^{-3}$ S cm^{-1} for D3 and D4, respectively. Thus, a distinctive difference between the low efficient monocation salts (D1, D2) and highly efficient multication salts (D3 and D4) can be observed with respect to the achieved conductivity values. Further, an increased polarity of the conjugated polymer in P1 facilitates the doping process.
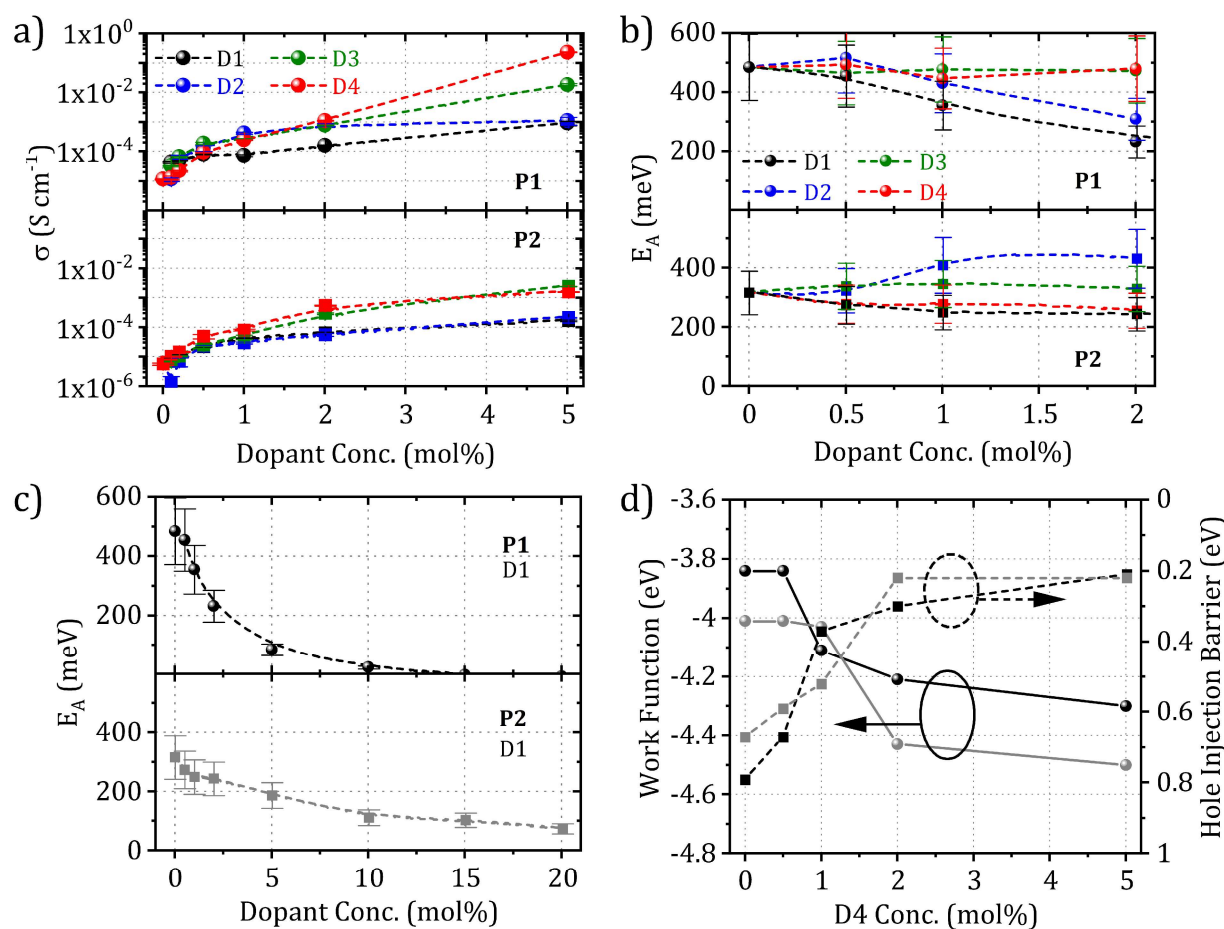
Figure 6.3. a) Electrical conductivity measurement. b) Evolution of the activation energies. c) E_A-progression of NOPF$_6$-doped films up to 20 mol% showing the drop of activation energy, which accompanies shift of the Fermi energy towards the transport level. d) Variation of work function (left *y*-axis, solid lines) and hole-injection barrier (right *y*-axis, dashed lines) of P1 (black) and P2 (gray) as a function of molar doping ratio from 0 to 5 mol% D4.

To gain an understanding of the charge transport mechanism, the thermal activation energies of the conductivity in doped polymers were determined. The activation energies E_A were calculated from Arrhenius plots by measuring the temperature dependent conductivity $\sigma(T)$ for a range between room temperature and 100 °C. From the Arrhenius-plots (**Figure S6.7**, Supporting Information), the activation energy values E_A were extracted using the Arrhenius equation $\sigma(T) = \sigma_0 e^{-E_A/(k_B T)}$, where k_B is the Boltzmann constant. The activation energy obtained by this consists of two processes: a contribution for the charge transfer salt dissociation and the contribution of the thermally activated

hopping, as described earlier by Schwarze et al.[42] The activation for charge transfer dissociation, schematically shown in **Equation 6.2**, is typically at least one order of magnitude greater than the activation for hopping.[42,43] Interestingly, we found drastic differences in E_A both, among the dopants, as well as between the two polymers. **Figure 6.3b** shows the activation energies of both doped polymers using different dopants for a dopant molar ratio up to 2 mol%. In the first glance, there is a distinct difference in behavior between NOPF$_6$ (D1) and the triarylamine cation salts (D2–D4). In the hydrophilic polymer P1, a steadily decreasing activation energy is obtained for D1 starting from 0 to 5 mol% (**Figure 6.3b**). This steady decline is very distinctive for an increased charge carrier density in organic semiconductors. By filling low lying, exponentially distributed trap states and shifting the Fermi level closer to the transport energy E_{Tr}, the hole injection barrier and the thermal activation energy for charge transport are lowered.[17] E_{Tr} delimits mobile from trapped charges, with only states higher in energy contributing to charge transport.[44] The hydrophobic polymer P2 exhibits a comparable behavior, although the decrease of the activation energy upon doping with D1 proceeds much slower than for P1 (**Figure 6.3b**). This is also observable in the doping regime beyond 2 mol% (**Table S6.3**, Supporting Information) and it is explained with the inferior compatibility of the NOPF$_6$ salt with the hydrophobic polymer. In order to fully understand the steady decrease in E_A, for D1, we measured additionally the E_A for dopant concentrations up to 20 mol% of D1 for both P1 and P2. **Figure 6.3c** clearly shows, that E_A asymptotically approaches zero for 20 mol% D1. The activation energy upon doping P2 with the oxidized triarylamine cations (D3–D4), which are HTM-dopants, remains, as in the polar polymer, almost constant. A slightly increasing activation energy is however found for D2 in polymer P2, which indicates an obstructed charge transport. On the contrary, in the case of the multication HTM-dopants D3 and D4, the activation energy for charge transport remains unchanged upon the introduction of dopants. In the context of hopping transport, this indicates a relatively unchanged distance between Fermi- and transport level. UPS experiments on the polymers P1 and P2 doped with D4 (**Figure 6.3d**) confirm the downshift of E_F toward the respective HOMO, with a distinct pinning at 200 meV above the valence band maximum for both polymers. Since the transport levels E_{Tr} in a Gaussian density of states (DOS) remains fairly independent of the charge carrier concentration, the downshift of the Fermi level E_F seems to be compensated by the additional broadening of the DOS by doping.[45] To

determine the impact of the (partially or fully) reduced HTM-dopant compared to a non-HTM dopant on the HOMO density of states and their distribution in polymers, ultraviolet photoelectron spectroscopy was carried out on 20 nm thin films of undoped P1 and P2 and their doped samples with NOPF$_6$ (non-HTM dopant) and spiro-MeOTAD^{4+}(PF$_6^-$)$_4$ (HTM-dopant). After measurement of the valence band maximum (VBM), the onset was fitted with a modified exponential Gaussian distribution to account for localized/tail states arising due to ionized dopants (**Equation S6.10**, Supporting Information). The broadening of the DOS was quantified by fitting **Equation S6.10** of the Supporting Information to the VBM (see also **Figure 6.4a**; numerical results summarized in **Table S6.7**, Supporting Information). A comparison of the standard deviation of the gaussian distribution of DOS (σ_{GDOS}) confirms that D1 (σ_{GDOS} = 120 meV) causes less change in the variance of the Gaussian part of the fit function than D4 (σ_{GDOS} = 198 meV) in P1. A similar broadening of DOS is observed in using an HTM-dopant like D4 in P2. Additionally, the most pronounced disorder, and exponential tailing of the pristine polymers was measured for the polar TEG-substituted P1, which is consistent with the experimental observations made by Borsenberger and Bässler, that static dipole moments increase the energetic disorder in organic semiconducting systems.[46] Together with the increased energetic disorder found *via* UPS experiments and the high number of dipoles (i.e., static disorder) added in the form of multiply charged small molecules, the constant activation energy for P1 and P2 using HTM-dopants can be attributed to a highly disordered system. However, at doping concentrations of 2 mol% and above, the use of multivalent dopants D3 and D4 result in doped polymers having conductivities orders of magnitude higher than D1 and D2. This advantage, however, comes along with the disadvantage, that a significant amount of static disorder is introduced by the highly charged HTM materials, causing no considerable decrease in activation energies for charge transport on increasing doping content.
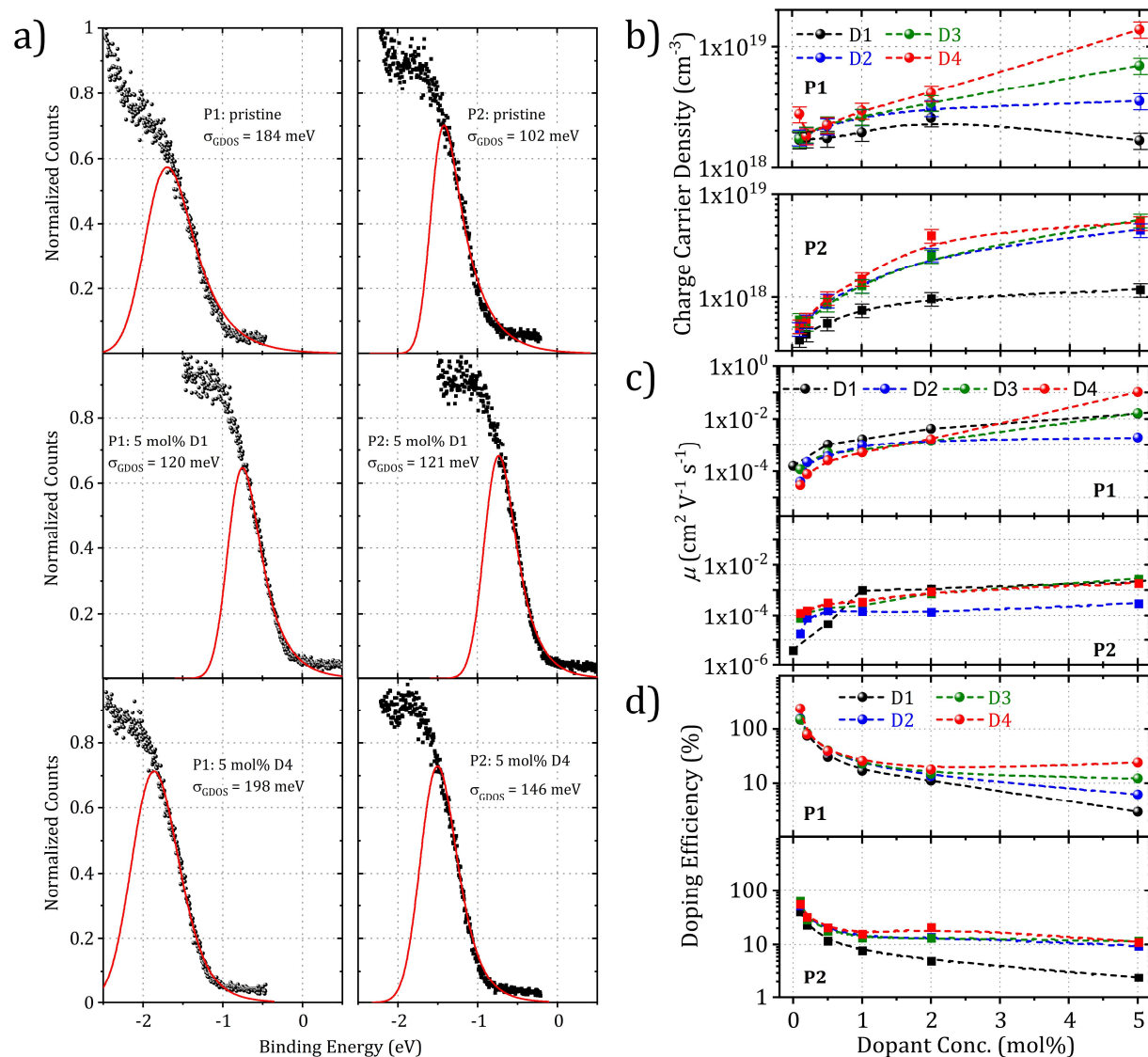
Figure 6.4. a) Valence band maxima of P1 and P2 doped with 0 mol% (top), 5 mol% D1 (center), and 5 mol% D4 (bottom) obtained from UPS and fitted with an exponentially modified Gaussian distribution (see Supporting Information for detailed calculation). *p*-doping with D4 induces a higher variance of the Gaussian distribution as compared to D1 doped polymers. b) Charge carrier density obtained from a calibration curve (see Supporting Information for details). c) Calculated charge carrier mobility μ of P1 and P2 doped with D1–D4, determined from **Equation 6.1** using the measured charge carrier concentration and conductivity. Holes were assumed as the majority carrier type in the *p*-doped systems, neglecting electron contribution. d) Doping efficiency of the polymers P1 and P2, upon doping with the different dopants D1–D4. The doping efficiencies of D3 and D4 are normalized to 100 % (denoting the uptake of two and four electrons, respectively).

Additionally, the difference in behavior of P1 and P2 toward the dopants can be explained as follows. As the ionization potential difference between P1 and P2 is almost negligible (≈ 0.05 eV), we do not expect the IP to cause any difference in the degree of ionization after doping by a significant amount. In addition, both polymers support an exothermic electron transfer to all dopants. Especially at higher doping ratios (i.e., 5 mol%), tail states should not impact the doping efficiency, as the Fermi level has well crossed all intragap and tail states at this point (**Figure 6.3d**). This leaves the polarity/side-chains as the only major difference in both polymers, as the possible cause for the difference in doping efficiency and ultimately the observed conductivity trend.

6.2.4 Charge Carrier Density

The number of introduced charge carriers N_D is an important figure of merit in unipolar (*p*- or *n*-type) doped systems and is directly linked to the elementary charge *e*, the hole mobility μ_h and conductivity σ *via* **Equation 6.1**.

$$\sigma = eN_D\mu_h \tag{6.1}$$

In doped systems, N_D is conveniently accessible *via* capacitance–voltage (Mott–Schottky) experiments on metal–insulator–semiconductor devices.[26] In metal–insulator–semiconductor devices, holes are either accumulated or depleted at the semiconductor–insulator interface upon applying an electrical bias at the metal contact. Spatial width and capacitance of this depletion- or space-charge layer is, inter alia, very sensitive to the amount of ionized donors N_D present in the bulk. Using impedance spectroscopy, the change in depletion layer capacitance and consequently N_D of the doped system can be monitored (see Supporting Information for detailed information). Therefore, we have measured the charge carrier densities (N_D) of polymer films doped with D1 from 0 to 20 mol% and correlated the resulting values with the respective polaron absorption intensities from optical absorption spectroscopy measurements. Since N_D correlates perfectly linear with the polaron peak integral obtained from UV/Vis studies, a calibration curve can be obtained to deduce N_D, once the polaron intensity is measured (**Figures S6.8** and **S6.9**, Supporting Information). Based on this calibration curve, the charge carrier

densities for both polymer films doped with the other three dopants D2–D4 were read out from the polaron absorption values. Details regarding the method are elaborated in the respective section of the Supporting Information. For both polymers, for the whole range of dopant concentration, the doped samples using triarylamine dopants D2–D4 exhibit considerably higher N_D values compared to NOPF$_6$. The charge carrier densities in the doped hydrophilic polymer P1 scale with the oxidation state of the HTM-dopants; D4 doping exhibiting almost 3–5 times the value of D2 doping. **Figure 6.4b** shows this clear trend for P1 above 2 mol% dopant. At the highest concentration of 5 mol%, the anticipated scaling of the charge carrier density with the oxidation state is perfectly expressed: the monovalent dopant D2 creates a carrier density of $3.5 \cdot 10^{18}$ cm^{-3}, which doubles to $6.9 \cdot 10^{18}$ cm^{-3} for D3 (dication) and quadruples for the fourfold oxidized D4, reaching a carrier density of $13.8 \cdot 10^{18}$ cm^{-3}. This correlation could not be observed in the doped hydrophobic polymer P2; indeed, the charge carrier density of D4 doped P2 films rises more strongly below 2 mol% dopant concentration, as compared to all the other dopants. Beyond 2 mol% in P2 however, the charge carrier densities generated by all three HTM-dopants D2–D4 merge and saturate reaching $5 \cdot 10^{18}$ cm^{-3} at 5 mol%. This is still almost five times the value obtained for NOPF$_6$-doped P2. Thus, the HTM-dopants induce drastically higher carrier densities than D1, which affords a saturated value of only $1.2 \cdot 10^{18}$ cm^{-3} at 5 mol%. The fact that for both, the polar polymer P1, and the nonpolar polymer P2, the redox dopant D1 performs worse than any of the HTM-dopants D2–D4 for the whole range of dopant concentrations up to 5 mol%, indicates the increased efficacy of doping conjugated polymers using triarylamine-cation based salts in general. Moreover, the higher the oxidation state of the dopant, the more efficient is the doping process.

6.2.5 Charge Carrier Mobility

The widely studied *p*-type dopants such as F$_4$TCNQ, and the fluorinated fullerene C$_{60}$F$_{36}$ are being reduced upon doping to form their anions such as F$_4$TCNQ$^-$, and C$_{60}$F$_{36}^-$, or charge transfer salts thereof.[7] Typically, these reduced species do not contribute to the charge transport, or may even hamper it, ultimately resulting in reduced charge carrier mobilities. Our dopants D2–D4, consisting of oxidized triarylamine hole conductors, are

able to transport charges in their pristine as well as partially oxidized states. The lower oxidized states (which are *de facto* the reduced dopant species after doping the polymer) are extensively used as charge transport layers for, e.g., solar cells.[47] We therefore examined if the use of cation salts of hole conductors as dopants can have additional contributions toward charge transport within the host:dopant mixture, as compared to $NOPF_6$, which has no HTM component at all. For this, first the zero-field charge carrier mobilities μ_0 of the pristine dopant precursors TPA-Br₃, MeOTPD, and spiro-MeOTAD were determined by impedance spectroscopy by fitting a Poole–Frenkel field-dependency (**Figure S6.10a**, Supporting Information). For this, negative differential susceptance measurements on hole-only FTO/semiconductor/Au devices were carried out. Holes are injected at one electrode if a sufficient electrical field F across the device is applied. By measuring the capacitive response of the biased device at different frequencies, an average carrier transit time for a given organic layer thickness and electrical field can be deduced. This ultimately yields μ_0 of the organic semiconductor after extrapolating $\mu(F)$ against zero electrical field. Details of calculation are published elsewhere and explained in the Supporting Information.[26] It was found, that all the pristine compounds possess similar values of μ_0 (MeOTPD: $2.6 \cdot 10^{-3}$ cm² V⁻¹ s⁻¹, followed by spiro-MeOTPD: $2.0 \cdot 10^{-3}$ cm² V⁻¹ s⁻¹ and TPA-Br₃: $1.3 \cdot 10^{-3}$ cm² V⁻¹ s⁻¹). Röhr et al. reported a similar value of $3.2 \cdot 10^{-3}$ cm² V⁻¹ s⁻¹ for spiro-MeOTAD from space-charge limited current measurements.[48] The impact of the HTM-dopants on charge carrier mobility of the doped polymer P1 and P2 was estimated by extracting the charge carrier mobility from the known parameters such as charge carrier density and conductivity using **Equation 6.1**. The results for both polymers doped with D1–D4 (0–5 mol%) are summarized in **Figure 6.4c**. Both, the polar P1 and the alkyl-substituted P2 improve in charge carrier mobility upon doping, regardless of the used dopant. This leads to the conclusion, that the presence of charged HTM dopants or their reduced products does not introduce trap states deeper in energy than already present in the disordered polymer semiconductor.[49] This is substantiated by the measured activation energy, which remains virtually constant upon doping with D3 or D4 (**Figure 6.3b**). The more polar P1 shows signs of filling energetically low-lying tail states below the gaussian HOMO DOS ("trap-filling"), as evidenced by lowered activation energy in the case of D1 and D2. Trap-filling substantially increases the charge carrier mobility at low doping ratios, consistent with the mobility data shown in **Figure 6.4c**).[17,22] The strong initial increase in μ_h tends

to flatten more for the alkyl-substituted polymer P2 and is in agreement with the initial steep drop of the hole-injection barrier and the Fermi-level pinning at > 2 mol% of D4 as seen in UPS experiments for both polymers (**Figure 6.3d**). When comparing the mobilities of the both doped polymers using the HTM dopants and NOPF$_6$, it appears that none of them affect the charge carrier mobility adversely and no considerable advantage is observed for the former, even though doping as such improves the charge carrier mobility.

6.2.6 Doping Efficiency

Besides fundamental electronic properties such as conductivity, charge carrier mobility, and charge carrier density, the doping efficiency (η_{Dop}) allows for comparison of our HTM-dopants versus NOPF$_6$. η_{Dop} is defined as the ratio of the number of free holes N_D (obtained by Mott–Schottky measurements) and the total number of dopant molecules N_A per unit volume. A higher η_{Dop} implies a more efficient dissociation of the bound charge transfer state formed by [Dopant$^{(n-x)+}$Polymer^{x+}] into free majority charge carriers as given in **Equation 6.2**, where D and P stand for dopant and polymer, respectively.

$$\left[D^{(n-x)}P^{x+}\right] \xrightarrow{k_B T} D^{(n-x)} + P^{x+}$$

(6.2)

One important point to note here is that the first step in the integer charge transfer doping reaction, i.e., the formation of the so-called charge transfer state is temperature independent.[50] This implies, that nearly all dopants introduced into the system form ionized CT states, which are coulombically bound semiconductor–dopant pairs. In a second step, *via* thermal activation, free charge carriers responsible for the conductivity increase can be generated from the CT states. The ratio between the total amount of dopant molecules in the bulk versus free charge carriers can be understood as the doping efficiency. As evident from **Figure 6.4d,** the polar polymer P1 displays an exponential decrease in η_{Dop} at the lowest doping ratios, to below 25 % ionization efficiency at 1 mol% dopant concentration. The pronounced loss in carrier generation efficiency with an increasing amounts of dopant molecules is known in the literature for organic

semiconductors. It can be explained by a free hole capture process by ionized dopant molecules, which become statistically more likely, the more dopant is present in the system.[22] Accumulation of unreacted dopant was detected in the absorption spectra for the highest doping concentration of 5 mol% D4 at 380 nm in **Figure 6.2d**. Consistent with our electrical conductivity and UV/Vis/NIR absorption studies, the more hydrophobic polymer P2 overall hinders the charge transfer salt dissociation, resulting in lower doping efficiency. This can be traced back to a decreased accessibility of the polymer backbone for dopant molecules and molecular miscibility. Ethylene glycol polar side chains are known to improve the dopant miscibility and doping efficacy for donor–acceptor copolymers.[51-53] Further, a large relative permittivity ε_r introduced by the TEG sidechains (ε_r(P1) = 5.41) helps to overcome Coulomb interaction of the charge transfer salt compared to the alkyl-substituted P2 with ε_r(P2) = 4.74 (**Figure S6.10b**, Supporting Information, for detailed calculation of dielectric constants). In both polymers, D4 offers the highest ratio of dissociated to total dopant molecules, closely followed by D3. To conclude, multivalent oxidized HTM dopants offer an advantage in carrier generation efficiency from their charge transfer salts compared to Magic Blue and NOPF$_6$, which especially manifests itself at high dopant concentrations of > 2 mol%.

6.3 Conclusion

We synthesized novel and stable HTM-dopants, dication (MeOTPD^{2+}(PF$_6^-$)$_2$, D3) and tetracation (spiro-MeOTAD^{4+}(PF$_6^-$)$_4$, D4) salts and comparatively studied their use as *p*-dopants or MEAs for two conjugated polymers belonging to the class of PDPPs differing in their polarity and dielectric constants. Their superiority over conventional one-electron oxidants such as NOPF$_6$ (D1) and Magic Blue (D2) for *p*-doping was clearly proven. We observed a fourfold amount of positively charged polarons in both polymers when using the tetracationic salt D4, resulting in a higher electrical conductivity and charge carrier density as compared to equivalent molar amounts of mono and divalent dopants. Unlike NOPF$_6$ (D1), a higher amount of energetic disorder is introduced in the density of states of doped polymer by MeOTPD^{2+}(PF$_6^-$)$_2$ and spiro-MeOTAD^{4+}(PF$_6^-$)$_4$, resulting in higher activation energies for charge transport. No negative effects on the charge carrier mobility were observed due to the presence of these dopants or their

reduced species. Finally, the doping efficiency of D4 remains the highest among all the dopants for the whole range of dopant concentration from 0 to 5 mol%. Thus, a highly efficient method of generating charge carriers in conjugated polymers is demonstrated using multiply charged salts of triarylamine derivatives to help decrease the dopant loading necessary for achieving strongly improved electronic properties, thereby overcoming issues associated with excess use of dopants. Synergistic effects between multivalent HTM dopants and hydrophilic polymers further boost the doping efficiencies. Our findings pave the way for a new and highly efficient route of doping conjugated polymers using MEA cation salts.

6.4 Acknowledgements

6.5 Conflicts of Interest

The authors declare no conflict of interest.

6.6 References

[1]   B. H. Lee, G. C. Bazan, A. J. Heeger, *Adv. Mater.* **2016**, *28*, 57.

[2]   Y. Hu, Z. D. Rengert, C. McDowell, M. J. Ford, M. Wang, A. Karki, A.T. Lill, G. C. Bazan, T.-Q. Nguyen, *ACS Nano* **2018**, *12*, 3938.

[3]   Y. Kim, S. Chung, K. Cho, D. Harkin, W.-T. Hwang, D. Yoo, J.-K. Kim, W. Lee, Y. Song, H. Ahn, Y. Hong, H. Sirringhaus, K. Kang, T. Lee, *Adv. Mater.* **2019**, *31*, 1806697.

[4]   I. H. Jung, C. T. Hong, U.-H. Lee, Y. H. Kang, K.-S. Jang, S. Y. Cho, *Sci. Rep.* **2017**, *7*, 44704.

[5]   H. Yan, J. G. Manion, M. Yuan, F. P. García De Arquer, G. R. Mckeown, S. Beaupré, M. Leclerc, E. H. Sargent, D. S. Seferos, *Adv. Mater.* **2016**, *28*, 6491.

[6]   Y. Zhang, H. Zhou, J. Seifter, L. Ying, A. Mikhailovsky, A. J. Heeger, G. C. Bazan, T.-Q. Nguyen, *Adv. Mater.* **2013**, *25*, 7038.

[7]   H. Hase, I. Salzmann, in *Handbook of Organic Materials for Electronic and Photonic Devices*, 2nd ed. (Ed: O. Ostroverkhova), Woodhead Publishing, Oxford, UK **2019**, pp. 349–383.

[8]   I. Salzmann, G. Heimel, M. Oehzelt, S. Winkler, N. Koch, *Acc. Chem. Res.* **2016**, *49*, 370.

[9]   J. Hynynen, D. Kiefer, L. Yu, R. Kroon, R. Munir, A. Amassian, M.Kemerink, C. Müller, *Macromolecules* **2017**, *50*, 8140.

[10]   B. Lüssem, M. Riede, K. Leo, *Phys. Status Solidi A* **2013**, *210*, 9.

[11]   R. Kroon, D. Kiefer, D. Stegerer, L. Yu, M. Sommer, C. Müller, *Adv. Mater.* **2017**, *29*, 1700930.

[12]   Y. Karpov, T. Erdmann, M. Stamm, U. Lappan, O. Guskova, M. Malanin, I. Raguzin, T. Beryozkina, V. Bakulev, F. Günther, S. Gemming, G. Seifert, M. Hambsch, S. Mannsfeld, B. Voit, A. Kiriy, *Macromolecules* **2017**, *50*, 914.

[13]   H. Li, E. Plunkett, Z. Cai, B. Qiu, T. Wei, H. Chen, S. M. Thon, D. H. Reich, L. Chen, H. E. Katz, *Adv. Electron. Mater.* **2019**, *5*, 1800618.

[14] Y. Xuan, X. Liu, S. Desbief, P. Leclère, M. Fahlman, R. Lazzaroni, M.Berggren, J. Cornil, D. Emin, X. Crispin, *Phys. Rev. B* **2010**, *82*, 115454.

[15] D. Kiefer, R. Kroon, A. I. Hofmann, H. Sun, X. Liu, A. Giovannitti, D.Stegerer, A. Cano, J. Hynynen, L. Yu, Y. Zhang, D. Nai, T. F. Harrelson, M. Sommer, A. J. Moulé, M. Kemerink, S. R. Marder, I. Mcculloch, M. Fahlman, S. Fabiano, C. Müller, *Nat. Mater.* **2019**, *18*, 149.

[16] G. Chauhan, R. Srivastava, A. Kumar, O. Rana, P. C. Srivastava, M. N. Kamalasanan, *Org. Electron.* **2012**, *13*, 394.

[17] S. Olthof, S. Mehraeen, S. K. Mohapatra, S. Barlow, V. Coropceanu, J.-L. Brédas, S. R. Marder, A. Kahn, *Phys. Rev. Lett.* **2012**, *109*, 176601.

[18] I. E. Jacobs, E. W. Aasen, J. L. Oliveira, T. N. Fonseca, J. D. Roehling, J. Li, G. Zhang, M. P. Augustine, M. Mascal, A. J. Moulé, *J. Mater. Chem.C* **2016**, *4*, 3454.

[19] F. Deschler, D. Riedel, A. Deák, B. Ecker, E. Von Hauff, E. Da Como, *Synth. Met.* **2015**, *199*, 381.

[20] J. Euvrard, A. Revaux, P.-A. Bayle, M. Bardet, D. Vuillaume, A. Kahn, *Org. Electron.* **2018**, *53*, 135.

[21] V. I. Arkhipov, E. V. Emelianova, P. Heremans, H. Bässler, *Phys. Rev. B* **2005**, *72*, 235202.

[22] M. L. Tietze, L. Burtone, M. Riede, B. Lüssem, K. Leo, *Phys. Rev. B* **2012**, *86*, 035320.

[23] B. Tan, S. R. Raga, A. S. R. Chesman, S. O. Fürer, F. Zheng, D. P. Mcmeekin, L. Jiang, W. Mao, X. Lin, X. Wen, J. Lu, Y.-B. Cheng, U. Bach, *Adv. Energy Mater.* **2019**, *9*, 1901519.

[24] W. H. Nguyen, C. D. Bailie, E. L. Unger, M. D. Mcgehee, *J. Am. Chem. Soc.* **2014**, *136*, 10996.

[25] W. Zhang, F. Zhang, B. Xu, Y. Li, L. Wang, B. Zhang, Y. Guo, J. M. Gardner, L. Sun, L. Kloo, *ACS Appl. Mater. Interfaces* **2020**, *12*, 33751.

[26] M. Goel, M. Siegert, G. Krauss, J. Mohanraj, A. Hochgesang, D. C. Heinrich, M. Fried, J. Pflaum, M. Thelakkat, *Adv. Mater.* **2020**, *32*, 2003596.

[27] A. I. Hofmann, R. Kroon, S. Zokaei, E. Järsvall, C. Malacrida, S. Ludwigs, T. Biskup, C. Müller, *Adv. Electron. Mater.* **2020**, *6*, 2000249

[28] P. Schmode, A. Savva, R. Kahl, D. Ohayon, F. Meichsner, O. Dolynchuk, T. Thurn-Albrecht, S. Inal, M. Thelakkat, *ACS Appl. Mater. Interfaces* **2020**, *12*, 13029.

[29] G. Krauss, F. Meichsner, A. Hochgesang, J. Mohanraj, S. Salehi, P. Schmode, M. Thelakkat, *Adv. Funct. Mater.* **2021**, *31*, 2010048.

[30] C. J. Mueller, E. Gann, C. R. Singh, M. Thelakkat, C. R. Mcneill, *Chem. Mater.* **2016**, *28*, 7088.

[31] B. Meng, J. Liu, L. Wang, *Polym. Chem.* **2020**, *11*, 1261.

[32] B. Meng, H. Song, X. Chen, Z. Xie, J. Liu, L. Wang, *Macromolecules* **2015**, *48*, 4357.

[33] H. Méndez, G. Heimel, A. Opitz, K. Sauer, P. Barkowski, M. Oehzelt, J. Soeda, T. Okamoto, J. Takeya, J.-B. Arlin, J.-Y. Balandier, Y. Geerts, N. Koch, I. Salzmann, *Angew. Chem., Int. Ed.* **2013**, *52*, 7751.

[34] I. Salzmann, G. Heimel, S. Duhm, M. Oehzelt, P. Pingel, B. M. George, A. Schnegg, K. Lips, R.-P. Blum, A. Vollmer, N. Koch, *Phys. Rev. Lett.* **2012**, *108*, 035502.

[35] C. Lambert, G. Nöll, *J. Am. Chem. Soc.* **1999**, *121*, 8434.

[36] Y. Su, X. Wang, X. Zheng, Z. Zhang, Y. Song, Y. Sui, Y. Li, X. Wang, *Angew. Chem., Int. Ed.* **2014**, *53*, 2857.

[37] S. Amthor, B. Noller, C. Lambert, *Chem. Phys.* **2005**, *316*, 141.

[38] C. Kvarnström, A. Petr, P. Damlin, T. Lindfors, A. Ivaska, L. Dunsch, *J. Solid State Electrochem.* **2002**, *6*, 505.

[39] D. J. Myers, J. Osteryoung, *Anal. Chem.* **1973**, *45*, 381.

[40] W. Zhang, L. Wang, Y. Guo, B. Zhang, V. Leandri, B. Xu, Z. Li, J. M. Gardner, L. Sun, L. Kloo, *Chem. Commun.* **2020**, *56*, 1589.

[41] A. Fediai, F. Symalla, P. Friederich, W. Wenzel, *Nat. Commun.* **2019**, *10*, 4547.

[42] M. Schwarze, C. Gaul, R. Scholz, F. Bussolotti, A. Hofacker, K. S. Schellhammer, B. Nell, B. D. Naab, Z. Bao, D. Spoltore, K. Vandewal, J. Widmer, S. Kera, N. Ueno, F. Ortmann, K. Leo, *Nat. Mater.* **2019**, *18*, 242.

[43] H. Matsui, D. Kumaki, E. Takahashi, K. Takimiya, S. Tokito, T. Hasegawa, *Phys. Rev. B* **2012**, *85*, 035308.

[44] J. O. Oelerich, F. Jansson, A. V. Nenashev, F. Gebhard, S. D. Baranovskii, *J. Phys.: Condens. Matter* **2014**, *26*, 255801.

[45] B. Hartenstein, H. Bässler, *J. Non-Cryst. Solids* **1995**, *190*, 112.

[46] P. M. Borsenberger, H. Bässler, *J. Chem. Phys.* **1991**, *95*, 5327.

[47] Z. Hawash, L. K. Ono, Y. Qi, *Adv. Mater. Interfaces* **2018**, *5*, 1700623.

[48] J. A. Röhr, X. Shi, S. A. Haque, T. Kirchartz, J. Nelson, *Phys. Rev. Appl.* **2018**, *9*, 044017.

[49] S.-J. Yoo, J.-H. Lee, J.-H. Lee, J.-J. Kim, *Appl. Phys. Lett.* **2013**, *102*, 183301.

[50] M. L. Tietze, J. Benduhn, P. Pahner, B. Nell, M. Schwarze, H. Kleemann, M. Krammer, K. Zojer, K. Vandewal, K. Leo, *Nat. Commun.* **2018**, *9*, 1182.

[51] D. Kiefer, A. Giovannitti, H. Sun, T. Biskup, A. Hofmann, M. Koopmans, C. Cendra, S. Weber, L. J. Anton Koster, E. Olsson, J. Rivnay, S. Fabiano, I. Mcculloch, C. Müller, *ACS Energy Lett.* **2018**, *3*, 278.

[52] J. Liu, L. Qiu, R. Alessandri, X. Qiu, G. Portale, J. Dong, W. Talsma, G. Ye, A. A. Sengrian, P. C. T. Souza, M. A. Loi, R. C. Chiechi, S. J. Marrink, J. C. Hummelen, L. J. A. Koster, *Adv. Mater.* **2018**, *30*, 1704630.

[53] J. Liu, G. Ye, H. G. O. Potgieser, M. Koopmans, S. Sami, M. I. Nugraha, D. R. Villalva, H. Sun, J. Dong, X. Yang, X. Qiu, C. Yao, G. Portale, S. Fabiano, T. D. Anthopoulos, D. Baran, R. W. A. Havenith, R. C. Chiechi, L. J. A. Koster, *Adv. Mater.* **2021**, *33*, 2006694.

6.7 Supporting Information

6.7.1 General Methods

All the materials were thoroughly dried under high vacuum prior to their use. The reactions sensitive to humidity and/or oxygen were conducted in flame-dried Schlenk type apparatuses under argon atmosphere and the doping experiments were performed in a nitrogen-filled glovebox. Anhydrous solvents were purchased from Sigma Aldrich / Acros Organics in sealed bottles and were used as received. Other solvents for chemical reactions, Soxhlet extractions etc. were freshly distilled in-house and reagents for syntheses were used as received from commercial sources if not stated otherwise. N,N,N′,N′-tetrakis(4-methoxyphenyl)benzidine (abbr. 4-MeO-TPD) was obtained from TCI Chemicals, Japan. $N^2,N^2,N^{2'},N^{2'},N^7,N^7,N^{7'},N^{7'}$-octakis(4-methoxyphenyl)-9,9'-spirobi[fluorene]-2,2',7,7'-tetraamine (abbreviated as "SpiroMeOTAD") was supplied by Sigma-Aldrich, Germany and used as received. 4-MeOTPD was dried under vacuum at rt for 1 h prior to use. Nitrosonium hexafluorophosphate was obtained from ThermoFischer, Germany and purified according to the synthetic procedure described below. Anhydrous dichloromethane and acetonitrile were supplied from ThermoFischer, Germany and used as received. Doped polymer solutions were fabricated by mixing of definite amounts of the respective polymer and dopant in dichloromethane; doped polymer films were similarly obtained by spin casting the respective polymer-dopant solution for 60 s at 1500 rpm. No further annealing was conducted. The polymerization reactions were conducted under microwave irradiation using a Biotage Initiator+ synthesis microwave machine. Solution NMR-spectra were recorded on a Bruker Avance spectrometer (300 MHz) at rt with deuterated solvents from Deutero GmbH and the chemical shifts are reported with respect to the residual solvent signal in units of (ppm). Gel permeation chromatography (GPC) measurements were performed on an instrument having an SDV linear XL gel column (particle size = 5 μm) with separation range from 100 to 3000000 Da (PSS, Mainz, Germany) together with a refractive index detector (1200 Series, Agilent Technologies). CHCl₃ (HPLC grade) was used as solvent (for dissolving polymer and as eluting solvent) with a flow rate of 0.5 mL min⁻¹ at room temperature. As internal standard toluene (HPLC grade) was used. The calibration was done with narrowly distributed polystyrene (PS) homopolymers (PSS calibration kit). An injection volume of

20 μL was used for the measurements. The sample was dissolved in $CHCl_3$ and filtered through a 0.22 μm PTFE filter before analysis. Optical absorption spectroscopy measurements were recorded using a Jasco V-670 spectrophotometer with a custom-built nitrogen flooded measurement chamber. Quartz cuvettes of an internal diameter of 1 cm were employed and for spectroelectrochemical absorption measurements, a Gamry Interface 1010T was used as the potentiostat in a conventional three-electrode setup (Pt-mesh WE, Pt-wire CE, Ag/AgCl RE). Ultraviolet photoelectron spectroscopy was performed on a PHI 5000 VersaProbe III machine equipped with a helium discharge radiation source providing stable and continuous He I and II lines, under ultrahigh vacuum (10^{-10} mbar). Samples for UPS measurements were obtained by spincoating on clean ITO (15 Ω $square^{-1}$), affording ca. 30 nm thick films (measured by using a dummy sample in a profilometer). The samples were transferred from the glovebox to the instrument in a nitrogen filled and sealed stainless steel transport vessel.

6.7.2 Monomer and Polymer Synthesis

The synthetic pathway toward the polymers was described by us earlier. (Krauss et al., *Adv. Funct. Mater.* **2021**, 2010048). The obtained polymers exhibited the following basic properties.

1H NMR:

PDPP[T]$_2${TEG}$_2$-3-MEET: (300 MHz, CDCl$_3$): d = 8.59 - 9.13 (br., 2 H), d = 6.41 - 7.15 (br., 3 H), d = 2.84 - 5.09 (br., 41 H).

PDPP[T]$_2${2-HD}$_2$-3-MEET: (300 MHz, CDCl$_3$): d = 8.76 - 9.27 (br., 2 H), d = 6.67 - 7.22 (br., 2 H), d = 3.53 - 4.76 (br., 8 H), d = 3.28 - 3.51 (br., 3 H), d = 0.44 - 2.14 (br., 66 H).

GPC:

PDPP[T]$_2${TEG}$_2$-3-MEET: M_n = 11 kg mol^{-1}, Đ = 2.5, X_N = 14.

PDPP[T]$_2${2-HD}$_2$-3-MEET: M_n = 14 kg mol^{-1}, Đ = 2.9, X_N = 18.

6.7.3 Dopant Synthesis

N^2,N^2,N$^{2'}$,N$^{2'}$,N^7,N^7,N$^{7'}$,N$^{7'}$-octakis(4-methoxyphenyl)-9,9'-spirobi[fluorene]-2,2',7,7'-tetraamine^{IV}, hexafluorophosphate salt (1:4)

Commercially available nitrosonium hexafluorophosphate was dried under vacuum for 3 d in a desiccator loaded with phosphorus pentoxide. A 250 mL flame-dried Schlenk flask was flushed with Ar and charged with 45 mL of anhydrous and degassed benzene. The solvent was cooled to 0 °C and dry nitrosonium hexafluorophosphate (2 g, 11.4 mmol) was added in small portions using air-free techniques to remove nitronium hexafluorophosphate. The mixture was stirred for 1 h at 0 °C. The solvent was removed and the purified nitrosonium hexafluorophosphate was dried under vacuum at rt and stored under inert conditions. Spiro-MeOTAD (107.6 mg, 87.8 µmol) was loaded into a flame-dried Schlenk flask flushed with Argon and dissolved in anhydrous dichloromethane (20 mL) cooled to 0 °C under strong stirring for 10 min. Nitrosonium hexafluorophosphate (103.8 mg, 593 µmol, 6 eq.) was loaded into a Schlenk flask flushed with Argon and dissolved in anhydrous acetonitrile (10 mL) and stirred at rt for 5 min. The nitrosonium hexafluorophosphate solution was added drop-wise to the ice-cold Spiro-MeOTAD solution using air-free techniques. Upon addition, the solution turned dark red with a gradual color change to royal blue. After complete addition, the mixture was allowed to heat up to rt and stirred for 20 min. The solution was precipitated in ice-cold, anhydrous hexane (500 mL), dried at rt in vacuum and stored under nitrogen. Yield: 127.9 mg (70.8 µmol, 81 %) of a dark-green powder.

N,N,N′,N′-Tetrakis(4-methoxyphenyl)benzidine^{II}, hexafluorophosphate salt (1:2)

4-MeO-TPD (115.4 mg, 190 µmol) was loaded into a flame-dried Schlenk flask, flushed with Ar and dissolved in anhydrous dichloromethane (20 mL) cooled to 0 °C under strong stirring for 10 min. Nitrosonium hexafluorophosphate (86.2 mg, 493 µmol, 2.6 eq.) was loaded into a Schlenk flask flushed with Ar and dissolved in anhydrous acetonitrile (10 mL) and stirred at rt for 5 min. The nitrosonium hexafluorophosphate solution was added drop-wise to the ice-cold 4-MeO-TPD solution using air-free techniques. Upon addition, the solution turned dark red with a gradual color change to dark blue. After

complete addition, the mixture was allowed to heat up to rt and stirred for 20 min. The solution was precipitated in ice-cold, anhydrous hexane (500 mL), dried at rt in vacuum and stored under nitrogen. Yield: 114 mg (127 μmol, 67 %) of a fine, dark-green powder.

6.7.4 Supporting Measurement Data
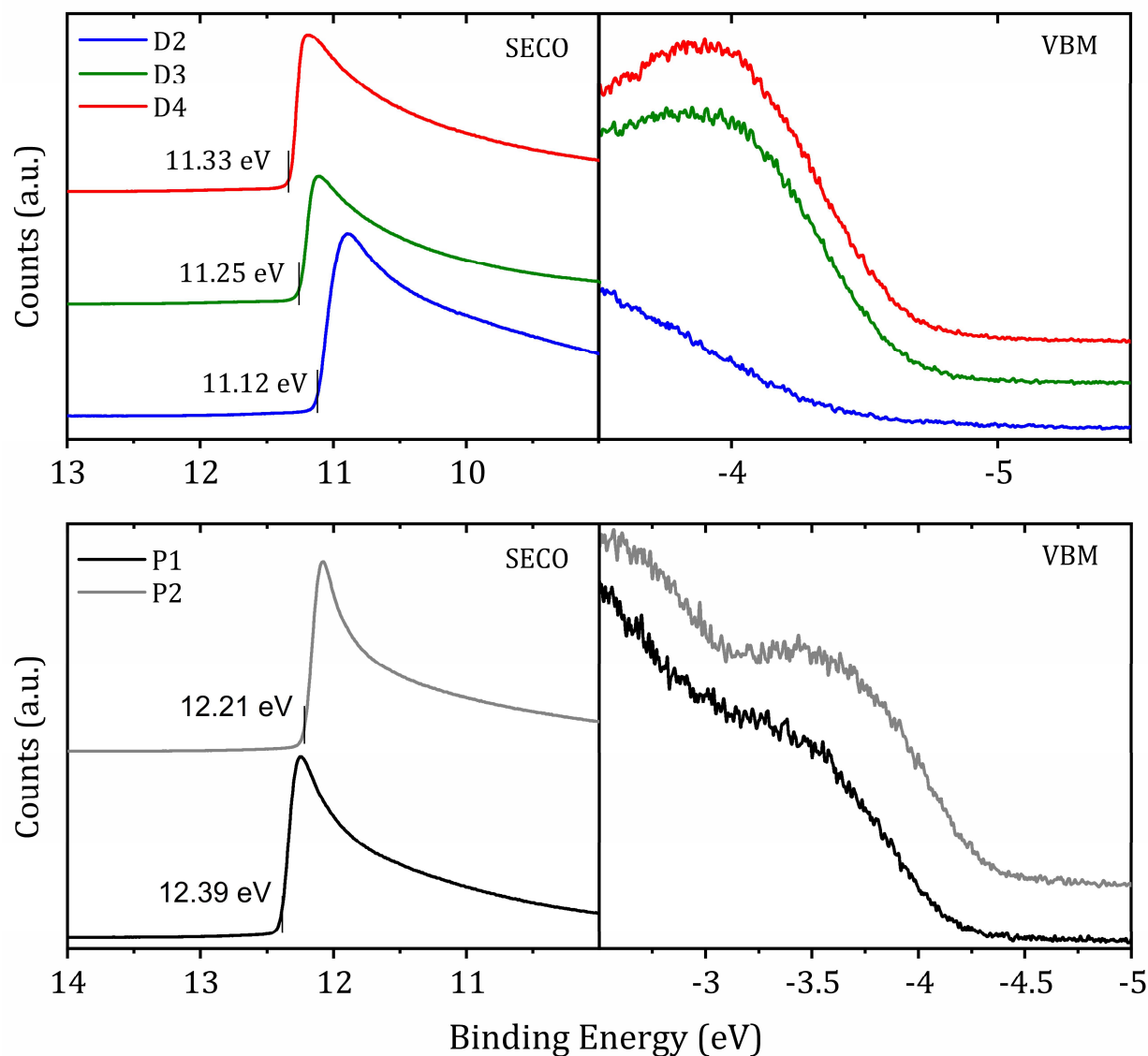
Figure S6.1. Ultraviolet photoelectron spectra showing the SECO (secondary electron cut-off, left) and VBM (valence band maximum, right) of D2 (blue), D3 (green), D4 (red), P1 (black) and P2 (grey), prepared as 20 nm thin films on ITO. Scaled w.r.t. Fermi Level (0 eV).
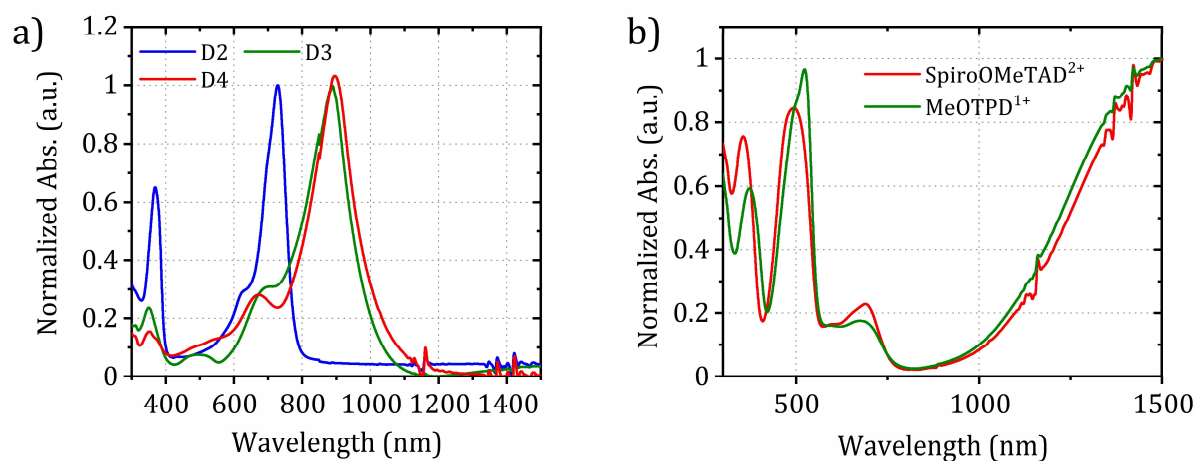
Figure S6.2. UV/Vis/NIR spectra of the pure HTM-dopants in acetonitrile solution (a), and the intermediately oxidized HTM-dopants (b).
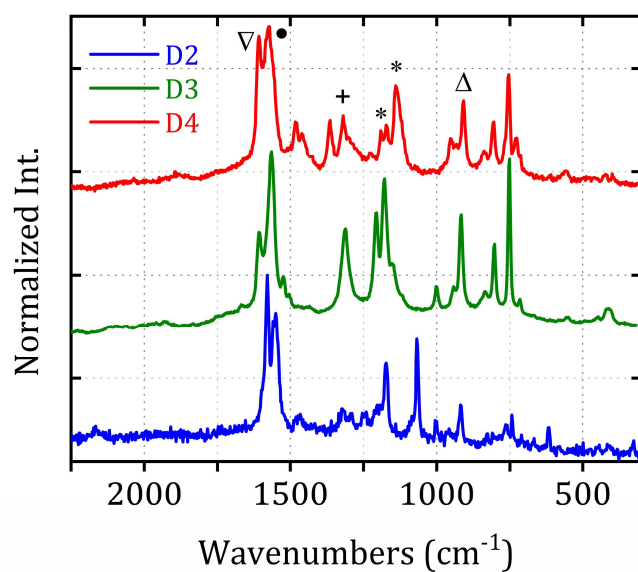
Figure S6.3. Raman spectra of the pure dopants D2, D3 and D4 measured on thin films on glass.
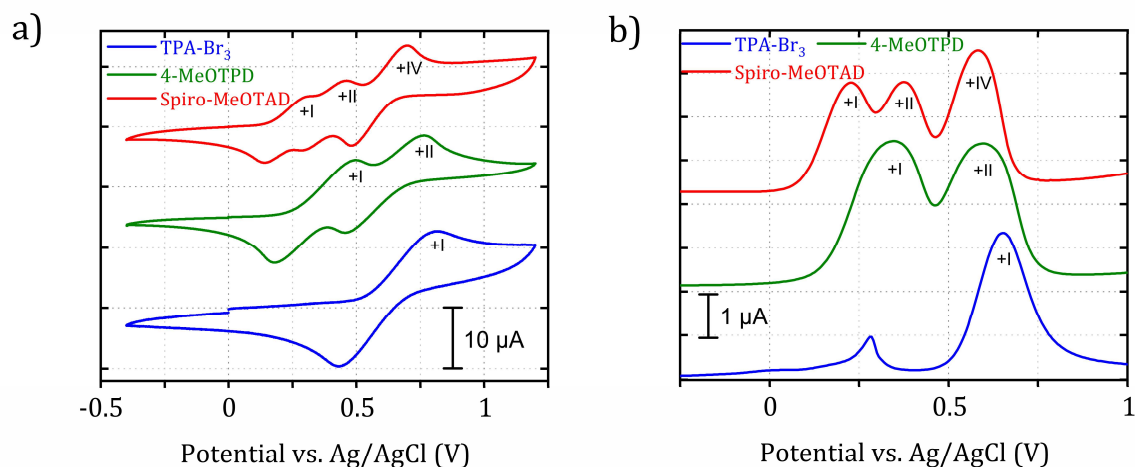
Figure S6.4. (a) Cyclic voltammograms and (b) differential pulse polarography (DPP) measured in dichloromethane solution using 0.1 M TBAPF$_6$ as the supporting electrolyte. A small redox current in the DPP measurement of Magic Blue at 260 mV vs. Ag/Ag+ indicates possible coupled by-products.
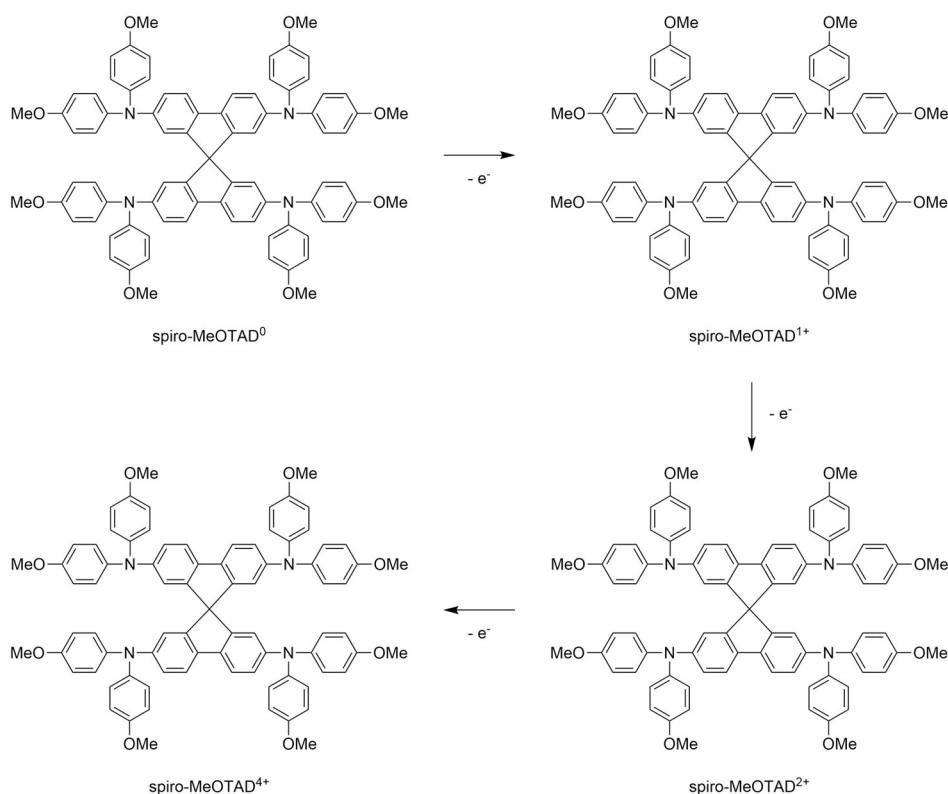
Figure S6.5. All the possible chemical structures of stepwise oxidation (removal of electrons) of spiro-MeOTAD.

Table S6.1. Cyclic voltammetry (CV) half wave $E^{1/2}$ potential (average of cathodic and anodic peaks) measured against Ag/AgNO$_3$ in DCM and peak-to-peak potential difference ΔE_p and differential pulse polarography (DPP) peak potential E_p for neutral tris(4-bromophenyl)amine (TPA-Br$_3$), 4-MeO-TPD and spiro-MeOTAD. Oxidation states of the corresponding peaks are given as (+x) in brackets. Measured in anhydrous dichloromethane with 0.1 M TBAPF$_6$.

Compound	CV		DPP
	$E^{1/2}(+x)$	ΔE_p	E_p
	(mV)	(mV)	(mV)
TPA-Br$_3$	628 (+I)	368 (+I)	650 (+I)
4-MeO-TPD	339 (+I)	314 (+I)	345 (+I)
	611 (+II)	302 (+II)	595 (+II)
Spiro-MeOTAD	223 (+I)	162 (+I)	230 (+I)
	374 (+II)	168 (+II)	375 (+II)
	590 (+IV)	216 (+IV)	585 (+IV)

X-Ray Photoelectron Spectroscopy

XPS measurements were carried out with a PHI 5000 VersaProbe III system fitted with an Al Kα excitation source ($h\nu$ = 1486.6 eV) and a dual neutralizer (electron gun and Ar$^+$) at 10^{-10} mbar. An X-ray source diameter of 100 mm was used to locally excite the samples; the corresponding photoemission with 45° take-off angle was collected at a multichannel analyzer. The survey and detailed spectra were measured with pass energies of 224 eV and 26/55 eV, respectively. The standard deviation on the reported energy values is ± 0.1 eV. The reproducibility of the observed results was confirmed by performing at least three measurements at different places of the samples. The spectra were analyzed with a Multipak software pack provided by the manufacturers. All emission signals were referenced to adventitious C1s peak at 284.8 eV. For atomic composition determination, the samples were transported to the instrument using a N$_2$-filled transport vessel to avoid air/O$_2$ contamination. For quantitative measurements, at least two areas of ca. $400 \cdot 400$ mm^2 were selected in each samples using secondary ion X-ray imaging

technique (SXI) to ensure spatial average composition of the dopants. The final reported atomic composition values are the average of 2 measurements. For quantitative analysis, the background of all spectra was corrected using the Shirley function. For XPS mapping experiments, a homogeneous sample area of 750 μm by 750 μm was selected with the help of SXI imaging. The photoelectrons of the selected area were collected using parallel acquisition mode of the detector with a resolution of 256 by 256 pixel. A pass energy of 55 eV, 4 frames per element and 20 ms time per step were chosen to increase the sensitivity. P1 and P2 were mapped according to their thiophene sulfur $2p_{3/2}$ peak at 161.5 eV, D2 according to the antimony $Sb3d_{5/2}$ peak at 539 eV, D3 and D4 to the fluorine 1s signal (688 eV). Prior to acquisition, the selected area was subjected to 30 s Ar sputtering ($2 \cdot 2$ mm, 2 kV, Zalar rotation) to remove surface residues. Finally, the color-coded images were overlaid to produce the mapped two-dimensional image.

Table S6.2. Comparison of the atomic composition of D3 and D4 between theoretical and
XPS determined values.

Elements	Theoretical composition (ratio of atoms)		XPS determined
	Spiro-MeOTAD^{2+}(PF$_6^-$)$_2$	Spiro-MeOTAD^{4+}(PF$_6^-$)$_4$	
N	4	4	55.2 %
P	2	4	44.8 %
N/P	2	1	1.2
P	2	4	14.3 %
F	12	24	85.7 %
P/F	0.17	0.17	0.17
	MeOTPD$^+$(PF$_6^-$)	MeOTPD^{2+}(PF$_6^-$)$_2$	
N	2	2	58.8 %
P	1	2	41.2 %
N/P	2	1	1.4
P	1	2	16.2 %
F	6	12	83.8 %
P/F	0.17	0.17	0.19

XPS determined values: atomic composition values are determined from ca.
$400 \cdot 400$ mm^2 area scan with 55 eV pass energy and 100 mm X-ray source size. The
values are the average from 2 measurements.
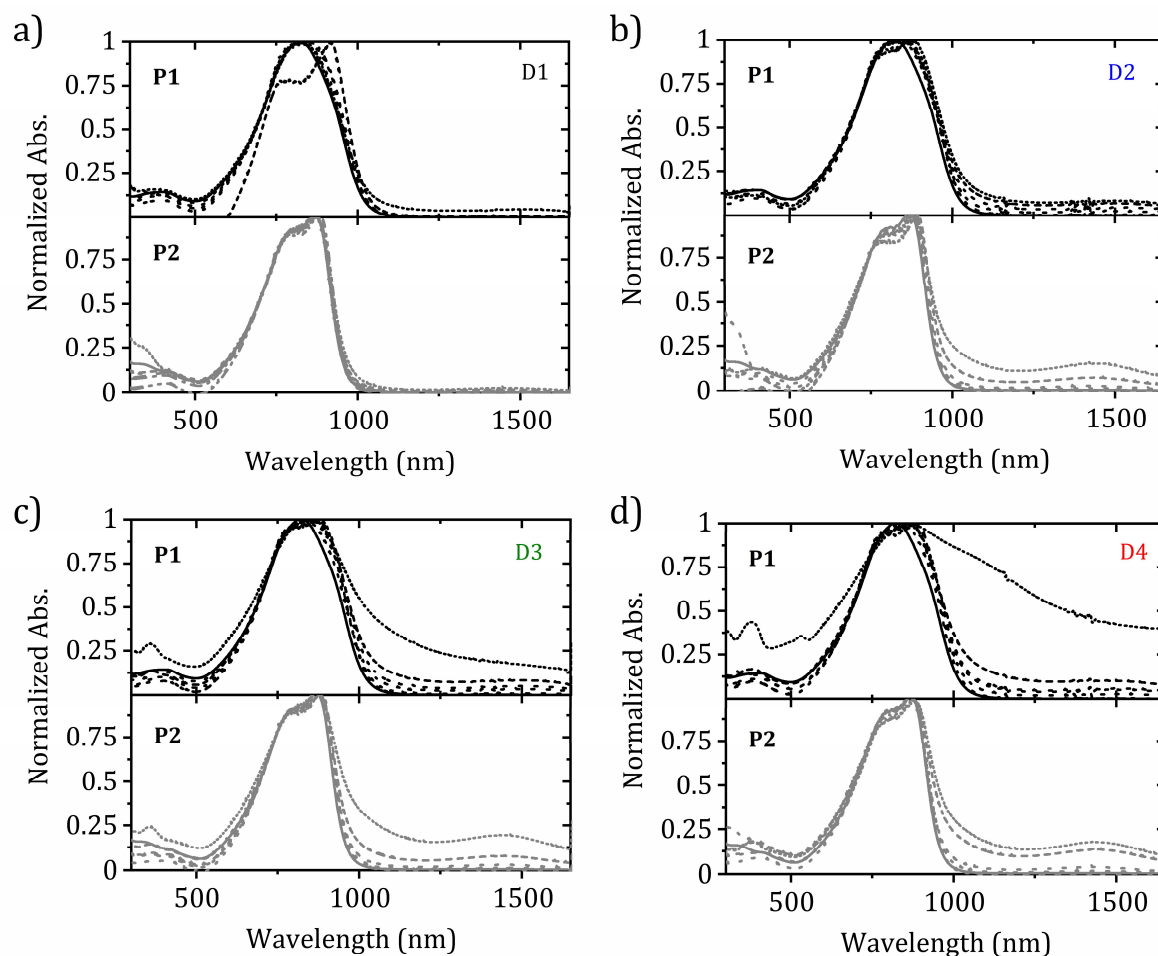
Figure S6.6. Solution (dichloromethane) UV/Vis/NIR progression of the two polymers P1 and P2 doped with D1 (a), D2 (b), D3 (c) and D4 (d) with the molar doping ratios of pristine (solid), 0.1 (dashed), 0.2 (dotted), 0.5 (dotted), 1 (dotted), 2 (dotted) and 5 mol% (dotted) in ascending order.

Electrical Conductivity

Electrical conductivities were measured using 30 nm thick interdigitated gold electrodes, patterned on thermally grown silicon oxide with a channel width of 2.5 μm and a channel length of 1 cm. The substrates were cleaned by sonication in isopropanol and acetone for 10 min each, followed by activation of the surface in an ozone plasma for 15 min at 50 °C. Polymer and doped polymer films were deposited by spin-coating from 5 mg mL^{-1} solutions (dichloromethane) at 1500 rpm in a nitrogen filled glovebox. I-V characteristics were measured using an Agilent Technologies B1500A Semiconductor Device Analyzer. The electrical conductivities were extracted from the linear fit of the I-V curve in the Ohmic region according to the **Equation S6.1** below.

$$\sigma = \frac{a \cdot L}{W \cdot d}$$

(S6.1)

Where σ: electrical conductivity, a: slope of the linear fit, L: channel length, W: channel width, d: film thickness. The film thicknesses were measured after the conductivity measurements, using a profilometer. The activation energies for the charge transport were extracted from temperature dependent electrical conductivity measurements. The sample preparation was done analogous to room-temperature electrical conductivity measurements. For the measurement, the devices were placed on a Linkam Scientific temperature control stage in a nitrogen filled glovebox and heated from rt to 100 °C in 5 K steps. The heating rate between each step was adjusted to 5 K min^{-1} and each temperature was kept constant for 30 s for equilibration before measuring the I-V characteristics. The activation energies were obtained from fitting the Arrhenius plot (ln σ vs. T^{-1}) with a linear curve and the Arrhenius equation yielded the activation energies.
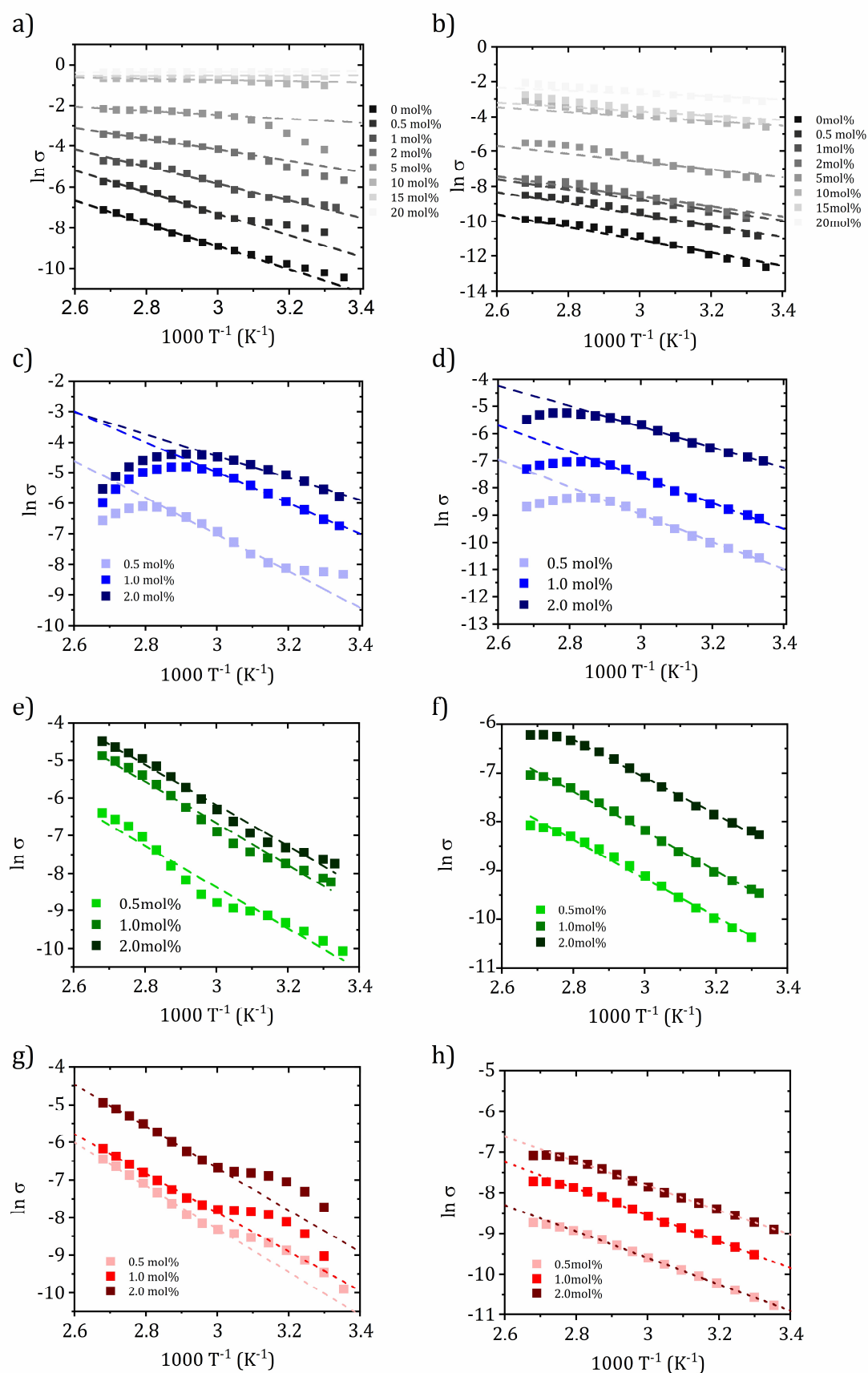
Figure S6.7. Arrhenius-plots of the polymer P1 (left side column) and P2 (right side column) for D1 (a, b), D2 (c, d), D3 (e, f) and D4 (g, h).

Table S6.3. Conductivity σ, thermal activation energy of conductivity E_A, charge carrier density N_D, doping efficiency η_{Dop} and hole mobility μ_h of P1 and P2 doped with D1 (NOPF$_6$).

System		σ (S cm^{-1})	E_A (meV)	N_D (cm^{-3})	η_{Dop} (%)	μ_h (cm V^{-1} s^{-1})
P1 : D1 PDPP[T]$_2${TEG}$_2$-3-MEET : NOPF$_6$	0 mol%	$1.16 \cdot 10^{-5}$	484.9	$1.1 \cdot 10^{18}$	-	0.0081
	0.1 mol%	$4.4 \cdot 10^{-5}$	-	$1.7 \cdot 10^{18}$	148	-
	0.2 mol%	$5.05 \cdot 10^{-5}$	-	$1.7 \cdot 10^{18}$	75	-
	0.5 mol%	$8.04 \cdot 10^{-5}$	455.6	$1.7 \cdot 10^{18}$	30	0.00107
	1 mol%	$7.36 \cdot 10^{-5}$	355.6	$1.9 \cdot 10^{18}$	17	0.00168
	2 mol%	$1.6 \cdot 10^{-4}$	232.5	$2.5 \cdot 10^{18}$	11	0.00429
	5 mol%	$9.13 \cdot 10^{-4}$	84.8	$1.6 \cdot 10^{18}$	3	0.01579
	10 mol%	-	24.3	-	-	-
	15 mol%	-	0	-	-	-
	20 mol%	-	0	-	-	-
P2 : D1 PDPP[T]$_2${2-HD}$_2$-3-MEET : NOPF$_6$	0 mol%	$6.15 \cdot 10^{-6}$	317.5	$3.7 \cdot 10^{18}$	-	0.0019
	0.1 mol%	$1.04 \cdot 10^{-5}$	-	$3.9 \cdot 10^{17}$	41	-
	0.2 mol%	$1.26 \cdot 10^{-5}$	-	$4.4 \cdot 10^{17}$	23	-

0.5 mol%	$2.38 \cdot 10^{-5}$	275.6	$5.6 \cdot 10^{17}$	12	$4.7 \cdot 10^{-5}$
1 mol%	$4.54 \cdot 10^{-5}$	251.4	$7.6 \cdot 10^{17}$	8	0.00104
2 mol%	$6.9 \cdot 10^{-5}$	245.8	$9.8 \cdot 10^{17}$	5	0.00116
5 mol%	$1.78 \cdot 10^{-4}$	188.9	$1.2 \cdot 10^{18}$	2	0.00217
10 mol%	-	114.3	-	-	-
15 mol%	-	105.5	-	-	-
20 mol%	-	76.5	-	-	-

Table S6.4. Conductivity σ, thermal activation energy of conductivity E_A, charge carrier density N_D, doping efficiency η_{Dop} and hole mobility μ_h of P1 and P2 doped with D2 (Magic Blue).

System		σ (S cm^{-1})	E_A (meV)	N_D (cm^{-3})	η_{Dop} (%)	μ_h (cm^2 V^{-1} s^{-1})
P1 : D2 PDPP[T]$_2${TEG}$_2$-3-MEET : Magic Blue	0 mol%	$1.16 \cdot 10^{-5}$	484.9	$1.1 \cdot 10^{18}$	-	0.0081
	0.1 mol%	$1.16 \cdot 10^{-5}$	-	$1.8 \cdot 10^{18}$	156	$4.1 \cdot 10^{-5}$
	0.2 mol%	$6.67 \cdot 10^{-5}$	-	$1.9 \cdot 10^{18}$	82	0.00022
	0.5 mol%	$1.3 \cdot 10^{-4}$	516.9	$2.2 \cdot 10^{18}$	38	0.00037
	1 mol%	$4.24 \cdot 10^{-4}$	431.1	$2.6 \cdot 10^{18}$	23	0.00101
	2 mol%	$8.01 \cdot 10^{-4}$	309.5	$3.1 \cdot 10^{18}$	14	0.00161
	5 mol%	0.00112	-	$3.5 \cdot 10^{18}$	6	0.00198
P2 : D2 PDPP[T]$_2${2-HD}$_2$-3-MEET : Magic Blue	0 mol%	$6.15 \cdot 10^{-6}$	317.5	$3.7 \cdot 10^{18}$	-	0.0019
	0.1 mol%	$1.45 \cdot 10^{-6}$	-	$5.0 \cdot 10^{17}$	53	$1.8 \cdot 10^{-5}$
	0.2 mol%	$7.5 \cdot 10^{-6}$	-	$5.9 \cdot 10^{17}$	31	$7.9 \cdot 10^{-5}$
	0.5 mol%	$2.49 \cdot 10^{-5}$	325.1	$9.4 \cdot 10^{17}$	20	0.00016
	1 mol%	$3.19 \cdot 10^{-5}$	410.8	$1.3 \cdot 10^{18}$	14	0.00015
	2 mol%	$6.03 \cdot 10^{-5}$	432.9	$2.6 \cdot 10^{18}$	14	0.00014
	5 mol%	$2.27 \cdot 10^{-4}$	-	$4.6 \cdot 10^{18}$	9	0.00031

Table S6.5. Conductivity σ, thermal activation energy of conductivity E_A, charge carrier density N_D, doping efficiency η_{Dop} and hole mobility μ_h of P1 and P2 doped with D3 (MeOTDP(PF$_6$)$_2$).

System		σ (S cm^{-1})	E_A (meV)	N_D (cm^{-3})	η_{Dop} (%)	μ_h (cm^2 V^{-1} s^{-1})
P1 : D3 PDPP[T]$_2${TEG}$_2$-3-MEET : MeOTDP(PF$_6$)$_2$	0 mol%	$1.16 \cdot 10^{-5}$	484.9	$1.1 \cdot 10^{18}$	-	0.0081
	0.1 mol%	$3.29 \cdot 10^{-5}$	-	$1.7 \cdot 10^{18}$	152	0.00012
	0.2 mol%	$6.53 \cdot 10^{-5}$	-	$1.9 \cdot 10^{18}$	82	0.00022
	0.5 mol%	$1.9 \cdot 10^{-4}$	465.1	$2.3 \cdot 10^{18}$	40	0.00052
	1 mol%	$2.65 \cdot 10^{-4}$	477.2	$2.6 \cdot 10^{18}$	23	0.00063
	2 mol%	$7.76 \cdot 10^{-4}$	472.9	$3.4 \cdot 10^{18}$	15	0.00142
	5 mol%	0.0185	-	$6.9 \cdot 10^{18}$	12	0.01653
P2 : D3 PDPP[T]$_2${2-HD}$_2$-3-MEET : MeOTDP(PF$_6$)$_2$	0 mol%	$6.15 \cdot 10^{-6}$	317.5	$3.7 \cdot 10^{18}$	-	0.0019
	0.1 mol%	$7.38 \cdot 10^{-6}$	-	$6.1 \cdot 10^{17}$	64	$7.5 \cdot 10^{-5}$
	0.2 mol%	$1.13 \cdot 10^{-5}$	-	$5.6 \cdot 10^{17}$	29	0.00012
	0.5 mol%	$2.7 \cdot 10^{-5}$	339.6	$8.6 \cdot 10^{17}$	18	0.001019
	1 mol%	$5 \cdot 10^{-5}$	347.8	$1.3 \cdot 10^{18}$	14	0.00024
	2 mol%	$3.12 \cdot 10^{-4}$	331.2	$2.6 \cdot 10^{18}$	13	0.00076
	5 mol%	0.00259	-	$5.7 \cdot 10^{18}$	12	0.00286

Table S6.6. Conductivity σ, thermal activation energy of conductivity E_A, charge carrier density N_D, doping efficiency η_{Dop} and hole mobility μ_h of P1 and P2 doped with D4 (Spiro-MeOTAD(PF$_6$)$_4$).

System		σ (S cm^{-1})	E_A (meV)	N_D (cm^{-3})	η_{Dop} (%)	μ_h (cm^2 V^{-1} s^{-1})
P1 : D4 PDPP[T]$_2${TEG}$_2$-3-MEET : Spiro-MeOTAD(PF$_6$)$_4$	0 mol%	$1.16 \cdot 10^{-5}$	484.9	$1.1 \cdot 10^{18}$	-	0.0081
	0.1 mol%	$1.32 \cdot 10^{-5}$	-	$2.7 \cdot 10^{18}$	241	$2.9 \cdot 10^{-5}$
	0.2 mol%	$2.24 \cdot 10^{-5}$	-	$1.8 \cdot 10^{18}$	79	$7.7 \cdot 10^{-5}$
	0.5 mol%	$9.24 \cdot 10^{-5}$	493.8	$2.2 \cdot 10^{18}$	39	0.00026
	1 mol%	$2.44 \cdot 10^{-4}$	446.9	$2.9 \cdot 10^{18}$	26	0.00052
	2 mol%	0.00112	479.7	$4.1 \cdot 10^{18}$	18	0.0017
	5 mol%	0.233	-	$1.4 \cdot 10^{19}$	24	0.10506
P2 : D4 PDPP[T]$_2${2-HD}$_2$-3-MEET : Spiro-MeOTAD(PF$_6$)$_4$	0 mol%	$6.15 \cdot 10^{-6}$	317.5	$3.7 \cdot 10^{18}$	-	0.0019
	0.1 mol%	$1.11 \cdot 10^{-5}$	-	$5.3 \cdot 10^{17}$	56	0.00013
	0.2 mol%	$1.58 \cdot 10^{-5}$	-	$6.2 \cdot 10^{17}$	32	0.00016
	0.5 mol%	$5.26 \cdot 10^{-5}$	279.7	$9.9 \cdot 10^{17}$	21	0.00033
	1 mol%	$8.7 \cdot 10^{-5}$	280.4	$1.5 \cdot 10^{18}$	16	0.00036

	2 mol%	$5.88 \cdot 10^{-4}$	257.8	$4.0 \cdot 10^{18}$	21	0.00091
	5 mol%	0.00167	-	$5.4 \cdot 10^{18}$	11	0.00195

Impedance Spectroscopy

Solid State Mott-Schottky Analysis

TEC-7 (XOP glass, $1" \cdot 1" \cdot 2.2$ mm, 6–8 Ω square^{-1}, ~ 500 nm FTO on glass) substrates were etched with dilute HCl/Zn-dust. After obtaining the etched electrode pattern, the substrates were brushed manually with sodium dodecyl sulfate and deionized water, followed by ultra-sonication in 2 vol% aqueous hellmanex-III solution, water, acetone and isopropanol. The substrates were blown dry with nitrogen and pre-treated with O_3/UV for 15 min at 50 °C. 100 nm of Al_2O_3 were deposited on the FTO-electrodes using ALD (H_2O/$Al(CH_3)_3$, 15 ms pulse duration, 150 °C, 5 s purge time, 1111 cycles), while leaving areas insulator-free for contacting the device during measurements. The aluminium oxide layer was passivated by spin coating 100 nm of BCB (10 vol% Cyclotene 3022-35 in toluene, 70 µL, 50 s, 3000 rpm) on top and soft curing for 10 s at 250 °C in air, followed by a hard bake at 250 °C for 1 h under Argon. The polymer:dopant-solutions were doctor bladed onto the substrates from DCM solutions (5 mg mL^{-1}, 40 µL, manual speed control, 60 µm blade height.) under inert atmosphere and used without further thermal annealing. To enhance the wettability, DCM was doctor bladed onto the substrates prior to polymer:dopant-coating and dried completely. Finally, Au electrodes were thermally evaporated using a shadow mask ($d_{Au} = 70$ nm). The impedance of the devices was measured with a two-electrode setup and varying electrical field (10 kHz to 10 Hz, 8 points per frequency decade, -1.5 to 1.5 V_{Bias} in 48 voltage steps, 7 mV$_{RMS}$) using a Metrohm Autolab PGSTAT204 equipped with an FRA32M module. The NOVA 2.1.4 Software package provided by Metrohm, Germany was used to process the impedance data. The Au top electrode was connected to the counter and reference electrode, the FTO contact to the working and sense electrode of the potentiostat. Devices under test were shielded from ambient light, external electrical fields and kept under inert atmosphere. From the imaginary Z'' and real Z' impedance, the capacitance of the organic layer was extracted assuming an R$_S$(RC) equivalent circuit (**Equation S6.2**).

$$\hat{Z}(i\omega)_{\text{R(RC)}} = R_{\text{Series}} + \cfrac{1}{i\omega C_{\text{Parallel}} + \cfrac{1}{R_{\text{Parallel}}}} \tag{S6.2}$$

Equation S6.2 can be solved for C_{Parallel} to yield

$$C_{\text{Parallel}} = \frac{Im(Z)}{(-Im(Z)^2 + (Re(Z) - R_{\text{S}})^2)\omega} \tag{S6.3}$$

The density of free charge carriers N_D was the extracted by plotting C^{-2} vs the Boltzmann corrected applied bias voltage V_{Bias} and fitting **Equation S6.4** to the linear depletion regime.

$$C_{\text{Parallel}}^{-2} = \frac{2}{\varepsilon_{\text{OSC}}\varepsilon_0 A^2 q N_D}\left(V_{\text{Bias}} - \frac{k_{\text{B}}T}{q}\right) \tag{S6.4}$$

where ε_{OSC} and ε_0 are the dielectric constants of the organic semiconductor layer (approximated with 3) and the vacuum permittivity, respectively. A^2 is the area of the organic layer in cm^2, q the elementary charge and k_{B} the Boltzmann constant in eV K^{-1}.
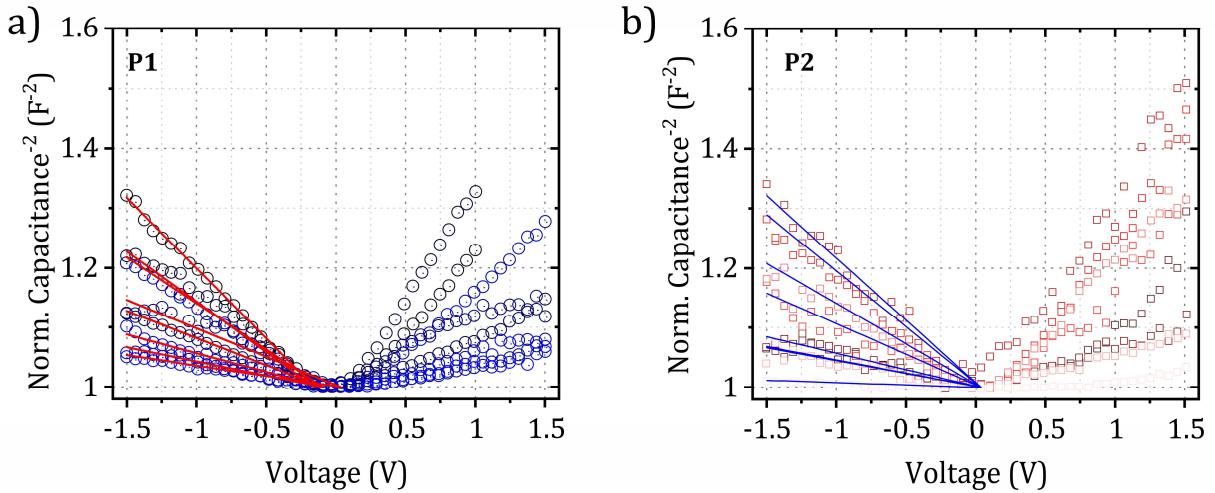
Figure S6.8. $1/C^2$ vs. applied bias voltage of metal-insulator-semiconductor (MIS) device structures of P1, resp. P2 doped with D1. The stack is comprised of FTO/Al$_2$O$_3$ (100 nm)/x-linked BCB (100 nm)/Polymer:Dopant (500 nm)/Au. A negative voltage applied to the Au top electrode results in the formation of a depletion zone at the insulator/semiconductor interface, where **Equation S6.4** is applied to calculate the charge carrier density N_D from the slope (Mott-Schottky measurement).
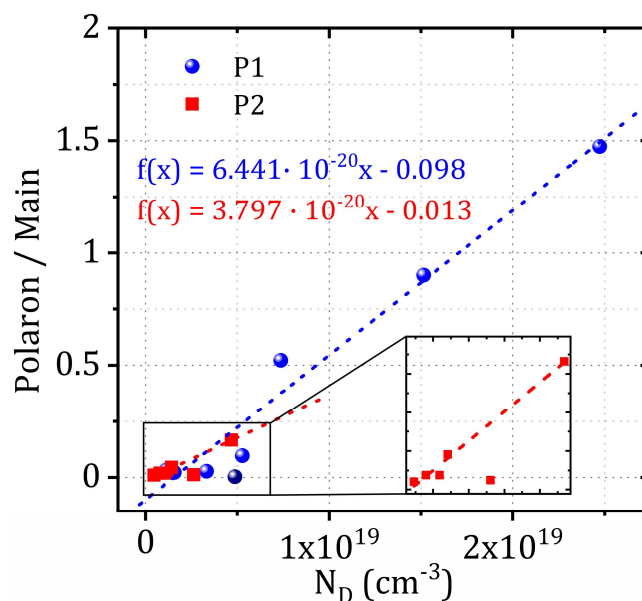
Figure S6.9. Linear correlations between measured charge carrier density N_D and measured absorption integral of polaron peak obtained by UV/Vis/NIR spectroscopy of solutions in DCM of P1 (blue) and P2 (red) doped with 0 to 20 mol% D1. N_D was obtained from Mott-Schottky measurements on metal-semiconductor-insulator devices (**Figure S6.8**). The obtained linear relationship was used to determine the charge carrier densities of P1 and P2 doped with D2, D3 and D4 from their respective polaron absorption integrals in solution, while keeping the concentrations of all species involved constant.

Negative Differential Susceptance Measurements

TEC-7 (XOP glass, $1" \cdot 1" \cdot 2.2$ mm, 6–8 Ω square^{-1}, ~ 500 nm FTO on glass) substrates were etched with dilute HCl/Zn-dust. After obtaining the etched electrode pattern, the substrates were brushed manually with sodium dodecyl sulfate and deionized water, followed by ultra-sonication in 2 vol% aqueous Hellmanex-III solution, water, acetone and isopropanol. The substrates were blown dry with nitrogen and pre-treated with O_3/UV for 15 min at 50 °C. The organic semiconductor films were doctor bladed onto the substrates from DCM solutions (5 mg mL^{-1}, 40 µL, manual speed control, 60 µm blade height) under inert atmosphere and used without further thermal annealing. To enhance the wettability, DCM was doctor bladed onto the substrates prior to coating and dried completely. To avoid edge effects, a part of the conductive electrodes was masked with

Kapton tape, which was removed after the OSC deposition. 100 nm of Au was thermally evaporated on top of the OSC layer using a shadow mask to complete the device stack. The impedance of the devices was measured with a two-electrode setup and increasing electrical field (1 MHz to 100 Hz, 25 points per frequency decade, 0-2 V_{Bias} in 15 voltage steps, 10 mV_{RMS}) using a Metrohm Autolab PGSTAT204 equipped with an FRA32M module. The NOVA 2.1.4 Software package provided by Metrohm, Germany was used to process the impedance data. The ITO back contact was connected to the working electrode (WE) and sense (S), while the Au top electrode was connected to the counter electrode (CE) and reference electrode (RE). Devices under test were shielded from ambient light and external electrical fields. From the imaginary Z'' and real Z' impedance, the capacitance of the organic layer was extracted assuming an R_S(RC) equivalent circuit (**Equation S6.2** and **S6.3**). The geometric capacitance C_{Geo} of each device was determined in the high frequency region of the C(f)-plot. Together with the measured capacitance, the mobility was extracted from the negative differential susceptance -ΔB at different electrical fields. The negative differential susceptance -ΔB can be calculated according to **Equation S6.5**.

$$-\Delta B = -\omega\left(C(\omega) - C_{geo}\right) \tag{S6.5}$$

The global maximum f_{max} of the $-\Delta B$(f)-plot was extracted and used to calculate the transit time τ_{tr}

$$\tau_{tr} = 0.56 f_{max}^{-1} \tag{S6.6}$$

Local maxima above the transit frequency without physical meaning were discarded. The mobility can then be extracted as

$$\mu = \frac{4}{3}\frac{d^2}{\tau_{tr}V_{Bias}} \tag{S6.7}$$

with d being the thickness of the organic layer. The zero-field mobility μ_0 was calculated by extrapolating the obtained Poole-Frenkel type field dependency.
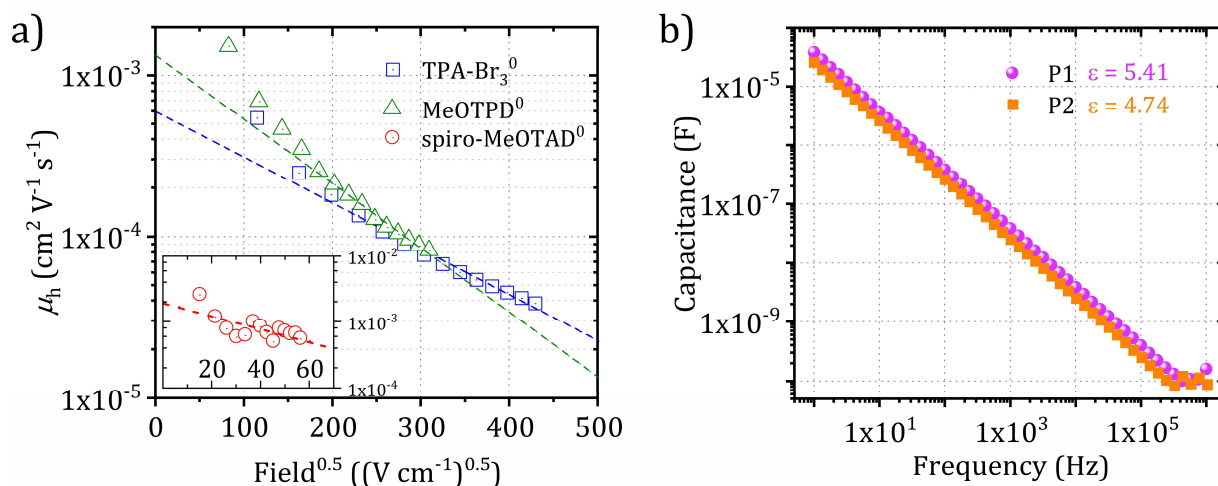
Figure S6.10. (a) Hole mobility μ_h of the pristine dopant molecules spiro-MeOTAD (red circles), MeOTPD (green triangles) and tris(4-bromo)phenylamine (TPA-Br$_3$, blue squares), measured by negative differential susceptance measurements on FTO/OSC/Au devices. The applied bias voltage was varied from 0 to 2 V with the working electrode connected to the Au top electrode, while the FTO contact was connected to the counter electrode in a two-electrode setup. The impedance was measured from 1 MHz to 10 Hz with 25 frequency steps per decade and 7 mV$_{RMS}$ amplitude of the AC signal superimposed on the DC bias. By plotting the square root of the applied electrical field vs. the natural logarithm of the measured mobility, the zero field-mobility μ_0 can be extracted from the y-intercept of a linear fit, if the mobility obeys a Poole-Frenkel type field dependency. (b) Frequency dependent capacitance of a metal-insulator-semiconductor (MIS) stack, compromised of FTO/Al$_2$O$_3$ (100 nm)/x-linked BCB (100 nm)/Polymer:Dopant (500 nm)/Au measured at -1.5 V Bias at complete depletion. The constant high frequency capacitance C_{min} above 200 kHz was used to calculate the dielectric constant of the polymer using **Equation S6.13**.

Ultraviolet Photoelectron Spectroscopy

UPS measurements were carried out with a PHI 5000 VersaProbe III system fitted with a He discharge light source providing stable and continuous He I and He II lines. For measurement, all samples were spun cast on clean ITO (15 Ω square^{-1}) substrates to produce ca. 20 nm thick films using dry solvents in a N$_2$ filled glovebox. The thickness of

the samples was measured by using dummy samples in a profilometer. The samples were directly transported to the UPS system by using a N_2 filled, sealed stainless steel transport vessel without exposing them to the ambient conditions. All measurements reported in this study were carried out with the He I (21.22 eV) line with -5 V sample biasing and the corresponding photoemission with 90° take-off angle was collected at the multichannel analyzer. The reproducibility of the signal position was confirmed by repeating the measurement at least in 2 spots from the same sample. The reference Fermi level was determined using a sputter cleaned gold foil. The standard deviation on the reported energy values is ± 0.15 eV, calculated using the full-width-half-maximum of the gold foils Fermi edge. To determine the impact of the (partially or fully) reduced dopant on the HOMO density of states and their distribution, ultraviolet photoelectron spectroscopy was carried out on 20 nm thin films of PDPP[T]$_2${TEG}$_2$-3- MEET and PDPP[T]$_2${2-HD}$_2$-MEET, both undoped as well as doped samples with either NOPF$_6$ or spiro-MeOTAD^{4+}(PF$_6$)$_4$. After measurement of the valence band maximum (VBM), the onset was fitted with an exponentially modified Gaussian distribution to account for localized/tail states arising due to ionized dopants (**Equation S6.8**).

$$
\begin{aligned}
g(E, & h, \mu, \sigma_{\text{GDOS}}, \tau) \\
&= \frac{h\sigma_{\text{GDOS}}}{\tau}\sqrt{\frac{\pi}{2}}\, exp\left(0.5\left(\frac{\sigma_{\text{GDOS}}}{\tau}\right)^2\right. \\
&\left. - \frac{E-\mu}{\tau}\right) erfc\left(\frac{1}{\sqrt{2}}\left(\frac{\sigma_{\text{GDOS}}}{\tau} - \frac{E-\mu}{\tau}\right)\right)
\end{aligned}
\tag{S6.8}
$$

where E is the energy w.r.t. vacuum level, h the peak height of the gaussian distribution, μ the center of the distribution, σ_{GDOS} the standard deviation of the gaussian distribution and τ the decay energy of the exponential tail. The parameters obtained by least squares fitting are summarized in **Table S6.7** below.

Table S6.7. Values obtained by fitting **Equation S6.8** to the VBM of P1 and P2 doped with 0 mol% and 5 mol% D4. $R^2 > 0.98$ for all fits.

Sample	h (1)	μ (eV)	σ_{GDOS} (meV)	τ (1)
P1, pristine	21.2	1.61	184	0.337
P1, 5 mol% D1	33.9	0.86	120	0.250
P1, 5 mol% D4	19.9	0.95	198	0.231
P2, pristine	18.0	1.31	102	0.294
P2, 5 mol% D1	33.1	0.82	121	0.218
P2, 5 mol% D4	17.3	0.86	146	0.215

Dielectric Constants of Semiconducting Polymers

FTO/Al$_2$O$_3$ (100 nm)/BCB (100 nm)/OSC/Au devices were prepared for measurement of the dielectric constant. The impedance of the devices was measured with a two-electrode setup and varying electrical field (1 Hz to 1 MHz, 8 points per frequency decade, -5 to 5 V$_{Bias}$ in 11 voltage steps, 1 V$_{RMS}$) using a Metrohm Autolab PGSTAT204 equipped with an FRA32M module. The NOVA 2.1.4 Software package provided by Metrohm, Germany was used to process the impedance data. The Au top electrode was connected to the counter and reference electrode, the FTO contact to the working and sense electrode of the potentiostat. Devices under test were shielded from ambient light, external electrical fields and kept under inert atmosphere. From the imaginary Z'' and real Z' impedance, the capacitance of the organic layer was extracted assuming an (RC) equivalent circuit[1]:

$$C(\omega) = C'(\omega) - iC''(\omega) \tag{S6.9}$$

where $C'(\omega)$ is the real part of the capacitance and $C''(\omega)$ the imaginary part (**Equation S6.10** and **S6.11**).

$$C'(\omega) = \frac{-Im(Z)}{\omega|Z(\omega)|^2} \tag{S6.10}$$

$$C''(\omega) = \frac{Re(Z)}{\omega|Z(\omega)|^2} \tag{S6.11}$$

To avoid influences of the space charge conduction, the real capacitance was extracted in the high frequency depletion regime of the MIS device. To achieve this condition, a negative bias was applied to the gold electrode, resulting in the formation of a hole depletion zone at the insulator/semiconductor interface. Since the organic semiconductor was measured in its pristine, i.e. intrinsic state, the depletion layer width can extent throughout the whole film thickness. The minimal, constant real capacitance C_{min} was then extracted from the saturated region at high frequencies (depletion region). Response from a possible inversion charge can be ruled out by the high measurement frequency not allowing enough minority carriers to form at the insulator/semiconductor interface. Since the film stack consists of two capacitors, C_{OSC} and $C_{Insulator}$ in series, C_{OSC} can then be extracted from C_{min}

$$C_{OSC} = \frac{C_{min}C_{Insulator}}{C_{Insulator} - C_{min}} \tag{S6.12}$$

In our devices, $C_{Insulator}$ itself consists of two separate stacks, therefore $1/C_{Insulator} = 1/C_{Al2O3} + 1/C_{BCB}$. Using the vacuum permittivity ε_0, the active area A_{OSC} and organic layer thickness d_{OSC} of the MIS device, one can extract the dielectric constant of the organic semiconductor ε_{OSC}

$$\varepsilon_{OSC} = \frac{C_{OSC}d_{OSC}}{\varepsilon_0 A_{OSC}} \tag{S6.13}$$

6.7.5 References

[1]   C. Wang, Z. Zhang, S. Pejić, R. Li, M. Fukuto, L. Zhu, G. Sauvé, *Macromolecules* **2018**, *51*, 9368.

7. Intricacies and Mechanism of p-Doping Spiro-MeOTAD Using Cu(TFSI)₂

Adrian Hochgesang[†], Simon Biberger[§], Jeannine Grüne[‡], John Mohanraj[†], Frank-Julian Kahle[§], Vladimir Dyakonov[‡], Anna Köhler[§‖] and Mukundan Thelakkat*[†‖]

[†] Applied Functional Polymers, University of Bayreuth, Universitätsstr. 30, 95440 Bayreuth, Germany

[§] Soft Matter Optoelectronics, University of Bayreuth, Universitätsstr. 30, 95440 Bayreuth, Germany

[‡] Experimental Physics IV, University of Würzburg, 97074 Würzburg, Germany

[‖] Bavarian Polymer Institute (BPI) and Bayreuth Institute of Macromolecular Research (BIMF), University of Bayreuth, Universitätsstr. 30, 95440 Bayreuth, Germany

* Corresponding Author
E-mail: mukundan.thelakkat@uni-bayreuth.de

Abstract

Copper salts are a popular choice as *p*-dopants for organic semiconductors, particularly in N^2,N^2,N$^{2\prime}$,N$^{2\prime}$,N^7,N^7,N$^{7\prime}$,N$^{7\prime}$-octakis(4-methoxyphenyl)-9,9$\prime$-spirobi[9H-fluoren]-2,2$\prime$,7,7$\prime$-tetramine (Spiro-MeOTAD) hole transport material for solar cells. While being exceptionally effective, no scientific consensus about their doping mechanism has been established so far. This study describes the thermodynamic equilibria of involved species in copper(II) bis(trifluoromethanesulfonyl)imide (Cu(TFSI)$_2$) doped, co-evaporated Spiro-MeOTAD. A temperature-independent formation of charge transfer states is found, followed by an endothermic release of free charge carriers. Impedance and electron paramagnetic resonance spectroscopy unravel low activation energies for hole release and hopping transport. As a result, (52.0 ± 6.4) % of the total Cu(TFSI)$_2$ molecules form free, dissociated holes at 10 mol% and room temperature. Cu^I species arising out of doping are stabilized by formation of a [Cu^I(TFSI)$_2$]$^-$ cuprate, inhibiting elemental copper formation. This Cu^I species presents a potent hole trap reducing their mobility, which can be averted by simple addition of a bathocuproine complexing agent. A nonlinear temperature-dependent conductivity and mobility that contradicts current charge transport models is observed. This is attributed to a combination of trap- and charge transfer state freeze-out. These insights may be adapted to other metal salts, providing guidelines for designing next-generation ultra-high efficiency dopants.

7.1 Introduction

Ever since the advent of organic solar cells and recent, but fast improvements in perovskite solar cells, a profound understanding of the fine interplay in these multilayer devices becomes a focus of research. With an ever-growing number of interfaces, extracting photogenerated charge carriers fast, efficient and selective is crucial for high-performance solar cells.[1] N^2,N^2,N$^{2\prime}$,N$^{2\prime}$,N^7,N^7,N$^{7\prime}$,N$^{7\prime}$-octakis(4-methoxyphenyl)-9,9$\prime$-spirobi[9H-fluoren]-2,2$\prime$,7,7$\prime$-tetramine (Spiro-MeOTAD) has found widespread use as a hole transport material (HTM) in solar cell research, where it is commonly *p*-doped (i.e., oxidizing Spiro-MeOTAD) by air (O$_2$) with the help of LiTFSI additives to increase the free

charge carrier density.[2,3] Li et al. first incorporated copper(I) thiocyanate and copper(I) iodide into Spiro-MeOTAD HTM and found distinct benefits such as improved power conversion efficiency and HTM conductivity over conventional dopants like LiTFSI/O$_2$ or the cobalt complex FK209.[4] This concept was refined by other groups designing stable copper(II) complexes with tunable valance band levels and solubilities by counter-ion choice.[5-7] We replaced the solution doping using copper salts by a solvent free and highly controlled co-evaporation route employing copper(II) bis(trifluoromethanesulfonyl)imide Cu(TFSI)$_2$ as a *p*-type dopant to yield conductive, uniform, and pinhole-free HTM layers. Our concept was previously successfully applied to conventional MAPbI$_3$ based 3D perovskite solar cells.[8] While practically proven to be useful in perovskite solar cells, the field still lacks a conclusive picture of the physical and chemical processes inside the Cu^{II} doped Spiro-MeOTAD bulk. Especially the role of dopant side products on charge transport is unclear, which turns out to be of quite complex nature. To close this gap, we herein report the occurring thermodynamic equilibria between redox states in co-evaporated, Cu(TFSI)$_2$ doped Spiro-MeOTAD necessary to draw a complete picture of the doping process and discuss the consequences thereof. First, the theoretically predicted and experimentally observed doping reaction of Cu(TFSI)$_2$ with Spiro-MeOTAD was investigated using ultraviolet photoelectron- and UV/Vis/NIR absorption spectroscopy. Temperature controlled optical spectroscopy experiments are used to gain insight into the formation of charge transfer (CT) states as the product of the doping reaction. *Via* electron paramagnetic resonance spectroscopy (EPR), electrical conductivity and impedance spectroscopy, possible endothermic release of free charge carriers by dissociation of the CT state was monitored. We quantitatively pin-point the activation energies for CT dissociation $E_{A,CT}$ by temperature dependent studies. A low $E_{A,CT}$ may result in high doping efficiencies even at increased dopant loadings, which will be experimentally verified in the course of this work. The mobility and thermodynamic equilibria of the bound and unbound charge carriers are investigated in detail by impedance- and EPR spectroscopy. Further, we determine the influence of the thermodynamic equilibria on the thermal activation energy for fundamental hopping processes $E_{A,Hop}$. Well-documented electronic properties of pristine Spiro-MeOTAD such as temperature-dependent mobility are thoroughly compared to that of Cu(TFSI)$_2$ doped samples. Distinct nonlinearities in conductivity, carrier concentration and mobility for Cu(TFSU)$_2$ doped Spiro-MeOTAD below 150 K are extensively studied. We try to shed light on the source of nonlinear behavior by investigating reversible CT- and trap state

recombination with the help of [Cu(MeCN)$_4$]BF$_4$ as a model Cu^I source. Additional focus is set on the influence of dopant products on charge transport in the bulk.

7.2 Results and Discussion

7.2.1 Charge Transfer Formation

We investigate the doping mechanism of Cu-salts in Spiro-MeOTAD by first considering the process of charge transfer formation in thin films. In a typical *p*-doping experiment, the dopant is required to possess unoccupied energy levels deeper in energy than the highest occupied molecular orbital (HOMO) of the organic semiconductor (OSC).[9,10] If this condition is met, an exothermic electron transfer from OSC to dopant can be expected. By using UV photoelectron spectroscopy (UPS) we measured the ionization potential (IP), which is by Koopmans-theorem in first approximation identical to the HOMO, and workfunction of Spiro-MeOTAD (**Figure 7.1a**).[11] The electron affinity EA with respect to vacuum level of Cu(TFSI)$_2$ was calculated from CV half-wave reduction potentials according to a known literature procedure (**Figure S7.1**, Supporting Information).[12] An electron affinity of EA = 6.15 eV of Cu(TFSI)$_2$ and IP = 5.03 eV of pristine Spiro-MeOTAD w.r.t. vacuum level were determined. Clearly, the EA of Cu(TFSI)$_2$ is positioned 1.12 eV deeper than the Spiro-MeOTAD HOMO, facilitating electron transfer. The removal of electrons from Spiro-MeOTAD upon doping is expected to result in a downshift of the workfunction toward the HOMO of the OSC. We monitored this electron transfer by UPS in a second experiment on co-evaporated Spiro-MeOTAD thin films with 0–10 mol% Cu(TFSI)$_2$ dopant ratio (**Figure 7.1b**). A continuous decrease of the workfunction from 4.25 eV down to 5.02 eV was recorded. This downshift was verified by a decreasing hole-injection barrier HIB (the difference between HOMO and workfunction) shown in **Figure 7.1b**. We noticed a slight variation in HOMO position during doping, which is responsible for the unexpectedly pronounced decrease of HIB between 2 and 4 mol% (see also summary of all UPS values collected in **Table S7.1**, Supporting Information). From **Figure 7.1b**, two distinct processes can be discerned: first, a strong initial HIB drop of ≈ 740 meV in the pristine state to 390 meV at 2 mol% Cu(TFSI)$_2$. This steep HIB gradient marks the region, where E_F moves through a lower density of states per energy interval compared to the deeper lying valence band. We assign these states lying higher in energy

as trap states, that is, the generated holes are being consumed entirely in passivating these trap states above the valence band up to 2 mol% Cu(TFSI)$_2$.[13] We clearly differentiate those trap states from trap states originating from dopant products, which are characterized in **Section 7.2.4**. Despite the high purity of Spiro-MeOTAD used in this work of 99.9 % (HPLC, see Supporting Information for manufacturer details), reducing impurities are common for organic semiconductors, shifting the Spiro-MeOTAD intrinsic carrier density from $\approx 9 \cdot 10^{14}$ cm^{-3} published by Abate et al. to $1.2 \cdot 10^{17}$ cm^{-3} in this work (see **Section 7.2.1**).[14] However, we propose the influence of these intrinsic trap states on subsequent doping experiments to be low, being fully passivated after 2 mol% Cu(TFSI)$_2$ (**Figure 7.1b**). Further, the characteristic slope change of E_F (dopant concentration) has also been associated with the Fermi level crossing an mid-gap acceptor level, which originates from dopant:host interaction.[15] Second, for doping concentrations greater than 2 mol%, the Fermi level E_F (e.g., workfunction) is pinned at ≈ 330 meV above the Spiro-MeOTAD valence band. At this stage it can be assumed, that the dopant releases free holes, which moves E_F closer to the HOMO with a shallow slope.[16-18] Fortifying the designated role as a hole conductor, the workfunction of 5.02 eV at 10 mol% Cu(TFSI)$_2$ allows for a very efficient injection of holes in the co-evaporated Spiro-MeOTAD films using high workfunction electrodes such as Au. Due to the twisted nature of the spiro-core inducing steric hindrance and bulky (nonplanar) form of the Spiro-MeOTAD, we expect Spiro-MeOTAD and Cu(TFSI)$_2$ to react according to an integer charge transfer. This infers that no hybridization of frontier orbitals (HOMO or lowest unoccupied molecular orbital) takes place and the system can be treated like a conventional redox-couple forming CT states upon doping.[19] Optical UV/Vis/NIR absorption spectroscopy was employed as a powerful tool to study the CT state evolution in 0–10 mol% Cu(TFSI)$_2$ doped Spiro-MeOTAD thin films (**Figure 7.1c**; **Figure S7.2**, Supporting Information). Simultaneous vacuum co-evaporation was used to deposit high-quality, pinhole-free thin films on glass, circumventing solvent influence and miscibility issues (see Supporting Information for experimental details).[8]
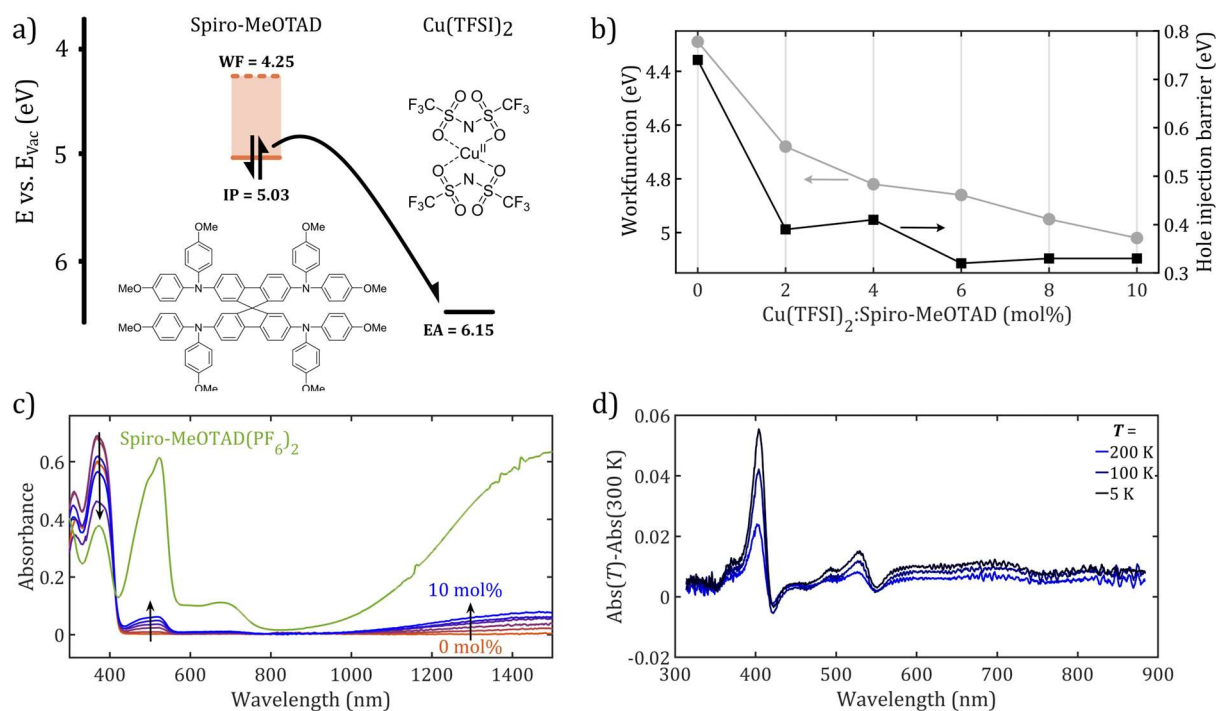
Figure 7.1. a) Energy level diagram of pristine Spiro-MeOTAD (orange) and Cu(TFSI)$_2$ (black) as determined by UPS (WF and IP of Spiro-MeOTAD) and CV (EA of Cu(TFSI)$_2$). b) Workfunction (left, grey circles) and hole-injection barrier HIB (right, black squares) of co-evaporated Spiro-MeOTAD films with increasing Cu(TFSI)$_2$ molar ratio. c) UV/Vis/NIR absorption spectra of co-evaporated films with increasing molar ratios of Cu(TFSI)$_2$ highlighting the formation of spectral features identical to that of chemically synthesized, pure Spiro-MeOTAD(PF$_6$)$_2$ (green). d) Difference in optical absorption of 10 mol% Cu(TFSI)$_2$ doped Spiro-MeOTAD thin film UV/Vis spectra obtained at 200 K (blue), 100 K (dark blue), and 5 K (black) to the spectrum obtained at 300 K (see **Figure S7.3**, Supporting Information).

The ground-state absorption of Spiro-MeOTAD at 370 nm is continuously bleached upon adding Cu(TFSI)$_2$, with new peaks emerging at 517 nm, 687 nm, and 1445 nm (see **Figure S7.2**, Supporting Information, for difference spectrum). The broad NIR absorption at 1445 nm was assigned to intervalence charge-transfer (IV-CT) from a positively charged radical-cation triphenylamine to the linking biphenyl bridge.[20] In addition, a characteristic fingerprint for charged Spiro-MeOTAD species is the absorption at 517 nm (as well as 687 nm).[21] We conclude a steady formation of charged Spiro-MeOTAD species upon co-evaporation with Cu(TFSI)$_2$, complementing earlier studies by Mohanraj et al.[8] To study the thermodynamic nature of the CT state formation, we carried out temperature

dependent absorption spectroscopy on co-evaporated films (**Figure 7.1d**, see Supporting Information, for spectra of all doping concentrations). No significant change in absorption intensity of the 517 nm band is observable. As a consequence, we conclude the formation of the CT states to be temperature independent, in line with experiments by Tietze et al. on doped small molecules.[22] Lastly, we want to shed light on the nature of the charged Spiro-MeOTAD species. Three stable oxidation states of Spiro-MeOTAD are known in literature, namely Spiro-MeOTAD^{1+}, Spiro-MeOTAD^{2+}, and Spiro-MeOTAD^{4+}.[23] UPS studies on Spiro-MeOTAD(PF$_6$)$_4$ revealed a HOMO energy of 5.25 eV, which is situated 0.90 eV above the EA of Cu(TFSI)$_2$. Consequently, all oxidation products of Spiro-MeOTAD are theoretically accessible by exothermic electron transfer to Cu(TFSI)$_2$, showcasing its capabilities as a powerful *p*-type dopant. For experimental identification of the formed oxidation state, we synthesized chemically pure Spiro-MeOTAD^{2+} by reacting Spiro-MeOTAD with two equivalents of the single-electron oxidant NOPF$_6$. Thin films of the obtained Spiro-MeOTAD(PF$_6$)$_2$ were characterized by UV/Vis/NIR spectroscopy (**Figure 7.1c**, green curve). We noted very similar optical absorption features between pure Spiro-MeOTAD(PF$_6$)$_2$ and the Cu(TFSI)$_2$ doped Spiro-MeOTAD. However, we cannot reliably distinguish the two oxidation states Spiro-MeOTAD$^{1+/2+}$ due to i) both states being almost degenerate in energy, with a separation of less than 110 mV versus Ag/Ag$^+$ resp. Fc/Fc$^+$ and ii) a very similar optical absorption spectral profile.[21,24] A comparison with Spiro-MeOTAD(PF$_6$)$_4$ absorption spectrum reveals, that Spiro-MeOTAD(PF$_6$)$_4$ is characterized by a broad peak at 875 nm, which is absent in our experiments (**Figure 7.1c**).[23] Therefore, both Spiro-MeOTAD^{1+} and Spiro-MeOTAD^{2+} are presumed as the most probable products of Spiro-MeOTAD doped with ≤10 mol% Cu(TFSI)$_2$. After proving the temperature-independent formation of charged Spiro-MeOTAD$^{1+/2+}$ CT states upon doping by optical absorption spectroscopy and UPS, the next step is to investigate the dissociation of the CT state and generation of mobile charge carriers. However, the CT state, being a salt, can be subject to strong coulombic binding energies in the range of > 100 meV.[22] Thus, a certain activation energy must be provided in order to separate CT states into free carriers. Only free charge carriers can contribute to the observed macroscopic conductivity in disordered organic semiconductors by thermally activated hopping processes. Our group has monitored and reported the change in electrical conductivity by measuring current-voltage scans of Spiro-MeOTAD:Cu(TFSI)$_2$ co-evaporated on top of interdigitated Au electrodes in a previous study.[8] Upon co-evaporating Cu(TFSI)$_2$, a linear increase followed by conductivity saturation (at 6 mol%

Cu(TFSI)$_2$) with an average value of $\approx 7 \cdot 10^{-4}$ S cm^{-1} was observed, in agreement with the constant HIB found in our UPS experiments above 6 mol% dopant. Elevated temperatures in the Spiro-MeOTAD effusion cell during evaporation do not significantly enhance the charge carrier density, as evidenced by the low conductivity ($1 \cdot 10^{-7}$ S cm^{-1}) of the evaporated pristine Spiro-MeOTAD sample. Increase in electrical conductivity values demonstrate the presence of mobile charge carriers in Spiro-MeOTAD:Cu(TFSI)$_2$ co-evaporated samples. Here, we intend to quantify this observation by determining the amount of free charge carriers p in the doped bulk *via* solid state Mott-Schottky experiments. More precisely, this analysis yields the density of ionized acceptors (from dopants) N_{A^-} in the bulk, which is equal to the density of free holes p in the hole conductor, since charge neutrality must be obeyed. This is achieved by measuring the voltage dependent capacitance C(V) of a metal-insulator-semiconductor device stack such as FTO/Al$_2$O$_3$/Hexamethyldisilazane/Cu(TFSI)$_2$:Spiro-MeOTAD/Au using impedance spectroscopy. Since the spatial width of a depletion layer (which in turn dictates its electrical capacitance) is very sensitive to the number of free carriers present in the semiconductor, measuring the series capacitance can give information about N_{A^-}. Applying a negative bias voltage causes the formation of a charge carrier depletion zone at the insulator/p-type semiconductor interface, which changes the overall device capacitance. By evaluating the slope dC^{-2}/dV of the device capacitance versus applied potential, the number of free carriers N_{A^-} can be evaluated (**Figure 7.2a**, see **Figure S7.4**, Supporting Information, for exemplary fit). In agreement with a very strong decrease in HIB and increase in conductivity when adding 2 mol% Cu(TFSI)$_2$, the charge carrier density rises from $1.2 \cdot 10^{17}$ cm^{-3} to $1.0 \cdot 10^{19}$ cm^{-3} at 1.5 mol% dopant. Above 1.5 mol%, N_{A^-} is increasing in a linear fashion up to $3.2 \cdot 10^{19}$ cm^{-3} at 10 mol% without showing saturation effects (**Figure 7.2b**). Having successfully quantified the density of free carriers, we focus on the density of bound CT states. Contrary to Mott–Schottky analysis, which is sensitive to only free charge carriers in the bulk, EPR detects all paramagnetic species within the sample volume. Specifically, EPR is used to determine the absolute sum of bound (in the form of a CT state) and free charge carriers. For measuring EPR, we co-evaporated Cu(TFSI)$_2$ and Spiro-MeOTAD onto poly(ethylene terephthalate) substrates of known area with a defined thickness, which were consequently sealed in quartz tubes under inert atmosphere. The EPR parameters are optimized for the highest signal of the 10 mol% doped film ($B_{mod} = 0.02$ mT, $P_{MW} = 0.8$ mW). As a fact, the presence of paramagnetic Cu^{II} ions is not affecting the results, as they cannot be resolved with the

optimized parameters (**Figure S7.5**, Supporting Information). Cu^{I} cations are diamagnetic due to a 4s^{0}3d^{10} electron configuration and therefore EPR inactive.[25] With increasing dopant concentration, the Lorentzian shaped EPR peak increases in area (**Figure 7.2c**). A *g*-value of 2.0026 was found, comparable to H-TFSI and Li-TFSI/O$_2$ doped Spiro-MeOTAD.[26-28] By convention, the EPR spectra (**Figure 7.2c**) are displayed as the first derivative of the original microwave absorption signal, thus double integration yields the absolute number of paramagnetic species N_{Spins}, normalized to unit volume and referenced to a sample with known spin concentration (**Figure 7.2b**). The quantity N_{Spins} includes all paramagnetic species per unit volume, whether bound to a counter ion (CT state) or free to move under the influence of an electric field (free holes p). N_{Spins} follows the same doping concentration dependent trend as N_{A^-}, yet we noticed a constant offset, which is equal to the states not detectable by Mott–Schottky measurements, the bound CT states. They contribute to about a factor of 4–6 in the range of 3–10 mol% doping ratio. It should be emphasized, that no information about the ratio between free and in CT states bound carriers can be deduced from the absolute number of spins N_{Spins}, owing to their high absolute error. Depending on the spin reference used, the absolute error is up to 1 order of magnitude, yet their relative values used in this work are exact. Hence, we used impedance spectroscopy to determine the ratio between bound and free charge carriers (see **Section 7.2.3**). Aiming to understand the evolution of ratio between N_{A^-} and N_{Spins} upon doping, we correlated both values with the UV/Vis/NIR CT state absorbance integral from our previous experiment (**Figure 7.1c**). Both N_{A^-} and N_{Spins} were found to increase monotonic and linearly with the absorbance integral (**Figure S7.6**, Supporting Information). This indicates, that no additional EPR silent species or bipolaron species are formed at up to 10 mol% Cu(TFSI)$_2$. Notably, the electrical conductivity saturates despite a monotonical increase in N_{A^-} and N_{Spins}, which hints to effects of the doping on the carrier mobility μ and will be discussed in the next paragraph in detail.
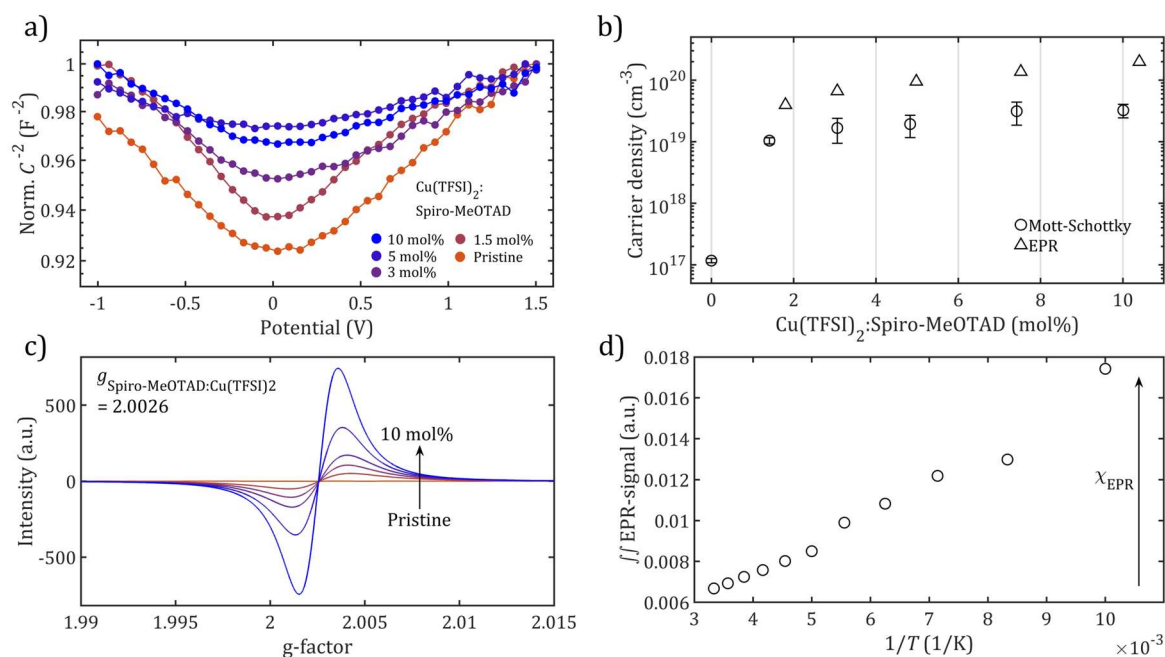
Figure 7.2. a) Exemplary, normalized C^{-2} versus applied potential plot of metal-insulator-semiconductor (MIS) devices fabricated with an FTO/Al₂O₃/Hexamethyldisilazane/Cu(TFSI)₂ doped Spiro-MeOTAD/Au structure. Negative potentials deplete the majority charge carriers (holes) from the interface, decreasing the capacitance. The positive slope in the positive potential range indicates low frequency inversion at the insulator/Spiro-MeOTAD interface. b) Charge carrier/spin densities obtained by Mott–Schottky (circles) and EPR (triangles) measurements. c) Doping concentration dependent EPR spectra of Cu(TFSI)₂ doped Spiro-MeOTAD thin films, co-evaporated on PET substrates. Modulation amplitude $B_{mod} = 0.02$ mT, microwave power $P_{MW} = 0.8$ mW. d) Double integral (proportional to spin susceptibility, i.e., spin density) of the EPR signal as a function of the inverse temperature proves localized spin species (Curie contribution). Doping concentration = 7.5 mol%.

Finally, for charge transport considerations later in this work, it is necessary to understand the degree of charge carrier localization in Cu(TFSI)₂ doped Spiro-MeOTAD. For this, we conducted temperature dependent EPR measurements on one typical sample (7.5 mol% Cu(TFSI)₂ doped Spiro-MeOTAD). The double integral of the EPR signal is proportional to the susceptibility X and was found to depend linearly on the inverse sample temperature $1/T$ in our experiment (**Figure 7.2d**).[29,30] It is well described by Curie contribution ($\approx N_{Spins}/T$), characteristic for localized spin species. The linear trend underlines the absence of additional paramagnetic species arising at different

temperatures, which would induce a deviation from $1/T$ behavior, fitting to temperature-independent formation of CT states.[30] By correcting the internal spin reference density to the cavity temperature, we verified a temperature-independent spin density $N_{Spins}(T)$ for a 7.5 mol% Cu(TFSI)$_2$ doped sample (**Figure S7.7**, Supporting Information). When extrapolating to the y-axis intercept, an offset remains in the magnitude of the determination inaccuracy. Nevertheless, Pauli contribution, that is, band like transport, is not typical for Spiro-MeOTAD even at high concentrations, as discussed below. Hence, free charge carriers are formed at room temperature in Cu(TFSI)$_2$ doped Spiro-MeOTAD, increasing the macroscopic bulk conductivity *via* hopping in mostly localized sites. To conclude, the ratio between free and in CT states bound charge carriers was determined and their changes upon varying the dopant concentration.

7.2.2 Charge Transport

As we quantified the nature and density of reaction products formed in Cu(TFSI)$_2$ doped Spiro-MeOTAD, we proceed further to complete the microscopic description of charge transport and thermally activated processes leading to free charge carriers. To select a proper model capable of describing the charge transport, we recorded the temperature dependent conductivity $\sigma(T)$ of co-evaporated Cu(TFSI)$_2$ doped Spiro-MeOTAD thin films from 400 K to 20 K in a He-cryostat (**Figure 7.3a**).
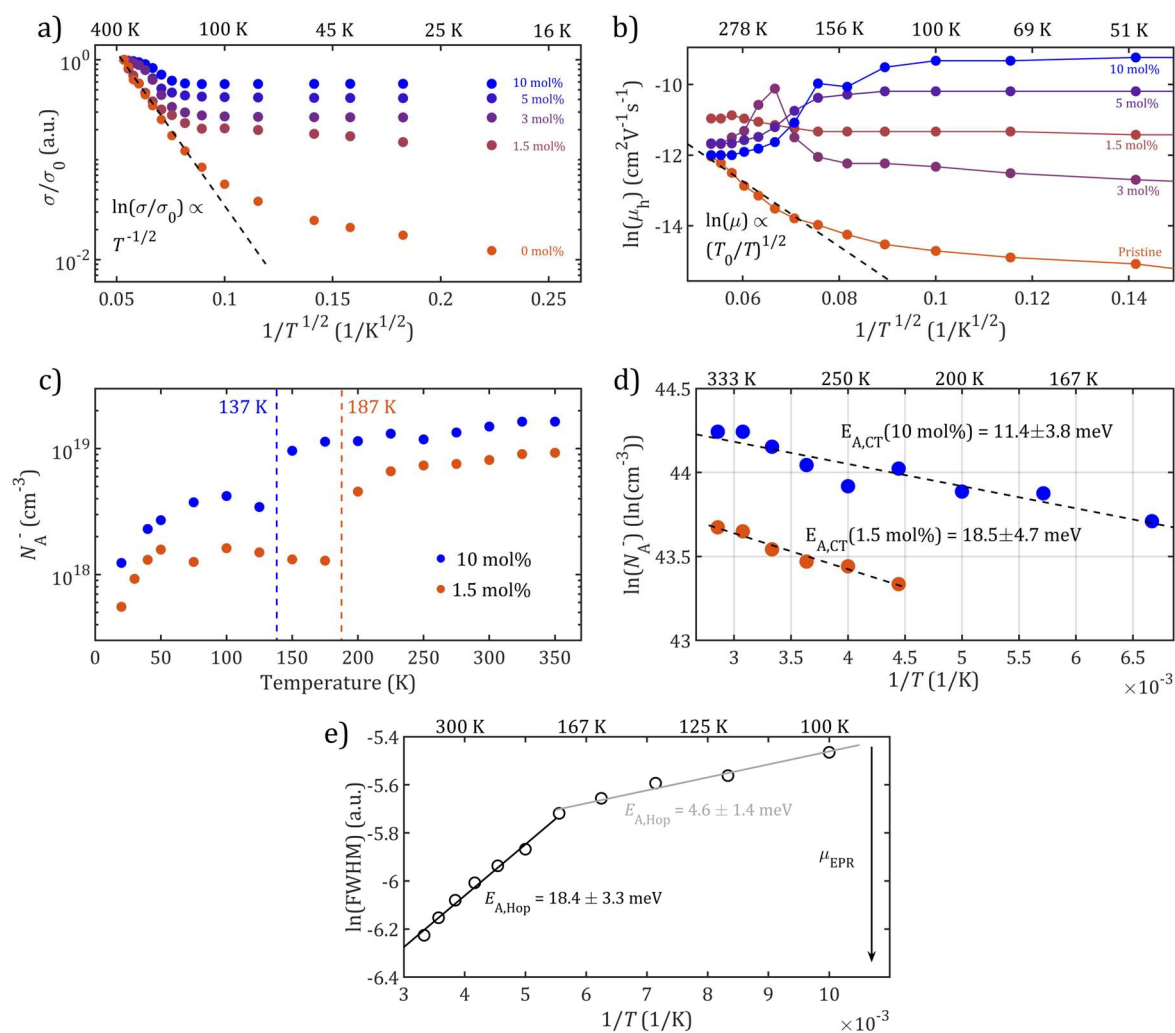
Figure 7.3. a) Temperature dependent, individually normalized conductivities σ measured on FTO/Cu(TFSI)$_2$:Spiro-MeOTAD/Au devices with different doping concentrations from 400 K to 20 K. b) Temperature dependent hole mobilities μ_h of Cu(TFSI)$_2$ doped Spiro-MeOTAD, determined from impedance measurements on FTO/Cu(TFSI)$_2$:Spiro-MeOTAD/Au devices using the negative differential susceptance $-\Delta B$. Black dashed fit line shows typical ES-VRH behavior $\ln(\mu_h) \propto (T_0/T)^{1/2}$ in the case of pristine Spiro-MeOTAD sample. All values were obtained at a constant electrical field $F = 100$ kV cm^{-1}. Full temperature scale measurements are shown in **Figure S7.10**, Supporting Information, detailed temperature dependent $-\Delta B$ versus frequency spectra in **Figure S7.11**, Supporting Information. c) Temperature dependent charge carrier densities $N_A{}^-(T)$ of 1.5 mol% and 10 mol% Cu(TFSI)$_2$ doped Spiro-MeOTAD, determined by Mott–Schottky measurements. A vertical dotted line demarcates the freeze-out points, for example, the thermal energy available below these marked values is not sufficient to dissociate the intimate CT pair. d) Arrhenius-type temperature dependency of $N_A{}^-(T)$ measured *via* Mott-Schottky experiments above the freeze-out point (150 K for 10 mol%

Cu(TFSI)$_2$ (blue), resp. 200 K for 1.5 mol% (orange)) with fitted activation energies $E_{A,CT}$. e) Logarithmic EPR linewidth (FWHM) of a 7.5 mol% Cu(TFSI)$_2$ doped Spiro-MeOTAD thin film as a function of inverse temperature. An activation energy for hole transport $E_{A,Hop}$ = (18.4 ± 3.3) meV (black fit) for higher temperature and (4.6 ± 1.4) meV (grey fit) below 160 K can be determined. Full temperature dependent EPR spectra can be found in **Figure S7.12**, Supporting Information.

Focusing on the pristine sample, a distinct linear region was found between 400 K and 150 K. We observed a positive slope dσ/dT, clearly indicating a temperature activated hopping behavior. Commonly, the popular Mott law is employed to model $\sigma(T)$ in organic semiconductors.[31] As it assumes a constant density of states surrounding the Fermi energy, which can hardly be assumed, we refer to Efros-Shklovskii variable range hopping (ES-VRH) accounting for a Coulomb gap surrounding E_F.[32,33] As Spiro-MeOTAD is disordered in terms of the energetic landscape with localized, spatially randomly distributed states (amorphous nature), the ES-VRH model is sufficient to explain the pristine case.[33] In addition, this model accounts for a Coulomb interaction of localized states introduced by the dopant molecules and hopping distances exceeding the nearest neighbor distance at low temperatures.[34,35] ES-VRH predicts the dependence $\ln(\sigma/\sigma_0) \propto T^{-1/2}$ and the experimental data on pristine Spiro-MeOTAD is in accordance to this.[34,36] In Cu(TFSI)$_2$ doped Spiro-MeOTAD samples, we noticed a restriction of the linear $\sigma(T)$ region to smaller temperature ranges (**Figure 7.3a**). Additionally, in all doped samples, a distinct temperature independent behavior is found below 150 K. Li et al. pointed out, that a temperature independent charge carrier transport in organic semiconductors may be explained sufficiently within the VRH model framework. At high carrier densities and low temperatures, Li proposed that the energy required for a carrier hop is provided entirely by the electric field across the device. This implies, that no thermal activation is necessary and the transport can be described as field-assisted tunnelling in the low temperature regime.[37] We could qualitatively adapt Lis modified VRH model to $\sigma(T)$ of Cu(TFSI)$_2$ doped Spiro-MeOTAD using N_A^- from Mott–Schottky measurements (**Figure 7.2b**; **Figure S7.13**, Supporting Information). Applying Lis theory, one could assume the origin of $\sigma(T)$ nonlinearities in Cu(TFSI)$_2$ doped Spiro-MeOTAD to stem from field-assisted tunnelling. Yet, carefully analyzing Lis model suggests a similar trend for the temperature dependent mobility $\mu(T)$ if the Fermi level E_F

and N_{A^-} are considered constant, i.e., a monotonic mobility decrease followed by a weakly temperature dependent region at lower temperatures. As a consequence, temperature dependent conductivity measurements are not sufficient to analyze the origin of nonlinear $\sigma(T)$, which shifts our focus toward temperature dependence of charge carrier mobility μ. To probe the temperature dependent mobility of free charge carriers in Cu(TFSI)₂ doped Spiro-MeOTAD, we carried out impedance spectroscopy experiments on FTO/Cu(TFSI)₂:Spiro-MeOTAD/Au metal-semiconductor devices employing the negative differential susceptance method (see Supporting Information for details). Using a metal-semiconductor device structure, holes are injected at one electrode if a sufficient electrical field F across the device is applied. By measuring the capacitive response of the biased device at different frequencies, an average carrier transit time for a given organic layer thickness and electrical field can be deduced, even at moderate bulk conductivities of doped semiconductor samples (where most common methods fail). Indium-tin-oxide/Li(TFSI) doped Spiro-MeOTAD/Au devices have recently been used to study the Spiro-MeOTAD charge carrier mobility *via* negative differential susceptance by Li et al. Carrier densities of up to $2.8 \cdot 10^{19}\,\mathrm{cm^{-3}}$ were reported using Mott–Schottky measurements, proving the applicability of this method for highly doped Spiro-MeOTAD samples.[38] Again, pristine Spiro-MeOTAD follows a temperature activated behavior, characterized by an increase in carrier mobility upon heating the sample up to 400 K. Between 350 K and 175 K, $\ln(\mu)$ is proportional to the inverse sample temperature. Closer analysis yields a slope of 0.5, thus resembling ES-VRH dependency for the hole mobility with $\ln(\mu) \propto \left(\frac{T_0}{T}\right)^{1/2}$, where $T_0 = 8.5 \cdot 10^3$ K. (**Figure 7.3b**).[39] We like to point out, that for the temperature range between 350 K to 20 K, a poor fit was found for $\ln(\mu) \propto \left(\frac{1}{T}\right)^2$ predicted by models using a Gaussian density of states distribution, which are often employed in literature to describe the electrical behaviour of doped organic semiconductors (**Figure S7.14**, Supporting Information).[40] Röhr et al. obtained comparable $\mu(T)$ of undoped Spiro-MeOTAD in space charge limited current device data fitted by Mott–Gurney law, verifying the negative differential susceptance method used in this experiment.[41] Consequently, $\sigma(T)$ and $\mu(T)$ of pristine Spiro-MeOTAD is described sufficiently by the ES-VRH model. To our surprise, doped samples are clearly subject to a different nature of charge transport, even increasing in charge carrier mobility upon cooling the sample below a threshold point of ≈ 150 K, followed by a temperature independent region between 150 K and 20 K (**Figure 7.3b**). We further note, that the

negative correlation $d\mu/dT < 0$ is exclusive to higher doping concentrations ≥ 5 mol%. At this point we want to highlight, that a negative temperature coefficient mobility is no unambiguous fingerprint of band-like transport typically found in metals. Exemplary, similar behavior was found in poly(2,5-bis(3-tetradecylthiophen-2-yl)thieno[3,2-b]thiophene) PBTTT field-effect transistors, explained by Luttinger liquid behavior.[42] Additionally, Spiro-MeOTAD, even at high doping ratios, cannot be described in terms of band transport due to the large amount of energetic disorder.[43] Thus, invoking VRH models, which expect a monotonic decrease in mobility and conductivity, are not able to explain the nonlinear charge transport in Cu(TFSI)$_2$ doped Spiro-MeOTAD samples. Based on the relationship $\sigma = qN_A^-\mu$ with q being the elementary charge, we formulate the lack of thermal energy at low temperatures to dissociate the CT-state as a possible cause for the nonlinearities found in Cu(TFSI)$_2$ doped Spiro-MeOTAD. Intuitively, this so-called carrier freeze-out would be reflected in $N_A^-(T)$, necessitating a quantification. For this, we coupled the Mott-Schottky experimental setup as described in an earlier paragraph with a helium cryostat. **Figure 7.3c** shows $N_A^-(T)$ measurements on 1.5 and 10 mol% Cu(TFSI)$_2$ doped Spiro-MeOTAD between 20 K and 350 K. Here we observe a sharp jump in carrier density at 137 K (for 10 mol% dopant) and 187 K (1.5 mol% dopant), which we denote as transition points. Above these transition points, N_A^- is proportional to the sample temperature. At lower temperatures, we noticed a decrease in free carrier concentration for both samples. Ultimately, N_A^- is not correlated to the sample temperature below these transition temperatures. We assign the distinct loss in free carrier concentration N_A^- at low temperatures to the recombination of free holes and counterion to re-form the bound CT state (freeze-out). Above the freeze-out, $N_A^-(T)$ can be well described by a Arrhenius type activation process, with the activation energy $E_{A,CT}$ corresponding to the CT state dissociation energy (**Figure 7.3d**).[22] $E_{A,CT}$ decreases from (18.5 ± 4.7) meV at 1.5 mol% Cu(TFSI)$_2$ to (11.4 ± 3.8) meV at 10 mol%, presumably due to increased energetic disorder, facilitating CT state dissociation.[22] These values are directly reflected in the freeze-out temperatures of 187 K and 137 K, which translate to thermal energy values of 16.1 meV (1.5 mol%) and 11.8 meV (10 mol%). $E_{A,CT}$ is in line with previously published results of disordered systems, ranging from 9 to 54 meV.[22] The measured freeze-out temperatures yield first evidence for our hypothesis, overlapping with the mid-point temperatures of nonlinear effects of $\sigma(T)$ and $\mu(T)$ (**Figure 7.3a,b**). We aim to fortify our hypothesis by approaching the thermodynamics of carrier hopping. Our previous $\mu(T)$ measurements (**Figure 7.3b**) clearly show an increase

in carrier mobility below the freeze-out. Therefore, we test the correlation between the average activation energy $E_{A,Hop}$ for carrier site transition (a "hop") and $N_{A^-}(T)$. The full width at half maximum (FWHM) of an EPR signal can be related to the average microscopic charge carrier mobility μ_{EPR} in doped organic systems.[30] In general, increasing microscopic mobility narrows the EPR linewidth due to averaging of hyperfine interactions (motional narrowing).[28,44] Subsequently, we determined $E_{A,Hop}$ by evaluating the FWHM of the EPR signal of a 7.5 mol% doped sample for different temperatures and applying Arrhenius fits (**Figure 7.3e**). With increasing temperature, the FWHM decreases continuously, indicating increasing mobility in doped samples. A distinct change in slope occurred for $\text{FWHM}_{EPR}(T)$ at ≈ 180 K, with a greater slope $d(\ln(\text{FWHM}_{EPR}))/d(1/T)$ above 180 K. The more decreasing EPR linewidth above 180 K is in contrast to impedance measurements (**Figure 7.3b**), where we observed a decrease in mobility upon increasing temperature between 150 K and 400 K for doped Spiro-MeOTAD. This can be explained by the fact that the linewidth of EPR is only affected by mobile polarons that arise after dissociation of CT states in this experiment (no active electron/hole injection *via* electrodes). In contrast, any trap states created simultaneously reduce the overall mobility of impedance spectroscopy by trapping the injected holes. We recorded an $E_{A,Hop}$ of (18.4 ± 3.3) meV above 180 K, with (4.6 ± 1.4) meV below for Arrhenius fits on $\text{FWHM}_{EPR}(T)$ (**Figure 7.3e**). The transition temperature of 180 K (≈ 16 meV thermal energy) fits to the CT state dissociation energies $E_{A,CT} = 11.4$–18.5 meV for 1.5 and 10 mol% Cu(TFSI)$_2$ doped Spiro-MeOTAD (**Figure 7.3c**). From $\text{FWHM}_{EPR}(T)$ and $N_{A^-}(T)$ experiments we conclude, that the CT state freeze-out is directly influencing the carrier mobility and it is consequently responsible for the nonlinear conductivity of Cu(TFSI)$_2$ doped Spiro-MeOTAD. Both $E_{A,Hop}$ and $E_{A,CT}$ can be verified by linking them to the macroscopic observed thermal activation energy for conductivity $E_{A,\sigma}$. We analyzed $E_{A,\sigma}$ by Arrhenius fits on temperature dependent conductivity measurements of co-evaporated Cu(TFSI)$_2$ doped Spiro-MeOTAD films (**Figure S7.15**, Supporting Information). Privitera et al. pointed out, that $E_{A,\sigma}$ is the sum of both CT state binding energy $E_{A,CT}$ and hole transport activation energy $E_{A,Hop}$.[30] As displayed in **Figure S7.16**, Supporting Information, $E_{A,\sigma}$ values ranging from (39.0 ± 7.0) meV to (130.0 ± 15.9) meV were recorded for the Cu(TFSI)$_2$ doped Spiro-MeOTAD system, with most samples having values below 100 meV. $E_{A,\sigma}$ of F$_4$TCNQ doped Spiro-MeOTAD was reported as ca. 170 meV, generally the thermal activation energies for conductivity are broadly distributed for small molecule organic semiconductors, ranging roughly from 38 to 467 meV.[45,46] In

comparison, Cu(TFSI)$_2$ doped Spiro-MeOTAD displays rather small $E_{A,\sigma}$ values. This result is remarkably well in line with an expected, approximated value of $E_{A,CT}$(10 mol%) + $E_{A,Hop}$(7.5 mol%) $\approx$ 30 meV. Higher measured $E_{A,\sigma}$ values are likely the result of additional factors such as electrostatic disorder of CT states (**Figure S7.16**, Supporting Information).[46] Summarizing, we were able to resolve all three major activation energy contributions to the doping process $E_{A,\sigma}$ (for conductivity), $E_{A,CT}$ (release of free charge carriers) and $E_{A,Hop}$ (hopping of free charge carriers). We conclude the nonlinear conductivity and mobility of Cu(TFSI)$_2$ doped Spiro-MeOTAD to be caused by reversible CT state freeze out.

7.2.3 Doping Efficiency

As discussed earlier, we found $E_{A,CT}$ of Cu(TFSI)$_2$ doped Spiro-MeOTAD to be low compared to other doped organic semiconductors, for example, in the case of N,N,N′,N′-tetrakis(4-methoxyphenyl)benzidine (4-MeO-TPD) doped with C$_{60}$F$_{36}$, $\approx$ 30 meV are required for CT state dissociation.[17] To test, if a low $E_{A,CT}$ facilitates carrier release in doped organic systems, we investigated the doping efficiency η_{Dop}. This figure of merit quantifies the ratio between free, dissociated charge carriers p and total density of dopant molecules in the system N_A as $\eta_{Dop} = p/N_A$. N_A^- was determined by Mott–Schottky experiments described in **Section 7.2.1**, where we assumed that the number of free holes p equals N_A^-. It is worth emphasizing, that the neutrality condition $p = N_A^-$ may not hold true for very high trap densities or a large number of free carriers bound in the CT state.[17,22] A detailed derivation of N_A can be found in the Supporting Information. Defining η_{Dop} *via* N_{Spins} and N_A^- was omitted due to the introduction of a large error source in absolute number of spins. As shown in **Figure 7.4a**, co-evaporated Cu(TFSI)$_2$ doped Spiro-MeOTAD retains a doping efficiency of up to (52.0 ± 6.4) % at 10 mol% dopant. Thus, in general η_{Dop} improves dramatically compared to other popular p-dopants, which drop below the 10.3 % mark at only 6.4 mol% in the case of the most efficient system in this series, C$_{60}$F$_{36}$ doped 4-MeO-TPD. Typically, η_{Dop} strongly decreases with increasing doping concentration, because charge carrier capture processes by dopant molecules become more likely.[17] In summary, the extraordinary low CT state binding energy $E_{A,CT}$

found in the Spiro-MeOTAD:Cu(TFSI)$_2$ system helps to greatly boost the doping efficiency compared to previously published *p*-dopants for organic systems.
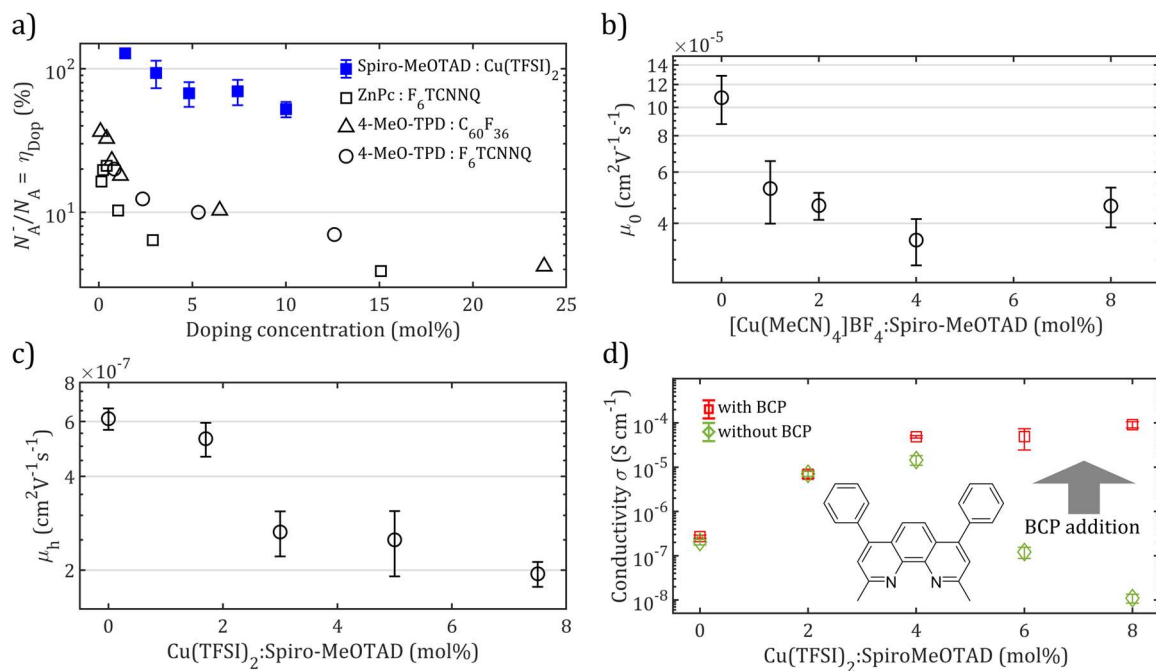
Figure 7.4. a) Doping efficiencies for different doping concentrations of Cu(TFSI)$_2$:Spiro-MeOTAD (blue squares). See Supporting Information for detailed information. Literature values for small molecule semiconductors: Zink-Phthalocyanine (abbr. ZnPc) doped with F$_6$TCNNQ (squares), 4-MeO-TPD doped with C$_{60}$F$_{36}$ (triangles) and F$_6$TCNNQ (circles).[17,22] b) Zero-field mobilities μ_0 of solution processed Spiro-MeOTAD thin films mixed with different molar amounts of [Cu(MeCN)$_4$]BF$_4$. c) Mobility μ of co-evaporated thin films of Cu(TFSI)$_2$ doped Spiro-MeOTAD using the CELIV method on FTO/Al$_2$O$_3$/Cu(TFSI)$_2$:Spiro-MeOTAD/Au devices. d) Thin film conductivities of solution processed, Cu(TFSI)$_2$ doped Spiro-MeOTAD without (green diamonds) and with bathocuproine (BCP, structure shown in graph) additive (red squares) at different dopant concentrations. BCP was added in equimolar amounts to Cu(TFSI)$_2$.

7.2.4 Hole Trapping

In our previous studies, no elemental Cu^0 was found in XPS studies of Cu(TFSI)$_2$ doped, co-evaporated Spiro-MeOTAD samples.[8] In turn, the Cu^I state can be assumed as the final product of the doping reaction. Supplementary to the XPS studies, we tested if the doping

reaction effectively stops at the Cu^I oxidation state. For this, a model Cu^I ion source, [Cu^I(MeCN)$_4$]$^+$BF$_4^-$ having the almost identical Cu^I/Cu^0 reduction potential compared to Cu(TFSI)$_2$ in acetonitrile solution, was mixed with Spiro-MeOTAD to verify, if [Cu^I(MeCN)$_4$]$^+$ can act as a dopant (**Figure S7.1**, Supporting Information).[47] Consequently, we prepared thin films from Spiro-MeOTAD mixed with increasing mole percent of [Cu^I(MeCN)$_4$]BF$_4$ in acetonitrile solution and conducted conductivity measurements (see **Figure S7.17**, Supporting Information, for details). Relative to pristine Spiro-MeOTAD, no increase in σ was found for up to 4 mol% [Cu^I(MeCN)$_4$]BF$_4$, the upper solubility limit of this complex in Spiro-MeOTAD. In line with XPS experiments, we conclude Cu^I to be the stable oxidation state formed after reacting Cu(TFSI)$_2$ and Spiro-MeOTAD. Penultimately, we want to clarify the role of products of the doping reaction in the macroscopic charge transport of Cu(TFSI)$_2$ doped Spiro-MeOTAD. The two possible ions arising out of doping reaction are TFSI$^-$ and Cu^I. Any detrimental influence of the TFSI$^-$ anion on the charge transport was rejected for up to 10 mol% dopant concentration based on the fact that both LiTFSI($\approx$ 50 mol%)/O$_2$ or Spiro-MeOTAD(TFSI)$_2$ (17 mol% optimum) doped Spiro-MeOTAD and are known in literature to surpass the hole mobility of pristine Spiro-MeOTAD.[24,38] One may raise the question, if unbound Cu^{II} is responsible for trapping mobile holes. Careful analysis of temperature dependent absorption helps to answer this question: i) The first step of CT state formation is temperature independent as reported in literature and verified to be valid as shown in **Figure 7.1d** for our system (see also **Figures S7.18**, **S7.7**, Supporting Information); thus, no unreacted Cu(TFSI)$_2$ should remain up to 10 mol% doping concentration ii) hypothetical Cu^{III} as the product of hole capture by Cu^{II} is highly unstable without suitable, stabilizing ligands.[22,48] Based on these findings, we focus on Cu^I as the main trapping center for holes in this system. Using impedance spectroscopy, the effect of [Cu^I(MeCN)$_4$]BF$_4$ on the Spiro-MeOTAD hole mobility was probed. In impedance spectroscopy experiments, a continuous decrease of the zero-field mobility $\mu_{h,0}$ from the pristine $(1.1 \pm 0.2) \cdot 10^{-4}$ cm^2 V^{-1} s^{-1} sample to $(4.6 \pm 0.7) \cdot 10^{-5}$ cm^2 V^{-1} s^{-1} in 8 mol% [Cu^I(MeCN)$_4$]BF$_4$:Spiro-MeOTAD was observed (**Figure 7.4b**; **Figure S7.19**, Supporting Information). Complementary charge extraction by linearly increasing voltage CELIV measurements on Cu(TFSI)$_2$ doped Spiro-MeOTAD revealed an identical trend of continuous decrease of the hole mobility μ_h in co-evaporated samples; from $(6.1 \pm 0.5) \cdot 10^{-7}$ cm^2 V^{-1} s^{-1} in the pristine sample to $(1.9 \pm 0.2) \cdot 10^{-7}$ cm^2 V^{-1} s^{-1} at 7.5 mol% Cu(TFSI)$_2$ (**Figure 7.4c**; **Figure S7.20**, Supporting Information). As show in our previous work, co-evaporated samples of

Cu(TFSI)$_2$ and Spiro-MeOTAD are uniform and pinhole-free, excluding morphological effects on carrier mobility in this experiment.[8] Yoo et al. studied evaporated triarylamine hole conductors, chemically and energetically very similar to Spiro-MeOTAD, doped with the transition metal oxide ReO$_3$ by impedance spectroscopy and found a profound loss in hole mobility. They attributed this effect to the ionized dopants acting as coulomb traps.[49] As a consequence, Cu^{I} is proposed to act as a hole trap by reversible oxidation to Cu^{II}, reducing the average mobility of holes μ_h in Spiro-MeOTAD. Further proof for Cu^{I} ions acting as hole traps is the distinct [Cu^{I}(TFSI)$_2$]$^-$ trap state freeze-out which recovers the mobility below ≈ 150 K for doping concentrations > 3 mol% (**Figure 7.3b**). Temperature dependent linewidth in EPR experiments verifies this hypothesis, as it suspects a lower charge carrier motion frequency above 180 K ($E_{A,trap} \approx 16$ meV) with higher $E_{A,Hop}$, characteristic for an increased average residence time on a "free" Cu^{I} trap site (**Figure 7.3e**).[50] Having identified Cu^{I} as a potent hole trap, we verified if it is possible to disrupt the accumulation of harmful [Cu^{I}(TFSI)$_2$]$^-$ species in doped Spiro-MeOTAD *via* selective ion complexation. 2,9-Dimethyl-4,7-diphenyl-1,10-phenanthroline (Bathocuproine, abbr. BCP) proves to be a suitable ligand to achieve the targeted selectivity, as it is known to form a stable tetrahedral bis-chelating complex with Cu^{I}.[51] Additionally, BCP stabilizes the copper(I) ion and inhibits further redox chemistry as it occurs in the hole trapping reaction.[52] We performed conductivity experiments on solution processed films, as co-evaporation does not allow sequential deposition without layered structure formation. First, Cu(TFSI)$_2$ was allowed to undergo a redox reaction with Spiro-MeOTAD in solution, then BCP was added in equimolar amounts to Cu(TFSI)$_2$ into the doped mixture solution to complex the resulting Cu^{I} ions. Cu^{I}(BCP)$_2$ complex formation was proven by UV/Vis/NIR spectroscopy in solution and thin films (**Figures S7.21**, **S7.22**, Supporting Information). Afterward, the solution was spun-cast onto commercial interdigitated gold electrodes to determine the thin film conductivity σ. Following an initial strong increase, the conductivity saturates at high doping concentrations and even starts to decrease due to loss in doping efficiency and detrimental effects of by-products such as [Cu^{I}(TFSI)$_2$]$^-$ (**Figure 7.4d**). To our surprise, σ was amplified by a factor of $0.8 \cdot 10^4$ in the presence of BCP compared to the sample without BCP at 8 mol% Cu(TFSI)$_2$. However, we also observed a loss in solution-processed Spiro-MeOTAD film quality and disrupted morphology upon adding Cu(TFSI)$_2$ and [Cu^{I}(MeCN)$_4$]BF$_4$, similar to our previous work (**Figures S7.23**, **S7.24**, Supporting Information).[8] This effect was mitigated upon adding BCP. We argue, that morphology

has minor influence on the bulk mobility, as both co-evaporated as well as solution-processed Cu(TFSI)$_2$:Spiro-MeOTAD display almost identical thin film conductivities.[8] Therefore, we conclude that any change in σ originates from Cu^I trap passivation. In essence, Cu^I species as the doping reaction side product was identified as a potent hole trap, whose detrimental effects may be mitigated by selective complexation.

7.2.5 Absence of Elemental Cu

A final piece of the puzzle is the question concerning why no further reduction of the remaining Cu^I to Cu^0 occurs. This is surprising, as studies have proven the capability of a Cu^I iodide salt to successfully oxidize Spiro-MeOTAD with a reported copper iodide workfunction of $\approx$ 5.5 eV.[4,53,54] To answer this question, we refer back to cyclic voltammetry measurements on Cu(TFSI)$_2$ solutions in acetonitrile performed earlier (**Figure S7.1**, Supporting Information). Half-wave potentials of -0.439 V versus Ag/AgNO$_3$ for Cu^0/Cu^I and $+1.51$ V versus Ag/AgNO$_3$ of the Cu^I/Cu^{II} redox couple were recorded. These values translate to a deep lying EA$_{Cu(II)/Cu(I)}$ = 6.15 eV, whereas the electron affinity EA$_{Cu(I)/Cu(0)}$ for the reduction to elemental copper is positioned at 4.20 eV in the presence of TFSI$^-$ anions and in acetonitrile. As explained earlier, with respect to the HOMO of Spiro-MeOTAD at 5.03 eV, the high EA$_{Cu(II)/Cu(I)}$ of Cu(TFSI)$_2$ results in an exothermic single electron transfer between Cu(TFSI)$_2$ and Spiro-MeOTAD, explaining the experimentally observed high doping efficiency. However, we noticed a low electron affinity of 4.20 eV for the reduction of [Cu^I(TFSI)$_2$]$^-$ to elemental copper, compared to 5.5 eV for CuI. Because the low EA implies an endothermic electron transfer to the HOMO of Spiro-MeOTAD, the doping reaction stops at copper(I) with the formation of [Cu^I(TFSI)$_2$]$^-$. We propose the EA$_{Cu(I)/Cu(0)}$ discrepancy between copper iodide and [Cu^I(TFSI)$_2$]$^-$ lies in the stabilization of the soft Lewis acid Cu^I by the adjacent ligands. Strikingly, Stricker et al. performed single crystal analysis on [1-ethyl-3-methylimidazolium]$^+$[Cu^I(TFSI)$_2$]$^-$, characterized by a d^{10} Cu^I ion coordinated linearly by the two TFSI$^-$ anions with an N$_{TFSI,1}$-Cu-N$_{TFSI,2}$ bond angle of 180.0°. In this compound, TFSI$^-$ behaves as a monodentate N-donor (κN) ligand. The same cuprate(I) anion [Cu^I(TFSI)$_2$]$^-$ is very likely formed during our solvent and oxygen free doping environment and responsible for the high stability (low EA$_{Cu(I)/Cu(0)}$) *via* complexation and

lower N_{TFSI}-Cu bond distance of ≈ 1.9 Å compared to I-Cu bond distance of 2.62 Å in γ-CuI.[55-57] To test the possibility for $[Cu^I(TFSI)_2]^-$ formation, we mixed equimolar amounts of Spiro-MeOTAD and Cu(TFSI)$_2$ in dichloromethane. A black, crystal-like salt was isolated by an anti-solvent approach (**Figure S7.25**, Supporting Information). A [Spiro-MeOTAD]$^+$[Cu^I(TFSI)$_2$]$^-$ composition was determined by elemental analysis (see Supporting Information). We conclude, that energetic mismatch between Cu^I and Spiro-MeOTAD prevents reduction of Cu(TFSI)$_2$ to elemental copper. In addition, $[Cu^I(TFSI)_2]^-$ anions are formed in Cu(TFSI)$_2$ doped Spiro-MeOTAD, further stabilizing the Cu^I state.

7.2.6 Doping Mechanism Overview

As a closing remark, we combined all our experimental findings to draw the complete doping mechanism between the *p*-dopant Cu(TFSI)$_2$ and Spiro-MeOTAD. We propose three consecutive steps in the doping reaction: i) formation of a coulombically bound CT state [Spiro-MeOTAD]$^{x+}$[Cu^I(TFSI)$_2^-$]$_x$, followed by ii) reversible, endothermic dissociation of the CT state into a free charge carrier and counterion and ultimately iii) transport of the free charge carriers with concurrent trapping involving the $[Cu^I(TFSI)_2]^-$ anions. This concept is in line with previously published results by Tietze et al. on the doping process of zinc phthalocyanine (ZnPc) and N,N,N′,N′-tetrakis(4-methoxyphenyl)-benzidine (MeO-TPD) using the *p*-dopant 1,3,4,5,7,8-hexafluorotetracyanonaphthoquinodimethane F$_6$TCNNQ.[22] The proposed mechanism is shown in **Scheme 7.1**.
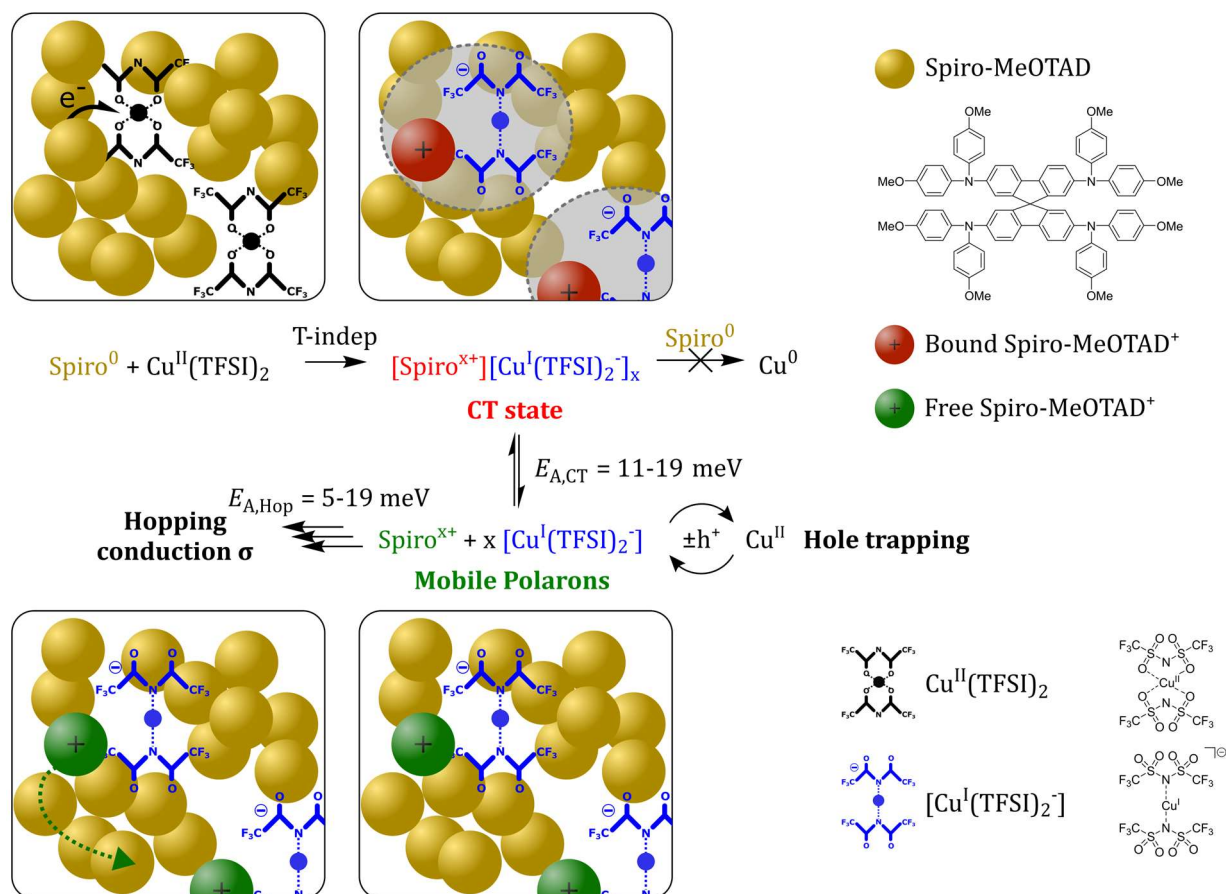
Scheme 7.1. Overview of the proposed individual reaction steps involving the small molecule hole-conductor Spiro-MeOTAD and *p*-dopant Cu(TFSI)$_2$. A temperature independent and irreversible redox reaction step first yields oxidized Spiro-MeOTAD$^+$ coulombically bound to the [Cu^I(TFSI)$_2$]$^-$ counter ion (charge transfer state). [Cu^I(TFSI)$_2$]$^-$ is generated as a side product of Cu(TFSI)$_2$ reduction. Here, Cu(II) is depicted as black-, Cu(I) as blue spheres. [Cu^I(TFSI)$_2$]$^-$ traps free holes with an average trap depth of $E_{A,Trap}$ = 16 meV. Mobile Spiro-MeOTAD^{x+} charge carriers are thermally released from the CT state with an activation energy $E_{A,CT}$ in the order of 11–19 meV. Further, the free charge carrier transport responsible for the macroscopic observed conductivity in doped Spiro-MeOTAD is thermally activated with 5–19 meV.

7.3 Conclusion

This report offers a comprehensive in-depth study of the doping process of Spiro-MeOTAD using Cu(II) salt, today one of the best hole collecting system in perovskite solar cells. The doping process itself is monitored by the observed shift of WF toward HOMO

level and consequent decrease in HIB and the complex doping process is fully elucidated. Impedance and electron paramagnetic resonance spectroscopy clearly indicate low activation energies for hole release and hopping transport. Remarkably small activation barriers favor unprecedented doping efficiencies of up to 50 % at 10 mol% doping using Cu(TFSI)$_2$. The reader is invited to recall **Scheme 7.1**, the central picture outlining all the important findings of this work regarding the mechanism. Prior to this study, many physical intricacies regarding Cu(TFSI)$_2$ as a *p*-dopant for Spiro-MeOTAD - and in general for molecular semiconductor systems - were poorly described in literature. We could verify the temperature-independent formation of charge transfer states, in line with general agreements on doped OSCs in literature. The CT states comprised of Spiro-MeOTAD^{x+} and [Cu^I(TFSI)$_2$]$^-$ were observed to dissociate with an activation energy of (11.4 ± 3.8) meV above ≈ 150 K. Due to complexation of Cu^I in the cuprate complex [Cu^I(TFSI)$_2$]$^-$, no further reduction to Cu^0 can be observed. Thermal activation in the range of 5–19 meV leads to free hole hopping in the doped Spiro-MeOTAD bulk. The hole mobility was found to be greatly influenced by reversible CT state freeze-out, causing macroscopic nonlinear temperature dependent conductivities, which cannot be explained within the framework of charge transport models. Cu^I as the dopant product was identified as a potent hole trap limiting the electrical properties. An improved understanding of this co-evaporated system provides guidelines to passivate these species using bathocuproine, resulting in vastly improved electrical conductivity. These findings complement not only earlier studies on co-evaporated Cu(TFSI)$_2$:Spiro-MeOTAD as a hole transport layer in solar cells, but provide crucial insight into copper salts as *p*-dopants for organic semiconductors.

7.4 Acknowledgements

7.5 Conflict of Interest

The authors declare no conflict of interest.

7.6 References

[1]   S. Yue, K. Liu, R. Xu, M. Li, M. Azam, K. Ren, J. Liu, Y. Sun, Z. Wang, D. Cao, X. Yan, S. Qu, Y. Lei, Z. Wang, *Energy Environ. Sci.* **2017**, *10*, 2570.

[2]   H. J. Snaith, M. Grätzel, *Appl. Phys. Lett.* **2006**, *89*, 262114.

[3]   T. Leijtens, J. Lim, J. Teuscher, T. Park, H. J. Snaith, *Adv. Mater.* **2013**, *25*, 3227.

[4]   M. Li, Z.-K. Wang, Y.-G. Yang, Y. Hu, S.-L. Feng, J.-M. Wang, X.-Y. Gao, L.-S. Liao, *Adv. Energy Mater.* **2016**, *6*, 1601156.

[5]   C. Chen, W. Zhang, J. Cong, M. Cheng, B. Zhang, H. Chen, P. Liu, R. Li, M. Safdari, L. Kloo, L. Sun, *ACS Energy Lett.* **2017**, *2*, 497.

[6]   J. Zhang, Q. Daniel, T. Zhang, X. Wen, B. Xu, L. Sun, U. Bach, Y.-B. Cheng, *ACS Nano* **2018**, *12*, 10452.

[7]   L. Qiu, X. Zheng, J. Zhang, Y. Yang, W. Cao, Y. Dong, D. Xia, X. Zhou, R. Fan, *ACS Appl. Mater. Interfaces* **2020**, *12*, 546.

[8]   J. Mohanraj, M. Stihl, E. Simon, O. von Sicard, G. Schmidt, M. Fleischer, C. Neuber, M. Thelakkat, *ACS Appl. Energy Mater.* **2019**, *2*, 3469.

[9]   I. Salzmann, G. Heimel, M. Oehzelt, S. Winkler, N. Koch, *Acc. Chem. Res.* **2016**, *49*, 370.

[10]   M. Goel, M. Siegert, G. Krauss, J. Mohanraj, A. Hochgesang, D. C. Heinrich, M. Fried, J. Pflaum, M. Thelakkat, *Adv. Mater.* **2020**, *32*, 2003596.

[11]   T. Koopmans, *Physica* **1934**, *1*, 104.

[12]   K. Gräf, M. A. Rahim, S. Das, M. Thelakkat, *Dyes Pigments* **2013**, *99*, 1101.

[13]   S. Olthof, S. Mehraeen, S. K. Mohapatra, S. Barlow, V. Coropceanu, J.-L. Brédas, S. R. Marder, A. Kahn, *Phys. Rev. Lett.* **2012**, *109*, 176601.

[14]   A. Abate, D. R. Staff, D. J. Hollman, H. J. Snaith, A. B. Walker, *Phys. Chem. Chem. Phys.* **2014**, *16*, 1132.

[15]   M. L. Tietze, P. Pahner, K. Schmidt, K. Leo, B. Lüssem, *Adv. Funct. Mater.* **2015**, *25*, 2701.

[16] J.-P. Yang, W.-Q. Wang, F. Bussolotti, L.-W. Cheng, Y.-Q. Li, S. Kera, J.-X. Tang, X.-H. Zeng, N. Ueno, *Appl. Phys. Lett.* **2016**, *109*, 093302.

[17] M. L. Tietze, L. Burtone, M. Riede, B. Lüssem, K. Leo, *Phys. Rev. B* **2012**, *86*, 035320.

[18] S. Olthof, W. Tress, R. Meerheim, B. Lüssem, K. Leo, *J. Appl. Phys.* **2009**, *106*, 103711.

[19] H. Méndez, G. Heimel, A. Opitz, K. Sauer, P. Barkowski, M. Oehzelt, J. Soeda, T. Okamoto, J. Takeya, J.-B. Arlin, J.-Y. Balandier, Y. Geerts, N. Koch, I. Salzmann, *Angew. Chem.* **2013**, *125*, 7905.

[20] C. Lambert, G. Nöll, *J. Am. Chem. Soc.* **1999**, *121*, 8434.

[21] S. Fantacci, F. De Angelis, M. K. Nazeeruddin, M. Grätzel, *J. Phys. Chem. C* **2011**, *115*, 23126.

[22] M. L. Tietze, J. Benduhn, P. Pahner, B. Nell, M. Schwarze, H. Kleemann, M. Krammer, K. Zojer, K. Vandewal, K. Leo, *Nat. Commun.* **2018**, *9*, 1182.

[23] G. Krauss, A. Hochgesang, J. Mohanraj, M. Thelakkat, *Macromol. Rapid Commun.* **2021**, *42*, 2100443.

[24] W. Zhang, L. Wang, Y. Guo, B. Zhang, V. Leandri, B. Xu, Z. Li, J. M. Gardner, L. Sun, L. Kloo, *Chem. Commun.* **2020**, *56*, 1589.

[25] H. Oshio, T. Watanabe, A. Ohto, T. Ito, U. Nagashima, *Angew. Chem. Int. Ed. Engl.* **1994**, *33*, 670.

[26] A. Abate, D. J. Hollman, J. Teuscher, S. Pathak, R. Avolio, G. D'Errico, G. Vitiello, S. Fantacci, H. J. Snaith, *J. Am. Chem. Soc.* **2013**, *135*, 13538.

[27] M. Namatame, M. Yabusaki, T. Watanabe, Y. Ogomi, S. Hayase, K. Marumoto, *Appl. Phys. Lett.* **2017**, *110*, 123904.

[28] T. Watanabe, T. Yamanari, K. Marumoto, *Commun. Mater.* **2020**, *1*, 96.

[29] K. Kang, S. Watanabe, K. Broch, A. Sepe, A. Brown, I. Nasrallah, M. Nikolka, Z. Fei, M. Heeney, D. Matsumoto, K. Marumoto, H. Tanaka, S. Kuroda, H. Sirringhaus, *Nat. Mater.* **2016**, *15*, 896.

[30] A. Privitera, R. Warren, G. Londi, P. Kaienburg, J. Liu, A. Sperlich, A. E. Lauritzen, O. Thimm, A. Ardavan, D. Beljonne, M. Riede, *J. Mater. Chem. C* **2021**, *9*, 2944.

[31]   N. F. Mott, *Philos. Mag.* **1969**, *19*, 835.

[32]   B. I. Shklovskii, A. L. Efros, *Electronic Properties of Doped Semiconductors*, Springer Berlin Heidelberg, Berlin, Heidelberg **1984**.

[33]   A. V. Nenashev, J. O. Oelerich, S. D. Baranovskii, *J. Phys. Condens. Matter* **2015**, *27*, 093201.

[34]   R. Fujimoto, Y. Yamashita, S. Kumagai, J. Tsurumi, A. Hinderhofer, K. Broch, F. Schreiber, S. Watanabe, J. Takeya, *J. Mater. Chem. C* **2017**, *5*, 12023.

[35]   R. Rosenbaum, *Phys. Rev. B* **1991**, *44*, 3599.

[36]   A. L. Efros, B. I. Shklovskii, *J. Phys. C Solid State Phys.* **1975**, *8*, L49.

[37]   L. Li, N. Lu, M. Liu, *J. Appl. Phys.* **2014**, *116*, 164504.

[38]   B. Li, S. Zhang, F. Xia, Y. Huang, X. Ran, Y. Xia, Y. Chen, W. Huang, *J. Appl. Phys.* **2020**, *128*, 085501.

[39]   M. Pei, J. Guo, B. Zhang, S. Jiang, Z. Hao, X. Xu, Y. Li, *Adv. Phys. X* **2020**, *5*, 1747945.

[40]   A. Köhler, H. Bässler, *Electronic Processes in Organic Semiconductors: An Introduction*, Wiley-VCH, Weinheim **2015**.

[41]   J. A. Röhr, X. Shi, S. A. Haque, T. Kirchartz, J. Nelson, *Phys. Rev. Appl.* **2018**, *9*, 044017.

[42]   J. D. Yuen, R. Menon, N. E. Coates, E. B. Namdas, S. Cho, S. T. Hannahs, D. Moses, A. J. Heeger, *Nat. Mater.* **2009**, *8*, 572.

[43]   D. Poplavskyy, J. Nelson, *J. Appl. Phys.* **2003**, *93*, 341.

[44]   Y. Matsuo, D. Son, Y. Shimoi, K. Marumoto, *Chem. Phys. Lett.* **2014**, *607*, 29.

[45]   K. A. Peterson, A. Patterson, A. Vega-Flick, B. Liao, M. L. Chabinyc, *Mater. Chem. Front.* **2020**, *4*, 3632.

[46]   M. Schwarze, C. Gaul, R. Scholz, F. Bussolotti, A. Hofacker, K. S. Schellhammer, B. Nell, B. D. Naab, Z. Bao, D. Spoltore, K. Vandewal, J. Widmer, S. Kera, N. Ueno, F. Ortmann, K. Leo, *Nat. Mater.* **2019**, *18*, 242.

[47]   A. Vaskevich, I. Rubinstein, *J. Electroanal. Chem.* **2000**, *491*, 87.

[48] A. M. Romine, N. Nebra, A. I. Konovalov, E. Martin, J. Benet-Buchholz, V. V. Grushin, *Angew. Chem., Int. Ed.* **2015**, *54*, 2745.

[49] S.-J. Yoo, J.-H. Lee, J.-M. Kim, J.-J. Kim, *Appl. Phys. Lett.* **2017**, *110*, 053303.

[50] H. Matsui, D. Kumaki, E. Takahashi, K. Takimiya, S. Tokito, T. Hasegawa, *Phys. Rev. B* **2012**, *85*, 035308.

[51] X. Ding, H. Xie, Y. J. Kang, *J. Nutr. Biochem.* **2011**, *22*, 301.

[52] R. P. Patel, D. Svistunenko, M. T. Wilson, V. M. Darley-Usmar, *Biochem. J.* **1997**, *322*, 425.

[53] P. Wang, J. Zhang, Z. Zeng, R. Chen, X. Huang, L. Wang, J. Xu, Z. Hu, Y. Zhu, *J. Mater. Chem. C* **2016**, *4*, 9003.

[54] S. Park, H. Lee, J. Lee, Y. Lee, Y. Yi, *Org. Electron.* **2014**, *15*, 3298.

[55] M. Stricker, B. Oelkers, C. P. Rosenau, J. Sundermeyer, *Chem. – Eur. J.* **2013**, *19*, 1042.

[56] N. Kuganathan, J. C. Green, *Chem. Commun.* **2008**, 2432.

[57] M. Kaiser, J. Göttlicher, T. Vitova, A. Hinz, *Chem. – Eur. J.* **2021**, *27*, 7998.

7.7 Supporting Information

7.7.1 Material and Equipment

Anhydrous solvents were purchased from Sigma-Aldrich / Acros Organics in sealed bottles and were used as received. N^2,N^2,N$^{2'}$,N$^{2'}$,N^7,N^7,N$^{7'}$,N$^{7'}$-octakis(4-methoxyphenyl)-9,9'-spirobi[fluorene]-2,2',7,7'-tetraamine Solarpur SHT-263 (abbreviated as "Spiro-MeOTAD") and copper(II)oxide were supplied by Sigma-Aldrich, Germany and used as received. Device grade, triple-sublimed copper(II)bis(trifluoromethanesulfonyl)imide (abbreviated as "Cu(TFSI)$_2$") for doping experiments was supplied by SIEMENS. 2,9-dimethyl-4,7-diphenyl1,10-phenanthroline (abbreviated as "BCP") was obtained in > 98 % purity from Sigma-Aldrich, Germany and used as received. Tetrakis(acetonitrile)copper(I)tetrafluoroborate was obtained from Sigma-Aldrich, Germany and purified by recrystallisation from anhydrous acetonitrile under inert atmosphere immediately prior to experiments to obtain white, flaky crystals. Spiro-MeOTAD(PF$_6$)$_2$ was synthesized according to a previously published procedure[1]. Film thicknesses were measured using a Veeco Dektak 150 Profilometer. Optical images of thin films were taken using a Zeiss Axio Imager A1m microscope. Scanning electron microscopy was performed with a Phenom Pro SEM by Thermo Fisher Scientific on thin films coated onto oxide-free silicon substrates. A 4-segmented detector and accelerating voltage of 10 kV were used. Ultraviolet photoelectron spectroscopy was performed on a PHI 5000 VersaProbe III machine equipped with a helium discharge radiation source providing stable and continuous He I and II lines, under ultrahigh vacuum (10^{-10} mbar). Room temperature UV/Vis/NIR absorption measurements were carried out using a V-670 JASCO spectrometer. Impedance data on devices was measured using a Metrohm Autolab PGSTAT204 equipped with an FRA32M module. The NOVA 2.1.4 Software package provided by Metrohm, Germany and custom MATLAB code was used to process the impedance data. Co-evaporation of Spiro-MeOTAD and Cu(TFSI)$_2$ was performed on a Balzers PLS 500 E equipped with quartz crystal microbalances and switchable shadow masks, for further information, see previous publications[2]. All temperature dependent mobility, charge carrier density and conductivity measurements were performed under helium atmosphere using an Optistat CF2 He cryostat from Oxford Instruments, UK. Al$_2$O$_3$ thin films for Mott-Schottky and CELIV metal-insulator-semiconductor devices were prepared by atomic layer deposition from trimethylaluminium and H$_2$O in a VEECO

Savannah Gen. 2 S300. EPR measurements were performed with an X-band spectrometer (Magnettech MS-5000) equipped with a continuous-flow helium cryostat (Oxford ESR 900). Density measurements were carried out using a Mettler Toledo XP205 digital balance equipped with either a Millipore water or cyclohexane reference liquid bath. Solid samples for density determination were fabricated by pressing Spiro-MeOTAD and anhydrous Cu(TFSI)$_2$ into pellets of 1 cm diameter at 8 tons pressure for 15 min.

*Synthesis of N^2,N^2,N$^{2'}$,N$^{2'}$,N^7,N^7,N$^{7'}$,N$^{7'}$-octakis(4-methoxyphenyl)-9,9'-spirobi[fluorene]-2,2',7,7'-tetraamine^I, [Cu(I)(bis(trifluoromethanesulfonyl)imide)$_2$] salt (1:1) (**1**)*

A 100 mL flame-dried Schlenk flask was evacuated and consecutively flushed with Ar three times. The flask was charged with 119.6 mg ($9.76 \cdot 10^{-5}$ Mol) Spiro-MeOTAD and 60.9 mg ($9.76 \cdot 10^{-5}$ Mol) Cu(TFSI)$_2$ under inert atmosphere. 25 mL anhydrous dichloromethane were added, which immediately lead to the formation of a dark-purple color. A condenser was attached and the solution was stirred at 50 °C under reflux conditions for 2 h. The solvent was removed under vacuum and the as obtained powder was dried under high vacuum for 1 h at rt. Single crystals were grown inside a glovebox by dissolving the compound in a minimal amount of anhydrous dichloromethane (ca. 1.5 mL) and placing the vial into another, bigger container. The outer container was filled with a small amount of anhydrous *n*-hexane and sealed hermetically to create a solvent saturated, inert atmosphere. After 24 h at rt., black single crystals 1.5 mm in diameter were collected from the bottom of the inner vial. The crystals were carefully suspended in anhydrous n-hexane to clean the surfaces, ultrasonicated for 10 sec and placed on a polyester/cellulose fabric to dry under inert atmosphere yielding 1 (119.3 mg, 66 %). Elemental analysis calculated (m%) for N^2,N^2,N$^{2'}$,N$^{2'}$,N^7,N^7,N$^{7'}$,N$^{7'}$-octakis(4-methoxyphenyl)-9,9'-spirobi[fluorene]-2,2',7,7'-tetraamineI , [Cu^I(TFSI)$_2$] salt (1:1) (1849.27 g mol^{-1}): C 55.206, H 3.706, N 4.545, S 6.936; found: C 56.41, H 3.87, N 4.63, S 7.19.

Synthesis of copper(II) bis(trifluoromethanesulfonyl)imide for density determination (2)

A 500 mL flask was loaded with copper(II)oxide nanopowder (500 mg, 6.29 mmol), which was subsequently dispersed in 150 mL Millipore H$_2$O under strong stirring at rt. Bis(trifluoromethane)sulfonimide (3.54 g, 12.6 mmol) was added in small portions. The dispersion was stirred at 80 °C for 4 h, until the black color completely disappears to form a light blue solution. Excess copper(II)oxide was removed by gravity filtration. The water was removed from the filtrate using a rotary evaporator, resulting in a blue, hydrated crystals. The hydrate was converted to the anhydrate by prolonged heating at 180 °C under high vacuum, yielding a white powder 2 (2.803 g, 71 %). The anhydrous copper(II)bis(trifluoromethanesulfonyl)imide was stored under Ar for further use.

7.7.2 General Methods

All doping experiments and oxygen/water sensitive reactions were carried out in a nitrogen filled mBraun Labmaster 130 glovebox.

Ultraviolet Photoelectron Spectroscopy

UPS measurements were carried out on a PHI 5000 VersaProbe III system fitted with a He discharge light source providing stable and continuous He I and He II lines, under ultrahigh vacuum (10^{-9} mbar). Samples for UPS measurements were obtained by thermal co-evaporation of controlled amounts of Cu(TFSI)$_2$ and spiro-MeOTAD on clean ITO (15 Ω square^{-1}), affording ca. 20 nm thick films (measured by using a dummy sample in a profilometer). The samples were transferred from the evaporation chamber to a N$_2$ filled glove box and further to the instrument in a nitrogen filled and sealed stainless steel transport vessel. Once the samples were loaded into the instrument main chamber, He I source (80 W) was used to induce photoelectrons and were collected at 90° take-off angle by using a multichannel semispherical analyzer. Both valence band maximum (VBM) and secondary electron cutoff (SECO) signals from the samples were measured by applying -5 V between the analyzer and the substrate. Both VBM and SECO spectra were collected at least from 3 different areas in 2 different samples, and only the reproducible measurements were considered for further calculations and discussion. The VBM and SECO binding energy values necessary to determine ionization potential and

workfunction, respectively, were obtained by linear extrapolation method. The Fermi level E_F of the samples (doped and pristine) were referenced to the Fermi level of sputter-cleaned Au foil. The energy resolution of the VBM and SECO is 0.15 eV, which was derived from the full-width half-maximum of the Au Fermi edge.

Table S7.1. Electron affinity, workfunction and hole-injection barrier of Cu(TFSI)$_2$ doped and pristine Spiro-MeOTAD, determined by UPS experiments.

Sample	Electron affinity EA (eV)	Workfunction WF (eV)	Hole injection barrier HIB (eV)
Pristine Spiro-MeOTAD	5.03 ± 0.15	4.29 ± 0.15	0.74 ± 0.15
2 mol% Cu(TFSI)$_2$:Spiro-MeOTAD	5.07 ± 0.15	4.68 ± 0.15	0.39 ± 0.15
4 mol% Cu(TFSI)$_2$:Spiro-MeOTAD	5.23 ± 0.15	4.82 ± 0.15	0.41 ± 0.15
6 mol% Cu(TFSI)$_2$:Spiro-MeOTAD	5.17 ± 0.15	4.86 ± 0.15	0.31 ± 0.15
8 mol% Cu(TFSI)$_2$:Spiro-MeOTAD	5.28 ± 0.15	4.95 ± 0.15	0.33 ± 0.15
10 mol% Cu(TFSI)$_2$:Spiro-MeOTAD	5.35 ± 0.15	5.02 ± 0.15	0.33 ± 0.15

Temperature Dependent UV/Vis/NIR

For investigating possibly temperature-dependent absorption features of the doped Spiro-MeOTAD we used a home-built absorption setup. The films were transferred in a continuous flow cryostat by Oxford instruments under helium atmosphere and the temperature between 300 K and 5 K is controlled by an Oxford Instruments ITC 502. For each temperature step the temperature was held constant for 15 min before the measurement. The optical density is calculated by analyzing the transmission spectra with a Shamrock SR-303i by Andor Technology equipped with CCD-camera (Andor iDus DU420-OE). For these experiments the (doped) Spiro-MeOTAD was evaporated on quartz glass.

Electrical conductivity

Electrical conductivities were measured using commercial Gen4 OFET substrates obtained from Fraunhofer IPMS, Germany. Every OFET substrate contains 30 nm thick interdigitated gold electrodes, patterned on thermally grown silicon oxide with a channel

width of 2.5 μm, 5 μm, 10 μm and 25 μm and a channel length of 1 cm. The substrates were cleaned by sonication in isopropanol and acetone for 10 min each, followed by activation of the surface in an ozone plasma for 15 min at 50 °C. 100 nm thick Cu(TFSI)$_2$:Spiro-MeOTAD films were deposited by co-evaporation. I-V characteristics were measured using an Agilent Technologies B1500A Semiconductor Device Analyzer. The electrical conductivities were extracted from the linear fit of the I-V curve in the Ohmic region according to **Equation S7.1** below:

$$\sigma = \frac{a \cdot L}{W \cdot d} \tag{S7.1}$$

Where σ: electrical conductivity, a: slope of the linear fit, L: channel length, W: channel width, d: film thickness. The film thicknesses were measured after the conductivity measurements, using a profilometer.

Solid State Mott Schottky Analysis

TEC-7 (XOP glass, 1" · 1" · 2.2 mm, 6 – 8 Ω square^{-1}, ~ 500 nm FTO on glass) substrates were etched with dilute HCl/Zn-dust. After obtaining the etched electrode pattern, the substrates were brushed manually with sodium dodecyl sulfate and deionized water, followed by ultrasonication in 2 vol% aqueous Hellmanex-III solution, water, acetone and isopropanol. The substrates were blown dry with nitrogen and pre-treated with O$_3$/UV for 15 min at 50 °C. 100 nm of Al$_2$O$_3$ were deposited on the FTO-electrodes using ALD (H$_2$O/Al(CH$_3$)$_3$, 15 ms pulse duration, 150 °C, 5 s purge time, 1111 cycles), while leaving areas insulator-free for contacting the device during measurements. The aluminium oxide layer was passivated by spin coating 100 nm of BCB (10 vol% Cyclotene 3022-35 in toluene, 70 μL, 50 sec, 3000 rpm) on top and soft curing for 10 sec at 250 °C in air, followed by a hard bake at 250 °C for 1 h under Argon. 100 nm of Cu(TFSI)$_2$:Spiro-MeOTAD films were co-evaporated onto the substrates. Finally, Au electrodes were thermally evaporated using a shadow mask (d_{Au} = 70 nm). The impedance of the devices was measured with a two-electrode setup and varying electrical field (10 kHz to 10 Hz, 8 points per frequency decade, -1.5 to 1.5 V$_{Bias}$ in 48 voltage steps, 7 mV$_{RMS}$) using a Metrohm Autolab PGSTAT204 equipped with an FRA32M module. The NOVA 2.1.4 Software package provided by Metrohm, Germany and custom MATLAB code was used to

process the impedance data. The Au top electrode was connected to the counter and reference electrode, the FTO contact to the working and sense electrode of the potentiostat. Devices under test were shielded from ambient light, external electrical fields and kept under inert atmosphere. From the imaginary Z'' and real Z' impedance, the capacitance of the organic layer was extracted assuming an R$_S$(RC) equivalent circuit:

$$\hat{Z}(i\omega)_{\text{R(RC)}} = R_{\text{Series}} + \cfrac{1}{i\omega C_{\text{Parallel}} + \cfrac{1}{R_{\text{Parallel}}}} \tag{S7.2}$$

which can be solved for C_{Parallel} to yield

$$C_{\text{Parallel}} = \frac{Im(Z)}{(-Im(Z)^2 + (Re(Z) - R_S)^2)\omega} \tag{S7.3}$$

The density of ionized acceptors N_A^- was the extracted by plotting C^{-2} vs the Boltzmann corrected applied bias voltage V_{Bias} and fitting **Equation S7.4** to the linear depletion regime.

$$C_{\text{Parallel}}^{-2} = \frac{2}{\varepsilon_{\text{OSC}}\varepsilon_0 A^2 q N_A^-}\left(V_{\text{Bias}} - \frac{k_B T}{q}\right) \tag{S7.4}$$

where ε_{OSC} and ε_0 are the dielectric constants of the organic semiconductor layer (approximated with 3) and the vacuum permittivity, respectively. A^2 is the area of the organic layer in cm^2, q the elementary charge and k_B the Boltzmann constant in eV K^{-1}. A minimum of 4 working MIS devices were evaluated per dopant concentration. An exemplary fit of **Equation S7.4** can be found in **Figure S7.4**.

Electron Paramagnetic Resonance Measurements

For EPR measurements on co-evaporated samples, PET foil of 13 μm thickness was used as a substrate. The PET foil was cut into a 2 cm by 5 cm sheet of pre-cut 2 mm stripes and fixed onto a metal carrier plate for co-evaporation of 100 nm Cu(TFSI)$_2$:Spiro-MeOTAD, yielding a constant sample volume of $1 \cdot 10^{-4}$ cm^3 for all doping concentrations. After deposition, the substrate was transferred to the glovebox and the 2 mm stripes were

carefully placed into pre-dried (50 °C, 2 h, vacuum) quartz EPR tubes. The tubes were subsequently sealed using UHU Plus Endfest 300 2-component glue under nitrogen, which was degassed under vacuum after mixing to exclude enclosed oxygen and water. For each doping concentration, at least two individual tubes were prepared to exclude experimental errors. Shipping of the EPR tubes to cooperation facilities was conducted in a hermetically sealed, nitrogen filled metal tube closed with ISO-KF blind flanges on both ends. EPR measurements were carried out in an X-band spectrometer (Magnettech MS-5000) with a resonance frequency of 9.42 GHz and a quality factor of $Q \sim 2000 - 3000$. The experimental settings were optimized to a modulation frequency of $B_{mod} = 0.02$ mT and microwave power of $P_{MW} = 0.8$ W. For temperature-controlled measurements, a continuous-flow helium cryostat (Oxford ESR 900) was used. For quantitative EPR, the double integral (DI) of the measured signals were compared with a reference sample with known spin number (internal reference of the spectrometer).

The spin number is then given by ($s = \frac{1}{2}$): $N_{Sample} = N_{Ref} \cdot \frac{DI_{Ref}}{DI_{Sample}} \cdot \frac{Q_{Sample}}{Q_{Ref}}$ and subsequently scaled up to the entire sample size. When determining N_{Sample}, a constant offset for each measurement occurs depending on the measurement of the reference sample.

Negative Differential Susceptance Mobility Measurement

TEC-7 (XOP glass, $1" \cdot 1" \cdot 2.2$ mm, $6 - 8$ Ω square^{-1}, ~ 500 nm FTO on glass) substrates were etched with dilute HCl/Zn-dust. After obtaining the etched electrode pattern, the substrates were brushed manually with sodium dodecyl sulfate and deionized water, followed by ultrasonication in 2 vol% aqueous Hellmanex-III solution, water, acetone and isopropanol. The substrates were blown dry with nitrogen and pre-treated with O$_3$/UV for 15 min at 50 °C. 100 nm of Cu(TFSI)$_2$:Spiro-MeOTAD films were co-evaporated onto the substrates. To avoid edge effects, a part of the conductive electrodes was masked with Kapton tape, which was removed after the OSC deposition. 100 nm of Au was thermally evaporated on top of the OSC layer using a shadow mask to complete the device stack. The impedance of the devices was measured with a two-electrode setup and increasing electrical field (1 MHz to 100 Hz, 25 points per frequency decade, 0 - 2 V$_{Bias}$ in 15 voltage steps, 10 mV$_{RMS}$) using a Metrohm Autolab PGSTAT204 equipped with an FRA32M module. The NOVA 2.1.4 Software package provided by Metrohm, Germany and custom

MATLAB code was used to process the impedance data. The ITO back contact was connected to the working electrode (WE) and sense (S), while the Au top electrode was connected to the counter electrode (CE) and reference electrode (RE). Devices under test were shielded from ambient light and external electrical fields. Based on frequency-dependent capacitance data of ITO/Spiro-MeOTAD:Cu(TFSI)$_2$/Au devices, a charge carrier mobility can be extracted based on unipolar space-charge limited current theory.[3] Extensive mathematical derivations can be found in the relevant literature.[4,5] Efficient electron/hole injection is required, as the transit-time effect responsible for the mobility determination using the negative differential susceptance method may only be observed, if the injection barrier is smaller than 0.4 eV.[6,7] As demonstrated for (doped) Spiro-MeOTAD, ITO forms ohmic contacts with low injection barriers suitable for this measurement.[8] First described by Martens et al., the mechanism for occurrence of a negative capacitive (= inductive) contribution in a biased, unipolar SCL diode can be formulated as: Injected charges move under the influence of an applied bias voltage, taking on a relaxed space-charge distribution. Upon applying an external AC stimulus (during impedance measurement, **Figure S7.8**), the AC current lags behind due to the finite transit time of the charge carriers across the film thickness, giving an inductive contribution in the measured admittance/impedance for a given frequency range.[9] The inductive contribution induces a characteristic negative capacitance region in a $C(f)$ plot (**Figure S7.9**). This frequency dependent relaxation time can be measured and visualized using the negative differential susceptance method (**Figure S7.11**); ultimately yielding the charge carrier mobility from the transit time. Above the characteristic transit frequency f_{max} the space charge is not able to redistribute within the AC period, and the capacitance approaches the purely geometrical capacitance, treating the organic layer as a regular dielectric.[6] Experimentally, the capacitance of the organic layer was extracted assuming an R$_S$(RC) equivalent circuit from the imaginary Z'' and real Z' impedance (**Figure S7.8**):

$$\hat{Z}(i\omega)_{\mathrm{R(RC)}} = R_{\mathrm{Series}} + \cfrac{1}{i\omega C_{\mathrm{Parallel}} + \cfrac{1}{R_{\mathrm{Parallel}}}} \tag{S7.5}$$

which can be solved for C_{Parallel} to yield

$$C_{\text{Parallel}} = \frac{Im(Z)}{(-Im(Z)^2 + (Re(Z) - R_{\text{S}})^2)\omega} \tag{S7.6}$$

For high parallel resistance, a total RC capacitance may also be calculated according to[10]

$$C_{\text{Series}} = \frac{-\sin(\theta)}{|Z|\omega} \tag{S7.7}$$

The geometric capacitance C_{Geo} of each device was determined in the high frequency region of the $C(f)$-plot (**Figure S7.9**). Together with the measured capacitance, the mobility was extracted from the negative differential susceptance $-\Delta B$ at different electrical fields. The negative differential susceptance $-\Delta B$ can be calculated from

$$-\Delta B = -\omega\big(C(\omega) - C_{geo}\big) \tag{S7.8}$$

$-\Delta B(f)$ displays a global maximum f_{max} (**Figure S7.11**, marked red), which are used to calculate the transit time τ_{tr}

$$\tau_{\text{tr}} = 0.56 f_{\text{max}}^{-1} \tag{S7.9}$$

Local maxima above the transit frequency without physical meaning were discarded. The mobility can then be extracted as

$$\mu = \frac{d^2}{\tau_{\text{tr}} V_{\text{Bias}}} \tag{S7.10}$$

with d being the thickness of the organic layer. The zero-field mobility μ_0 was calculated by extrapolating the obtained Poole-Frenkel type field dependency.

MIS-CELIV (Metal-Insulator-Semiconductor Charge Extraction by Linearly Increasing Voltage)

The MIS-CELIV technique was employed to extract the hole mobility at room temperature. For the MIS-architecture a 25 nm thin insulating layer (Al$_2$O$_3$) was deposited on an FTO-covered substrate *via* atomic layer deposition (H$_2$O/Al(CH$_3$)$_3$, 15 ms pulse duration, 150 °C, 5 s purge time, 278 cycles). These substrates were then transferred to a thermal evaporator where the (doped) Spiro-MeOTAD and the gold contacts were evaporated. By applying a triangular voltage ramp with a waveform generator (RIGOL DG4102) charges were firstly injected and accumulated at the semiconductor-insulating layer and then extracted again *via* the gold contact. The sample response was amplified by a DHPCA-100 (Femto) and recorded with a Tektronix TDS3000 oscilloscope. The obtained data was analyzed according to Sandberg et al.[11] The mobility was calculated by using **Equation S7.11**.

$$\mu = \frac{\pi^2 d_s^2 (1 + f)}{8A * t^2} \left[1 + \frac{\pi^4 k_B T}{2eA * t} \right]^{-1} \tag{S7.11}$$

where d_s is the thickness of the Spiro-MeOTAD, f is the ratio between the between the geometric capacitance of the Spiro-MeOTAD and the insulator layer ($f = \frac{\epsilon_s d_i}{\epsilon_i d_s}$), A is the voltage ramp and t is the time in which the current signal rises from the plateau value j_0 to the 2·j_0 value.

7.7.3 Supporting Measurement Data
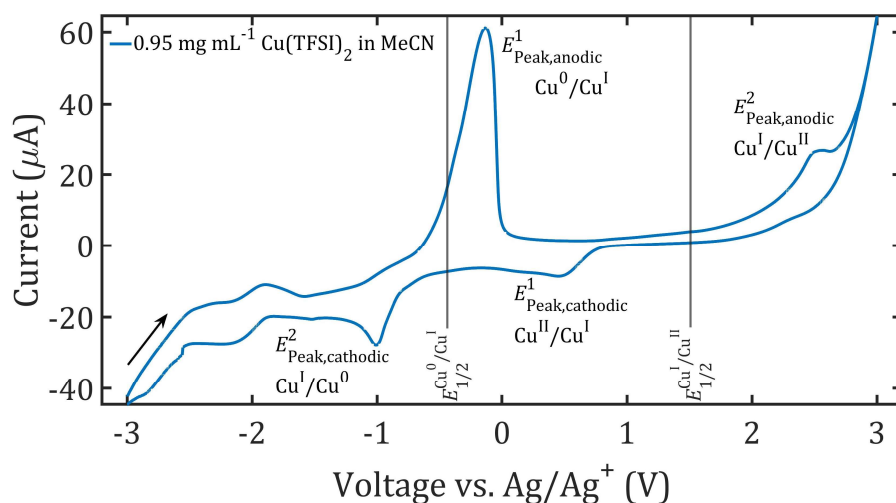
Figure S7.1. Cyclic voltammogram of Cu(TFSI)$_2$ in anhydrous MeCN (0.95 mg mL^{-1}) at 295 K, all voltages referenced to an Ag/AgNO$_3$ non-aqueous reference electrode. The working and counter electrode consists of two platinum disk electrodes with a diameter of 1 mm. $E^1_{Peak,anodic}$ = -131.8 mV; $E^2_{Peak,anodic}$ = +2.567 V; $E^1_{Peak,cathodic}$ = +452.2 mV; $E^2_{Peak,cathodic}$ = -1.008 V; $E^{Cu(0)/Cu(I)}_{1/2}$ = -438.5 mV; $E^{Cu(I)/Cu(II)}_{1/2}$ = +1.510 V.
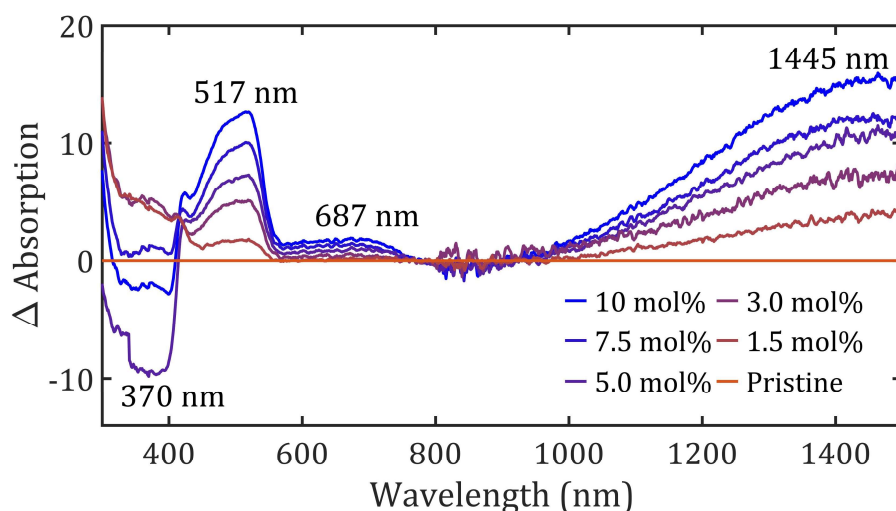
Figure 7.2. Differential plot of Cu(TFSI)$_2$ doped Spiro-MeOTAD UV/Vis/NIR absorbance compared to pristine Spiro-MeOTAD for different doping concentrations given in the legend (**Figure 7.1c**).
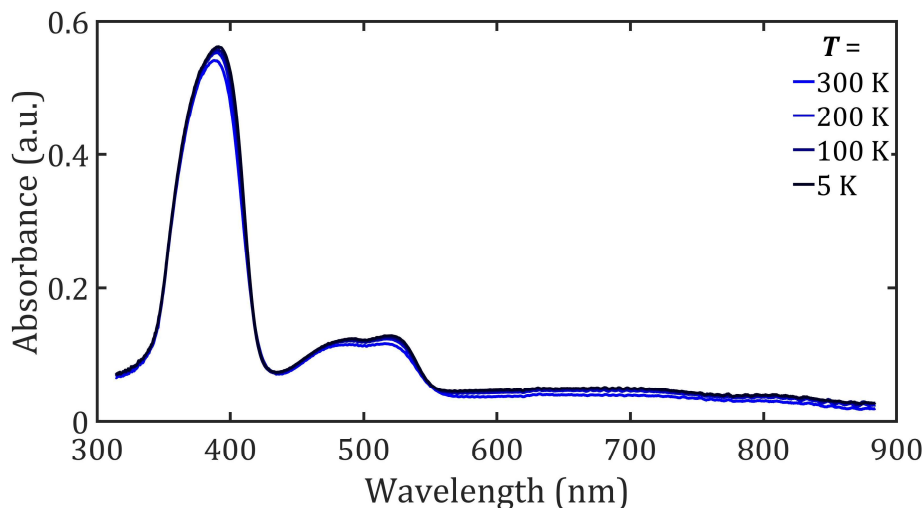
Figure 7.3. Temperature dependent UV/Vis/NIR absorption spectra of 10 mol% Cu(TFSI)$_2$ doped Spiro-MeOTAD thin films under inert atmosphere at 300 K to 5 K.
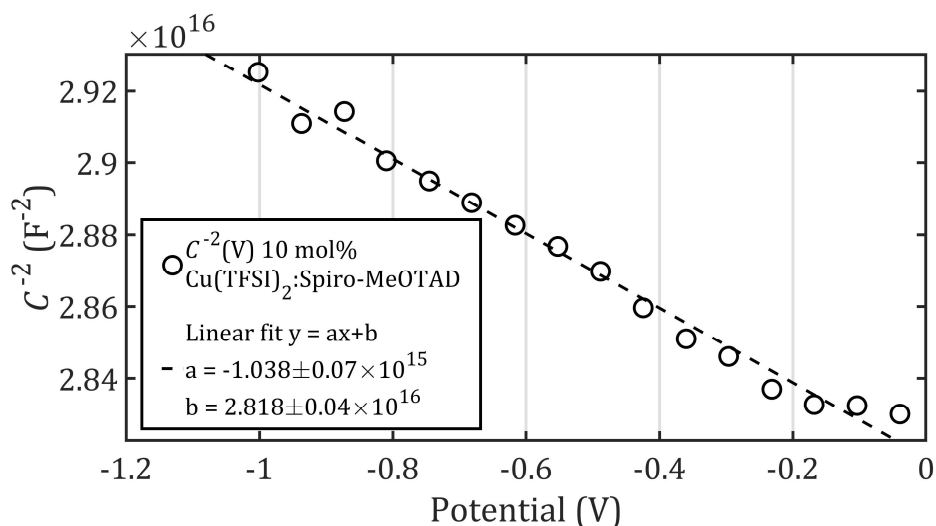
Figure 7.4. Exemplary fit of **Equation S7.4** to the voltage dependent inverse squared capacitance of 10 mol% doped, co-evaporated films in a FTO/Al$_2$O$_3$/Hexamethyldisilazane/Cu(TFSI)$_2$ doped Spiro-MeOTAD/Au structure. The slope yields a charge carrier density N_{A^-} of $(2.8 \pm 0.2) \cdot 10^{19}$ cm^{-3} for $\varepsilon_{OSC} = 3$, $A^2 = 0.04$ cm^2 and $T = 300$ K in this sample.
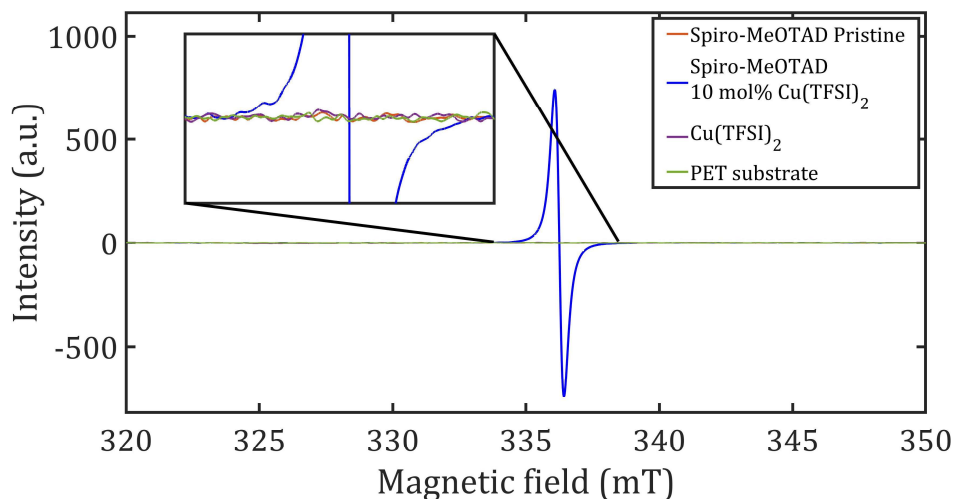
Figure 7.5. EPR spectra for different samples investigating Spiro-MeOTAD doped with Cu(TSFI)$_2$. Doping concentration of 10.4 mol% leads to a Lorentzian EPR signal while undoped Spiro-MeOTAD shows no intrinsic doping. The PET-substrate and Cu(TFSI)$_2$ have no measurable EPR signal. EPR parameters (modulation amplitude B_{mod} and microwave power P_{MW}) were optimized for highest signal of 10.4 mol%.
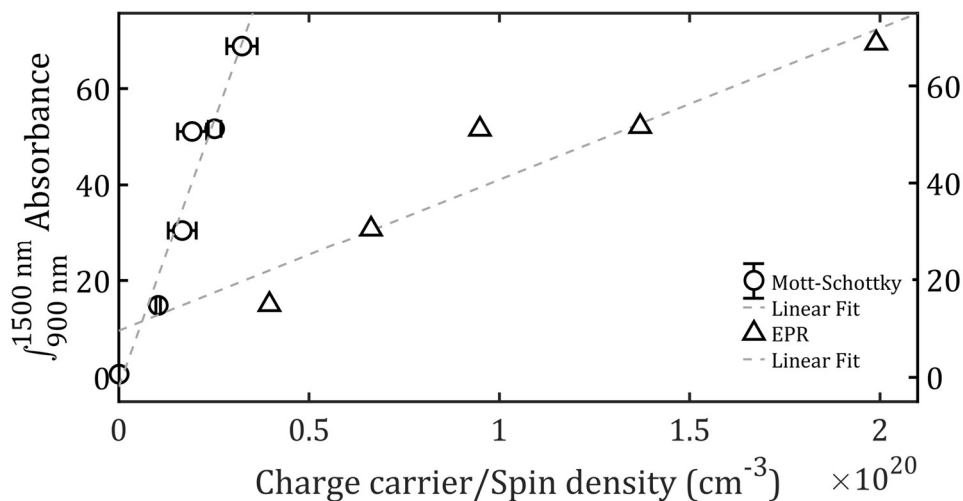
Figure 7.6. Linear correlation (grey dotted line) between charge carrier density N_{A^-} obtained from Mott-Schottky experiments (black circles), as well as spin density N_{Spins} obtained from EPR experiments (black triangles) and the integral of the polaron peak between 900 nm and 1500 nm for a series of doped films (see UV/Vis/NIR of doped, co-evaporated thin films in **Figure 7.1c**).
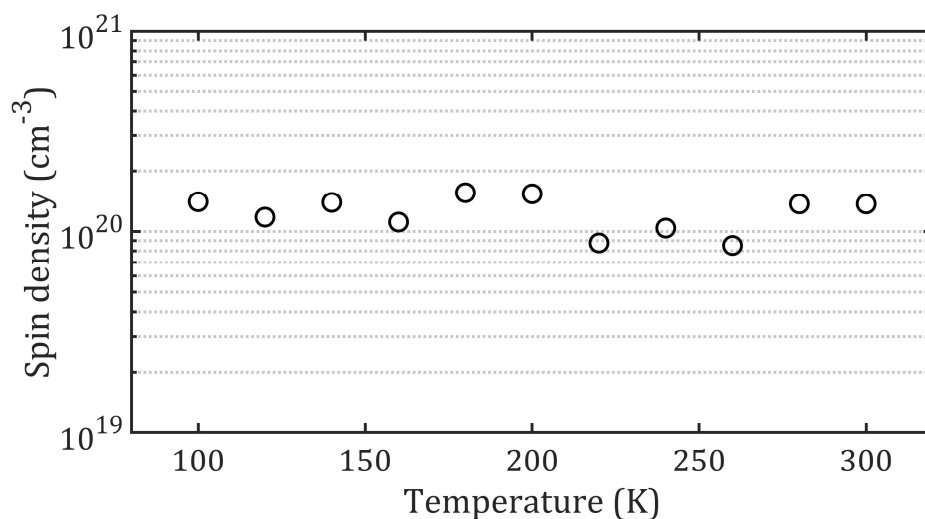
Figure S7.7. Spin density of 7.5 mol% Cu(TFSI)$_2$ doped Spiro-MeOTAD sample as a function of the temperature. Here, the spin density was referenced to the internal spin reference corrected for the cavity temperature. $B_{mod} = 0.02$ mT, microwave power $P_{MW} = 0.8$ mW.
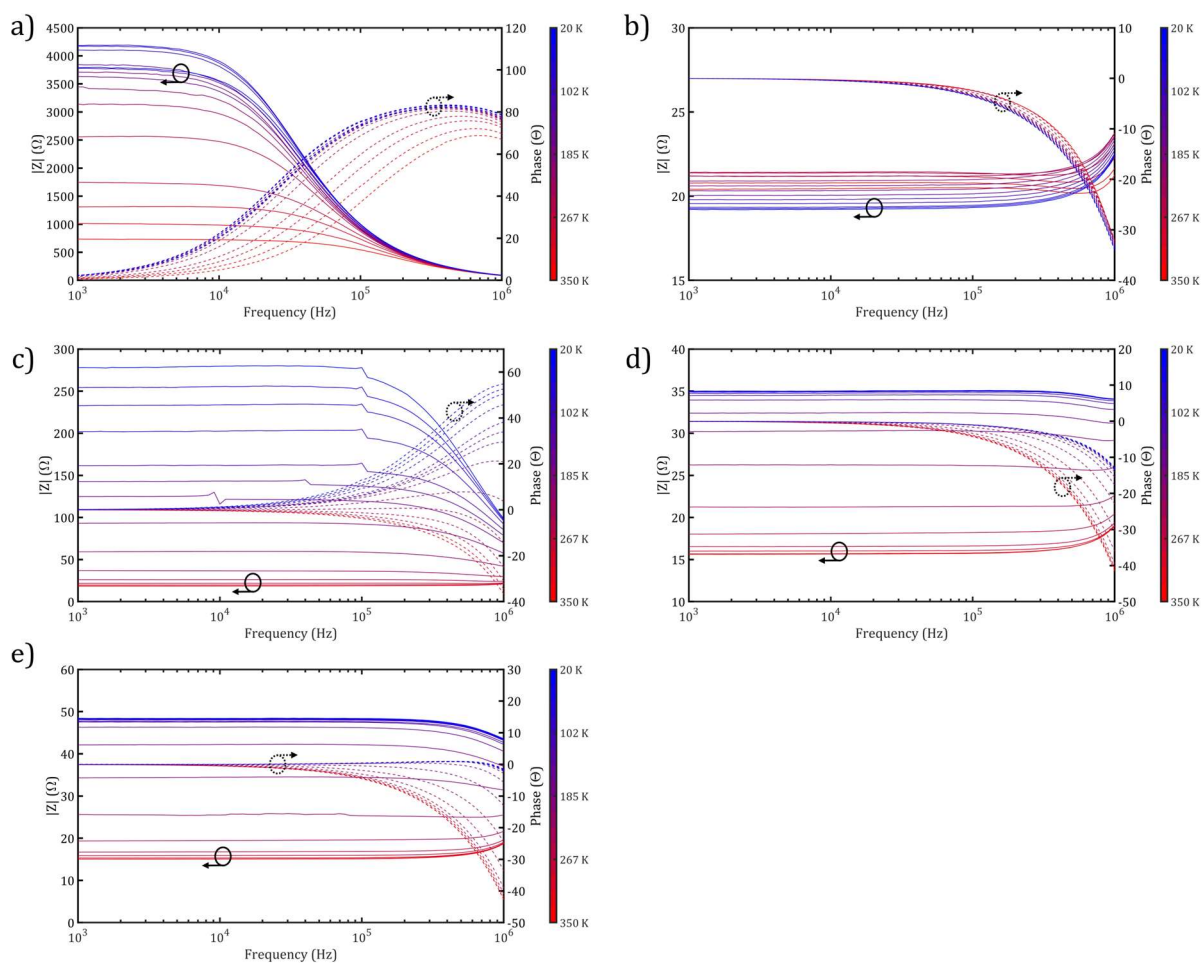
Figure S7.8. Temperature- (color bar) and frequency (x-axis) dependent impedance |Z| (left y-axis, solid lines) and phase angle (right y-axis, dashed lines) of Cu(TFSI)$_2$ doped Spiro-MeOTAD. Determined from impedance measurements on FTO/Cu(TFSI)$_2$:Spiro-MeOTAD/Au devices inside a He cryostat from 350 K to 20 K with a) 0 mol%, b) 1.5 mol%, c) 3 mol%, d) 5 mol% and e) 10 mol% Cu(TFSI)$_2$. The electrical field was kept constant at F = 100 kV cm^{-1}.
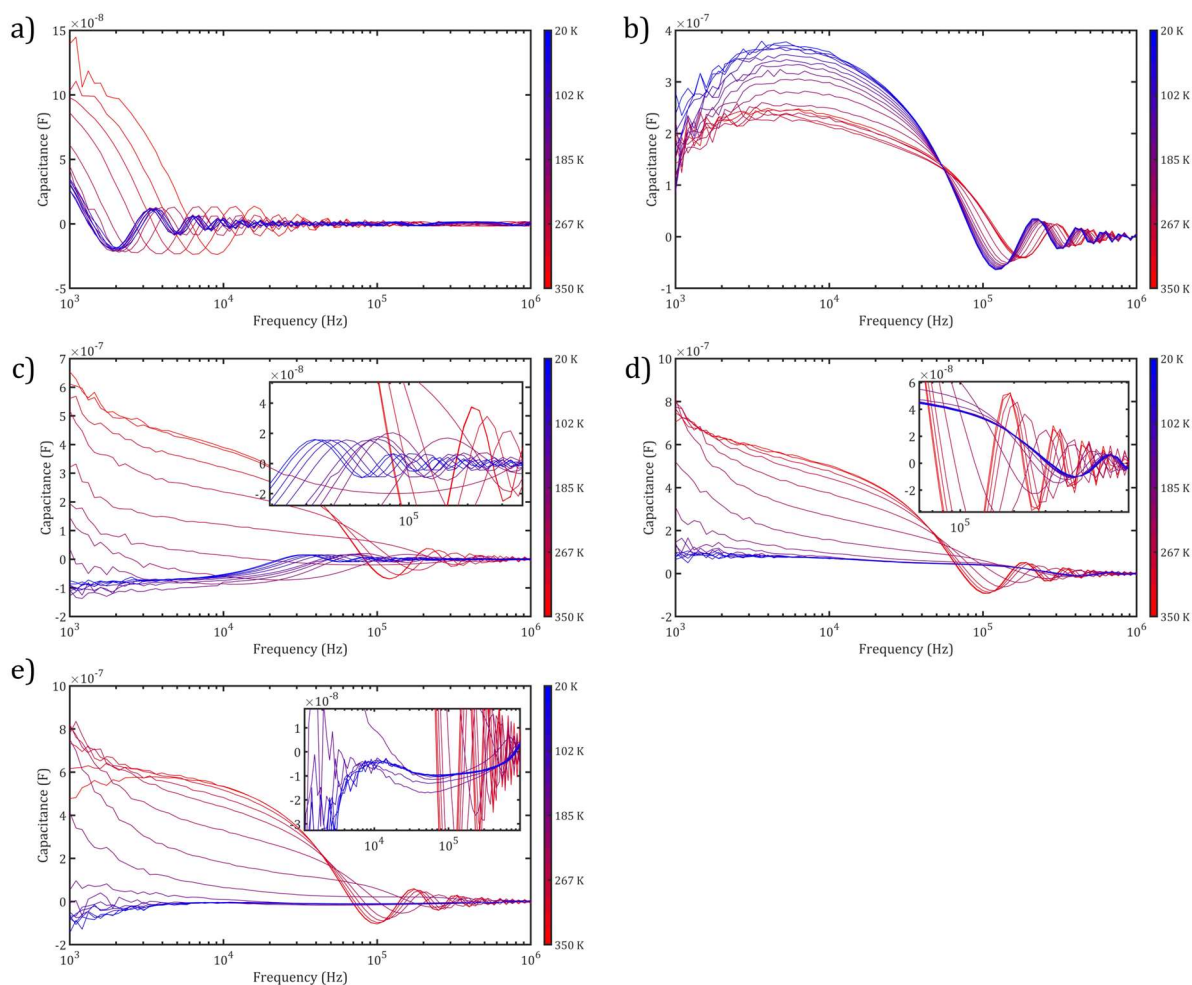
Figure S7.9. Temperature- (color bar) and frequency (x-axis) dependent capacitance C of SpiroMeOTAD doped with a) 0 mol%, b) 1.5 mol%, d) 3 mol%, e) 5 mol% and f) 10 mol% Cu(TFSI)₂. C was calculated according to **Equation S7.6** or **Equation S7.7** from the impedance data shown in **Figure S7.7**. Determined from impedance measurements on FTO/Cu(TFSI)₂:Spiro-MeOTAD/Au devices inside a He cryostat from 350 K to 20 K. For 3 mol%, 5 mol% and 10 mol%, insets are given for better visualization of the low-temperature $C(f)$ behaviour (axis units identical main plot). The electrical field was kept constant at F = 100 kV cm⁻¹.
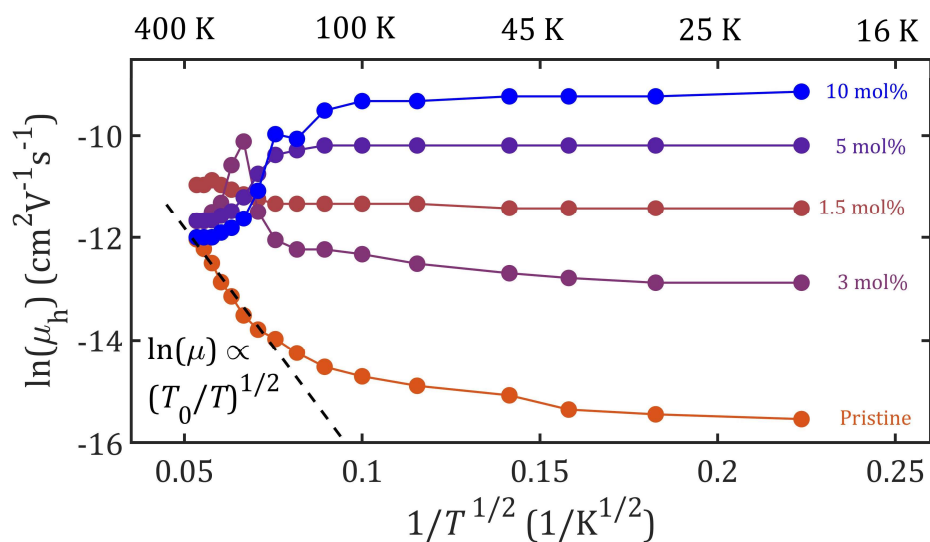
Figure S7.10. Temperature dependent hole mobilities μ_h of Cu(TFSI)$_2$ doped Spiro-MeOTAD, determined from impedance measurements on FTO/Cu(TFSI)$_2$:Spiro-MeOTAD/Au devices using the negative differential susceptance $-\Delta B$. Black dashed fit line shows typical ES-VRH behaviour $\ln(\mu_h) \propto (T_0/T)^{1/2}$ in the case of pristine Spiro-MeOTAD sample. All values were obtained at a constant electrical field F = 100 kV cm^{-1}.
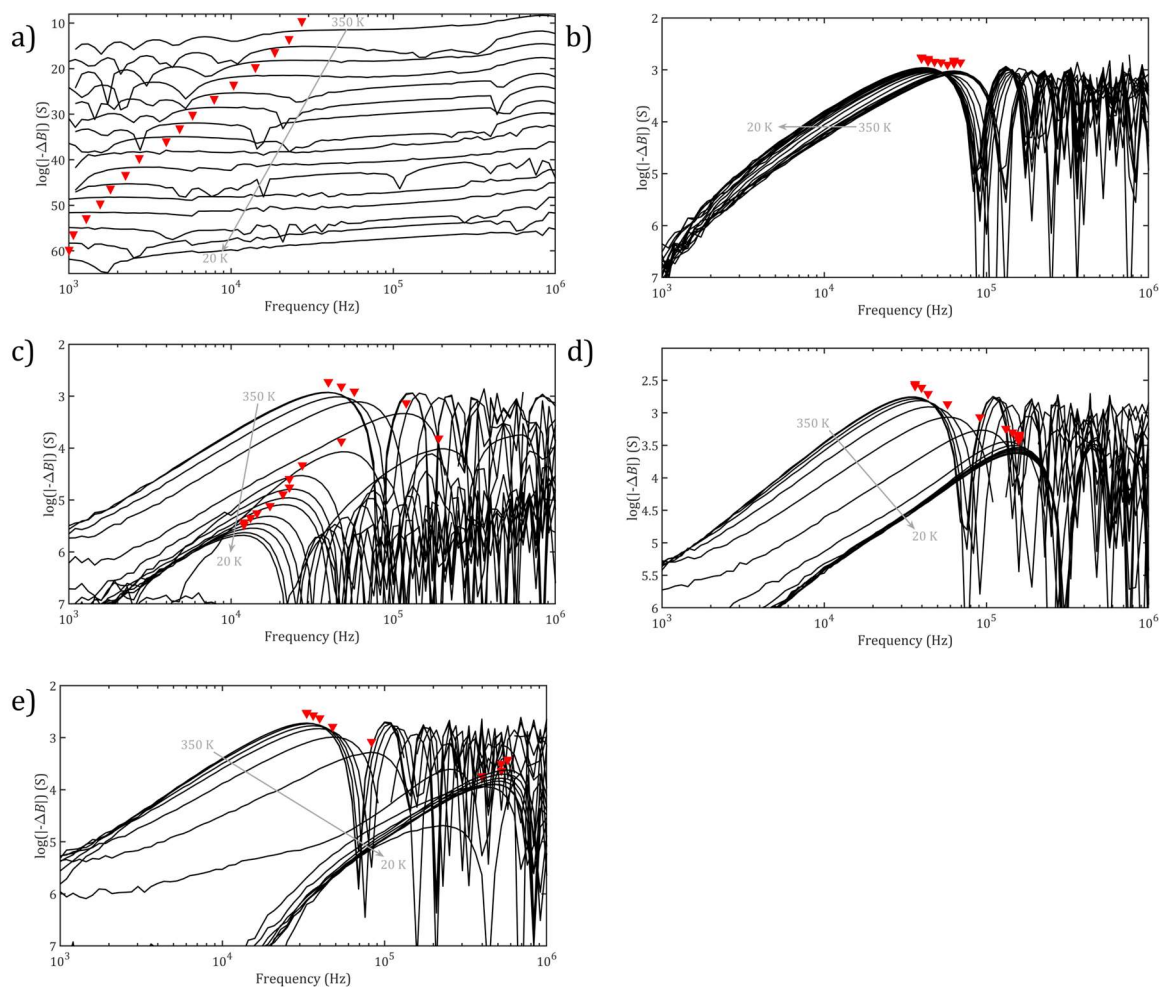
Figure S7.11. Temperature dependent logarithmic negative differential susceptance log(-ΔB) of Cu(TFSI)$_2$ doped Spiro-MeOTAD, determined from impedance measurements on FTO/Cu(TFSI)$_2$:Spiro-MeOTAD/Au devices inside a He cryostat from 350 K to 20 K. From the peak transition frequencies marked with red triangles, the temperature dependent hole mobility μ_h can be obtained, depicted in **Figure 7.3b**. Following Cu(TFSI)$_2$ concentrations were measured: a) 0 mol%, b) 1.5 mol%, c) 3 mol%, d) 5 mol%, e) 10 mol%. The electrical field was kept constant at F = 100 kV cm^{-1}.
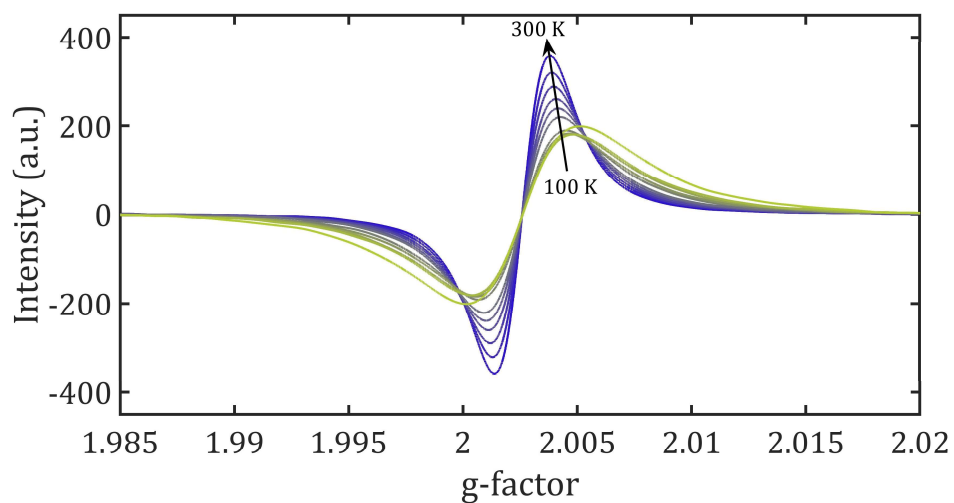
Figure S7.12. Temperature dependent EPR spectrum of Spiro-MeOTAD co-evaporated with 7.5 mol% Cu(TFSI)$_2$ going from 100 K (starting temperature) to 300 K.
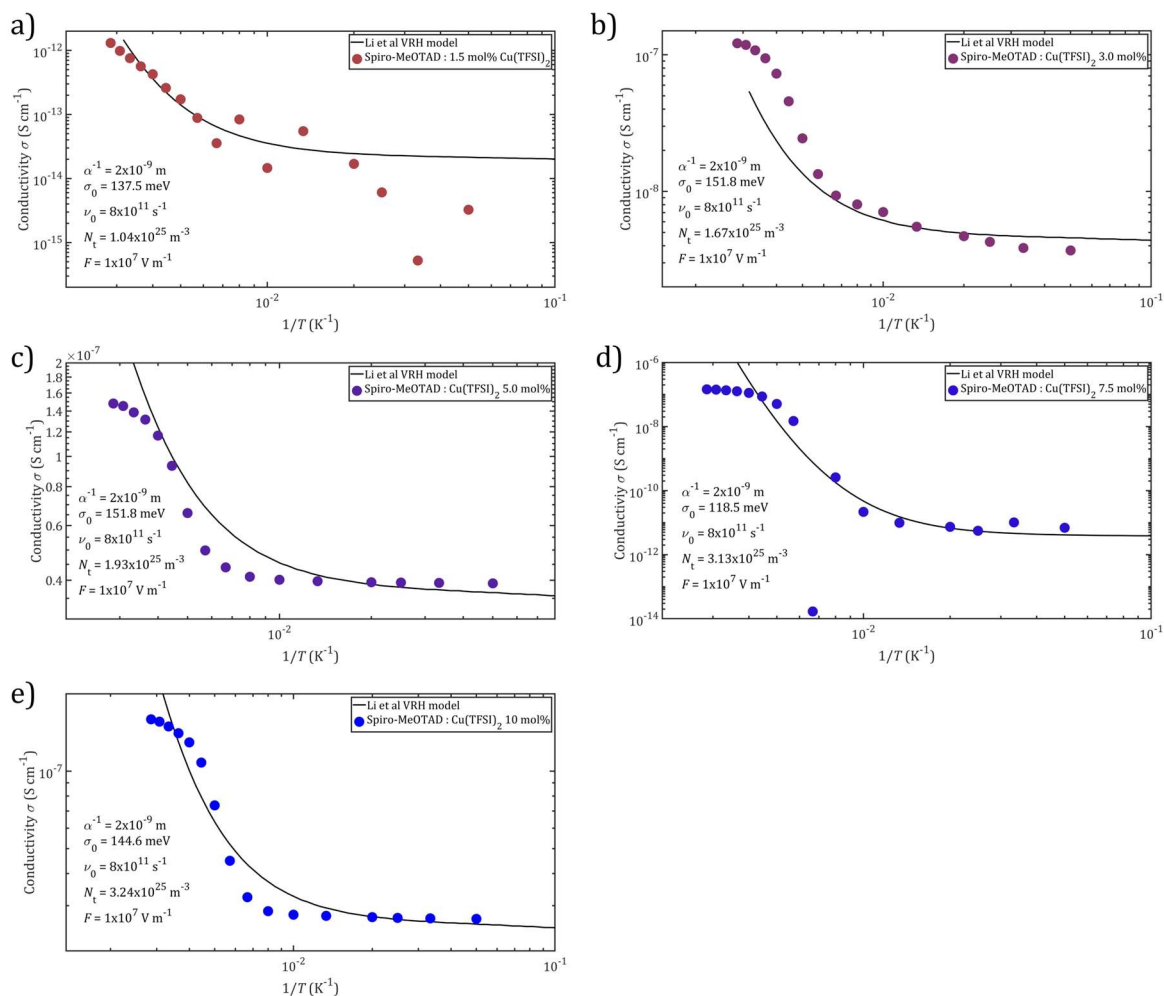
Figure S7.13. Temperature dependent conductivities (circles) of a) 1.5 mol%, b) 3.0 mol%, c) 5.0 mol%, d) 7.5 mol%, e) 10 mol% Cu(TFSI)$_2$ doped, co-evaporated FTO/Cu(TFSI)$_2$:Spiro-MeOTAD/Au devices (data taken from **Figure 7.3a**). A variable range hopping model modified by Li et al. for high carrier densities and electrical fields was fitted (solid lines) with the parameters shown in each plot as a calculation input.[12] Here, α^{-1} is the inverse localized length, σ_0 the Gaussian DOS width, ν_0 the attempt-to-jump frequency, N_t the charge carrier density and F the electrical field (assuming 100 nm active layer thickness).
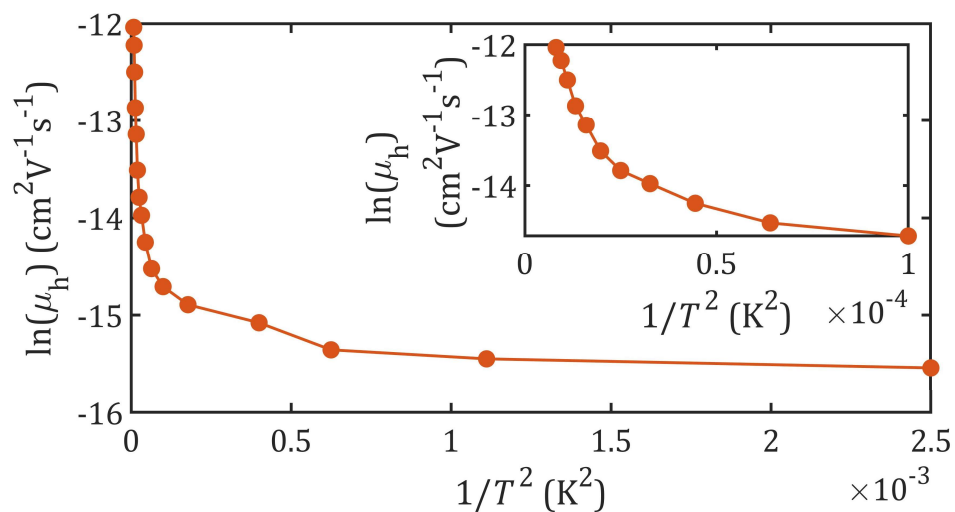
Figure S7.14. Logarithmic hole mobility μ_h of pristine evaporated Spiro-MeOTAD versus the inverse square root of the temperature (data taken from **Figure 7.3b**). The inset shops a detailed plot of μ_h between 350 K and 100 K.
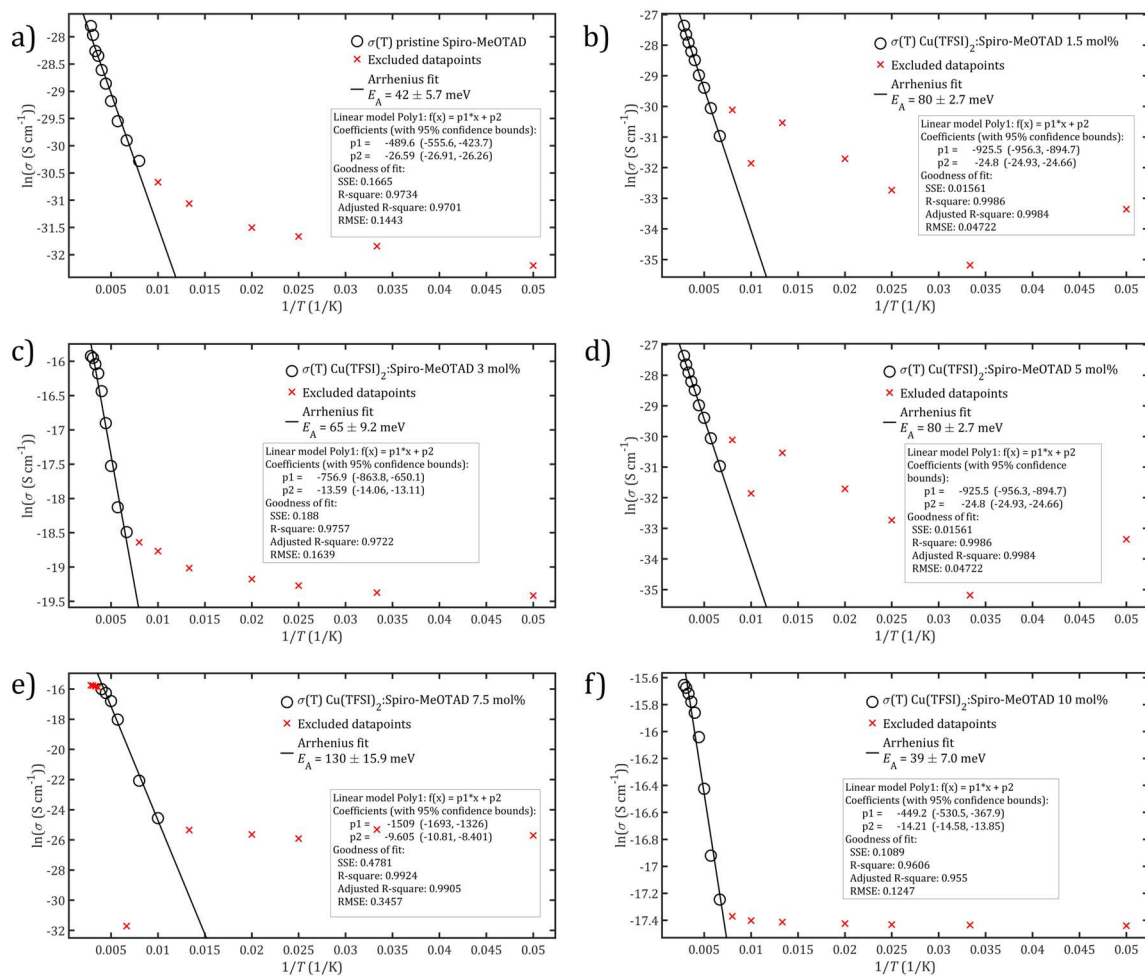
Figure S7.15. Temperature dependent conductivities (circles) of a) 0 mol% b) 1.5 mol%, c) 3.0 mol%, d) 5.0 mol%, e) 7.5 mol%, f) 10 mol% Cu(TFSI)$_2$ doped, co-evaporated FTO/Cu(TFSI)$_2$:SpiroMeOTAD/Au devices (100 nm active layer thickness; data taken from **Figure 7.3a**). Excluded datapoints below non-linearity shown in red crosses. Solid lines represent the linear Arrhenius fit to yield the thermal activation energy of conductivity $E_{A,\sigma}$ for the temperature range 400 K to 350 K summarized in **Figure S7.16**.
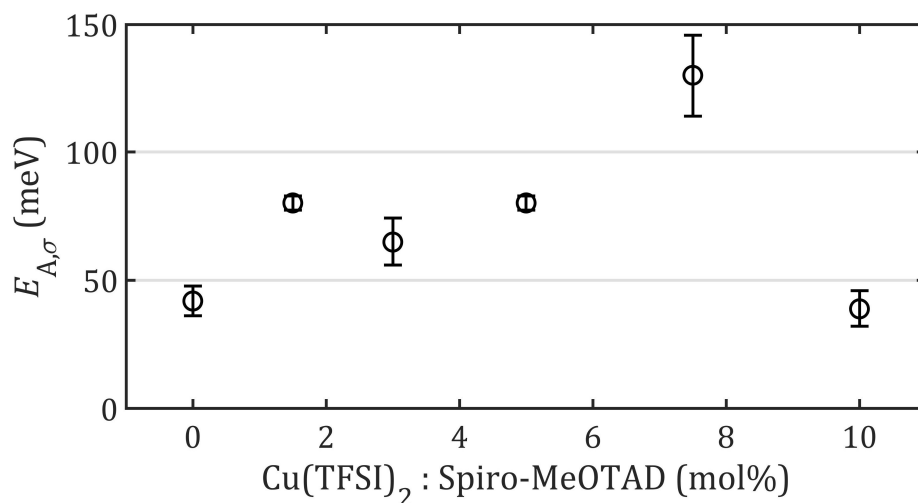
Figure S7.16. Thermal activation energy of conductivity E$_{A,\sigma}$ of 0 – 10 mol% Cu(TFSI)$_2$ doped, co-evaporated Spiro-MeOTAD thin films (100 nm).
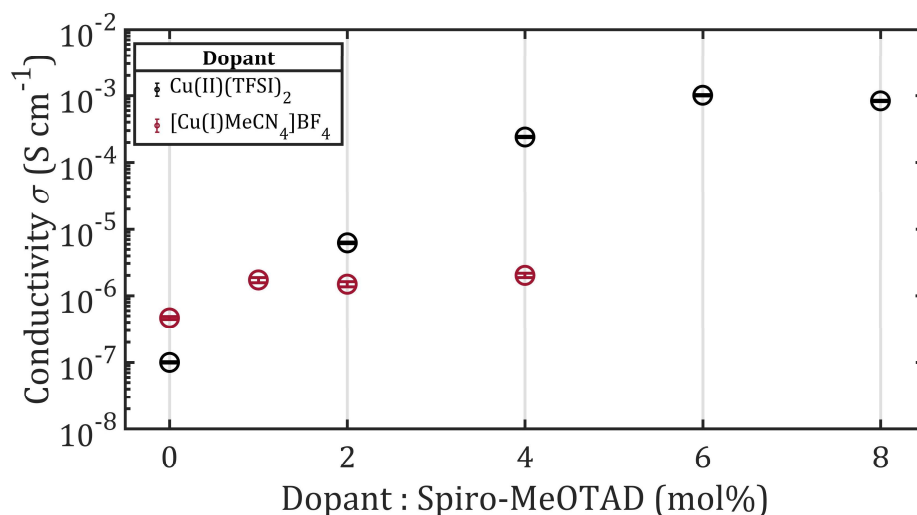
Figure S7.17. Thin film conductivities of Cu(TFSI)$_2$ doped, co-evaporated Spiro-MeOTAD (black circles) and a solution processed [Cu(MeCN)$_4$]BF$_4$:Spiro-MeOTAD mixture (red circles) at different doping/additive concentrations (black circles).
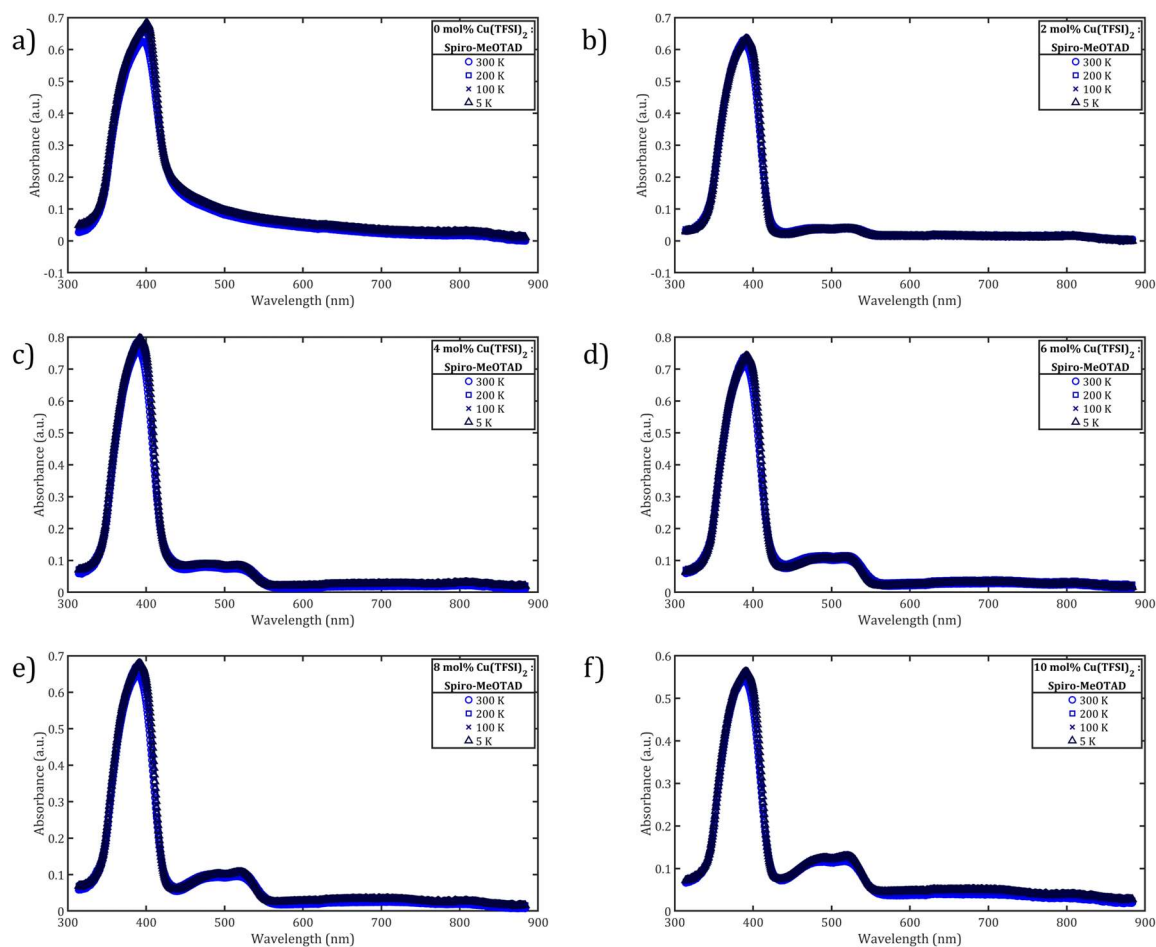
Figure S7.18. Temperature dependent thin film absorption measurements of co-evaporated Spiro-MeOTAD:Cu(TFSI)$_2$ samples at various doping ratios ranging from 0 mol% a) to 10 mol% f). Measured at 300 K (blue circles), 200 K (blue boxes), 100 K (black crosses) and 5 K (black triangles).
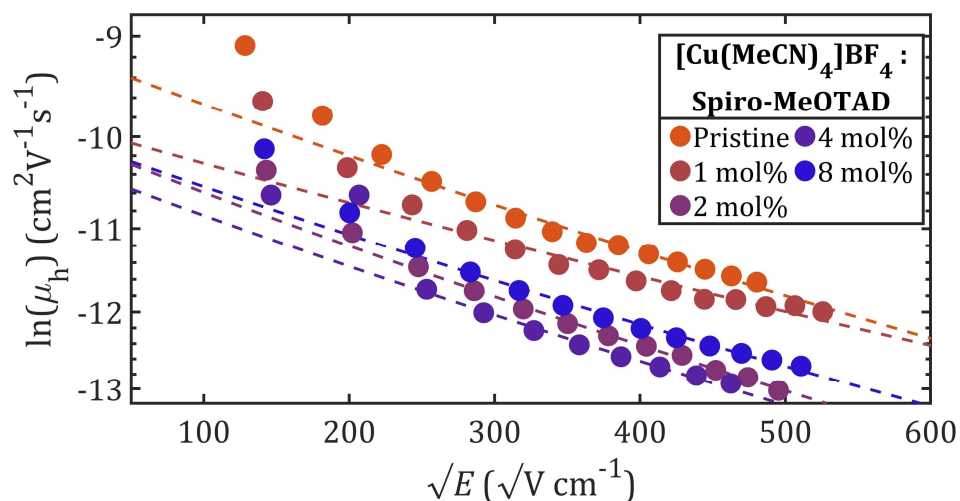
Figure S7.19. Field dependent mobility of solution processed Spiro-MeOTAD thin films mixed with different molar amounts of [Cu(MeCN)$_4$]BF$_4$. Linear fits yield the zero-field mobility μ_0 at the y-intercept. All μ_h values measured using the -ΔB method on FTO/[Cu(MeCN)$_4$]BF$_4$:Spiro-MeOTAD/Au devices.
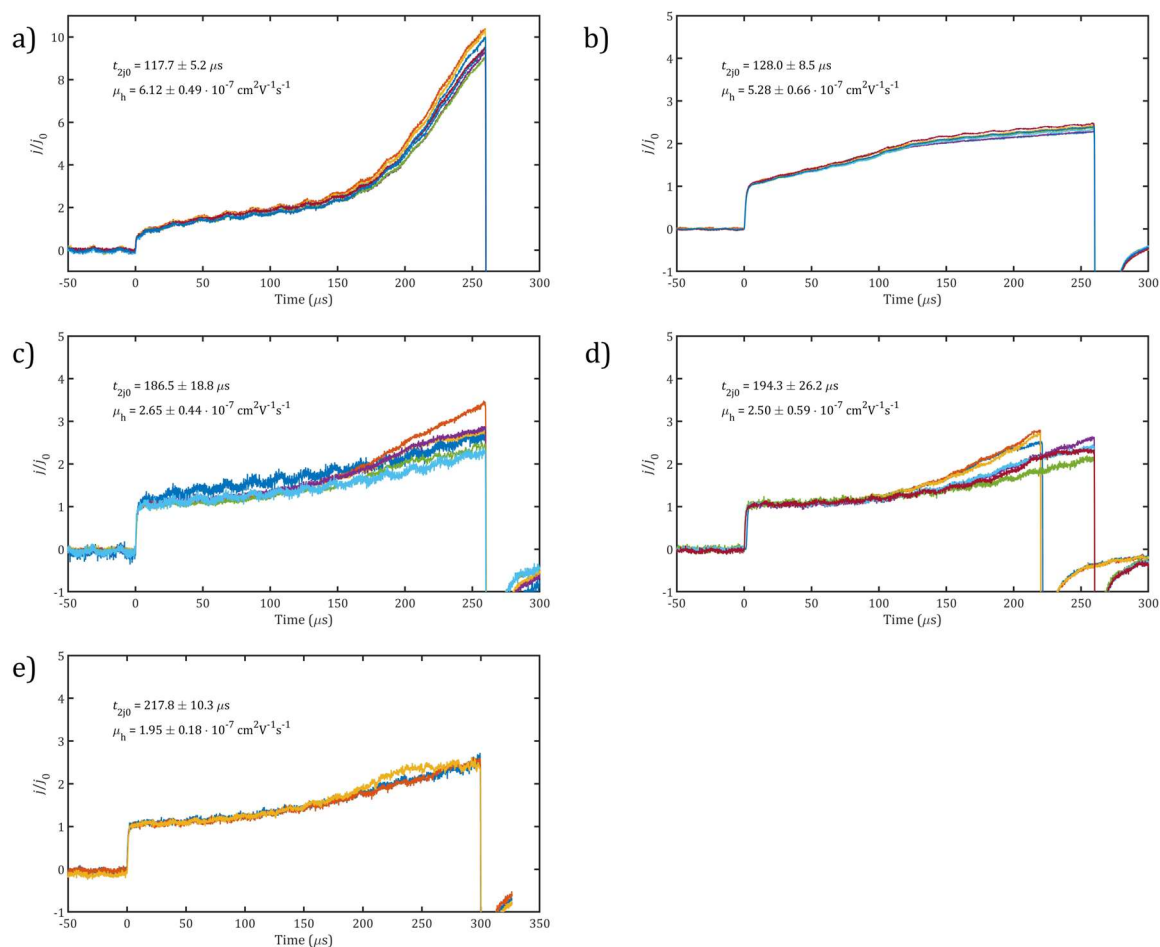
Figure S7.20. CELIV measurements on FTO/Al₂O₃ (25 nm) /Spiro-MeOTAD:Cu(TFSI)₂ (200 nm)/Au devices. An offset voltage of -3 V was applied and the charges were extracted using a ramp of 0.05 V μs⁻¹. a) pristine Spiro-MeOTAD, b) 1.5 mol% of Cu(TFSI)₂, c) 3.0 mol% of Cu(TFSI)₂, d) 5 mol% of Cu(TFSI)₂, e) 7.5 mol% of Cu(TFSI)₂.
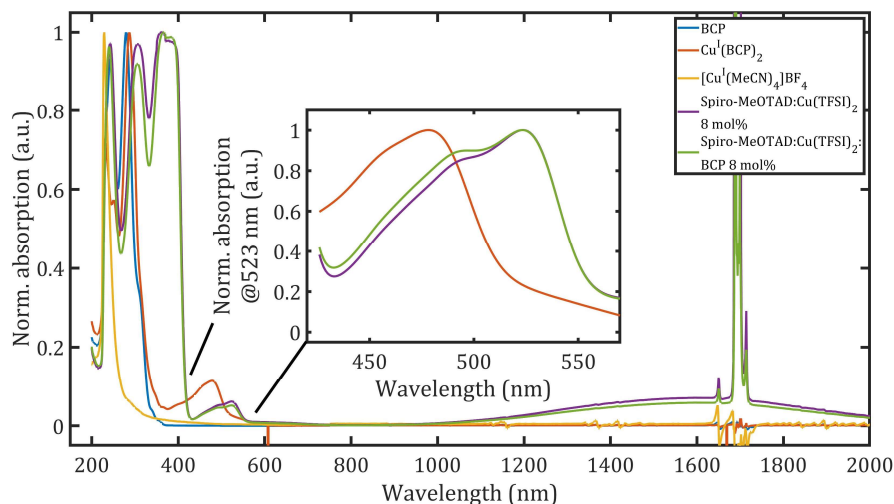
Figure S7.21. Normalized UV/Vis/NIR solution spectra of BCP (blue), $Cu^I(BCP)_2$ (red), $[Cu^I(MeCN)_4]BF_4$ (yellow), Spiro-MeOTAD:$Cu(TFSI)_2$ 8 mol% (purple) and Spiro-MeOTAD:$Cu(TFSI)_2$:BCP 8 mol% (green, 1:1 molar ratio $Cu(TFSI)_2$:BCP) in DCM (0.02 mg mL^{-1} of BCP, $Cu^I(BCP)_2$ and Spiro-MeOTAD). The inset shows the region of the oxidized Spiro-MeOTAD HOMO/HOMO-1/LUMO/LUMO-1 transition peak at 523 nm, normalized to this peak absorption. The formation of $Cu^I(BCP)_2$ complex (red) increases the absorption at 478 nm for the solution with BCP (green) compared to the solution without BCP (purple). All spectra measured under inert atmosphere and in anhydrous solvents.
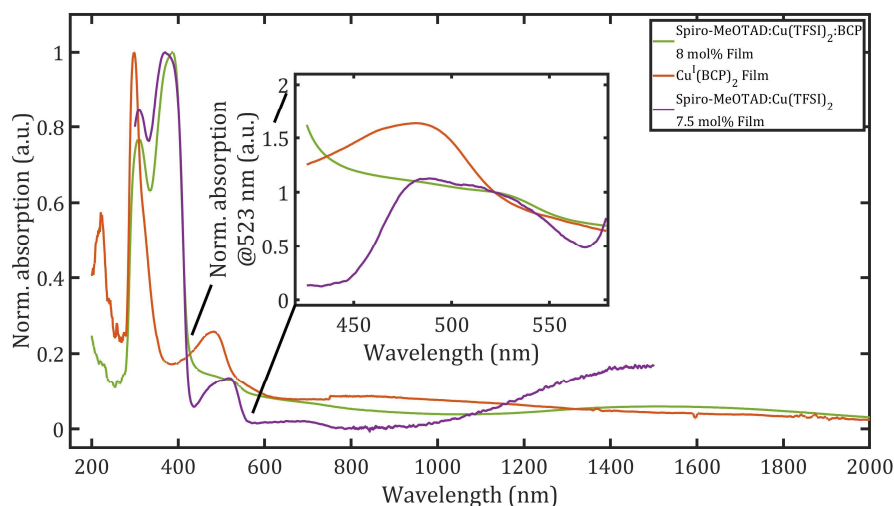
Figure S7.22. Normalized UV/Vis/NIR thin film spectra on quartz substrates of solution processed Cu^I(BCP)$_2$ (red), co-evaporated Spiro-MeOTAD:Cu(TFSI)$_2$ 7.5 mol% (yellow) and solution processed Spiro-MeOTAD:Cu(TFSI)$_2$:BCP 8 mol% (blue, 1:1 molar ratio Cu(TFSI)$_2$:BCP). The inset shows the region of the oxidized Spiro-MeOTAD HOMO/HOMO-1/LUMO/LUMO-1 transition peak at 523 nm, normalized to this peak absorption. The formation of Cu^I(BCP)$_2$ complex (red) increases the absorption below 478 nm for the film with BCP (blue) compared to the solution without BCP (yellow). All spectra measured under inert atmosphere.
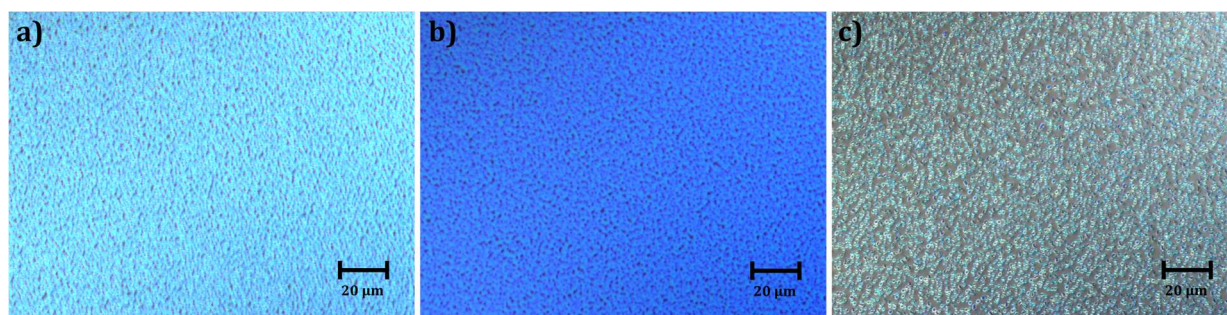
Figure S7.23. Unpolarized light microscopic images with a magnification of 50x showing the morphology of solution processed films of a) Cu(TFSI)$_2$(8 mol%):Spiro-MeOTAD, b) Cu(TFSI)$_2$(8 mol%):BCP(8 mol%):Spiro-MeOTAD, c) [Cu(MeCN)$_4$]BF$_4$(8 mol%):Spiro-MeOTAD. Scale bar: 20 µm.
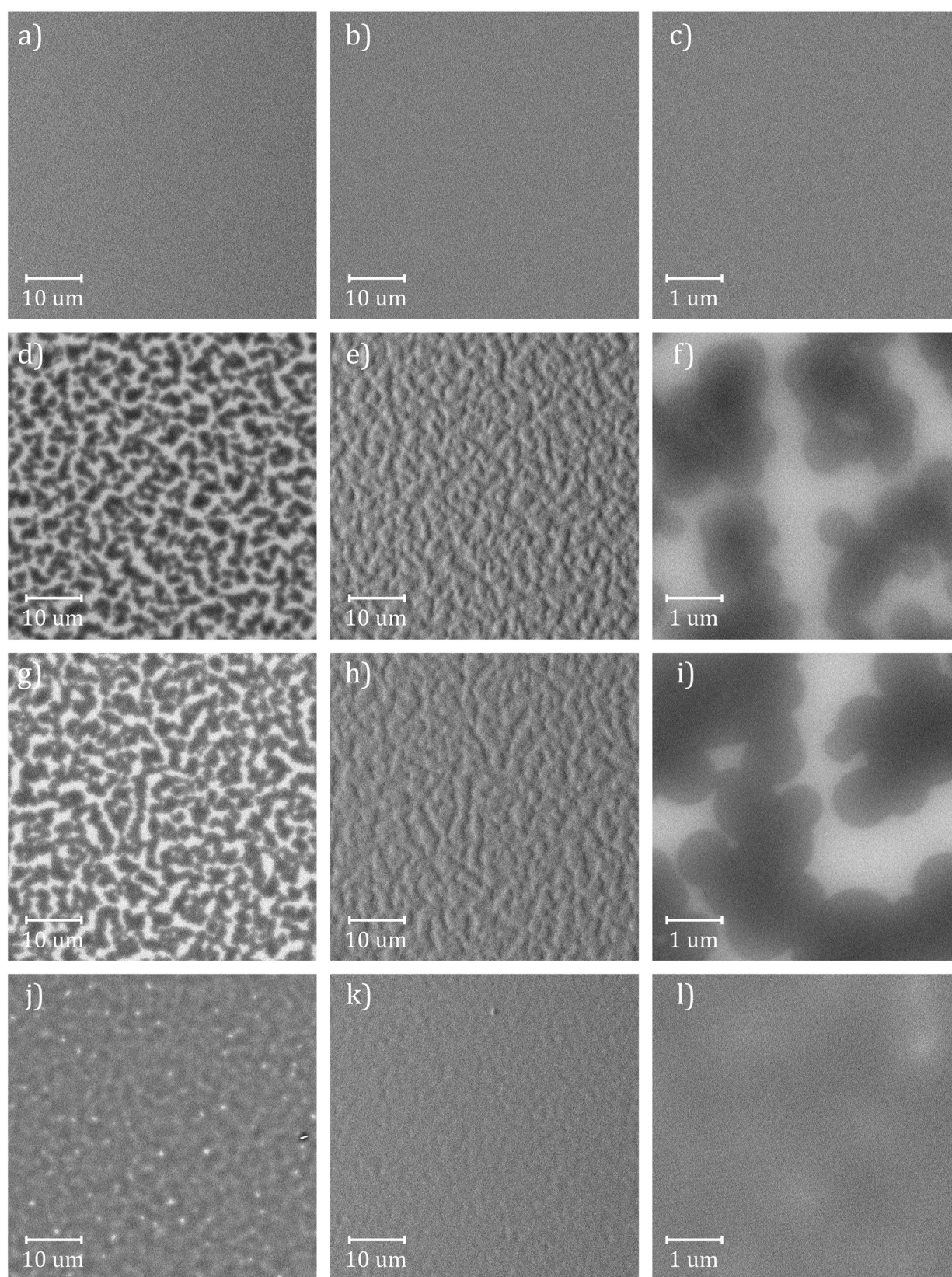
Figure S7.24. SEM micrographs of pristine Spiro-MeOTAD a)-c), [Cu(MeCN)₄]BF₄(8 mol%):SpiroMeOTAD d)-f), Cu(TFSI)₂(8 mol%):Spiro-MeOTAD g)-i) and Cu(TFSI)₂(8 mol%):BCP(8 mol%):Spiro-MeOTAD j)-l) thin films (ca. 100 nm) on

silicon substrates at two different magnifications. b), e), h) and k) were recorded using the topographic detector mode.

Figure S7.25. Microscopic images of [Spiro-MeOTAD]$^+$[Cu^I(TFSI)$_2$]$^-$ crystals before the hexane washing step. Lines in the background are 2 mm by 1 mm.

Doping Efficiency Calculation

The doping efficiency η_{Dop} was calculated from the amount of ionized Cu^I dopant molecules N_{A^-} obtained from Mott-Schottky measurements, and the total number of dopants N_A per unit volume. From the mole fraction of the dopant $x_{Cu(TFSI)2}$ and molar masses of Spiro-MeOTAD M_{Spiro} and Cu(TFSI)$_2$ $M_{Cu(TFSI)2}$, the average molar mass $\bar{M}$ of the mixture at a given doping concentration can be determined.

$$x_{Cu(TFSI)2} = \frac{C_{Dop}}{100} \tag{S7.12}$$

$$\bar{M} = x_{Cu(TFSI)2}M_{Cu(TFSI)2} + \left(1 - x_{Cu(TFSI)2}\right)M_{Spiro} \tag{S7.13}$$

Which in turn gives the mass fraction $w_{Cu(TFSI)2}$ of the dopant (**Equation S7.14.**).

$$w_{Cu(TFSI)2} = x_{Cu(TFSI)2}\frac{M_{Cu(TFSI)2}}{\bar{M}} \tag{S7.14}$$

From $w_{Cu(TFSI)2}$, the average density ρ_{mix} of the solid mixture is calculated. For Spiro-MeOTAD and Cu(TFSI)$_2$, densities of $\rho_{Spiro} = (1.159 \pm 0.003)$ g cm^{-3} and $\rho_{Cu(TFSI)2} = (2.925 \pm 0.019)$ g cm^{-3} were determined experimentally.

$$\rho_{mix} = \frac{1}{\dfrac{w_{Cu(TFSI)2}}{\rho_{Cu(TFSI)2}} + \dfrac{1 - w_{Cu(TFSI)2}}{\rho_{Spiro}}} \tag{S7.15}$$

Using ρ_{mix}, $\bar{M}$ and the Avogadro constant $N_{Avogadro}$, the absolute number of molecules per unit volume N_0 (dopant and Spiro-MeOTAD) for a given doping concentration can be found.

$$N_0 = \frac{N_{Avogadro}\rho_{mix}}{\bar{M}} \tag{S7.16}$$

For a certain doping concentration C_{Dop} and volume, the number of dopant molecules/acceptors N_A present is calculated according to **Equation S7.17**.

$$N_A = \frac{C_{Dop}}{100} N_0 \tag{S7.17}$$

Which can be used to determine the percentage of ionized acceptors η_{Dop} from the density of ionized acceptors N_A^- determined by Mott-Schottky experiments.

$$\eta_{Dop} = 100 \frac{N_A^-}{N_A} \tag{S7.18}$$

The error of η_{Dop} may be determined by propagation of uncertainty, considering the main error sources ρ_{Spiro}, $\rho_{Cu(TFSI)2}$ and N_A^- as not correlated.

$$N_A = \frac{C_{Dop}}{100} N_0$$

7.7.4 References

[1] G. Krauss, A. Hochgesang, J. Mohanraj, M. Thelakkat, *Macromol. Rapid Commun.* **2021**, *42*, 2100443.

[2] J. Mohanraj, M. Stihl, E. Simon, S. von Sicard, G. Schmidt, M. Fleischer, C. Neuber, M. Thelakkat, *ACS Appl. Energy Mater.* **2019**, *2*, 3469-3478.

[3] S. Ishihara, T. Okachi, H. Naito, *Thin Solid Films* **2009**, *518*, 452-456.

[4] N. D. Nguyen, M. Schmeits, *Phys. Rev. B* **2007**, *75*, 075307.

[5] H. C. F. Martens, H. B. Brom, P. W. M. Blom, *Phys. Rev. B* **1999**, *60*, R8489.

[6] T. Okachi, T. Nagase, T. Kobayashi, H. Naito, *Thin Solid Films* **2008**, *517*, 1331.

[7] T. Okachi, T. Nagase, T. Kobayashi, H. Naito, *Jpn. J. Appl. Phys.* **2008**, *47*, 8965.

[8] B. Li, S. Zhang, F. Xia, Y. Huang, X. Ran, Y. Xia, Y. Chen, W. Huang, *J. Appl. Phys.* **2020**, *128*, 085501.

[9] H. C. F. Martens, W. F. Pasveer, H. B. Brom, J. N. Huiberts, P. W. M. Blom, *Phys. Rev. B* **2001**, *63*, 125328.

[10] E. J. Meijer, A. V. G. Mangnus, C. M. Hart, D. M. de Leeuw, T. M. Klapwijk, *Appl. Phys. Lett.* **2001**, *78*, 3902-3904.

[11] O. J. Sandberg, M. Nyman, S. Dahlström, S. Sandén, B. Törngren, J.-H. Smått, R. Österbacka, *Appl. Phys. Lett.* **2017**, *110*, 153504.

[12] L. Li, N. Lu, M. Liu, *J. Appl. Phys.* **2014**, *116*, 164504.

8. Highly Efficient n-Doping via Proton Abstraction of an Acceptor1-Acceptor2 Alternating Copolymer toward Thermoelectric Application

Adrian Hochgesang[†], Andreas Erhardt[†], John Mohanraj[§], Meike Kuhn[‡], Eva M. Herzig[‡], Selina Olthof[§], and Mukundan Thelakkat[†∥]*

[†] Applied Functional Polymers, University of Bayreuth, Universitätsstr. 30, 95440 Bayreuth, Germany

[§] Department of Physical Chemistry, University of Cologne, Greinstraße 4-6, Köln 50939, Germany

[‡] Dynamics and Structure Formation – Herzig Group, University of Bayreuth, Universitätsstraße 30, Bayreuth 95447, Germany

[∥] Bavarian Polymer Institute (BPI), University of Bayreuth, Universitätsstr. 30, 95440 Bayreuth, Germany

* Corresponding Author
E-mail: mukundan.thelakkat@uni-bayreuth.de

8. HIGHLY EFFICIENT N-DOPING VIA PROTON ABSTRACTION OF AN ACCEPTOR1-ACCEPTOR2 ALTERNATING COPOLYMER TOWARD THERMOELECTRIC APPLICATIONS

Abstract

Electron transporting (n-type) polymers are the coveted complementary counterpart to more thoroughly studied hole transporting (p-type) semiconducting polymers. Besides intrinsic stability issues of the doped form of n-type polymer towards ubiquitous oxidizing agents (H_2O and O_2), the choice of suitable n-dopants and underlying mechanism of doping is an open research field. Using a low LUMO, n-type unipolar acceptor1-acceptor2 copolymer poly(DPP-TPD) in conjunction with bulk n-doping using Cs_2CO_3 these issues can be addressed. A solid-state acid-base interaction between polymer and basic carbonate increases the backbone electron density by deprotonation of the thiophene comonomer while forming bicarbonate, as revealed by NMR and optical spectroscopy. Comparable to N-DMBI hydride/electron transfer, Cs_2CO_3 proton abstraction doping shifts the poly(DPP-TPD) work function towards the LUMO. Thereby, the anionic doped state is resilient against O_2 but is susceptible towards H_2O. Based on GIWAXS, Cs_2CO_3 is mostly incorporated into the amorphous regions of poly(DPP-TPD) with the help of hydrophilic side chains and has minor impact on the short-range order of the polymer. Cs_2CO_3 proton abstraction doping and the acceptor1-acceptor2 copolymer architecture creates a synergistic n-doped system with promising properties for thermoelectric energy conversion, as evidenced by a remarkable power factor of $(5.59 \pm 0.39)\ \mu W\ m^{-1}\ K^{-2}$.

8.1 Introduction

Organic semiconductors (OSCs) offer unique benefits over their inorganic counterparts, most notably the solution processability, flexibility, and chemical structure tailoring leading to tunable electronic properties. These properties allow them to be employed in a multitude of applications previously dominated by inorganic semiconductors, such as organic photovoltaics, organic field-effect transistors, or organic light-emitting diodes.[1–3] Pristine organic semiconductors are of intrinsic nature, implying a low free carrier density well within the realm of electrical insulators. Manipulation of the charge carrier density *via* chemical doping is a crucial tool to transform intrinsic semiconductors into conducting, unipolar materials. Most notably, doping results in an increase in electrical conductivity.[4] The resulting doped materials can, for example, be applied as charge transport layers in solar cells or as active materials in thermoelectric generators.[5,6] Chemical doping processes are redox reactions (oxidation for *p*-type materials, reduction for *n*-type materials), resulting in polarons on the host material. The doped system consists of two parts, the OSC and the dopant; each of which we will focus on separately.

Donor-acceptor (abbr. D-A) polymers are a popular approach for high-performance *n*-type OSCs. By combining electron-deficient acceptor and electron-rich donor moieties in the polymer backbone, the band gap can be reduced by orbital overlap and HOMO and LUMO positions can be tuned separately.[7,8] A major breakthrough for *n*-type D-A OSCs was achieved by the introduction of poly(NDI2OD-T2) (N2200) by Guo et al.[9] Despite offering a field-effect electron mobility of 0.1 to 0.85 cm^2 V^{-1} s^{-1} for N2200, the structure of D-A polymers must be carefully optimized.[10] Functionalization of the electron rich monomer with electron withdrawing functionalities was demonstrated to weaken the donor character of the respective segment and thus leads to increased *n*-type character of the polymer.[11,12] The electron rich character of the donor monomer can further be increased by incorporating motifs, considered electron deficient themselves in the classical context, leading to acceptor₁-acceptor₁ homopolymers and polymers with heteroacceptor monomers (acceptor₁-acceptor₂).[13] Common acceptor units include benzobis(thiadiazole) (BBT), isoindigo (IID) or diketopyrrolo(pyrrole) (DPP) and naphthylamide (NDI).[14–17] Linking two different acceptor moieties (acceptor₁-acceptor₂) has distinct advantages over acceptor₁-acceptor₁ homopolymers, which suffer from high

dihedral angles, loss of conjugation/planarity and as a consequence low *n*-type charge transport mobility, even though theoretical studies predicted planar structures with low dihedral angles.[18–21] For example, improved packing and coplanar backbone conformation of acceptor1-acceptor2 polymers was reported using fluorinated benzothiadiazole monomers in combination with NDI units by Wang et al.[22] Generally, a higher acceptor fraction of comonomers in semiconducting copolymers results in a more unipolar electron transport and lowers the LUMO value.[23] Especially the LUMO position plays two important roles in *n*-type OSCs: First, a low LUMO value ensures efficient electron injection from high work function electrodes like gold. Second, it was reported that electron acceptor materials and their respective doped states can be stable under ambient conditions if the LUMO of the pristine material exceeds 4.0 eV – a sought-after characteristic, reflected in the sparse chemical space of stable *n*-type OSCs.[24]

With these requirements in mind, we synthesized a hydrophilic alternating acceptor1-acceptor2 *n*-type polymer poly(DPP-TPD) (**Figure 8.1**).[25,26] We use the synergistic effects of a diketopyrrolopyrrole and thienopyrrolodione (TPD) acceptor to tune both HOMO and LUMO concurrently, and also to increase the stability of the *n*-doped state. Additionally, planarizing the backbone *via* imide C=O···H-(thiophene) non-covalent interactions and the deep HOMO energy of TPD enhance the unipolar electron transport. We tackle the problem of solubility by N-functionalization of the acceptor moieties with methoxy-capped ethylene glycol groups in both acceptor moieties. Simultaneously, these polar side chains can increase the compatibility of the polymer host material and the *n*-dopant and its counter-ion, as reported by Krauss et al. and Kroon et al.[27,28]

In order to *n*-dope poly(DPP-TPD), the highest (singly) occupied molecular orbital of the *n*-dopant must be located in the vicinity or lower in energy compared to the LUMO of the polymer.[29] This opens up a variety of potential *n*-dopants, one of the most popular being 4-(2,3-Dihydro-1,3-dimethyl-1H-benzimidazol-2-yl)-N,N-dimethylbenzenamine (N-DMBI) and derivatives thereof.[30–33] The N-DMBI *n*-doping mechanism, being based on either hydride or direct electron transfer to the OSC, has been described in detail by Bardagot et al. and Zeng et al.[32,34] Another less-thoroughly investigated *n*-type dopant is Cs_2CO_3, which is reported to effectively facilitate electron injection from a wide range of metal electrodes, when commonly applied *via* evaporation on top of the acceptor material, or as thin individual interface layers on diverse metals in organic light emitting diodes

and solar cells [35–41]. Compared to N-DMBI and other organic electron donors, alkali metal carbonates are a promising alternative, being far more abundant and cheaper. No detailed studies of bulk doping using carbonates are reported so far. Moreover, only speculative explanations of the doping mechanism, ranging from integer charge transfer from either the alkali metal cation or CO_3^{2-} to the OSC or indirect doping *via* the thermal degradation intermediate cesium oxide, exist.[35–41] In the context of OLED research, the viability of further alkali carbonates as *n*-type dopants has been demonstrated, suggesting redox activity of the carbonate anion.[37,42–45] Liu et al. investigated the thermoelectric performance enhancement of a fullerene derivative doped by thermally evaporated Cs_2CO_3, but did not comment further on the underlying mechanism.[46] The authors like to point out the distinct difference between carbonate-doping of small molecule semiconductors such as 1,10-phenanthroline or bathocuproine and semiconducting polymers. The former have strong tendencies to complex and bind metal ions, facilitating reaction pathways not achievable in polymers.[47]
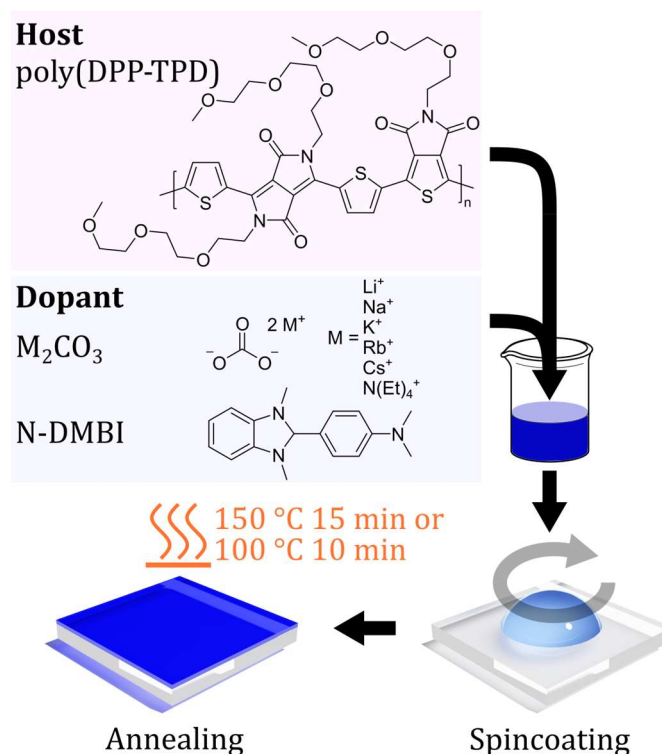
Figure 8.1. Device preparation and chemical structure of the *n*-type host polymer poly(DPP-TPD) as well as the investigated dopants N-DMBI and various carbonate salts.

In this work, we investigate the mechanism of doping the acceptor₁-acceptor₂ polymer poly(DPP-TPD) using carbonates and evaluate the strategy towards thermoelectric applications. First, the poly(DPP-TPD) characteristics and impact of carbonate doping compared to N-DMBI on the electrical conductivity is studied. To investigate underlying electronic processes, UV/Vis/NIR spectroscopy, X-ray-, ultraviolet- and inverse photoelectron spectroscopy (abbr. XPS, UPS, IPES) as well as impedance spectroscopy, NMR and thermoelectric measurements are applied. Furthermore, the mechanism of doping is elucidated. Finally, GIWAXS and scanning electron microscope (abbr. SEM) measurements are employed to determine the morphology and topology of poly(DPP-TPD) and changes thereof during doping.

8.2 Discussion

All the synthetic details of the monomers and polymer and their characterization are given in the supporting information. In short, direct arylation polymerization was used to obtain the polymer with an average molecular weight of 20.6 kg mol^{-1} (GPC).[48] To understand the charge transport properties of this strong acceptor$_1$-acceptor$_2$ copolymer poly(DPP-TPD), we fabricated field-effect transistors and measured the output- and transfer characteristics (**Figure 8.2a**, full transfer scan in shown in **Figure S8.1**). We recorded an average electron mobility of $\mu_e = 4.4 \cdot 10^{-4}$ cm^2 V^{-1} s^{-1} with very little current flowing in the p-type region, rendering poly(DPP-TPD) suitable as a host for n-doping experiments.
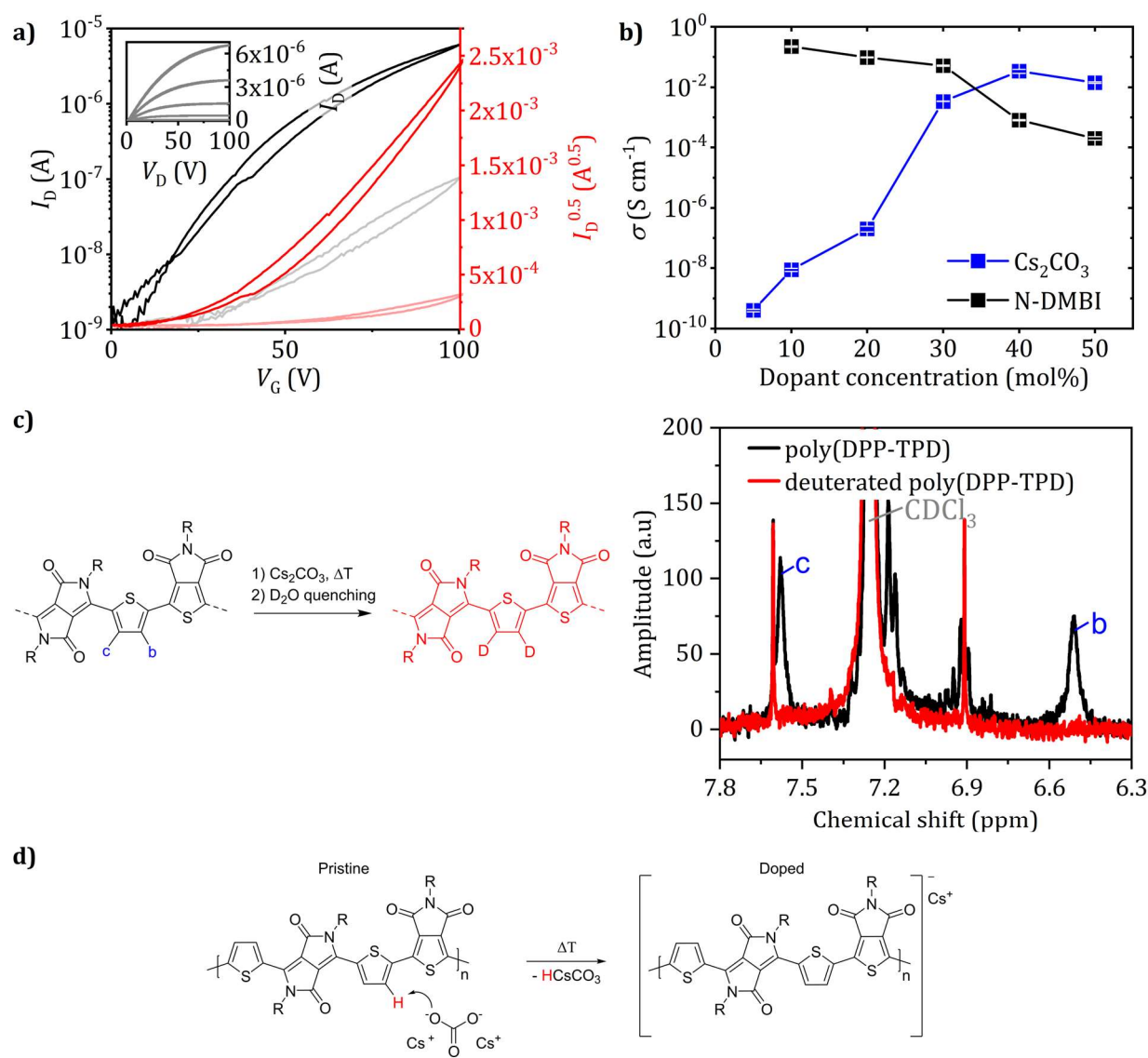
Figure 8.2. a) Organic field-effect transistor transfer characteristics of pristine poly(DPP-TPD). Left y-axis: Drain current I_D vs. gate potential V_G, right y-axis: square root of the drain current $I_D^{0.5}$ vs. gate potential used for mobility determination (see SI). The inset shows the output characteristics with gate voltage variation from 0 to 100 V in 20 V steps. b) Thin film conductivity values of poly(DPP-TPD), doped with various amounts of N-DMBI and Cs_2CO_3. c) left: Sketch showing the deprotonation and subsequent deuteration mechanism of the poly(DPP-TPD) backbone. Right: ^{1}H-NMR of pristine poly(DPP-TPD) in $CDCl_3$ (black curve) showing the two signals b and c of the thiophene protons of the poly(DPP-TPD) backbone. After doping with Cs_2CO_3 and quenching the doped poly(DPP-TPD) in D_2O, the corresponding positions are deuterated and not visible in the NMR spectrum (red curve). d) Proposed Brønsted acid-base doping mechanism between Cs_2CO_3 and poly(DPP-TPD).

In a first step, the feasibility of bulk doping of poly(DPP-TPD) using Cs_2CO_3 was examined *via* electrical conductivity measurements of the doped systems. Cesium carbonate and N-DMBI (as a reference) were mixed with poly(DPP-TPD) in different doping concentrations. The solutions were spin coated onto interdigitated Au electrodes from HFIP solutions under glovebox conditions (< 1 ppm H_2O and O_2). The thin film conductivities σ were obtained from the slope of linear I/V-curves and geometric parameters (see SI for details). It was found, that both dopants require thermal activation for the doping reaction to proceed (**Figure 8.6a**). Hence, the substrates were annealed at 150 °C for 15 min (Cs_2CO_3) or 100 °C for 10 min (N-DMBI) under inert atmosphere. **Figure 8.2b** summarizes the thin film conductivities of Cs_2CO_3 and N-DMBI doped poly(DPP-TPD). Both dopants induce an increase in σ over multiple orders of magnitude compared to pristine poly(DPP-TPD) ($1.0 \cdot 10^{-11}$ S cm^{-1}). In the case of N-DMBI doping the highest conductivity value of 0.22 S cm^{-1} was achieved at 10 mol% dopant concentration; the conductivity slowly decreasing up to 30 mol% and radically above this level of doping. We argue that the loss in σ upon exceeding 10 mol% N-DMBI originates from doping efficiency losses. As shown later, in the case of N-DMBI and Cs_2CO_3, the dopant is accumulated in fully amorphous polymer regions. We observe a stark contrast between N-DMBI reaching the highest conductivity at 10 mol% (0.22 S cm^{-1}) and carbonates showing a saturation effect starting from 30 mol% and a maximum conductivity of 0.034 S cm^{-1}. The discrepancy and trend in σ hints toward different doping reactions for both dopants. To verify the feasibility of bulk doping by Cs_2CO_3, we measured the absolute values of ionization potential and electron affinity using inverse and regular UPS experiments on Cs_2CO_3 and poly(DPP-TPD) thin films (**Table S8.1**-**S8.5, Figure S8.2**). An ionization potential of (6.5 ± 0.11) eV for Cs_2CO_3 was determined, far exceeding the electron affinity of poly(DPP-TPD) (3.3 ± 0.60) eV. Thus, an electron transfer from Cs_2CO_3 HOMO to poly(DPP-TPD) LUMO is energetically unfavorable. By impedance spectroscopy, we studied the contribution of ion diffusion (by Cs^+ or CO_3^{2-}) to the observed current flow. For this, poly(DPP-TPD) was dissolved in HFIP, doped with 30 mol% Cs_2CO_3 and spun-cast onto interdigitated Au electrodes. After annealing at 150 °C for 15 min, the electrical impedance was recorded under inert atmosphere before and after polarization at 5 V for 40 min. The phase angle ϕ of the current flowing through the device remains constant at 0 ° between 10 Hz and 10 mHz independent of polarization, indicating purely ohmic behavior without diffusion processes (**Figure S8.3**).
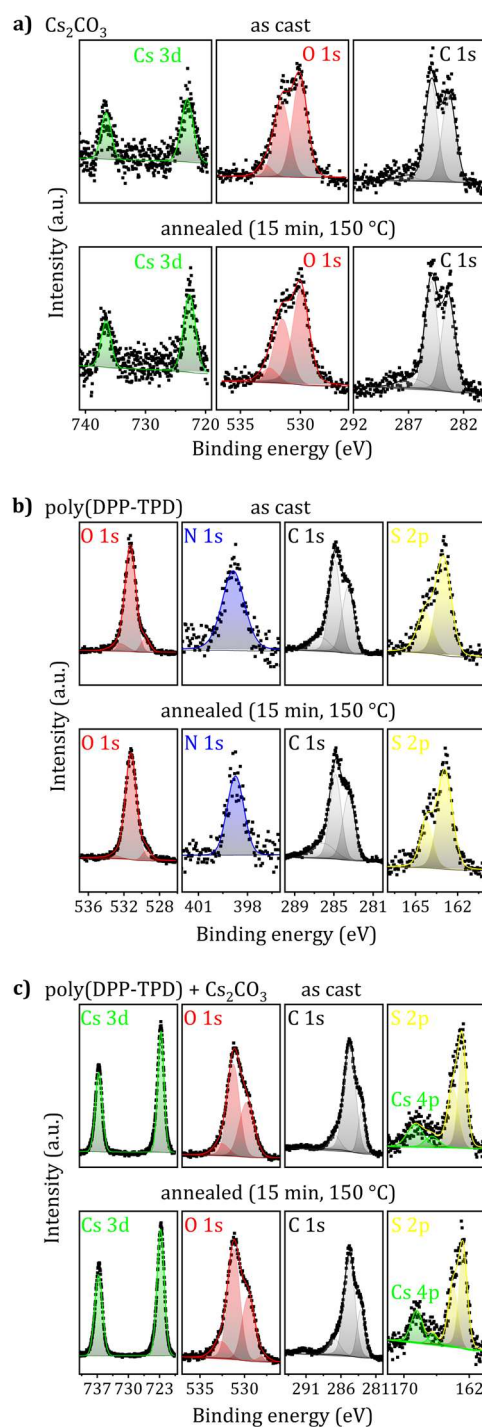
Figure 8.3. XPS detail spectra of a) Cs_2CO_3, b) pristine poly(DPP-DTT) and c) poly(DPP-TPD) doped with 30 mol% Cs_2CO_3 O 1s, N 1s, C 1s and S 2p regions. The spectra were recorded before (upper panels) and after (lower panels) annealing. Black squares are data points, lines are the fitted spectra and shaded areas the deconvoluted contributions to the total fitted spectrum.

To verify if the annealing leads to the formation of side products such as Cs_2O and if it contributes to doping, we conducted XPS spectroscopy as follows. The C 1s, O 1s and Cs 3d core level peaks of Cs_2CO_3 powder were monitored at rt and after *in-situ* heating to 150 °C for 15 min under vacuum (**Figure 8.3**). No change in peak area or position occurred, hence the absence of Cs_2CO_3 side-products during the doping experiments can be concluded. TGA measurements on Cs_2CO_3 powder affirm this with a decomposition onset temperature of > 500 °C (**Figure S8.4**). In contrast to Cs_2CO_3, which is stable at these conditions, Li_2CO_3 shows minor degradation in XPS studies (**Figure S8.5**). Besides the carbonate C 1s peak at 291 eV, a lower BE component at 285 eV increased in intensity after annealing.[49] We attribute the lower BE C 1s peak to either bicarbonate formation or C-C bonds formed during decomposition.[50] Having excluded ion diffusion and dopant decomposition, we turn our attention towards alternative reaction pathways to explain the mechanism of *n*-doping poly(DPP-TPD) with carbonates. To gain deeper insight on the mechanism of the *n*-doping process using carbonates, XPS analysis on thin poly(DPP-TPD) and Cs_2CO_3 films coated onto quartz substrates as well as doped films was conducted (**Figure 8.3**). The C 1s peaks of pristine poly(DPP-TPD) appear at 283.5, 285 and 286 eV, originating from sp^2 C=C, sp^3 C-C and C-O-C ethylene glycol side chain binding energies (convoluted with C=O), respectively.[51,52] O 1s of poly(DPP-TPD) has distinct binding energies at 529.5 eV (aromatic C=O), 531.3 eV (C-O-C side chain) and 532.8 eV (Si-O-Si substrate).[53,54] Sulfur of the poly(DPP-TPD) thiophene donor moiety was detected at 162.9 eV ($2p_{3/2}$) and 164.2 eV ($2p_{1/2}$), consistent with measurements on DPP-DTT by Wei et al.[55] N 1s could not be resolved in pristine poly(DPP-TPD) XPS experiments. The pristine poly(DPP-TPD) film sample was annealed at 150 °C for 15 min under vacuum and the photoelectron spectrum as recorded again. We observed no change in peak position or intensity, therefore we conclude the polymer to be stable under annealing conditions used for Cs_2CO_3 doping.

Next, a doped system consisting of 30 mol% Cs_2CO_3 in as-cast and annealed state was analyzed using XPS (**Figure 8.3**). We selected a higher pass energy of 55 eV and a large number of integration cycles of 12 to resolve components with a low atomic concentration such as N 1s. The samples were heated at 150 °C for 15 min under inert atmosphere to promote the doping reaction and subsequently, the XPS spectra were recorded after cooling back to rt. No significant change in O 1s and N 1s peak positions and intensities were recorded before and after annealing. In doped samples, an additional C 1s peak at

291.3 eV emerges, associated with the π-π* shake-up peak or aromatic systems.[56,57] Further, two high BE peaks at 166.8 and 168.8 eV appear in the S 2p region, which are absent in the pure poly(DPP-TPD) spectrum. To identify the origin of these peak, we also replaced Cs_2CO_3 with the alkali-metal free bis(tetraethylammonium)carbonate $(NEt_4)_2CO_3$ as dopant and repeated the XPS experiment on doped poly(DPP-TPD). In this case, no high BE peaks were recorded between 165 eV and 170 eV before and after annealing at 150 °C for 15 min (**Figure S8.6**). This led us to believe, that the peaks at 166.8 eV and 168.8 eV are originating from Cs 4p transitions at the sample surface and are not associated with highly oxidized sulfur species. Similarly, the Cs 3d peaks located at 736.8 eV (Cs $3d_{3/2}$) and Cs $3d_{5/2}$ at 722.7 eV did not change position, intensity or FWHM during annealing (**Figure 8.3**). Chen et al. and Wu et al. reported a shift of the Cs 3d binding energy towards higher energies in experiments involving evaporated Cs_2CO_3 as interlayers between electron transport layer and metals and related it to electron transfer from Cs to semiconductor.[35,58] Nevertheless, no such shift was found in our experiment. This finding confirms the neutral role of the Cs^+ spectator cation in bulk doping of poly(DPP-TPD). We also infer from XPS results, that the polymer backbone is not subject to chemical degradation during doping.

As the only remaining species, the interaction between CO_3^{2-} and poly(DPP-TPD) was investigated in detail with ATR-FTIR spectroscopy under anhydrous conditions (**Figure S8.7**). A 30 mol% Cs_2CO_3 doped poly(DPP-TPD) powder was prepared by removing the solvent under vacuum after stirring the doped HFIP solution for 5 min at rt. ATR-FTIR spectra were measured before and after annealing under inert atmosphere at 150 °C for 15 min. The resulting spectra are compared to the pristine poly(DPP-TPD) polymer. Upon thermal treatment, a distinct sharp transition appears at 2918 cm⁻¹, assigned to O-H stretching vibrations. As water was excluded during measurement, we argue this peak to originate from HCO_3^- formed during doping. This was confirmed by ATR-FTIR of $CsHCO_3$ powder (**Figure S8.7**).[59] As the experiment was conducted in the solid state, we conclude that the poly(DPP-TPD) has to be deprotonated during the annealing process to form HCO_3^- species. Further, a shift in the C-O-C ether stretching modes from 1093 cm⁻¹ (in pristine poly(DPP-TPD)) to 1086 cm⁻¹ after doping and annealing was observed, which can be attributed to coordination of Cs^+ cations by the ethylene glycol side chains.[60,61] As the ethylene glycol side chain protons are not in conjugation with the main chain, deprotonation leading to enhanced conductivity has to

occur at the polymer backbone. The sole protons of poly(DPP-TPD) are located at the 3,4 thiophene positions. Deprotonation leads to a strong increase in unsaturated C-H vibration at 1016 cm^{-1}.[62,63] as observed in FTIR (**Figure S8.7**)

Based on our findings, we propose a Brønsted acid-base interaction between Cs_2CO_3 and poly(DPP-TPD) during doping, deprotonating the thiophene moiety and forming $CsHCO_3$ as a product. To verify the proton abstraction mechanism, ^{1}H-NMR spectroscopy was conducted. The thiophene protons of the pristine poly(DPP-TPD) polymer are detected downfield at 6.51 and 7.58 ppm. The authors note, that even prolonged stirring in $CDCl_3$ at rt causes no change in the thiophene proton peak integral, hence the pristine polymer does not exchange protons with the solvent without dopant. If our hypothesis holds true, quenching the Cs_2CO_3 doped poly(DPP-TPD) in D_2O should cause the thiophene anion to be deuterated, rendering them invisible to the proton NMR. To prove this experimentally, we prepared a poly(DPP-TPD) HFIP solution, to which a 1:1 molar ratio of Cs_2CO_3 in aqueous solution was added. After removing the solvent under vacuum at 50 °C, the solid mixture was transferred to a glovebox, annealed at 150 °C for 15 min in the solid state and immediately quenched with D_2O. Afterwards, a ^{1}H-NMR spectrum was recorded again in $CDCl_3$ (**Figure 8.2c**). Both proton signals are missing in the quenched spectrum, hence we conclude the proposed deprotonation (or proton abstraction) mechanism to be correct (**Figure 8.2d**). The peak at ca. 7.1 ppm can be assigned to thiophene protons of homocoupling defects, i.e., two thiophene monomers are directly coupled during the direct arylation polymerization reaction. As these protons are also labile, they too are absent in the ^{1}H-NMR spectrum after deprotonation and deuteration. Further, we note, that the side chain protons are not affected by the doping procedure (see **Figure S8.8**, **S8.9** for full ^{1}H-NMR spectra).

Based on the proposed proton abstraction mechanism, we argue that less basic carbonates should induce a lower density of negative charges on poly(DPP-TPD) or do so with a higher activation energy. We investigated the impact of carbonate basicity by monitoring the thin film conductivity of poly(DPP-TPD) doped with different carbonates such as Li_2CO_3, Na_2CO_3, K_2CO_3 and Rb_2CO_3. Poly(DPP-TPD) was dissolved in HFIP with varying amounts of aqueous dopant stock solution added and spin coated onto interdigitated Au electrodes. Within the series of alkali metal carbonates, the maximum achieved conductivity correlates with the increasing cation ionic radius and in turn the

carbonate basicity (**Figure 8.4a**).[64] Particularly the soft Lewis acids Cs+ and Rb+ ion help to improve the doping efficiency by increasing the alkali metal carbonate basicity.[65] Though HFIP exerts a considerable Brønsted acidity, we found no correlation to the doping reaction, as it also proceeds in strictly anhydrous aprotic solvents and occurs only in solid state during annealing. Specifically, poly(DPP-TPD), doped with 30 mol% Cs_2CO_3 exhibits a conductivity of $(1.9 \pm 0.31) \cdot 10^{-4}$ S cm^{-1}, when cast from a mixture of hot DMSO and NMP (**Figure S8.10**). However, the host polymer is only sparsely soluble in the used solvent mixture, resulting in heterogeneous films and thus decreased conductivity. Further, in contrast to earlier literature affiliating Cs+ with the *n*-doping reaction, we could replace the alkali metal ions with an all organic bis(tetraethylammonium) cation in the doping experiment, forming $(NEt_4)_2CO_3$.[35] After annealing poly(DPP-TPD) thin films mixed with $(NEt_4)_2CO_3$, the dopant reacts similar to the inorganic carbonates tested, showcasing the neutral role of the cations in this study (**Figure 8.4a**). We argue that the carbonate lattice energy plays a decisive role in deprotonating the thiophene donor moiety, ultimately leading to an enhanced electrical conductivity. Summarizing, electrical conductivity, XPS, NMR and ATR-FTIR measurements fortified the role of the carbonate anion as the active species during a proton abstraction doping mechanism. *Via* counter ion choice, the carbonate basicity and hence dopant activity can even be tailored. Moreover, this is not specific for Cs_2CO_3, but common to any carbonate, even an organic carbonate such as bis(tetraethylammonium) carbonate.

8.2.1 Frontier orbital measurement

Charge carrier density changes on the host due to doping are usually directly reflected in a change of the work function, i.e., the Fermi position E_F. It is generally accepted, that *n*-doping leads to an E_F upward shift towards the LUMO position, increasing the hole injection barrier (abbr. HIB, the distance between E_F and HOMO) and concurrently decreasing the electron injection barrier (distance between E_F and LUMO).[30,66] To quantify the E_F shift, we measure UPS and IPES on 30 mol% N-DMBI and Cs_2CO_3 doped poly(DPP-TPD) thin films, which were prepared on top of ITO/PEDOT:PSS substrates. The doped films were measured before and after annealing under inert atmosphere. As our carbonate case study involves a deprotonation step which is fundamentally different from

simple electron transfer, we refrain from frontier orbital models based on integer charge transfer or charge transfer complex formation.[67,68] First, we address the 30 mol% N-DMBI doped poly(DPP-TPD) reference system. Relative to pristine poly(DPP-TPD), the HIB increases from (1.0 ± 0.10) eV to (1.3 ± 0.10) eV in the doped system (**Table S8.1**, **Figure 8.4b**). Concurrently, the electron injection barrier is decreased from (1.1 ± 0.60) eV to (0.20 ± 0.60) eV. Therefore, poly(DPP-TPD) is *n*-doped by N-DMBI; the doping mechanism being either hydride or electron transfer from N-DMBI as reported earlier by Bardagot et al. and Zeng et al.[32,34] Next, the dopant was changed to Cs_2CO_3 (30 mol%) and the UPS spectrum recorded again. Similar to N-DMBI, the HIB changes from (1.0 ± 0.10) eV in pristine poly(DPP-TPD) to (1.3 ± 0.10) eV after annealing with Cs_2CO_3, while the electron injection barrier decreases from (1.1 ± 0.60) eV to (0.30 ± 0.60) eV (**Table S8.2**, **Figure 8.4b**). We conclude, that the proton abstraction by CO_3^{2-} leads to a shift of the Fermi level towards the LUMO of poly(DPP-TPD), thus *n*-doping the polymer.

We also note, that the LUMO of both N-DMBI and Cs_2CO_3 doped poly(DPP-TPD) shifts to lower values, whereas the HOMO position remains constant. However, the electron affinity is not expected to change during chemical doping, which is also confirmed by UV/Vis/NIR measurements on poly(DPP-TPD) thin films doped with 30 mol% Cs_2CO_3 (**Figure S8.11**). No significant changes occurred after annealing, demonstrating a stable band gap. This suggests that the onset of the unoccupied states observed for the Cs_2CO_3 doped samples is not the LUMO, but rather originates from gap states that form in this film. The origin of these states positioned at ca. $0.30 - 0.50$ eV below the pristine poly(DPP-TPD) LUMO at (3.3 ± 0.6) eV however, remains obscure.
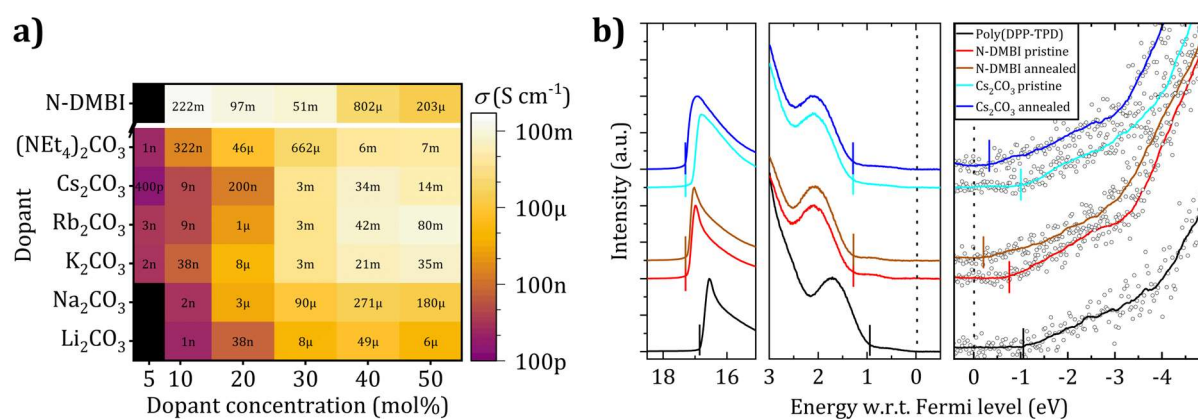
Figure 8.4. a) Heat map of dopant- and doping content dependent conductivity of poly(DPP-TPD) with various alkali metal carbonates, as well as $(NEt_4)_2CO_3$ and N-DMBI. Conductivity was extracted in all cases from the linear slope of the I/V characteristics of the solution processed materials between interdigitated gold electrodes on Si/SiO$_2$ substrates. b) Frontier orbitals of poly(DPP-TPD) (black lines) doped with N-DMBI (pristine: red lines, annealed at 100 °C for 10 min under inert conditions: dark brown lines) and Cs$_2$CO$_3$ (pristine: cyan lines, annealed at 150 °C for 15 min under inert conditions: dark blue lines). Secondary electron cutoff (left) and valence band maximum (middle) were measured by UPS, conduction band minimum (right) by IPES.

Having quantified the position of the frontier orbitals in doped and pristine poly(DPP-TPD), we can correlate the stability of the doped state to the proposed proton abstraction mechanism. The LUMO position plays a decisive role in stability considerations of conventional *n*-doped organic semiconductors (by means of either hydride or electron transfer): If the LUMO of the pristine polymer is situated below 3.7 eV, the *n*-doped state is stable with respect to the reduction of H$_2$O, whereas if it is even lower (< 4.0 eV), it is resilient against both H$_2$O and O$_2$ reduction (achieving "ambient stability").[24,69] Based on these findings, we expect Cs$_2$CO$_3$ doped poly(DPP-TPD) to be unstable against oxidation by H$_2$O and O$_2$ with E_{LUMO} = (3.6 ± 0.6) eV (**Table S8.2**). To study the ambient stability of Cs$_2$CO$_3$ doped polymer, we drop-casted poly(DPP-TPD) doped with 30 mol% Cs$_2$CO$_3$ onto interdigitated electrodes under inert atmosphere. The doped substrates were transferred into a Schlenk flask and the electrodes connected to a potentiostat to record the current over time at fixed potential of 1 V, monitoring the change in conductivity. At one point, the samples are exposed to either ambient atmosphere (38 % relative humidity, 26 °C), 95 % relative humidity atmosphere (28 °C) or pure dry oxygen (**Figure S8.12**). It is to be noted

that in both ambient atmosphere as well as high humidity atmosphere, dissolved oxygen in moist air is present compared to just dry oxygen which has no moisture in it. It can be seen that the doped state is far more resilient towards dry O_2 than H_2O+O_2 in the atmosphere. We conclude, that the stability of poly(DPP-TPD) doped by proton abstraction is mostly governed by the presence of H_2O.

8.2.2 Impact of doping on the polymer microstructure

Complimentary to previous mechanistic considerations, the impact of doping on the polymer topology and morphology was investigated. To evaluate possible de-mixing of the doped materials at high doping contents, SEM images of the pristine polymer were compared to poly(DPP-TPD) doped with 30 mol% N-DMBI or Cs_2CO_3 (**Figure 8.5**, for comparison with non-annealed samples see **Figure S8.13, S8.14**). Upon high magnification, a structure or patterns are recognizable for all samples. It was concluded to be caused by the fast-evaporating solvent used for film fabrication rather than dopant segregation, as the inhomogeneous features are as pronounced in the undoped polymer as in the doped systems. To study the dopant aggregation of poly(DPP-TDP) in detail, atomic force microscopy (AFM) was conducted in tapping mode on doped and pristine thin films (**Figure 8.5, Figure S8.15**). A similar structure as in SEM-experiments caused by the fast evaporation of HFIP during film preparation is observed in all films. No change in topography was detected for pristine poly(DPP-TPD) before and after annealing at 150 °C for 15 min. After doping with 30 mol% N-DMBI, no aggregates were found on the surface of the film before and after annealing. This is in agreement with AFM experiments by Ye et al. who reported excellent solubility of N-DMBI in *n*-type semiconducting polymers with glycol ether side chains.[70] For Cs_2CO_3 doped poly(DPP-TPD), phase-separated particles are detected, which increase in size and surface density after annealing. Based on our proposed doping mechanism (**Figure 8.2d**), we argue that the observed particles are composed of $CsHCO_3$ after annealing. In this context, we like to mention that the alkylated Poly(DPP-TPD) counterpart with branched C_8H_{17}-C_6H_{13} side chains is very poorly miscible with Cs_2CO_3 and neither uniform films nor reproducible data could be obtained from those doped films.
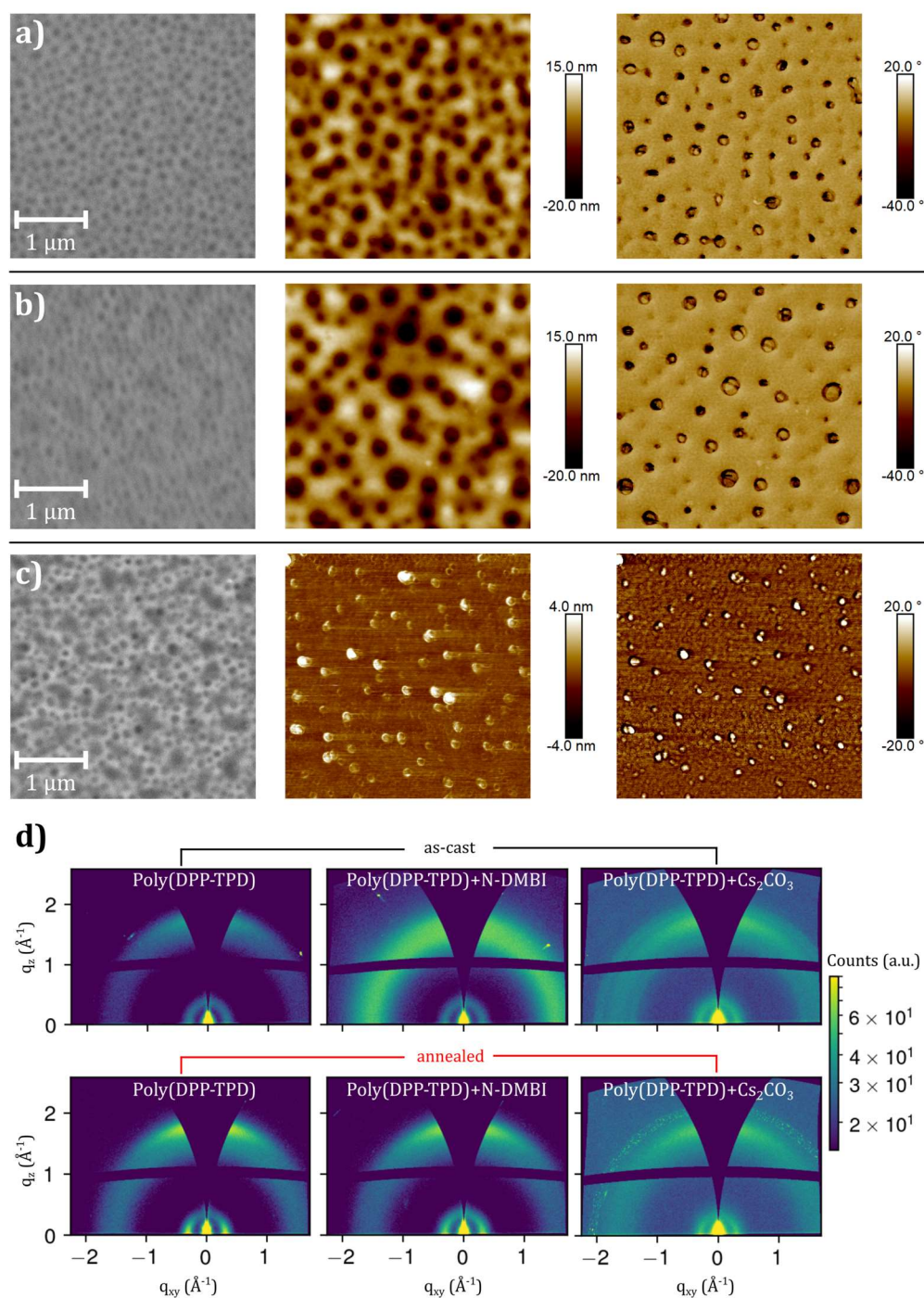
Figure 8.5. SEM micrographs (50k magnification, left) and AFM tapping mode images (middle: topography, right: phase) of a) pristine poly(DPP-TPD) b) poly(DPP-TPD) doped with 30 mol% N-DMBI and c) poly(DPP-TPD) doped with 30 mol% Cs_2CO_3. All films were annealed (N-DMBI doped samples: 100 °C, 10 min, Cs_2CO_3 doped and pristine samples: 150 °C, 15 min) prior to measurement. d) 2D-GIWAXS patterns of pristine poly(DPP-TPD) (left), poly(DPP-TPD) doped with N-DMBI (middle) and poly(DPP-TPD) doped with Cs_2CO_3 (right). The upper panels show the as-cast samples, the lower panels after annealing under inert atmosphere (N-DMBI: 100 °C, 10 min, Cs_2CO_3: 150 °C, 15 min).

Deeper insight into the thin film morphology was attempted using grazing-incidence wide-angle X-ray scattering (GIWAXS) experiments, performed on the pristine as well as doped polymer on Si/SiO_x substrates. Intensive 100 signals at $Q_{xy} = 0.31$ Å^{-1}, corresponding to the polymer-polymer lamellar distance and 010 reflexes at $Q_z = 1.75$ Å^{-1}, caused by the polymer π-π stacking are revealed (**Figure 8.5d**). The absence of higher order peaks, however, indicates a low overall ordering in all investigated materials. Upon thermal annealing of the as-cast materials, the peak full width at half maximum (FWHM) determined from line-cuts does not change, suggesting no significant change of domain size (**Figure S8.16**). The low structural impact of annealing can be explained by the high melting point of the host polymer, which could not be detected using DSC experiments up to 200 °C (**Figure S8.17**). Using Flash-DSC, we could extend the temperature range past the decomposition temperature of poly(DPP-TPD) by recording the heat flow at large heating and cooling rates up to 2000 K min^{-1} (**Figure S8.18**). The absence of phase transitions in both experiments shows the overall amorphous behavior of the sample.[71]

Thus, annealing for 15 min at $T = 150$ °C does not enable sufficient polymer segment mobility to enable the formation of highly ordered structures. Despite the poor ordering, a preferential face-on orientation of the polymers with respect to the substrate can be seen in most cases. Interestingly, the N-DMBI doped samples did form this oriented structure only during thermal treatment, whilst samples without any dopant and with added Cs_2CO_3 demonstrated a preferential orientation already before thermal treatment. Line cuts of the undoped polymer reveal that the π-π stacking signal is the sum of two overlapping signals. By comparison of the vertical (ver) and horizontal (hor) cut, a significant shift of the peak ratios can be seen, suggesting that the sharp signal at q = 1.75 Å^{-1} corresponds predominantly to a short range ordered, oriented material fraction, while the second signal at q = 1.46 Å^{-1} is caused by isotropically distributed short range ordered material, where a slightly larger π-π stacking distance is realized. Molecular rearrangements during the doping process of poly(DPP-TPD) with N-DMBI can be monitored by comparison of the scattering patterns of undoped and doped materials. Compared to neat poly(DPP-TPD), the N-DMBI doped films show slightly broader 100 signals, suggesting a reduced short-range order caused by dopant incorporation. However, the absence of a shift in the peak position shows that dopant molecules do not affect lamellar expansion of the host material and thus likely do not accumulate there. Instead, location in the fully amorphous domains can be assumed. 010 signals of annealed

poly(DPP-TPD) and annealed N-DMBI doped material are identical, indicating no structural change in the π-π stacking. The deviation of the material prior to annealing (see line cuts in **Figure S8.16**) can be explained by the reorientation of isotropic domains to face-on ordered domains.

In a similar matter, the structural changes correlated to Cs_2CO_3 doping can be investigated. Compared to pristine poly(DPP-TPD), only insignificant changes in FWHM and q-value of the 100 signals are apparent in the vertical line cut (**Figure S8.16**), hinting no substantial change of coherence length and lamellar distance. Likewise, upon annealing, only small shifts of the scattering signal peaks are observable, if at all. The most pronounced changes of approximately -0.02 $Å^{-1}$ are found in the 100 signals of the polymer doped with Cs_2CO_3. These signal shift, however, lie in the margin of error for the measurement, e.g. caused by deviations in sample position between measurements. Therefore, we consider this change as insignificant and conclude that the majority of dopant must be located in the amorphous domains. 2D scattering images as well as line cuts reveal the presence of ordered impurities in the Cs_2CO_3 doped samples at q values of $Q = 1.41$ $Å^{-1}$ and $Q = 1.95$ $Å^{-1}$ in the pristine and $Q = 2.07$ $Å^{-1}$ in the annealed state. These impurities are initially mostly short-range ordered with defined peaks suggesting a small amount of long-range order (**Figure S8.16**). Interestingly, the original peaks obtained from the ordered domains change position during annealing. This agrees well with the proposed doping reaction, where Cs_2CO_3 is consumed during annealing to form $CsHCO_3$, leading to different scattering patterns of the inhomogeneities. We argue, that the $CsHCO_3$ forms individual crystallites with random orientation after annealing, resulting in well-defined Bragg peaks.

8.2.3 Thermoelectric performance

The competitive electrical conductivity of proton abstraction doping compared to N-DMBI doping enables possible use of such doped polymers in thermoelectric energy conversion. First the temperature dependence of doping using various alkali metal carbonates at different annealing temperatures of 25, 100, 150 and 200 °C was studied by measuring the electronic conductivity of the resulting doped polymers using 30 mol% dopants

(**Figure 8.6a**). It is obvious that the conductivity for lower annealing temperatures scales with the basicity and ion radius of the alkali metal carbonate as explained in **Figure 8.4a**. However, at 150 °C and above, all the three carbonates, K_2CO_3, Rb_2CO_3 and Cs_2CO_3 show saturation conductivities. To quantify the thermoelectric properties of the pristine and Cs_2CO_3-doped poly(DPP-TPD), the polymer was dissolved in HFIP with varying amounts of dopant and drop-casted onto Al_2O_3 substrates. The sample was mounted on to a thin film adapter of the ZEM-3 thermoelectric system and annealed in-situ under 0.8 bar helium atmosphere at 150 °C for 15 min prior to measurement. Throughout the range of 10 – 60 mol% Cs_2CO_3, the Seebeck coefficient S exerts a negative sign, a fingerprint for electron majority carriers (**Figure 8.6b**).
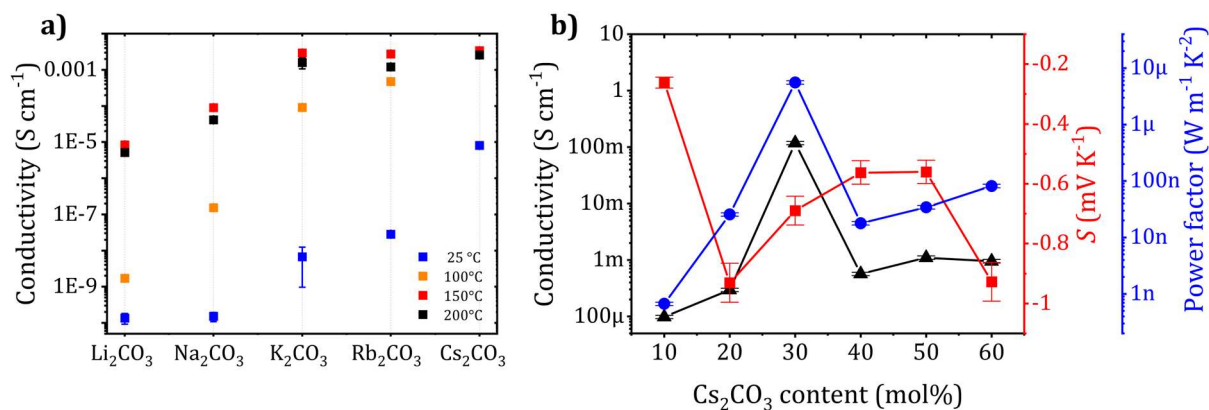
Figure 8.6. a) Temperature dependent conductivity of poly(DPP-TPD) doped with 30 mol% of Li_2CO_3, Na_2CO_3, K_2CO_3, Rb_2CO_3 and Cs_2CO_3 after annealing at different temperature for 15 min each consecutively. The data points for Cs_2CO_3 annealed at 100 °C, 150 °C and 200 °C are closely grouped. b) Thermoelectric properties of poly(DPP-TPD) as a function of the Cs_2CO_3 doping ratio. Black triangles: Thin film conductivity, blue circles: Seebeck coefficient, red squares: power factor.

We conclude, that the intragap states observed in UPS experiments are most likely localized and charge transport is dominated by the LUMO states lower in energy. Since conductivity is the highest at 30 mol% doping, the power factor $PF = \sigma S^2$ of 30 mol% Cs_2CO_3 doped poly(DPP-TPD) shows a maximum with $PF = (5.6 \pm 0.39) \cdot 10^{-6}$ W m^{-1} K^{-2} (for full data see **Table S8.6**). Between 20 mol% and 50 mol%, S decreases by a factor of ca. 0.5 from (931 ± 65.1) µV K^{-1} to (560 ± 39.2) µV K^{-1}. We attribute this loss in Seebeck

coefficient to the decreased distance between Fermi level and mean energy of charge carriers (here approximated with the conduction band minimum, e.g. LUMO, see **Figure 8.4b**) upon doping, a phenomenon well documented in literature.[72,73] The *PF* maximum is mostly governed by the conductivity maximum at 30 mol%, which is not only observed for Cs_2CO_3, but also for Na_2CO_3 and Li_2CO_3 (**Figure 8.4a**, Rb_2CO_3 and $(NEt_4)_2CO_3$ level off significantly). Combined with the observed crystallite formation in GIWAXS and AFM experiments, we argue that the crystallization of both carbonate and bicarbonate causes less dopants to be available for the deprotonation reaction as opposed to a homogeneously mixed polymer:dopant system at lower doping ratios.

This thermoelectric performance is competitive towards recently published *n*-type acceptor-acceptor polymers. Wang et al. reported a naphthalenediimide-bithiazole based acceptor-acceptor copolymer poly(NDI2OD-Tz2), which achieved a *PF* of $1.5 \cdot 10^{-6}$ W m^{-1} K^{-2} upon vapor-doping with tetrakis(dimethylamino)ethylene.[74] Liu et al. characterized the thermoelectric performance of the similar all-acceptor copolymer PNDI2TEG-2Tz with hydrophilic ethylene glycol side chains and achieved a *PF* of $(4.5 \pm 0.2) \cdot 10^{-6}$ W m^{-1} K^{-2}, doped with 21 mol% N-DMBI.[75] Using a pyridine-flanked DPP-core, Yang et al. synthesized the polymer PDPF with a *PF* of $(4.65 \pm 0.23) \cdot 10^{-6}$ W m^{-1} K^{-2} with 5 mol% N-DMBI.[76] By introducing the even more electron-deficient acceptor pyrazine as a DPP flanking unit in conjunction with 3,3'-dicyano-2,2'-bithiophene comonomers, Yan et al. demonstrated a *PF* of $57.3 \cdot 10^{-6}$ W m^{-1} K^{-2} with 40 mol% N-DMBI.[77] To the best of our knowledge, this is the first report of double donor-acceptor polymers doped with common carbonates for thermoelectric applications and opens up new possibilities towards alternative doping pathways to obtain very high conductivity as well as appreciably good power factor.[78]

8.3 Conclusion

A successful synergy between a polymer semiconductor and *n*-dopant to form a stable and highly conductive system could lead to advances in thermoelectric research by providing the complementary counterpart to *p*-doped systems. By combining the concept of a hydrophilic acceptor1-acceptor2 copolymer poly(DPP-TPD) with proton abstraction

doping, we provide a profound background to carbonate base doping and feasibility for thermoelectric applications. CO_3^{2-} is identified as the active dopant, deprotonating labile poly(DPP-TPD) thiophene protons during annealing and shifting the Fermi level towards the polymer LUMO. The conductivity hereby scales with the basicity and ion radius of the alkali metal carbonate, achieving similar performance to N-DMBI. During proton abstraction doping, no change in the short range ordered polymer microstructure was observed, probably with Cs_2CO_3 and N-DMBI residing in the fully amorphous domains of the polymer. We successfully applied the carbonate doped poly(DPP-TPD) as an *n*-type thermoelectric material, achieving a competitive power factor of $(5.6 \pm 0.39) \cdot 10^{-6}$ W m^{-1} K^{-2}. These findings could pave the way for a more efficient, universal *n*-doping protocol of *n*-type semiconducting polymers, promoting both the fields of facile and efficient doping as well as the realization of organic thermoelectric generators, which is at present lacking suitable *n*-doped counterparts.

8.4 Experimental section/methods

8.4.1 General methods

Thermoelectric measurement

For thermoelectric measurements, a ZEM-3 Seebeck coefficient and resistance measurement system equipped with a high-resistance option was used. The machine was supplied by ULVAC, Japan. Aluminium oxide substrates ($0.5 \cdot 4 \cdot 10$ mm, unpolished surface) were cleaned by 15 min ultrasonication in 4 consecutive baths of 5 vol% Hellmanex DI water, DI water, acetone and isopropanol. The substrates were blown dry with N$_2$ and treated with O$_3$ at 50 °C for 15 min. Poly(DPP-TDP) was dissolved in HFIP (10 mg mL^{-1}). Cs$_2$CO$_3$ was dissolved in Millipore water (resistance > 20 MΩ cm^{-1}, 10 mg mL^{-1}). The appropriate amount of the Cs$_2$CO$_3$ stock solution was added to the poly(DPP-TPD) solution for a given molar ratio of dopant. The solution was drop-casted onto the aluminium oxide substrate under ambient atmosphere (50 °C, covered by petri dish to avoid coffee ring effect, $3 \cdot 30$ µL doped solution). Afterwards, the substrate was mounted onto the ceramic thin film holder and contacted with nickel stripes and silver paste. The silver paste was allowed to dry for a short period of time. Afterwards, the sample was transferred into the measurement chamber, which was then purged by three consecutive pump-flush cycles with helium 5.0. The sample was heated to 150 °C for 15 min under 800 mbar helium atmosphere for better heat transfer. Then, the sample was allowed to cool to rt and the measurement was started. To determine the Seebeck, two sets of base temperatures were used (30 °C and 50 °C), each with 3 ΔT values of 20 °C, 30 °C and 40 °C.

Photoelectron Spectroscopy

The photoelectron spectroscopy measurements were performed in a custom designed multichamber UHV system at a base pressure of p $\sim 10^{-9}$ mbar, using a Phoibos 100 hemispherical analyzer (Specs). The UPS was done by using a monochromatic He source (VUV 5000, VG Scienta, hν = 21.22 eV) at an electron pass energy of 2 eV. A sample bias of -8 V was applied during measurements to observe the high energy cutoff. The experimental resolution at this low pass energy setting is only determined by thermal broadening and is in the range of 100 meV (ΔE = 4 k_BT).

Measurements of the unoccupied DOS were performed by inverse photoelectron spectroscopy. Here, a low energy electron gun (ELG-2, Kimball) was used at 2 μA emission current together with a bandpass photon detector (SrF2/NaCl bandpass, IPES 2000, Omnivac). The energy resolution, as determined from the width of an Ag Fermi edge, is approximately 600 meV. For all the measurements, the samples were transferred into the ultrahigh vacuum system under nitrogen atmosphere and were therefore not exposed to air.

X-ray photoelectron spectroscopy

XPS measurements were carried out with a PHI 5000 VersaProbe III system fitted with an Al Ka excitation source (hν = 1486.6 eV) and a dual neutralizer (electron gun and Ar$^+$) at 10^{-10} mbar. An X-ray source diameter of 100 mm was used to locally excite the samples; the corresponding photoemission with 45° take-off angle was collected at a multichannel analyzer. The survey and detailed spectra were measured with pass energies of 224 eV and 26/55 eV, respectively. The standard deviation on the reported energy values is ± 0.1 eV. The spectra were analyzed with a Multipak software pack provided by the manufacturers. All emission signals were referenced to adventitious C 1s peak at 284.8 eV or the Au 4f7/2 peak at 84.0 eV. The samples were transported to the instrument using a N2-filled transport vessel to avoid air/O2 contamination. For quantitative analysis, the background of all spectra was corrected using the Shirley function.

Organic field-effect transistor measurements

Bottom gate/bottom contact organic field effect transistors (OFET Gen4) were purchased from Fraunhofer IPMS. *n*-doped silicon (doping at the surface n ∼ 3 · 10^{17} cm^{-3}) was used as the surface and gate electrode. The dielectric consists of a 230 ± 10 nm layer of silicon oxide. Each substrate consisted of 16 devices with a constant channel width *W* of 10 mm and varying channel lengths *L* of 2.5 – 20 μm. The source and drain electrodes were a 30 nm thick gold layer on a 10 nm ITO adhesion layer. The devices were prepared by cleaning in acetone and subsequently in isopropanol in an ultrasonic bath for 15 min, followed by 15 min treatment in an ozone oven at 50 °C. The SiO2 surface was passivated by 2 h treatment in hexamethylenedisilazane vapor at 100 °C. The devices were rinsed with isopropanol and dried with nitrogen. Thin polymer films were spun cast from

5 mg mL^{-1} HFIP solutions at a spinning speed of 3000 rpm under ambient conditions. All devices were stored and measured under nitrogen atmosphere. The I-V-characteristics were measured using an Agilent B1500 semiconductor parameter analyzer. Using **Equation S8.1** the charge carrier mobility μ was calculated from the slope of the $(I_D)^{0.5}$–V_G plots, where V_t is the threshold voltage and C_i the SiO$_2$ insulator capacitance.

$$I_D = \frac{W}{2L} C_i \mu (V_G - V_t)^2 \tag{S8.1}$$

Grazing-incidence small-angle X-ray scattering (GIWAXS)

GIWAXS on neat films coated of silicon substrates was performed in vacuum at rt on a laboratory system at the University of Bayreuth (Xeuss 3.0, Xenocs SAS, Grenoble, France) with a Cu Kα source ($\lambda = 1.54$ Å), a Dectris EIGER 2R 1 m detector, and a sample-to-detector distance of 52.5 mm. Scattering experiments were carried out on 0.5 cm by 0.5 cm Si/SiO$_x$ substrates due to decreased scattering background compared to glass. Q-profiles are cake cuts covering an azimuthal angle of 70° – 110° for the cuts in the vertical direction and 0° – 20° as well as 160° – 180° for the cuts in the horizontal direction.

Matrix-assisted laser desorption/ionization time-of-flight mass spectroscopy (MALDI-ToF MS)

MALDI-ToF measurements were performed using a Bruker AutoFlex Max mass spectrometer equipped with a Smartbeam II laser. The analyte was embedded in the matrix material trans-2-[3-(4-tert-Butylphenyl)-2-methyl-2-propenylidene]malononitrile (DCTB) or dithranol in the matrix : analyte mass ratio 10 : 1.

Atomic force microscopy (AFM)

The polymer films were characterized by Tapping Mode AFM in air / under ambient conditions using a Dimension Icon (Bruker Nano Inc.) equipped with a NanoScope V controller. AFM cantilevers (OMCL-AC160-TS-R3) with a nominal spring constant of 26 N m^{-1} and a typical resonant frequency of 300 kHz, where purchased from Olympus.

Tapping Mode AFM images were acquired at scan sizes of 2 µm · 2 µm using a scan rate of 1 Hz and a pixel density of 512 · 512 pixels. The AFM height sensor and phase images were processed with NanoScope Analysis 1.80 (Bruker Nano Inc.).

8.4.2 Chemicals

Solvents were purchased from abcr, Germany and used as-received. Deuterated DSMO (99.8 %) and D_2O (99.95 %) was supplied by Deutero, Germany. Lithium carbonate (≥ 99 %), potassium carbonate (≥ 99 %), rubidium carbonate (99.8 %) and cesium carbonate (≥ 99 %) were purchased from Sigma-Aldrich, USA, sodium carbonate (99.5 %) was purchased from Grüssing, Germany. The carbonates were dried at 200 °C under high vacuum and stored under inert atmosphere until further use. $CsHCO_3$ (99.99 %) was purchased from Alfa Aesar, USA. N-DMBI (98 %) was sourced from Sigma-Aldrich. Tetraethylammonium carbonate was synthesized by bubbling CO_2 through a 25 wt% tetraethylammonium hydroxide solution in methanol at rt for 12 h. The solvent was removed under vacuum, the educt was dried under vacuum at 75 °C for 3 d and stored under N_2 until further use. ^{1}H-NMR (300 MHz, DMSO-d_6, δ, referenced to residual solvent peak at 2.54 ppm): 3.21 (m, 8H, -CH_2-), 1.15 (m, 11H, -CH_3); ^{13}C-NMR (300 MHz, DMSO-d_6, δ, referenced to residual solvent peak at 39.53 ppm): 51.4 (-CH_2-), 7.13 (-CH_3); (**Figure S8.19**, **S8.20**). Monomer and polymer synthesis are given in the supporting information. The various steps of sidechain synthesis, polymerization etc. were adapted from reports of Thelakkat et al., Reynolds et al., and LeClerc et al. and the procedure was optimized for microwave synthesis, followed by Soxhlet extraction for oligomer, catalyst, and additive removal.[79–81] The polymer was then again precipitated in water and methanol to ensure quantitative removal of Cs_2CO_3 residues, as proven *via* XPS (**Figure S8.21**). The molecular mass of the resulting polymer was determined to be 20.6 kg mol^{-1} with a dispersity of 1.8 *via* GPC (HFIP, PMMA standards, **Figure S8.22**).

8.5 Acknowledgements

8.6 References

[1]   X. Xu, L. Yu, H. Meng, L. Dai, H. Yan, R. Li, Q. Peng, *Adv. Funct. Mater.* **2022**, 8.

[2]   P. H. Wöbkenberg, D. D. C. Bradley, D. Kronholm, J. C. Hummelen, D. M. de Leeuw, M. Cölle, T. D. Anthopoulos, *Synthetic Metals* **2008**, *158*, 468.

[3]   F. Rodella, R. Saxena, S. Bagnich, D. Banevičius, G. Kreiza, S. Athanasopoulos, S. Juršėnas, *Journal of Materials Chemistry C* **2021**, 12.

[4]   M. Goel, M. Siegert, G. Krauss, J. Mohanraj, A. Hochgesang, D. C. Heinrich, M. Fried, J. Pflaum, M. Thelakkat, *Adv. Mater.* **2020**, *32*, 2003596.

[5]   H. Un, S. A. Gregory, S. K. Mohapatra, M. Xiong, E. Longhi, Y. Lu, S. Rigin, S. Jhulki, C. Yang, T. V. Timofeeva, J. Wang, S. K. Yee, S. Barlow, S. R. Marder, J. Pei, *Adv. Energy Mater.* **2019**, *9*, 1900817.

[6]   J. Mohanraj, M. Stihl, E. Simon, O. von Sicard, G. Schmidt, M. Fleischer, C. Neuber, M. Thelakkat, *ACS Appl. Energy Mater.* **2019**, *2*, 3469.

[7]   M. Goel, C. D. Heinrich, G. Krauss, M. Thelakkat, *Macromol. Rapid Commun.* **2019**, *40*, 1800915.

[8]   C. B. Nielsen, M. Turbiez, I. McCulloch, *Adv. Mater.* **2013**, *25*, 1859.

[9]   X. Guo, M. D. Watson, *Org. Lett.* **2008**, *10*, 5333.

[10]   H. Sun, X. Guo, A. Facchetti, *Chem* **2020**, *6*, 1310.

[11]   Z. Yuan, B. Fu, S. Thomas, S. Zhang, G. DeLuca, R. Chang, L. Lopez, C. Fares, G. Zhang, J.-L. Bredas, E. Reichmanis, *Chem. Mater.* **2016**, *28*, 6045.

[12]   C. J. Mueller, C. R. Singh, M. Fried, S. Huettner, M. Thelakkat, *Adv. Funct. Mater.* **2015**, *25*, 2725.

[13]   D. Qu, T. Qi, H. Huang, *Journal of Energy Chemistry* **2021**, *59*, 364.

[14]   H. Yan, Z. Chen, Y. Zheng, C. Newman, J. R. Quinn, F. Dötz, M. Kastler, A. Facchetti, *Nature* **2009**, *457*, 679.

[15]   T. Kono, D. Kumaki, J. Nishida, S. Tokito, Y. Yamashita, *Chem. Commun.* **2010**, *46*, 3265.

[16]   T. Lei, J.-Y. Wang, J. Pei, *Acc. Chem. Res.* **2014**, *47*, 1117.

[17]   L. Bürgi, M. Turbiez, R. Pfeiffer, F. Bienewald, H.-J. Kirner, C. Winnewisser, *Adv. Mater.* **2008**, *20*, 2217.

[18]   M. M. Durban, P. D. Kazarinoff, C. K. Luscombe, *Macromolecules* **2010**, *43*, 6348.

[19]   W. Khelifi, H. Awada, S. Blanc, G. H. Roche, L. Hirsch, B. Oboho, F. Castet, A. Bousquet, C. Lartigau-Dagron, *Applied Sciences* **2022**, *12*, 4494.

[20]   U. Salzner, *J. Chem. Phys.* **2021**, *154*, 054309.

[21]   T. Hasegawa, M. Ashizawa, J. Hiyoshi, S. Kawauchi, J. Mei, Z. Bao, H. Matsumoto, *Polym. Chem.* **2016**, *7*, 1181.

[22]   Y. Wang, T. Hasegawa, H. Matsumoto, T. Michinobu, *J. Am. Chem. Soc.* **2019**, *141*, 3566.

[23]   Y. Shi, H. Guo, M. Qin, Y. Wang, J. Zhao, H. Sun, H. Wang, Y. Wang, X. Zhou, A. Facchetti, X. Lu, M. Zhou, X. Guo, *Chem. Mater.* **2018**, *30*, 7988.

[24]   S. Griggs, A. Marks, H. Bristow, I. McCulloch, *J. Mater. Chem. C* **2021**, *9*, 8099.

[25]   K. H. Hendriks, G. H. L. Heintges, M. M. Wienk, R. A. J. Janssen, *J. Mater. Chem. A* **2014**, *2*, 17899.

[26]   S.-W. Chang, T. Muto, T. Kondo, M.-J. Liao, M. Horie, *Polym J* **2017**, *49*, 113.

[27]   G. Krauss, A. Hochgesang, J. Mohanraj, M. Thelakkat, *Macromol. Rapid Commun.* **2021**, *42*, 2100443.

[28]   D. Kiefer, A. Giovannitti, H. Sun, T. Biskup, A. Hofmann, M. Koopmans, C. Cendra, S. Weber, L. J. Anton Koster, E. Olsson, J. Rivnay, S. Fabiano, I. McCulloch, C. Müller, *ACS Energy Lett.* **2018**, *3*, 278.

[29]   K. Walzer, B. Maennig, M. Pfeiffer, K. Leo, *Chem. Rev.* **2007**, *107*, 1233.

[30]   Z. Bin, J. Li, L. Wang, L. Duan, *Energy Environ. Sci.* **2016**, *9*, 3424.

[31]   Y. Sun, C. Di, W. Xu, D. Zhu, *Adv. Electron. Mater.* **2019**, *5*, 1800825.

[32] O. Bardagot, C. Aumaître, A. Monmagnon, J. Pécaut, P.-A. Bayle, R. Demadrille, *Appl. Phys. Lett.* **2021**, *118*, 203904.

[33] P. Wei, J. H. Oh, G. Dong, Z. Bao, *J. Am. Chem. Soc.* **2010**, *132*, 8852.

[34] Y. Zeng, W. Zheng, Y. Guo, G. Han, Y. Yi, *J. Mater. Chem. A* **2020**, *8*, 8323.

[35] C.-I. Wu, C.-T. Lin, Y.-H. Chen, M.-H. Chen, Y.-J. Lu, C.-C. Wu, *Appl. Phys. Lett.* **2006**, *88*, 152104.

[36] K. C. Kwon, K. S. Choi, B. J. Kim, J.-L. Lee, S. Y. Kim, *J. Phys. Chem. C* **2012**, *116*, 26586.

[37] M.-H. Chen, D.-S. Leem, C. T. Lin, G. R. Lee, T.-W. Pi, J.-J. Kim, C.-I. Wu, in (Eds.: F. So, C. Adachi), San Diego, CA, **2008**, p. 70511C.

[38] A. Barbot, C. Di Bin, B. Lucas, B. Ratier, M. Aldissi, *J Mater Sci* **2013**, *48*, 2785.

[39] J. Huang, Z. Xu, Y. Yang, *Adv. Funct. Mater.* **2007**, *17*, 1966.

[40] J. S. Yang, D. C. Choo, T. W. Kim, Y. Y. Jin, J. H. Seo, Y. K. Kim, *Thin Solid Films* **2010**, *518*, 6149.

[41] H.-H. Liao, L.-M. Chen, Z. Xu, G. Li, Y. Yang, *Appl. Phys. Lett.* **2008**, *92*, 173303.

[42] P.-C. Kao, J.-H. Lin, J.-Y. Wang, C.-H. Yang, S.-H. Chen, *Synthetic Metals* **2010**, *160*, 1749.

[43] J. S. Swensen, *J. Photon. Energy* **2011**, *1*, 011008.

[44] T.-W. Lee, T. Noh, B.-K. Choi, M.-S. Kim, D. W. Shin, J. Kido, *Appl. Phys. Lett.* **2008**, *92*, 043301.

[45] J.-W. Ma, S.-W. Hwang, C.-C. Chang, S. F. Hsu, C. H. Chen, *SID Symposium Digest* **2006**, *37*, 964.

[46] J. Liu, M. P. Garman, J. Dong, B. van der Zee, L. Qiu, G. Portale, J. C. Hummelen, L. J. A. Koster, *ACS Appl. Energy Mater.* **2019**, *2*, 6664.

[47] Z. Bin, G. Dong, P. Wei, Z. Liu, D. Zhang, R. Su, Y. Qiu, L. Duan, *Nat Commun* **2019**, *10*, 866.

[48]   A. Erhardt, A. Hochgesang, C. R. McNeill, M. Thelakkat, *Adv. Electron. Mater.* **2023**, 2300026.

[49]   K. N. Wood, G. Teeter, *ACS Appl. Energy Mater.* **2018**, *1*, 4493.

[50]   A. Shchukarev, D. Korolkov, *Open Chemistry* **2004**, *2*, 347.

[51]   T. R. Gengenbach, G. H. Major, M. R. Linford, C. D. Easton, *Journal of Vacuum Science & Technology A* **2021**, *39*, 013204.

[52]   K. C. Kwon, K. S. Choi, B. J. Kim, J.-L. Lee, S. Y. Kim, *J. Phys. Chem. C* **2012**, *116*, 26586.

[53]   G. M. Bancroft, H. W. Nesbitt, R. Ho, D. M. Shaw, J. S. Tse, M. C. Biesinger, *Phys. Rev. B* **2009**, *80*, 075405.

[54]   M. C. Ruiz-Cañas, H. I. Quintero, L. M. Corredor, E. Manrique, A. R. Romero Bohórquez, *Polymers* **2020**, *12*, 1152.

[55]   P. Wei, Z. Shen, X. Qin, P. Zhang, L. Bu, Q. Chen, S. V. Roth, G. Lu, *Small* **2022**, *18*, 2105896.

[56]   J. A. Gardella, S. A. Ferguson, R. L. Chin, *Appl Spectrosc* **1986**, *40*, 224.

[57]   W. R. Salaneck, H. R. Thomas, *Solid State Communications* **1978**, *27*, 685.

[58]   F.-C. Chen, J.-L. Wu, S. S. Yang, K.-H. Hsieh, W.-C. Chen, *Journal of Applied Physics* **2008**, *103*, 103721.

[59]   W. Hage, A. Hallbrucker, E. Mayer, *J. Am. Chem. Soc.* **1993**, *115*, 8427.

[60]   J.-H. Wang, C.-C. Cheng, O. Altukhov, F.-C. Chang, S.-W. Kuo, *Polymers* **2013**, *5*, 937.

[61]   M. Rayung, M. M. Aung, M. S. Su'ait, L. Chuah Abdullah, A. Ahmad, H. N. Lim, *ACS Omega* **2020**, *5*, 14267.

[62]   H.-D. Jin, F. Zheng, W.-L. Xu, W.-H. Yuan, M.-Q. Zhu, X.-T. Hao, *J. Phys. D: Appl. Phys.* **2014**, *47*, 505502.

[63]   H. Shirakawa, S. Ikeda, *Polym J* **1971**, *2*, 231.

[64]   R. D. Shannon, *Acta Cryst A* **1976**, *32*, 751.

[65]   D. Liu, T. Thomas, H. Gong, F. Li, Q. Li, L. Song, T. Azhagan, H. Jiang, M. Yang, *Org. Biomol. Chem.* **2019**, *17*, 9367.

[66]   C. Gaul, S. Hutsch, M. Schwarze, K. S. Schellhammer, F. Bussolotti, S. Kera, G. Cuniberti, K. Leo, F. Ortmann, *Nature Mater* **2018**, *17*, 439.

[67]   I. Salzmann, G. Heimel, M. Oehzelt, S. Winkler, N. Koch, *Acc. Chem. Res.* **2016**, *49*, 370.

[68]   H. Méndez, G. Heimel, S. Winkler, J. Frisch, A. Opitz, K. Sauer, B. Wegner, M. Oehzelt, C. Röthel, S. Duhm, D. Többens, N. Koch, I. Salzmann, *Nat Commun* **2015**, *6*, 8560.

[69]   D. M. de Leeuw, M. M. J. Simenon, A. R. Brown, R. E. F. Einerhand, *Synthetic Metals* **1997**, *87*, 53.

[70]   G. Ye, J. Liu, X. Qiu, S. Stäter, L. Qiu, Y. Liu, X. Yang, R. Hildner, L. J. A. Koster, R. C. Chiechi, *Macromolecules* **2021**, *54*, 3886.

[71]   Z. Peng, L. Ye, H. Ade, *Mater. Horiz.* **2022**, *9*, 577.

[72]   G. Zuo, X. Liu, M. Fahlman, M. Kemerink, *Adv. Funct. Mater.* **2018**, *28*, 1703280.

[73]   Y. Zou, D. Huang, Q. Meng, C. Di, D. Zhu, *Organic Electronics* **2018**, *56*, 125.

[74]   S. Wang, H. Sun, T. Erdmann, G. Wang, D. Fazzi, U. Lappan, Y. Puttisong, Z. Chen, M. Berggren, X. Crispin, A. Kiriy, B. Voit, T. J. Marks, S. Fabiano, A. Facchetti, *Adv. Mater.* **2018**, *30*, 1801898.

[75]   J. Liu, G. Ye, B. van der Zee, J. Dong, X. Qiu, Y. Liu, G. Portale, R. C. Chiechi, L. J. A. Koster, *Adv. Mater.* **2018**, *30*, 1804290.

[76]   C.-Y. Yang, W.-L. Jin, J. Wang, Y.-F. Ding, S. Nong, K. Shi, Y. Lu, Y.-Z. Dai, F.-D. Zhuang, T. Lei, C.-A. Di, D. Zhu, J.-Y. Wang, J. Pei, *Adv. Mater.* **2018**, *30*, 1802850.

[77]   X. Yan, M. Xiong, J.-T. Li, S. Zhang, Z. Ahmad, Y. Lu, Z.-Y. Wang, Z.-F. Yao, J.-Y. Wang, X. Gu, T. Lei, *J. Am. Chem. Soc.* **2019**, *141*, 20215.

[78]   A. Tripathi, Y. Lee, S. Lee, H. Y. Woo, *J. Mater. Chem. C* **2022**, *10*, 6114.

[79]   G. Krauss, F. Meichsner, A. Hochgesang, J. Mohanraj, S. Salehi, P. Schmode, M. Thelakkat, *Adv. Funct. Mater.* **2021**, *31*, 2010048.

[80]   R. M. W. Wolfe, J. R. Reynolds, *Org. Lett.* **2017**, *19*, 996.

[81]   J.-R. Pouliot, L. G. Mercier, S. Caron, M. Leclerc, *Macromol. Chem. Phys.* **2013**, *214*,
        453.

8.7 Supporting information

Monomer and polymer synthesis

Poly(DPP[T]$_2${TEG}-TPD{TEG})/**poly(DPP-TPD)**:

The monomers TPD{TEG} (0.04 g, 0.15 mmol, 1 eq.) and DPP[T]$_2${TEG}-Br$_2$ (0.113 g, 0.15 mmol, 1 eq.), ligands pivalic acid (4.6 mg, 0.045 mmol, 0.3 eq.) and tris(2-methoxyphenyl)phosphine (4.2 mg, 0.012 mmol, 0.08 eq.), the base Cs$_2$CO$_3$ (0.114 g, 0.35 mmol, 2.32 eq.) and catalyst Pd-Hermann (2.8 mg, 3.0 µmol, 0.02 eq.) were weighed *in this order* in a microwave vial under ambient conditions. A stir bar was added and the vial was sealed with a septum. By puncturing the septum with a syringe and placed in a Schlenk flask. After application of high vacuum on the solids for 15 minutes, the vessels were backfilled with argon, followed by removal of the syringe with the microwave vial still in the Schlenk flask. 0.6 mL (0.25 M, relative to monomer TPD{TEG}) anhydrous *o*-xylene is added to the vial and purged for 20 minutes under rapid stirring. Polymerization is conducted for 2 h at 160 °C under microwave irradiation. Afterwards, the polymerization mixture is diluted with chloroform, precipitated in methanol and filtered through a cellulose Soxhlet thimble. Oligomer, catalyst and additive residues are removed by extraction with methanol, followed by 2-butanone. The remaining polymer is redissolved in hexafluoroisopropanol and precipitated in water, to ensure quantitative carbonate removal. 0.082 g (62 %) polymer is obtained as a black powder.

^{1}H-NMR (300 MHz, CDCl$_3$, δ): 7.56 (s, 2 H), 6.5 (s, 2 H), 2.70 – 4.60 (broad, 56 H). GPC (HFIP, PMMA standards): Mn = 20.6 kg mol^{-1}, Đ = 1.8.

2,5-bis(2-(2-(2-methoxyethoxy)ethoxy)ethyl)-3,6-di(5-bromothiophen-2-yl)pyrrolo[3,4-c]pyrrole1,4(2H,5H)-dione/**DPP[T]$_2${TEG}-Br$_2$**

A dried Schlenk flask was charged with DPP[T]$_2${TEG} and kept under HV for 15 min. After backfilling with argon, anhydrous CHCl$_3$ was added. The solution was cooled to 0 °C under stirring, the flask wrapped in aluminium foil and N-bromosuccinimide was added under Ar counter flow. The ice bath was removed and the reaction allowed to progress at rt for 4 d. After workup with aq. NaHCO$_3$ (sat.), the solution was concentrated and poured into a large excess of methanol. The solution was stored overnight at -25 °C to encourage crystallization. The crystalline product was filtered, and washed with cold methanol. After

column chromatography (silica, gradient DCM -> ethyl acetate, product in second fraction), and subsequent solvent removal, 2.7 g (3.6 mmol, 53 %) pure product are obtained as metallic red powder.

^{1}H-NMR (300 MHz, CDCl$_3$, δ): 8.49 (d, J = 4.14 Hz, 2 H), 7.21 (d, J = 4.33 Hz, 2 H), 4.17 (t, J = 5.93 Hz, 4 H), 3.78 (t, 4 H), 3.46 - 3.67 (m, 16 H), 3.35 (s, 6 H). ^{13}C-NMR (300 MHz, CDCl$_3$, δ): 42.4 (s, 2 C), 59.0 (s, 2 C), 68.9 (s, 2 C), 70.6 (d, 4 C), 70.8 (s, 2 C), 71.9 (s, 2 C), 107.9 (s, 2 C), 119.3 (s, 2 C), 131.1 (s, 2 C), 131.4 (s, 2 C), 134.8 (s, 2 C), 139.4 (s, 2 C), 161.2 (s, 2 C). DIP-MS: 300 [M]$^+$, 272, 244, 216, 188, 163, 135, 111.

2,5-bis(2-(2-(2-methoxyethoxy)ethoxy)ethyl)-3,6-di(thiophen-2-yl)pyrrolo[3,4-c]pyrrole1,4(2H,5H)-dione/**DPP[T]₂{TEG}**

A dried Schlenk flask was charged with DPP[T]$_2$ (4.0 g, 13.3 mmol, 1 eq.), freshly dried (HV, 500 °C) K$_2$CO$_3$ (7.37 g, 53.3 mmol, 4 eq.) and 18-crown-6 (0.176 g, 0.67 mmol, 0.05 eq.) and kept under HV for 15 min. After careful backfilling the flask with argon, anhydrous DMF (82.5 mL, 0.16 M, relative to DPP[T]$_2$) was added. The dispersion was heated to 110 °C for 1 h and subsequently cooled to 0 °C, where TEG-Br (9.99 g, 44.0 mmol, 3.3 eq.) was added slowly. The reaction mixture was allowed to heat to room temperature and heated to 130 °C for 24 h. After the reaction mixture reached rt, it was washed with brine three times. The combined aqueous phases were extracted with chloroform. The combined organic phases were dried over MgSO$_4$, followed by filtration and complete solvent removal in vacuo. The dry crude product was redissolved in a small amount of chloroform, poured into a large excess of MeOH and stored at -25 °C overnight. 2.0 g (3.4 mmol, 25 %) pure product are obtained as red crystals.

^{1}H-NMR (300 MHz, CDCl$_3$, δ): 8.75 (dd, J = 3.96 Hz, 1.13 Hz, 2 H), 7.63 (dd, J = 4.90 Hz, 1.13 Hz, 2 H), 7.23 - 7.28 (m, 2 H), 4.27 (t, J = 6.31 Hz, 4 H), 3.78 (t, 4 H), 3.45 - 3.67 (m, 16 H), 3.34 (s, 6 H). ^{13}C-NMR (300 MHz, CDCl$_3$, δ): 41.9 (s, 2 C), 59.0 (s, 2 C), 68.9 (s, 2 C), 70.6 (s, 4 C), 70.7 (s, 2 C), 71.9 (s, 2 C), 107.9 (s, 2 C), 128.4 (s, 2 C), 129.6 (s, 2 C), 130.8 (s, 2 C), 134.7 (s, 2 C), 140.4 (s, 2 C), 161.5 (s, 2 C). MALDI-TOF MS m/z: [M]$^+$ calcd for C$_{28}$H$_{36}$N$_2$O$_8$S$_2$, 592.190; found, 592.319.

3,6-di(thiophen-2-yl)-2,5-bis(2-hexyldodecyl)-pyrrolo[3,4-c]pyrrole-1,4-dione/**DPP[T]₂**

In a three-necked 500 mL round-bottom flask sodium-2-methylbutan-2-oleate (19 g, 172 mmol) was dissolved in dry 2-methylbutan-2-ol (70 mL) at 100 °C. Thiophene-2-

carbonitrile (12.5 g, 115 mmol) was added in one part and diethyl succinate (10 g, 57 mmol) were added slowly (3 mL h^{-1}) using a syringe-pump and the resulting dark red mixture was stirred overnight at 100 °C. Thereafter, it was cooled to 65 °C and methanol (200 mL) was added carefully. Acetic acid (11 mL) was added to neutralize the mixture and precipitate the crude product which was filtered off, while still warm. The crude solid was washed with methanol and water, dried at 40 °C in vacuo and used as obtained. Yield: 8.8 g (29 mmol, 51 %) of a dark red solid.

^{1}H-NMR (300 MHz, DMSO-d$_6$, δ): 10.39 (br. s., 2 H), 7.35 (dd, J = 3.86, 1.22 Hz, 2 H), 7.10 (dd, J = 4.90, 1.13 Hz, 2 H), 6.44 (dd, J = 4.90, 3.77 Hz, 2 H). ^{13}C-NMR (300 MHz, DMF-D$_7$, δ): 162.0 (s, 2 C), 136.7 (s, 2 C), 132.3 (s, 2 C), 131.7 (s, 2 C), 131.6 (s, 2 C), 128.9 (s, 2 C), 109.3 (s, 2 C). MALDI-TOF MS m/z: [M]$^+$ calcd for C$_{14}$H$_8$N$_2$O$_2$S$_2$, 300.000; found, 299.963.

1-(bromomethoxy)-2-(2-methoxyethoxy)ethane**/TEG-Br**

2-(2-(2-methoxyethoxy)ethoxy)ethan-1-ol (TEG-OH, 20 g, 122 mmol, 1 eq.) and CBr$_4$ (52.5 g, 158 mmol, 1.3 eq.) are dissolved in DCM (200 mL, 0.61 M, relative to TEG-OH) and cooled to 0 °C. PPh$_3$ (44.7 g, 171 mmol, 1.4 eq.) is dissolved in DCM (50 mL, 3.41 M, relative to PPh$_3$) and added dropwise *via* an addition funnel. The reaction mixture is stirred for 45 min at this temperature, then it is allowed to heat to rt and react at this temperature for another 45 min. The reaction mixture was poured into a 1:4 (v:v) mixture of diethyl ether and hexane, followed by filtration over a silica plug. Upon solvent removal *in vacuo*, the mixture partially solidified. The crude mixture was distilled in vacuo, first without active cooling to avoid bromoform solidification. 27.2 g (120 mmol, 98 %) pure product was obtained as colourless liquid.

^{1}H-NMR (300 MHz, CDCl3, δ): 3.80 (t, J = 6.4 Hz, 2H), 3.71 – 3.62 (m, 6H), 3.58 – 3.52 (m, 2H), 3.46 (t, J = 6.3 Hz, 2H), 3.37 (s, 3H).

5-((2-(2-methoxyethoxy)ethoxy)methyl)-4H-thieno[3,4-c]pyrrole-4,6(5H)-dione**/TPD{TEG}**

A Schlenk flask is charged with TPD (2 g, 13 mmol, 1 eq.) and freshly dried (HV, 500 °C) K$_2$CO$_3$ (3.60 g, 26.1 mmol, 2 eq.). Anhydrous DMF (52 mL) is added, followed by addition of previously HV-degassed TEG-Tos (4.07 g, 12.8 mmol, 0.98 eq.). The reaction is stirred at 110 °C overnight. After cooling to room temperature, the product solution was stirred

with water and extracted three times with DCM. The combined organic phases were dried with MgSO$_4$. During solvent removal in vacuo, a solid formed that was purified by recrystallization from boiling methanol to yield 2.6 g (56.7 mmol, 87 %) white solid product.

^{1}H-NMR (300 MHz, CDCl$_3$, δ): 7.80 (s, 2H), 3.70 – 3.78 (m, 2H), 3.60 – 3.67 (m, 2H), 3.63 – 3.41 (m, 8H), 3.30 (s, 3H). ^{13}C-NMR (300 MHz, CDCl$_3$, δ): 37.6 (s, 1 C), 58.9 (s, 1 C), 70.0 (s, 1 C), 70.4-70.6 (s, 3 C), 71.8 (s, 1 C), 125.8 (s, 2 C), 136.4 (s, 2 C), 162.4 (s, 2 C). MALDI-TOF MS m/z: [M+Na]$^+$ calcd for C$_{13}$H$_{17}$NO$_5$S, 322.069; found, 322.010.

Thieno[3,4-c]pyrrole-4,6(5H)-dione/**TPD**

3,4-Thiophenedicarboxylic acid (13 g, 75.5 mmol, 1 eq.), water (7.55 mL) and ammonia (25 % in water, 51.4 g, 755 mmol, 10 eq.) are added to a round bottom flask, equipped with glass beads. The reaction mixture was heated to 95 °C and allowed to remain at this temperature to react, accompanied with removal of the solvent. When no solvent remained, a condenser was attached to the flask and the temperature increased to 260 °C. The product partly resublimes on the condenser, but is mostly contained in the flask, together with dark impurities. After 4 h at 260 °C, the reaction is cooled to rt and all solids collected together and resublimed on a coldfinger, to yield 9.3 g (60.7 mmol, 80 %) white solid.

^{1}H NMR (300 MHz, DMSO-d$_6$, δ): 11.25 (b, 1H), 8.25 (s, 2H). ^{13}C-NMR (300 MHz, DMF-D$_7$, δ): 127.0 (s, 2 C), 137.9 (s, 2 C), 163.5 (s, 2 C).

(2-(2-methoxyethoxy)ethoxy)methyl 4-methylbenzenesulfonate/**TEG-Tos**

2-(2-(2-methoxyethoxy)ethoxy)ethan-1-ol (26.3 g, 160 mmol, 1 eq.) and tosyl chloride (32.1 g, 168 mmol, 1.05 eq.) are dissolved in DCM (114 mL, 1.4 M relative to TEG-OH) and cooled to 0 °C. KOH (35.9 g, 641 mmol, 4 eq.) is added portion wise and slowly. The ice bath is allowed to thaw and the reaction is stirred for 3 d. After workup with diluted HCl, the solution is dried with MgSO$_4$ and the solvent is removed. 50 g (157 mmol, 98 %) pure compound are obtained without further purification as colourless liquid.

^{1}H-NMR (300 MHz, CDCl$_3$, δ): 7.85 – 7.74 (m, 2H), 7.34 (dd, J = 8.6 Hz, 0.6 Hz, 2H), 4.19 – 4.11 (m, 2H), 3.72 – 3.64 (m, 2H), 3.63 – 3.56 (m, 6H), 3.55 – 3.48 (m, 2H), 3.36 (s, 3H), 2.44 (s, 3H). ^{13}C-NMR (300 MHz, CDCl$_3$, δ): 21.41 (s, 1 C), 58.72 (s, 1 C), 68.41 (s, 1 C), 69.30

(s, 1 C), 70.29 (s, 2 C), 70.43 (s, 1 C), 71.69 (s, 1 C), 127.74 (s, 2 C), 129.76 (s, 2 C), 132.81 (s, 1 C), 144.73 (s, 1 C).
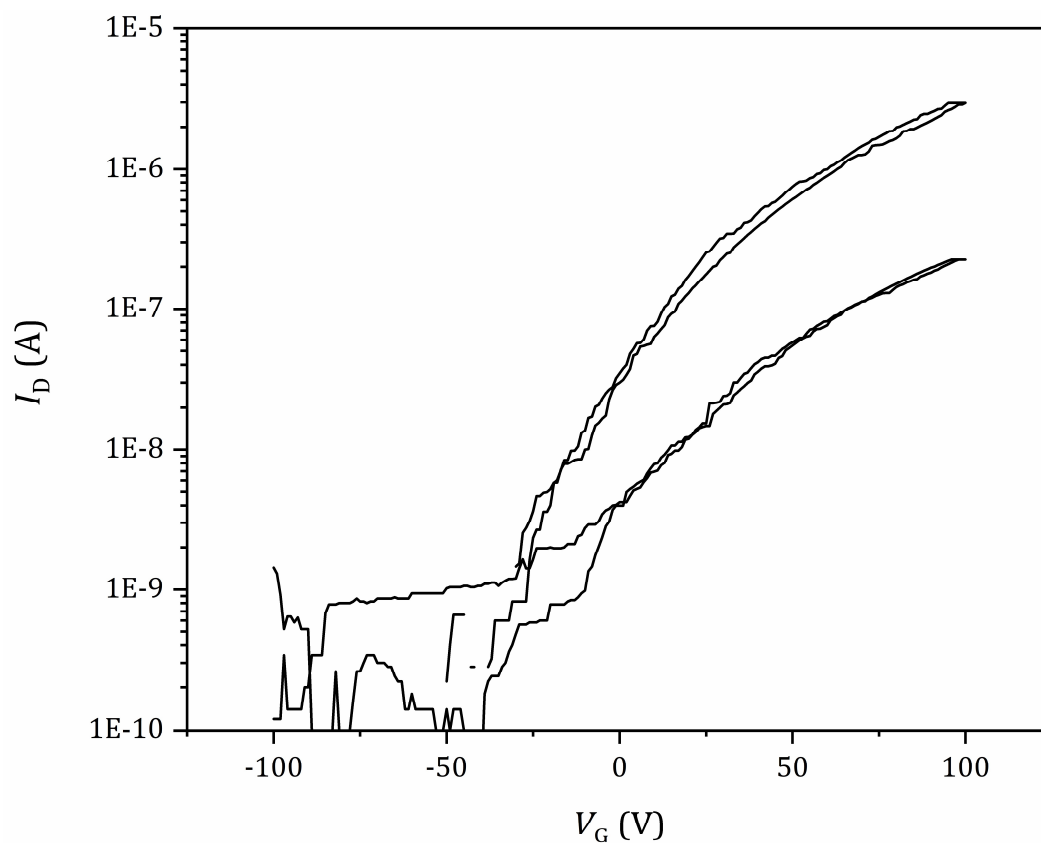
Figure S8.1. Transfer curve of poly(DPP-TPD) thin film organic transistors between -100 V and 100 V gate potential with 1 V step size. The drain potential was fixed at 5 V (lower curve) and 60 V (upper curve).
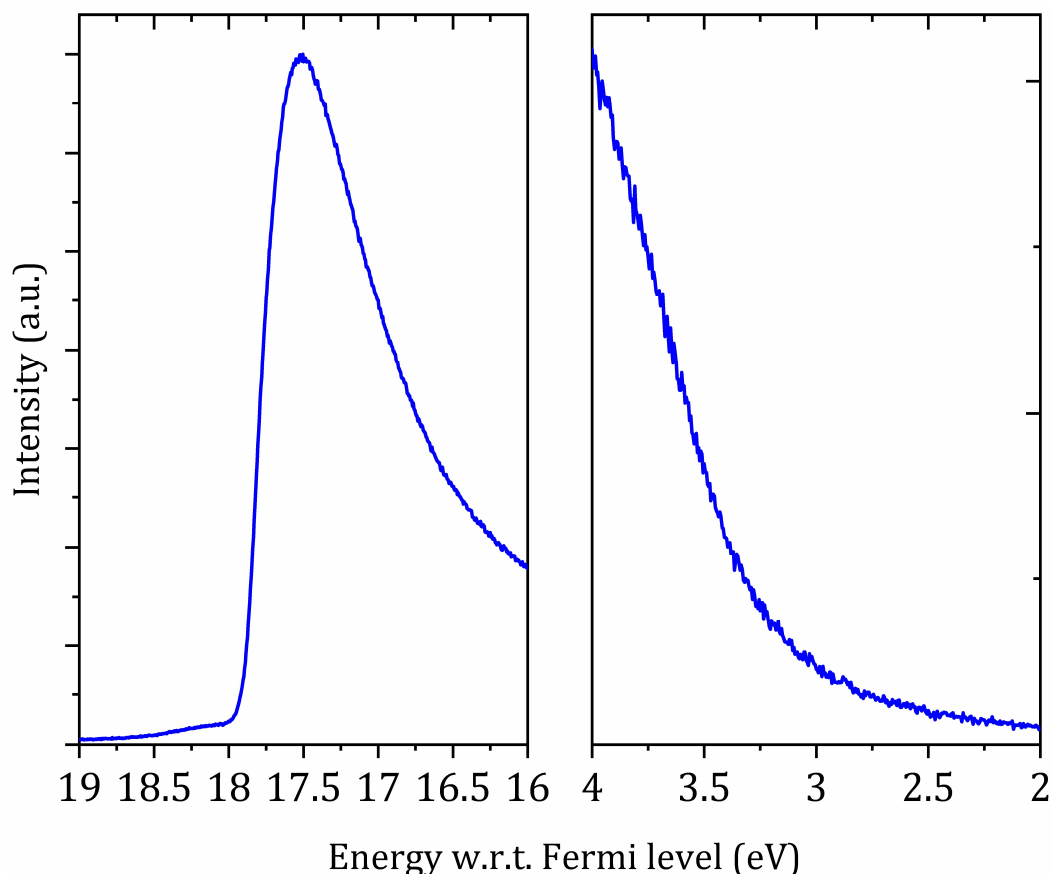
Figure S8.2. Secondary electron cutoff (SECO, left) and valence band maximum (VBM, right) of Cs_2CO_3 thin films (20 nm on ITO), as determined by UPS.
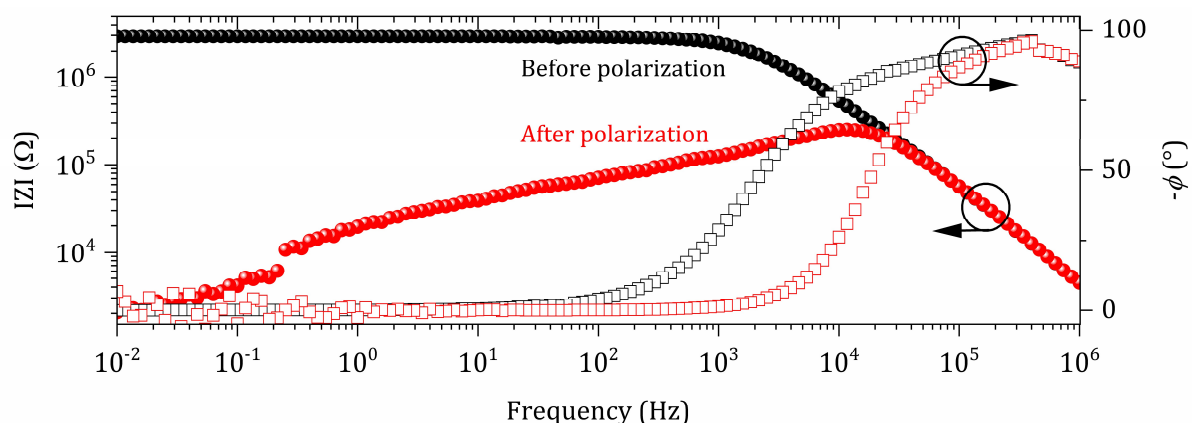
Figure S8.3. Bode plot of poly(DPP-TPD) doped with 30 mol% Cs_2CO_3 after annealing at 150 °C for 15 min thin films spin-coated onto gold interdigitated electrodes (Channel length L = 2.5 μm, channel width W = 1 cm) on SiO_2. Data without applied potential (before polarization, black curve) and at 5 V (after polarization, red curve) is shown, with the magnitude of the impedance |Z| on the left y-axis (circles) and negative phase shift -φ on the right x-axis (squares).
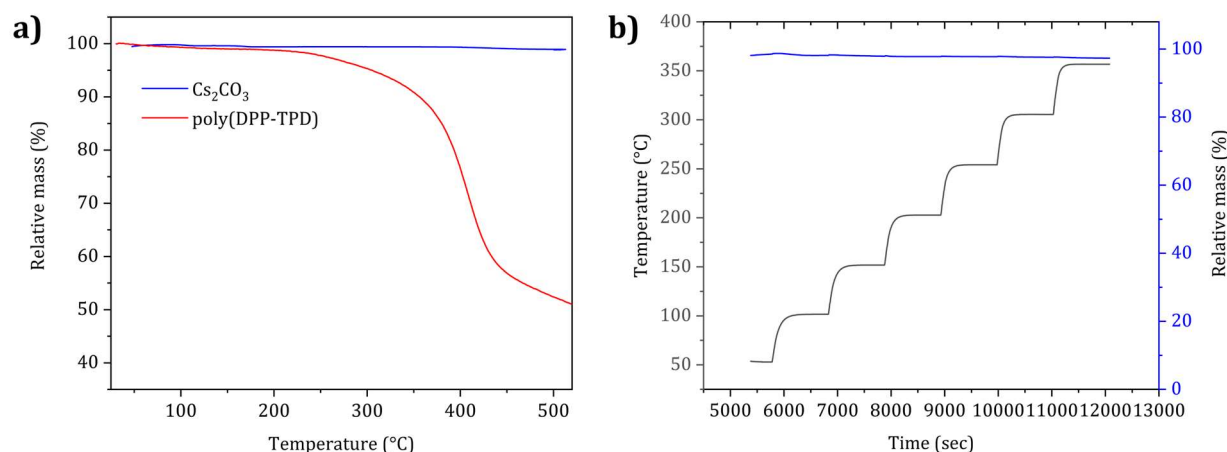
Figure S8.4. a) Thermal gravimetric analysis (TGA) of poly(DPP-TPD) (red) and Cs_2CO_3 (blue). b) Isothermal gravimetric analysis of Cs_2CO_3 from 50 °C to 350 °C with settle times of 15 min at each step of 50 °C. Cs_2CO_3 was dried in-situ at 250 °C for 1 h prior to measurement. Heating rate: 10 K min^{-1} or 20 K min^{-1} (isothermal analysis), 30 mL min^{-1} N_2 flow.
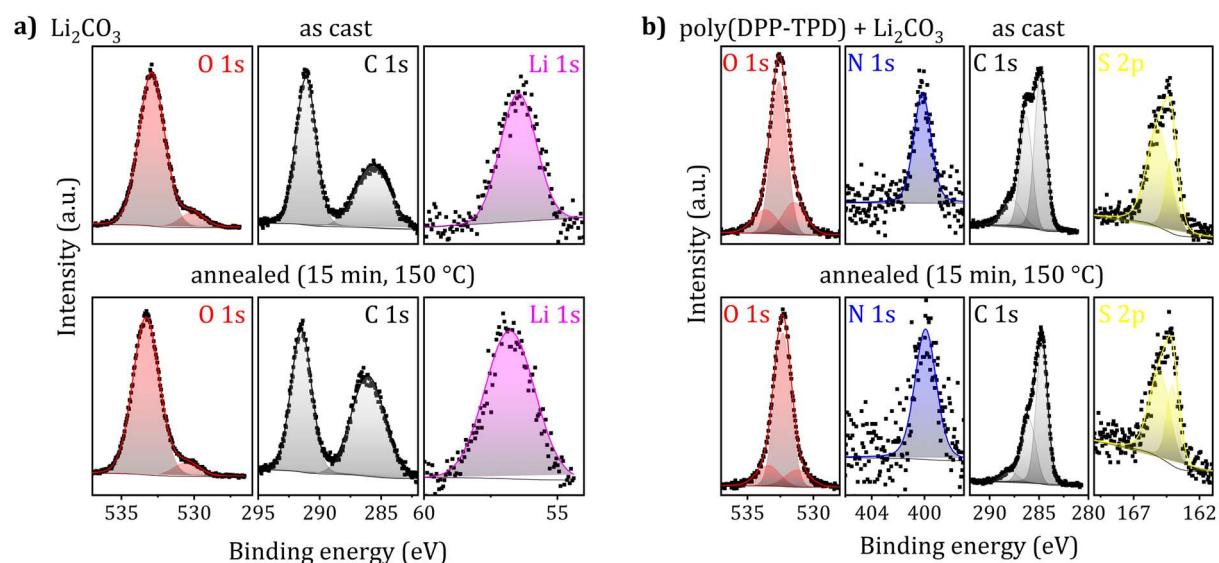
Figure S8.5. XPS detail spectra of a) Li_2CO_3 and b) poly(DPP-TPD) doped with 30 mol% Li_2CO_3 O 1s, N 1s, C 1s and S 2p regions. The spectra were recorded before (upper panels) and after (lower panels) annealing. Black squares are data points, lines are the fitted spectra and shaded areas the deconvoluted contributions to the total fitted spectrum.
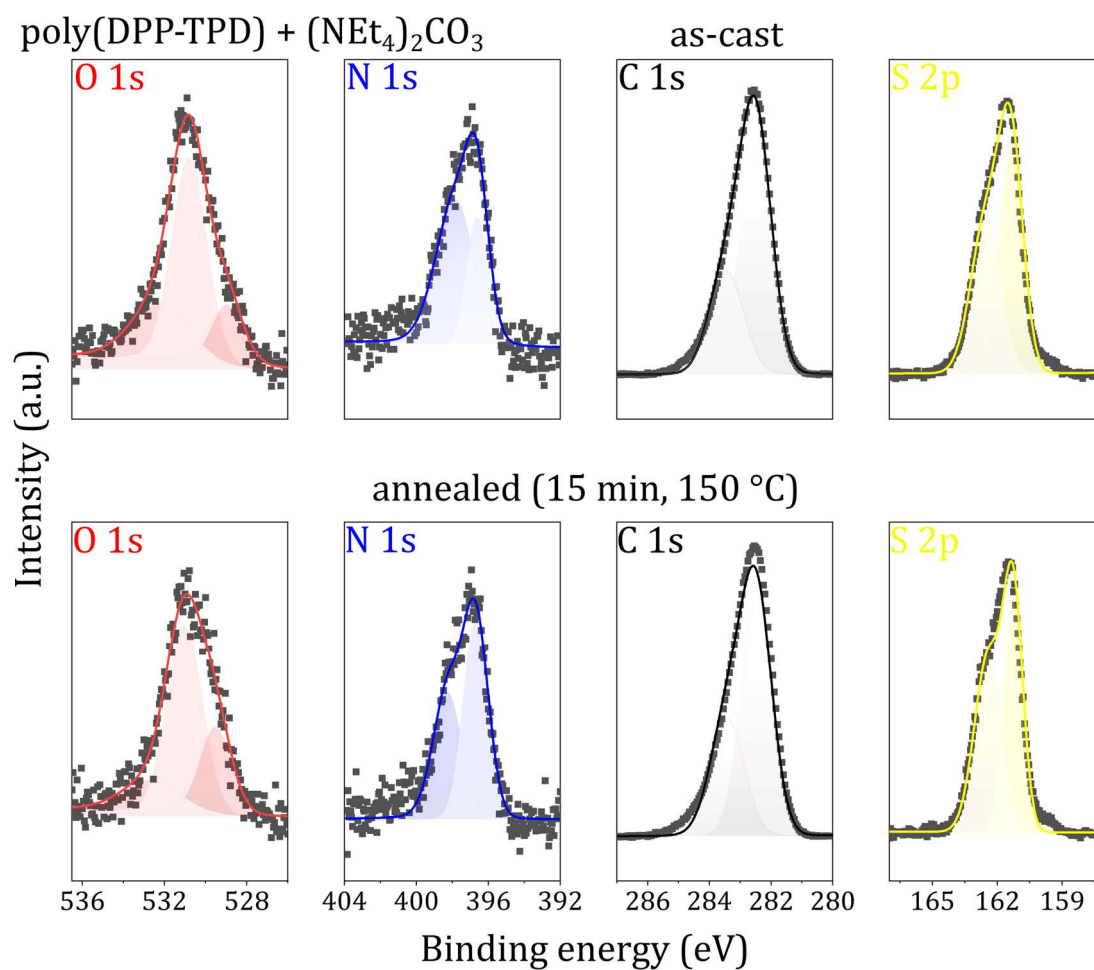
Figure S8.6. XPS detail spectra of poly(DPP-TPD) doped with 30 mol% $(NEt_4)_2CO_3$ O 1s, N 1s, C 1s and S 2p regions. The spectra were recorded before (upper panels) and after (lower panels) annealing. Black squares are data points, lines are the fitted spectra and shaded areas the deconvoluted contributions to the total fitted spectrum.
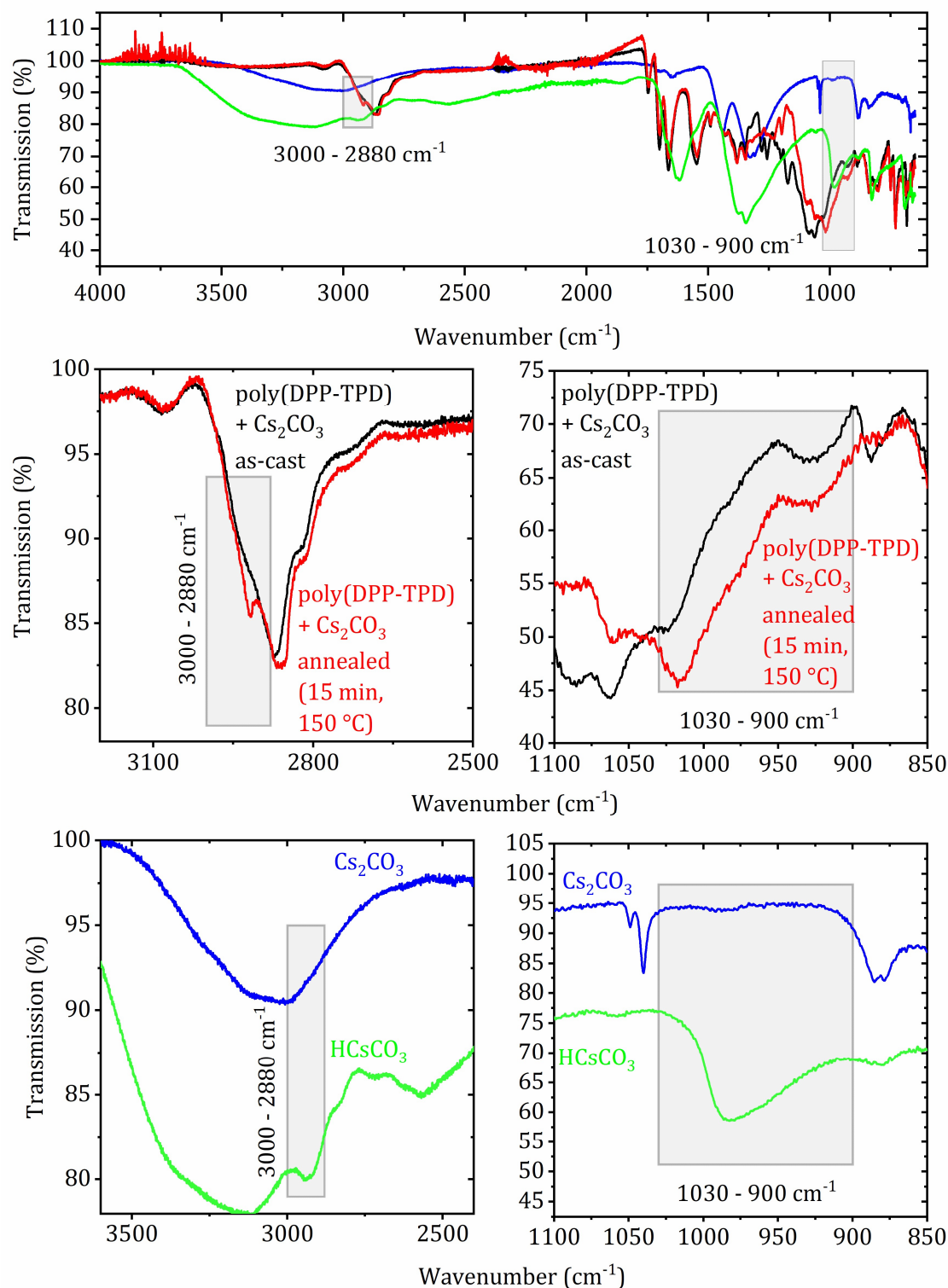
Figure S8.7. FTIR spectra of $CsHCO_3$ powder (green), Cs_2CO_3 powder (blue), poly(DPP-TPD) doped with $30\,mol\%$ Cs_2CO_3 as-cast (black) and poly(DPP-TPD) doped with $30\,mol\%$ Cs_2CO_3 after annealing (red).
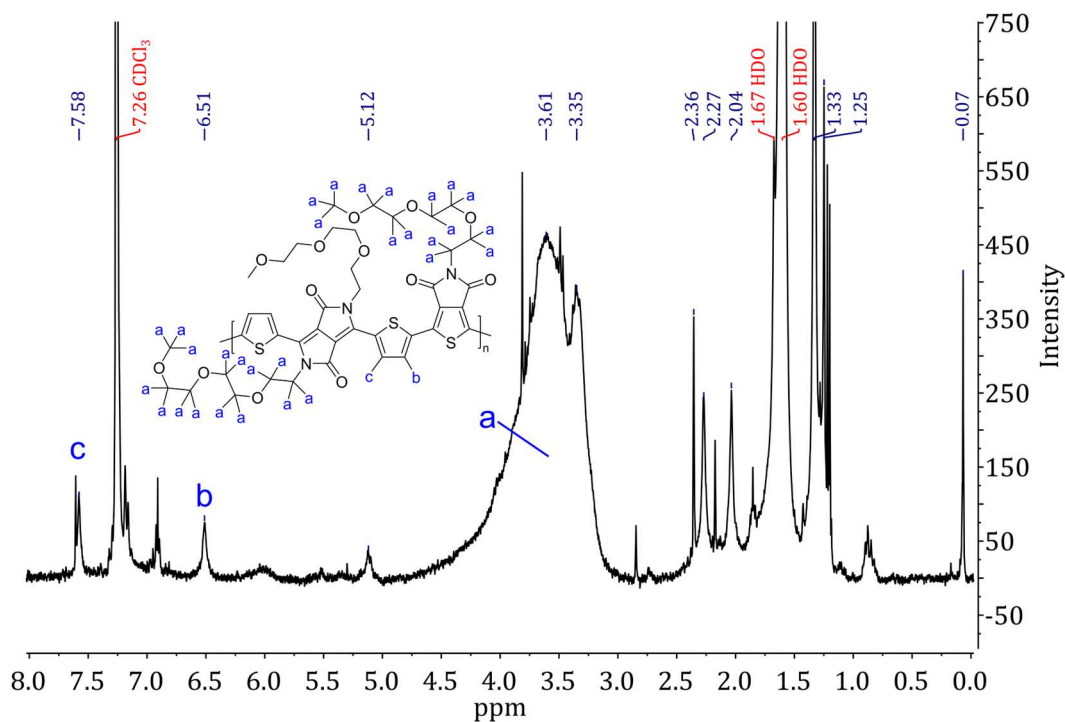
Figure S8.8. ^{1}H-NMR of pristine poly(DPP-TPD) in CDCl$_3$, 512 scans.
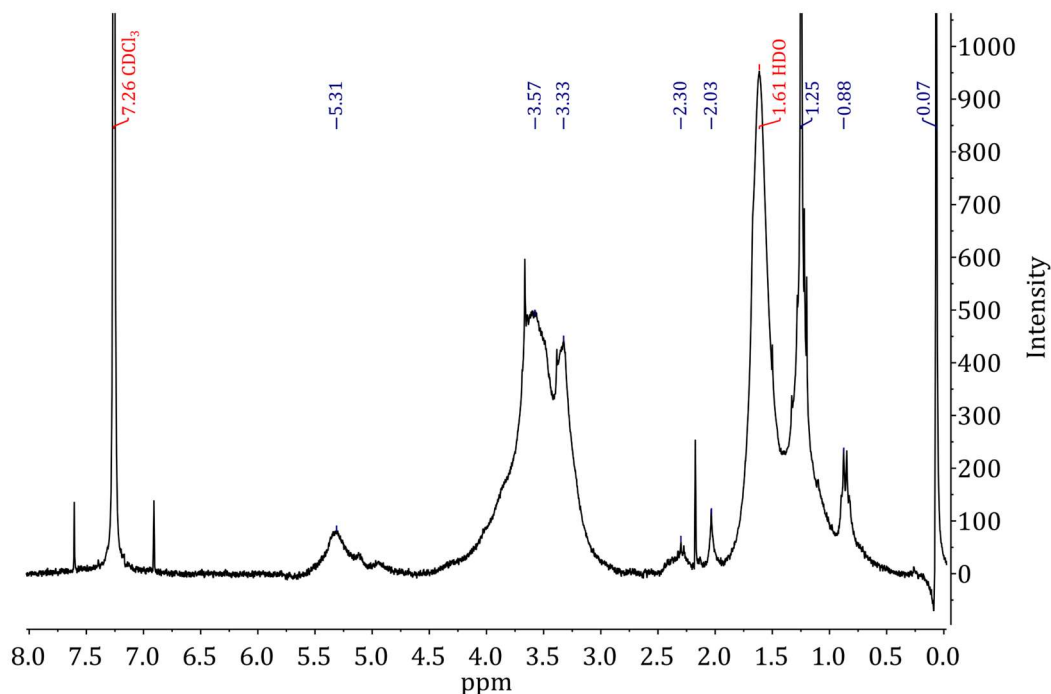
Figure S8.9. ^{1}H-NMR of poly(DPP-TPD) doped with 100 mol% Cs$_2$CO$_3$ after D$_2$O quench
in CDCl$_3$, 512 scans.
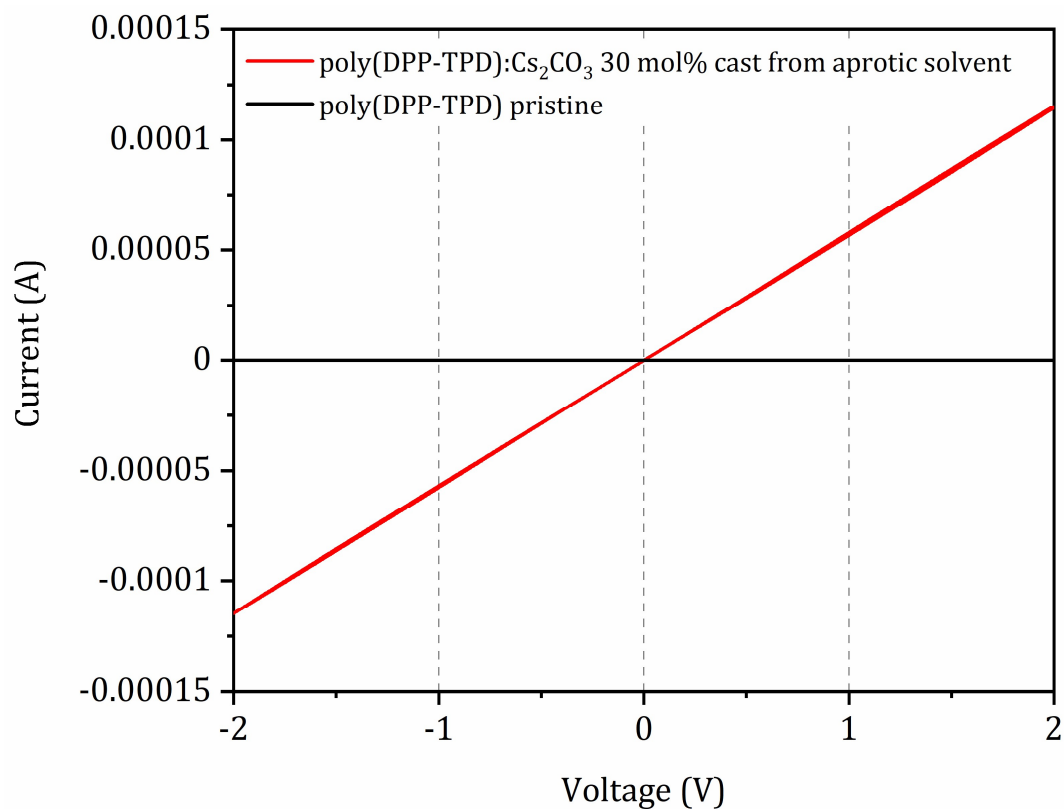
Figure S8.10. Current-voltage characteristics of poly(DPP-TPD) in the pristine state (black) and doped with 30 mol% Cs₂CO₃ using an aprotic solvent mixture (DMSO for Cs₂CO₃ stock solution, NMP for poly(DPP-TPD) stock solution) (orange). Channel length L = 2.5 μm, channel width W = 1 cm.
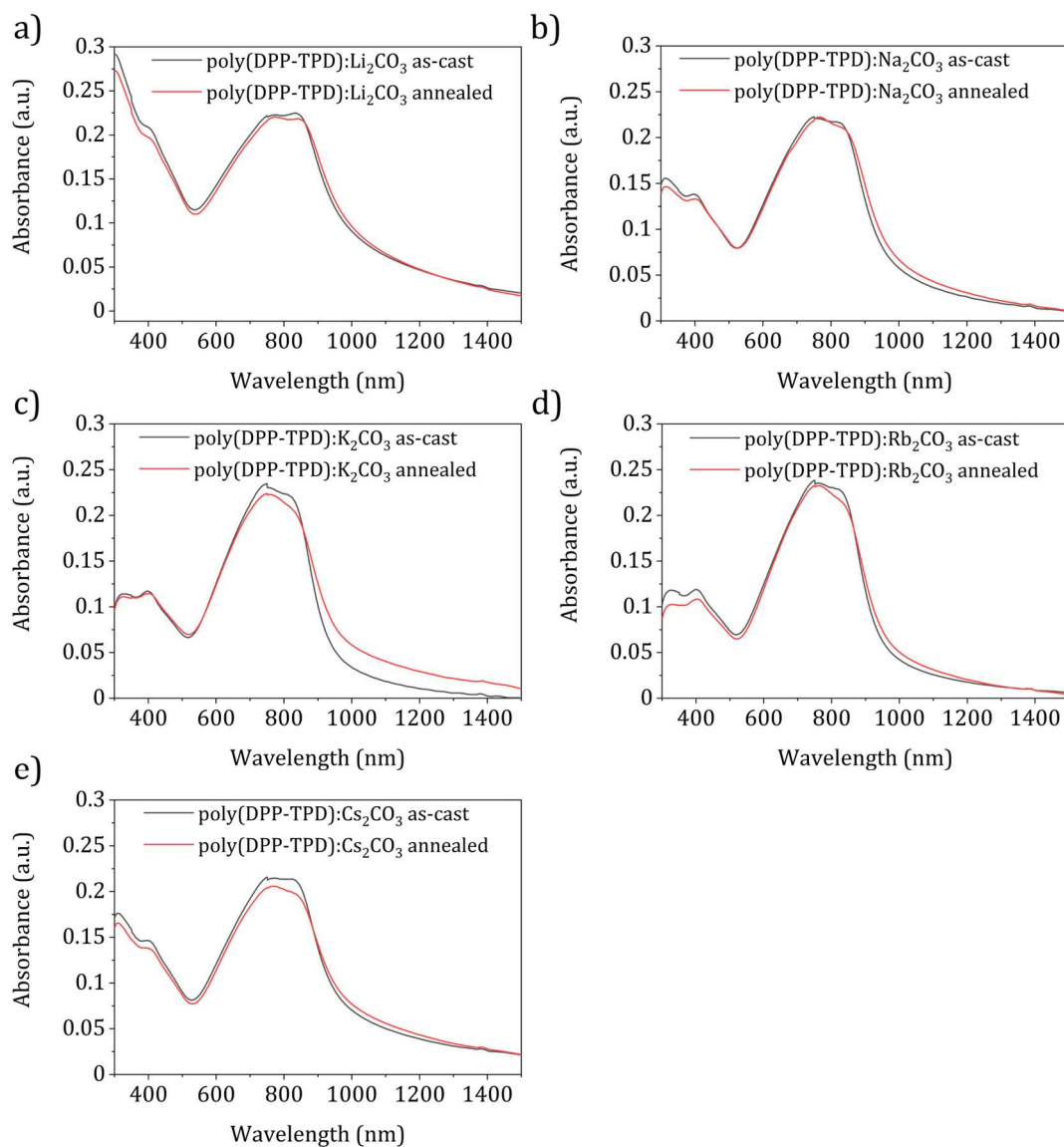
Figure S8.11. UV/Vis/NIR thin film spectra of a) Li_2CO_3-, b) Na_2CO_3-, c) K_2CO_3-, d) Rb_2CO_3-, e) Cs_2CO_3-doped poly(DPP-TPD) (all doped with 30 mol% dopant) on quartz under inert atmosphere. The spectra are shown before (black curve) and after (red curve) annealing at 150 °C for 15 min.
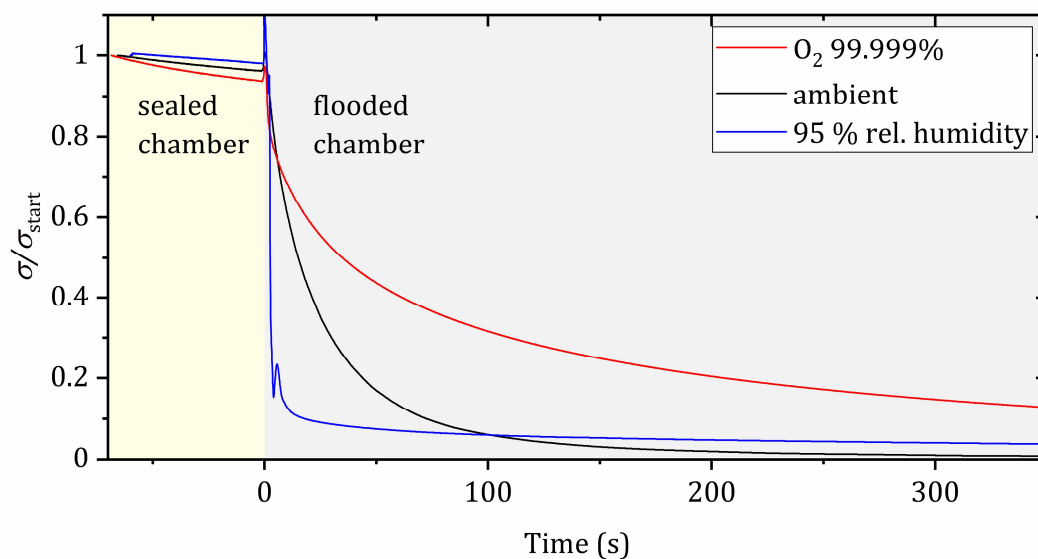
Figure S8.12. Normalized current flowing through interdigitated electrodes coated with 30 mol% doped and annealed poly(DPP-TPD) under different atmospheres. The change between "sealed chamber" and "flooded chamber" represents the point of opening the flask to the corresponding atmosphere. The channel length L is 11.8 μm, the channel width W = 163.05 mm.
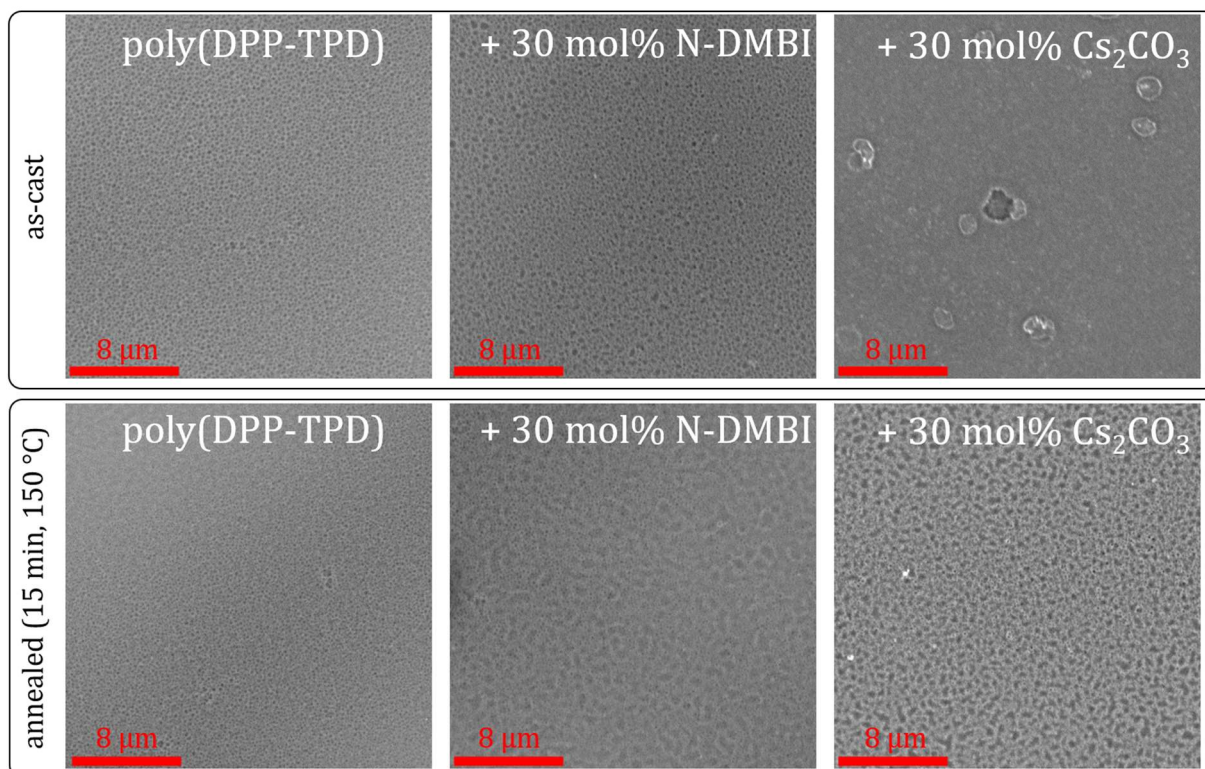
Figure S8.13. SEM micrographs of as-cast (upper panels) and annealed (lower panels) pristine poly(DPP-DTT) (left), poly(DPP-TPD) doped with 30 mol% N-DMBI (middle) and poly(DPP-TPD) doped with 30 mol% Cs_2CO_3 (right) at 10k magnification.
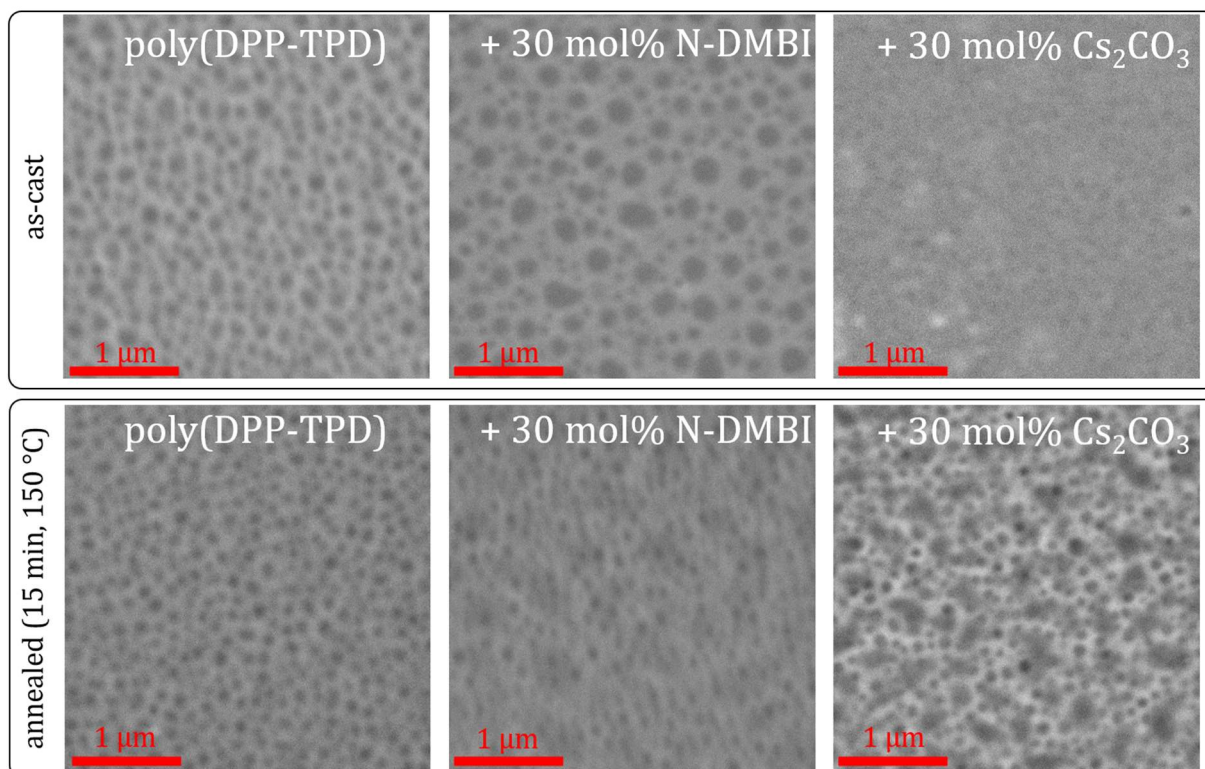
Figure S8.14. SEM micrographs of as-cast (upper panels) and annealed (lower panels) pristine poly(DPP-DTT) (left), poly(DPP-TPD) doped with 30 mol% N-DMBI (middle) and poly(DPP-TPD) doped with 30 mol% Cs$_2$CO$_3$ (right) at 50k magnification.
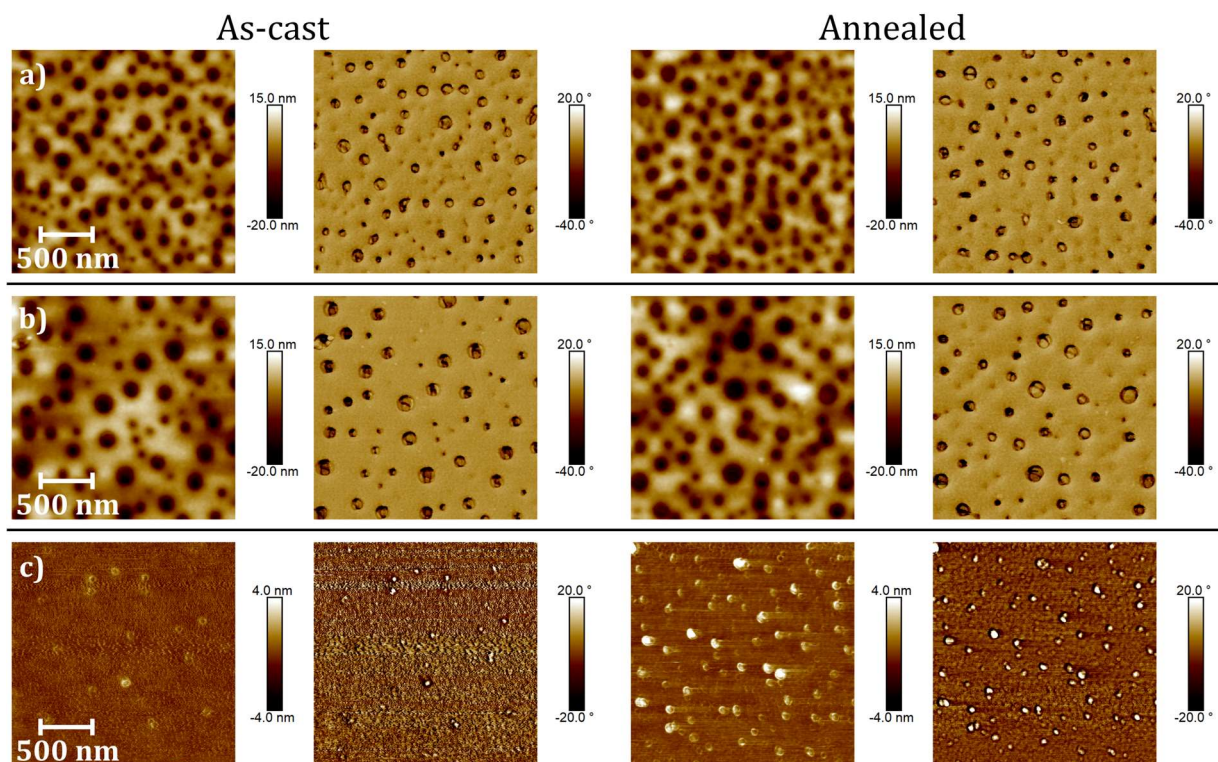
Figure S8.15. AFM tapping mode images of a) pristine poly(DPP-TPD) b) poly(DPP-TPD) doped with 30 mol% N-DMBI and c) poly(DPP-TPD) doped with 30 mol% Cs$_2$CO$_3$. The films were measured as-cast (left) and annealed (right, N-DMBI doped samples: 100 °C, 10 min, Cs$_2$CO$_3$ doped and pristine samples: 150 °C, 15 min). For each sample, topography and phase data was recorded.
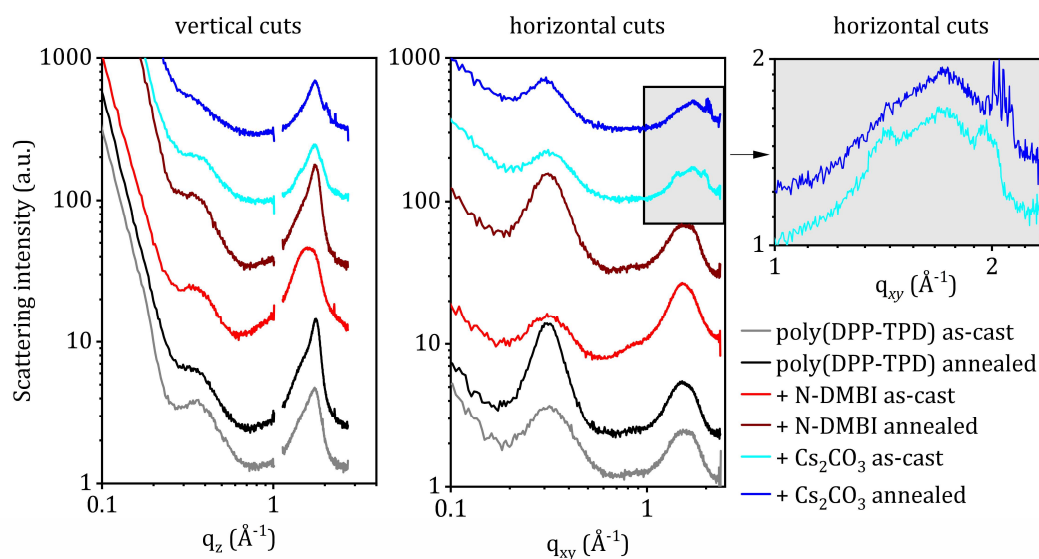
Figure S8.16. Vertical and horizontal line cuts of the GIWAXS images of annealed poly(DPP-TPD), as well as composites with 30 mol% Cs_2CO_3 or N-DMBI prior and after annealing for 15 min at 150 °C. Crystalline heterogeneities are apparent in the magnified clipping.
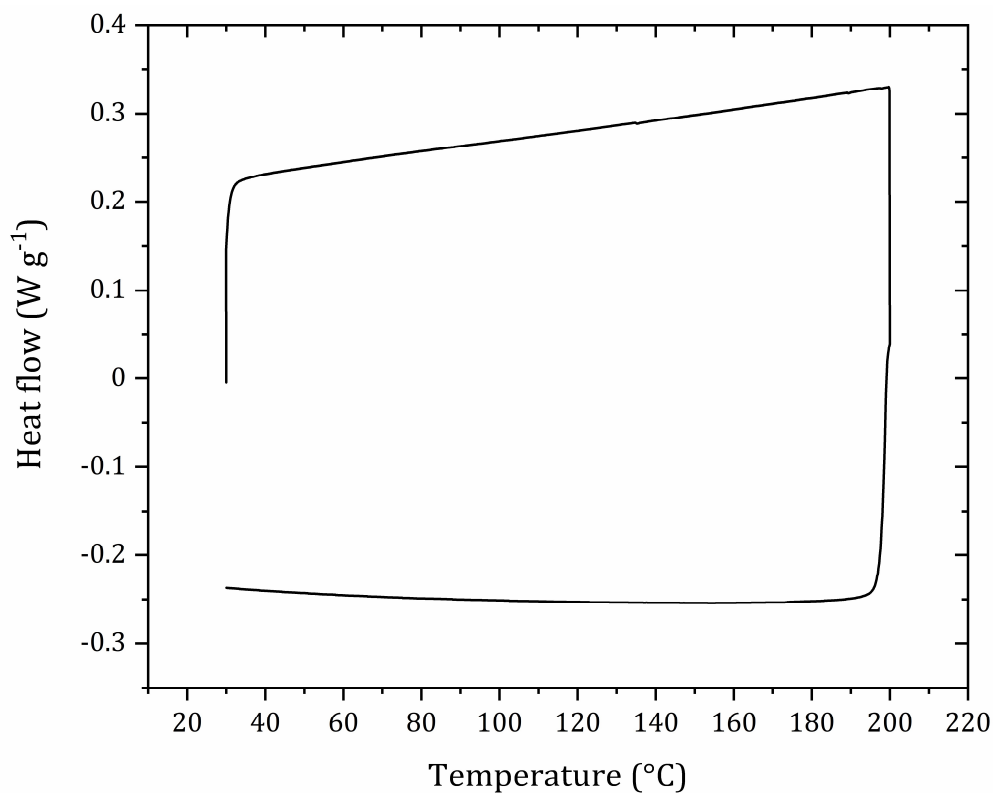
Figure S8.17. Differential scanning calorimetry heat flow curves of poly(DPP-TPD) from 30 °C to 200 °C at a heating range of 10 K min^{-1} under N_2 (10 mL min^{-1}). Shown is the second heating/cooling cycle. Measured on a DSC 3+ by Mettler Toledo.
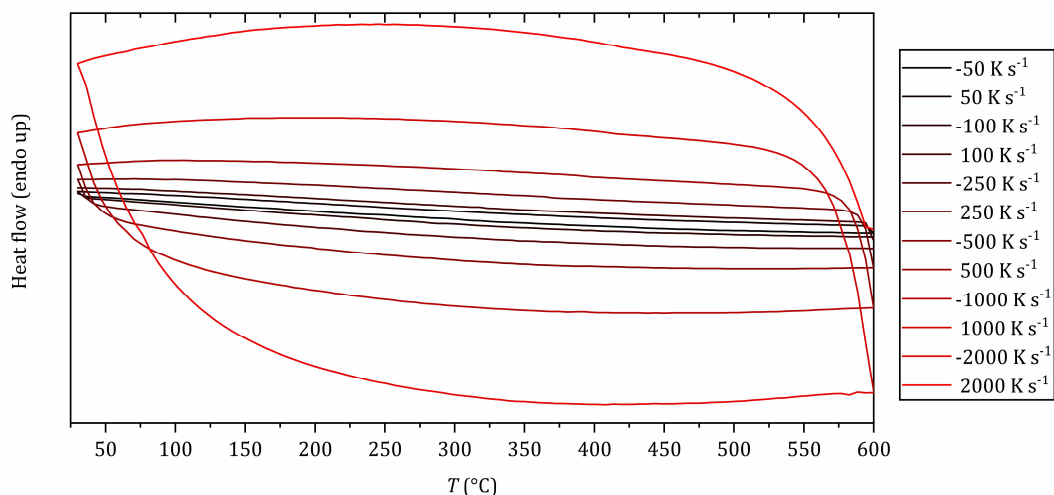
Figure S8.18. Flash differential scanning calorimetry heat flow curves of poly(DPP-TPD) for different heating rates ranging from 50 K s^{-1} to 2000 K s^{-1}. Measured on a Flash DSC 1 by Mettler Toledo.
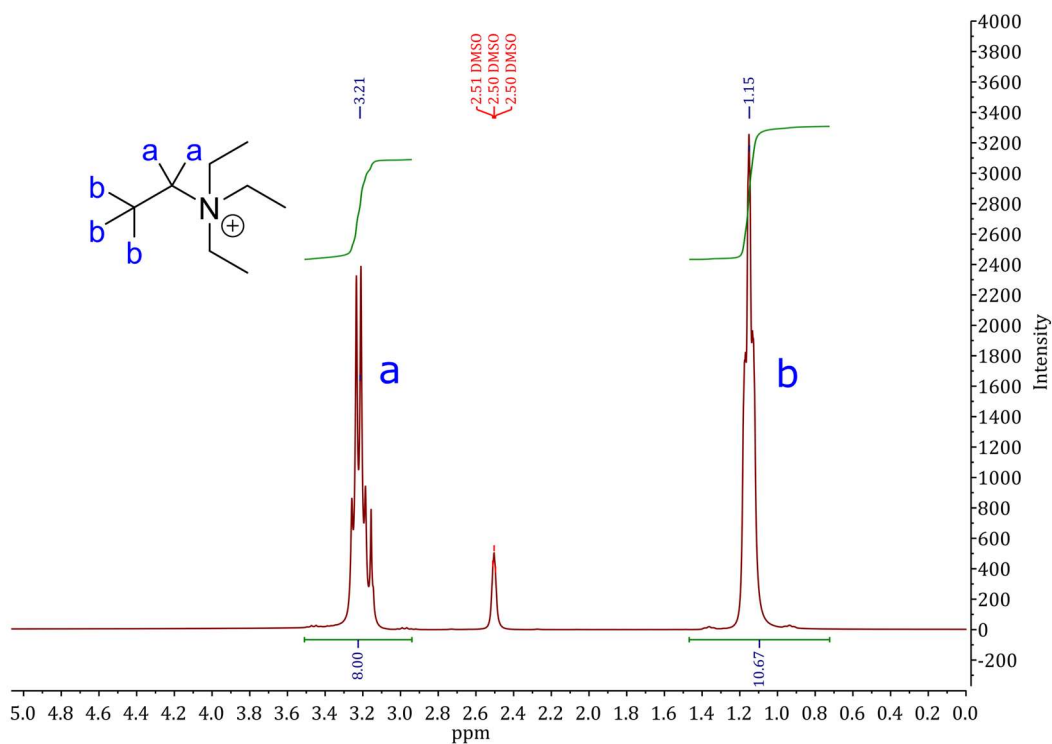
Figure S8.19. ^{1}H-NMR of (NEt$_4$)$_2$CO$_3$.
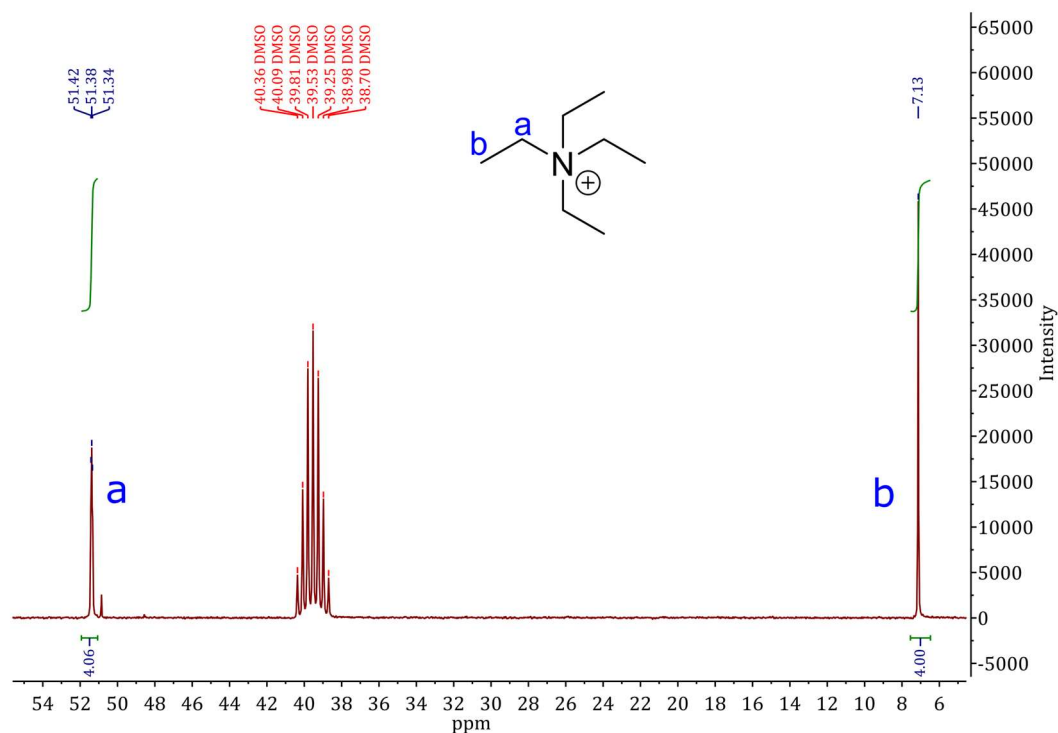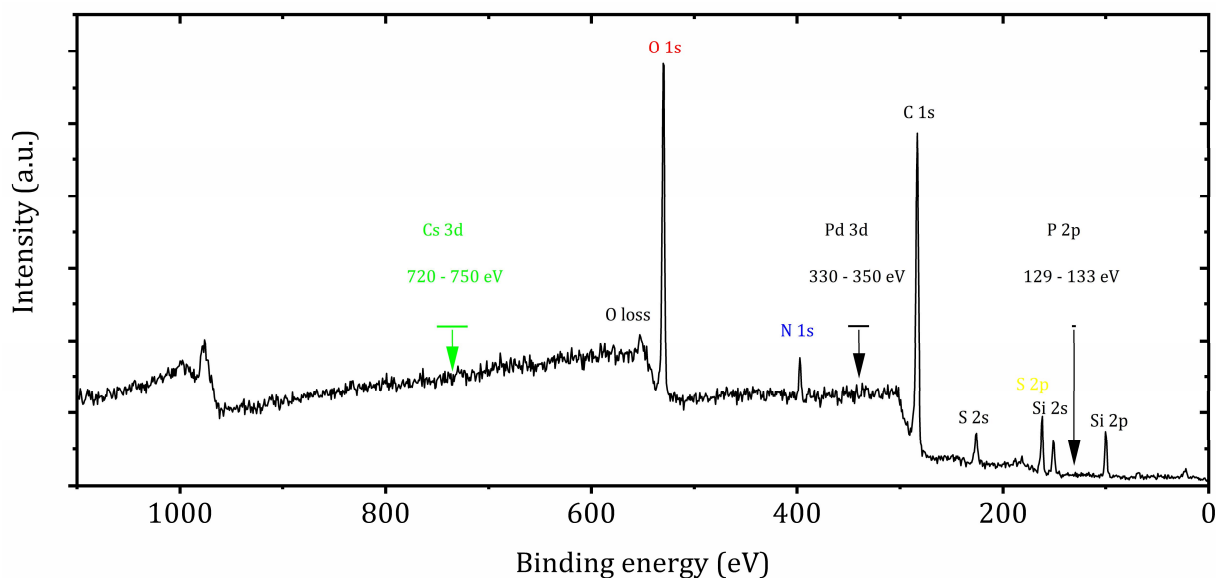
Figure S8.20. ^{13}C-NMR of $(NEt_4)_2CO_3$.

Figure S8.21. XPS survey spectrum of poly(DPP-TPD) after Soxhlet purification, indicating the absence of Cs 3d, Pd 3d, and P 2p signals. The Si signals are originating from the tape used to fixate the polymer onto the sample holder.
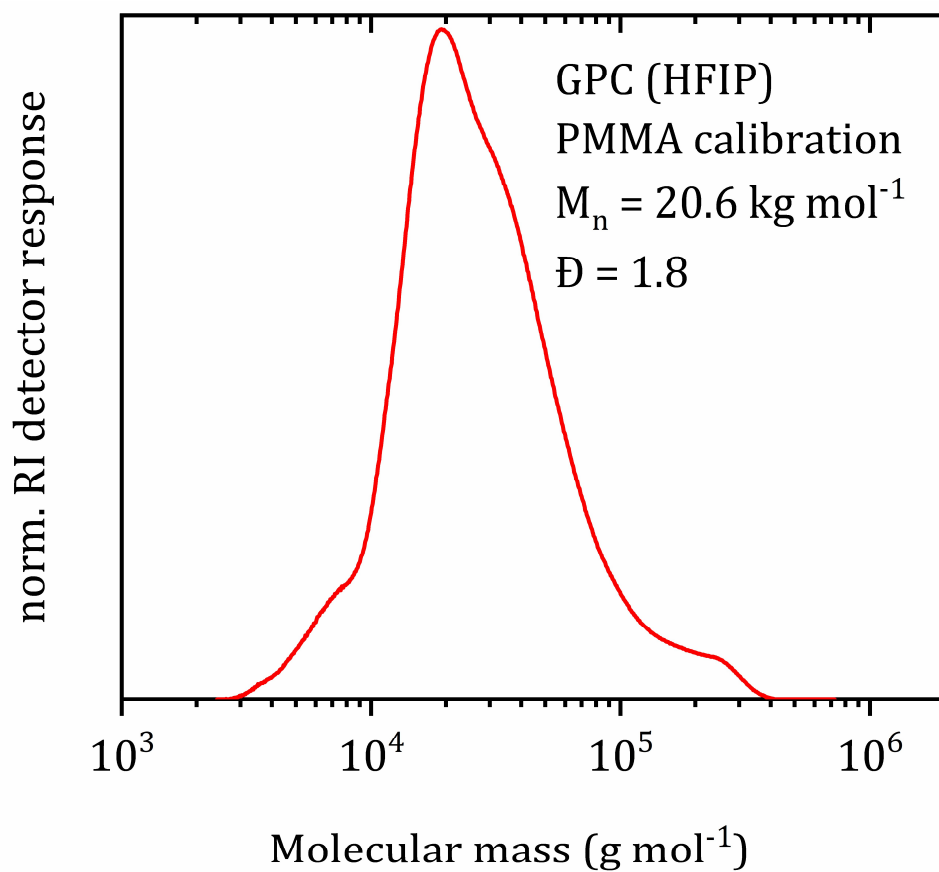
Figure S8.22. GPC elugramm of poly(DPP-TPD) (HFIP, PMMA calibration).

Table S8.1. Work function (WF), HOMO position, hole-injection barrier (HIB, HOMO-WF) and LUMO position values of 30 mol% N-DMBI doped poly(DPP-TPD) as determined by UPS and IPES.

	WF [eV]	HOMO [eV]	HIB [eV]	LUMO [eV]
Poly(DPP-TPD)	4.4 ± 0.10	5.4 ± 0.10	1.0	3.3 ± 0.60
Poly(DPP-TPD): N-DMBI pristine	4.0 ± 0.10	5.3 ± 0.10	1.3	3.2 ± 0.60
Poly(DPP-TPD): N-DMBI 10 min @ 100 °C	4.0 ± 0.10	5.3 ± 0.10	1.3	3.8 ± 0.60

Table S8.2. Work function (WF), HOMO position, hole-injection barrier (HIB, HOMO-WF) and LUMO position values of 30 mol% Cs_2CO_3 doped poly(DPP-TPD) as determined by UPS and IPES.

	WF [eV]	HOMO [eV]	HIB [eV]	LUMO [eV]
Poly(DPP-TPD)	4.4 ± 0.10	5.4 ± 0.10	1.0	3.3 ± 0.60
Poly(DPP-TPD):Cs_2CO_3 pristine	4.1 ± 0.10	5.4 ± 0.10	1.3	3.1 ± 0.60
Poly(DPP-TPD):Cs_2CO_3 15 min @ 150 °C	3.9 ± 0.10	5.2 ± 0.10	1.3	3.6 ± 0.60

Table S8.3. Work function (WF), HOMO position and hole-injection barrier (HIB, HOMO-WF) values of 30 mol% Li_2CO_3 doped poly(DPP-TPD) as determined by UPS.

	WF [eV]	HOMO [eV]	HIB [eV]
Poly(DPP-TPD)	4.4 ± 0.10	5.4 ± 0.10	1.0
Poly(DPP-TPD):Li_2CO_3 pristine	3.8 ± 0.10	5.1 ± 0.10	1.3
Poly(DPP-TPD):Li_2CO_3 15 min @ 150 °C	3.8 ± 0.10	5.2 ± 0.10	1.4

Table S8.4. Work function (WF), HOMO position and hole-injection barrier (HIB, HOMO-WF) values of 30 mol% $(NEt_4)_2CO_3$ doped poly(DPP-TPD) as determined by UPS.

	WF [eV]	HOMO [eV]	HIB [eV]
Poly(DPP-TPD)	4.4 ± 0.10	5.4 ± 0.10	1.0
Poly(DPP-TPD):$(NEt_4)_2CO_3$ pristine	3.6 ± 0.10	5.0 ± 0.10	1.4
Poly(DPP-TPD):$(NEt_4)_2CO_3$ 15 min @ 150 °C	3.7 ± 0.10	5.0 ± 0.10	1.3

Table S8.5. Work function (WF), HOMO position and hole-injection barrier (HIB, HOMO-WF) values of $(NEt_4)_2CO_3$ and Cs_2CO_3 as determined by UPS.

	WF [eV]	HOMO [eV]	HIB [eV]
$(NEt_4)_2CO_3$	2.7 ± 0.10	5.9 ± 0.10	3.2
Cs_2CO_3	3.2 ± 0.10	6.4 ± 0.10	3.3

Table S8.6. Film thickness d, thin film conductivity σ, Seebeck coefficient S and power factor PF of poly(DPP-TPD) doped with various molar concentrations of Cs_2CO_3.

Doping concentration [mol%]	d [nm]	σ [S cm^{-1}]	S [μV K^{-1}]	PF [W m^{-1} K^{-2}]
10	2038	$(9.8 \pm 0.68) \cdot 10^{-5}$	$-(262 \pm 18.3)$	$(6.7 \pm 0.47) \cdot 10^{-10}$
20	2696	$(3.0 \pm 0.21) \cdot 10^{-4}$	$-(931 \pm 65.1)$	$(2.6 \pm 0.18) \cdot 10^{-8}$
30	3226	$(1.2 \pm 0.048) \cdot 10^{-1}$	$-(690 \pm 48.3)$	$(5.6 \pm 0.39) \cdot 10^{-6}$
40	4447	$(5.7 \pm 0.40) \cdot 10^{-4}$	$-(563 \pm 39.4)$	$(1.8 \pm 0.13) \cdot 10^{-8}$
50	4960	$(1.1 \pm 0.077) \cdot 10^{-3}$	$-(560 \pm 39.2)$	$(3.4 \pm 0.24) \cdot 10^{-8}$
60	1962	$(9.5 \pm 0.67) \cdot 10^{-4}$	$-(928 \pm 64.9)$	$(8.2 \pm 0.57) \cdot 10^{-8}$

9. List of publications

9.1 Publications arising from this thesis

1. Philip Schmode, <u>Adrian Hochgesang</u>, Mahima Goel, Florian Meichsner, Martina Fried and Mukundan Thelakkat: „A Solution-Processable Pristine PEDOT Exhibiting Excellent Conductivity, Charge Carrier Mobility, and Thermal Stability in the Doped State", *Macromol. Chem. Phys.* **2021**, *222*, 2100123.

2. Gert Krauss, <u>Adrian Hochgesang</u>, John Mohanraj and Mukundan Thelakkat: „Highly Efficient Doping of Conjugated Polymers Using Multielectron Acceptor Salts", *Macromol. Rapid Commun.* **2021**, *42*, 2100443.

3. <u>Adrian Hochgesang</u>, Simon Biberger, Jeannine Grüne, John Mohanraj, Frank-Julian Kahle, Vladimir Dyakonov, Anna Köhler and Mukundan Thelakkat: "Intricacies and Mechanism of p-Doping Spiro-MeOTAD Using Cu(TFSI)$_2$", *Adv. Electron. Mater.* **2022**, *8*, 2200113.

4. <u>Adrian Hochgesang</u>, Andreas Erhardt, John Mohanraj, Meike Kuhn, Eva M. Herzig, Selina Olthof, and Mukundan Thelakkat: "Highly Efficient n-Doping via Proton Abstraction of an Acceptor$_1$-Acceptor$_2$ Alternating Copolymer toward Thermoelectric Applications", *Adv. Funct. Mater.* **2023**, 2300614. DOI:10.1002/adfm.202300614.

9.2 Additional publications during the PhD involving my contributions

5. Mahima Goel, Marie Siegert, Gert Krauss, John Mohanraj, <u>Adrian Hochgesang</u>, David C. Heinrich, Martina Fried, Jens Pflaum and Mukundan Thelakkat: „HOMO–HOMO Electron Transfer: An Elegant Strategy for p-Type Doping of Polymer

Semiconductors toward Thermoelectric Applications", *Adv. Mater.* **2020**, *32*, 2003596.

6. Andreas Erhardt, <u>Adrian Hochgesang</u>, Florian Meichsner and Mukundan Thelakkat: „High electron mobility and tuneable glass transition temperature in fullerene-functionalized polynorbornenes", *J. Mater. Chem. C* **2022**, *10*, 6419-6428.

7. Gert Krauss, Florian Meichsner, <u>Adrian Hochgesang</u>, John Mohanraj, Sahar Salehi, Philip Schmode and Mukundan Thelakkat: „Polydiketopyrrolopyrroles Carrying Ethylene Glycol Substituents as Efficient Mixed Ion-Electron Conductors for Biocompatible Organic Electrochemical Transistors", *Adv. Funct. Mater.* **2021**, *31*, 2010048.

8. Andreas Erhardt, <u>Adrian Hochgesang</u>, Christopher R. McNeill and Mukundan Thelakkat: „A competitive n-Type OECT Material via Copolymerization of Electron Deficient Building Blocks", *Adv. Electron. Mater.* **2023**, DOI:10.1002/aelm.202300026, forthcoming.

9. Aruna K Kunhiramana, Akash Prabhu S, Muhammad Rahees P, Ajay Rakkesh R and <u>Adrian Hochgesang</u>: "MoS$_2$/CoS$_2$ Heterostructure Decorated on Carbon Nanostructure as a Hybrid Electrocatalyst for Hydrogen Evolution Reaction in Acidic Medium", *J. Power Sources* **2023**, POWER-D-23-00942, submitted.

10. Acknowledgements

True to the motto „Alles hat ein Ende, nur die Wurscht hat zwei", a long chapter in my life at the University Bayreuth is finally coming to an end. Yet I'm very lucky to have gained precious experience and new friends during my stay. I am immensely grateful for everybody who joined me along the way, inside and outside of uni life.

First, special thanks to my doctor father Prof. Mukundan Thelakkat. I thoroughly enjoyed the professional and productive atmosphere in his AFuPo group. Also, a big thanks for the pleasant culture of scientific discussion (an art which seems to be more and more forgotten nowadays) and assistance during harsh times, which provided crucial impulse to my work. Thanks for the freedom of choice for my research topics, the funding and provision of necessary work equipment – as a PhD student, we had everything a chemist could wish for!

I thank Alexander Kern for the fact, that this work would have been finished at least 6 months earlier without him in our group. Unfortunately, we always discovered technical problems and laboratory equipment which required our full attention. Thank you for the professional expertise around the lab ("Eierlegende Wollmilchsau") – you truly do keep the lights on in MC1.

I'd like to thank John Mohanraj for the introduction into the team and work all the way back during my bachelor thesis. The following years you always had an open ear for scientific problems and transferred a lot of knowledge, which helped me immensely to be where I am now. I wish you all the very best for your future!

Hereby, I would like to thank the PNS Keylab alumnis, especially Jonas Mayer, Philipp Ramming, Yu Zhong, David Heinrich and Chetan Raj Singh. You brought more life into the lab and the mutual assistance was worth gold during my first weeks in PNS.

Thank you, Mahima Goel, for the help during my first publication and initiation of the whole doping and thermoelectrics "adventure", where you helped me to overcome some

11. Eidesstattliche Versicherungen und Erklärungen

(§ 9 Satz 2 Nr. 3 Promotionsordnung BayNAT)

Hiermit versichere ich eidesstattlich, dass ich die Arbeit selbstständig verfasst und keine

anderen als die von mir angegebenen Quellen und Hilfsmittel benutzt habe

(vgl. Art. 97 Abs. 1 Satz 8 BayHIG).

(§ 9 Satz 2 Nr. 3 Promotionsordnung BayNAT)

Hiermit erkläre ich, dass ich die Dissertation nicht bereits zur Erlangung eines akademischen Grades eingereicht habe und dass ich nicht bereits diese oder eine gleichartige Doktorprüfung endgültig nicht bestanden habe.

(§ 9 Satz 2 Nr. 4 Promotionsordnung BayNAT)

Hiermit erkläre ich, dass ich Hilfe von gewerblichen Promotionsberatern bzw. – vermittlern oder ähnlichen Dienstleistern weder bisher in Anspruch genommen habe noch künftig in Anspruch nehmen werde.

(§ 9 Satz 2 Nr. 7 Promotionsordnung BayNAT)

Hiermit erkläre ich mein Einverständnis, dass die elektronische Fassung meiner Dissertation unter Wahrung meiner Urheberrechte und des Datenschutzes einer gesonderten Überprüfung unterzogen werden kann.

(§ 9 Satz 2 Nr. 8 Promotionsordnung BayNAT)

Hiermit erkläre ich mein Einverständnis, dass bei Verdacht wissenschaftlichen Fehlverhaltens Ermittlungen durch universitätsinterne Organe der wissenschaftlichen Selbstkontrolle stattfinden können.

- -

Ort, Datum, Unterschrift